

**Validation and Testing of a Numerical Model for the
Design and Up-Scaling of Low Temperature Difference Stirling Engines**

by

Matthias Lottmann

A thesis submitted in partial fulfillment of the requirements for the degree of

Master of Science

Department of Mechanical Engineering

University of Alberta

Abstract

This thesis presents the experimental validation, testing and review of a numerical model for low temperature difference Stirling engines (LTDSEs). The research of LTDSEs is motivated by the potential use of low temperature heat as an unconventional sustainable energy source.

An experimental setup was designed with a gamma-type LTDSE that has a working space volume of 4.6 liters, source and sink temperatures of 150 °C and 5 °C, charge pressure between 200 kPa and 450 kPa (gauge), and a maximum shaft power of 15 W. The system allowed automated control of the setpoint through source and sink temperatures, pressure, and torque load; and automated acquisition of data consisting of temperatures, average and instantaneous pressures, crankshaft angle and shaft torque.

The engine was modeled as a simplified axisymmetric geometry with the numerical model, *MSPM*. It was found that two model input parameters have a significant influence on the model predictions and are at the same time difficult to measure experimentally. One is the heat transfer between the heat source/sink medium and the heat exchanger, which was not accounted for by *MSPM* and was then implemented as a custom heat transfer coefficient. Two different estimates for these coefficients, one analytical and one from CFD analysis, were tested in the subsequent model validation. The other parameter is the leakage of piston seals. The power piston was modeled with a leak-free seal and the displacer piston was tested with both a leak-free seal and no seal.

The experimental validation of this model focused on the thermodynamic model at constant engine speed, so that the modeling of the gas processes could be assessed without influences of mechanical friction from the mechanism model. The model variants with the different heat transfer

coefficients and displacer piston seals differed substantially from each other in their agreement with the experimental data. Consistent predictions of the heat input and rejection rates within 20 % and the gas temperatures within 3 % or 10 °C were achieved by one model variant. However, no model predicted the indicated cycle work consistently. The observed model deviations suggest that if the sensitive coefficients of source/sink heat transfer and seal leakage for both seals would be determined more rigorously through experiments or other analyses, the model agreement could be improved to a reliable level. Therefore, the key outcome of this validation is that overall, *MSPM* predicted the performance of the given LTDSE well, and it shows promising potential to model future LTDSE designs, but its accuracy relies sensitively on the heat transfer resistances and seal leakages to be well defined.

MSPM was used to scale up a similar LTDSE model to an output power of kilowatts, and to model an existing commercial LTDSE. The model gave a reasonable estimate of this engine's performance, but the accuracy could not be assessed conclusively due to lack of detailed engine specifications and experimental data. This analysis showed that the regenerator plays an important role for engines even with low source temperatures, and *MSPM* demonstrated its ability to optimize the regenerator properties. The study also indicated that the heat exchangers for an LTDSE should be chosen to minimize flow friction and heat transfer resistances. This favours geometries with large surface areas and short conduction distances such as shell-and-tube heat exchangers.

The presented studies are limited in scope because mechanical friction and seal leakage were not investigated in detail, and they were based on a small variety of engine and heat exchanger geometries, and only laminar heat exchanger flow conditions. The experimental setup was unsuccessful in measuring the heat exchanger pressure drop, so the effects of flow friction could not be validated. Furthermore, the use of steady state flow correlations out of scope in an oscillating

flow system was identified as a weakness of *MSPM*. The model was also found to produce questionable results with working gases other than air and at high pressures above 120 bar, which limits the scope of the model in its current state. On this basis, future work should validate the pressure drop, investigate and model seal leakage, expand the variety of validation data, implement and validate mechanism models with friction, and review the implementation of working gases and the steady-state assumption in *MSPM*.

Preface

This thesis is an original work by Matthias Lottmann. Aspects of this research have been published in the following conference publication:

M. Lottmann and D. Nobes, “Validation of a Numerical Model for Reciprocating Thermodynamic Machines by Examining Heat Transfer in a Low Temperature Difference Stirling Engine,” *Proceedings of the Canadian Society for Mechanical Engineering International Congress 2022*, Jun. 2022, doi: <https://doi.org/10.7939/r3-ey5z-m827>.

The author also authored the following publications which did not directly contribute to this thesis:

M. Lottmann *et al.*, “Early Development Of A 100 Watt Low Temperature Difference Stirling Engine,” *Progress in Canadian Mechanical Engineering*, vol. 4, 2021, doi: <https://doi.org/10.32393/csme.2021.193>.

M. Lottmann *et al.*, “Development of a 100-Watt-Scale Beta-Type Low Temperature Difference Stirling Engine Prototype,” in *19th International Stirling Engine Conference (ISEC 2021)*, 2021, vol. 313. doi: [10.1051/e3sconf/202131308004](https://doi.org/10.1051/e3sconf/202131308004).

Acknowledgements

The author would like to thank his supervisor,

Dr. David S. Nobes,

for his persistent support and calm advice;

his lab mates

Linda Hasanovich,

Connor Speer,

Steven Middleton,

Michael Nicol-Seto,

Calynn Stumpf,

Jason Michaud,

David Miller,

who rode the Stirling boat together and supported this project with invaluable knowledge;

his colleagues, co-op students, friends, and his parents, who supported him from near and far.

The author is endlessly grateful to his wife, Habiba, who was the single source of strength behind him from start to finish through all the challenges this endeavour entailed.

Financial support for this research was provided by the following funding bodies:

Natural Sciences and Engineering Research Council (NSERC) of Canada

Alberta Innovates Energy and Environment Solutions

Future Energy Systems

Table of Contents

| | |
|---|--------|
| Abstract..... | ii |
| Preface..... | v |
| Acknowledgements..... | vi |
| Table of Contents..... | vii |
| List of Tables | xvii |
| List of Figures..... | xx |
| List of Symbols and Abbreviations..... | xxviii |
| Chapter 1. Introduction and Literature Review..... | 1 |
| 1.1 Motivation..... | 1 |
| 1.1.1 Stirling Engines..... | 2 |
| 1.2 Stirling Engine Components and Cycle..... | 4 |
| 1.2.1 The Ideal Stirling Cycle | 5 |
| 1.2.2 The Real Stirling Cycle..... | 8 |
| 1.2.3 Compression Ratio | 9 |
| 1.3 Losses and Impediments of Real Stirling Engines | 10 |
| 1.3.1 Flow Friction and Pressure Drop | 10 |
| 1.3.2 Mechanical Friction and Forced Work..... | 11 |
| 1.3.3 Leakage | 13 |
| 1.3.4 Imperfect Regenerator..... | 14 |
| 1.3.5 Heat Conduction and Gas Spring Hysteresis | 14 |
| 1.3.6 Dead Volume..... | 14 |
| 1.3.7 Heat Transfer Resistances | 15 |

| | | |
|------------|--|----|
| 1.4 | Review of Low Temperature Difference Engines | 17 |
| 1.4.1 | Solar LTDSEs | 17 |
| 1.4.2 | Lloyd's Rotating Displacer | 18 |
| 1.4.3 | Japanese (Saitama University) | 18 |
| 1.4.4 | Cool Energy Inc. | 19 |
| 1.4.5 | Free-Piston and Thermoacoustic LTDSEs | 20 |
| 1.4.6 | Conclusions | 20 |
| 1.5 | Modeling of Stirling Engines..... | 21 |
| 1.5.1 | 1 st Order: Analytical | 21 |
| 1.5.2 | 2 nd Order: Ideal with Losses..... | 23 |
| 1.5.3 | 3 rd Order: Discretized | 24 |
| 1.5.4 | Modeling of LTDSEs | 25 |
| 1.5.5 | Higher Order or CFD Modeling..... | 27 |
| 1.6 | Thesis Objectives and Outline | 28 |
| Chapter 2. | Experimental Stirling Engine Setup and Procedures..... | 30 |
| 2.1 | <i>Raphael</i> Experimental Stirling Engine | 30 |
| 2.1.1 | History of the <i>Raphael</i> Engine | 30 |
| 2.1.2 | Overview of the <i>Raphael</i> Engine | 33 |
| 2.1.3 | Heat Exchanger Geometry of <i>Raphael</i> Engine | 37 |
| 2.2 | Data Acquisition and Setpoint Control Equipment | 42 |
| 2.2.1 | Pressure and Temperature Measurement Locations..... | 43 |
| 2.2.2 | Pressure Sensors | 45 |
| 2.2.3 | Temperature Sensors | 46 |
| 2.2.4 | Mean Pressure Control | 47 |

| | | |
|-------|---|----|
| 2.2.5 | Heating / Cooling Systems and Temperature Control | 48 |
| 2.2.6 | Torque Control and Measurement..... | 49 |
| 2.2.7 | Crank Angle and Speed Measurement | 49 |
| 2.2.8 | DAQ System and Software | 50 |
| 2.2.9 | Data Sampling Duration and Frequencies..... | 53 |
| 2.3 | Sample of Raw Data | 57 |
| 2.4 | Calibration of Sensors and Pumps | 60 |
| 2.4.1 | Temperature Sensor Calibration..... | 60 |
| 2.4.2 | Pump Flow Rate Calibration..... | 61 |
| 2.4.3 | Specific Heat of Heat Transfer Fluids..... | 62 |
| 2.4.4 | Pressure and Torque Sensor Calibration | 64 |
| 2.5 | Experiment Operating Procedures | 65 |
| 2.5.1 | Warm-up and Preparation for Experiment | 65 |
| 2.5.2 | Start-up and Steady State | 66 |
| 2.5.3 | Data Acquisition Procedure | 67 |
| 2.6 | Reaching Steady State in Experiment..... | 68 |
| 2.6.1 | Time to Steady State (TTSS) | 68 |
| 2.6.2 | Experiment to Determine TTSS Between Setpoints | 70 |
| 2.6.3 | Experiment to Determine TTSS After Start-up..... | 72 |
| 2.6.4 | Oscillating Behaviour Caused by Temperature-Speed Interaction | 76 |
| 2.6.5 | Time to Steady State: Conclusions..... | 77 |
| 2.7 | Experimental Data Processing | 78 |
| 2.7.1 | Apply Calibration to Raw Measured Data | 78 |
| 2.7.2 | Mean Temperature Calculations | 80 |

| | | |
|------------|--|----|
| 2.7.3 | Heat Flow Rate Calculations..... | 81 |
| 2.7.4 | Pressure Calculations | 82 |
| 2.7.5 | Engine Speed Calculation from Crankshaft Angle | 82 |
| 2.7.6 | Speed and Pressure Data Averaging | 83 |
| 2.7.7 | Mean Speed, Torque, Shaft Power and Efficiency | 84 |
| 2.7.8 | Determination of Engine Volumes..... | 85 |
| 2.7.9 | Indicated Work and Power..... | 85 |
| 2.8 | Experimental Repeatability..... | 86 |
| 2.9 | Chapter Conclusion..... | 89 |
| Chapter 3. | Numerical Model <i>MSPM</i> and Modeling of the <i>Raphael</i> Engine..... | 90 |
| 3.1 | Overview of the Model | 90 |
| 3.1.1 | Thermodynamic Model of <i>MSPM</i> | 93 |
| 3.1.2 | Mechanical Model of <i>MSPM</i> | 94 |
| 3.2 | Assumptions and Simplifications of <i>MSPM</i> | 95 |
| 3.2.1 | Ideal Gas Model, Single Phase..... | 95 |
| 3.2.2 | Radiation, Fluid Inertia, Gravity Neglected | 95 |
| 3.2.3 | Axisymmetric Two-Dimensional Geometry..... | 95 |
| 3.2.4 | Uniform Pressure..... | 96 |
| 3.2.5 | One-Dimensional Flow | 96 |
| 3.2.6 | Quasi-Steady Flow and Turbulence | 96 |
| 3.2.7 | Fully Developed Flow..... | 97 |
| 3.2.8 | Isothermal Heat Sources..... | 98 |
| 3.2.9 | No Contact Resistance to Heat Conduction | 98 |
| 3.2.10 | Mechanisms are Kinematic and Linked | 98 |

| | | |
|------------|--|-----|
| 3.3 | Previous Validation Work on <i>MSPM</i> | 99 |
| 3.4 | Model of <i>Raphael</i> Engine in <i>MSPM</i> | 101 |
| 3.4.1 | Numerical Mesh and Heat Exchangers | 102 |
| 3.4.2 | Heat Exchanger Circumferential Temperature Gradient | 105 |
| 3.4.3 | Piston Seals: Two Model Variants | 106 |
| 3.4.4 | Heat Transfer with Environment..... | 108 |
| 3.5 | Numerical Data Acquisition and Processing | 111 |
| 3.5.1 | Model Outputs and Sample Data | 111 |
| 3.5.2 | Simulation Setup | 114 |
| 3.5.3 | Numerical Data Processing | 115 |
| 3.6 | Introducing Custom Heat Transfer Coefficients to <i>MSPM</i> | 116 |
| 3.6.1 | Analytical Estimation of Liquid Heat Transfer Coefficients for <i>Raphael</i> Model 117 | |
| 3.6.2 | CFD Estimation of Liquid Heat Transfer Coefficients for <i>Raphael</i> Model..... | 121 |
| 3.7 | Chapter Conclusion..... | 125 |
| Chapter 4. | Experimental Validation of <i>MSPM</i> Model..... | 126 |
| 4.1 | Scope of Validation..... | 126 |
| 4.1.1 | Validation Metrics..... | 128 |
| 4.1.2 | Experimental Datasets for Validation | 129 |
| 4.1.3 | Model Variants for Validation | 130 |
| 4.2 | Analysis of Indicator Diagrams | 132 |
| 4.2.1 | Indicator Diagram Samples..... | 132 |
| 4.2.2 | Indicated Work vs. Speed and Pressure | 134 |
| 4.2.3 | Indicated Work and Indicator Overlap vs. Reynolds Number | 136 |

| | | |
|--------|--|-----|
| 4.2.4 | Comparison of Model Variants | 138 |
| 4.2.5 | Comparison of Reynolds Number from Model and Theory | 144 |
| 4.3 | Analysis of Heat Consumption and Rejection | 148 |
| 4.4 | Analysis of Gas Temperatures | 151 |
| 4.5 | Analysis of Heat Exchanger Pressure Drop..... | 157 |
| 4.5.1 | Experimental Pressure Drop Measurements vs. Model and Theory | 157 |
| 4.5.2 | Experiment: Varying Positions of Dynamic Pressure Sensors | 163 |
| 4.5.3 | Conclusions and Suggestions for Pressure Drop Measurement..... | 167 |
| 4.6 | Analysis of In-Cycle Speed Variations..... | 170 |
| 4.7 | Model Sensitivity to Settings and Input Parameters..... | 172 |
| 4.7.1 | Sensitivity to Initial Conditions..... | 172 |
| 4.7.2 | Repeatability of Model Results in Repeated Runs..... | 174 |
| 4.7.3 | Effect of Neglecting Heat Conduction in Different Components..... | 175 |
| 4.7.4 | Numerical Mesh Sensitivity Study..... | 178 |
| 4.7.5 | Sensitivity to Source and Sink Temperatures | 181 |
| 4.7.6 | Sensitivity to Source and Sink Liquid Heat Transfer Coefficients | 183 |
| 4.7.7 | Sensitivity to Regenerator Properties | 189 |
| 4.7.8 | Summary: Total Estimated Uncertainty in Model Indicated Work | 191 |
| 4.8 | Shaft Power and Thermal Efficiency | 192 |
| 4.9 | Experimental Uncertainty | 196 |
| 4.9.1 | Measured Variables..... | 197 |
| 4.9.2 | Calculated Variables | 197 |
| 4.10 | Chapter Conclusion..... | 200 |
| 4.10.1 | Summary of Results..... | 200 |

| | | |
|------------|--|-----|
| 4.10.2 | Discussion..... | 202 |
| Chapter 5. | Scaling Up an LTDSE Using the <i>MSPM</i> Model | 204 |
| 5.1 | Scaling Parameters..... | 205 |
| 5.2 | Making a Scalable Model | 207 |
| 5.2.1 | Scaling of Volumes and Heat Exchanger Properties with Diameter | 207 |
| 5.2.2 | Model Geometry in <i>MSPM</i> | 211 |
| 5.2.3 | Tube Bank Heat Exchangers: Sizing and Advantages | 212 |
| 5.2.4 | Liquid Heat Transfer Coefficients for Tube Bank Heat Exchanger..... | 214 |
| 5.3 | Scaling Study | 217 |
| 5.3.1 | Optimizing Pressure and Speed..... | 217 |
| 5.3.2 | Results of Scaling Up..... | 219 |
| 5.3.3 | Estimating Realistic Power and Required Scale | 220 |
| 5.3.4 | Performance with Different Working Gases..... | 220 |
| 5.3.5 | Conclusion of Scaling Study..... | 223 |
| 5.4 | Comparison to ThermoHeart™ Commercial LTDSE | 224 |
| 5.4.1 | <i>MSPM</i> Model of ThermoHeart™ Engine | 224 |
| 5.4.2 | Estimating Regenerator Properties..... | 227 |
| 5.4.3 | Validation at Varying Source Temperature | 229 |
| 5.5 | Chapter Conclusion..... | 232 |
| Chapter 6. | Conclusions and Future Work | 234 |
| 6.1 | Review of Thesis Goals | 234 |
| 6.1.1 | Acquire detailed experimental data with a lab scale LTDSE..... | 234 |
| 6.1.2 | Validating the <i>MSPM</i> model..... | 235 |
| 6.1.3 | Investigate upscaling LTDSEs and model a large LTDSE using <i>MSPM</i> | 236 |

| | | |
|-------------|---|-----|
| 6.1.4 | Assess capabilities of <i>MSPM</i> Model..... | 237 |
| 6.2 | Future Work..... | 239 |
| 6.2.1 | Experimental Work and Validating <i>MSPM</i> | 239 |
| 6.2.2 | Expanding the <i>MSPM</i> Model..... | 240 |
| | References..... | 242 |
| Appendix A. | Uncertainty Analysis Methods | 256 |
| A.2.1 | Cyclic and Averaged Data..... | 259 |
| A.2.2 | Specifications of DAQ and Control System..... | 260 |
| Appendix B. | Uncertainty in Measured Variables | 263 |
| B.8.1 | Calibration: 2022-06-13 | 270 |
| Appendix C. | Uncertainty in Calculated Variables..... | 274 |
| C.1 | Heater and Cooler Liquid Flow Rates | 274 |
| C.1.1 | Calibration Oct 2021 | 275 |
| C.2.1 | Liquid Temperature Difference..... | 278 |
| C.2.2 | Cooler Heat Capacity..... | 279 |
| C.2.3 | Heater Heat Capacity..... | 279 |
| C.3.1 | Raw Pressures for entire Data Sample | 280 |
| C.3.2 | Cycle Averaged Pressures | 281 |
| C.5.1 | Raw speed for entire data sample (<i>f_{raw}</i>) | 283 |
| C.5.2 | Speed for each cycle angle (<i>fθ</i>)..... | 284 |
| C.5.3 | Average Speed (<i>f</i>)..... | 284 |
| C.7 | Thermal Efficiency | 286 |
| C.8 | Indicated Work..... | 287 |
| C.8.1 | Pressure Uncertainty..... | 288 |

| | | |
|-------------|--|-----|
| C.8.2 | Volume Uncertainty | 289 |
| Appendix D. | Improvements Made to <i>MSPM</i> Model | 291 |
| D.1 | GUI Functionality | 292 |
| D.2 | Issues with Mechanism Code..... | 293 |
| D.3 | Additional Test Set Parameters..... | 293 |
| D.4 | Model.m..... | 293 |
| D.5 | Simulation.m..... | 294 |
| D.6 | Matrix.m..... | 295 |
| D.7 | Node.m..... | 295 |
| D.8 | NodeContact.m | 296 |
| D.9 | Face.m..... | 296 |
| D.10 | Material.m..... | 296 |
| D.11 | Sensor.m..... | 296 |
| Appendix E. | Results of Model Sensitivity Study for Liquid Heat Transfer Coefficients.. | 297 |
| Appendix F. | Drawing Package of <i>Raphael</i> Engine..... | 304 |
| Appendix G. | Experimental Data Processing Code | 324 |
| G.1 | Starting Point of Experimental and Model Data Processing ('post_process.m'). | 324 |
| G.2 | Engine Specifications to Calculate Volumes ('T2_ENGINE_DATA')..... | 326 |
| G.3 | Reading and Calibration of Raw Experimental Data ('calibrate.m') | 331 |
| G.4 | Processing of Experimental Data and Calculation of Variables ('reduce.m')..... | 347 |
| G.5 | Secondary Functions | 359 |
| G.5.1 | Calculation of Cycle Averaged Pressures and Speed ('PV_data_avg')..... | 359 |
| G.5.2 | Calculate Flow Rate of Heater Fluid from Calibration Data at Setpoint Temperature ('SIL_180_flow_rate_calc')..... | 360 |

| | | |
|-------------|---|-----|
| G.5.3 | Calculate Specific heat of Heater Fluid from Calibration Data at Setpoint Temperature ('SIL_180_specific_heat_calc')..... | 362 |
| G.5.4 | Engine Volume Calculations ('volume')..... | 364 |
| Appendix H. | Model Data Processing Code | 366 |
| H.1 | MSPM Data Processing ('DataExtract.m')..... | 366 |

List of Tables

| | |
|--|-----|
| Table 2.1: Properties of <i>Raphael</i> engine..... | 34 |
| Table 2.2: Properties of <i>Raphael</i> engine heat exchangers and regenerator. | 41 |
| Table 2.3: Measured variables with symbols..... | 42 |
| Table 2.4: Controlled setpoint parameters with symbols..... | 42 |
| Table 2.5: Names of pressure and temperature sensor locations. | 44 |
| Table 2.6: Experimental ‘time to steady state’ for LTDSEs from literature. | 69 |
| Table 2.7: Equations for calculated temperatures..... | 80 |
| Table 2.8: Equations for heat flow rate calculations..... | 81 |
| Table 2.9: Equations for calculated pressures..... | 82 |
| Table 2.10: Equations for speed, torque, shaft power and efficiency..... | 84 |
| Table 2.11: Equations for indicated work and power. | 85 |
| Table 3.1: Mesh properties of <i>Raphael</i> model (with displacer piston seal, see Section 3.4.3) | 105 |
| Table 3.2: ‘Environment’ parameters of <i>Raphael</i> model..... | 108 |
| Table 3.3: Calculation results of natural convection coefficients for heater and cooler..... | 110 |
| Table 3.4: Reynolds number calculation for liquid flow in source channels..... | 119 |
| Table 3.5: Analytical calculation results for custom liquid heat transfer coefficients..... | 120 |
| Table 3.6: CFD study boundary conditions and results for liquid heat transfer coefficients [47]. | 123 |
| Table 4.1: List of experimental datasets used for validation. | 129 |
| Table 4.2: List of model variants used for validation, differing in representation of the displacer piston seal and the source and sink convection heat transfer coefficients. | 130 |

| | |
|---|-----|
| Table 4.3: Resulting changes in indicated work and heat flows from disabling (for PP and CC: enabling) heat conduction in the listed bodies in the <i>MSPM</i> model of <i>Raphael</i> | 177 |
| Table 4.4: Uncertainties of relevant measured variables | 197 |
| Table 4.5: Uncertainties of relevant calculated variables | 199 |
| Table 5.1: Properties of heat exchangers and regenerator of the scaling model from this chapter and the <i>Raphael</i> engine. | 213 |
| Table 5.2: Calculation of liquid heat transfer coefficients for tube bank heat exchangers... 216 | |
| Table 5.3: Engine volumes predicted by <i>MSPM</i> to reach shaft power goals with different working fluids. ‘Realistic’ estimate assumes model overpredicts shaft power by 41 %. Unrealistic predictions with helium and hydrogen indicated by (*). | 222 |
| Table 5.4: Properties of ThermoHeart™ engine as published in or estimated from [20], [57]. | 225 |
| Table 6.1: Specifications of data acquisition and setpoint control equipment. | 260 |
| Table 6.2: RTD measurement uncertainties..... | 263 |
| Table 6.3: TC measurement uncertainties | 264 |
| Table 6.4: Mean pressure measurement uncertainties | 265 |
| Table 6.5: Dynamic pressure measurement uncertainties..... | 266 |
| Table 6.6: Torque measurement uncertainties | 267 |
| Table 6.7: Angle measurement uncertainties..... | 268 |
| Table 6.8: Timestamp uncertainties | 269 |
| Table 6.9 – Atmospheric pressure sensor measurement uncertainties | 270 |
| Table 6.10 – Barometer calibration variables and uncertainties..... | 271 |
| Table 6.11: Cooler flow rate uncertainties..... | 274 |
| Table 6.12: Fluid mass uncertainties | 275 |
| Table 6.13: Recorded time uncertainties | 276 |

| | |
|--|-----|
| Table 6.14: Heat flow rate uncertainty values | 278 |
| Table 6.15: Speed uncertainty values | 283 |
| Table 6.16: Shaft power uncertainty values..... | 285 |
| Table 6.17: Thermal efficiency uncertainty values..... | 286 |
| Table 6.18 –Sources of volume uncertainties..... | 289 |

List of Figures

| | |
|---|----|
| Figure 1.1: Schematic of gamma Stirling engine with kinematic crank mechanism..... | 4 |
| Figure 1.2: Ideal Stirling cycle processes on schematic engine..... | 6 |
| Figure 1.3: Ideal Stirling cycle indicator diagram. | 7 |
| Figure 1.4: A real Stirling cycle indicator diagram, overlaid on the ideal cycle curve (dashed). | 8 |
| Figure 1.5: Indicator diagram of engine and buffer pressure, showing forced work areas. ... | 12 |
| Figure 1.6: Illustration of heat transfer resistances for convection and conduction between gas and source. | 15 |
| Figure 2.1: Photo of experimental setup with annotations. | 30 |
| Figure 2.2: Solid model of <i>Raphael</i> engine with key components annotated. | 33 |
| Figure 2.3: Photo of as-built <i>Raphael</i> engine with annotations..... | 34 |
| Figure 2.4: Horizontal cross section view of heater / cooler gas channel geometry from solid model. Detail of gas side fin / channel geometry. Dimensions in millimeters. | 38 |
| Figure 2.5: Vertical half-section view of upper displacer cylinder area from solid model showing heater geometry. Blue arrow indicates gas flow path. | 39 |
| Figure 2.6: Photo of regenerator matrix, made of tubular gauze and polyester fiber material. | 40 |
| Figure 2.7: Vertical section view of solid model showing pressure and temperature measurement locations..... | 43 |
| Figure 2.8: Diagram of pressure supply system..... | 47 |
| Figure 2.9: Diagram of heating and cooling systems with liquid flow loops. | 48 |
| Figure 2.10: Photo of <i>Raphael</i> crankshaft with annotation of installed instruments..... | 49 |
| Figure 2.11: Diagram showing flow of data and control signals in DAQ system. | 51 |

| | |
|--|----|
| Figure 2.12: Screenshots of DAQ software in NI LabVIEW showing (a) live monitoring of voltage inputs and (b) automated experiment controls. | 52 |
| Figure 2.13: Spectral analysis samples of pressure and torque signals acquired at $fVC = 1000$ Hz. Frequency shown on logarithmic axis and normalized with mean engine speed f . (a) Pressure pPC at setpoint $pset = 450$ kPa. (b) Shaft Torque at setpoint $pset = 200$ kPa..... | 55 |
| Figure 2.14: Sample plots of raw data from voltage and counter measurements. (a) speed from crank angle data, (b) torque, (c,d) mean and dynamic pressures (first 5 seconds). | 58 |
| Figure 2.15: Sample plots of raw temperature data. (a) hot side gas thermocouples, (b) cold side gas thermocouples, (c) liquid RTD temperatures..... | 59 |
| Figure 2.16: Comparison of measured temperature error over calibration temperature range before (a) and after (b) calibration is applied. For all RTD and TC sensors. | 61 |
| Figure 2.17: Plot and fit equation of heater liquid flow rate vs. setpoint temperature. | 62 |
| Figure 2.18: Plot of <i>Sil 180</i> specific heat estimate vs. temperature..... | 64 |
| Figure 2.19: Plots of first long time experiment, torque change, 60 minutes. (a) speed, (b) RTD temperatures, (c) hot side gas temperatures, (d) cold side gas temperatures. Moving average with 1 minute interval applied to (a) and (b). | 71 |
| Figure 2.20: Plots of first long time experiment, pressure and torque change, 30 minutes. (a) speed, (b) hot side gas temperatures. Moving average with 1 minute interval applied to (a). | 72 |
| Figure 2.21: Plots of 7-hour long time experiment. (a) speed, (b) torque, (c) shaft power, (d) mean pressures. Right axis showing deviation from the final-hour average (blue horizontal line). Moving average applied to speed (1 min interval), torque (5 min interval), pressures (1 min interval)..... | 74 |
| Figure 2.22: Plots of 7-hour long time experiment. (a,b) heat exchanger liquid temperature drops with deviation from final-hour average (blue horizontal line), (c,d) hot and cold side gas temperatures. Moving average with 1 minute interval applied to all curves. | 75 |
| Figure 2.23: Example plot of speed samples and averaged curve from a 10 second datapoint. | 84 |

| | |
|---|-----|
| Figure 2.24: Indicated work for three setpoints with $p_{set} = 100$ kPa, and similar speeds. Comparison of five datasets acquired with four different dynamic pressure sensors..... | 86 |
| Figure 2.25: Gas temperatures of setpoint with $p_{set} = 100$ kPa, comparing data from five experiments with similar speeds ($f = 211$ - 213 rpm). (a) Hot side and (b) cold side temperatures. | 87 |
| Figure 3.1: Schematic of <i>MSPM</i> model. Left: Thermodynamic model (Groups) built in GUI and discretized into Mesh. Right: Mechanical model..... | 92 |
| Figure 3.2: Model of <i>Raphael</i> engine rendered in <i>MSPM</i> . Left: full model, center: enlarged view with connecting pipe and crankcase cropped. Symmetry axis at center. | 101 |
| Figure 3.3: Numerical mesh in displacer cylinder and heat exchangers of <i>Raphael</i> model, as rendered by <i>MSPM</i> . Showing centers and bounds of gas and solid nodes. | 103 |
| Figure 3.4: Mesh detail of heater and regenerator. (a) Gas nodes and faces, ‘S’ is source channel, (b) Solid nodes and faces, (c) Gas and solid nodes (centermarks only), and mixed faces between them. | 104 |
| Figure 3.5: The two model versions, (a) without and (b) with displacer piston seal, rendered in <i>MSPM</i> , showing the displacer piston and heat exchanger section with gas nodes (blue/pink) and gas faces (green). Seal in (b) highlighted..... | 107 |
| Figure 3.6: Sensor locations in <i>Raphael</i> engine model rendered in <i>MSPM</i> | 111 |
| Figure 3.7: Sample plots of (a) Th, reg and (b) cooler Reynolds number from <i>MSPM</i> , model variant B, setpoint $p_{set} = 400$ kPa, $f = 207$ rpm. | 112 |
| Figure 3.8: Sample indicator diagrams for (a) working space and (b) crankcase from <i>MSPM</i> , model variant B, setpoint $p_{set} = 400$ kPa, $f = 207$ rpm. Blue curves have positive work (clockwise), red curves have negative work. Circle denotes starting point (angle zero)..... | 113 |
| Figure 3.9: Cross section of one half of the heater, as shown in <i>MSPM</i> . Gas channel on left, source channel (red outline, dimensioned) on right. Solid nodes (red dots) and faces (green lines) are rendered to show heat flow path between source channel and fins. | 118 |
| Figure 3.10: Gas and liquid computational domains of CFD study. The solid domain (not shown) is between gas and liquid domains. Adapted from Hasanovich [47]. | 121 |

| | |
|--|-----|
| Figure 4.1: Schematic of model validation areas and scope of this chapter (green). | 127 |
| Figure 4.2: Sample indicator diagrams from model variant A. Showing experiment and model data, and overlapping area as measure of similarity of shapes, (a) Lowest $Re_{HX, avg}$ datapoint, (b) Highest $Re_{HX, avg}$ datapoint. | 133 |
| Figure 4.3: Indicated work over engine speed, experiment and model variant A, all datasets. | 135 |
| Figure 4.4: Relative deviation of indicated work from model to experiment, over engine speed, model variant A, all datasets. | 136 |
| Figure 4.5: Relative deviation of indicated work from model to experiment, over average heat exchanger Reynolds number, model variant A, all datasets. | 137 |
| Figure 4.6: Indicator diagram overlap ratio over average heat exchanger Reynolds number, model variant A, all datasets. | 138 |
| Figure 4.7: Indicated work from all model variants A to D and experiment. (a) Absolute values over engine speed, (b) Relative deviation between model and experiment over average heat exchanger Reynolds number. | 140 |
| Figure 4.8: Comparison of indicator diagrams from experiment and all model variants for datapoints with (a) lowest $Re_{HX, avg}$, (b) highest $Re_{HX, avg}$. $Re_{HX, avg}$ is from equation (68). | 143 |
| Figure 4.9: Relative deviation of heat exchanger Reynolds number $Re_{HX, avg}$ between model variants and theoretical estimate from equation (68), plotted over the theoretical estimate. | 147 |
| Figure 4.10: Heater and Cooler heat flow rates over average heat exchanger Reynolds number, experiment and all model variants A to D, all datasets. | 149 |
| Figure 4.11: Relative deviation of Heater and Cooler heat flow rates over average heat exchanger Reynolds number, all model variants A to D, all datasets. | 150 |
| Figure 4.12: Gas temperature profile along locations in working space from Expansion Space (left) to Crankcase (right). Data from experiment and all model variants for datapoints with (a) lowest $Re_{HX, avg}$, (b) highest $Re_{HX, avg}$. $Re_{HX, avg}$ is the estimate from equation (68). Data exists only at the marker positions, dashed lines are for readability. | 152 |

| | |
|---|-----|
| Figure 4.13: Deviation of expansion space (T_e) and power piston space (TPP) gas temperatures predicted by model variants A to D from experiment, over average heat exchanger Reynolds number.(a) Absolute deviation in $^{\circ}\text{C}$, (b) relative deviation in %..... | 155 |
| Figure 4.14: Pressure drop over crank position, for 8 different datapoints, from experiment (solid lines) and model variant A (dashed lines). | 158 |
| Figure 4.15: Average pressure drop over heat exchanger Reynolds number from equation (68), for all 59 datapoints. Experiment, model variant A, and analytical estimate from equation (70). | 161 |
| Figure 4.16: Crank positions where pressure drop is zero over heat exchanger Reynolds number from equation (68), for all 59 datapoints. Data from experiment and model variant A. | 162 |
| Figure 4.17: Comparison of dynamic pressure measurements from all four sensors at position 0 (displacer cylinder head) . Setpoints with higher (a) and lower (b) speed. | 164 |
| Figure 4.18: Comparison of dynamic pressure measurements from all four sensors at position 2 (power piston cylinder) . Setpoints with higher (a) and lower (b) speed. | 165 |
| Figure 4.19: Indicator diagrams from all pressure sensors for setpoint with $f = 200 - 210$ rpm. | 166 |
| Figure 4.20: Indicated work from all pressure sensors for three setpoints, over speed. | 167 |
| Figure 4.21: Engine speed variation over crank position, comparison between experiment and model variant D. For the two setpoints with lowest (a) and highest (b) $Re_{HX, avg}$ | 171 |
| Figure 4.22: Comparison of indicated work model results when starting from different initial conditions ‘from Snapshot’ and ‘from Scratch’ (left axis). Relative deviation between them (right axis). Source heat transfer coefficients vary between the datapoints. Data to the left of the black vertical line is from ‘no seal’ model, to the right from ‘with seal’ model. | 173 |
| Figure 4.23: Indicated work model results repeatability over 25 repetitions of the same setpoint. For a hypothetical setpoint with $p_{mean} = 300$ kPa and $f = 150$ rpm. Model Variant D. | 175 |
| Figure 4.24: <i>Raphael</i> engine model in <i>MSPM</i> showing the bodies for which the effect of neglecting heat conduction was studied..... | 176 |

Figure 4.25: Indicated work and heat flow rates over ‘Node Factor’ which scales the mesh density. Shown relative to the respective values of the default model with ‘Node Factor’ of 1. 179

Figure 4.26: Number of nodes, faces and runtime of the computation over the ‘Node Factor’.
..... 180

Figure 4.27: Indicated work and heat flow rates over varying source temperature (a) and sink temperature (b). Model variant A. Shown relative to the values at the setpoint temperatures. .. 181

Figure 4.28: 3D plot of the model deviation in *Wind* over the source and sink liquid heat transfer coefficients. For setpoints with highest (red) and lowest (blue) *Re_{HX, avg}*. For model versions ‘No_Seal’ (a) and ‘With_Seal’ (b). 185

Figure 4.29: **For model version ‘With_Seal’**. RSS deviation in *Wind* from two setpoints, and difference in deviation (DD) between setpoints, over the source and sink liquid heat transfer coefficients. 3D view. 186

Figure 4.30: For model version ‘With_Seal’. RSS deviation in *Wind* from two setpoints, and difference in deviation (DD) between setpoints, over the source and sink liquid heat transfer coefficients. (a) trend over *h_{Source}* with lines of equal *h_{Sink}* annotated, (b) trend over *h_{Sink}* with lines of equal *h_{Source}* annotated. 187

Figure 4.31: Sensitivity of indicated work to varying regenerator porosity (a) and wire diameter (b). Red are the nominal properties used for model validation; black lines are estimated boundaries of uncertainty in regenerator properties. 190

Figure 4.32: Shaft Power of *Raphael* engine over speed. Data from experiment and all model variants, for all setpoints. Colour indicates charge pressure. 193

Figure 4.33: Shaft (Thermal) Efficiency of *Raphael* engine over speed. Data from experiment and all model variants, for all setpoints. Colour indicates charge pressure. 194

Figure 4.34: Uncertainty in indicated work over engine speed, for all datapoints 199

Figure 5.1: Illustration of tube bank heat exchanger, cross section perpendicular to gas flow direction. Tubes arranged in a rectangular grid with each tube taking a rectangular share of the cross section area. 208

Figure 5.2: Model used for scaling study, as rendered in *MSPM*. 211

Figure 5.3: Shaft power (a) and shaft (thermal) efficiency (b) of the scaling model with tube bank heat exchangers at varying pressure (absolute) and speed. Values at maximum power and efficiency annotated. Area of power within 5 % of maximum is highlighted by green crosses. 218

Figure 5.4: Shaft power predicted by scaling up engine volume, mean pressure or speed while scaling number of heat exchanger tubes equally. (a) Factor up to 10, (b) Factor up to 100 (volume only). ‘Realistic’ values assume that model predictions are 41 % higher than the actual shaft power would be. Starting from $V = 4.55 \text{ L}$, $p_{mean} = 13 \text{ bar}$, $f = 210 \text{ rpm}$ (max shaft power). 219

Figure 5.5: Shaft power predicted by scaling up engine volume and number of heat exchanger tubes, with different working fluids. (a) Factor up to 10, (b) Factor up to 100. 221

Figure 5.6: Model of ThermoHeart™ engine as rendered in *MSPM*. Expansion piston at minimum volume and compression piston at maximum volume. 227

Figure 5.7: Shaft power (a,c) and thermal efficiency (b,d) predicted by *MSPM* model with $T_{source} = 150 \text{ °C}$ (a,b) and $T_{source} = 400 \text{ °C}$ (c,d), with varying regenerator wire diameter (x-axis) and porosity (colour). Black horizontal lines are experimental data [20], red lines in (a,c) are shaft power predictions expected from *MSPM* assuming 41 % overprediction. 228

Figure 5.8: Shaft power (a), thermal efficiency (b), and heat input rate (c) predicted by *MSPM* model compared to experimental data [20] over source temperature. 231

Figure 6.1: Gravity correction table for mercury barometer..... 272

Figure 6.2: Temperature correction table for mercury barometer 273

Figure 6.3: Effect of all pressure and volume uncertainties combined on indicator diagram 287

Figure 6.4: Effect of pressure uncertainty on indicator diagram 288

Figure 6.5: Effect of power piston bore and stroke uncertainty on indicator diagram 290

Figure 6.6: Effect of crank angle uncertainty on indicator diagram 290

Figure 6.7: Updated GUI highlighting new mesh viewing options. 292

Figure 6.8: **For model version ‘No_Seal’**. RSS deviation in *Wind* from two setpoints, and difference in deviation (DD) between setpoints, over the source and sink liquid heat transfer

coefficients. (a) trend over h_{Source} with lines of equal h_{Sink} annotated, (b) trend over h_{Sink} with lines of equal h_{Source} annotated..... 298

Figure 6.9: **For model version ‘No_Seal’**. RSS deviation in Q_{Source} from two setpoints, and difference in deviation (DD) between setpoints, over the source and sink liquid heat transfer coefficients. (a) trend over h_{Source} with lines of equal h_{Sink} annotated, (b) trend over h_{Sink} with lines of equal h_{Source} annotated..... 299

Figure 6.10: **For model version ‘No_Seal’**. RSS deviation in Q_{Sink} from two setpoints, and difference in deviation (DD) between setpoints, over the source and sink liquid heat transfer coefficients. (a) trend over h_{Source} with lines of equal h_{Sink} annotated, (b) trend over h_{Sink} with lines of equal h_{Source} annotated..... 300

Figure 6.11: **For model version ‘With_Seal’**. RSS deviation in $Wind$ from two setpoints, and difference in deviation (DD) between setpoints, over the source and sink liquid heat transfer coefficients. (a) trend over h_{Source} with lines of equal h_{Sink} annotated, (b) trend over h_{Sink} with lines of equal h_{Source} annotated..... 301

Figure 6.12: **For model version ‘With_Seal’**. RSS deviation in Q_{Source} from two setpoints, and difference in deviation (DD) between setpoints, over the source and sink liquid heat transfer coefficients. (a) trend over h_{Source} with lines of equal h_{Sink} annotated (cropped to show minimum), (b) trend over h_{Sink} with lines of equal h_{Source} annotated..... 302

Figure 6.13: **For model version ‘With_Seal’**. RSS deviation in Q_{Sink} from two setpoints, and difference in deviation (DD) between setpoints, over the source and sink liquid heat transfer coefficients. (a) trend over h_{Source} with lines of equal h_{Sink} annotated, (b) trend over h_{Sink} with lines of equal h_{Source} annotated..... 303

List of Symbols and Abbreviations

Roman Alphabet Symbols

| Symbol | Description | Unit |
|-------------|-----------------------------|--------|
| A | Area | m^2 |
| AR | Aspect Ratio | - |
| CR | Compression Ratio | - |
| D | Diameter | m |
| D_h | Hydraulic Diameter | m |
| Gr | Grashof number | - |
| H | Height | m |
| L | Length, Thickness, Distance | m |
| N_f | Friction Factor | - |
| N_w | West Number | - |
| Nu | Nusselt Number | - |
| P | Power | W |
| Pr | Prandtl Number | - |
| \dot{Q} | Heat Flow Rate | W |
| R | Specific Gas Constant | J/kg K |
| $R_{1,2,3}$ | Heat Transfer Resistance | K/W |
| Ra | Rayleigh Number | - |
| Re | Reynolds Number | - |
| S | Stroke Length | m |

| Symbol | Description | Unit |
|-----------|--------------------------------------|--------------------|
| S_T | Tube Spacing | m |
| T | Temperature | °C, K |
| U | Flow Velocity | m/s |
| V | Volume | m ³ |
| W | Width | m |
| W_{ind} | Indicated Work | J |
| X | Diameter Scaling Factor | - |
| c, c_p | Specific Heat Capacity | J/kg K |
| f | Speed / Frequency | rpm or Hz |
| g | Gravitational Acceleration | m/s ² |
| h | Convection Heat Transfer Coefficient | W/m ² K |
| k | Thermal Conductivity | W/m K |
| l_p | Perimeter Length | m |
| \dot{m} | Mass Flow Rate | kg/s |
| n, N | Number of Items | - |
| p | Pressure | Pa |
| t | Time | s |
| u | Uncertainty | various |
| x | Measured Variable | various |
| y | Calculated Variable | various |

Greek Alphabet Symbols

| Symbol | Description | Unit |
|----------|---------------------------------------|--------------------|
| α | Thermal Diffusivity | m ² /s |
| β | Coefficient of Volume Expansion | 1/K |
| | Regenerator Porosity | - |
| Δ | Prefix indicating change or increment | - |
| η | Efficiency | % or dimensionless |
| θ | Cycle or Crankshaft Angle | ° or rad |
| μ | Dynamic Viscosity | Pa s |
| ν | Kinematic Viscosity | m ² /s |
| ρ | Density | kg/m ³ |
| τ | Torque | Nm |

Abbreviations

| Abbreviation | Meaning |
|--------------|---|
| CC | Crankcase |
| CFD | Computational Fluid Dynamics |
| CHP | Combined Heat and Power |
| DAQ | Data Acquisition |
| DD | Difference between Deviations / Difference in Deviation |
| <i>DTECL</i> | Dynamic Thermal Energy Conversion Lab |
| GUI | Graphical User Interface |
| ID | Internal Diameter |
| LTDSE | Low Temperature Difference Stirling Engine |
| <i>MSPM</i> | Modular Single Phase Model |
| OD | Outer Diameter |
| ORC | Organic Rankine Cycle |
| PEI | Polyetherimide |
| PP | Power Piston |
| PTFE | Polytetrafluoroethylene |
| RSS | Root Sum Square |
| RTD | Resistance Temperature Detector |
| TC | Thermocouple |
| TTSS | Time To Steady State |

Chapter 1. Introduction and Literature Review

1.1 Motivation

Climate change caused by greenhouse gas emissions from fossil energy use presents an unprecedented challenge to the global energy sector. The latest predictions demand a substantial shift to low-emission energy sources over the next 30 years [1]. In addition, climate change is not only caused by energy use, but also threatens the security of worldwide energy supply, especially electricity, because of extreme weather and water scarcity [2]. At the same time, the global share of electricity in total energy supply will be doubled or tripled from 2019 to 2050 if the energy sector is sufficiently decarbonized [1]. This is also true for Canada, where total energy use is declining, but electricity demand is predicted to grow by 47% until 2050 [3]. Therefore, regions that rely heavily on fossil fuels for electricity generation, such as the province of Alberta with 53 % of electricity generated from natural gas and 36 % from coal as of 2019 [4], are facing a growing pressure to replace these capacities with renewables. However, renewable electricity sources in Alberta are mostly solar and wind, which are intermittent as they depend on unsteady environmental conditions and lack the reliability to replace baseload capacity [5].

These factors have increased the interest in the utilization of unconventional resources that may have been evaluated as uneconomical before. Low temperature heat is a resource widely available in central to northwestern Alberta in the form of geothermal energy [6]. An electrical power potential of around 712 MW exists here at temperatures from 120 °C up to about 150 °C [6], which could cover about 8 % of the province-wide electricity demand of 274.5 PJ in 2019 [4]. In addition, low temperature heat is commonly discarded as a by-product of energy intensive industries. An estimated 236 MW of heat below 230 °C from industrial areas near Edmonton could be utilized to directly reduce local greenhouse gas emissions [7].

The utilization of low temperature heat for power generation has not been economically viable with conventional technology since the conversion efficiency for any technology is limited by the difference between heat source and rejection temperature. Two competing technologies are the organic Rankine cycle (ORC) and reciprocating heat engines such as the Stirling engine. While the ORC uses turbomachinery and is viable for large scales in terms of power and size at a steady

operating point, Stirling machines have the advantage of lower complexity and possibly higher efficiency at small scales [8]. A study of numerous applications suggested that they may be more economical than ORCs in a power range between 1 kW and several hundred kilowatts [9].

1.1.1 Stirling Engines

The Stirling engine, patented by Robert Stirling more than 200 years ago [10], is a heat engine powered by the temperature difference between a heat source and heat sink. Since its inception, it has seen several periods of increased research interest and some uses, but never achieved sustained success because it was overshadowed by the advances of other technologies, most notably the internal combustion engine [11]. Today Stirling engines are being researched and developed for utilizing various unconventional energy sources including solar [12]–[14]; biomass [15], [16]; waste heat from combustion engines [17], [18], cement production [19], and other sources [20]; geothermal [21]; waste gas combustion [22], [23]; and cryogenic exergy from LNG regasification [24]. Stirling engines have become established in decentralized combined heat and power (CHP) applications during the past 20 years, usually fuelled by natural gas or biomass [25]. Free piston Stirling engines have no mechanical linkages and offer superb durability. They are in ongoing development by NASA as radioisotope generators for space power supply, with some units exceeding 10 years of maintenance-free operation [26], [27].

Low temperature difference Stirling engines (LTDSEs), as referred to in this work, operate at source temperatures up to 150 °C and sink temperatures above 0 °C. Kolin [28] and Senft [29] first developed small-scale demonstration engines with power output below 1 W, with Senft's machine running off a temperature difference of 0.5 °C [29]. At the author's research group, *DTECL* (Dynamic Thermal Energy Conversion Lab), Stumpf [30] and Speer [31] built lab-scale LTDSEs that achieved on the order of 10 W shaft power.

To investigate the technical and economical viability of LTDSEs for power generation from low temperature heat, the technology must be advanced to a useful scale with a unit power in the kilowatt range. A 2016 review of the state of research [32] concluded that large-scale LTDSEs could be built inexpensively and be successful despite low efficiency when using abundant heat sources such as waste heat. A key challenge to this effort is modeling the performance of LTDSEs

[33]. This thesis aims to address this problem by validating a numerical model that was specifically developed to model the performance of LTDSEs.

1.2 Stirling Engine Components and Cycle

A Stirling engine is a closed cycle, reciprocating heat engine that uses a constant mass of working gas, such as air or helium [34], [35]. Heat is supplied to and rejected from the working gas externally through heat exchangers, enabling it to utilize any source of heat [34]. No chemical reactions occur inside the engine. Heat is also supplied continuously, giving it the advantage of low noise and longevity over internal combustion engines [34]. A Stirling machine has two pistons acting on the working gas that can be arranged in different layouts which have been termed alpha, beta, and gamma [34]. Figure 1.1 shows the components of a Stirling engine in the gamma layout.

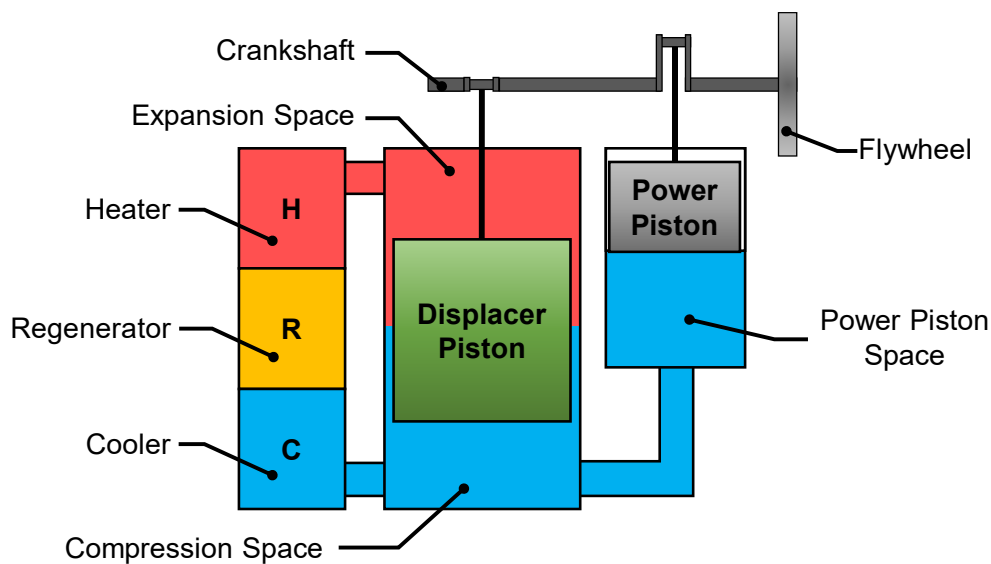


Figure 1.1: Schematic of gamma Stirling engine with kinematic crank mechanism

Most of the working gas is in the expansion and compression spaces, where it is at a high temperature, and in the compression space at a lower temperature. The double-acting displacer piston moves the gas back and forth between the spaces through the heater, regenerator and cooler, changing its temperature, which causes a pressure change in the working space. The power piston, usually connected to the cold side of the engine, expands the gas volume while most gas is in the expansion space and pressure is high, and compresses while most gas is in the compression space and pressure is low. Thereby a net indicated work is extracted from the gas by the power piston. In kinematic engines like the one shown in Figure 1.1, the pistons are linked via a mechanism to a flywheel. The power piston transfers energy to the flywheel and the displacer piston is powered by energy from the flywheel.

While the heat exchangers (heater and cooler) exchange heat with an external source and sink, respectively, the regenerator does not. It acts like a ‘heat sponge’, absorbing heat from the gas while it moves from hot to cold, and returning this heat to the gas when it moves back to the hot side. Thus, it reduces the amounts of heat taken from and rejected to the heat exchangers, increasing the efficiency of the cycle. The regenerator was a key component of Stirling’s original invention [10] as it decreased the fuel consumption compared to non-regenerative engines. It is usually a porous material capable of storing and transferring heat effectively.

The beta layout has the same components as the gamma, but both pistons are coaxial and share one cylinder [34]. The alpha layout uses two opposing pistons with the heat exchangers and regenerator between them, and both pistons share the tasks of displacement and volume change [34].

1.2.1 The Ideal Stirling Cycle

For simplicity, the processes outlined above can be described by an idealized thermodynamic cycle with the following assumptions [35], [36]:

- The working fluid is an ideal gas.
- There are no friction or conduction losses and no leaks.
- All processes are discontinuous, reversible, and occur at infinitesimal speed.
- Perfect heat transfer and regenerator: All heating and cooling during the isochoric processes is done by the regenerator. The regenerator achieves the temperature changes between heater and cooler temperature. Heat addition and rejection is isothermal.

The ideal Stirling cycle consists of four processes [35], [36], which are illustrated using a gamma engine in Figure 1.2. If heat is supplied to the heater at a temperature T_{source} and rejected from the cooler at T_{sink} , the ideal processes are:

- 1 to 2: Isochoric heating. Gas is heated from T_{sink} to T_{source} by the heat stored in the regenerator. Note how the regenerator temperature is changing.
- 2 to 3: Isothermal expansion and heat addition. Volume is expanded while temperature is held constant at T_{source} by adding heat from the source.

- 3 to 4: Isochoric cooling. Gas is cooled back to T_{sink} by transferring heat to the regenerator.
- 4 to 1: Isothermal compression and heat rejection. Volume is compressed at constant temperature T_{sink} by rejecting heat to the sink.

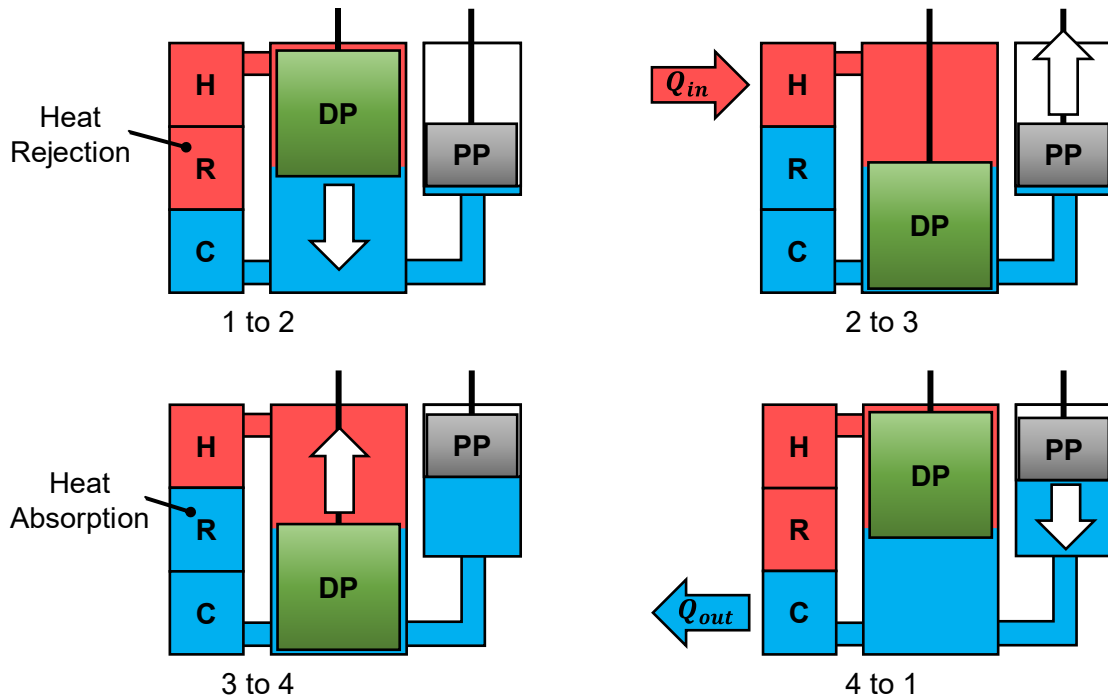


Figure 1.2: Ideal Stirling cycle processes on schematic engine.

The cycle is characterized by its indicator diagram (pressure vs. volume) which is shown in Figure 1.3. The indicated work (W_{ind}), which is the theoretical cycle work output of the engine, is represented by the area enclosed by the indicator curve. The difference between the maximum and minimum pressures of the cycle is called the pressure swing.

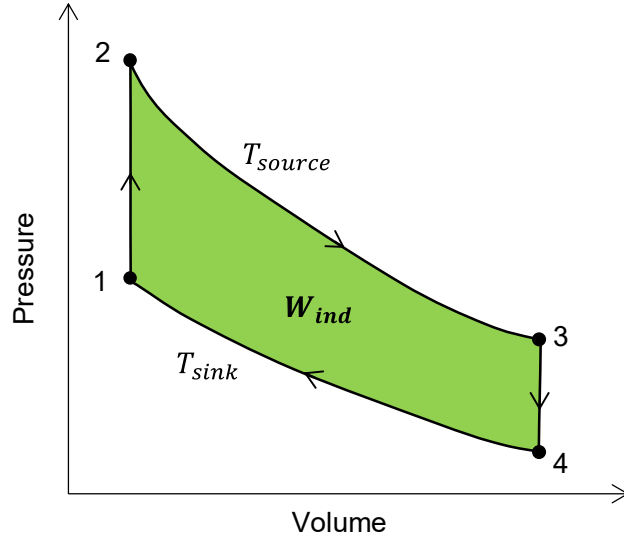


Figure 1.3: Ideal Stirling cycle indicator diagram.

The indicated work is calculated by integrating the pressure-volume curve:

$$W_{ind} = \oint p dV \quad (1)$$

where: W_{ind} = indicated work (J)

p = working space pressure (Pa)

V = working space volume (m³)

As the ideal cycle is reversible, and expansion and compression are isothermal with the gas at source and sink temperature, respectively, the efficiency of the ideal engine is equal to the Carnot efficiency (η_{Carnot}), which is the theoretical maximum for any heat engine [35]. However, this efficiency only applies to the hypothetical scenario of infinitesimal speed and power output [37].

$$\eta_{Carnot} = 1 - \frac{T_{Sink}}{T_{Source}} \quad (2)$$

where: T_{Sink} = sink (cooler) temperature (K)

T_{Source} = source (heater) temperature (K)

For a Stirling engine, the cycle goes in a clockwise direction as shown in Figure 1.3. If the direction is reversed, the machine acts as a heat pump or refrigerator that takes work input to extract heat at a lower temperature and reject it at a higher temperature [35].

1.2.2 The Real Stirling Cycle

The ideal cycle helps to illustrate the heat transfer and volume change processes in a Stirling engine, but cannot be achieved by a real machine. This is mainly because real thermodynamic processes are irreversible and must occur at a finite speed for the engine to produce any power.

Firstly, a practical engine operates at some frequency that does not allow infinite time for the working gas to remain isothermal during expansion and compression, or even enough time for it to reach the ideal temperatures T_{source} and T_{sink} while passing through the heat exchangers. In practice, the working spaces are nearly adiabatic, meaning they exchange little heat with the gas, and the gas temperature is strongly affected by compression and expansion [34], [35]. Therefore, the indicator curve of a real engine, as illustrated in Figure 1.4, does not touch the isotherms of the ideal cycle curve during expansion and compression.

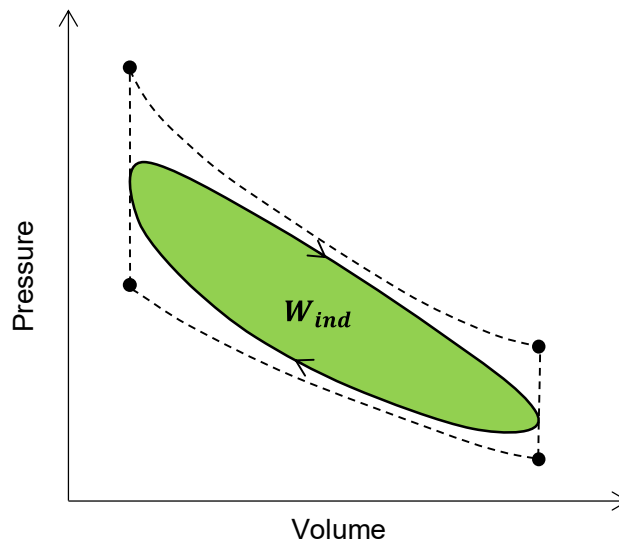


Figure 1.4: A real Stirling cycle indicator diagram, overlaid on the ideal cycle curve (dashed).

Secondly, the pistons usually do not move discontinuously, but simultaneously and with nearly sinusoidal motion profiles that are either imposed by a kinematic mechanism or, in the case of free piston engines, the result of pressure variations [34]. The displacer and power pistons are usually phased 90° apart so that expansion occurs while most of the gas is in the expansion space [36], but the overlapping piston motions mean that the pressure swing cannot be fully utilized to extract work. Consequently, the indicator curve becomes rounded and W_{ind} decreases, as shown in Figure 1.4. Despite this, the Carnot efficiency can still be achieved independently of piston motions if compression and expansion are reversible [35].

Lastly, there are other loss mechanisms that cause additional deviation from the ideal cycle. For example, leakage across piston seals diminishes the pressure swing. Viscous flow friction does the same and requires work to overcome. These factors are discussed in Section 1.3. The efficiency of a real engine depends on the complex interaction of heat transfer and energy losses. For heat engines that have irreversible, finite-time heat transfer but are otherwise ideal, and operate at maximum power output, the Chambadal–Novikov or Curzon-Ahlborn efficiency (η_{CNCA}) is valid [37] and has been used to analyze numerous heat conversion systems [9]. It is calculated as [37]:

$$\eta_{CNCA} = 1 - \sqrt{\frac{T_{Sink}}{T_{Source}}} \quad (3)$$

1.2.3 Compression Ratio

The compression ratio (CR) is defined as the ratio between the maximum (V_{max}) and minimum (V_{min}) volume of the working space, which occur at the extremes of expansion and compression:

$$CR = \frac{V_{max}}{V_{min}} \quad (4)$$

CR is a key parameter for engine design and optimization as it relates directly to the amounts of mechanical work that passes through the mechanism and causes mechanical friction. The maximum CR an engine can operate at depends on the ratio of source and sink temperature [38], and it was shown experimentally that smaller CR are preferable for LTDSEs [28].

1.3 Losses and Impediments of Real Stirling Engines

Losses are mechanisms that reduce the performance of an engine compared to the idealized assumptions of isothermal or adiabatic working spaces. They impact the performance by increasing the heat input and rejection rates, or decreasing the output of indicated or mechanical work. For modeling Stirling machines, apart from the thermodynamic processes, it has long been a challenge to predict these losses [39], [40] as they vary strongly with engine geometry and their effects can be interdependent [33]. At the author's research group *DTECL*, it was found through experimental trials of LTDSEs and comparison to simple models that losses have an exaggerated effect on LTDSE due to their low power density compared to more common high temperature engines [31], [41]–[43]. Middleton [33] showed analytically how losses have stronger effects at lower source temperatures. This section discusses some of the most important loss mechanisms relating to LTDSEs.

1.3.1 Flow Friction and Pressure Drop

The movement of the working gas through the engine space incurs losses from viscous flow friction. This occurs predominantly where the flow is forced through geometries with small cross-sectional areas, such as the porous regenerator and the heat exchangers. Any other flow obstructions and changes in flow direction also contribute to this loss. The energy lost to friction manifests as a drop in pressure along the flow geometry, which influences the overall pressure acting upon the pistons. For a gamma engine as shown in Section 1.2, the pressure drop from flow friction in the heat exchangers causes a net pressure on the displacer piston that opposes the piston motion, so that work must be input to the piston to overcome the pressure difference. It also affects the pressure acting on the power piston and can reduce the indicated work.

For internal flow, such as in a heat exchanger duct, the Darcy-Weisbach equation [44] relates pressure drop to a dimensionless friction factor, geometry and flow properties:

$$\Delta p = N_f \frac{L}{D_h} \frac{\rho U^2}{2} \quad (5)$$

where: Δp = pressure drop (Pa)

N_f = friction factor (-)

L = length of flow geometry (m)

D_h = hydraulic diameter of flow geometry (m)

ρ = fluid density (kg/m³)

U = flow velocity (m/s)

N_f depends on the flow geometry and Reynolds number, which is defined as [45]:

$$Re = \frac{\rho U D_h}{\mu} \quad (6)$$

where: Re = Reynolds number (-)

μ = dynamic viscosity of the fluid (Pa s)

The relation between Re and N_f depends on the geometry and the laminar or turbulent state of the flow [45], but Δp always increases with fluid viscosity, flow velocity due to the square term in equation (5), and with the length of the flow geometry. This has the consequence that LTDSEs operate at lower frequencies than high temperature engines and require heat exchangers with a short length and large cross-section area to minimize flow losses [33], [46].

1.3.2 Mechanical Friction and Forced Work

Mechanical friction occurs anywhere moving components are in contact, such as sliding seals on pistons and rods, and the bearings and linkages of kinematic mechanisms. Particularly for engines with low power density like LTDSEs, the work lost to mechanical friction can take away a significant share of the indicated work and even exceed it, rendering the engine inoperable [41].

This is because the work traveling through a mechanism can be excessive in an ill-designed Stirling cycle due to so-called forced work. Senft [38] termed and researched this concept extensively, and detailed discussions were given by researchers at *DTECL* [30], [31], [41]–[43].

The power piston is acted on by two opposing pressures – the engine pressure from the working space and the pressure on the piston’s back side, called the buffer pressure. The buffer can be open to the atmosphere, in which case the buffer pressure is constant, or it can be a closed volume like a crankcase, in which case the buffer pressure oscillates opposite to the engine pressure. Figure 1.5 shows the indicator curves of both pressures overlaid. Different periods of the cycle are marked by the letters a to d. During the periods a-b and c-d the net pressure on the piston is aligned with its direction of travel. Therefore, the piston transfers work to the mechanism and flywheel, which is called efficacious work [38], and the engine speed increases. During the periods b-c and d-a the net piston force opposes its motion, and forced work is taken from the flywheel to overcome the pressure [38]. This slows the engine. The alternating periods of efficacious and forced work cause an oscillation of the engine speed. The forced work taken from the flywheel must have been produced by the engine in previous cycles. Hence this work passes through the mechanism twice, and both times some work is lost to mechanical friction.

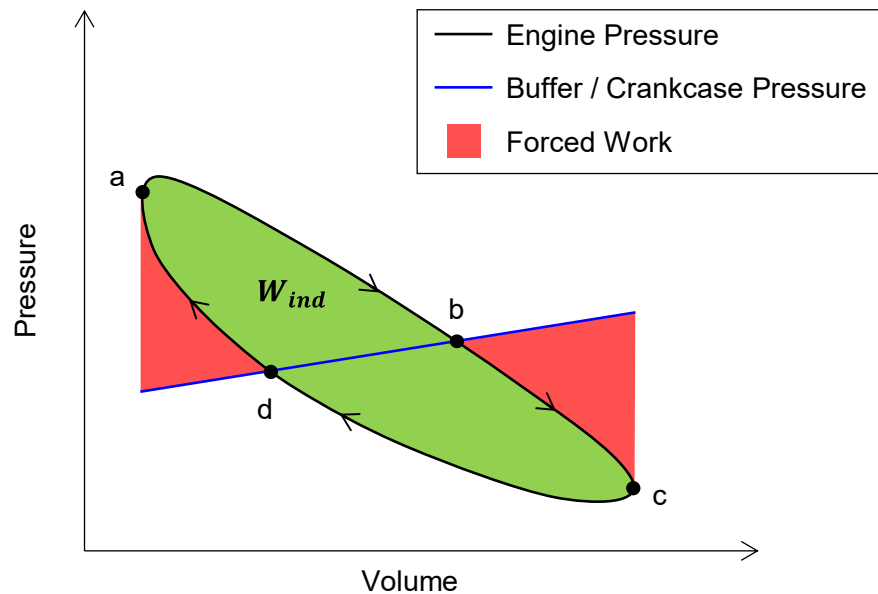


Figure 1.5: Indicator diagram of engine and buffer pressure, showing forced work areas.

The amount of forced work is equal to the areas between the indicator curves during forced work periods, as illustrated in Figure 1.5. It depends on the shape of the engine and buffer pressure

cycles. It can be shown that forced work is minimized when the buffer pressure is constant and equal to the mean engine pressure [38]. This means that the buffer or crankcase volume should be maximized to minimize the buffer pressure swing.

The energy losses caused by forced work depend on the mechanical conversion efficiency of the mechanism [38]. Since the compression ratio (CR) defines the horizontal width of the indicator curve (volume change), both indicated work and forced work increase with CR , and there is an optimal CR at which the net shaft work is maximized. This CR will be higher for a more efficient mechanism.

Because of forced work, the mechanical friction loss is linked to both the mechanism efficiency and the indicator curve shape. Therefore, the mechanism and the thermodynamic cycle must both be modeled accurately to predict the performance of LTDSEs as they are strongly impacted by losses relative to their power output.

1.3.3 Leakage

Most moving seals are not perfect, but allow some leakage as a result of the pressure difference across them. Sliding seals also incur a loss from mechanical friction, and there is a trade-off between a tighter seal that minimizes leakage and a looser seal that minimizes friction. For LTDSEs it is usually preferable to minimize friction, which means they may suffer from more significant seal leakage. The lower operating speed of LTDSEs (Section 1.3.1) further exaggerates the effect of leaks, allowing more gas to pass a leak before the pressure across the seal reverses.

Leakage through the displacer piston seal allows hot and cold gas from the expansion and compression spaces to mix, reducing the effective temperature difference and thereby the pressure swing. Leaks between the working space and buffer space, for example past the power piston seal, decrease the pressure swing directly. In both cases the indicated cycle work is diminished. West [34] noted that the dynamic leak rate of a seal in operation is difficult to measure and leakage may cause otherwise unexplained losses of power. Experimental work on various seals is presented by Hargreaves [35].

1.3.4 Imperfect Regenerator

As discussed in Section 1.2.2, perfect isothermal heat transfer is not realizable, and therefore the regenerator cannot heat the gas to the temperatures of the source and sink. The remaining heat must be supplied by the source and rejected by the sink, hence the imperfection of the real regenerator increases the necessary heat supply rate and diminishes the engine's efficiency [39]. LTDSEs are usually forced to use a higher porosity regenerator to limit flow friction losses [46], which further reduces the amount of heat that can be regenerated. These factors severely limit the thermal efficiency LTDSEs can achieve, in addition to the already low Carnot limit.

1.3.5 Heat Conduction and Gas Spring Hysteresis

Losses of heat by conduction through the solid geometry of an engine are caused by two mechanisms [33]. Firstly, heat is steadily conducted from the heat source to the sink and between source, sink and the surroundings. Materials with low thermal conductivity should be used, especially between the heat exchangers, to limit this loss. Secondly, the temperature oscillation in the working space and crankcase causes heat to be transferred to the walls at a higher temperature and returned to the gas at a lower temperature. Although no net heat is transferred over the cycle, work is lost due to the temperature difference [34]. This loss is called gas spring hysteresis. Both losses have a greater effect on LTDSEs relative to their power output [33].

1.3.6 Dead Volume

Any volume in the working space that is not swept by a piston is called 'dead' volume [36] as it does not participate in the thermodynamic cycle. This includes heat exchangers, regenerator, piston clearances and any ducting between components. Generally, dead volume should be minimized because it reduces the share of the working gas that goes through heating and cooling and thereby decreases the pressure swing [38], but in some circumstances added dead volume can improve the power output slightly [46]. The effects of dead volume on LTDSEs were investigated by Hoegel [46] and Hasanovich [47].

1.3.7 Heat Transfer Resistances

It can be shown by an empirical formula that engine power is significantly more sensitive to changes in source temperature at low temperatures [33]. This indicates that a small improvement in heat transfer, yielding improved gas temperatures, can boost the performance of LTDSEs significantly. LTDSEs are particularly limited by heat transfer as heat flow is always proportional to a temperature difference. Heat flow rates can be improved by increasing the surface area of the heat exchangers, but this usually also leads to increased flow friction and dead volume. This trade-off shows how different loss mechanisms are coupled.

Another factor limiting heat flow is the path of heat flow between the heat source or sink of known temperature and the working gas. This can be considered as a chain of heat transfer resistances analogous to an electrical circuit [45]. For any heat exchanger geometry, heat is transferred by three processes: By convection between the gas and the heat exchanger gas surface, by conduction between the surfaces on the gas and source/sink sides, and by some process between the source medium and the surface. For LTDSEs using geothermal and waste heat, sources and sinks are likely to be fluid streams, such as exhaust gases, cooling water or heat transfer oils. Therefore, heat transfer at the source/sink would be by convection. This heat transfer chain is illustrated in Figure 1.6 for the simplified case of a plane wall.

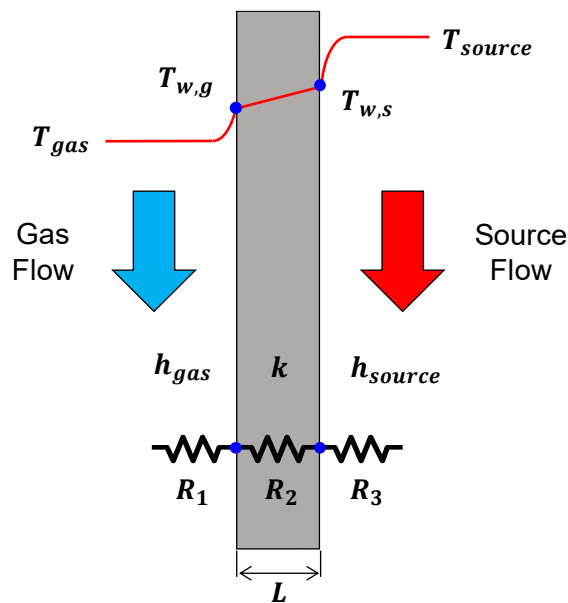


Figure 1.6: Illustration of heat transfer resistances for convection and conduction between gas and source.

The resistances and the heat flow rate through the series of resistances are calculated as [45]:

$$R_1 = \frac{1}{h_{gas} A_s}, \quad R_2 = \frac{t}{k A_s}, \quad R_3 = \frac{1}{h_{source} A_s} \quad (7)$$

$$\dot{Q} = \frac{T_{source} - T_{gas}}{R_1 + R_2 + R_3} \quad (8)$$

where: $R_{1,2,3}$ = heat transfer resistances (K/W)

h_{gas} = convection heat transfer coefficient on gas side (W/m² K)

h_{source} = convection heat transfer coefficient on source side (W/m² K)

A_s = surface area (m²)

L = conduction distance (m)

k = wall thermal conductivity (W/m K)

\dot{Q} = heat flow rate (W)

T_{source} = source temperature (K)

T_{gas} = gas temperature (K)

The heat flow rate is a function of the convection heat transfer coefficients in both flows, the conduction distance and conductivity of the wall between them, and the surface area through which heat is transferred. For non-planar or finned geometries the surface area and conduction distance can vary across the geometry. Equation (8) shows that if one of the resistances is much greater than the others, it will dominate the heat flow rate and become a heat transfer bottleneck. If the speed or pressure of any engine is increased to increase output power, at some point it will encounter a power limit due to heat transfer or flow friction. The heat transfer limit depends on the convection and conduction resistances (equation (7)). It is a particular challenge for Stirling engine models to estimate the convective heat transfer coefficients as these are difficult to measure experimentally and depend on the conditions of the unsteady, oscillating flow.

1.4 Review of Low Temperature Difference Engines

As discussed in Section 1.1, LTDSEs started at the small scale (milliwatts) [28], [29] and advanced to the lab scale (~ 10 W), for example the experimental engines tested at *DTECL* [30], [31], [41], [42]. Countless experimental and modeling studies have been carried out at this scale, some were reviewed by Stumpf [30] and Speer [31]. In a review by Wang et al. [32] almost all LTDSEs with a temperature difference below 150 °C had a power below 10 W. As the goal of this work is to scale up this technology, only large-scale LTDSEs from the literature that achieved or may have achieved a useful work output outside of a lab environment are discussed here. Some of the engines have source temperatures above 150 °C but are mentioned because their concept may be applied to lower temperatures.

1.4.1 Solar LTDSEs

Numerous Stirling engines and similar heat engines have been designed to utilize solar power [14], [32], most for concentrated sunlight at temperatures above 250 °C. Some LTDSEs for unconcentrated sunlight were designed. Early developments were unconventional devices and likely never achieved notable success [14], [48]. Boutammachte and Knorr [13] built a large-diameter low-cost engine that achieved about 20 W shaft power from direct sunlight in a field test, with a gas temperature difference between 30 °C and 50 °C. It was used to pump water at a slow but steady rate and is a rare example of useful mechanical work generated from a very low temperature difference.

A group at UC Berkeley [49], [50] researched solar free-piston LTDSEs. They aimed to achieve manufacturing costs of less than 1 USD/Watt by using low-cost materials and manufacturing [49]. Their small experimental engine achieved 9 W of electrical power with expansion and compression space temperatures of 184 °C and 22 °C, respectively [49]. They planned to develop a larger engine with 2.5 kW of power from a source temperature difference of 100 °C while pressurized with nitrogen to 75 bar [49]. However, only a much-simplified kinematic gamma-type engine with about 0.8 liters of swept volume was built [50]. It was tested at scaled-down conditions of 16 bar and a speed of 10 Hz, where it produced 120 W of electrical power from a temperature difference of 50 °C [50]. No further publications of this project were found.

1.4.2 Lloyd's Rotating Displacer

Lloyd [51] designed an unconventional LTDSE featuring a rotating displacer piston and wedge-shaped heat exchangers in a cylinder of 800 mm diameter. The displacer, with a swept volume of 130 liters, was powered by a servo motor allowing discontinuous motion, and a conventional power piston situated in a smaller cylinder was coupled to an output shaft by a crank linkage. The machine was to be filled with air at 10 bar, operate at 2 Hz and output 500 W of power from source and sink temperatures of 90 °C and 20 °C, respectively. It was partially assembled and the displacer mechanism tested, but no further progress was made. The design was scaled only using simple empirical models for volume and compression ratio, hence it is questionable whether it could have reached its targeted performance.

1.4.3 Japanese (Saitama University)

Pioneers of large-scale kinematic LTDSEs appeared to be a research group led by Iwamoto at Saitama University in Japan, who built numerous engines in the 1990s [52]. They also developed their own engine scaling method based on nondimensional parameters [53]. Their first large LTDSE was a gamma-type with a short-stroke displacer piston that had a diameter of 800 mm and swept volume of 40 liters [54]. It was filled with air at 1 bar and developed a shaft power of 146 W at 143 rpm while heated at 130 °C and cooled at 40 °C. Its thermal efficiency was about 3.5 %.

Later the Japanese group aimed to reach 1 kW shaft power and produced a larger LTDSE with several innovations [55]. It was an alpha-type with coaxial pistons that were both connected to a crankshaft on the same side by passing one piston rod through the other piston. A mechanism resembling a Scotch yoke allowed both pistons to connect to one crank throw while maintaining a phase angle between them and minimizing side loads on the pistons. The pistons used a unidirectional seal to minimize leakage between the working space and crankcase [55], [56]. The swept volume was about 20 liters, charged with nitrogen, and source and sink temperatures were 130 °C and 20 °C, respectively. At a speed of 175 rpm, 750 W of shaft power were achieved at a pressure of 8 bar, and 500 W at 5 bar, with a thermal efficiency of about 5 % [55]. This was a large machine, with a piston diameter of 400 mm and a mass around 2 tons, and may be the earliest example of an LTDSE producing sufficient power for a small-scale application like CHP.

Later this engine was commercially developed, which is presented in a 2021 paper [16]. This machine, called *AP2-10/300*, is pressurized with helium at 41 bar (absolute) and operates with heat from biomass combustion. At its minimum source temperature of 250 °C and a sink temperature of 30 °C it generates 10 kW of electrical power at 12 % thermal efficiency and a speed of 1400 rpm. Its speed can be adjusted to adapt to a changing electrical load, which is an advantage of kinematic engines over free-piston or thermoacoustic engines [16]. This engine has two parallel thermodynamic cycles resembling the previous alpha engine but with much smaller swept volume of 2 liters per cycle. The piston layout is unique, with one piston split in two parts, of which one part is connected rigidly to the opposing piston to act as a displacer, and the other part is detached and acts as a power piston. This allows the pistons and heat exchangers to have a large cross section with minimal flow friction while reducing the piston forces by 60 % compared to a regular alpha layout, which significantly improves the efficiency and compactness of the mechanism [16]. The machine is part of the power and heating system of a building and can also act as a heat pump using surplus renewable electricity to provide heating. The *AP2-10/300* engine and its application exemplify what could be possible with a mature large-scale LTDSE, and its design can inform the development of lower temperature systems.

1.4.4 Cool Energy Inc.

For source temperatures as low as 150 °C there appears to be only one commercially available system, the ThermoHeart® by Cool Energy Inc [20], [57]. This engine was developed for diverse sources of heat between 150 °C and 400 °C that can be fed to the engine via a heat transfer oil [20]. The unit consists of four alpha-type cycles with shell-and-tube heat exchangers [57], weighs about 4 tons and operates with nitrogen at 20 to 40 bar [20]. The pistons drive a rotary-cam mechanism on a shaft that is parallel to the piston axes, which allows the entire system to be contained in a compact cylindrical pressure vessel [57]. The electrical output is 3 kW at 6 % efficiency with a source of 150 °C, and 25 kW at an astonishing 30 % efficiency with a 400 °C source, with rejection at 20 °C [20]. Since 2019 pilot test engines are in commercial operation [20]. The targeted service interval is 20,000 hours [20]. Qualities of the ThermoHeart® design that could inform future LTDSE development are mainly the layout of heat exchangers and regenerator for minimal flow friction, the compact mechanism and pressure vessel, and the manufacturing challenges that have been solved to achieve market readiness.

Cool Energy Inc. is also developing a 40 kW engine with a focus on low cost and maintenance by using a simple construction with concrete components [58]. Temperatures between 150 °C and 350 °C are targeted and pilot engines may have been built, but little more information is available. The company also developed a comprehensive thermodynamic and mechanical model which is proprietary and not published [57].

1.4.5 Free-Piston and Thermoacoustic LTDSEs

Large-scale LTDSEs can be built as free-piston machines and perform well. This was proven in the 1980s by an engine built for NASA that demonstrated 5 kW of power at 11 % efficiency from 237 °C and 42 °C source and sink temperature [59], which is 29 % of the Carnot limit. However, these engines have been researched little at low temperatures due to their high development cost and complexity [32].

Wang et al. [32] found that thermoacoustic engines may be viable for low temperatures as they can achieve low cost, and high efficiency and reliability. An acoustic power of more than 1 kW has been achieved with a temperature difference of 79 °C, but more efficient methods to extract electric power are needed [32].

1.4.6 Conclusions

This review of the state of power generation from LTDSEs showed that few engines have ever been developed to maturity for real-world application, and that the body of research and published information is scarce. Some developments are likely unpublished because of commercial interests. Furthermore, no system exists that can utilize the targeted temperature range below 150 °C.

1.5 Modeling of Stirling Engines

Numerous modeling approaches have been researched to predict the performance of Stirling engines. The first analytical model was published by Schmidt [60] in 1871, and a surge in numerical models have been developed since the 1960s when computer-based solving of iterative algorithms became possible [61]. Modeling Stirling machines is not trivial as they are not linear or steady flow systems, but involve transient, oscillating flow and heat transfer, and complex interactions between thermodynamic and mechanical processes. This means they cannot be divided into smaller, simpler, independent subsystems but must be analyzed as a whole. In the literature, models are commonly categorized into orders of complexity, which were termed by Martini [39] and Chen and Griffin [61].

1.5.1 1st Order: Analytical

First order models are idealized representations of the engine cycle or empirical correlations that yield an analytical, closed form solution without numerical solving [39], [61]. They offer an order-of-magnitude estimate of engine power with few input parameters, which is useful in the early design stage of an engine. A common empirical parameter that is based on experimentally observed trends is the West number [34]:

$$N_W = \frac{P_{shaft}}{p_{mean} V_{sw} f} \frac{T_{Source} - T_{Sink}}{T_{Source} + T_{Sink}} \quad (9)$$

where: N_W = West number (-)

P_{shaft} = shaft power (W)

p_{mean} = mean cycle pressure (Pa)

V_{sw} = swept volume of power piston (m³)

f = mean engine speed (Hz)

Based on engines with source temperatures mostly above 400 °C, N_W was estimated at 0.25 [34]. For LTDSEs, values between 0.025 and 0.035 have been suggested based on correlation with experimental data [62]. The West number demonstrates the basic parameters that determine the

power output of a Stirling engine – pressure, volume, speed, and the temperature factor – while neglecting all loss mechanisms. Thus, it can be used to approximately compare the performance of different engines.

The most detailed 1st order model is the ideal isothermal analysis by Schmidt [60]. It has been discussed in detail by Urieli and Berchowitz [40], Speer [31], and Middleton [33]; Senft [38] presented the model equations for gamma-type engines. In short, the model divides the working space into isothermal volumes with assumed gas temperatures and makes similar assumptions to the ideal cycle. It is assumed that the working gas is an ideal gas and the pressure is uniform anywhere in the working space. Then, by applying the ideal gas law to each isothermal volume and considering that the total mass of gas is constant, an expression for the pressure as a function of the different volumes is obtained. For a kinematic mechanism the volumes are defined by the cycle phase angle [40]:

$$p(\theta) = m R \left(\sum_i \frac{V_i(\theta)}{T_i} \right)^{-1} \quad (10)$$

where: $p(\theta)$ = engine pressure as function of cycle angle (Pa)

θ = cycle or crankshaft angle ($^\circ$ or rad)

m = total mass of working gas (kg)

R = specific gas constant of working gas (J/kg K)

$V_i(\theta)$ = working space volumes, may depend on cycle angle (m^3)

T_i = constant temperatures of working space volumes (K)

The volumes V_i can be the expansion space, compression space, heat exchangers, dead volume, and any other space that can be assigned a temperature T_i . This constitutes a general isothermal model, but the additional assumption of the Schmidt model is that the volume variations $V_i(\theta)$ are sinusoidal [31], which is approximately true for common mechanisms like the Scotch yoke and the simple crank. This makes it possible to solve the pressure $p(\theta)$ analytically. Thus, the Schmidt model estimates the indicator curve and indicated work for an engine of known volume proportions, but neglects any losses, and does not consider the effects of engine speed.

1.5.2 2nd Order: Ideal with Losses

Second order models solve the thermodynamic cycle using an idealized model and calculate losses separately which are then subtracted from the ideal power output and heat input [61]. The ideal model can assume the working spaces to be isothermal (previous Section), or adiabatic (no heat exchanged with the gas), or semi-adiabatic in which case heat transfer in the working spaces is considered [61]. The included losses vary between models but usually include those discussed in Section 1.3. It is important that the losses are independent of each other, that is, they are decoupled, and the effects they might have on the cycle and on each other are not modeled [61]. Some loss calculations may rely on arbitrary correction factors [61]. The advantages of 2nd order models are their simplicity and low computational complexity compared to higher order models, and the separation of losses from the cycle which allows the impact of each loss to be quantified [31].

A vast array of 2nd order analyses has been developed and used to model commercial and research engines [39], [61]. Recent models in the academic literature were reviewed by Ahmed et al. [63], and some commercial models listed by Middleton [33]. The models by Urieli and Berchowitz [40], [64] are widely used; Speer [31] described them in detail and reviewed recent applications. Their *Simple* model includes imperfect heat transfer and flow friction losses into an ideal adiabatic cycle. It uses a quasi-steady method to estimate pressure drop. Speer [31] used this model on experimental LTDSEs and found that it overpredicted the power output despite additional loss calculations that had been implemented. The model deviation became worse when the source temperature was reduced. It was determined that the model failed to account for the effect of losses on LTDSEs and consequently predicted engines to work while they were unable to run in reality [41]. Mechanical friction and leakage through imperfect seals were particularly underestimated [31], [43]. These findings indicated that a more sophisticated approach, encompassing the interactions and coupled losses within the whole thermodynamic and mechanical system, would be necessary to successfully model LTDSEs.

1.5.3 3rd Order: Discretized

Third order models do not rely on an idealized cycle, instead they discretize the engine geometry into a nodal network on which the governing equations of the thermodynamic processes are solved. These are usually the conservation of mass, momentum, and energy, and an equation of state for the working gas [39], [61] which can be the ideal gas law in the simplest case. Simplifications can be applied to the equations, for example, inertia and kinetic energy of the gas are often neglected [61]. The model is also discretized in the temporal dimension, and the system is solved numerically with implicit or explicit finite-differencing schemes [61]. These methods bear similarities to computational fluid dynamics (CFD), but 3rd order models usually discretize the flow in only one dimension and are therefore less computationally expensive [33]. Kinematic and dynamic models of mechanical components can be coupled with the thermodynamic model to simulate an entire engine.

Depending on their generality, 3rd order models can also model a greater variety of geometries and can be powerful tools for exploring and optimizing designs. Furthermore, they can produce information that is difficult to obtain experimentally or with simpler models, such as instantaneous temperatures [33]. Most importantly, 3rd order models are considered to be more accurate than lower order models because they use fewer assumptions and empirical correlations, and they solve all processes simultaneously and interdependently, so that coupled effects of losses are accounted for. This suggests that it should be possible to design a 3rd order model which can reliably predict the performance of LTDSEs.

The nodal analysis of Stirling engines was pioneered by Finkelstein [65] starting in the 1960s. Other early models were reviewed by Chen and Griffin [61]. Heat transfer and flow friction were treated as quasi-steady in early 3rd order models because only steady-state correlations were available [61], but research on oscillating flow has advanced and some more recent models account for some effects of unsteady, accelerating flow, for example the *Sage* [66] model developed by Gedeon. *Sage* is commercially available and was developed mainly to design free-piston engines and Stirling cryocoolers. It uses implicit numerical schemes in space and time [66], which were also used in Gedeon's model from 1978 [67] and make the model more computationally efficient than explicit solvers. The drawback of the implicit time scheme is that the solution is cyclical and transient-speed simulations are not possible.

Some recent 3rd order models were reviewed by Middleton [33] and Hasanovich [47]. Application of these models to LTDSEs were not found in the literature and their code is usually not published, therefore little can be said about their applicability to LTDSEs. Some additional works should be mentioned. The code called *SETAM-NTUA* by Rogdakis et al. [68] is a 3rd order thermodynamic model with a kinematic mechanism implementation. The 3rd order model *kpsim* was first developed by Kuehl [69] and discussed in detail in a recent paper [70]. It features a graphical representation of modular engine components, much like *Sage* [66], where the thermodynamic cycle is coupled to mechanical components. Both these models do not support transient speed simulations and have so far only been validated at high temperatures. Xiao et al. [71] combined *Sage* [66] with loss calculations from a 2nd order model, which significantly improved the model predictions of a high temperature engine.

1.5.4 Modeling of LTDSEs

The development of lab-scale LTDSEs at *DTECL* has so far relied on highly iterative experimental work [30], [31], [41], [42] because little research exists on their design and on models that can reliably predict and optimise their performance [31], [33], [43]. This section reviews modeling efforts that have been done on low temperature machines and for which there is evidence of experimental validation.

Possibly the first model with specific consideration of low temperature sources was published in 1982 by Shoureshi [72]. It was a 2nd order adiabatic analysis with correlations for mechanical friction and imperfect heat transfer losses. However, it was validated only against data from high temperature engines available at the time.

Miller [43] reviewed some models that were validated with LTDSEs. These works were using small-scale gamma engines and found that models generally overestimated the indicated work or power output. Yousefzadeh et al. [73] used such an engine with a temperature difference of 30 °C and found good agreement of their 2nd order model, albeit with few datapoints. Small LTDSEs in the milliwatt power range have been modeled by simple 1st or 2nd order methods because of their simple geometry; they usually lack a regenerator and dedicated heat exchangers. It is questionable if these results and models are transferable to larger, more complex machines.

Kraitong [74] optimized a small LTDSE using a 2nd order model, CFD analysis, and a genetic algorithm. The algorithm was able to improve the shaft power of the engine notably. Optimization methods such as this one could potentially be applied to other models and larger LTDSEs. Kraitong [74] also noted a lack of heat transfer and flow friction correlations for oscillating flow in the low temperature regime.

Sage [66] has recently been used to model LTDSEs [46], [47]. Hasanovich [47] validated *Sage* against the same experimental engine used in this thesis and found that gas temperatures were predicted well, but indicated work only agreed qualitatively and was overestimated by the model. In the author's own experience, *Sage* showed difficulties converging when modeling an LTDSE. Lloyd [51] reported similar problems and was unable to model a physically large LTDSE in *Sage*. Additional factors make *Sage* undesirable for LTDSE research. Firstly, the model code is proprietary and not open to researchers. Secondly, it cannot simulate transient cases with varying engine speed due to its implicit temporal scheme. The ability to predict transient and in-cycle variations of engine speed was identified as necessary to model the effect of different mechanisms and piston motions on engine performance [42]. Lastly, the model interface and handling of input and output data are not user-friendly and require considerable learning effort.

To fill this research gap and accelerate the development of LTDSE, the model *MSPM* [33] was developed at *DTECL*. The goal of this 3rd order, two-dimensional, model is to provide a complete system analysis of closed-cycle reciprocating machines, especially aimed at the low temperature regime, that is accessible to research [33]. The model assumes axisymmetric geometry and uses a coupled thermodynamic and mechanical solver and has a graphical user interface (GUI). Similar coupling of a thermodynamic cycle and dynamic mechanism model was done by Yang et al. [75] with a 2nd order adiabatic model and by Hooshang et al. [76] with a 3rd order code. Both models predicted dynamic speed well compared to experiments.

If proven reliable, the *MSPM* model could be used to predict the performance of LTDSE designs and advance their development considerably. To achieve this, it must be experimentally validated.

1.5.5 Higher Order or CFD Modeling

A detailed understanding of the flow field in Stirling engines can only be obtained through multi-dimensional flow analysis or CFD (computational fluid dynamics). CFD was used to optimize geometrical parameters of a small-scale LTDSE [77], [78]. A finite-element simulation of the flow in a Stirling shell-and-tube heat exchanger was compared in 3D and 1D, and found heat transfer and efficiency to be optimal when gas flow in the heat exchanger is symmetrical [18]. 3D studies can be useful to determine if the symmetry assumption in a simpler model is valid [18]. The CFD analysis by Mahkamov [79] on a high temperature engine was two-dimensional and axisymmetric, similar to the *MSPM* model, and predicted power better than a 2nd order model.

Rogdakis et al. [80] carried out a 3D CFD study of an entire high temperature engine and found results to be similar to their 3rd order model *SETAM-NTUA* [68]. They found that gas temperatures were not uniform in the engine working spaces and that vortical structures were forming [80]. Kuban et al. [81] carried out a full 3D CFD analysis of an engine working space. The flow was found to be strongly asymmetric even in symmetrical components, and areas of high vorticity and turbulence were found that may cause significant flow losses. They proposed this may cause significant error for models assuming any symmetry, such as *MSPM*.

Though it can provide detailed flow and temperature information that is otherwise impossible to obtain, full-engine CFD is not feasible for modeling the overall performance of engines because of its complexity. CFD analysis of oscillating, compressible flow with moving boundaries requires large numbers of mesh elements and substantial computing power. For example, a single engine cycle in Kuban's study [81] took up to 43 hours to compute using 24 CPU cores. In contrast, 3rd order models like *Sage* or *MSPM* provide sufficient details for most design purposes within minutes. CFD can play a useful role in engine design to study localized flow details. For example, velocity and temperature distributions as well as empirical heat transfer and friction correlations for heat exchangers [82] and regenerators [83] have been obtained this way.

1.6 Thesis Objectives and Outline

The overarching goal of this thesis is to investigate and advance the scale-up of low temperature difference Stirling engines. This is pursued by reviewing and experimentally validating a numerical model which has the potential to advance the development of LTDSEs. The work presented in this thesis follows these objectives:

- Acquire detailed experimental data with an existing lab-scale LTDSE.
- Using this data, validate the numerical model *MSPM* to quantify its accuracy and identify deviations.
- Utilize the *MSPM* model for a scaling study that estimates the size of an LTDSE for a given power output, and to model an existing large-scale LTDSE.
- Assess the capability of *MSPM* as a design tool for future LTDSE development, and recommend next steps for further validation and development of the model.

The remaining thesis Chapters are structured as follows:

Chapter 2 gives an overview of the experimental LTDSE and data acquisition equipment used to obtain the experimental data for the model validation. Procedures for calibration, warm-up, data acquisition and processing are described and the criteria for achieving steady state conditions with this engine are discussed.

Chapter 3 describes the model *MSPM*, the validation of which forms the core part of this thesis. The model's assumptions are discussed critically, improvements made to the model are introduced, and the model geometry and procedures used for the following validation are presented.

In Chapter 4, the thermodynamic model of *MSPM* is validated against experimental data at steady state, using indicator diagrams, heat flow rates and gas temperatures as metrics. A sensitivity study investigates whether model deviations are caused by model deficiencies or inaccurate input parameters. An analysis of experimental uncertainty concludes the Chapter.

In Chapter 5, the *MSPM* model is used to optimize the working point and scale up an LTDSE from the size investigated in previous Chapters to a useful power scale. The performance with different working gases is explored. Additionally, an approximate model of a real commercial

large-scale LTDSE is built in *MSPM* and compared to published data of this engine at different source temperatures.

Chapter 6 concludes this thesis by evaluating the thesis objectives and suggesting future opportunities for experimental research and developing the *MSPM* model.

Chapter 2. Experimental Stirling Engine

Setup and Procedures

This chapter describes the experimental Stirling engine and data acquisition setup used to obtain the data for validating the model in Chapter 4. Procedures followed to acquire and process data as well as experimental uncertainties are discussed.

2.1 *Raphael* Experimental Stirling Engine

The experimental engine, called the *Raphael*, is installed on a cart, and is operated alongside peripheral devices such as heating and cooling baths, a pressure supply system, and data acquisition (DAQ) equipment. Figure 2.1 shows the experimental setup. The following sections describe the components of the setup.

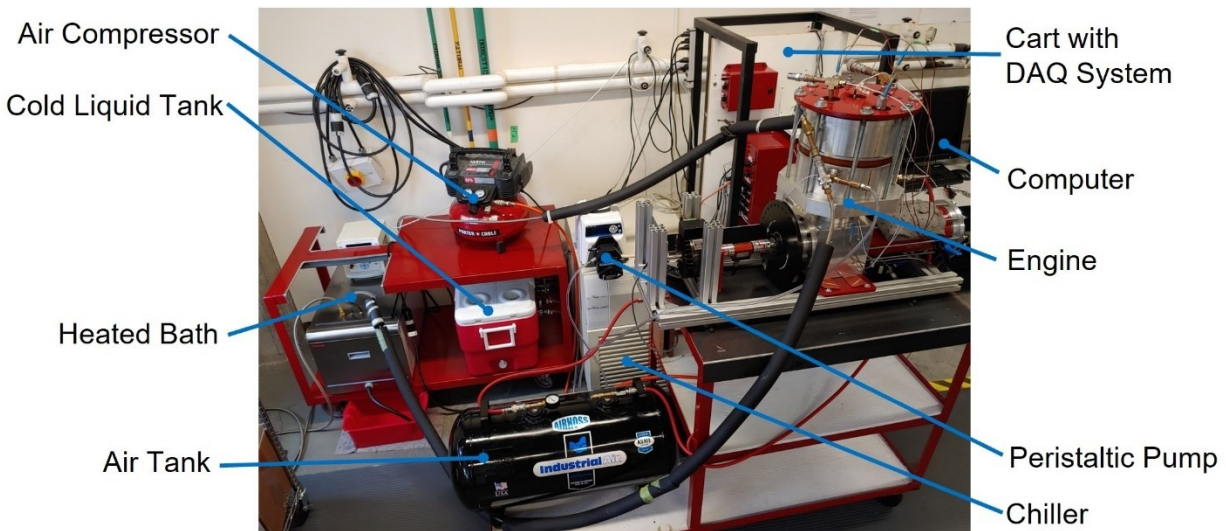


Figure 2.1: Photo of experimental setup with annotations.

2.1.1 History of the *Raphael* Engine

The origin of the *Raphael* engine design lies in the *ST05G-CNC* Stirling engine, which was developed by Viebach [84] in the 1990s to promote microgeneration from biofuel combustion. The hot side heat exchanger of the *ST05G-CNC* consists of steel tubes that absorb heat from combustion gases [84]. The complete drawing package of this design was available online until

the company ceased operations, but an archived copy of their website [84] is still accessible. *ST05G-CNC* engines and modified versions have been used by researchers to optimize engine parameters and to validate various models. The following are examples of recent publications of this work.

Bert et al. [85] used an *ST05G-CNC* engine with electric resistance heaters instead of the original tube heater. They operated the engine at source temperatures between 200 °C and 700 °C with air and helium as working gases, and validated a 2nd order model. Using particle swarm optimization, they also found the theoretically optimal piston kinematics at a single operating point to be close to a discontinuous saw-wave motion.

Hooshang et al. [86] experimentally validated results from a third-order model of an engine similar to the *ST05G-CNC*. They then used an artificial neural network to optimize the modelled engine at source temperatures of 350 °C to 400 °C [86]. In another work they measured and modeled the dynamic behaviour of the engine speed [76].

Alfarawi et al. [87] simulated the *ST05G-CNC* in a second-order model that is an extended version of the *Simple* model by Urieli and Berchowitz [40]. They also performed a two-dimensional CFD study of the working space which was validated experimentally and provided an estimate of the flow field and temperature distribution in the volume spaces [88]. Their work covered source temperatures of 450 °C and 600°C.

Kuban et al. [81] analysed the *ST05G-CNC* engine's working spaces using 3D CFD. Source temperatures were between 300 and 500 °C. Turbulence in the connecting pipe was found to potentially cause considerable flow losses [81]. The flow was strongly asymmetrical and complex vortical structures formed in the expansion and compression spaces [81]. This cannot be predicted by a one-dimensional model assuming symmetry, like *MPSM*. However, the operating conditions in this study are not comparable to the experiments in this thesis as the source temperatures were higher and either speed or pressure was more than twice of the highest used in this thesis for each of their studied cases.

At *DTECL*, Speer [31] built a modified version of the *ST05G-CNC*, called the *HTG*, with an electrically powered heater that resembled a solar heat source. The effect of several design modifications to reduce the minimum source temperature of the engine was investigated [31].

Experimental results showed that a reduction of the power piston diameter, leading to a smaller compression ratio, and an increase of the crankcase volume led to an improved low temperature performance and enabled the engine to operate with a source temperature as low as 144 °C [31]. A reduced compression ratio and larger crankcase are beneficial for LTDSEs as explained in Section 1.3.2. The data was also compared to second order isothermal and adiabatic models, and it was found that the simplified, decoupled losses calculated by these models are inaccurate in the low temperature regime and cause a significant overestimation of engine performance [31].

Informed by the results of the *HTG*, Speer [89] developed a prototype named *Raphael* for the company Terrapin Geothermics aimed at utilizing geothermal heat at source temperatures below 150 °C. The *Raphael* was again based on the *ST05G-CNC*, thus turning this design into an LTDSE. The main changes from the *ST05G-CNC* were a reduced compression ratio and a roughly four-times increase in displacer swept volume by increasing the displacer piston diameter. The design also used identical annular-finned heat exchangers as heater and cooler that increased the heat exchanger volume and surface area substantially and enabled the use of a liquid heat source medium [89].

Components of the *Raphael* were experimentally optimized for shaft power at Terrapin Geothermics, especially the power piston seal and the regenerator material [89]. Later, this same engine was acquired by *DTECL* to serve as a source of experimental data for the model validation in this thesis work as well as a platform to test improvements to components like the heat exchangers and the piston seal.

2.1.2 Overview of the *Raphael* Engine

Raphael is a gamma-type LTDSE with displacer piston and power piston arranged at a 90° angle. From an internal volume of about 4.7 liters it generates a maximum shaft power of 15 W when running at source and sink temperatures of 150 °C and 5 °C, respectively, a charge pressure of 450 kPa, and a speed of 130 rpm. A solid model rendering of the engine is shown in Figure 2.2 with a section cut to show its internals. A view of the real engine from a similar angle is given in Figure 2.3, where liquid supply hoses, air supply manifold, and some sensors can be seen installed. Table 2.1 contains the most relevant parameters of the engine, specifically those relevant to the validation of the thermodynamic model. A drawing package showing all parts of the engine in assembly drawings and more detailed part drawings of the heat exchangers is included in Appendix F.

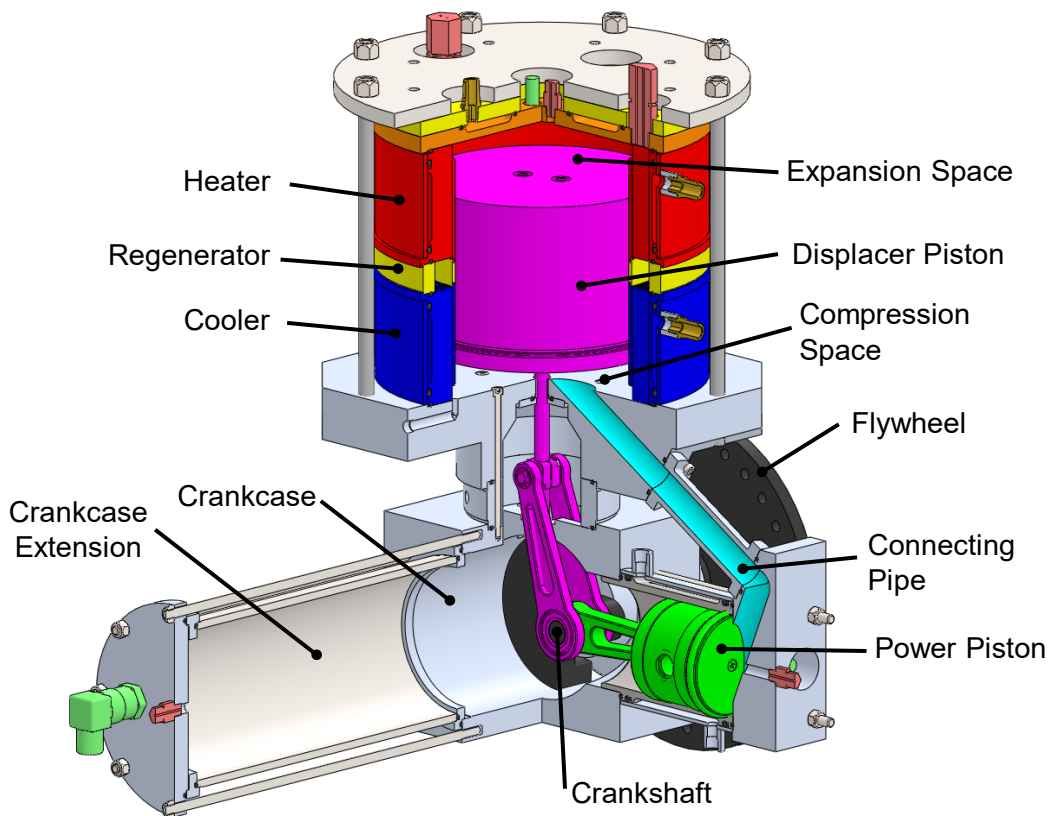


Figure 2.2: Solid model of *Raphael* engine with key components annotated.

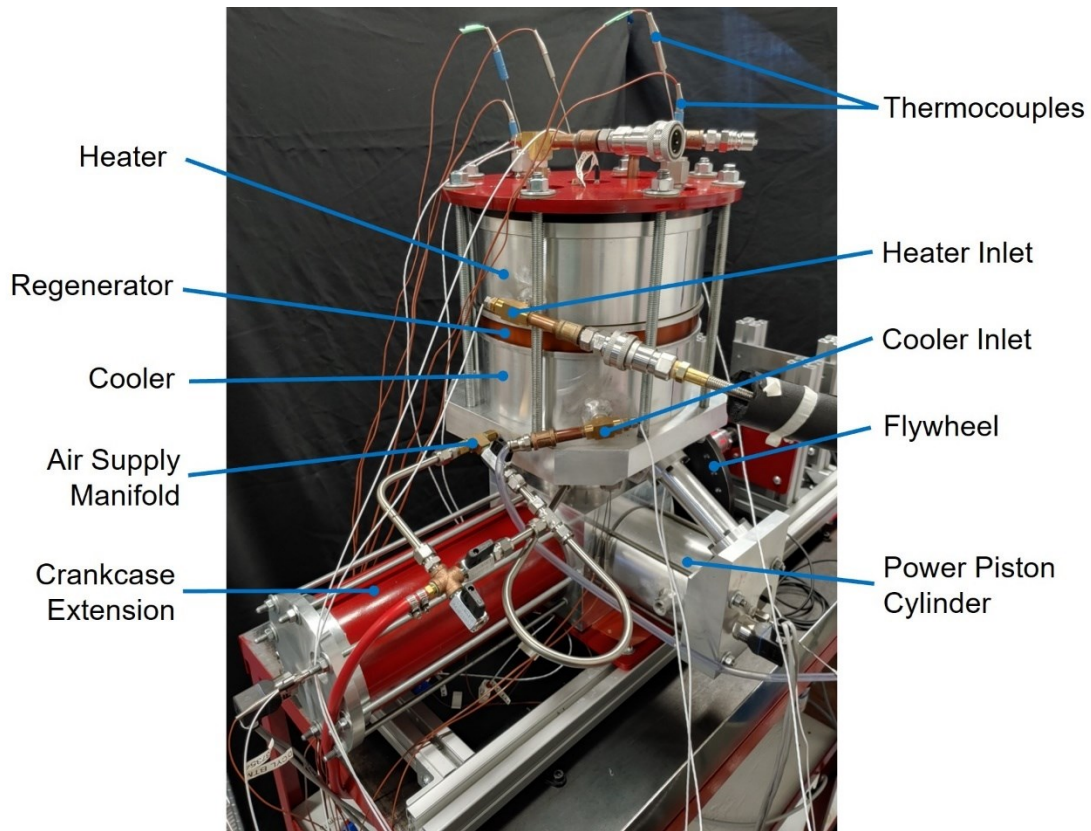


Figure 2.3: Photo of as-built *Raphael* engine with annotations.

Table 2.1: Properties of *Raphael* engine.

| | | |
|----------------|--|---|
| General | Outer dimensions (Length × Width × Height) | 646 × 425 × 602 mm |
| | Total mass | 75 kg (approx.) |
| | Materials | 6061 Aluminum (majority) |
| | | Carbon Steel |
| | | Polyurethane Foam, General Plastics FR-4718 [90] (Displacer piston) |
| | Polyetherimide / PEI (Figure 2.2, yellow) | |

| | | |
|--|---|---|
| General | Working fluid | Air |
| | Compression ratio | 1.1035 |
| | Piston phase angle | 90 degrees |
| | Charge pressure (experiments) | 0 – 450 kPa |
| | Speed / Frequency (typical) | 90 – 300 rpm |
| | Source / Sink Temperature (typical) | 150 / 5 °C |
| Volumes | Displacer piston swept volume | 2.36 L |
| | Power piston swept volume | 0.43 L |
| | Total dead volume (incl. heat exchangers) | 1.83 L |
| | Maximum Working Space Volume | 4.62 L |
| | Crankcase / Buffer volume (minimum) | 6.87 L |
| Displacer Piston | Piston Diameter | 198 mm |
| | Bore Diameter | 200 mm |
| | Stroke | 75 mm |
| | Seal | PTFE lip, 0.13 mm thick |
| | Connecting rod length | 130 mm |
| Power Piston | Diameter | 85.725 mm |
| | Stroke | 75 mm |
| | Seal | Crown seal, Carbon graphite filled PTFE |
| | Connecting rod length | 146 mm |
| Flywheel (incl. crankshaft) | Mass | 9.36 kg |
| | Moment of inertia | 0.0673 kg m ² |

The displacer piston is made of rigid polyurethane tooling foam and sits in the vertical displacer cylinder. The heat exchangers are in an annulus surrounding the displacer cylinder. The rod at the bottom of the displacer piston passes through two polytetrafluoroethylene (PTFE) bushings that provide linear guidance. The annular gap between the displacer piston and its bore is sealed by a very thin (0.13 mm) and flexible PTFE lip. This seal is loose and has no force pressing it against the bore, so it likely allows a considerable leak flow rate compared to the power piston seal which is much tighter. However, unlike the power piston, the spaces separated by the displacer piston do not have a large pressure difference between them, so leakage is not as critical here. From experience with other LTDSEs, loose displacer piston seals like the one used here have proven superior due to their low friction [89].

The power piston operates in its own horizontal cylinder that is connected to the displacer cylinder via a connecting pipe (Figure 2.2, light blue). It is guided in the bore by wear rings. The power piston seal is critical to engine performance as it needs to seal against the pressure differential between working space and crankcase, which has been measured to reach up to 80 kPa in this engine. At the same time, mechanical friction and wear are sensitive to the seal design and to the normal force between seal and cylinder wall. An ill-designed seal can drastically reduce the engine's performance or prevent it from running altogether, as difficulties with the *HTG* piston seal have shown [31]. Several seal geometries and materials were tested on *Raphael* by Speer [89]. Best performance was observed with a crown seal made of graphite-reinforced PTFE that is backed by a nitrile O-ring pressing it against the bore [89]. This seal was used for all experimental results in this work; its dimensions can be found at the end of the drawing package in Appendix F.

A slider-crank mechanism links the pistons to the crankshaft through connecting rods. Both pistons are connected to a single crank pin, meaning that the phase angle between the piston motions is equal to the physical angle of 90° between them. The piston axes and the crankshaft axis all meet in a point at the center of the crankcase. The crankcase extension has the purpose of increasing the crankcase volume, which reduces the crankcase pressure swing and thereby decreases the forced work and gas spring hysteresis loss (see Section 1.3). The displacer and power piston cylinders and the crankcase extension are each built as a stack of components that are compressed by tie rods on the outside, which allows for easy (dis)assembly.

All parts of the engine, including heater and cooler, are made of 6061 aluminium, except for the following. The inner part of the power piston cylinder, the crankshaft assembly, the crankcase extension pipe, the top plate of the displacer cylinder head, and fasteners such as tie rods are carbon steel. The regenerator walls and the plate below the displacer cylinder top (Figure 2.2, yellow) are made of polyetherimide (PEI) for thermal insulation against heat losses through conduction.

2.1.3 Heat Exchanger Geometry of *Raphael* Engine

The geometry of the heat exchangers is shown in detail here because these are the most critical thermodynamic components and need to be represented accurately in the model. All relevant heat exchanger parameters are summarized in Table 2.2 at the end of this section.

Heater, cooler and regenerator in the *Raphael* are stacked on top of each other and form an annulus that surrounds the displacer cylinder. As shown in Figure 2.2 the cooler and compression space are in the bottom where the power piston space is connected, which is favorable for the power piston seal as it will be operating at a relatively low temperature.

Figure 2.4 shows a section view of the heat exchanger geometry. Heater and cooler are two identical modules that transfer heat between the working gas on the inside and a liquid heat transfer medium that flows circumferentially through a channel on the outside (source channel). The section view in Figure 2.4 is aligned so that both the liquid inlet and outlet are sectioned, and the entire liquid flow path (colored red) is visible. The central component ('cartridge') that transfers heat through convection with the fluids and conduction between inside and outside is made from a single piece of aluminum. The empty space on the inside of the heat exchanger is occupied by the displacer piston. The inside has longitudinal fins that run parallel to the gas path and form rectangular channels through which the working gas flows. These can be seen in detail in Figure 2.4. Since it fills an annular space, the fins are tapered radially towards the inside. This shape was manufactured by cutting the channels axially into a solid block using a waterjet cutter [89]. Two channels are oversized to allow for thermocouples to be inserted to measure gas temperatures within the heat exchangers.

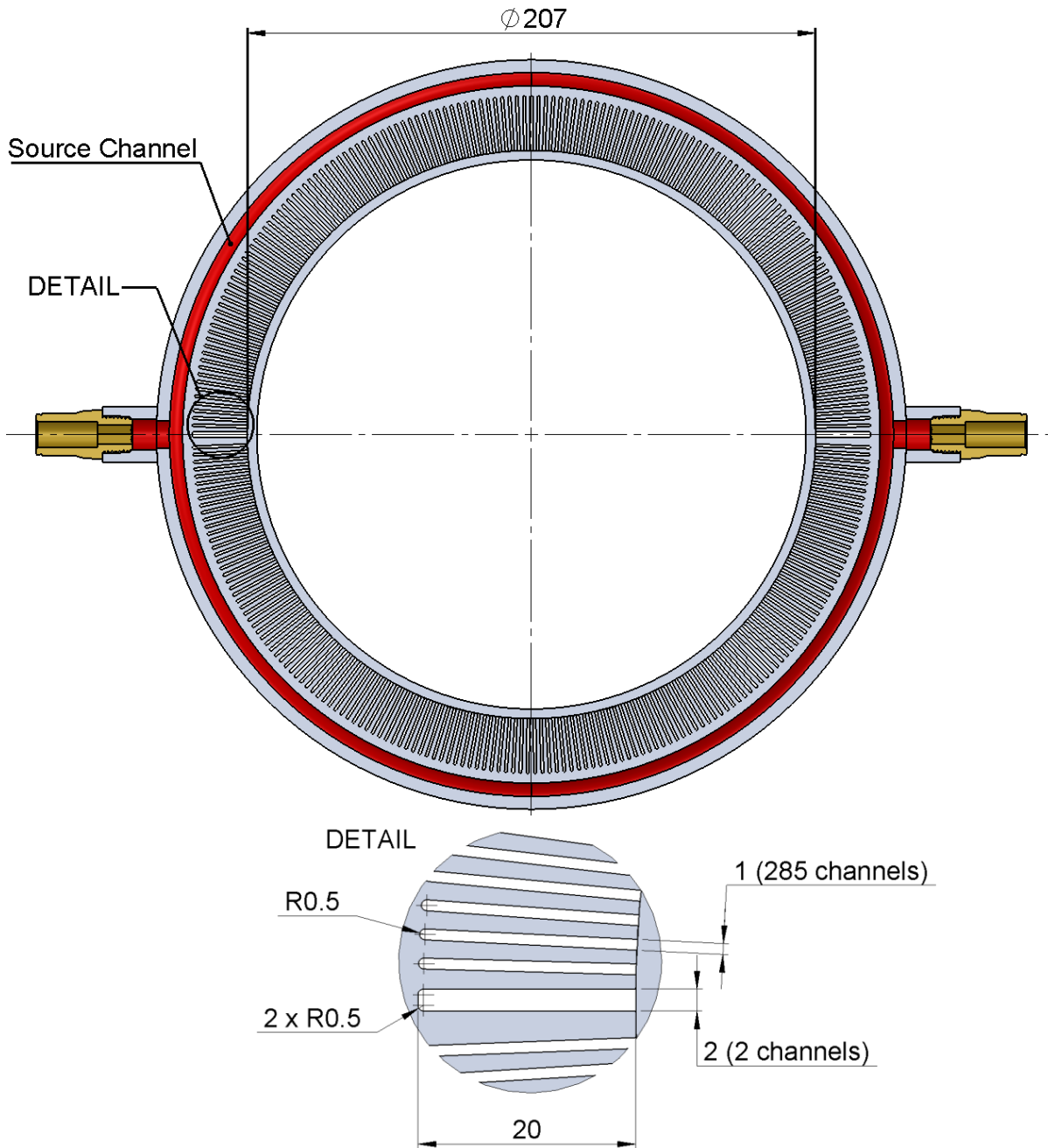


Figure 2.4: Horizontal cross section view of heater / cooler gas channel geometry from solid model. Detail of gas side fin / channel geometry. Dimensions in millimeters.

Figure 2.5 shows a vertical cross section of the upper part of the displacer cylinder including the heater and parts of the regenerator, displacer piston and displacer cylinder head. The left side of the image is the displacer cylinder centerline. Here, the source channel, the path of heat flow between source and working gas, and the gas flow path (blue arrow) can be seen. The displacer piston forces the air radially through a gap between the cylinder and the annulus, around a 180°

turn, axially through the heat exchanger stack, and radially back into the cylinder at the bottom side.

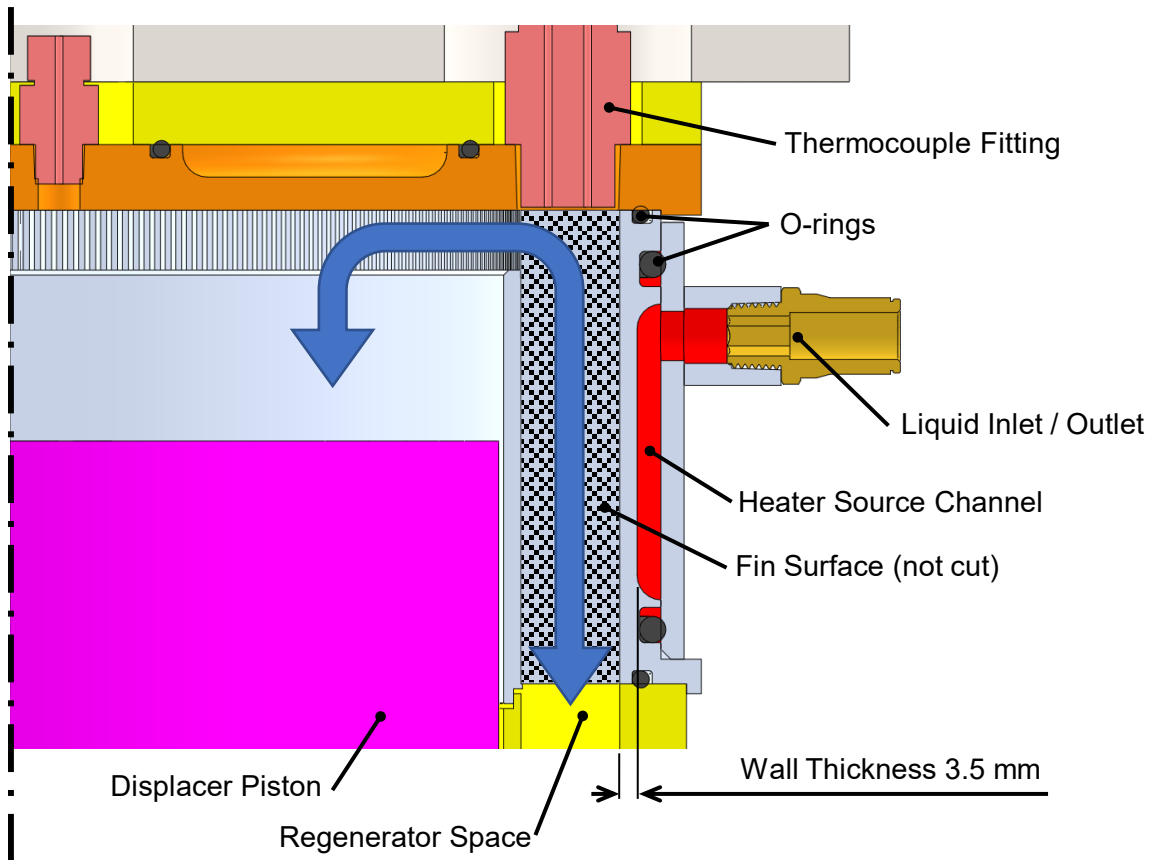


Figure 2.5: Vertical half-section view of upper displacer cylinder area from solid model showing heater geometry. Blue arrow indicates gas flow path.

The area shaded red in Figure 2.5 highlights the wetted volume of the heat source medium, which is a silicone oil for the heater and a water-ethylene glycol mixture for the cooler. This medium enters through an inlet, flows circumferentially around the cylinder, and exits through an outlet 180° apart from the inlet. The source channel has a nearly rectangular cross section with rounded edges, and no fins. Heat convects from the source medium to the wall, conducts through the 3.5 mm strong wall to reach the base of the fins on the gas side, then conducts further into the fins before convecting to the working gas. With this type of heat exchanger, the heat flow path is long and poses a high resistance to heat transfer compared with one where the heat exchanging media are closer together, such as an intercooler core or a plate-and-frame type. However, its advantage for this application is that it can be easily integrated into a cylindrical pressure vessel without requiring additional dead volume for ducting. The regenerator is housed in an annular

space between heater and cooler with the same inner and outer diameters as the heat exchanger gas channels. It is made of a matrix of random polyester fibers contained inside tubular gauze and can be seen in Figure 2.6. The porosity was varied between experiments. A thermocouple fitting can be seen above the gas channel that allows for two thermocouples to be inserted between the fins at different positions along the gas flow path.



Figure 2.6: Photo of regenerator matrix, made of tubular gauze and polyester fiber material.

Figure 2.2 and Figure 2.5 also show an orange-colored plate on top of the heater that marks the ‘ceiling’ of the displacer cylinder. It has a source channel similar to that of the heater, which allows the displacer cylinder head to be used as an additional heating surface and increase the temperature in the expansion space. However, during the experiments for Chapter 4 this heater was not used and disconnected from the liquid cycle because of leak issues. This allows for the accuracy of the finned heat exchangers in the model to be observed in isolation with no other heat sources or sinks affecting the results.

Similarly, the power piston cylinder can be cooled by pumping liquid through a channel in the cylinder wall, thus lowering the temperature in the power piston space. This additional cooler was expected to bring a gain in engine power because it would cool the gas in the power piston space during expansion so that the gas temperature would be lower during the following compression, which would increase the pressure swing. However, it did not cause a notable effect when tested experimentally [89]. During the experiments for Chapter 4 this cooler was not active.

Table 2.2: Properties of *Raphael* engine heat exchangers and regenerator.

| | | |
|--|---|---|
| Heater / Cooler (identical) | Depth (fin / channel length), all fins | 96 mm |
| | Fin / channel width, all fins | 20 mm |
| | Number of regular fins / channels | 287 |
| | Regular fin thickness | 1.46 mm (mean) |
| | Regular fin spacing / channel height | 1 mm |
| | Number of irregular channels | 2 |
| | Height of irregular channels | 2 mm |
| | Gas volume | 0.552 L |
| | Gas flow cross section area | 57.5 cm ² |
| | Gas surface area | 11,180 cm ² |
| | Heat source medium | Silicone oil, Fisher Scientific <i>Sil 180</i> [91] |
| | Heat source temperature | 135 – 150 °C (varies) |
| | Heat sink medium | Water – Ethylene Glycol 70:30 mixture |
| | Heat sink temperature | 5 °C |
| | Source channel height (aprx. rectangular) | 55.5 mm |
| | Source channel width (radial) | 4.8 mm |
| | Wall thickness between source and gas | 3.5 mm |
| Regenerator | Inner diameter / Outer diameter | 207 mm / 247 mm |
| | Depth (gas path length) | 25.4 mm |
| | Material | Random polyester fibers Diameter 0.1 mm Porosity 94 - 97 % (varies) |

2.2 Data Acquisition and Setpoint Control Equipment

This section details all hardware and software that was used for data acquisition and setpoint control in the experiment. The setup consists of sensors and control devices, a DAQ chassis with input/output modules, and a PC from which all data acquisition and control is managed. The raw data acquired consists of pressures, temperatures, crank angle, speed, and shaft torque. Table 2.3 lists all measured variables with their symbols. Setpoint parameters being controlled are the engine mean pressure, source and sink temperatures, and load torque. Table 2.4 shows the setpoint parameters and their symbols. The specifications of all sensors and hardware are listed in Appendix A.2.2.

Table 2.3: Measured variables with symbols.

| | |
|--|--------------------------|
| Heater / Cooler Liquid Inlet / Outlet Temperatures | T_{RTD0} to T_{RTD3} |
| Gas Temperatures | T_{TC0} to T_{TC9} |
| Mean Pressures | p_{m0} and p_{m1} |
| Dynamic Pressures | p_{d0} to p_{d3} |
| Atmospheric Pressure | p_{atm} |
| Shaft Torque | τ_{raw} |
| Crankshaft Angular Position | θ |
| Time for Voltage / Counter Data | t_{VC} |

Table 2.4: Controlled setpoint parameters with symbols.

| | |
|----------------------------------|--------------|
| Source Temperature (Heated Bath) | T_{Source} |
| Sink Temperature (Chiller) | T_{Sink} |
| Setpoint Pressure | p_{set} |
| Setpoint Torque | τ_{set} |

2.2.1 Pressure and Temperature Measurement Locations

Figure 2.7 shows the locations of pressure and temperature measurements on the engine body. Heater, cooler and pistons are colored for better readability. Each sensor is assigned a name based on its location in Table 2.5.

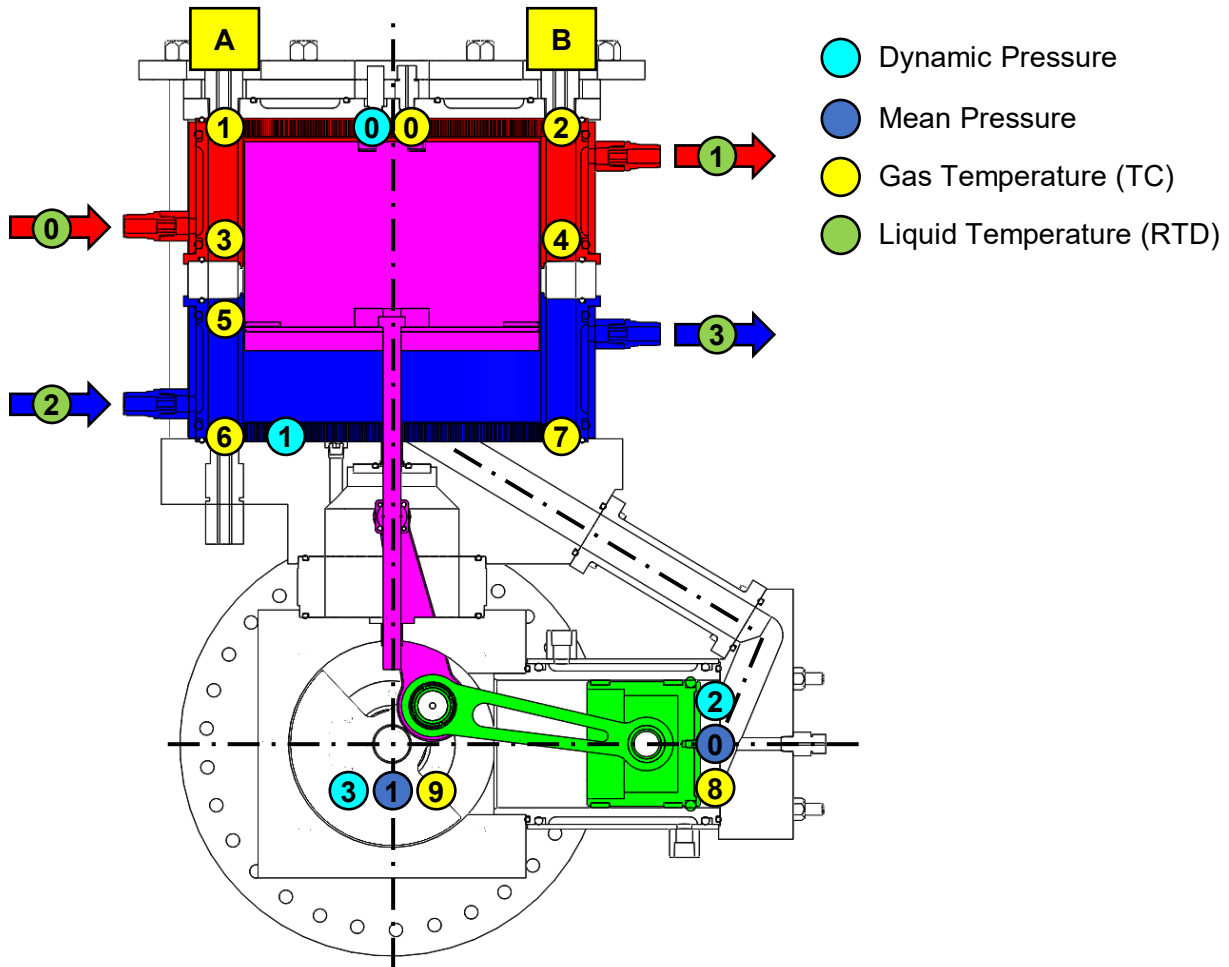


Figure 2.7: Vertical section view of solid model showing pressure and temperature measurement locations.

Table 2.5: Names of pressure and temperature sensor locations.

| Sensor Type | Number | Name |
|---------------------------------|--------|--|
| Mean Pressure | 0 | Power Cylinder |
| | 1 | Crankcase |
| Dynamic Pressure | 0 | Expansion Space |
| | 1 | Compression Space |
| | 2 | Power Cylinder |
| | 3 | Crankcase |
| Gas Temperature / Thermocouples | 0 | Expansion Space |
| | 1 | Heater / Expansion Space Interface, A Side |
| | 2 | Heater / Expansion Space Interface, B Side |
| | 3 | Heater / Regenerator Interface, A Side |
| | 4 | Heater / Regenerator Interface, B Side |
| | 5 | Cooler / Regenerator Interface, A Side |
| | 6 | Cooler / Compression Space Interface, A Side |
| | 7 | Cooler / Compression Space Interface, B Side |
| | 8 | Power Cylinder |
| | 9 | Crankcase |
| Liquid Temperature / RTDs | 0 | Heater Inlet |
| | 1 | Heater Outlet |
| | 2 | Cooler Inlet |
| | 3 | Cooler Outlet |

2.2.2 Pressure Sensors

Mean pressure and dynamic pressure are measured separately by different sensors and added together to obtain the overall pressure (see section 2.7). Since the mean pressure of the working space is assumed to be uniform, it is measured only at one location in the power piston cylinder. Dynamic pressure varies spatially and is additionally measured at the top and bottom of the displacer cylinder. The pressure drop across the heat exchangers can be calculated from these measurements.

The mean pressures of the working space and crankcase are measured using diaphragm pressure sensors (PMP300 FSH03103, FUTEK [92]). These measure relative pressure against the atmosphere. Their analog voltage output is read by the DAQ analog input module. The range of the mean pressure sensors (200 psi / 1379 kPa) is large because it needs to cover the maximum rated engine charge pressure (150 psi [89] / 1034 kPa), but this means they are too inaccurate to measure variables that are small compared to their range, such as the pressure swing (min. 23 kPa) and heat exchanger pressure drop (ca. 0.1 – 5 kPa).

To measure pressure swing and pressure drop more accurately and with minimal temporal delay, dynamic pressure is measured with flush-mounted piezoelectric sensors (113B28, PCB Piezotronics [93]) that are designed to capture high-frequency oscillations in the kilohertz-range. This approach is similar to Speer's [31], who adopted flush-mounted sensors after measuring the differential pressure across the regenerator with an outboard pressure transducer and discovering that the tubing between engine volume and sensor distorted the transient pressure measurement. The dynamic pressure sensors are controlled and read by a signal conditioner which provides an analog voltage output that is read by the analog input module of the DAQ system (see section 2.2.8). The sensors measure changes in pressure relative to the mean, and as such require a dynamic pressure with a minimum frequency of 0.5 Hz [93] to produce reliable data. Their response to a static pressure decays to zero within a few seconds. Since the lowest observed engine speed is about 1.5 Hz this application is considered to be within the sensors' valid operating range.

The thermodynamic processes within the engine depend on the density of the working fluid, which is a function of the absolute pressure. A comparison between data acquired at different times, locations or by different authors is only valid in terms of absolute pressure, meaning that the local atmospheric pressure must be recorded during each experiment. This is done using the

integrated barometric sensor in a smartphone, which was calibrated against a reference barometer (see section 2.4.4). All data in this work is presented as absolute pressure for the sake of usefulness to other researchers.

2.2.3 Temperature Sensors

Gas temperatures are measured with thermocouples (TCs) (TJFT72-T-SS-116G-6-SMPW-M, Omega [94]) that are inserted into the working space through compression seal fittings which seal them airtight. Their measurement tips were positioned at the locations shown in Figure 2.7. Heat exchanger temperatures are measured at two angular positions on the displacer cylinder spaced 180° apart (A and B side). The B side is closer to the duct connecting displacer and power piston spaces, and the A side is opposite from it. This asymmetry could cause different gas flow conditions between the two sides. Figure 2.7 suggests that the A and B sides are also aligned with the locations of heater and cooler liquid inlets and outlets, but that is not true for the real setup. The photograph in Figure 2.3 shows that the cooler inlet is positioned about 45 degrees from the B side and the heater inlet is approximately central between A and B. As can be seen in Figure 2.7 the temperature at the cooler-regenerator interface is measured only on one side (No. 5) because the engine design did not allow sensor access on the other side.

TCs were chosen because their response time, depending on the type and geometry of their measurement tip, can be low enough to register the cyclic temperature oscillation. The TC used here was a T-type with a 0.02-inch diameter grounded junction. According to the manufacturer, the response time should be about 0.9 seconds, but this is measured at a wind speed four to fifteen times higher than the average flow speed expected in the heat exchangers [95]. Thus, the response time in this application with lower speeds, meaning slower heat transfer between the thermocouple and its environment, would likely be greater. One engine cycle takes 0.6 seconds at a low-end speed of 100 rpm, which means that the TCs cannot resolve the transient gas temperatures accurately and only mean temperatures can be measured. The TCs were connected to the thermocouple input modules of the DAQ system.

Temperatures of the heat transfer liquids are measured using resistance temperature detectors (RTDs) (RTD-810, Omega [96]) which are placed into the liquid supply hoses right before the heat exchanger inlets and outlets. RTDs were selected because they had been found to be more

reliable in water than TCs [31]. A fast response time is not necessary here since temperatures in the source media are expected to change much more slowly than in the working space. The RTDs are connected to a RTD input module in the DAQ system.

2.2.4 Mean Pressure Control

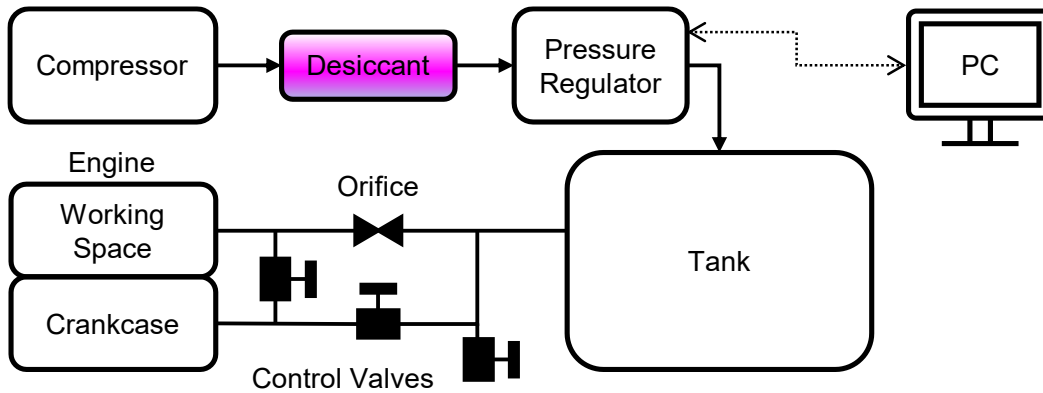


Figure 2.8: Diagram of pressure supply system

Figure 2.8 shows the setup used to control the charge pressure or mean pressure in the engine. Air at 150 psi is supplied by a compressor. Between the compressor and the engine is an electronic pressure regulator (QB3TANEEZP150PSGGBR, Proportion Air [97]) that regulates the pressure following a control voltage from the DAQ analog output module. The regulator is designed to hold a static pressure, so it may interfere with the engine's pressure swing if it was connected to the working space directly. To dampen the amplitude of pressure oscillation that the regulator observes, a 20-gallon air tank and a flow restrictor with a 0.025-inch diameter orifice were added between the regulator and the pressure inlet of the engine. The tank serves as a buffer space and the orifice limits the amount of air that passes back and forth between the engine and this buffer space during each engine rotation due to the engine pressure swing. At the same time, the orifice ensures that a change in engine mean pressure through leakage or temperature changes is still seen and corrected by the regulator. A module desiccant dryer is also part of the pressure line to remove moisture from the pressurized air.

There are separate pressure inlets for the engine working space and the crankcase. A set of ball valves allows to pressurize both spaces simultaneously or only the working space, and to bypass the orifice to accelerate the pressure change. During engine operation only the working space

pressure is regulated because the crankcase and working space pressures slowly equalize through minor leaks past the power piston seal and the bushing of the displacer rod.

2.2.5 Heating / Cooling Systems and Temperature Control

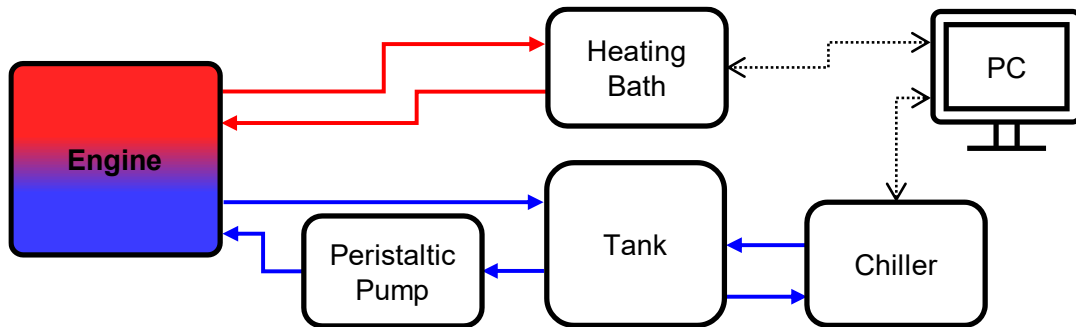


Figure 2.9: Diagram of heating and cooling systems with liquid flow loops.

Figure 2.9 illustrates the heating and cooling systems and the associated flow loops. Heat is supplied by an electric heated bath (Sahara PC201 S-45, ThermoFisher [98]) which heats about 41 litres of source medium (silicone oil) to a setpoint temperature and also circulates it through the engine's heater. The temperature is controlled from the PC directly via digital interface. The heating power going into the heater is calculated from the circulation pump flow rate, the medium's heat capacity and the temperatures measured at the heater inlet and outlet (see section 0). Initially, a peristaltic pump was to be used for circulation because this would allow to accurately control the flow rate, but it was found that the source medium at 150 °C would leak through the peristaltic pump tubing [89]. The built-in pump of the heated bath was used instead.

About 35 litres of heat sink medium (water – ethylene glycol) were stored in an insulated tank. The medium is cooled and circulated through the tank by an electric recirculating chiller (Merlin M150LR T1, ThermoFisher [99]). The temperature is again controlled directly from the PC. A peristaltic pump (Masterflex L/S [100]) is used to circulate the medium from the tank through the engine's cooler so that the flow rate can be controlled independently of the chiller. The cooling power or heat rejected by the engine is calculated similarly to the heating power.

2.2.6 Torque Control and Measurement

The engine speed is controlled by applying a torque load to the crankshaft. The resulting torque as well as the angular position and speed of the crankshaft are measured. Figure 2.10 shows the outside section of the crankshaft behind the flywheel with the installed devices.

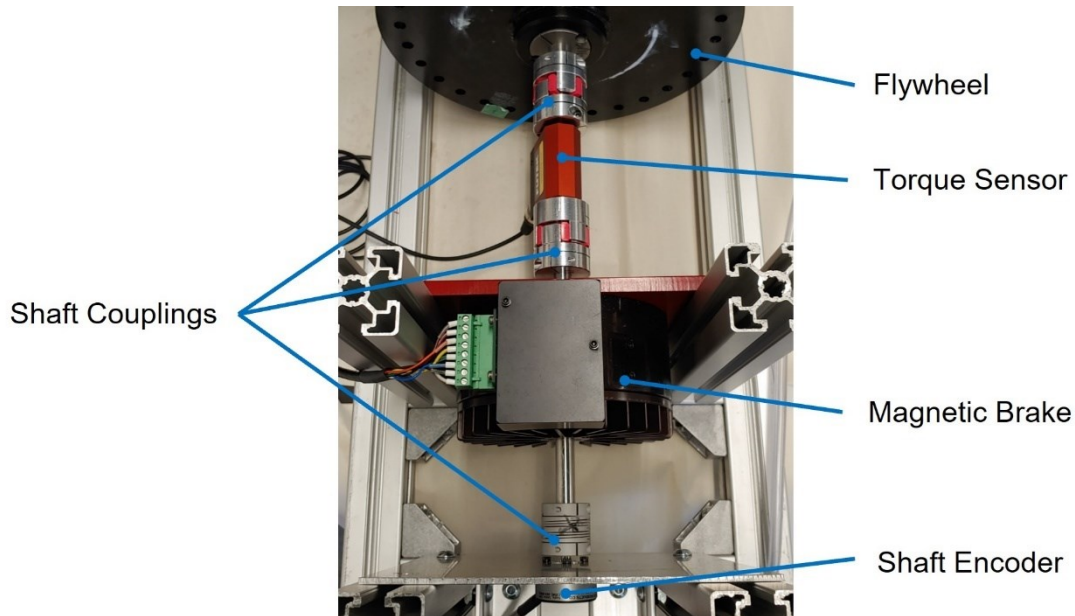


Figure 2.10: Photo of *Raphael* crankshaft with annotation of installed instruments.

Torque was applied by a magnetic brake (MBZ-5.7, Magnetic Brake Systems [101]) that is powered via electric current from a dedicated circuit. The setpoint torque is controlled by an analog voltage from the DAQ. This setpoint is only a rough estimate for the real torque that is transferred, which varies with rotational speed and also alternates in direction due to the alternating phases of forced work and efficacious work over the engine cycle (see Section 1.3.2). Therefore, the real, transient torque is measured between the flywheel and the brake by a non-contact torque sensor (TRS600 FSH01997, FUTEK [102]). It provides an analog voltage signal to the DAQ.

2.2.7 Crank Angle and Speed Measurement

The rotational speed of the crankshaft was measured and output as analog voltage by a sensor in the magnetic brake. This measurement is used for live monitoring of the engine speed, but it shows a significant zero-offset (ca. 7 rpm when engine stationary) and cannot be considered accurate for data analysis. It also does not provide information about the angular position.

An analog incremental shaft encoder (15S-19M1-0500NV1ROC-F03-S1, Encoder Products Company [103]) is installed at the end of the crankshaft to provide a crank angle measurement at 500 pulses per rotation, from which the instantaneous engine speed at any point in the cycle can be calculated. An alignment pulse that is sent once per rotation makes it possible to measure the angular position. The pulses from the encoder are read by a counter module on the DAQ. The angular position measurement is necessary to link the dynamic pressure data to corresponding positions of the pistons and thus generate the indicator diagram.

2.2.8 DAQ System and Software

The input and output of all analog signals from sensors and control devices is handled by a commercial DAQ system (cDAQ-9189, National Instruments Inc. [104]). The different types of inputs/outputs are sent and received by different DAQ modules that sample the data and perform digital-analog conversion. All modules are bundled on a chassis which communicates with a PC via Ethernet. To summarize the DAQ and control system, Figure 2.11 illustrates the system of devices and data flows between them. All of the instruments and devices of the system are listed in Appendix A.2.2.

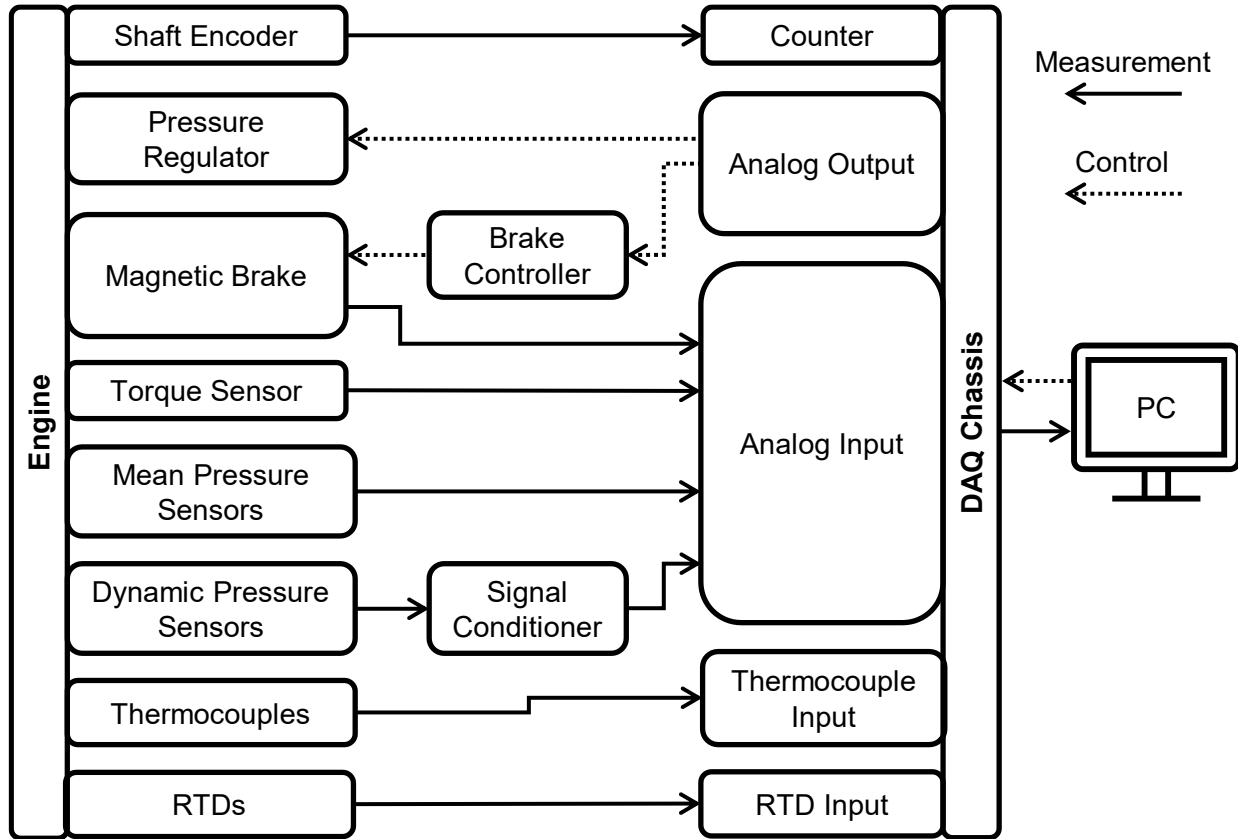
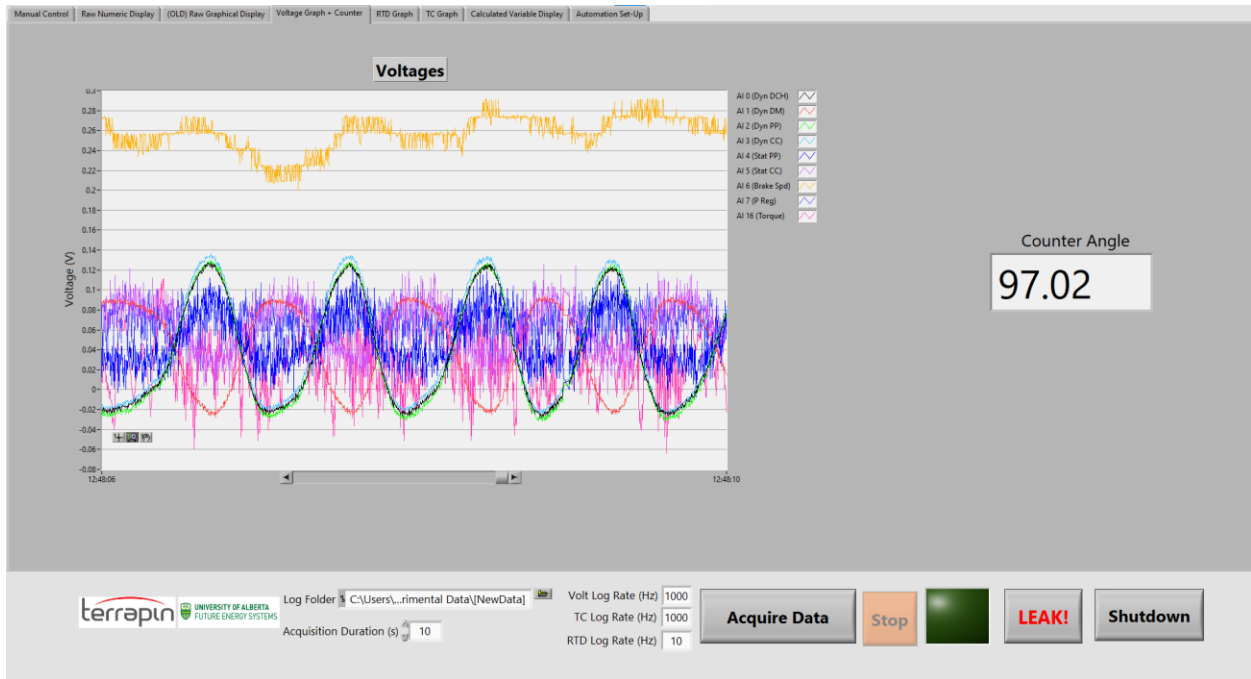
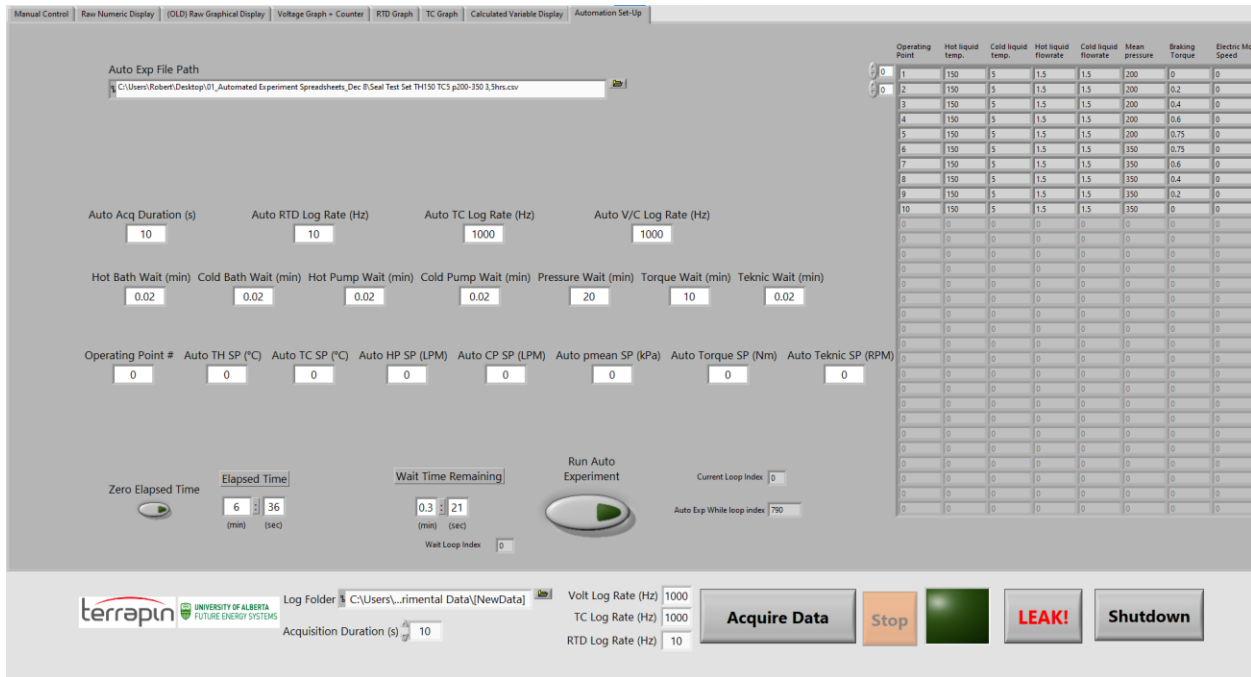


Figure 2.11: Diagram showing flow of data and control signals in DAQ system.

The user controls all setpoint parameters and data acquisition through custom developed software (LabVIEW, National Instruments Inc.). Figure 2.12 shows different parts of the software user interface. The program allows live monitoring of all sensor readings, manual setpoint control, manual acquisition of single datapoints, and automated experiments in which datasets are recorded at setpoints from a pre-defined list with defined wait times between the setpoints. Data is stored in the form of three text files per datapoint: Thermocouple data, RTD data, and analog voltage and counter data. The time for each sample is also stored. These are then fed into a custom processing scheme (MATLAB, The MathWorks Inc.) which applies calibration and obtains calculated variables (see section 2.7).



(a)



(b)

Figure 2.12: Screenshots of DAQ software in NI LabVIEW showing (a) live monitoring of voltage inputs and (b) automated experiment controls.

2.2.9 Data Sampling Duration and Frequencies

The frequencies at which the measured variables were sampled and the duration of each datapoint when acquiring regular datasets for Chapter 4 were determined by considering the maximum engine speed and the samples per crank angle resolution required.

To gather sufficient data for averaging, the aim was to record at least $n_{cyc} = 15$ engine cycles. The engine had not been able to run at a speed below 100 rpm, therefore $f_{min} = 90 \text{ rpm} = 1.5 \text{ Hz}$ was chosen as an absolute minimal speed. The acquisition duration was determined as:

$$t_{datapoint} = \frac{n_{cyc}}{f_{min}} = \frac{15}{1.5 \text{ s}^{-1}} = 10 \text{ s} \quad (11)$$

The data from pressure sensors, torque sensor and shaft encoder must be sampled at a high resolution as their crank angle-dependent values are used. The purpose of the experimental data is the comparison against the *MSPM* model, which uses a speed-dependent time step of $n_{MSPM} = 200$ intervals per engine cycle as the resolution for the output data. It was considered appropriate to sample the experiment data at minimally the same resolution. The highest engine speed observed at steady state was $\sim 240 \text{ rpm}$, so with some upward buffer $f_{max} = 300 \text{ rpm} = 5 \text{ Hz}$ was taken as the maximum speed. The sampling frequency for voltages and encoder counter signal follows as:

$$f_{VC} = n_{MSPM} f_{max} = 200 * 5 \text{ Hz} = 1000 \text{ Hz} \quad (12)$$

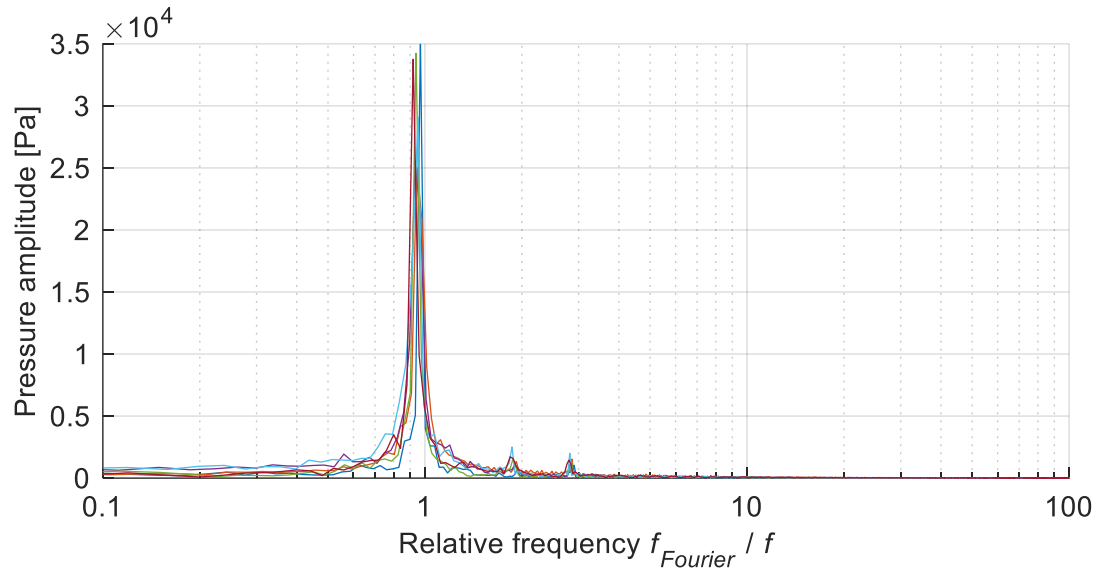
To verify that the chosen sampling frequency was sufficient to capture any frequencies present in the signals, the sampling rate theorem as stated by Wheeler and Ganji [105] was utilized. It states that the sampling rate must be higher than twice the highest frequency in the signal to be able to capture and reconstruct the original signal completely [105] as defined by:

$$f_{sample} > 2 f_{max,signal} \quad (13)$$

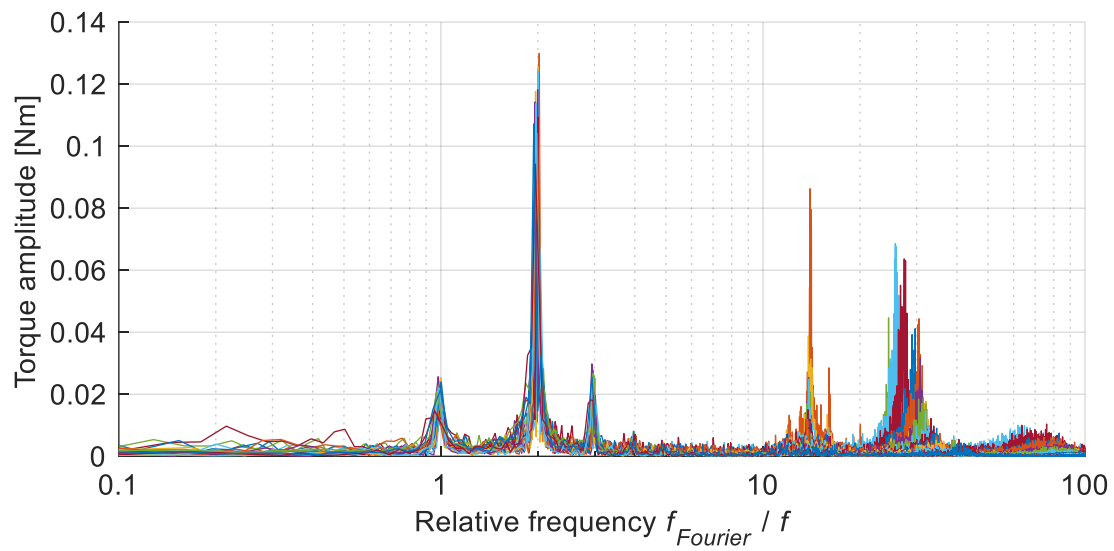
To find the highest recorded frequency in the sensor voltage signals, a spectral analysis by fast Fourier transform (FFT) was performed on the signals (MATLAB, The MathWorks Inc.). This method shows the amplitudes and frequencies, up to one half of the sampling frequency, of any waveforms that represent the signal. Dynamic pressure and torque signals were analysed as these are the only variables of which the transient data is used.

Figure 2.13 (a) shows the resulting frequencies and amplitudes in the dynamic pressure data of a dataset. Each line represents one datapoint with 10,000 samples. Frequencies are shown relative to the average engine speed f for each setpoint because any peaks are expected at frequencies that are multiples of f . All curves have a large peak close to the engine speed, which is the first harmonic [105]. Much smaller peaks with amplitudes of less than 10 % of the first harmonic can be seen at the second and third harmonics. The domination of the first harmonic confirms the expectation that the pressure oscillation is dominated by the engine speed as it is caused by the piston motions.

Figure 2.13 (b) shows the same plot for the torque sensor data of a different dataset. The dominant frequency with the largest peak here is the second harmonic. This shows that the main oscillation of torque occurs at double the engine speed. It is likely caused by the transitions between intervals of efficacious and forced work that occur twice per cycle (see Section 1.3.2) and are also transitions between acceleration and deceleration of the engine speed, thus affecting the measured torque. The first and third harmonics are also significant in all curves. Some datapoints show peaks at the 14th harmonic, between 24 and 31 times f , and around $60 f$. These frequencies and amplitudes vary between datapoints, which suggests they may be caused by resonance effects at certain engine speeds.



(a)



(b)

Figure 2.13: Spectral analysis samples of pressure and torque signals acquired at $f_{VC} = 1000$ Hz. Frequency shown on logarithmic axis and normalized with mean engine speed f . (a) Pressure p_{PC} at setpoint $p_{set} = 450$ kPa. (b) Shaft Torque at setpoint $p_{set} = 200$ kPa.

The highest found frequencies with a potentially relevant amplitude are shown in Figure 2.13 (b) and are below $100 f$. Thus, following the sampling rate theorem:

$$f_{VC} > 2 * 100 f_{max} = 200 \times 5 \text{ Hz} = 1000 \text{ Hz} \quad (14)$$

This result matches with the value for f_{VC} found with equation (12) and therefore the sampling frequency was chosen appropriately.

As discussed in section 2.2.3 the thermocouple and RTD temperature measurements were only used as averages so they may be sampled at a lower frequency. The thermocouple input module was set to the most accurate sampling mode ‘high resolution’ to minimize the error in the mean temperature data. This limits the frequency to:

$$f_{TC} = 1.8 \text{ Hz} \quad (15)$$

which yields 18 samples per datapoint considering $t_{datapoint}$. Since the thermocouples readings are not expected to oscillate significantly due to their response time, this number of samples should be sufficient to calculate an average temperature.

The RTD frequency is neither limited by the DAQ nor required to be higher than the thermocouple frequency. It was chosen arbitrarily as

$$f_{RTD} = 10 \text{ Hz} \quad (16)$$

2.3 Sample of Raw Data

A sample of raw data obtained with the setup described in previous sections is presented here for a qualitative assessment. In Figure 2.14 plots (a) and (b) show engine speed (calculated from angle θ) and torque τ_{raw} for a setpoint with $p_{set} = 450$ kPa and $\tau_{set} = 1.04$ Nm. This datapoint has a high setpoint pressure, meaning that the efficacious and forced work exchanged with the flywheel are relatively large, and a low speed, meaning that the energy of the flywheel is low. This combination leads to the strongest speed and torque oscillations of any recorded datapoint which are seen in both curves. The data appears very regular with few outlier samples which suggests that the cycle averaged data will be of good quality.

Plots (c) and (d) in Figure 2.14 show the readings of all pressure sensors for a setpoint with $p_{set} = 450$ kPa and $f = 130$ rpm. The curves of dynamic pressure are visibly smoother than those of mean pressure, suggesting that the mean pressure sensors would likely be inadequate to produce accurate indicator diagrams. The crankcase mean pressure p_{m1} is visibly lower than the working space mean pressure p_{m0} . The dynamic pressures p_{d0} to p_{d2} measured at different locations in the working space are overlapping as the differences between them are small compared to the pressure swing.

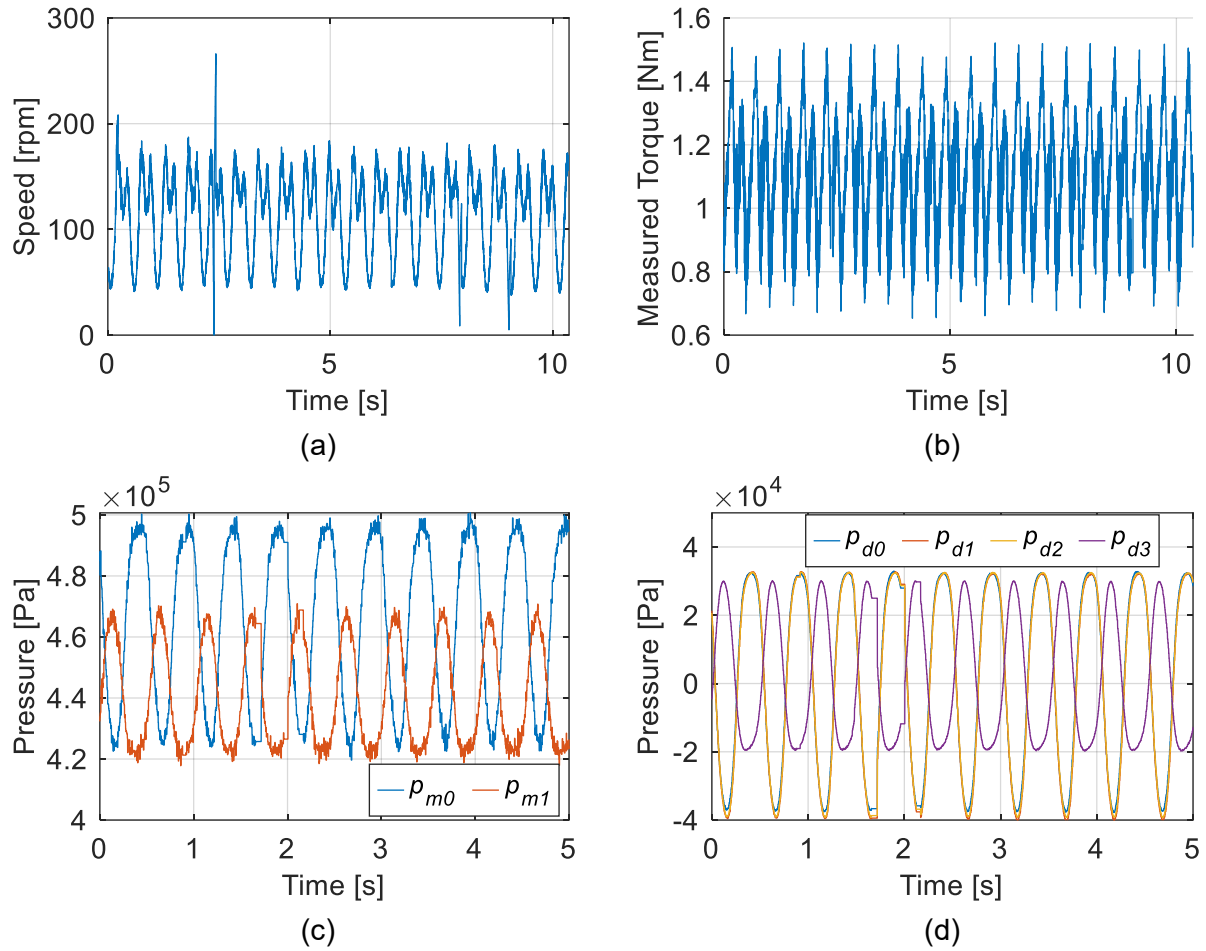


Figure 2.14: Sample plots of raw data from voltage and counter measurements. (a) speed from crank angle data, (b) torque, (c,d) mean and dynamic pressures (first 5 seconds).

Figure 2.15 shows raw temperature data from TCs and RTDs for a setpoint with $p_{set} = 400$ kPa and $f = 129$ rpm. The TC sampling frequency is not a multiple of the engine speed:

$$\frac{f_{TC}}{f} = \frac{1.8 \text{ Hz}}{129 \text{ rpm} / (60 \frac{\text{rpm}}{\text{Hz}})} = \frac{1.8 \text{ Hz}}{2.15 \text{ Hz}} \cong 0.84 \quad (17)$$

This means that TC data is taken at different positions in the engine cycle. However, no significant changes are visible in any of the TC plots, confirming that the TC response time is too long to register the cyclic fluctuations as explained in section 2.2.3.

There appears to be large temperature differences between TC 3 and 4, and between TC 6 and 7. These pairs of sensors are located at equal positions on the A and B sides of the heat exchangers. The differences between them are unexpected and suggest there may be a strong preferential gas flow or source / sink temperature difference between the two sides.

In Figure 2.15 (c) the RTD readings are nearly constant during one datapoint. The liquid temperature drop between inlet and outlet is greater for the cooler than for the heater.

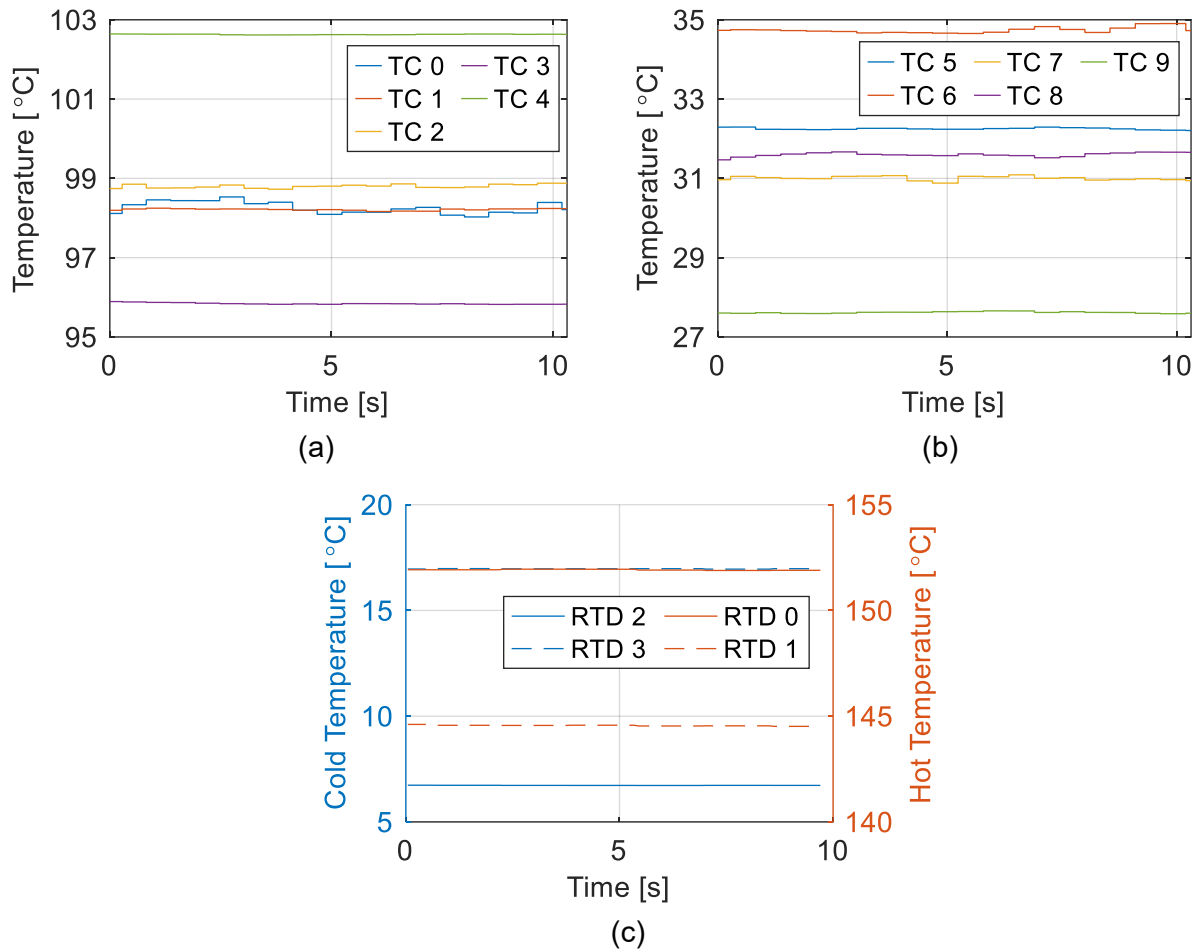


Figure 2.15: Sample plots of raw temperature data. (a) hot side gas thermocouples, (b) cold side gas thermocouples, (c) liquid RTD temperatures.

2.4 Calibration of Sensors and Pumps

Methods used to calibrate sensors and pumps, sources of calibration data, and assumptions made related to these are described in this section.

2.4.1 Temperature Sensor Calibration

All temperature sensors must be calibrated against some reference to minimize the influence of each sensor's individual bias on the processed data. Ideally this reference would be a known 'true' temperature like the melting point of water, which would allow to remove the absolute error of each separate sensor from the system. However, because of the complexity of performing such a calibration across the experiment's temperature range, a relative calibration method was used instead. It is based on the procedure followed by Speer [31] with a similar setup.

All sensors (TCs and RTDs) were bundled together and immersed into the heat source or sink liquid at different temperatures. In the experiment, all temperatures must be between sink and source temperature, therefore the calibration temperatures were chosen from 5 °C to 20 °C with increments of 5 °C and from 30 °C to 160 °C with increments of 10 °C. To calibrate at 5 °C to 20 °C the sensors were placed into the heat sink liquid tank and for 30 °C to 150 °C into the heated bath. At each calibration temperature a 10-second data sample was acquired. The data from each sensor was averaged over the sample. Then, for each calibration temperature the average measurement from all sensors was used as the 'true' reference temperature. The deviations of each sensor from this reference were calculated and third-order polynomial fits were applied to this data to obtain a correction function for each sensor. The raw temperature data from experiments were passed through these functions to yield data corrected for the 'true' mean temperature. Thus, the sensors were calibrated relative to each other, which removes any deviations between their measurements at the same temperature. If the deviation of the 'true' mean temperature from the actual temperature is roughly constant across the relevant temperature range, then this calibration would reduce the uncertainty in measured temperature differences, such as between the heat exchanger liquid inlets and outlets. This is likely, but cannot be proven without a known reference temperature, therefore the calibration is not considered in the uncertainty analysis in Appendix B.1 and B.2. The procedure does not improve the absolute accuracy of individual temperature measurements.

Figure 2.16 compares the deviation of all sensor readings from the reference temperature before and after applying the calibration curves. The remaining errors after calibration are due to the deviations of the polynomial fit functions from the data they were fit to. Deviations exist because the data was not always smooth. This is likely due to inconsistencies in sensor placement during the calibration causing slight temperature differences between sensors, and could be improved with a calibration apparatus that would immerse all sensors in a defined and repeatable way. The polynomial fit has a desired smoothing effect on the data.

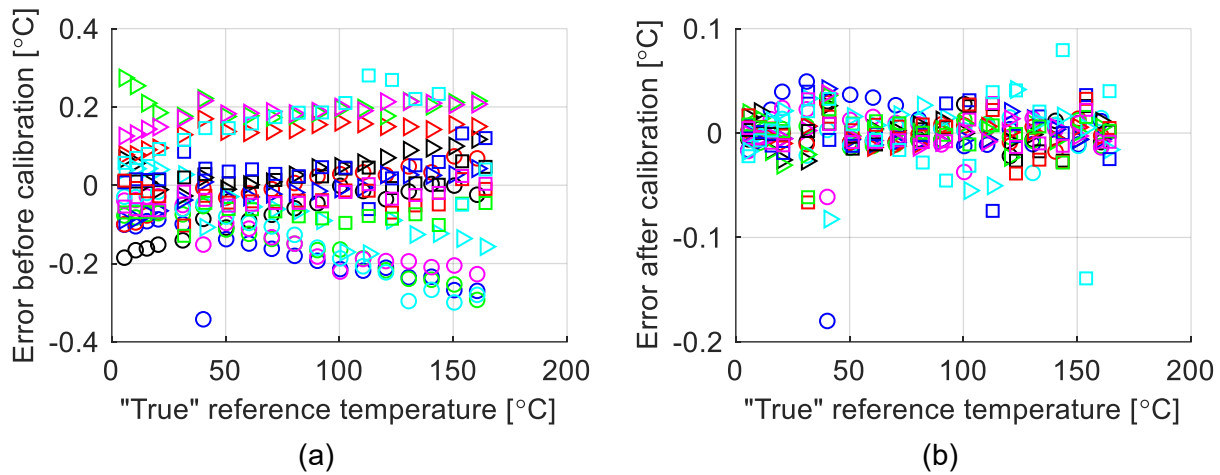


Figure 2.16: Comparison of measured temperature error over calibration temperature range before (a) and after (b) calibration is applied. For all RTD and TC sensors.

Figure 2.16 shows that the range of errors decreased through calibration from ± 0.4 °C to ± 0.2 °C and most points are within ± 0.05 °C. This is supported by the root sum square of all error values which reduces from 2.26 before to 0.41 after calibration.

2.4.2 Pump Flow Rate Calibration

The mass flow rates of the heat transfer liquids through heater and cooler must be known accurately to calculate the heat flow rates into and out of the system (see section 0). The pump settings remained unchanged between experiments, so the calibration needed to be performed only once.

First, the source and sink flow rates were adjusted so that the engine in operation would cause a temperature change of more than 5 °C between the liquid inlets and outlets, which is greater than the uncertainty in the measured RTD temperature difference (see Appendix C.2.1). Then the mass

flow rates were measured by taking timed samples of the liquids from the return lines to the heated bath / tank. For the cooling side, the sink temperature was constant across all experiments and a positive displacement pump was used, so the flow rate would be constant and only one measurement at 5 °C was taken. On the heating side, the source temperature was varied between experiments, which affects the fluid density and therefore the mass flow rate. The turbine pump of the heated bath could only be controlled in terms of power and would produce a varying flow rate depending on the pressure drop in the flow loop and the fluid’s viscosity. Therefore, the flow rate was measured at a range of source temperatures. The calibration procedure is described in Appendix C.1. A third order polynomial fit was used to obtain a function for the heater flow rate over temperature. Figure 2.17 shows the resulting plot and equation. The cooler flow rate was significantly lower at 0.0236 kg/s.

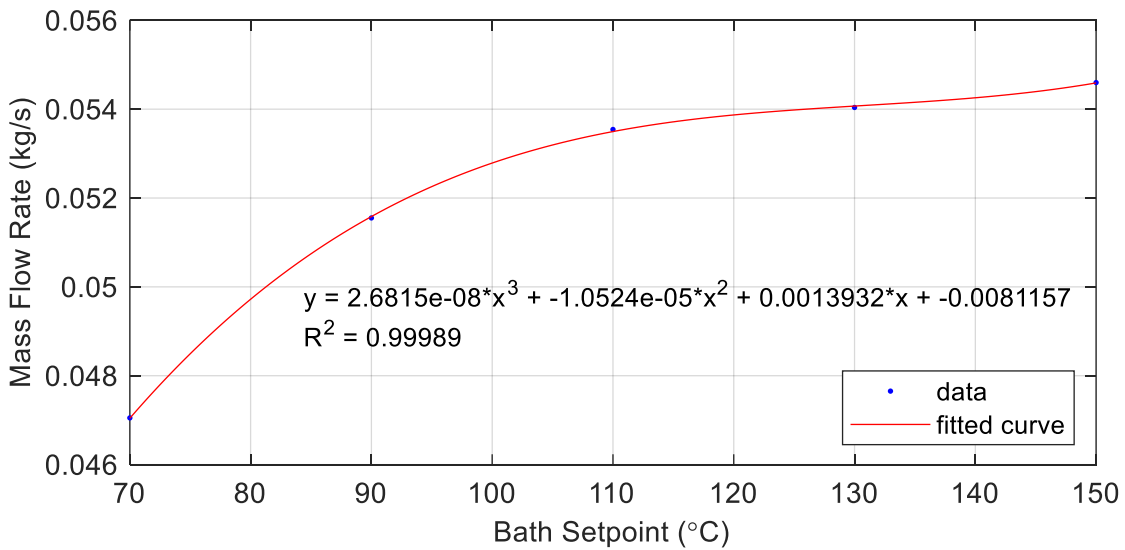


Figure 2.17: Plot and fit equation of heater liquid flow rate vs. setpoint temperature.

2.4.3 Specific Heat of Heat Transfer Fluids

Another variable critical to calculate heat flow rates is the specific heat of the source and sink liquids. The sink medium was a mixture of distilled water and ethylene glycol that had been mixed at a known ratio but was topped up and diluted with more water during previous experiments. Its specific heat was determined by measuring its density, determining its mixture ratio and finding the specific heat from available fluid data. The ethylene glycol mass fraction was determined to

be around 30 % and the corresponding specific heat was calculated as $c_p = 3770 \text{ J/kg K}$. This is documented in Appendix 0

For the source medium *Sil 180* [91] the supplier gives the specific heat only at 20 °C. Comparing this value to data of similar silicone oils showed that the specific heat is expected to change significantly over the experimental temperature range, and that the properties of two fluids with similar chemical formulas (Polydimethylsiloxane) can be different, possibly due to different molecule lengths. Another factor was the fluid's age of more than three years, which was beyond the supplier's recommended use time and may cause a deviation from its original properties. As a result, the temperature-dependent specific heat of the fluid could only be estimated by extrapolation using the trend in the data of a similar fluid.

Density and viscosity are provided for *Sil 180* over the relevant temperature range. Comparing these to a range of other silicone-based heat transfer fluids, *Sil 180* was found to be most similar to a product named *SYLTHERM 800* (The Dow Chemical Company) [106]. Their density is equal to within 1.2 % while viscosity deviates by up to 33 %. Their specific heat at 20 °C differs by 6.5 %. Using the data of specific heat over temperature for *SYLTHERM 800* and adding the offset at 20 °C to it, an estimated specific heat curve for *Sil 180* was created that can be seen in Figure 2.18. Though based on the assumption of similarity between the fluids, this solution was expected to be more accurate than applying the value for 20 °C to the entire temperature range.

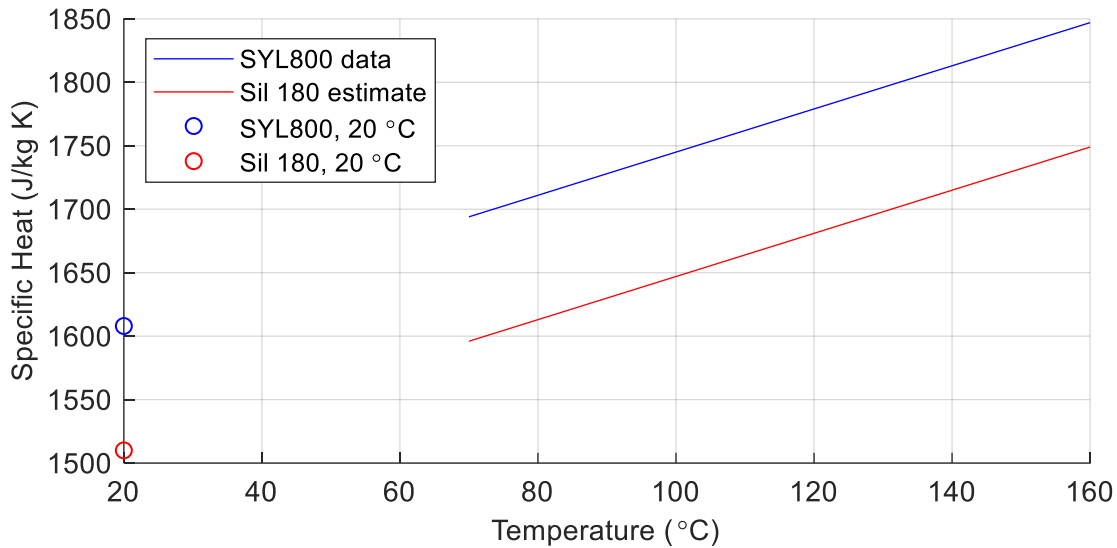


Figure 2.18: Plot of *Sil 180* specific heat estimate vs. temperature.

2.4.4 Pressure and Torque Sensor Calibration

The static and dynamic pressure sensors and the torque sensor were calibrated by the manufacturers when purchased. Linear curves were fitted to the calibration data from the manufacturers and used to process the experimental data. At the time of the experiments the recalibration time recommended by the manufacturers (one year) had been surpassed by several years for all sensors. This must be kept in mind as a potential source of error, but it cannot be quantified as there is no data on sensor drift over time from the manufacturers. It was assumed that any drift in these sensors would be much smaller than the deviations between experimental and model data observed in Chapter 4. If the accuracy of the indicator diagrams and the shaft power will have to be improved for future analysis of smaller model deviations, the sensors should be sent to the factory for recalibration.

The atmospheric pressure sensor of the mobile device was calibrated against a mercury barometer. The barometer reading was corrected for latitude and temperature. A constant offset between the barometer and the sensor was determined and corrected for in the mean pressure data, and the error in the barometer reading was applied. See Appendix B.8.1 for documentation.

2.5 Experiment Operating Procedures

In this section the procedures followed to acquire experimental data reliably are outlined, and the time intervals chosen for warm-up and between datapoints are explained. First, the engine was stationary while going through a warm-up period until the temperatures of the source and sink media reach their setpoints. At this point, the temperature difference between heater and cooler is close to the source and sink temperature, causing the engine to run at a high speed when started and gradually slowing down while the internal temperatures move towards a steady state. When considered steady, data recording can begin. As the setpoint is changed for each datapoint, steady state must be reached again. The criteria for steady state are investigated in section 2.6.

2.5.1 Warm-up and Preparation for Experiment

1. Check experimental setup and workspace for defects and hazards:
 - Liquids on floor, anywhere along liquid flow loops.
 - Cables and tubes are no tripping hazards, correctly plugged in and organized.
 - Loose tools and components are safe from falling / rolling away and organized.
2. Power up computer. Enable power for DAQ system, compressor, pump, heater, chiller. Turn on dynamic pressure sensor signal conditioner.
3. Run NI MAX software (National Instruments), find the DAQ chassis and run 'Self-test' to ensure that data acquisition will work correctly.
4. Run LabVIEW software and verify that all instruments are working properly.
5. Set source temperature and turn on heated bath.
 - Ensure all installed sensors on hot side are rated for set temperature.
 - Ensure hot components are not in contact with anything not heat resistant.
 - Check entire hot liquid system for leaks.
6. Check desiccant dryer next to pressure regulator and replace if necessary.
 - To restore used material, place in oven at 350 °F for 15 minutes.

7. Align shaft encoder:
 - While viewing encoder angle in LabVIEW, rotate crankshaft until angle jumps to 0° .
 - Rotate crankshaft so that marker on flywheel faces horizontally towards the side opposite the power piston. This position should coincide roughly with angle 0° .
 - If need to re-align, remove dynamic pressure sensor from power cylinder head.
 - Use a dial gauge through the sensor hole to align piston top dead center with angle 180° . Tighten the encoder coupling when done and reinstall sensor.
8. Set sink temperature and turn on chiller.
9. Open cold liquid tank and ensure that chiller is circulating fluid!
 - If not, locate the chiller return tube by the label on the back panel of the chiller.
 - Lift up the tube as high as possible to get the circulation started.
 - If unsuccessful, turn chiller OFF immediately!
10. Start the peristaltic pump for the cold liquid.
 - Ensure that pump head is closed!
 - Check entire cold liquid system for leaks.
11. Ensure valves on manifold are in correct position and set charge pressure.
12. Before starting engine, wait until temperatures are close to a static steady state.
 - Heated bath and chiller have reached setpoint temperatures
 - RTD temperatures have stabilized
 - This takes about 1 hour for the heated bath at 130°C and 15 minutes for the chiller.

2.5.2 Start-up and Steady State

1. Close air valves on manifold.
2. De-cog magnetic brake to ensure no torque is applied.
3. Start engine by pushing flywheel in direction of arrows.
4. Make sure setpoint parameters are set equal to first setpoint of planned experiment.
5. Let engine run for specified steady state time (see section 2.6).
 - 1 hour was used for experiments in Chapter 4.

2.5.3 Data Acquisition Procedure

1. Ensure that temperatures and speed have not changed significantly for over the past ~15 minutes before taking any data.
2. Set output folder and take a manual datapoint to ensure that data is logged correctly.
3. Record atmospheric pressure at start and end of experiment. Use the mean for processing.
4. Start acquisition manually or automated using list of setpoints and acquisition parameters.
 - All datasets in Chapter 4 have constant mean pressure, only torque changes between setpoints, to minimize the wait time between setpoints for steady state.
 - Wait time depends on parameter change between setpoints (see section 2.6).
 - 10 minutes was used for experiments in Chapter 4.

2.6 Reaching Steady State in Experiment

In Chapter 4, the experimental data is compared to a model which assumes a ‘numerically perfect’ steady state where the remaining change in the solution variables between cycles is arbitrarily small. Therefore, it is critical that the data is acquired when the engine is close to a steady state of operation.

The timescale of reaching steady state and the engine’s dynamic behaviour during this time depend on the engine geometry and the difference between the engine’s initial (unsteady) thermal state and final (steady) thermal state at the setpoint. This topic has been studied little as SEs are usually designed to operate at a steady state without interruption for long periods of time, hence unsteady behaviour has been of low interest. Findings presented in this section aim to determine a ‘time to steady state’ (TTSS) using the *Raphael* engine as an example.

2.6.1 Time to Steady State (TTSS)

The thermal state of an engine is essentially the distribution of thermal energy in its working gas and solid components at a given time. The working gas has a small volumetric heat capacity due to its low density compared to the solids, and most of the gas undergoes a temperature swing in the heat exchangers during each cycle, meaning that gas temperatures react much more quickly to changes of the operating point than solid temperatures. In solids, thermal energy is transferred only by conduction and the ‘reaction speed’ of a material to temperature changes is quantified by its thermal diffusivity (α) as defined in equation (18):

$$\alpha = \frac{k}{\rho c_p} \quad (18)$$

where: α = thermal diffusivity (m²/s)

k = thermal conductivity (W/m K)

ρ = density (kg/m³)

c_p = specific heat capacity (J/kg K)

Thus, the TTSS depends primarily on the time that a temperature change takes to propagate between the gas, the heat source/sink and the solids that undergo temperature changes, by convection and conduction. This is related to the thermal diffusivity of the solids and the heat transfer resistances posed by convection. In a similar way, this applies to the convergence time of a time-resolved numerical model like *MSPM* [33]. This was observed while producing data with *MSPM* for the validation in Chapter 4 as the model converged more quickly when convective heat transfer resistances at the source and sink were reduced. It may be possible to deduce a parameter with unit (seconds / °C) that quantifies the TTSS for a machine and a given change in gas temperatures, but that would exceed the scope of this analysis.

It is difficult to model the transient behaviour of an engine without a detailed and validated transient model of its solid structure and heat transfer mechanisms. For prior experiments at *DTECL* the TTSS was determined by observing gas temperatures and/or engine speed, and assuming steady state when the curves of these parameters appeared to plateau [30], [31], [41]–[43]. Table 2.6 shows the wait times found using this method. The source temperatures and speed of the engines used were similar to those of *Raphael*. The TTSS determined in sections 2.6.2 and 2.6.3 is also listed below.

Table 2.6: Experimental ‘time to steady state’ for LTDSEs from literature.

| Source | TTSS from start-up | Max time observed | TTSS between setpoints | Max time observed |
|-----------------|---|-------------------|------------------------|-------------------|
| Speer [31] | 10 min | - | Until speed constant | - |
| Miller [43] | 10 min | - | 5 min | - |
| Stumpf [30] | Until baths return to setpoint temperatures | - | 2 min | - |
| Nicol-Seto [42] | 30 min | - | 2 min | - |
| Michaud [41] | 45 min | 60 min | 3 min | 5 min |
| This work | 60 min | 420 min | 10 min | 60 min |

Michaud [41] observed the transient behaviour for one hour after start-up and for five minutes after a setpoint change, albeit with an alpha-type engine that had a very different geometry from *Raphael* and was powered by an electric motor. The other authors did not note the maximum time observed, which indicates that long-time transient behaviour past the time when speed and temperatures first appear to plateau has not been investigated. This may have been because the main purpose of these experiments was not model validation, but experimental optimization of engine parameters.

2.6.2 Experiment to Determine TTSS Between Setpoints

To assess the TTSS for the validation data in Chapter 4 more rigorously, long-time experiments were carried out. Appropriate values for TTSS from start-up and between setpoints had to be found that achieve an acceptable ‘accuracy’ of the ‘experimental steady state’ and limit the duration of the experiment to be able to acquire a dataset in one uninterrupted experiment on one workday.

For first experiment the following setpoints were run in direct succession, with $T_{source} = 135\text{ }^{\circ}\text{C}$, $T_{sink} = 5\text{ }^{\circ}\text{C}$ and an acquisition frequency of 1 Hz:

1. Start-up at $p_{set} = 200\text{ kPa}$, $\tau = 0.5\text{ Nm}$, record for 90 minutes
2. Torque change to $\tau_{set} = 0.6\text{ Nm}$, record for 60 minutes
3. Pressure and torque change to $p_{set} = 350\text{ kPa}$, $\tau_{set} = 0.3\text{ Nm}$, record for 60 minutes

Setpoint 1 revealed that after 90 minutes all gas temperatures had passed a maximum or minimum corresponding to the high speed after start-up. But rather than plateauing, some were now changing in the other direction, which meant that observation over an even longer period was necessary to draw conclusions.

For setpoint 2 the data seen in Figure 2.19 shows the engine’s response to a torque change by 0.1 Nm which is similar to the largest torque increments used for the datasets in Chapter 4. After about 10 minutes the engine speed (a), liquid temperatures (b) and gas temperatures (c,d) have reached values from which none of them deviated by more than 2 rpm, or 0.5 °C respectively, over the remaining 50 minutes. The speed curve shows an oscillation with a period of about 4 minutes, but it appears to oscillate about a steady mean. Therefore, no significant changes were expected past 10 minutes after a torque change, and this was chosen as the TTSS between setpoints.

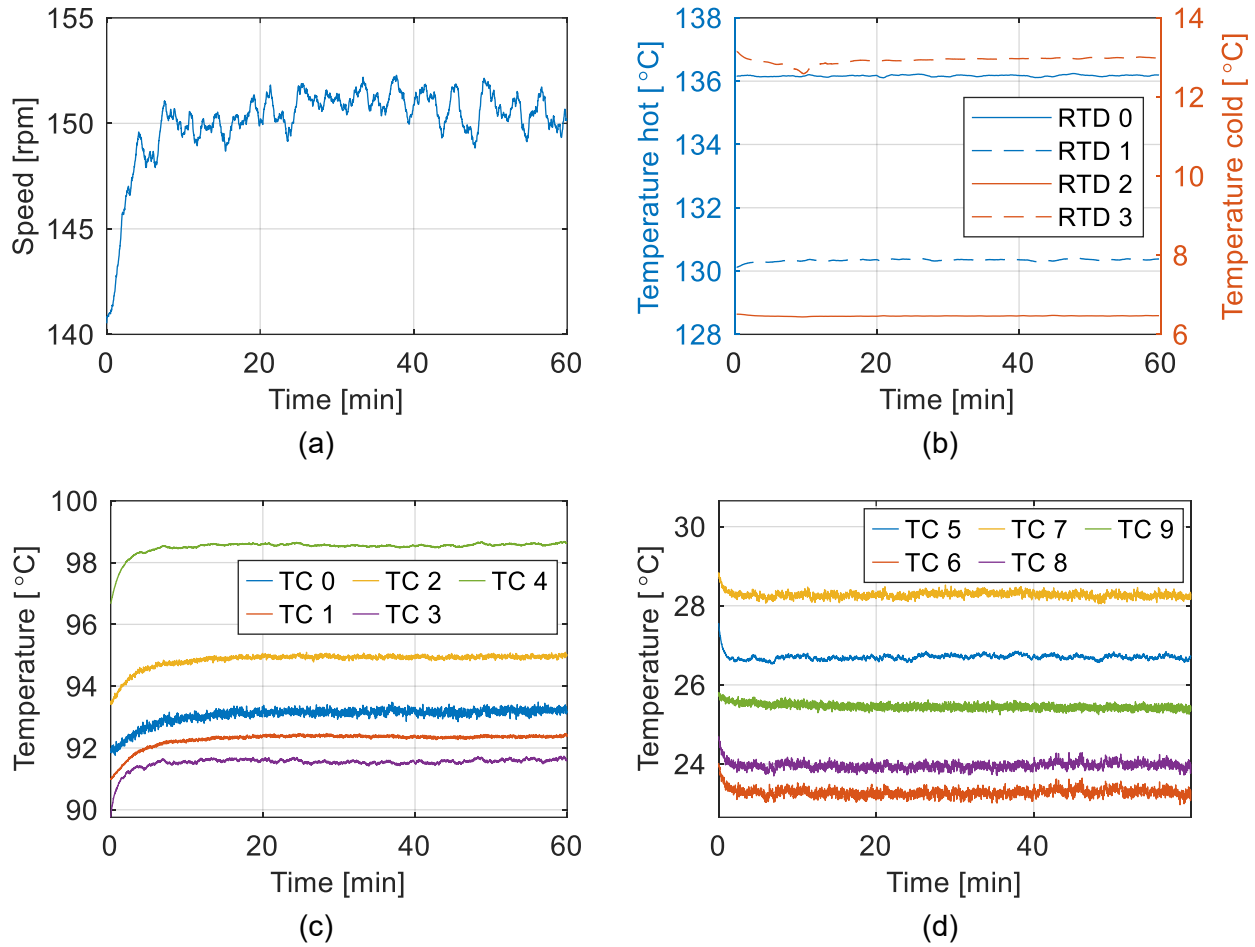


Figure 2.19: Plots of first long time experiment, torque change, 60 minutes. (a) speed, (b) RTD temperatures, (c) hot side gas temperatures, (d) cold side gas temperatures. Moving average with 1 minute interval applied to (a) and (b).

Figure 2.20 displays the speed and hot side gas temperature data of setpoint 3 for the first 30 minutes. The engine stalled after 35 minutes, likely because the piston seal used at the time was underperforming due to wear. The length of time it ran before ultimately stalling, and the observation that the parameters in Figure 2.20 were not approaching steady values after 30 minutes showed that the TTSS after changing the mean pressure is much longer than after changing torque, possibly comparable to the TTSS after start-up. Thus, it was decided to keep p_{set} constant for each dataset and treat a pressure change like a new start-up.

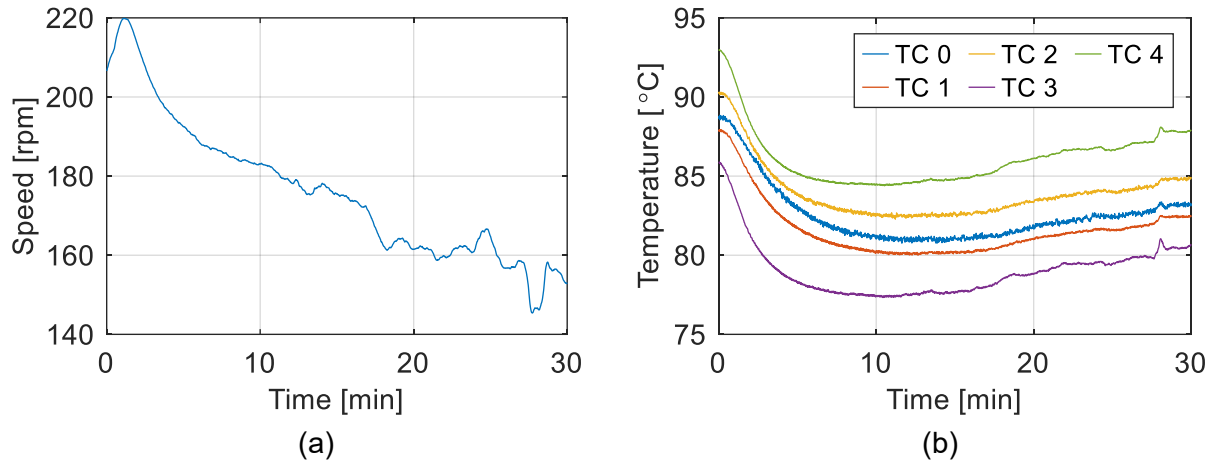


Figure 2.20: Plots of first long time experiment, pressure and torque change, 30 minutes. (a) speed, (b) hot side gas temperatures. Moving average with 1 minute interval applied to (a).

2.6.3 Experiment to Determine TTSS After Start-up

To determine TTSS after start-up a second experiment was run for 7 hours, which is longer than a feasible wait time for a single-day experiment can be. The acquisition frequency was increased to 10 Hz. It had been observed that higher p_{set} and T_{source} lead to longer times for engine speed and temperatures to plateau, so these parameters were set to the maximum used for experiments in Chapter 4:

1. $T_{source} = 135$ °C, $p_{set} = 450$ kPa, start-up and set $\tau_{set} = 0.3$ Nm immediately, record for 7 hours

Figure 2.21 (a-c) shows the measured speed, torque, and resulting shaft power in blue. Note that the torque changed over time even though the brake was set to a constant setpoint the entire time. This may be because the actual torque applied by the brake varies with speed. From hour 5 onwards these variables appeared to oscillate around a steady mean. Because of this observation, the average during the final hour, represented by the horizontal blue lines, was assumed to be a valid estimate for the final steady-state value. The relative deviation from this value, plotted in orange, can be used to quantify how close the engine is to a ‘power steady state’, at which shaft power and the variables it is derived from are no longer changing significantly.

It was decided to use 1 hour as the TTSS after start-up because the deviation in shaft power and torque at that time was below 5 %, which is a not insignificant but well-defined deviation from

steady state, and at the same time this allowed to run experiments in a relatively quick succession. As seen in Chapter 4 this deviation is small compared to the average model error observed at this point. If the model error can be reduced reliably to below 10 %, new experimental data should be taken with a TTSS of around 3 hours for a deviation of less than 2 % in speed, torque, and shaft power.

Figure 2.21 (d) shows the mean pressure measured in the power cylinder and crankcase. The working space pressure was constant apart from occasional spikes, possibly caused by the pressure regulator opening its valve in coarse increments. The crankcase pressure was initially similar to the working space as expected, but after 20 minutes decreased suddenly by about 5 % before stabilizing at a level below the working space pressure. The cause for this shift is unclear. It may have been caused by the piston seal or the displacer rod bushing, through which air leaks between the spaces, changing their geometry due to warming up in a way that made the leak biased towards the working space. That would allow air to leave the crankcase until a pressure difference would exist across the leak that would again balance the net leakage to zero. This deviation between crankcase and working space pressure may lead to a slight decrease in shaft power due to increased forced work (see Section 1.3.2), but has little effect on indicated work and the validation of the thermodynamic model.

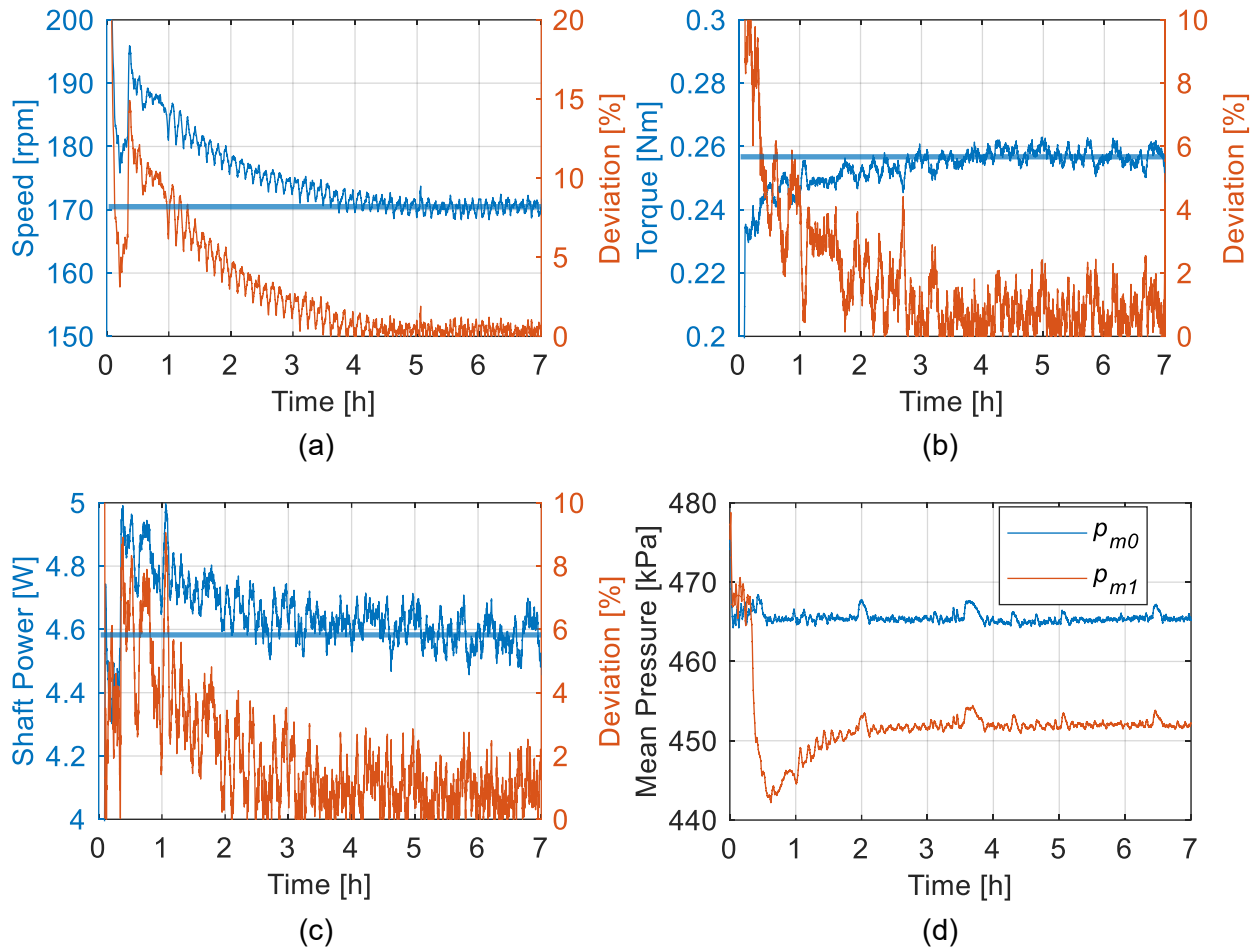


Figure 2.21: Plots of 7-hour long time experiment. (a) speed, (b) torque, (c) shaft power, (d) mean pressures. Right axis showing deviation from the final-hour average (blue horizontal line). Moving average applied to speed (1 min interval), torque (5 min interval), pressures (1 min interval).

Figure 2.22 shows the progression of temperatures during the 7-hour experiment. In (a) and (b) the heater and cooler liquid temperature drop between inlet and outlet are shown along with their deviation from the final-hour average. Inlet temperatures were at a constant level while the outlet temperatures changed following the heat demand and rejection in the engine. The deviation for both fell below 5 % within 1 hour. Thus, a 5 % deviation from steady state applies to the source and sink heat flow rates in the experimental data in Chapter 4 which are proportional to the liquid temperature drops.

Figure 2.22 (c) and (d) show that the hot and cold side gas temperatures appeared to move towards steady values on a longer time scale compared to the other variables. They reached extrema after 1 to 5 hours, then started changing in the other direction and did not appear to plateau

after 7 hours. This suggested that it takes a much longer TTSS to achieve a ‘thermal steady state’, where all temperatures are reasonably steady, than a ‘power steady state’ as described earlier. However, at 1 hour the average difference between hot and cold side gas temperatures is within 5 % of the value after 7 hours. Based on this observation it was concluded that the earlier determined TTSS of 1 hour after start-up is still appropriate considering temperatures, and a possible deviation from steady state of roughly 5 % must be kept in mind for all variables used for validation in Chapter 4.

The crankcase temperature increased by about 8 °C over the first 4 hours, but it has little effect on engine performance and is not shown for that reason. TC 5 is not shown as it was not installed.

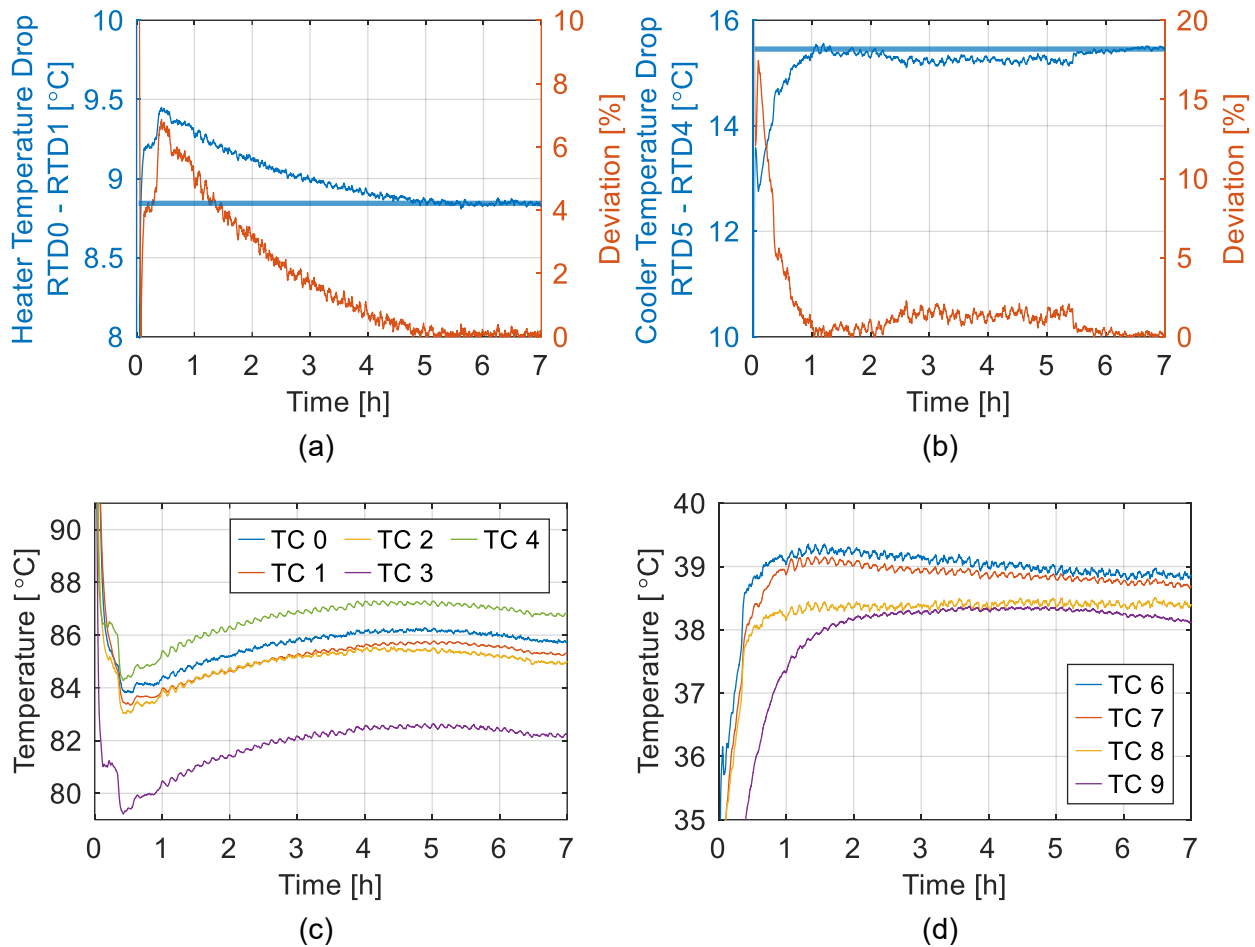


Figure 2.22: Plots of 7-hour long time experiment. (a,b) heat exchanger liquid temperature drops with deviation from final-hour average (blue horizontal line), (c,d) hot and cold side gas temperatures. Moving average with 1 minute interval applied to all curves.

2.6.4 Oscillating Behaviour Caused by Temperature-Speed Interaction

The plots in Figure 2.21 and Figure 2.22 reveal that all measured parameters show oscillating behaviour while approaching steady state. Especially visible in Figure 2.21 (a) but present in all curves is a small-scale oscillation with a period of about 7 minutes and amplitude of up to 4 % of the final-hour average depending on the parameter. Additionally, a large-scale oscillation seems to be present in Figure 2.22 (c) and (d) since the gas temperatures did not plateau but changed direction. The period may be much longer than the duration of this experiment. This pattern might also be followed by the other parameters but may not yet be visible after 7 hours. The period and amplitude of these oscillations are likely linked to the thermally relevant geometry of the engine as described in section 2.6.1. Similar behaviour may be present in any thermodynamic machine operating at a cyclic quasi-steady state.

The root cause behind the oscillating behaviour are reciprocal interactions between the hot-cold temperature difference and the engine speed that act like a feedback loop. This becomes clear when comparing Figure 2.21 (a) and Figure 2.22 (c) and (d). At start-up the temperature difference is high, causing a high power and thus a high speed. In turn, the high speed leads to a rapid decrease of the temperature difference because heat is transferred from heater to cooler during each engine cycle. Then, speed decreases due to the reduced temperature difference driving the process, allowing in turn the temperature difference to increase again, and this sequence repeats over and over. There appear to be two such oscillations with different periods for the *Raphael* engine as explained above. The large-scale oscillation is dampened as the parameters move towards steady values, but the small-scale oscillation did not appear to decrease in amplitude during the experiment and may continue indefinitely, at least for the particular setpoint conditions tested.

The oscillating trends in long-time Stirling engine data described here are a new insight into how cyclic thermodynamic machines respond to changes in operating conditions and approach steady-state conditions. Further research could investigate how to reduce the TTSS, observe longer time periods than shown here, and compare the behaviour of different engines. The long-time data could also be used to validate a transient model by simulating the unsteady conditions after start-up.

2.6.5 Time to Steady State: Conclusions

Experiments observing the *Raphael* engine for up to 7 hours were conducted to determine wait times that should be followed after engine start-up and change of setpoint before acquiring data. From analysing the trends of speed, torque, shaft power, liquid temperature drop at the heat exchangers and gas temperatures it was decided that a ‘time to steady state’ of 1 hour after start-up and 10 minutes after a torque change should be followed. This way, the deviation from steady state for all variables used for validation in Chapter 4 should be limited to about 5 %.

Comparing these results to Table 2.6 shows that the wait times from literature, which are mostly qualitative estimates, are insufficient for obtaining data with the *Raphael* engine for comparison with a steady state model. This is also expected to apply to other machines depending on the geometry and materials of their heat exchangers and other thermally relevant structures.

The validity of this analysis could be verified by obtaining and analysing the following additional data:

- Observe the TTSS after various torque increments, at higher p_{set} and T_{source} , for longer time.
- Acquire data with high frequency in short intervals rather than continuously with low frequency. Then assess steady state based on indicator diagram instead of shaft power.

2.7 Experimental Data Processing

The following is an overview of the processing scheme used to calibrate, convert, and organize the experimental data saved by the DAQ software. The calculated variables for all setpoints of a dataset are each saved into a '.mat' file that is accessible for plotting and analysis. The corresponding MATLAB code can be found in Appendix G. The original code developed by Speer [31] was improved and extended for the current experimental setup.

2.7.1 Apply Calibration to Raw Measured Data

The raw data from the text files is corrected via calibration methods described in section 0 and then stored in a single file for each dataset.

For RTD and thermocouple data the calibration curves are obtained from calibration data as follows:

- For each RTD calibration file (representing one calibration temperature):
 1. Extract data vectors of all RTDs.
 2. Calculate and store average reading for each RTD.
 3. Calculate 'true' reference as the average of all readings (see section 2.4.1).
 4. Calculate and store correction term for each RTD as the deviation of average reading from 'true' reference.
- For each RTD, apply 3rd order polynomial fit to map from RTD reading to correction term. Store fit coefficients to later apply to experiment data.
- Repeat the same procedure as for RTDs on the thermocouple calibration files.

For pressure and torque sensors, linear fits are applied to the data from the sensor calibration certificates from the manufacturers, and fit coefficients stored.

Then, calibration curves and conversion factors are applied to the raw experimental data. For each experimental datapoint, represented by 3 text files:

- From RTD file, read raw RTD data vectors, RTD time vector and setpoint parameters.
- From TC file, read raw TC data vectors and TC time vector.
- From Voltage/Counter file, read raw voltage/counter data vectors and time vector.

- Format the time vectors so they start at 0 and have constant spacing.
- Apply RTD and TC calibration to raw data using correction terms from calibration data.
- Apply pressure and torque sensor calibration fits to raw data.
- Convert brake speed reading to (rpm) and average it.
- Manually input the measured atmospheric pressure and apply correction term (see Appendix B.8)

The calibrated data from all setpoints, comprised of the variables listed in Table 2.3, is stored in a '.mat' file.

2.7.2 Mean Temperature Calculations

For each setpoint the temperatures used for analysis are obtained as averages of the calibrated data following the equations in Table 2.7.

Table 2.7: Equations for calculated temperatures.

| | | |
|---|---|------|
| Expansion Space Temperature | $T_e = \text{mean}(T_{TC0})$ | (19) |
| Heater Inlet Temperature (avg.) | $T_{h,inlet} = \text{mean}(\text{mean}(T_{TC1}), \text{mean}(T_{TC2}))$ | (20) |
| Heater/Regenerator Interface Temperature (avg.) | $T_{h,reg} = \text{mean}(\text{mean}(T_{TC3}), \text{mean}(T_{TC4}))$ | (21) |
| Cooler Inlet Temperature (avg.) | $T_{k,inlet} = \text{mean}(\text{mean}(T_{TC7}), \text{mean}(T_{TC8}))$ | (22) |
| Cooler/Regenerator Interface Temperature | $T_{k,reg} = \text{mean}(T_{TC5})$ | (23) |
| Regenerator Temperature (log mean) | $T_{reg} = \frac{T_{h,reg} - T_{k,reg}}{\ln(T_{h,reg}/T_{k,reg})}$ | (24) |
| Power Piston Space Temperature | $T_{PP} = \text{mean}(T_{TC9})$ | (25) |
| Crankcase Temperature (avg.) | $T_{CC} = \text{mean}(T_{TC10})$ | (26) |
| Heater Liquid Inlet Temperature | $T_{source,in} = \text{mean}(T_{RTD0})$ | (27) |
| Heater Liquid Outlet Temperature | $T_{source,out} = \text{mean}(T_{RTD1})$ | (28) |
| Cooler Liquid Inlet Temperature | $T_{sink,in} = \text{mean}(T_{RTD2})$ | (29) |
| Heater Liquid Outlet Temperature | $T_{sink,out} = \text{mean}(T_{RTD3})$ | (30) |

2.7.3 Heat Flow Rate Calculations

Liquid flow rates, specific heats, and heat flow rates for heater and cooler are calculated using the equations in Table 2.8.

Table 2.8: Equations for heat flow rate calculations.

| | |
|--|---|
| $\dot{m}_{Cooler} = 0.0235576 \text{ kg/s}$ | Measured for setpoint 5 °C |
| $c_{cold} = 3770 \text{ J/kg K}$ | 30 % ethylene glycol in water, 5 °C [107] |
| $\dot{Q}_{Cooler} = \dot{m}_{Cooler} c_{cold} (T_{sink,out} - T_{sink,in})$ (31) | |
| $\dot{m}_{Heater} = \dot{m}_{Heater}(T_{Heater})$ | See Figure 2.17 |
| $c_{hot,in} = c_{hot,in}(T_{source,in}), \quad c_{hot,out} = c_{hot,out}(T_{source,out})$ | See Figure 2.18 |
| $\dot{Q}_{Heater} = \dot{m}_{Heater} (c_{hot,in} T_{source,in} - c_{hot,out} T_{source,out})$ (32) | |

2.7.4 Pressure Calculations

The analysis of the indicator diagram and pressure drop in Chapter 4 is based on combined pressure data from the mean and dynamic pressure sensors. Mean pressures for working space and crankcase are given as absolute pressure to make the data comparable to other experiments. These variables are calculated from the measured atmospheric, mean and dynamic pressures as shown in Table 2.9.

Table 2.9: Equations for calculated pressures.

| | |
|--|---|
| Expansion Space Pressure | $p_{Exp} = \text{mean}(p_{m0}) + p_{d0}$ (33) |
| Compression Space Pressure | $p_{Com} = \text{mean}(p_{m0}) + p_{d1}$ (34) |
| Power Piston Cylinder Pressure | $p_{PC} = \text{mean}(p_{m0}) + p_{d2}$ (35) |
| Crankcase Pressure | $p_{CC} = \text{mean}(p_{m1}) + p_{d3}$ (36) |
| Absolute Mean Working Space Pressure | $p_{mean} = p_{atm} + \text{mean}(p_{Exp}, p_{Com}, p_{PC})$ (37) |
| Absolute Mean Crankcase Pressure | $p_{mean,CC} = p_{atm} + \text{mean}(p_{CC})$ (38) |
| Heat Exchanger + Regenerator Pressure Drop | $\Delta p_{HX} = p_{Exp} - p_{Com}$ (39) |

2.7.5 Engine Speed Calculation from Crankshaft Angle

The raw engine speed f_{raw} (rpm) is calculated from the measured crankshaft angle θ (°) and counter time t_{VC} (s). First, θ_{raw} is converted into a monotonically increasing angle θ_{mono} . Then, angular speed (°/s) is calculated by dividing angle increments by time increments for each sample. A moving average over an interval of 40 samples is used. This corresponds to about 75° of crank rotation at a high-end speed of 300 rpm and 1 kHz sampling frequency. The averaging reduces the random fluctuations in the encoder data without smoothing the real variations of speed over crank

angle. Finally, the data is converted from ($^{\circ}/s$) to (rpm). For each sample i , this operation is represented by equation (40):

$$f_{raw,i} = \frac{\theta_{mono,i+20} - \theta_{mono,i-20}}{t_{VC,i+20} - t_{VC,i-20}} * \frac{60 \text{ rpm}}{360 \text{ }^{\circ}/s} \quad (40)$$

2.7.6 Speed and Pressure Data Averaging

The raw data of speed and pressures span the entire acquisition duration and contain multiple engine revolutions. This data is now condensed into one average revolution by averaging all samples corresponding to the same crankshaft angular position in whole degrees.

- Round the measured angles θ to whole degrees.
- As the speed/pressure data corresponds to the angle data, each speed/pressure sample can now be assigned an angle in whole degrees.
- For each whole degree angle (1° to 360°), average all speed/pressure samples corresponding to that angle.

The resulting data is:

- Average speed for each degree of crank angle: f_{θ}
- Average pressures for each degree of crank angle:

$$p_{Exp,avg}, p_{Com,avg}, p_{PC,avg}, p_{CC,avg}, p_{d2,avg}$$

Figure 2.23 shows an example of the speed data of a datapoint consisting of 10,000 samples and the resulting curve of averaged speed f_{θ} .

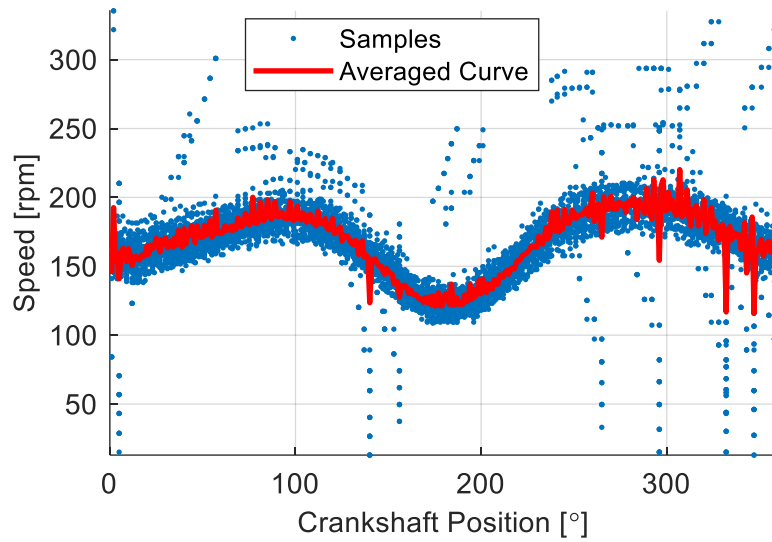


Figure 2.23: Example plot of speed samples and averaged curve from a 10 second datapoint.

2.7.7 Mean Speed, Torque, Shaft Power and Efficiency

With the averaged shaft speed and torque, shaft power and thermal efficiency were calculated following Table 2.10.

Table 2.10: Equations for speed, torque, shaft power and efficiency.

| | |
|---------------------------|---|
| Average Speed [rpm] | $f = \text{mean}(f_{\theta})$ |
| Average Shaft Torque [Nm] | $\tau = \text{mean}(\tau_{raw})$ |
| Shaft Power [W] | $P_{shaft} = \tau f * \frac{2\pi \text{ rad/s}}{60 \text{ rpm}}$ (41) |
| Thermal Efficiency [-] | $\eta_{shaft} = P_{shaft} / \dot{Q}_{Heater}$ (42) |

2.7.8 Determination of Engine Volumes

To form the indicator diagram, the volumes of the working space and crankcase were calculated for each whole degree crankshaft position from the engine geometry. The volumes contributed or displaced by all components contacting the engine volumes were measured in the engine solid model in SOLIDWORKS®. The volume variations by the displacer piston, its rod, and the power piston at each crankshaft position were determined from the mechanism geometry. Table 2.1 lists the most important volumes. For all data, a crank angle of 0° corresponds to the start of compression, maximum working space volume, with the power piston in bottom dead center position. The results are V_{total} and V_{CC} (total working space volume and crankcase volume).

2.7.9 Indicated Work and Power

With the averaged pressure and volume data from previous sections, the area of the power piston p-V diagram (indicated work) was determined by trapezoidal numerical integration. The dynamic pressure $p_{d2,avg}$ was used for W_{ind} instead of the full power piston pressure $p_{PC,avg}$. These pressures differ only by a constant offset between them as seen in equation (35), so the area of the indicator curve and therefore W_{ind} are not affected. The benefit is that the mean pressure p_{m0} does not need to be considered in the uncertainty of W_{ind} .

Table 2.11 shows the mathematical operations. The pressure and volume data are circular with index i , meaning that indices (0 and 360) and (1 and 361) refer to the same value.

Table 2.11: Equations for indicated work and power.

| | |
|--|---|
| Working Space Volume change (central differences) | $dV_{total,i} = \frac{V_{total,i+1} - V_{total,i-1}}{2}$ |
| Indicated Work [J] (trapezoidal integration) | $W_{ind} = \oint p_{d2,avg} dV_{total} \cong \sum_{i=1}^{360} p_{d2,avg,i} dV_{total,i} \quad (43)$ |
| Indicated Power [W] | $P_{ind} = W_{ind} f \frac{1}{60} \frac{\text{Hz}}{\text{rpm}} \quad (44)$ |

2.8 Experimental Repeatability

In this section the repeatability of the experiments with this setup is analyzed qualitatively by comparing the data from a dataset that was acquired several times. Three datapoints at $p_{set} = 100$ kPa with different torques were recorded five times. Dynamic pressure sensors were swapped into different positions between the datasets to assess the deviations between individual sensors. The engine was stopped and returned to warmed-up condition between the repeated experiments. Indicated work and gas temperatures are compared here as they are the most relevant variables for the validation in Chapter 4.

Figure 2.24 shows the indicated work calculated from the pressure data acquired with the dynamic pressure sensor mounted in the power piston space for each experiment. Experiments 1 and 5 used sensor A, which was also used to acquire all the data for Chapter 4. Sensor C deviated visibly by 13 % on average from the other sensors, which produced values within 3 % of one another. This shows that there may be a considerable discrepancy between outputs of individual sensors that is not accounted for in the uncertainty analysis. The deviation between the experiments using sensor A was also within 3 %, thus a repeatability error around 3 % in W_{ind} should be expected.

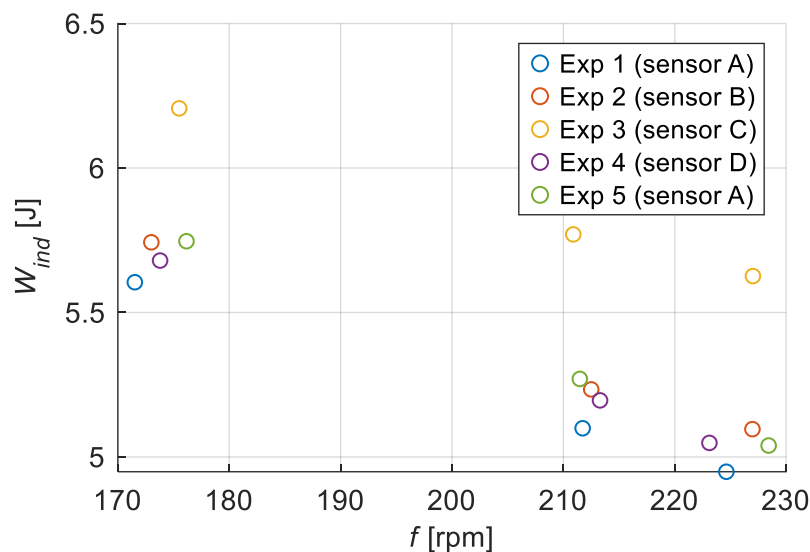


Figure 2.24: Indicated work for three setpoints with $p_{set} = 100$ kPa, and similar speeds. Comparison of five datasets acquired with four different dynamic pressure sensors.

Figure 2.25 shows the gas temperatures measured during the same five experiments for one of the setpoints shown in Figure 2.24. They are plotted over the thermocouple position numbers (see Figure 2.7) and split into hot side (a) and cold side (b). The pairs of positions displayed closer to each other on the x-axis (e.g. 1 and 2) are those that are at the same locations on the A and B sides of the engine, respectively.

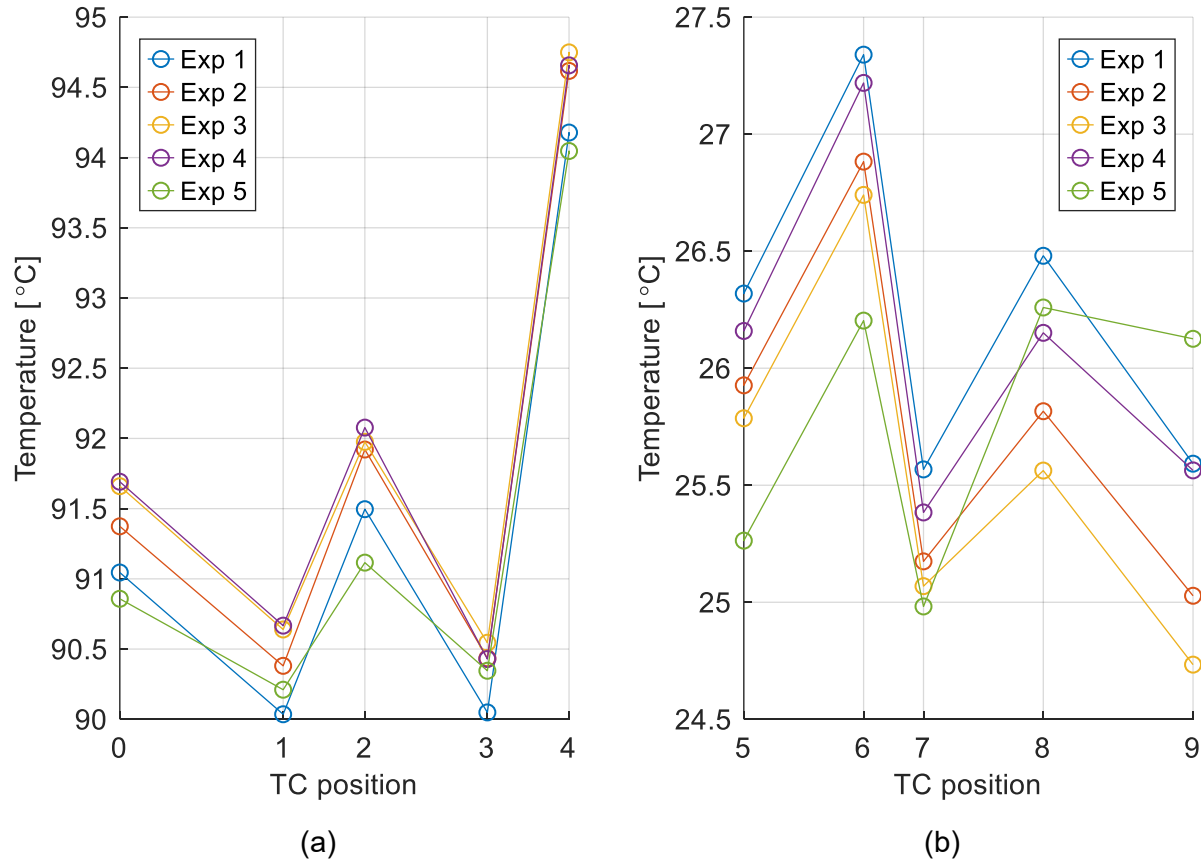


Figure 2.25: Gas temperatures of setpoint with $p_{set} = 100$ kPa, comparing data from five experiments with similar speeds ($f = 211$ - 213 rpm). (a) Hot side and (b) cold side temperatures.

Overall, the readings deviated from each other by 0.5 °C to 1.1 °C depending on position. When inspecting the hot side (a) and cold side (b) separately, the temperatures measured in experiments 1 to 4 had a consistent order (low to high) at all locations. Experiment 5 did not follow that order and its curve crossed the other curves. The relative consistency of the deviations and order indicates that the deviations are likely not primarily due to random noise, but due to small differences in the operating conditions (e.g. heat exchanger wall temperatures) between experiments. These exist because after the steady state wait time of one hour the temperatures are

still changing and cannot be considered steady, as was found in section 2.6. Hence, a repeatability error in the range of 1 °C in gas temperature data should be expected.

Surprisingly the largest temperature differences among the hot and cold side data are not between different locations along the heat exchanger axis, but between A and B side. Positions on the B side (2, 4, 7) are significantly hotter on the hot side and colder on the cold side than their respective positions on the A side (1, 3, 6). This cannot be explained by the location of the liquid connections relative to A and B sides because the heater liquid inlet and outlet are positioned centrally between A and B (see section 2.2.3). Thus, the heater temperatures are expected to be similar on A and B sides unless preferential flow of the gas through one side over the other plays a role. The gas temperatures being closer to the source and sink temperatures on the B side suggests the gas may be preferentially moving through the A side at higher velocities. One cause of this may be an uneven distribution of the regenerator material. It was reportedly difficult to spread the fiber material evenly throughout the gauze tube [89] (see Figure 2.6), which may have caused local variations in porosity that would lead to gas preferentially flowing through areas of higher porosity and lower flow resistance. The trends in temperature profiles observed here were found to be similar in the data from the other two setpoints shown in Figure 2.24.

2.9 Chapter Conclusion

An experiment has been set up to gather performance data from a gamma-type LTDSE running at source and sink temperatures of 150 °C and 5 °C, respectively, and achieving around 15 W of shaft power. The data acquisition system measures temperatures of the working gas and the heat source/sink liquids, instantaneous pressures, crankshaft angular position and shaft torque. Controlled setpoint parameters are the source and sink temperatures, mean pressure, and brake torque. Setpoint control and data acquisition are fully computer-controlled. A list of all equipment that is part of the setup can be found in Appendix A.2.2. A sample of experimental data was shown, and the methods of acquiring and processing data for the work in Chapter 4 were discussed. Calibration procedures for temperature sensors, pumps, and pressure sensors as well as the estimation of properties of the heat transfer fluids were documented.

The setup serves to provide the experimental data for the validation of a model in Chapter 4. The engine was observed for up to seven hours after start-up to find that wait times of one hour after start-up and ten minutes after changing the setpoint torque are necessary to ensure that the recorded data is within about 5 % of the expected values at the steady-state conditions that the model assumes. The repeatability of indicated work was estimated at 3 %, but a rigorous analysis of uncertainty will be performed in Chapter 4 with relation to the experimental data.

Chapter 3. Numerical Model *MSPM* and Modeling of the *Raphael* Engine

The numerical model *MSPM* was developed in the author's research group and aims to provide an openly available tool for researchers to develop and optimize Stirling engines, particularly LTDSEs, and other reciprocating thermodynamic machines. This thesis presents the first comprehensive validation effort of the model in Chapter 4. In this Chapter, an overview is given of the working principles of *MSPM*, the most important assumptions followed by the model are discussed, the model representation of the *Raphael* engine used for the validation in Chapter 4 is described, procedures followed for simulation setup and data processing are explained, and improvements made to the model code and functionality are listed. All work with *MSPM* was done in MATLAB R2019a Update 9 (The MathWorks Inc.).

3.1 Overview of the Model

MSPM ('Modular Single Phase Model') was developed in MATLAB and published as a thesis work by Middleton [33] in 2021. It has the following objectives and features that distinguish it from existing models:

- The model focuses on the low temperature and pressure regime and LTDSE, instead of high temperature engines with combustion heat sources. This means that most energy losses like viscous flow friction, mechanical friction, and leakage must be modeled more precisely. At the same time, some simplifications become viable, such as using the ideal gas model and ignoring radiation heat transfer. [33]
- The complexity of the model strikes a balance where it works on a discretized geometry and the effects of losses are coupled, which makes it more complex and accurate than 2nd order models, but assumes one-dimensional flow, which makes it a 3rd order model [39], [61] and requires much less computational power than a higher order analysis such as CFD.
- Dynamic / transient simulations with varying engine speed are supported so that, once validated, speed could be predicted instead of predefined.

- A graphical user interface (GUI) displays the model geometry visually (rather than abstractly) and allows arbitrary geometries to be built from modular elements (hence the name of the model). Interactions between the elements are inferred and discretization into a nodal network is automatic with minimal user input required.
- Data is output in numerical and graphical form, with the kind of data and the locations where it is acquired in the geometry being customizable by the user.
- Any number of test cases with varying operating conditions and geometry parameters can be run automatically in batches. This facilitates testing variations of design parameters and operating points, and conducting sensitivity analysis.
- The code is openly accessible, making it possible to modify and add improvements on any level.

MSPM, its mathematical foundations and numerical methods are described in detail by its author [33]. Here, the logic and important elements of the model are summarised. Figure 3.1 illustrates the model elements, which are represented as objects in the code, and their relationships. The left side shows the thermodynamic model, starting at the top with the interactable elements that the user configures through the GUI. These elements are then discretized into a network (mesh) of finite elements. The thermodynamic model interacts with the mechanical model (Mechanical System) on the right, which is configured through numerical inputs and not visualized.

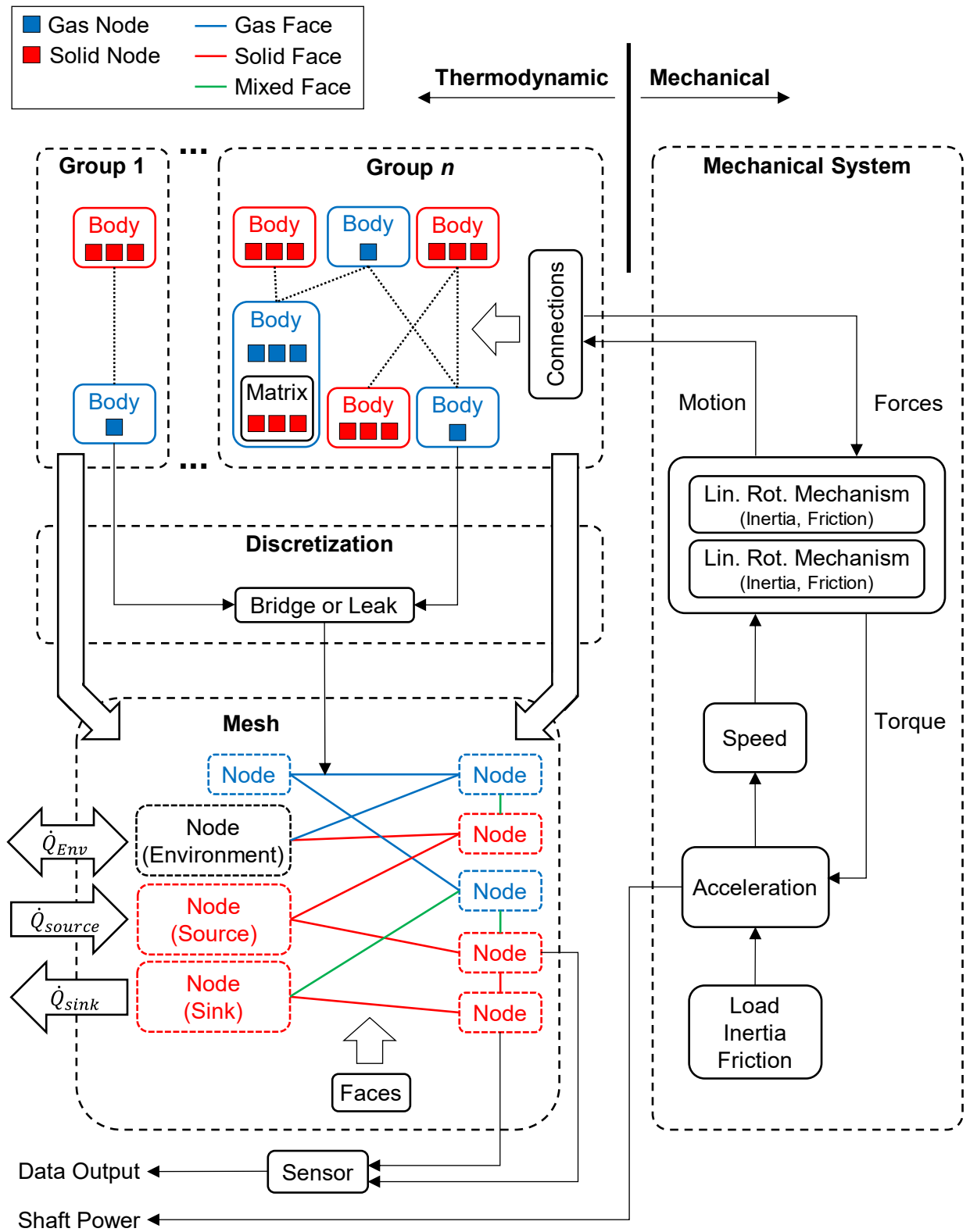


Figure 3.1: Schematic of MSPM model. Left: Thermodynamic model (Groups) built in GUI and discretized into Mesh. Right: Mechanical model.

3.1.1 Thermodynamic Model of MSPM

All processes related to the flow of gas and heat occur in the thermodynamic model; it represents the physical geometry of the engine working space and the structures around it that are relevant to heat conduction. The model assumes an axisymmetric geometry which is discretized in two dimensions – axial and radial. The cross section of this geometry is rendered two-dimensionally in the GUI. The geometry is built using *Bodies*, which are cylindrical or annular elements of material, either gas or solid. A *Group* is a collection of *Bodies* that share one central symmetry axis. Each *Body* is bounded by four *Connections*, essentially the upper, lower, inside, and outside surfaces of the *Body*, and two *Bodies* sharing a *Connection* can interface with each other. A *Gas Body* can contain a *Matrix* component which represents the solid structure of a heat exchanger or regenerator.

The geometry of *Bodies* is then discretized into a numerical mesh comprised of *Nodes* and *Faces*, which represent volume elements (gas or solid) and the interfaces between them, respectively. Each *Body* can be discretized into one or several *Nodes*, and the mesh structure and density can be defined automatically by a meshing algorithm for areas where strong gradients in temperature or pressure are expected, such as heat exchangers and conductive walls. In Figure 3.1 the colours indicate the type of *Body*, *Node* or *Face*, and the small red and blue squares represent the *Nodes* that a *Body* will generate. A *Gas Body* with a *Matrix* has both *Gas* and *Solid Nodes* with *Faces* between them. *Faces* can be one of three types: *Solid*, which transport only heat by conduction; *Gas*, which additionally transport mass and energy through advection, turbulence, and are used to calculate flow friction; and *Mixed*, which simulate convective heat transfer at a solid-gas interface. Heat sources and sinks are represented as isothermal *Nodes* with defined temperatures, and can be created by a heat exchanger *Matrix* or a separate isothermal *Body*. *Nodes* on the outside surface of the geometry also exchange heat with the *Environment* with a constant convection coefficient. *Faces* can also be added manually between *Bodies* that are not in contact in the modeled geometry. This is done by a *Bridge*, which can connect two *Groups* into one geometry, or a *Leak*, which creates a leakage between two gas *Bodies* with the leak rate depending on the pressure difference between them. For each time step, this thermodynamic model is solved numerically for internal energy, mass, temperature and turbulence in each *Node*, as well as heat flow, volume flow rates and pressure drop for each *Face* [33].

3.1.2 Mechanical Model of MSPM

After solving a time step in the thermodynamic model, the mechanical model comes into play. The *Mechanical System* represents the crankshaft and flywheel to which one or several *Linear to Rotational Mechanisms* are connected. These are kinematic linkages between the rotating crankshaft and the translating pistons, such as simple crank mechanisms or Scotch yokes. The entire *Mechanical System* operates at one rotational speed, and this speed is translated by the *Mechanisms* into linear motion that is applied to *Connections* in the thermodynamic model, thus moving *Bodies* like pistons along their axis. In return, the forces acting on a moving surface are processed by the respective *Mechanism*, accounting for friction and inertia within the linkage, into forces and torque that are applied to the crankshaft. The *Mechanical System* takes the combined *Mechanism* loads, external torque load, and the crankshaft friction and flywheel inertia to calculate shaft power and, if simulating transient behaviour, the angular acceleration applied to the system. The resulting speed is applied to the thermodynamic model in the following time step. This cycle can be repeated indefinitely and allows the transient simulation of the entire system.

3.2 Assumptions and Simplifications of *MSPM*

The following are assumptions made in the development of the model that contribute to its simplicity, but also may incur error in the model predictions. This discussion includes the reasoning of Middleton [33] and the author's own comments.

3.2.1 Ideal Gas Model, Single Phase

The working fluid is a gas and undergoes no phase changes. It is modeled as an ideal gas, which is sufficiently accurate for the moderate pressures and temperatures usually encountered in LTDSE. For air, to keep errors below 2 %, the pressure should not exceed 40 bar and temperatures should be roughly above 0 °C [108]. If this is not met, the expected error should be gauged through the compressibility factor of the gas, which could be implemented into *MSPM* as an advanced gas model. Errors will differ for different gases.

3.2.2 Radiation, Fluid Inertia, Gravity Neglected

Heat transfer through thermal radiation was expected to be negligible in LTDSE due to the strong dependency of radiation on temperature [33]. Kinetic and potential energy of the fluid are neglected for the low density of gases [33]. These simplifications reduce model complexity and computing time.

3.2.3 Axisymmetric Two-Dimensional Geometry

The thermodynamic model is made of axisymmetric cylindrical or annular bodies. This was justified as most pistons and cylinders, heat exchangers and ducts in well designed Stirling engines are circular because they need to be compact and pressure-retaining [33]. There is no discretization around the axis, which makes the geometry two-dimensional, and it can be easily rendered in the GUI as a cross-section along the symmetry axis with the bodies represented by rectangles. No variations along the circumferential direction are possible, such as preferential flow due to asymmetric components or temperature variations due to asymmetric heat exchanger temperatures.

3.2.4 Uniform Pressure

Pressure is uniform for all gas spaces that are connected to each other. This assumption is also central to the Schmidt model (Section 1.5.1) and forms the basis for solving the volume flow rate in *MSPM*. It also means that acoustic effects are neglected as these are pressure variations. However, since the pressure drop from flow friction requires slight pressure differences between nodes, it is determined in a separate process where the Darcy-Weisbach equation [44] for pressure drop is applied to each gas face. The equation system is solved along with the condition that the sum of the partial pressures of all nodes multiplied with their volumes is equal to the product of total volume and average pressure, which closes the equation system. The piston forces and, finally, the shaft power calculated from these pressures therefore reflect the flow friction loss.

3.2.5 One-Dimensional Flow

Flow can move between nodes axially and radially, but flow parameters like hydraulic diameter, Reynolds and Nusselt numbers are calculated based on the assumed main direction of flow. This simplifies the gas domain into a one-dimensional pipe network. This model applies well in ducts such as heat exchangers where flow is guided in one direction, but does not represent more complex flow, such as recirculation in larger volumes like the compression and expansion space, and nodes with strong axial and radial flow, for example a 90° bend.

3.2.6 Quasi-Steady Flow and Turbulence

The nature of the oscillating flow in the working space is only reflected in open gas volumes, where turbulence is generated and decayed based on the Valensi number which represents oscillatory fluid inertia [33]. In matrixes, flow is assumed to be fully developed and quasi-steady, and flow acceleration plays no role. Nusselt number and friction factor are based on Reynolds number correlations for steady flow, and laminar and turbulent correlations are blended using a steady state transition criterion. This was justified with the argument that flow through fine geometry develops rapidly due to small Reynolds numbers [33]. For LTDSEs, which tend to operate at lower speed and pressure, this assumption may be more applicable than for high temperature machines.

However, the *Sage* model [66] considers oscillation dependent properties in matrixes for laminar, but not for turbulent flow. Steady-state and oscillating flow correlations for turbulent flow were compared in the *kpsim* model [70], and the oscillating correlations affected gas temperatures but did not affect heat flow rates and power output notably. This indicates that the quasi-steady assumption may be applicable for turbulent matrix flow, but in laminar cases, which include the *Raphael* heat exchangers, it may lead to significant error. Organ [109] strongly discourages from using any steady flow correlations in Stirling analysis.

Additionally, some correlations might have been used out of scope, for example the laminar Nusselt number for rectangular channel and finned surface heat exchangers is 8.23 [33], which is the analytical solution for parallel plates and does not account for the channel's aspect ratio [45]. All correlations used by *MSPM* should be reviewed regarding their validity for the modeled geometries and oscillating flow.

3.2.7 Fully Developed Flow

Flow is assumed to always be fully developed, and the hydrodynamic entrance length, in which the Nusselt number is greater than in developed flow, is neglected. In heat exchangers with internal flow and Reynolds numbers in the high end of the laminar regime, the entrance length can be significant and amount up to 115 times the hydraulic diameter, as shown by [45]:

$$L_h = 0.05 Re D_h = 115 D_h \quad (45)$$

With $Re = 2300$

This means that for the *Raphael* engine at the same Reynolds number, the entire length of the heat exchanger would be within the entrance length ($L = 96$ mm, $D_h = 1.9$ mm, see Table 2.2). Therefore, this simplification could reduce heat transfer rates notably. The Nusselt number calculations for adjacent nodes would need to be interdependent and affected by the overall length of the flow structure to implement entrance length effects. This issue of having a node-based, not surface-based Nusselt number was also identified as an error source by Middleton [33].

3.2.8 Isothermal Heat Sources

Heat sources and sinks are modeled as isothermal solid nodes, there is no consideration of heat transfer resistances of real heat sources like the convection from a heat transfer liquid to a wall. Stirling engines and especially LTDSEs are limited by heat transfer performance, hence the complete path of heat transfer between source and gas should be considered in models. An improvement to this is presented in Section 3.6. Also, no other heat source models are implemented in *MSPM*, such as constant heat flux (e.g. electrical heater) or radiation heat sources (e.g. flame, solar).

3.2.9 No Contact Resistance to Heat Conduction

In the model, two bodies in contact conduct heat between them as if they are perfectly joined. In reality, components may be only in loose contact or have rough surfaces which inhibits conduction heat transfer between them.

3.2.10 Mechanisms are Kinematic and Linked

Only kinematic mechanisms can be modeled, in which all moving components are linked and move at same angular velocity. Free pistons that oscillate independently cannot be modeled.

3.3 Previous Validation Work on *MSPM*

In the original work developing *MSPM* some tests to validate the model were conducted [33]. These comprised of simple heat conduction and gas compression and expansion problems compared against analytical solutions, as well as validation of indicated work and indicator diagram shapes against a small set of 12 datapoints from an experimental engine operating with different piston motion profiles [42]. For this engine, operating at atmospheric pressure only and speeds between about 36 and 135 rpm, *MSPM* underestimated indicated work by 22 % on average, and it did not predict the superior performance of a mechanism with square wave motion that produced about 15 % higher indicated work in the experiment [33]. This indicates that the model might have underestimated heat transfer or overestimated the flow friction of heat exchangers and regenerator since a square wave motion causes more abrupt gas flow with higher velocity.

In-cycle speed variations were analyzed, and the ratio of minimum to maximum cycle speed was predicted more closely at higher speed [33]. A sensitivity study on heat transfer and flow friction parameters found that the heat exchanger Nusselt number affected the indicated work most significantly, and the friction factor played a notable role only at higher engine speed [33]. This points toward heat transfer effectiveness being a key limiting factor for the performance of LTDSEs.

MSPM was also compared against the *Sage* model [66] simulating an alpha engine. Running at high pressure (5 MPa) and source/sink temperatures of 150 °C/ 40 °C, *MSPM* underpredicted heat transfer leading to shaft power being underpredicted by 30 to 60 % [33]. This may have been caused by *MSPM*'s lack of oscillation-dependent correlations for laminar Nusselt number and friction factor (see Section 3.2.6), as well as error incurred from the ideal gas model at high pressure and moderate temperature [33]. Tests at low temperatures (95 °C/ 5 °C) and pressure (1 atm) found *MSPM* overpredicting heat transfer and underpredicting pressure drop, which was also attributed to the steady-state laminar correlations [33]. However, the accuracy of *Sage* at low temperatures is questionable, and certain conclusions can only be drawn from comparisons against well-documented experimental data.

These validation efforts gave some pointers at which of the model's assumptions might be sources of significant error, but a more complete picture of *MSPM*'s accuracy and statements

regarding its reliability can only be gained through more extensive experimental validation. This should involve different heat exchanger and regenerator geometries, and a larger number of datapoints taken at varying pressures and heat exchanger Reynolds numbers covering the laminar and turbulent regimes.

3.4 Model of *Raphael* Engine in *MSPM*

The *Raphael* engine described in Chapter 2 was modeled in *MSPM* to gather numerical data for the validation in Chapter 4. The visual rendering of the thermodynamic model from *MSPM* is displayed in Figure 3.2. The full model is seen on the left, and due to its height an enlarged and cropped view in which the relevant components are visible is shown at the center. All model dimensions were obtained from the *Raphael* solid model and the drawing package found in Appendix F.

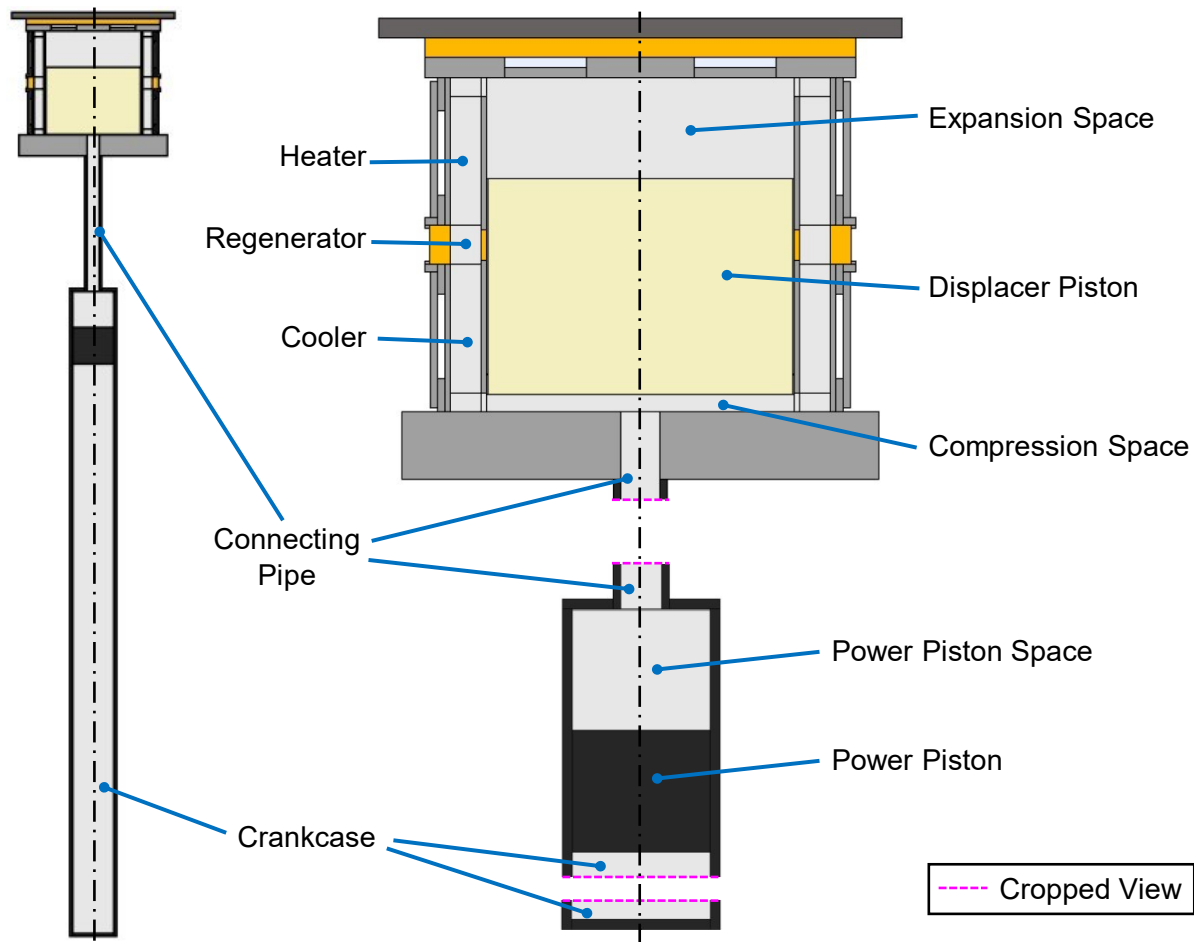


Figure 3.2: Model of *Raphael* engine rendered in *MSPM*. Left: full model, center: enlarged view with connecting pipe and crankcase cropped. Symmetry axis at center.

Since the modeled geometry in *MSPM* is axisymmetric, the 90° layout of the real *Raphael* engine (see Figure 2.2) could not be replicated in the model. Instead, the whole engine was modeled as a single Group symmetric about the indicated center axis. The modeled lengths of the

connecting pipe and the crankcase were defined so that their gas volume matched the real engine. Due to this simplification, the shape of the connecting pipe, power piston cylinder and crankcase was not modeled, meaning that solid heat conduction in these areas and the effect of the bend in the connecting pipe on the flow are not replicated. A minor loss coefficient could be implemented to simulate the latter. This is expected to have little effect on the overall thermodynamic performance because the majority of heat transfer, flow friction losses, and temperature gradients occur in the displacer cylinder and heat exchangers which are modeled with their accurate shape and materials. The base below the compression space ('displacer mount') is rectangular in reality but was modeled as a cylinder with equal volume. The piston connecting rods were not modeled, therefore the gas volume occupied by the displacer piston rod, conduction through it, and the leak through the displacer rod bushing between the compression space and the crankcase were neglected. Measurement instruments and their ports were not modeled as their heat conduction and the effect of thermocouples interfering with the flow were assumed negligible. Components of the mechanism were not modeled as they have minimal effect on the thermodynamic processes. The piston seals were represented as either perfect or non-existent, which is explained in Section 3.4.2.

As the validation will be limited to the thermodynamic outputs (e.g. indicated work), the mechanical model was set to be frictionless and follow the true motion of the pistons accounting for the dimensions of the crank mechanism. To run transient tests and validate the mechanical model, friction functions for the mechanism would need to be determined, and the crank mechanism implementation in the code would need to be completed.

3.4.1 Numerical Mesh and Heat Exchangers

Figure 3.3 shows the nodes that make up the numerical mesh of the displacer cylinder. Open volumes like the expansion and compression space each have only a single gas node, while the gas bodies with a matrix (heat exchangers and regenerator) have several as they are discretized in the axial direction. Solid bodies are discretized by the automatic mesher, except for the displacer piston which was set to 2 by 5 nodes to reduce computational effort (see Section 4.7.3). Gas and solid nodes are overlapping in the heat exchangers and regenerator to simulate the porous matrixes.

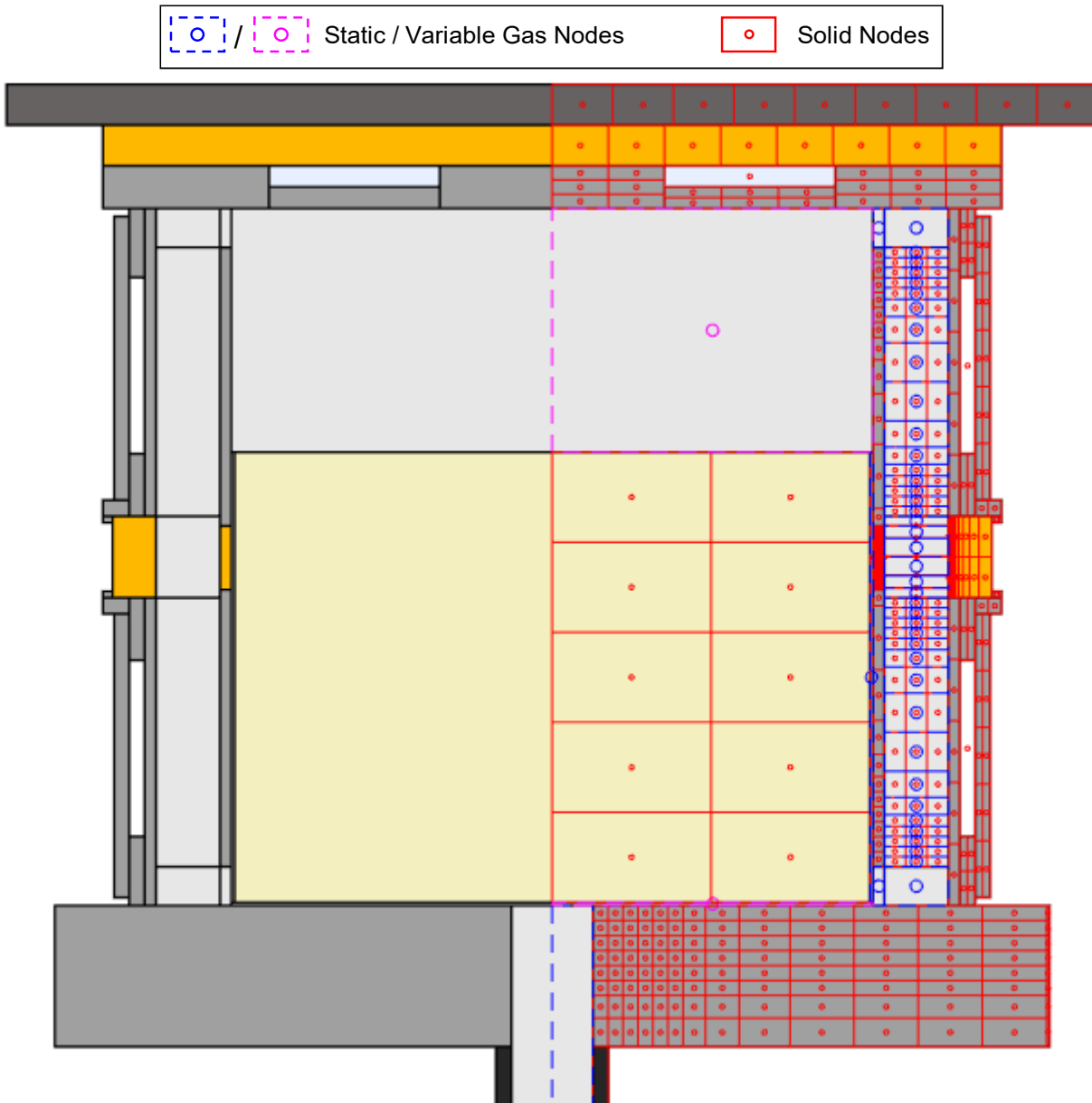


Figure 3.3: Numerical mesh in displacer cylinder and heat exchangers of *Raphael* model, as rendered by *MSPM*. Showing centers and bounds of gas and solid nodes.

The mesh of the heater and regenerator is shown in more detail in Figure 3.4. Heater and cooler are identical. The regenerator is a ‘Random Fiber’ matrix and the heat exchanger gas channel is a ‘Fin Enhanced Surface’ matrix with the fins connected to the outside (right) wall of the gas channel. Figure 3.4 (a) shows the gas nodes and faces along the vertical flow direction. The liquid source channel (white, marked ‘S’) is an isothermal body in the outside wall. In Figure 3.4 (b) the solid nodes and faces are seen. The heat exchanger fins are represented by three nodes radially across the gas channel which are connected by faces to the outside channel wall and the source

channel. The regenerator solid nodes are rendered very thin as their thickness is proportional to the regenerator porosity. Figure 3.4 (c) shows only the centermarks of all nodes and the mixed faces that connect gas and solid nodes. The gas nodes interact with all walls and the solid nodes of the matrix.

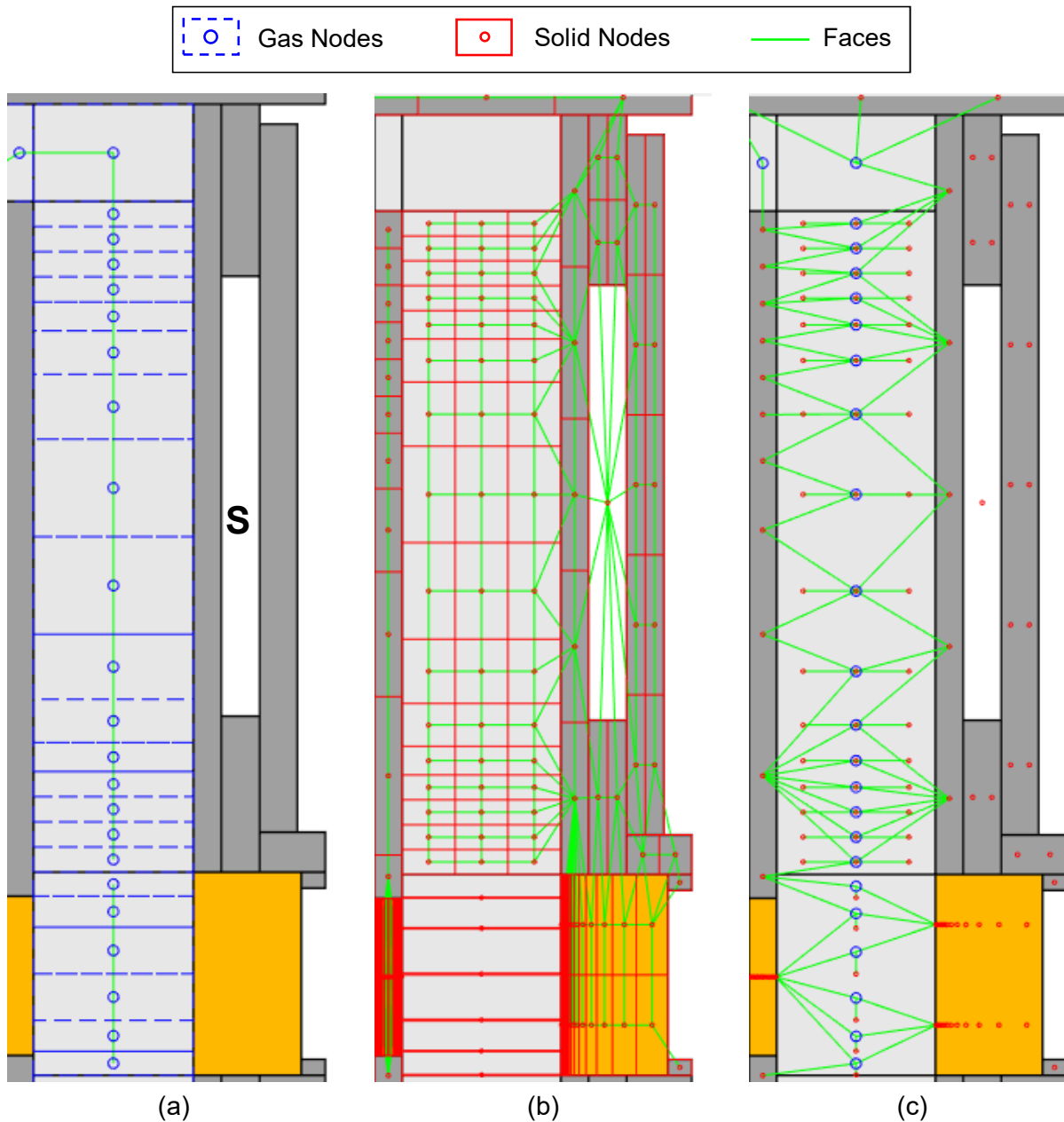


Figure 3.4: Mesh detail of heater and regenerator. (a) Gas nodes and faces, 'S' is source channel, (b) Solid nodes and faces, (c) Gas and solid nodes (centermarks only), and mixed faces between them.

The mesher settings and statistics of the resulting mesh are listed in Table 3.1. The maximum Courant and Fourier numbers are used by the solver to choose a time step that will resolve gas flow and heat conduction appropriately [33]. It can be seen that solid nodes and faces make up the majority of mesh elements due to the large temperature gradients in solids.

Table 3.1: Mesh properties of *Raphael* model (with displacer piston seal, see Section 3.4.3)

| Mesher Settings | All Default |
|------------------------|-----------------|
| Maximum Courant Number | 0.025 (Default) |
| Maximum Fourier Number | 0.025 (Default) |
| Gas Nodes | 50 |
| Gas Faces | 48 |
| Solid Nodes | 387 |
| Solid Faces | 820 |
| Mixed Faces | 318 |

3.4.2 Heat Exchanger Circumferential Temperature Gradient

As shown in Section 2.1.3 the heating and cooling liquids flow through the heat exchangers circumferentially, which means there will be a circumferential gradient in source and sink temperature between the liquid inlets and outlet in the real engine. This may cause uneven heat transfer. However, *MSPM* cannot replicate any variations in circumferential direction because of its axisymmetric assumption. Instead, the mean between measured inlet and outlet temperature is applied to the entire heat exchanger in the model.

The effect of this temperature gradient was investigated by Wang et al. [110] on a Stirling heat pump with similar heat exchangers modeled in *Sage* [66]. With a source temperature gradient of 40 °C between inlet and outlet, which is much greater than in the *Raphael*, they found an insignificant drop in efficiency due to colder and warmer gas mixing in the working spaces. Therefore, the effect of asymmetric temperature for the *Raphael* is likely negligible.

3.4.3 Piston Seals: Two Model Variants

The implementation of seals in the model can be critical for its accuracy because seals influence the thermodynamic performance of an engine through leakage and the mechanical output through friction. In the case of the *Raphael* model used for validation in Chapter 4 the mechanical model is not of interest, thus seal friction is not relevant. Seal leakage, however, affects the pressure and flow rates in the working space and must be considered when validating the thermodynamic model. In *MSPM* seal leakage can be modeled either as a physical gap between piston and bore, or by a ‘leak connection’ which can be added manually between two gas spaces. The ‘leak connection’ allows for a certain gas flow rate, which is a function of the pressure difference between the spaces, to pass through.

For a real seal the leak rate cannot be confidently modeled without measuring it experimentally. The power and displacer piston seals in the *Raphael* engine are in contact with their bores, but they still leak because of imperfections in the seal-wall contact that could be caused, for example, by surface roughness, wear, and flexibility of the seal. These effects are difficult to predict without experimental data, and there is also no reference data for the *Raphael*’s seals as the seal geometries and the application are non-standard. Thus, to model the leak rates accurately, an experimental setup would need to be developed to measure the leak rates as a function of pressure differential. This would go past the scope of this work, therefore the seals in the model will be approximated as either ‘perfect’, meaning no leakage, or ‘non-existent’, meaning that the gap between piston and bore is left open. These cases represent lower and upper bounds for the leak rate of a real seal which must be between these extremes.

Section 2.1.2 describes the seals of the *Raphael* engine. The power piston seal has little flexibility and sits tightly in its bore. It has been observed experimentally that the pressure change from leakage through this seal within the duration of one engine cycle is minimal. This indicates that the power piston seal can likely be approximated as ‘perfect’ without incurring significant error in the model. Thus, the power piston is modeled with no gap to its bore and is leak-free. On the other hand, the displacer piston has a much larger gap of 1 mm with its bore and its seal is a flexible lip designed for low friction. A more substantial leak rate is expected here but this type of seal has been proven in LTDSEs to achieve a high power output compared to alternatives, which means that it still performs much better than the ‘non-existent’ representation would. Therefore,

two versions of the displacer piston seal will be tested in Chapter 4 – the ‘non-existent’ version which is expected to underestimate the engine performance, and the ‘perfect’ version which will likely overpredict performance. Figure 3.5 shows a view of both model versions in *MSPM*. A part of the displacer piston and the heat exchangers are shown. The body of the seal that prevents flow through the appendix gap is highlighted in Figure 3.5 (b), it is the only difference between the versions. The seal is attached to the displacer piston and is modeled in the same position as its real counterpart. Also, the network of gas nodes and faces shows the effect of the seal on the gas path.

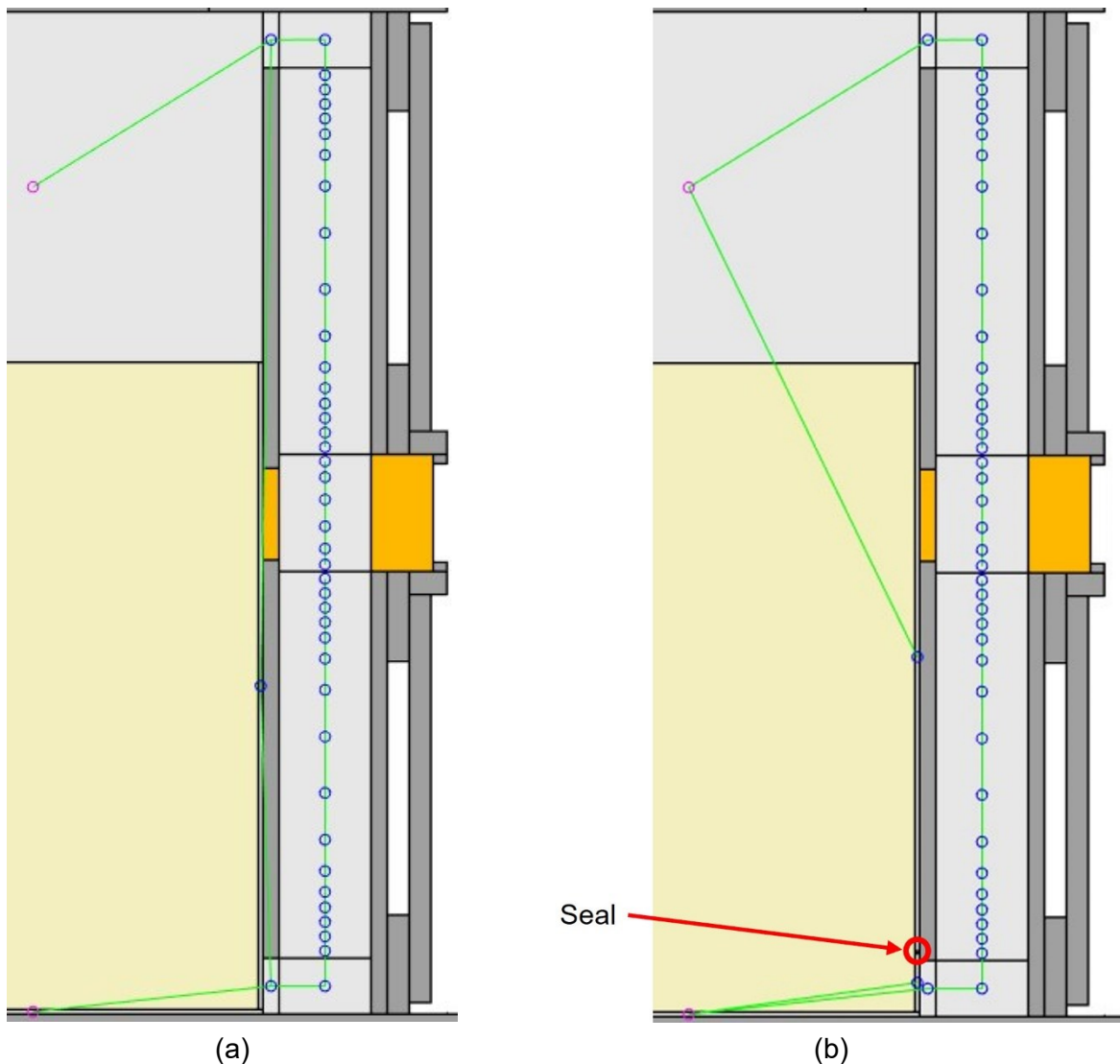


Figure 3.5: The two model versions, (a) without and (b) with displacer piston seal, rendered in *MSPM*, showing the displacer piston and heat exchanger section with gas nodes (blue/pink) and gas faces (green). Seal in (b) highlighted.

3.4.4 Heat Transfer with Environment

The air surrounding the engine is modeled as a node with fixed temperature and convection coefficient that exchanges heat with the outside surfaces of the model. The parameters used for this ‘Environment’ are listed in Table 3.2.

Table 3.2: ‘Environment’ parameters of *Raphael* model

| Gas | Air |
|-------------|----------------------|
| Pressure | 1 atm |
| Temperature | 298 K |
| h | 5 W/m ² K |

These parameters are the model defaults, except for the heat transfer coefficient h , which was determined analytically as follows. As there was no forced air movement around the engine in the lab, the engine surface would be subjected to natural convection which can be described by the Grashof number [45]:

$$Gr_L = \frac{g \beta (T_s - T_\infty) L^3}{\nu^2} \quad (46)$$

where: $g = 9.81 \text{ m/s}^2 =$ gravitational acceleration

$\beta =$ coefficient of volume expansion (1/K), equals $1/T$ for ideal gases

$T_s =$ surface temperature (°C)

$T_\infty =$ temperature far from surface (°C)

$L =$ characteristic length of geometry (m)

$\nu =$ kinematic viscosity of the fluid (m²/s)

All fluid properties are taken at the film temperature [45]:

$$T_f = \frac{T_s + T_\infty}{2} \quad (47)$$

Since only one value for h can be applied to all surfaces, it was derived for the surfaces that were expected to contribute most to environment heat loss, which is the outside of the heater and cooler. Both have a vertical length of $L = 0.096$ m and a diameter of $D = 0.273$ m. Their surface temperatures are assumed to match the source and sink temperatures. All parameters and calculation results for both heater and cooler are given in Table 3.3. The following condition determines if the surface can be treated as a vertical plate [45]:

$$D \geq \frac{35 L}{Gr_L^{1/4}} \quad (48)$$

$$0.273 \text{ m} \geq 0.0824 \text{ m}$$

This was calculated with the smaller Grashof number. Hence the Nusselt number correlation for a vertical plate can be used [45]:

$$Nu_L = \left(0.825 + \frac{0.387 Ra_L^{1/6}}{\left(1 + \left(\frac{0.492}{Pr} \right)^{9/16} \right)^{8/27}} \right)^2 \quad (49)$$

where: $Ra_L = Gr_L Pr =$ Rayleigh number [45]

$Pr =$ Prandtl number of fluid

Finally, the heat transfer coefficients are obtained from the Nusselt number definition [45]:

$$h = \frac{Nu_L k}{L} \quad (50)$$

where: $k =$ thermal conductivity of fluid (W/m K)

These heat transfer coefficients are expected to be higher than they would be for the other convective surfaces, such as the displacer cylinder head and base, because the heater and cooler have the most extreme temperatures compared to the surroundings. Also, the true coefficients may

be smaller as the surface temperatures will not match the source and sink temperatures in reality. Therefore, the value $h = 5 \text{ W/m}^2 \text{ K}$ was used in the model as an estimate of the overall average.

Table 3.3: Calculation results of natural convection coefficients for heater and cooler.

| Parameter | Heater | Cooler |
|------------------|---|---|
| T_s | 423.15 K | 278.15 K |
| T_∞ | 298 K | |
| T_f | 360.6 K | 288.1 K |
| $\beta = 1/T_f$ | $2.77 \cdot 10^{-3} \text{ 1/K}$ | $3.47 \cdot 10^{-3} \text{ 1/K}$ |
| $\nu (T_f) [45]$ | $2.17 \cdot 10^{-5} \text{ m}^2/\text{s}$ | $1.47 \cdot 10^{-5} \text{ m}^2/\text{s}$ |
| L | 0.096 m | |
| Gr_L | $6.397 \cdot 10^6$ | $2.767 \cdot 10^6$ |
| $Pr (T_f) [45]$ | 0.7132 | 0.7323 |
| Ra_L | $4.562 \cdot 10^6$ | $2.027 \cdot 10^6$ |
| Nu_L | 25.0 | 20.1 |
| $k (T_f) [45]$ | 0.03024 W/m K | 0.02476 W/m K |
| h | $7.89 \text{ W/m}^2 \text{ K}$ | $5.18 \text{ W/m}^2 \text{ K}$ |

3.5 Numerical Data Acquisition and Processing

In this section it will be outlined which model outputs were used and how they were processed to obtain the datasets used in Chapter 4.

3.5.1 Model Outputs and Sample Data

Gas temperatures were acquired by ‘Sensor’ outputs placed in the model at locations corresponding to the experimental measurement locations (see Figure 2.7). Heat exchanger Reynolds numbers were measured at the center of both heat exchangers. Figure 3.6 shows the locations of all sensors in *MSPM*.

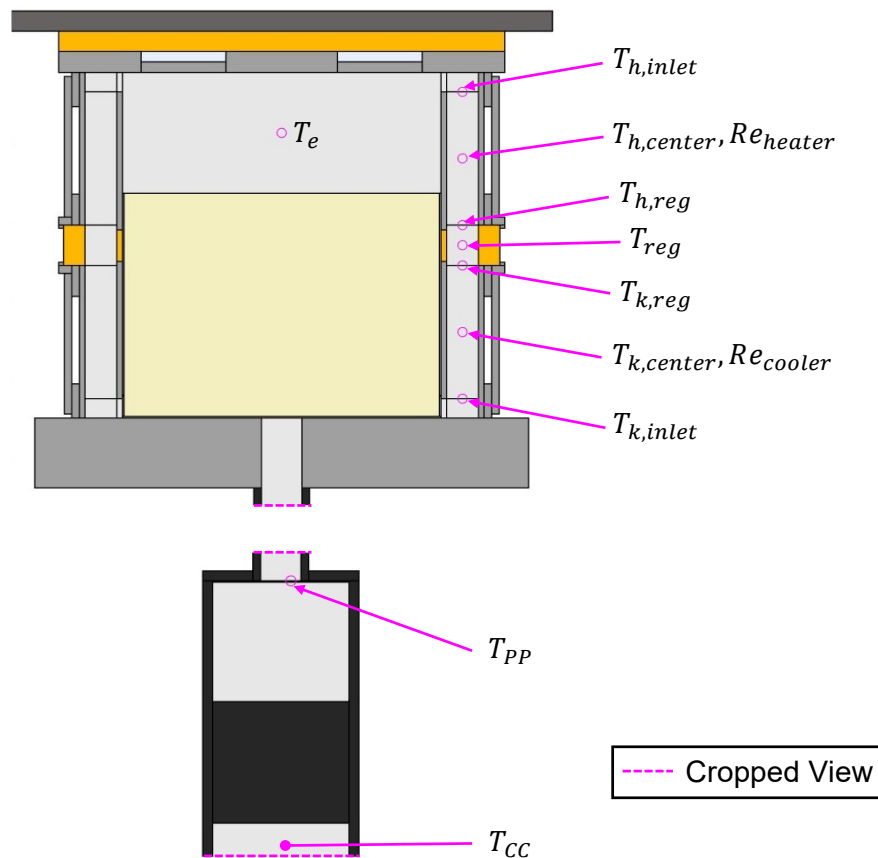
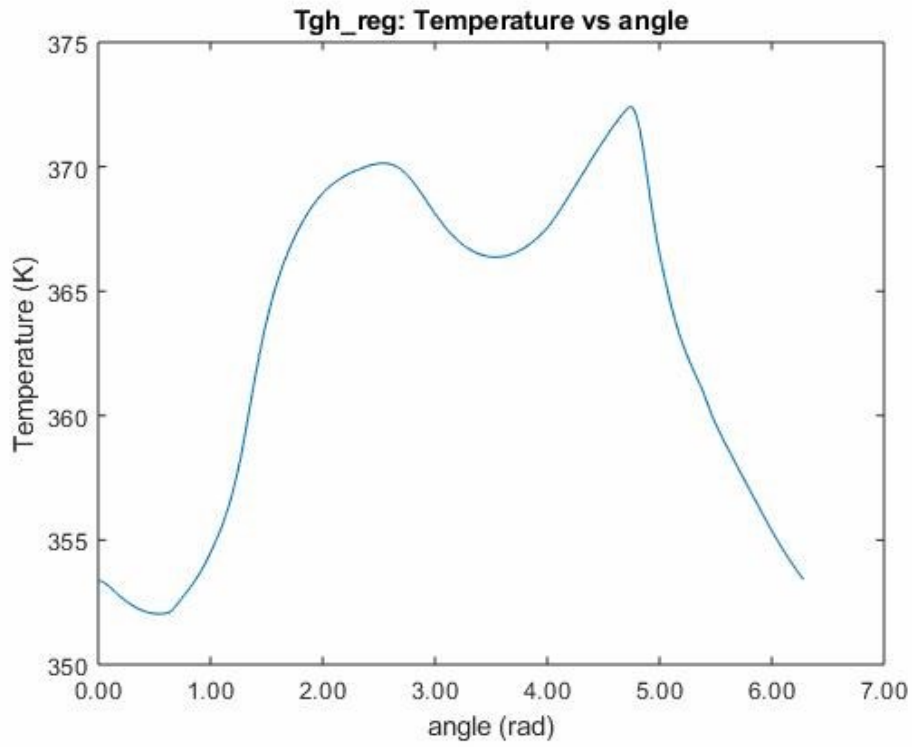
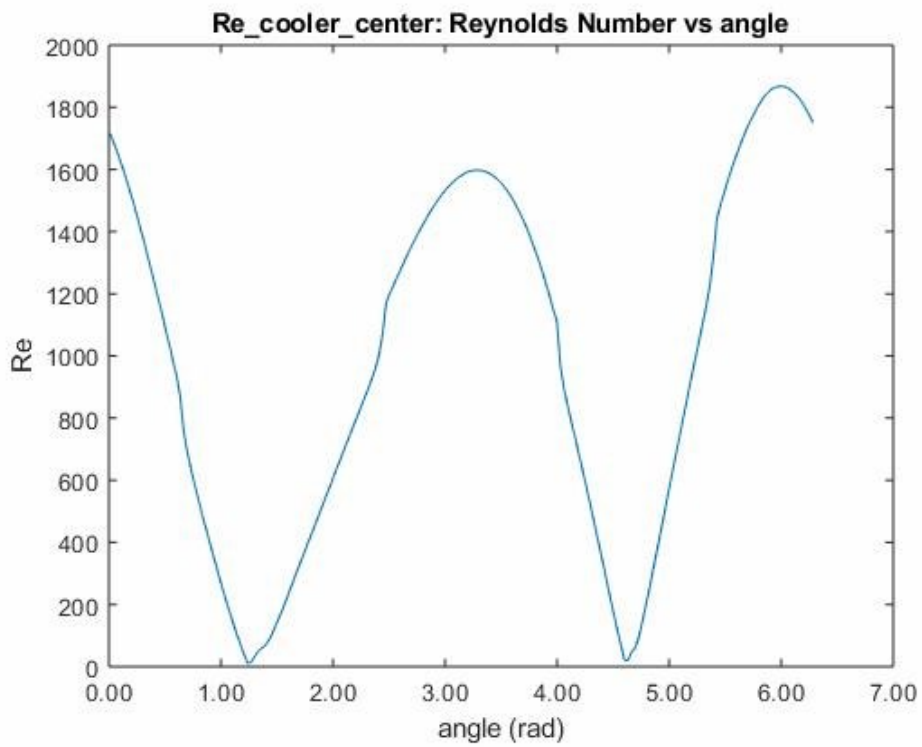


Figure 3.6: Sensor locations in *Raphael* engine model rendered in *MSPM*.

Each sensor outputs data dependent on the crank angle position. A sample of raw temperature and Reynolds number data is given in Figure 3.7. Figure 3.8 shows sample indicator diagrams. These figures are raw outputs directly from the model.



(a)



(b)

Figure 3.7: Sample plots of (a) $T_{h,reg}$ and (b) cooler Reynolds number from *MSPM*, model variant B, setpoint $p_{set} = 400$ kPa, $f = 207$ rpm.

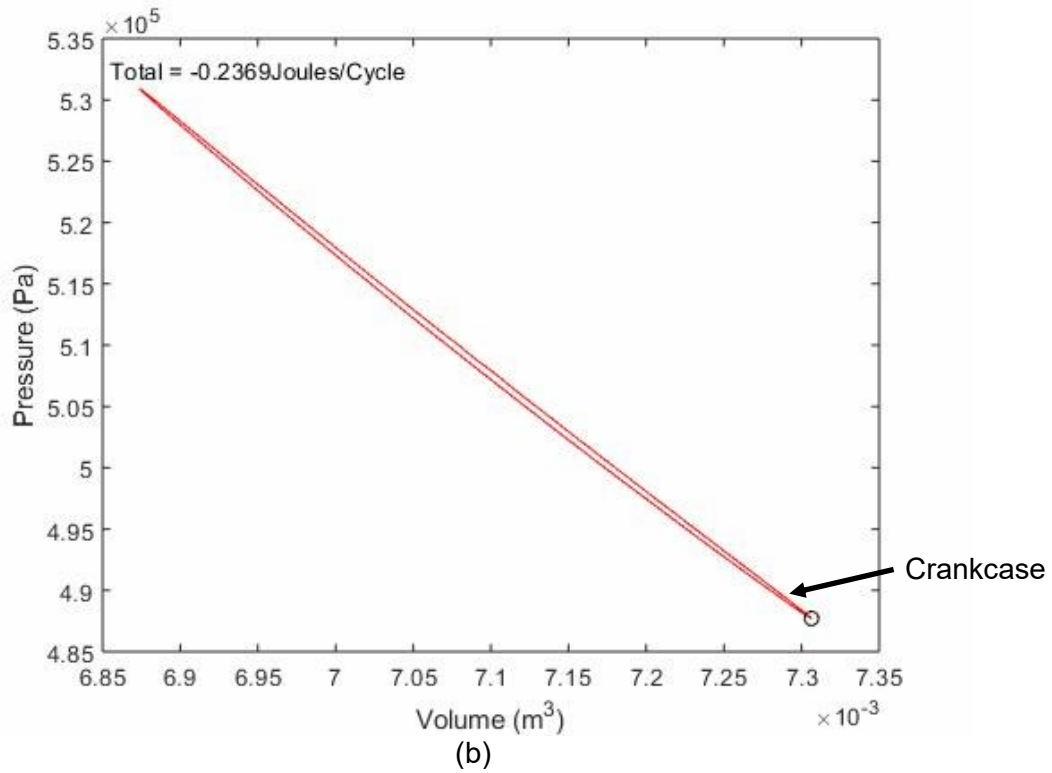
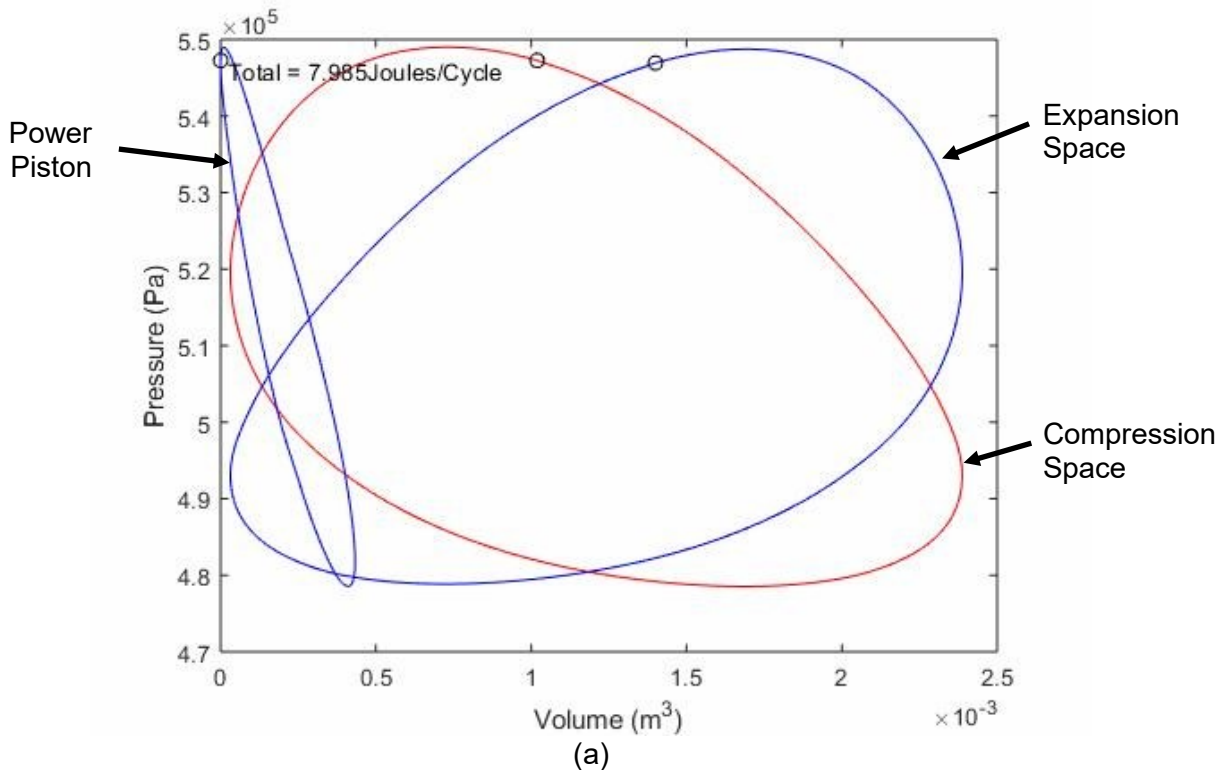


Figure 3.8: Sample indicator diagrams for (a) working space and (b) crankcase from *MSPM*, model variant B, setpoint $p_{set} = 400$ kPa, $f = 207$ rpm. Blue curves have positive work (clockwise), red curves have negative work. Circle denotes starting point (angle zero).

At angle zero, which corresponds to minimum engine volume and the middle of the heating phase with air moving to the expansion space, the heat exchanger Reynolds number is close to its maximum (Figure 3.7 (b)), and the temperature between heater and regenerator is low as the air is coming from the cooler and the heat stored in the regenerator is mostly depleted (Figure 3.7 (a)). This agrees with expectations and indicates that the thermodynamic cycle is modeled correctly. Figure 3.8 shows that each variable volume gas space produces its own indicator plot. For validation in Chapter 4 only the power piston indicator was used as it compares directly to experimental pressure measured in the power piston cylinder. The total indicated work transferred to the mechanism also includes the expansion and compression space work (caused by flow friction) and the crankcase work (caused by gas spring hysteresis). Additional data including shaft power, transient speed and heat flow rates to source, sink and environment were taken from the ‘Statistics’ output file which *MSPM* generates for each run.

3.5.2 Simulation Setup

The input parameters for each run were taken directly from the processed experimental data described in Section 2.7. These are the source temperature (mean of $T_{source,in}$ and $T_{source,out}$), sink temperature (mean of $T_{sink,in}$ and $T_{sink,out}$), absolute pressure p_{mean} , and speed f . Simulation settings were (SS = true) and (movement_option = ‘C’) to run at constant speed until steady state is reached, (simTime = 600 s) to ensure more than enough time to converge to steady state, and the default (max_dt = 0.1 s).

3.5.3 Numerical Data Processing

The model data was processed similarly to the experimental data (Section 2.7). Each model run is saved by *MSPM* in a separate folder, and data is extracted folder by folder, eventually storing the dataset in a single MATLAB file for easy plotting. The following is a summary of the processing steps. The corresponding code is found in Appendix H.

Predefined inputs are atmospheric pressure p_{atm} (to obtain gauge pressure from *MSPM*'s absolute pressure) and engine layout (to assign indicator data correctly). First, choose the folder containing folders of *MSPM* datapoints to process. Then, for each folder (datapoint):

- Read setpoint parameters (T_{source} , T_{sink} , p_{mean}) from folder name
- Find and load 'Statistics.mat' file
- Find and load PV data files of working space and, if present, crankcase
- Extract pressure and volume data, subtracting p_{atm} to obtain gauge pressure
- Find and load relevant sensor data files (temperatures, Reynolds number), and store name and data of each. Convert temperatures from Kelvin to Celsius.
- Calculate working space and crankcase mean pressures
- Close the PV data loops by adding first value at the end, then calculate indicated work for all spaces using trapezoidal integration
- From 'Statistics' file, calculate shaft power, mean and transient speed, and heat flow rates to source, sink, and environment (by summing data of heat per crank angle increment and multiplying with speed)
- Calculate efficiencies from indicated work, speed, shaft power and source heat flow rate

Finally, all data is written to a MATLAB structure and stored in a file.

3.6 Introducing Custom Heat Transfer Coefficients to *MSPM*

In preliminary testing of the *Raphael* engine model in *MSPM* it was found that the model would overpredict the engine power output. Heat flow rates of the heat source and sink were much higher in model results than in the experimental data for equal setpoints. The cause for this was found to be the heat transfer process of convection in the source channel of the heat exchangers which was not represented in the model, as discussed in Section 3.2.8. *MSPM* solves the gas flow and heat transfer through conduction and solid-gas convection, but has no representation for liquid flow and convection in the heat source and sink, which are represented highly simplified as isothermal solid bodies with perfect heat transfer to their neighbouring nodes. As discussed in Section 1.3.7 the series of heat transfer resistances between heat source and working gas are critical in limiting the performance of a real Stirling engine, so it is not surprising that omitting one of them leads to overestimation of the engine performance.

To correct this error and represent all heat transfer processes, a custom heat transfer coefficient was introduced to *MSPM* which can be used to model any heat transfer resistances that *MSPM* cannot simulate at this point. This coefficient h_{custom} with the unit (W/m² K) can be specified in the GUI for any body of solid material and is added as an additional resistance term to the conductance calculation for all faces that connect the parent body's nodes to other solid nodes. Thus, it can be used to represent any mechanism that causes a heat transfer resistance between bodies modeled as solid, such as contact resistance between surfaces or convection in a heat source. This added functionality is in line with the future opportunity 'Source/Sink Simulation' suggested by Middleton [33]. In its current form the coefficient must not be used on non-solid bodies or bodies with more than one node because it will be applied even to faces within the body, which will cause unphysical results. This could be fixed by a more sophisticated implementation of this feature in the code.

In the *Raphael* engine model described in Section 3.4 this functionality is used to add a convective heat transfer coefficient to the isothermal bodies representing the heat exchanger source channels. These coefficients will model the heat transfer resistance caused by convection from the source/sink liquids to the channel walls which is not modeled by *MSPM*. The values of h_{custom} for source and sink are input parameters to the model and must be determined before any valid comparison between model and experimental data can take place. The coefficients could be

obtained from experimental data through Newton's law of cooling if all other parameters are known:

$$\dot{Q} = h_{custom} A_{s,liquid} (T_{\infty} - T_s) \quad (51)$$

where: \dot{Q} = heat flow rate (W)

h_{custom} = convective heat transfer coefficient (W/m² K)

$A_{s,liquid}$ = surface area of source channel walls (m²)

T_{∞} = bulk temperature of liquid medium (°C or K)

T_s = wall surface temperature (°C or K)

However, the solid wall surface temperature is not known from experiments, so the following two approaches were taken instead to estimate the heat transfer coefficient values:

1. Using analytical or empirical correlations for the Nusselt number from literature based on flow characteristics in the source channel.
2. Estimating the surface temperature through a CFD study and using equation (51).

The resulting coefficients from both approaches are used in Chapter 4 to carry out the validation of the *MSPM* model. It should be noted that the accuracy of both approaches depends on the accuracy of the properties of the heat transfer liquids. Especially in the case of the heater, as currently there is no information from the supplier of the silicone oil about the temperature dependence of its thermal conductivity and specific heat. This means that the results of the following sections are estimates with considerable margins of inaccuracy.

3.6.1 Analytical Estimation of Liquid Heat Transfer Coefficients for *Raphael* Model

Figure 3.9 shows the cross section of the heater in *MSPM* with the solid nodes and faces drawn. The view is normal to the flow of the liquid in the source channel, which is shown with its dimensions annotated. The red outline illustrates the walls of the channel that are affected by the custom heat transfer coefficient. The real channel is rounded at the short sides (see Figure 2.5), but

in the model and for this calculation it is assumed to be rectangular with the height chosen so that its surface area is equal to that of the real geometry.

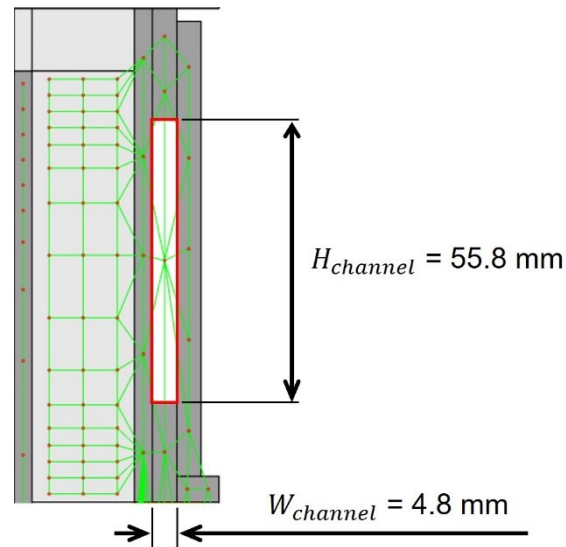


Figure 3.9: Cross section of one half of the heater, as shown in *MSPM*. Gas channel on left, source channel (red outline, dimensioned) on right. Solid nodes (red dots) and faces (green lines) are rendered to show heat flow path between source channel and fins.

Internal forced convection is governed by the Reynolds number [45] as given by

$$Re = \frac{\rho U D_h}{\mu} = \frac{U D_h}{\nu} \quad (52)$$

where: ρ = fluid density (kg/m^3)

U = flow velocity (m/s)

D_h = hydraulic diameter of the channel (m)

μ = dynamic viscosity of the fluid (Pa s)

ν = kinematic viscosity of the fluid (m^2/s)

The flow velocity is obtained from the calibrated pump mass flow rates as:

$$U = \frac{\dot{m}}{2 A_{cross} \rho} \quad (53)$$

where: \dot{m} = mass flow rate (kg/s)

$$A_{cross} = H_{channel} W_{channel} = 268.8 \text{ mm}^2 = \text{channel cross section area}$$

With the factor of two because the flow is split between both semi-circular sides of the channel symmetrically. The hydraulic diameter is [45]:

$$D_h = 4 \frac{A_{cross}}{l_p} = 8.84 \text{ mm} \quad (54)$$

where: $l_p = 2 (H_{channel} + W_{channel}) = 121.2 \text{ mm} = \text{channel perimeter}$

If the flow is laminar, meaning Re is below 2300, the Nusselt number (Nu) is independent of Re [45]. To determine this, the Reynolds number is calculated for both the flow of the ethylene glycol water mixture in the cooler and the silicone oil in the heater using the above equations. The flow and fluid properties and the resulting Re are listed in Table 3.4. Fluid properties have been taken at temperatures that result in a conservatively high estimate for Re .

Table 3.4: Reynolds number calculation for liquid flow in source channels.

| Parameter | Cooler (30 % Ethylene glycol – water) | Heater (Silicone oil <i>Sil 180</i>) |
|-------------------------------------|---|--|
| \dot{m} (kg/s) (Section 2.4.2) | 0.0236 | 0.0546 (150 °C) |
| ρ (kg/m ³) | 1054 (0 °C) [107] | 932 (measured, 21.5 °C) |
| U (m/s) | 0.04165 | 0.1090 |
| Viscosity | $\mu = 1.7 \text{ cP} = 0.0017 \text{ Pa s}$ (26.7 °C) [107] | $\nu = 2 \text{ cSt} = 2 \cdot 10^{-6} \text{ m}^2/\text{s}$ (200 °C) [111] |
| Re | 228 | 482 |

Both resulting values for Re are well within the laminar range. Therefore, the laminar Nusselt number for both cases depends only on the aspect ratio of the channel [45] which is:

$$AR = \frac{H_{channel}}{W_{channel}} = 11.625 \quad (55)$$

The constant surface temperature case of the analytical Nusselt number solution was assumed here because the heat source and sink were modeled as isothermal. The closest values are given for AR of 8 and infinity (parallel plates) [45]. Based on these the Nusselt number was estimated at

$$Nu_{analytical} \cong 7 \quad (56)$$

Finally, the convective heat transfer coefficients were determined from the Nusselt number definition following:

$$Nu_{analytical} = \frac{h_{analytical} D_h}{k} \quad (57)$$

$$h_{analytical} = \frac{Nu_{analytical} k}{D_h} \quad (58)$$

where: k = fluid thermal conductivity (W/m K)

Thus, as long as the liquid flow remains laminar, the convection coefficient scales proportionally with the thermal conductivity of the heat transfer fluid. The resulting coefficient values are listed in Table 3.5. These values should be taken only as rough estimates because the calculations assume a simple, fully developed flow and the estimated Nusselt number is only approximate.

Table 3.5: Analytical calculation results for custom liquid heat transfer coefficients.

| Parameter | Cooler (30 % Ethylene glycol – water) | Heater (Silicone oil <i>Sil 180</i>) |
|---------------------------------------|---------------------------------------|---------------------------------------|
| k (W/m K) | 0.484 [112] | 0.1 [111] |
| $h_{analytical}$ (W/m ² K) | 383.2 | 79.3 |

3.6.2 CFD Estimation of Liquid Heat Transfer Coefficients for *Raphael* Model

A Computational Fluid Dynamics (CFD) study was performed on the heat exchanger to characterize the liquid flow in the source channel of which there is no experimental data, and to estimate the heat transfer coefficients at steady state. This work was done and documented in detail by Hasanovich [47]. The SOLIDWORKS® Flow Simulation solver was used to simultaneously model the liquid flow and its heat transfer with the channel wall, the heat conduction through the solid geometry of the heat exchanger, and the gas flow and heat transfer in the finned gas channels. The computational domain can be seen in Figure 3.10. Symmetry was assumed about the vertical plane that intersects the liquid inlet and outlet as the liquid flow is expected to split evenly and move symmetrically through the two symmetrical semi-circular channels, and the gas flow in this domain can only be affected by the temperature changes caused by the liquid, so it follows the same symmetry.

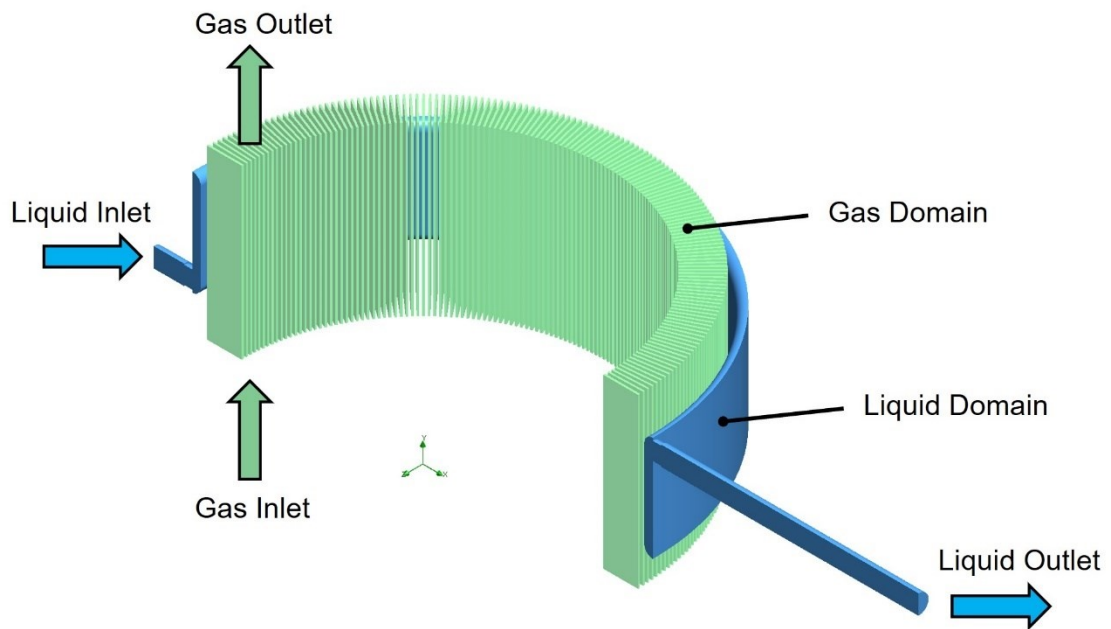


Figure 3.10: Gas and liquid computational domains of CFD study. The solid domain (not shown) is between gas and liquid domains. Adapted from Hasanovich [47].

The simulation required ~ 14 million mesh cells due to the complex setup modeling three components (liquid, solid, gas) and was run at steady state to reduce computational resource requirements and because the interest was only in steady state heat transfer coefficients for the

convection on the liquid side. Mesh independence studies were undertaken for the liquid and gas domain to determine this mesh size. As CFD simulations cannot be regarded reliable without validation, both the liquid and gas side models were compared against analytical estimates for pressure drop, surface temperatures and exit temperatures. The model was found to follow trends with varying boundary conditions (gas pressure and velocity, liquid flow rate and boundary temperatures), and deviations from the analytical estimates were attributed to complex flow geometry that could not be analytically modeled. However, an experimental validation of the CFD study or measurement of the liquid heat transfer coefficients would be needed to reliably determine these important model input parameters.

For boundary conditions, the gas inlet temperature T_i was taken as the regenerator mean effective temperature, which is an estimate originating from Urieli and Berchowitz [40] for the gas temperature entering heater / cooler during the heating / cooling phase:

$$T_i = \frac{T_{source} - T_{sink}}{\ln\left(\frac{T_{source}}{T_{sink}}\right)} \quad (59)$$

where: T_i = gas inlet temperature (K)

T_{source} = source temperature (K)

T_{sink} = sink temperature (K)

With T_{source} and T_{sink} of 150 °C and 5 °C, respectively, as in the experiment. The engine pressure and speed were chosen as a mean of the experimental dataset values. Gas inlet velocity was calculated as the mean from the average engine speed assuming that all air displaced by the displacer piston passes through the heat exchangers. Gas outlet pressure was equated to the chosen engine pressure.

The liquid inlet temperature was set equal to T_{source} or T_{sink} . The liquid outlet pressure was defined as the mean atmospheric pressure measured in experiments. The liquid flow rates and fluid parameters were the same as in Table 3.4. To obtain the convective heat transfer coefficient for the inner wall of the source channel, equation (51) was rearranged for h_{custom} :

$$h_{custom} = \frac{\dot{Q}}{A_{s,liquid} (T_{\infty} - T_s)} \quad (60)$$

The unknown parameters were extracted from the CFD solution. The heat flow rate \dot{Q} was measured for the inner wall surface, the fluid temperature T_{∞} was taken as the spatial average of the entire liquid domain, and the surface temperature T_s was averaged across the inner wall surface. The wall surface area $A_{s,liquid}$ is known from the solid model. All these boundary conditions, the simulation results and the calculated heat transfer coefficients (h_{CFD}) are listed in Table 3.6. The heat flow rate and temperature values used here differ slightly from those given by Hasanovich [47] because they were taken from preliminary results of the CFD study. The simulation was repeated with varying gas boundary conditions to simulate engine pressures (absolute) from 300 to 570 kPa and speeds from 100 to 240 rpm, covering the range of the experimental data (see Table 4.1). The resulting variations in the heat transfer coefficients were smaller than 5 %.

Table 3.6: CFD study boundary conditions and results for liquid heat transfer coefficients [47].

| Parameter | Cooler (30 % Ethylene glycol – water) | Heater (Silicone oil <i>Sil 180</i>) |
|--|---------------------------------------|---------------------------------------|
| Gas Inlet Temperature (°C) | 72.4 | |
| Liquid Outlet Pressure (kPa) | 92.955 | |
| Gas Outlet Pressure (kPa) | 435 | |
| Speed (rpm) | 170 | |
| \dot{Q} (W) | 832.7 | 544 |
| $A_{s,liquid}$ (m ²) | 0.05232 | |
| T_{∞} (°C) | 12.6 | 135.8 |
| T_s (°C) | 34.2 | 98.8 |
| h_{CFD} (W/m ² K) | 735.1 | 281.3 |
| h_{CFD} variation (max-min estimate) | 21.4 (3 %) | 13 (4.6 %) |

3.7 Chapter Conclusion

MSPM is a 3rd order numerical model for Stirling engines and other reciprocating thermodynamic systems. It models the flow of a compressible ideal gas, conduction and convection heat transfer, flow friction, and turbulence effects in an axisymmetric, two-dimensional discretized geometry. This is coupled with a mechanical model that enables simulations with variable engine speed. The model was developed with emphasis on predicting the performance of LTDSEs by accounting for relevant energy losses. The most notable potential weaknesses were identified as the assumption of steady developed flow in matrixes, the use of steady state correlations for systems that are characterized by unsteady oscillating flow, and the inability to model imperfect heat transfer from an isothermal heat source.

The *Raphael* engine described in Chapter 2 was modeled in *MSPM* to conduct an experimental validation of the model which is documented in Chapter 4. The power piston seal was assumed to be leak-free and frictionless, and the displacer piston seal was, for lack of data, modeled in two variants as leak-free or non-existent. Heat transfer resistance from convection between the heat source/sink liquids and the heat exchanger walls was found to significantly affect the engine performance, so a custom heat transfer coefficient was implemented to simulate this. Two estimates for this coefficient's values for the heater and cooler of the *Raphael* were made by analytical correlations and CFD analysis, and both estimates will be tested in Chapter 4.

As documented in Appendix D, the model was further improved by adding functionality to analyze the mesh, and additional model parameters to be varied during automated tests. The discretization of a heat exchanger type was implemented to model the *Raphael* heat exchangers. The calculation of several flow-relevant parameters was corrected, which is expected to improve the model accuracy notably.

More work on *MSPM* is needed to validate if the model can become a useful engine design tool. Most importantly, the applicability of the quasi-steady flow assumption and correlations should be thoroughly verified, and the implementation of a kinematic mechanism with friction should be completed so that an entire thermodynamic and mechanical engine can be modeled and validated.

Chapter 4. Experimental Validation of *MSPM* Model

This chapter presents a validation of the numerical model *MSPM* described in Chapter 3 using experimental data obtained with the LTDSE setup explained in Chapter 2. The validation work is limited to certain parts of the model, which are outlined in the first section. Then the deviations between data from the real engine and several variants of its model representation in *MSPM*, as shown in Section 3.4, are analyzed. Finally, the sensitivity of the model to changes in setpoint parameters, geometry and model parameters is studied.

4.1 Scope of Validation

As discussed in Section 3.3 the experimental validation work on *MSPM* until now has been limited to the indicator diagram shape and work at atmospheric pressure only, and a glance at speed fluctuations. A rigorous validation of the model should consider every process that transfers or converts a significant amount of energy. This includes thermodynamic and mechanical processes, which *MSPM* simulates in separate thermodynamic and mechanical models that are coupled through their outputs. Several improvements have also been made to the model which are documented in Section 3.6 and Appendix D, and which are expected to improve the model accuracy compared to the original *MSPM* code.

This chapter presents a more rigorous validation with more datapoints at different pressure levels and a variety of metrics. The analysis is focused on the thermodynamic model only and at constant speed, with the mechanical model playing no role. There are two reasons for this limitation. Firstly, the available experimental data offers a range of pressure and temperature measurements that allow for a detailed study of the thermal performance, primarily heat transfer. However, data concerning the mechanical model is limited to the overall shaft power and engine speed, which would not provide enough detail to track down sources of error in the model. Secondly, little can be said about the accuracy of the mechanical model until the thermodynamic model has independently been verified to provide reliable outputs, since the reaction forces of the mechanism depend on the pressure forces from the thermodynamic side. The thermal model can be analyzed independently by defining the speed as constant and observing the indicated power of the engine, but the shaft power is comprised of indicated power less losses and therefore the model

error in shaft power can be caused by both the thermodynamic and mechanical model. Figure 4.1 shows a proposed scheme for the validation process of all areas of *MSPM*, where the scope of this work is highlighted in green.

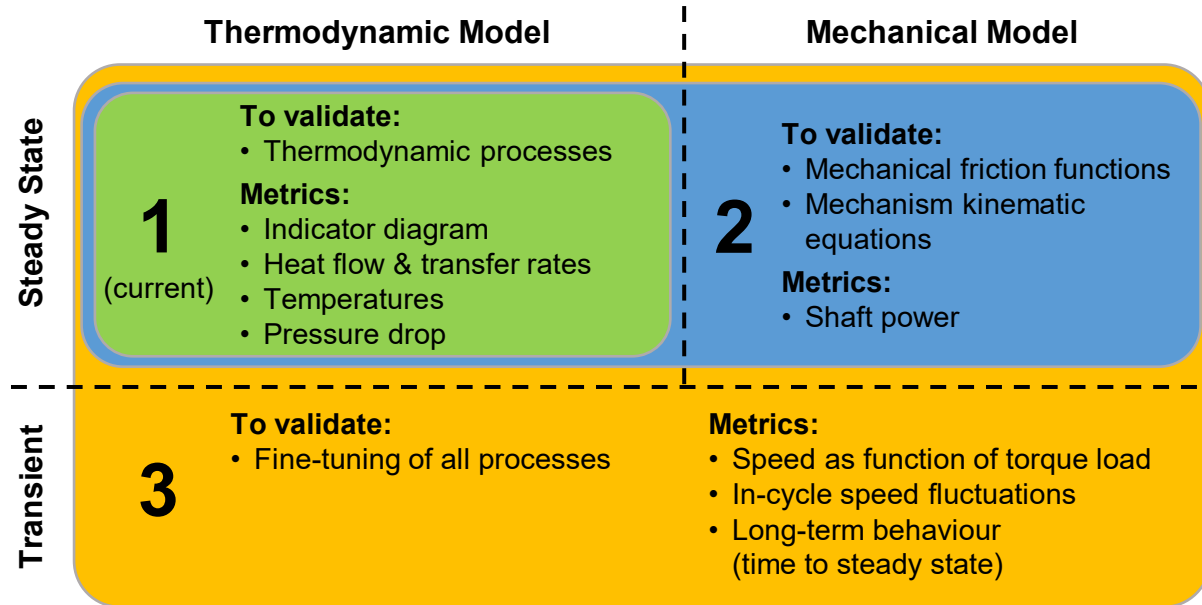


Figure 4.1: Schematic of model validation areas and scope of this chapter (green).

Following this scheme, the overall model can be validated in three phases that each depend on the results of the previous phase. The first phase is the subject of this chapter and is limited to steady-state results of the thermodynamic model, for which experimental data was acquired as described in Chapter 2. For future work the second step would be to examine the mechanical model at steady state, for which the mechanism friction would first need to be quantified. That could be done experimentally by measuring the friction work or torque caused by different parts of a mechanism separately while powering the mechanism externally, for example with a servo motor. Finally, when the model can predict the thermal (indicated) and mechanical (shaft) output with sufficient accuracy, transient cases can be modeled with the goal of predicting speed and the progression towards steady state as a function of applied load. At this point, the model would be able to simulate the entire system's behaviour which is controlled by source temperature, mean pressure and load, similar to a real engine.

4.1.1 Validation Metrics

The thermodynamic model deals with changes in gas properties (pressure, temperature) and thermal energy exchanged between the simulation domain and sources, sinks, and the environment. Important factors are the heat flow path between source/sink and gas, which consists of solid-gas convection, conduction, and solid-liquid convection; as well as flow friction, and turbulence effects. The latter cannot be directly measured with the experiment setup and are insignificant in this case because Reynolds numbers in the heat exchangers are all laminar, as shown in the following sections. The following are the parameters used as validation metrics:

- **Indicator diagram** area (indicated work W_{ind}) and shape as the primary result of the thermodynamic processes.
- **Heat flow rates** of the heat source and sink to analyze scale of heat transfer with gas and heat loss through conduction.
- **Mean gas temperatures** to analyze the effect of heat transfer at specific locations in the working space.
- **Pressure drop** between compression and expansion space as metric for flow friction in heat exchangers and regenerator, which is a significant loss mechanism for LTDSEs.

The indicator diagram is a characteristic measure for the thermodynamic performance of a cyclic machine. The enclosed area of the cycle loop, equal to the indicated work W_{ind} , is commonly used to compare Stirling machines and models. However, the shape of the diagram is a much stronger measure than the area for the accuracy of the thermodynamic model because it reflects the instantaneous gas pressure at each point in the cycle rather than the cumulative result. Two indicator diagrams with equal area can have dissimilar shapes. Therefore, in addition to W_{ind} , the indicator diagram shape will be compared between experiment and model results to verify if the trend in predicted cycle pressures is close to reality.

Though a common metric in Stirling engine literature, the thermal efficiency is not used in this analysis because it would be calculated from two other variables - indicated work and source heat flow rate. Instead, these variables are evaluated directly so that the model deviation in each of them can be observed separately.

4.1.2 Experimental Datasets for Validation

Four experimental datasets are compared to the results of *MSPM*. Table 4.1 lists the datasets with their most important parameters. Each dataset was acquired at a constant setpoint pressure p_{set} , source and sink temperatures T_{Source} and T_{Sink} while varying the applied load torque τ_{set} . Each set has datapoints from zero torque (free running) to the highest torque the engine was capable of before stalling. Zero torque corresponds to the highest engine speed and maximum torque to the lowest speed. The engine stalls when an increase in torque leads to a decrease in speed below some value where the momentum stored in the flywheel is too small to overcome the forced work of the cycle. This minimum speed depends on the flywheel moment of inertia and the amount of forced work, which increases with mean pressure. Thus, the minimum speed is higher in datasets recorded at higher pressure. Datasets 2 and 3 have setpoint pressures in the range where the engine achieves its maximum shaft power, which is around 350 to 400 kPa. All datapoints were acquired following the steady state procedures described in Section 2.5. The measured mean pressures varied slightly between datapoints, so they are given as the mean and maximum variation for each dataset.

Table 4.1: List of experimental datasets used for validation.

| No. | Number of datapoints | p_{set} (kPa) | T_{Source}, T_{Sink} ($^{\circ}\text{C}$) | τ_{set} (Nm) | f (rpm) | p_{mean} (absolute, kPa) | $p_{mean,CC}$ (absolute, kPa) |
|-----|----------------------|-----------------|---|-------------------|------------|----------------------------|-------------------------------|
| 1 | 22 | 200 | 150, 5 | 0 to 1.04 | 238 to 111 | 307.4 ± 2.6 | 309.9 ± 3.6 |
| 2 | 18 | 350 | 150, 5 | 0 to 0.97 | 174 to 124 | 457.0 ± 1.7 | 442.9 ± 10.0 |
| 3 | 20 | 400 | 150, 5 | 0 to 1.04 | 207 to 129 | 509.5 ± 2.8 | 492.1 ± 6.8 |
| 4 | 29 | 450 | 150, 5 | 0 to 1.00 | 154 to 130 | 560.8 ± 2.3 | 547.2 ± 7.0 |

Note that $p_{mean,CC}$ is slightly higher than p_{mean} in the first dataset but notably smaller in the other datasets. This may have been caused by replacing the power piston seal after the first dataset had been acquired. At that time, the seal had worn out so that the power output of the engine had significantly decreased. Since this seal separates the working space from the crankcase, the new seal likely had a smaller leak rate and allowed for a larger pressure difference to build up between

the spaces. The notable effect of the worn seal on power began suddenly and was not yet notable while the first dataset was being recorded, which leads to the assumption that the seal swap had a small, but not significant effect on the engine’s performance and the resulting validation data.

4.1.3 Model Variants for Validation

As discussed in Section 3.6 the convective heat transfer coefficients for convection between the heat source/sink liquids and the heat exchanger wall was added as an input parameter to the model. Two estimates for these parameters were made from analytical heat transfer equations and from a CFD study, and the estimates differed substantially. Since these estimates are not informed by experimental data, the heat transfer coefficient values h_{Source} and h_{Sink} cannot be defined with certainty, but at the same time they significantly affect the model results. Therefore, this chapter compares the results obtained with both estimates from Sections 3.6.1 and 3.6.2. Additionally, two versions of the displacer piston seal (‘non-existent’ and ‘perfect’) were introduced in Section 3.4.2 which will also be compared. In total this means that four model variants will be compared against experimental data in this chapter. Table 4.2 lists their parameters.

Table 4.2: List of model variants used for validation, differing in representation of the displacer piston seal and the source and sink convection heat transfer coefficients.

| Variant | Name | Displacer Piston Seal | h_{Source} (W/m ² K) | h_{Sink} (W/m ² K) |
|---------|------------------------|-----------------------|-----------------------------------|---------------------------------|
| A | No_Seal_h_analytical | ‘non-existent’ | 79.3 | 383.2 |
| B | No_Seal_h_CFD | ‘non-existent’ | 281.3 | 735.1 |
| C | With_Seal_h_analytical | ‘perfect’ | 79.3 | 383.2 |
| D | With_Seal_h_CFD | ‘perfect’ | 281.3 | 735.1 |

The CFD estimate of the heat transfer coefficients is multiple times higher than the analytical estimate. Therefore, the CFD variants are anticipated to predict a better performing engine. Similarly, the ‘perfect’ seal will likely outperform the versions that lack a seal. The properties of the real engine are expected to be somewhere in the range between these model variants. Due to

the significant uncertainty in these model parameters the focus of the validation in the following sections is not to strictly compare absolute values, but to identify trends in the model results that line up with the experimental data. The agreement of trends can indicate that the model may be predicting the thermodynamic processes and the relation between operating parameters and engine performance correctly, but a systematic deviation in the results may be caused by inaccuracies in the model representation of the engine or deficiencies in the code that could be identified and corrected.

4.2 Analysis of Indicator Diagrams

Indicator diagrams and indicated work are an indirect measure of the heat transfer in the engine but are the most important design output for a model to predict because they define the usefulness of a design. Therefore, they are used as the primary validation metric. Sections 4.2.1 to 4.2.3 show only data from model variant A and describe how indicator diagrams were first analyzed against engine speed and pressure, which were then combined into the single measure of Reynolds number. In Section 4.2.4 the model variants are compared.

4.2.1 Indicator Diagram Samples

This section analyzes the indicator diagrams from model variant A. The indicator diagram for each setpoint is defined by the data of total engine volume and pressure measured in the power piston working space, over crank angle. Figure 4.2 compares sample indicator diagrams from the datapoints with the lowest (a) and highest (b) average Reynolds number in the heat exchanger flow. The heat exchanger Reynolds number ($Re_{HX,avg}$) serves as a measure for the thermal load on the heat exchangers and is explained in Section 4.2.5. The experimental and model curves are overlaid, and the area covered by both is highlighted and calculated as the overlap area. A custom algorithm was developed to determine the overlap curve. Pressure is plotted as the difference with respect to the mean of each curve so that both curves are centered on zero pressure. This means the overlap is independent of the slight differences in mean pressure that occur between experiment and model. The percentage of overlapping area is calculated with respect to both the experiment and model curves. The overlap percentage is an approximate measure of the similarity in shape between the indicator curves.

With the two overlap values, two scenarios can occur. Firstly, if one curve is completely enclosed by the other, one of the overlap values is 100 % and the other is equal to the ratio of the curve areas (indicated work). In this scenario, it is likely that both curves have similar shapes, but if the inner curve has a much smaller area than the outer curve, it could vary significantly in shape from the outer curve without affecting the overlap percentage. In this case the overlap criterion does not prove the similarity of shapes and a manual check is required. Secondly, if both overlap values are well below 100 % then neither curve encloses the other, which indicates that their shapes definitely cannot be considered similar. In short, if either of the overlap values are small or both

are below 100 %, the indicator curve shapes may be dissimilar and should be analyzed. The overlap percentage is no accurate metric of shape similarity and is only intended as a simple measure to support the analysis of indicated work. If indicated work and overlap observe similar trends between the datapoints, it follows that the indicator diagram shapes are consistent between the datapoints and it is sufficient to analyze only the indicated work.

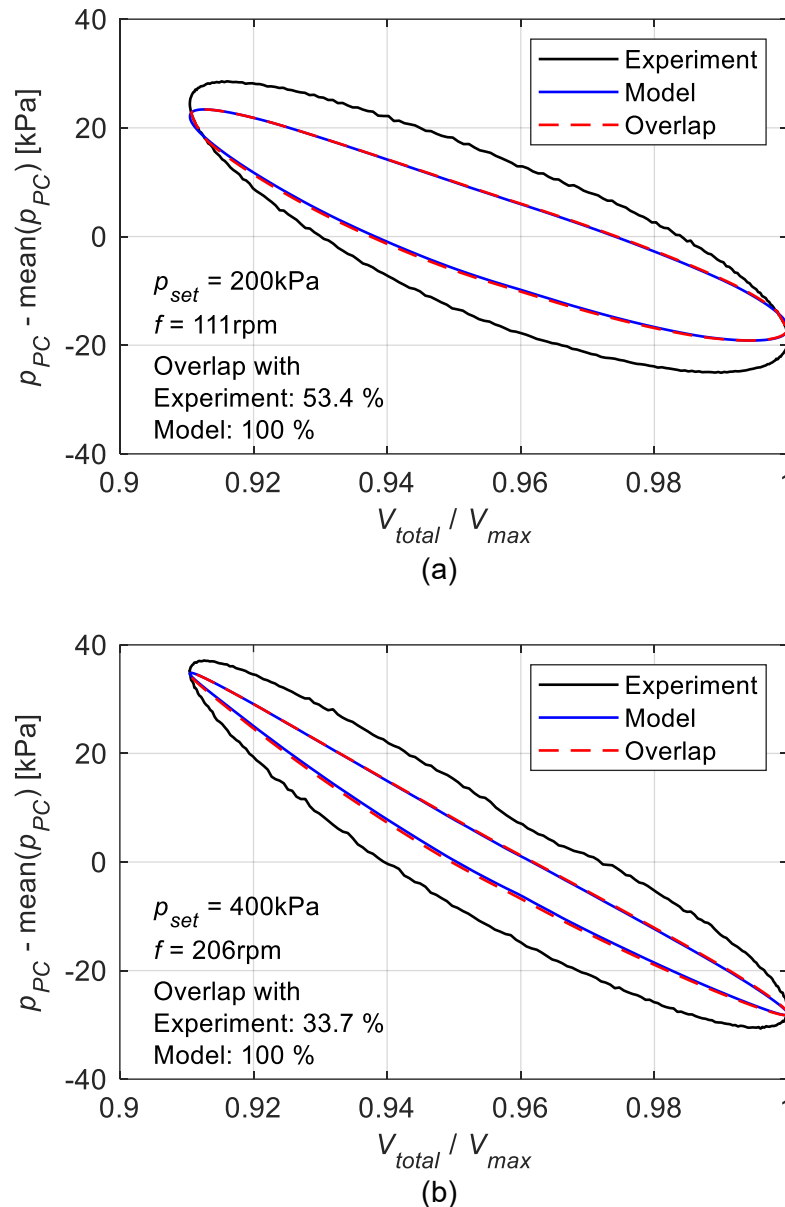


Figure 4.2: Sample indicator diagrams from model variant A. Showing experiment and model data, and overlapping area as measure of similarity of shapes, (a) Lowest $Re_{HX,avg}$ datapoint, (b) Highest $Re_{HX,avg}$ datapoint.

In Figure 4.2 it can be seen that for both the low (a) and high (b) Reynolds number cases the model curve is completely enclosed by the experiment curve and the model strongly underpredicts the area (W_{ind}) of the indicator diagram. Both plots have the same axis limits so the curve shapes can be directly compared. The experimental curve in (b) is more slender in the vertical direction compared to (a), which means that the temperature-induced pressure difference between expansion (upper curve) and compression (lower curve) is smaller in the high Reynolds number case. This indicates that the heat exchangers are running into a heat transfer limit in case (b) and are not able to provide enough thermal energy to produce the same level of indicated work as in case (a). The indicator shape is well replicated by the model in both cases as the overlaid curves are close to parallel for the most part. The underprediction of W_{ind} by model variant A is likely due to the low estimate of the heat transfer coefficients and the ‘non-existent’ displacer piston seal that this variant uses. This supports the initial expectation that these parameters would lead to the model predicting a low engine performance.

4.2.2 Indicated Work vs. Speed and Pressure

The indicated work results from the experiment and model variant A for all four datasets are plotted over engine speed in Figure 4.3. Colors represent the different datasets which are denoted by their setpoint pressure p_{set} .

Looking at the experimental data (circles), all datapoints are close to following a single linear trend and W_{ind} does not appear to have a strong dependence on p_{set} . This confirms the observation from Figure 4.2 that the heat exchangers are encountering a heat transfer limit which prevents them from producing a higher indicated work at higher pressures. W_{ind} decreases with increasing speed and the highest indicated work of each dataset is achieved at the lowest speed tested. This is expected as the residence time of the gas inside the heat exchangers is longer at lower speed, which leads to a greater temperature change, pressure swing and thus indicated work.

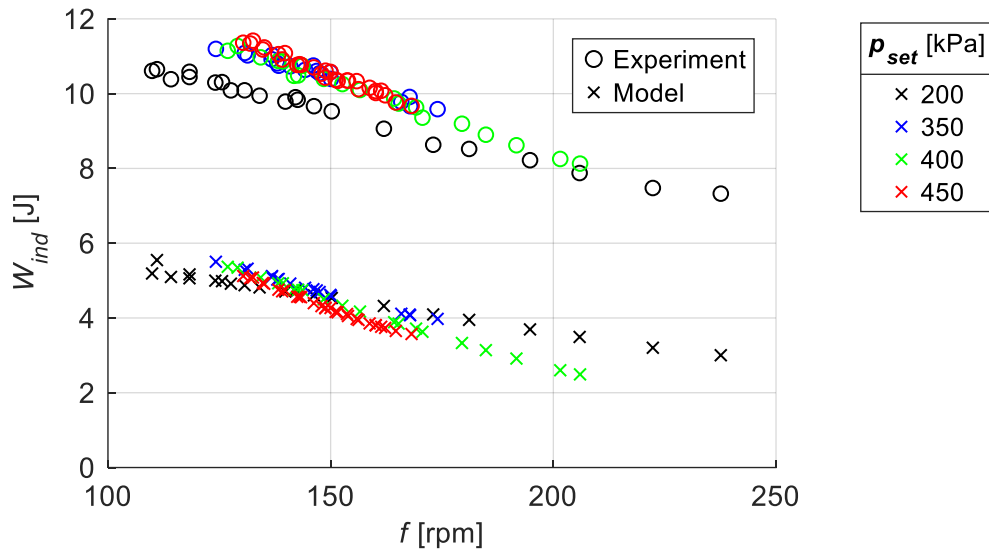


Figure 4.3: Indicated work over engine speed, experiment and model variant A, all datasets.

The model results (\times 's) underestimate W_{ind} by about 50 % or more at all datapoints, which is in line with the observation from Figure 4.2. However, the downward trend of W_{ind} over f appears very similar to the experimental data, and the weak dependency on p_{set} is also captured relatively closely by the model. The experiment shows the highest overall values of W_{ind} at a p_{set} of 400 kPa to 450 kPa while the model estimates the maximum at a lower pressure. These observations suggest that model variant A has a source of systematic error that causes a relatively consistent underprediction of the indicated work, but the trends in changes of W_{ind} and the indicator diagram shapes between setpoints are generally reflected by the model, including the heat transfer limit at higher set point pressures. The model predicts the optimal p_{set} to be lower than the experimental data shows, but the differences in W_{ind} with pressure are small compared to the effect of speed.

The trends of model and experiment indicated work relative to each other are more visible when shown as the relative deviation between the two, which is displayed in Figure 4.4. In this plot a horizontal trend would indicate that the model deviation is consistent across a dataset. For model variant A the model deviation follows a worsening trend from around 50 % at low speed and pressure to almost 70 % at high speed and pressure. The slope of the lowest pressure dataset ($p_{set} = 200$ kPa) is smaller than that of the other datasets, meaning that the trend of W_{ind} over speed was predicted better at lower pressure. This is in line with the conclusion from Figure 4.3 that model variant A reaches a heat transfer limit at a lower pressure than the real engine, which causes the model to underestimate W_{ind} increasingly at higher pressures.

The points the three datasets with $p_{set} \geq 350$ kPa show clear linear trends that all appear to have a similar slope, but are slightly offset from each other based on p_{set} . This shared trend suggested that it may be possible to collapse all datapoints onto a single curve, independent of pressure, by plotting them over a different variable. Since W_{ind} depends mostly on heat transfer, and the convective heat transfer coefficients in *MSPM* are based on correlations that are functions of the Reynolds number in the heat exchangers, it seemed likely that W_{ind} could be correlated with a cycle-average of the Reynolds number. This hypothesis is explored in the following section.

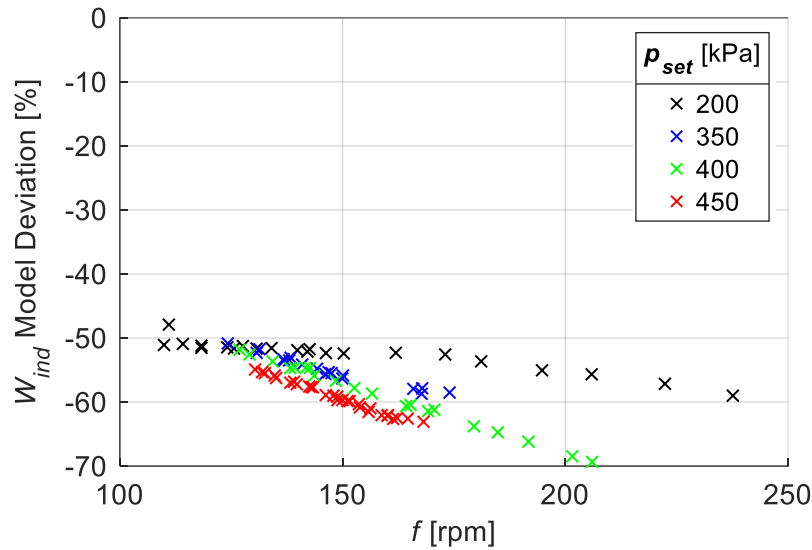


Figure 4.4: Relative deviation of indicated work from model to experiment, over engine speed, model variant A, all datasets.

4.2.3 Indicated Work and Indicator Overlap vs. Reynolds Number

Indicated work is compared over the cycle averaged Reynolds number in the gas channels of the heat exchangers, $Re_{HX,avg}$. The values for $Re_{HX,avg}$ used here were taken directly from the model results as the average of the Reynolds number data measured in the central gas nodes of the heater and cooler. Alternatively, an estimate for $Re_{HX,avg}$ can also be calculated from experimentally measured pressure, heat exchanger gas temperature, and engine speed. A comparison between the Reynolds numbers from the model and this estimate will be given in section 4.2.5.

The trend of the deviation in W_{ind} over $Re_{HX,avg}$ for model variant A is shown in Figure 4.5. As hypothesized in the previous section, most datapoints now fall on one linear trendline, except for the points with a Reynolds number of less than 500 which follow a slightly different slope. It appears that $Re_{HX,avg}$ is a suitable parameter over which to identify trends in the results of the thermodynamic model, and it will be used in the following section to compare the four model variants. The goal is to find the model variant that makes the most reliable predictions in terms of the overall deviation and the consistency of the deviation between setpoints with varying Reynolds numbers.

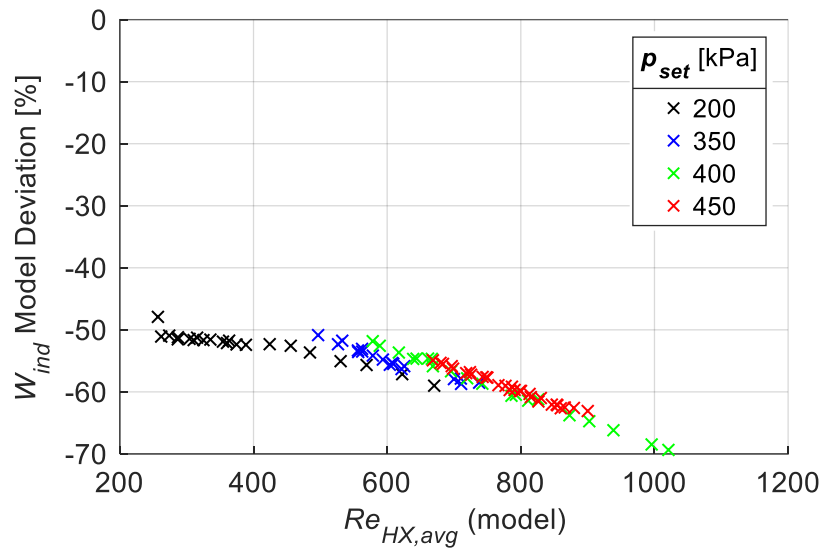


Figure 4.5: Relative deviation of indicated work from model to experiment, over average heat exchanger Reynolds number, model variant A, all datasets.

To support the analysis of indicated work and verify that the indicator diagram shapes follow a similar trend to W_{ind} , Figure 4.6 shows the percentage of overlap of the experimental and model indicator curves for the same datapoints. In this case, the trend is identical to that in Figure 4.5 because the indicator curve from the model is completely enclosed by the experimental curve for all datapoints.

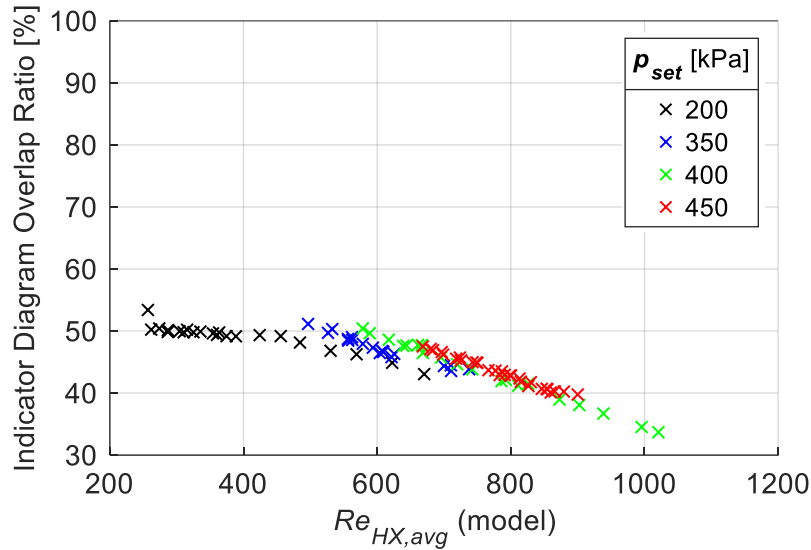


Figure 4.6: Indicator diagram overlap ratio over average heat exchanger Reynolds number, model variant A, all datasets.

4.2.4 Comparison of Model Variants

This section forms the core part of the validation of the thermodynamic model in *MSPM* where the predictions of indicated work from the four variants of the *Raphael* engine model shown in Table 4.2 are compared. The predicted W_{ind} from all variants is shown along with the experimental measurements in Figure 4.7 (a). For analysis of the model error, Figure 4.7 (b) presents the W_{ind} deviation over the heat exchanger Reynolds number analogous to the previous section. The model variants are represented by different markers.

Figure 4.7 (a) shows that variants B and D predict substantially higher values for W_{ind} than variants A and C, which is expected due to the higher liquid heat transfer coefficients in B and D. The trends of A and C compare somewhat to the underestimation of W_{ind} observed in previous validation of the model (Section 3.3). It also stands out that B and D predict the highest indicated work to occur at the highest charge pressure (450 kPa), indicating that there is no heat transfer limit restricting the performance, while A and C predict the maximum at lower pressures. This illustrates that the resistances to heat transfer in the heat exchangers are critical as they limit the thermodynamic work an engine can attain and the operating pressure at which the maximum work is achieved.

Figure 4.7 (b) shows that all variants produce vastly differing results that vary from -70 % to +70 % deviation in W_{ind} and each have different trends over the Reynolds number. The lowest deviation overall is achieved by variant B with an average absolute deviation of 9 %. However, none of the models made predictions that could be considered consistent, meaning a steady level of deviation over varying Reynolds numbers. Variant A follows a negative gradient (slope) while B has a positive gradient, and for both the gradient decreases from low to high Reynolds numbers which suggests the curves may be described by parabolic function and have a maximum at some $Re_{HX,avg}$. Variant C follows a linear downward trend and D appears to show relatively consistent values over the tested Reynolds number range for each dataset. However, for variant D the four datasets appear as clearly distinct lines, which shows that its predictions are dependent on the setpoint pressure p_{set} and the deviation is not a function of $Re_{HX,avg}$ alone. This behaviour also appears to be present in variant C but with a much less significant offset between the datasets. Thus, it seems that for models that include the displacer piston seal (C and D), especially when combined with a strong heat exchanger performance enabled by the high estimate for the heat transfer coefficients (D), the model deviation in indicated work is more strongly related to engine pressure than to the Reynolds number.

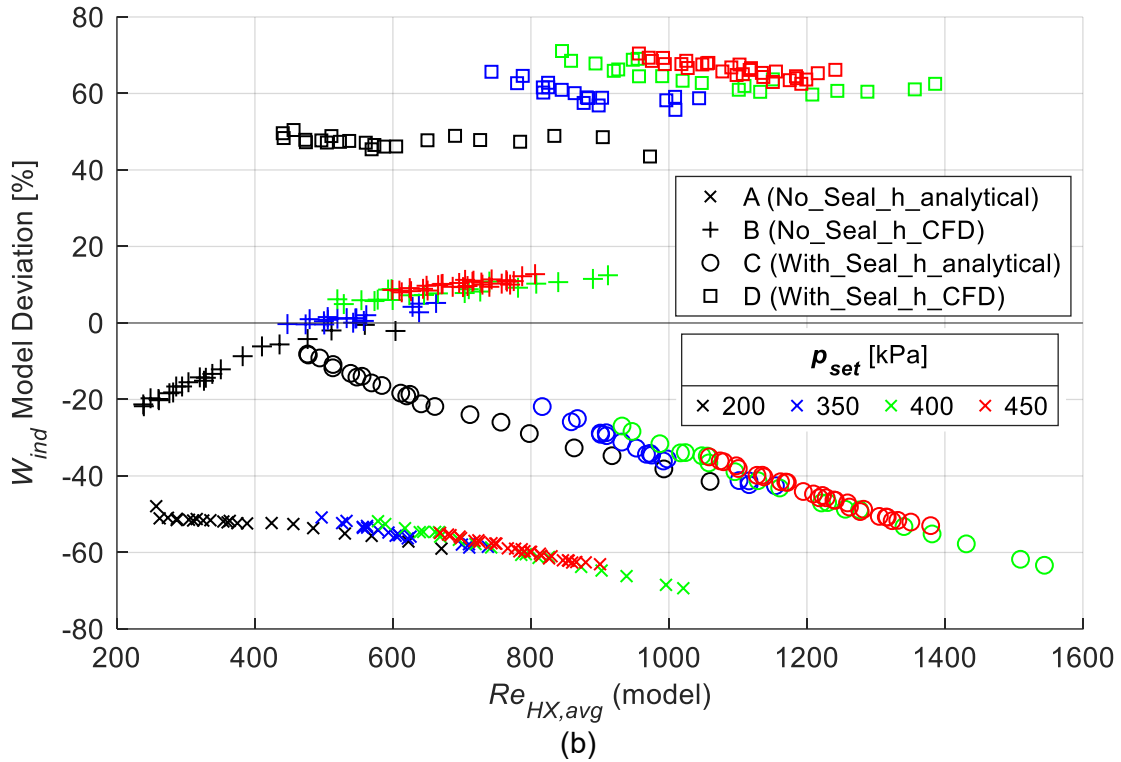
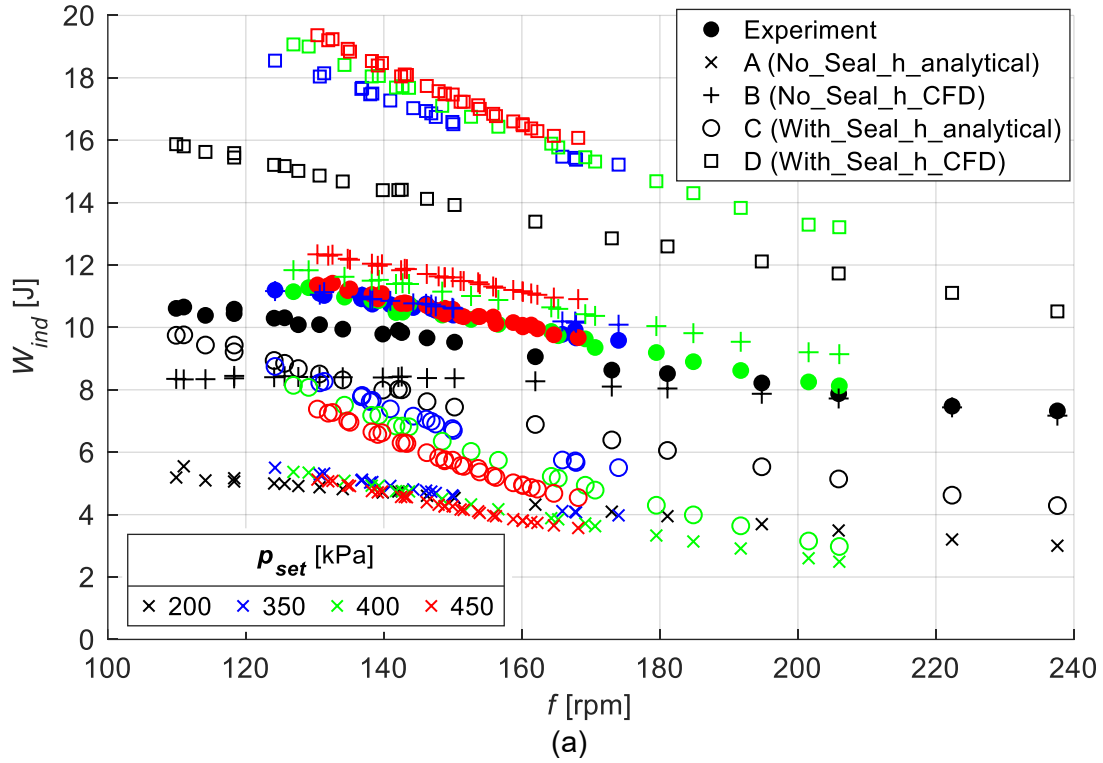


Figure 4.7: Indicated work from all model variants A to D and experiment. (a) Absolute values over engine speed, (b) Relative deviation between model and experiment over average heat exchanger Reynolds number.

The two parameters that differ between the variants, namely the presence of the displacer piston seal and the choice of source heat transfer coefficients, affect the indicated work in the way that was expected in Section 4.1.3. Variant A predicts the lowest values, compared to which variant B with the CFD-estimated heat transfer coefficients gives much higher values with a deviation between -20 % and +20 %, as well as an upward trend over $Re_{HX,avg}$ that contrasts the downward trend of variant A. A similar comparison can be drawn between variants C and D where both the range of deviation values and the gradient are significantly higher for variant D. The effect of the heat transfer coefficients appears consistent in that increasing them causes an increase in both the values of W_{ind} and its gradient over the Reynolds number.

The effect of the displacer piston seal is different. The model variants with the seal, C and D, also have substantially higher values of W_{ind} than their counterparts without the seal, A and B, respectively. However, the gradients in the data of variants C and D are reduced compared to A and B. It seems that an improvement of the displacer piston seal, of which only the extreme cases of a ‘non-existent’ and a ‘perfect’ seal are shown here, leads to an increased indicated work and a decreased gradient of the W_{ind} deviation over $Re_{HX,avg}$. Another significant difference caused by the presence of the seal is in the range of $Re_{HX,avg}$ of the model variants. Much higher Reynolds numbers, by a factor of about 1.5 to 2, are recorded with variants C and D compared to A and B. This must be caused by the leak flow in the variants without a modeled seal that is able to leak through the displacer piston gap instead of passing through the heat exchangers, reducing the flow rate and therefore the Reynolds number in the heat exchangers. Since the Reynolds number is proportional to flow rate (assuming density is unchanged), the ratio of $Re_{HX,avg}$ between a ‘test’ case with seal leakage and a case with a ‘perfect’ seal should indicate the share of the flow caused by the displacer piston that is ‘lost’ to seal leakage, as:

$$\frac{\dot{m}_{Leak}}{\dot{m}_{DP,total}} = \frac{Re_{HX,avg}(\text{perfect seal}) - Re_{HX,avg}(\text{test})}{Re_{HX,avg}(\text{perfect seal})} = 1 - \frac{Re_{HX,avg}(\text{test})}{Re_{HX,avg}(\text{perfect seal})} \quad (61)$$

where: \dot{m}_{Leak} = leak flow rate in ‘test’ case (kg/s)

$\dot{m}_{DP,total}$ = total flow rate caused by movement of displacer piston (kg/s)

This ratio is a model estimate for the relative significance of the displacer piston leak in the ‘test’ case. It could be used to quantify the leak rate for different variants of a piston and its seal during the design stage of an engine, for example to compare different widths of the appendix gap. With a validated model that is confirmed to produce reliable results, the leak rate for the seal of an existing engine could also be found by tuning the modeled seal until the resulting predictions of W_{ind} and other metrics agree with experimental data. In Section 4.2.5 the Reynolds number data from Figure 4.7 will be analyzed quantitatively.

To summarize, both the effectiveness of the displacer piston seal and the range of the source heat transfer coefficients greatly affect the model predictions for indicated work. An increase to either of the parameters causes corresponding increases in the range of W_{ind} . The gradient of the W_{ind} deviation over the Reynolds number is increased by the heat transfer coefficients but decreased by the seal effectiveness. This means that the gradient can be controlled to some extent by balancing these two parameters. The primary goal for optimizing the model is to get a deviation that is consistent over all setpoints, therefore a gradient of zero is desired. The observations from Figure 4.7 suggest that it might be possible to obtain such a consistent model by varying the heat transfer coefficients and the seal effectiveness in between the four extreme cases presented here. For instance, using model variant C and increasing h_{source} and h_{sink} could potentially increase the values and gradient of the curve such that a consistent deviation around 0 % could be achieved. This will be discussed in section 4.7.6 through a sensitivity study on the heat transfer coefficients. As a note, the analytical and CFD estimates of the heat transfer coefficients can be seen as extreme cases since both were obtained through valid methods but differed significantly from each other.

In addition to W_{ind} , the indicator diagram shape was compared for all model variants. Like with Figure 4.6 the plot of the indicator overlap ratio showed the same trends as the indicated work in Figure 4.7 because for all datapoints one curve almost completely encloses the other. A direct comparison of the indicator diagrams for the two extreme setpoints with the highest and lowest Reynolds number is drawn from Figure 4.8. Generally, the shapes of all model curves agree with the experimental results as they are mostly parallel, and the deviations in W_{ind} are caused by deviations in pressure that exist consistently along the entire length of the curve. Variant C in setpoint (a) and variant B in setpoint (b) are by far the closest to the experimental curves, each with a deviation in W_{ind} of about 10 %. Inspecting these curves more closely reveals that most of

their deviation occurs in the ‘top left’ and ‘bottom right’ parts of the plot, meaning the first half of the expansion and compression phases, respectively. Thus, efforts to reduce the deviations should focus on these parts of the engine cycle. It should also be noted that all model curves are smooth and have no visible discontinuities, which indicates that the solutions are numerically consistent and achieved a low convergence residual. In preliminary testing this was not always the case for models that produced incoherent results.

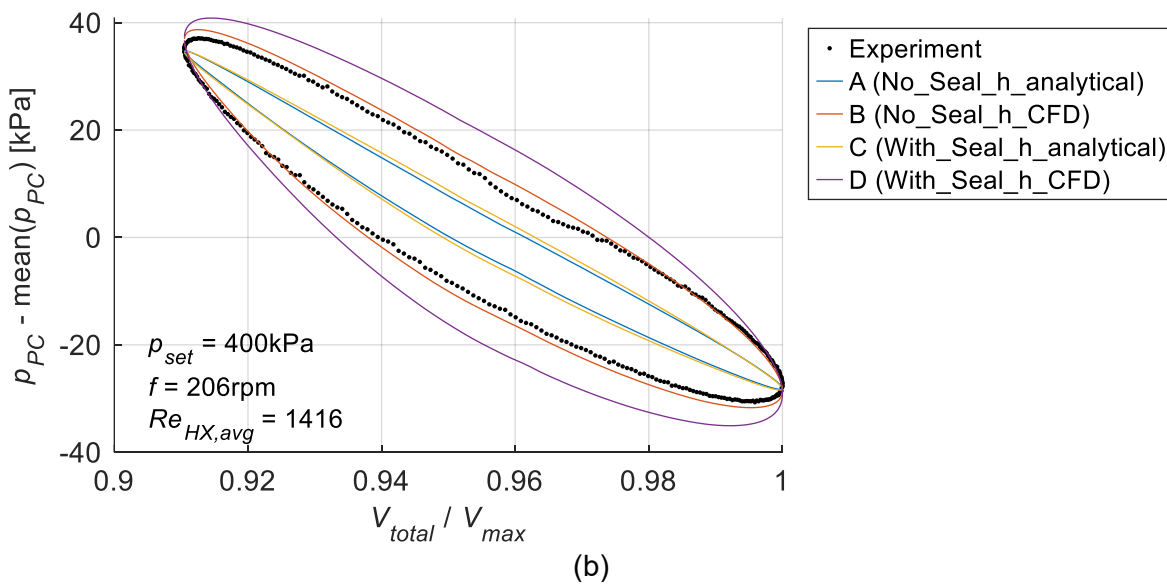
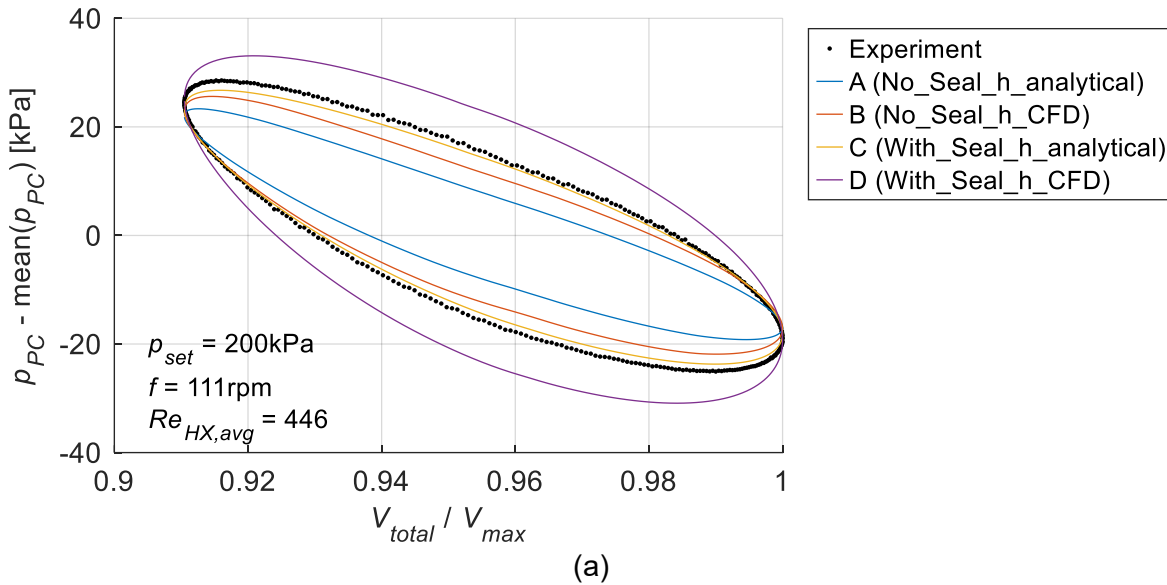


Figure 4.8: Comparison of indicator diagrams from experiment and all model variants for datapoints with (a) lowest $Re_{HX,avg}$, (b) highest $Re_{HX,avg}$. $Re_{HX,avg}$ is from equation (68).

In practice, a model like *MSPM* needs to make predictions about proposed engine designs or modifications for which no experimental data is available. Unfortunately, as found from the above analysis of four model variants, the predictions of *MSPM*'s thermodynamic model depend heavily on parameters that cannot be accurately estimated without experimental data. Therefore, *MSPM* at this point can not be expected to return reliable predictions unless the analysis is supported by experiments, CFD studies, or other data that help to define the model input parameters with certainty.

4.2.5 Comparison of Reynolds Number from Model and Theory

To put into context the Reynolds number values that are output by the model, an estimate for $Re_{HX,avg}$ was calculated from experimental data using the theoretical average flow velocity and gas properties in the heat exchangers following equation (62). Note that this does not necessarily represent the true Reynolds number since the flow velocity was never measured experimentally.

$$Re_{HX,avg} = \frac{\rho_{HX,avg} U_{HX,avg} D_{h,HX}}{\mu(T_{HX,avg})} \quad (62)$$

where: $\rho_{HX,avg}$ = average fluid density in heat exchanger (kg/m³)

$U_{HX,avg}$ = average flow velocity in heat exchanger (m/s)

$D_{h,HX}$ = hydraulic diameter of heat exchanger gas channel (m)

$T_{HX,avg}$ = mean temperature of heat exchanger gas flow (°C)

$\mu(T_{HX,avg})$ = dynamic viscosity of air at the mean temperature (Pa s)

(linear interpolation of data from [113])

The temperature and Re vary slightly between heater and cooler, but since this is only an approximation of the average, the mean between heater and cooler inlet temperatures is used:

$$T_{HX,avg} = \text{mean}(T_{h,inlet}, T_{k,inlet}) \quad (63)$$

Density is obtained from the ideal gas law using the mean temperature and pressure:

$$\rho_{HX,avg} = \frac{p_{mean}}{R T_{HX,avg}} \quad (64)$$

where: p_{mean} = mean absolute working space pressure (Pa)

$R = 287 \text{ J/kg K}$ = specific gas constant of air

The flow velocity is linked to the average velocity of the displacer piston and assumes that all of the air displaced by the piston actually passes through the heat exchangers:

$$U_{HX,avg} = \frac{A_{DP}}{A_{HX}} U_{DP,avg} \quad (65)$$

where: A_{DP} = frontal area of displacer cylinder (m^2)

A_{HX} = flow cross section area of heat exchanger (m^2)

$U_{DP,avg}$ = average velocity of displacer piston (m/s)

The average piston velocity is simply obtained from the distance traveled per cycle and the cycle rate (speed):

$$U_{DP,avg} = 2 S f \quad (66)$$

where: S = displacer piston stroke (m)

f = mean engine speed (Hz)

he hydraulic diameter of the rectangular gas channel is [45]:

$$D_{h,HX} = 4 \frac{A_{HX,channel}}{l_{P,HX}} = 1.905 \text{ mm} \quad (67)$$

where: $A_{HX,channel} = H_{channel,HX} W_{channel,HX} = 20 \text{ mm}^2 =$ gas channel cross section area

$$l_{P,HX} = 2 (H_{channel,HX} + W_{channel,HX}) = 42 \text{ mm} = \text{gas channel perimeter}$$

$$H_{channel,HX} = 1 \text{ mm} = \text{gas channel height}$$

$$W_{channel,HX} = 20 \text{ mm} = \text{gas channel width}$$

From equations (62) to (67) follows the below expression for the theoretical estimate of the heat exchanger Reynolds number. It is proportional to the mean working space pressure and engine speed as long as all other parameters can be assumed constant.

$$Re_{HX,avg} = \frac{2 p_{mean} A_{DP} S f D_h}{R T_{HX,avg} A_{HX} \mu(T_{HX,avg})} \quad (68)$$

$$Re_{HX,avg} \propto p_{mean} f$$

The assumption made for equation (65) is equivalent to the model variants C and D that assume a perfect displacer piston seal. Therefore, variants C and D are expected to have Reynolds number values close to the estimate from equation (68), and variants A and B should be much lower. Figure 4.9 compares the $Re_{HX,avg}$ from the model and the theoretical estimate. The relative deviation of the model results from the estimate is plotted over the estimated $Re_{HX,avg}$ as the reference. The expectation is confirmed. Variant D is remarkably close to the estimate at less than 2 % deviation. Variant C is about 10 % higher, likely because it uses the lower, analytical set of heat transfer coefficients, which lead to lower overall gas temperatures, which in turn increase the Reynolds number. Variants A and B show values between 25 % and 50 % below the estimated $Re_{HX,avg}$, and A is above B for the same reason described above. There is also a clear upwards trend for A and B, meaning that at lower Reynolds numbers the model $Re_{HX,avg}$ is relatively smaller compared to the theoretical estimate than at higher Reynolds numbers. An explanation for this may be that the relative significance of the leak through the displacer piston gap becomes smaller as

the Reynolds number is increased because flow friction in the narrow gap may increase with the Reynolds number at a greater rate than flow friction through the heat exchangers and regenerator, thus limiting the leak flow rate relative to the heat exchanger flow rate at higher Reynolds numbers. It is also likely that at higher speed, leakage is less significant because of the reduced time between reversals of the leak flow direction.

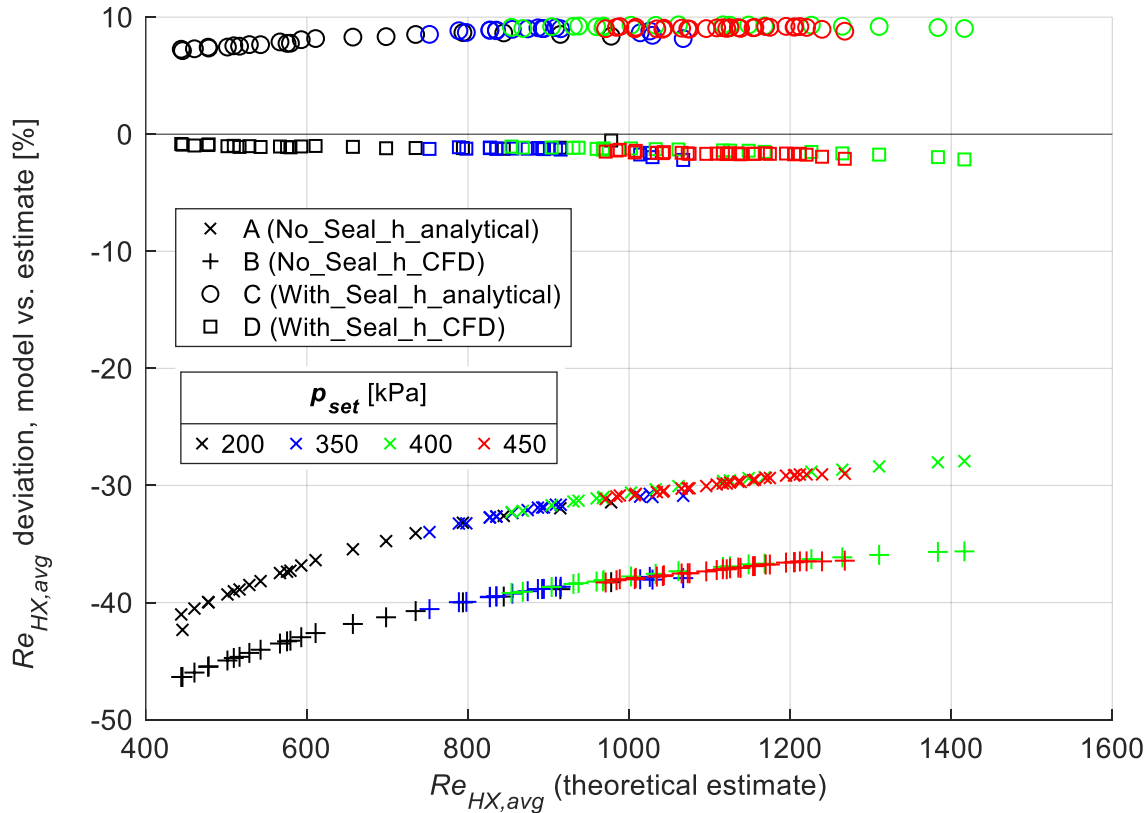


Figure 4.9: Relative deviation of heat exchanger Reynolds number $Re_{HX,avg}$ between model variants and theoretical estimate from equation (68), plotted over the theoretical estimate.

These observations show that *MSPM*'s predictions of the gas flow in the heat exchangers, as characterized by the average Reynolds number, and the effect of the displacer piston seal on the flow, agree with theoretical expectations. As discussed in the derivation of equation (61), the analysis of $Re_{HX,avg}$ could be used to quantify the unknown leak rate of a setup if experimental data of W_{ind} is available and the model is validated, or to validate the leak rate predicted by the model if experimental data of the leak rate is available.

4.3 Analysis of Heat Consumption and Rejection

The heat flow rates going into the heater and out of the cooler are a more direct metric of heat transfer than W_{ind} and are of interest as they define the thermal efficiency of the engine. They factor in not only the effective heat transfer between heat source / sink and the working gas but also the ineffective heat losses through conduction between source and sink and convection with the environment. Thus, they are a measure for the overall accuracy of the heat flows predicted by the thermodynamic model and of the engine geometry represented in the model. However, as discussed in Chapter 2.4.3 the temperature dependent heat capacity of the heater's heat transfer liquid could only be estimated from limited available data. This means the experimental heater flow rate is subject to a large margin of uncertainty and can only be compared to model results in terms of trends. Due to this limitation the heat flow rates are used as a secondary metric.

Figure 4.10 is a combined plot of the heat flow rates of the heater and cooler from experimental data and the four model variants, with the same 89 datapoints as used in previous sections. All red datapoints are from the heater and all blue points from the cooler. They are plotted over the estimated Reynolds number from equation (68) so that all results are shown at equal $Re_{HX,avg}$ and a direct comparison of the heat flow values is possible.

Firstly, looking at the experimental data only, measured heat flow rates range between about 500 W and 1200 W and increase with $Re_{HX,avg}$ as the amount of heat exchanged with the working gas increases. At $Re_{HX,avg}$ greater than 800 most experimental datapoints show \dot{Q}_{Cooler} to be greater than \dot{Q}_{Heater} , which is impossible due to conservation of energy. This clearly illustrates the aforementioned uncertainty in the experimental \dot{Q}_{Heater} . The actual heater flow rate is most likely higher than the cooler flow rate by about the same margin that the model data shows. This margin between \dot{Q}_{Heater} and \dot{Q}_{Cooler} is expected to be relatively constant over all datapoints as it represents mostly the heat lost to the environment, apart from a small share (ca. 15 W for *Raphael*) that becomes shaft power. The energy balance of the system in equation (69) shows this. The heat flow to the environment should be nearly constant because most of the heat is lost directly through the outer walls of the heat exchangers and depends on the source and sink temperatures which are constant. Energy lost to viscous and mechanical friction leaves the system as heat and is included in the \dot{Q} terms:

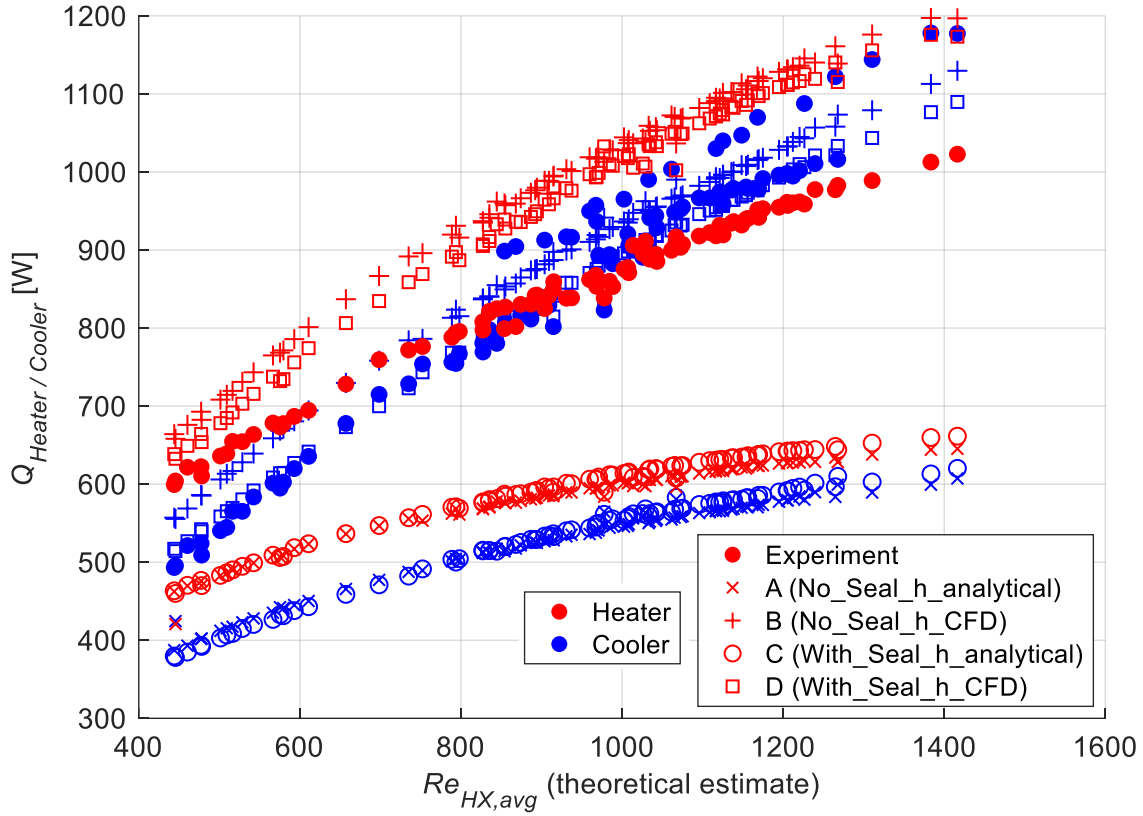


Figure 4.10: Heater and Cooler heat flow rates over average heat exchanger Reynolds number, experiment and all model variants A to D, all datasets.

$$\dot{Q}_{Heater} = \dot{Q}_{Cooler} + \dot{Q}_{Environment} + P_{shaft} \quad (69)$$

where: $\dot{Q}_{Environment}$ = flow rate of heat lost to environment (W)

Looking at the model data, there is a consistent margin between \dot{Q}_{Heater} and \dot{Q}_{Cooler} , fulfilling the expectation. Model variants A and C predict nearly identical heat flow rates that are significantly lower and do not show the strong upwards trend with $Re_{HX,avg}$ compared to the experimental values. The predictions of variants B and D are also very similar in values and trends, but they also match the experimental data well. While their cooler flow rates are very accurate, their heater flow rates deviate notably from the experiment at higher Reynolds numbers, but this is likely due to the uncertainty of the experimental data for the heater. The variants making similar predictions are the pairs that share the same heat transfer coefficients (analytical and CFD-

derived), which shows that the heat flow rates depend strongly on the heat transfer coefficients but are almost unaffected by the displacer piston seal and the changes in $Re_{HX,avg}$ that it causes. This makes sense while the heat exchanger flow is laminar as in this case the Nusselt number and heat transfer coefficient in the gas channel are constant and not affected by $Re_{HX,avg}$.

To quantify the model error in the heat flow rates, Figure 4.11 shows the relative deviation of the model results with respect to the experimental values. Variants A and C have a significant deviation that increases with $Re_{HX,avg}$ from about 20 % to almost 50 %. Variants B and D, which share the CFD-derived heat transfer coefficients, show a strong agreement for the cooler that is consistently within 15 % with an average of 4 %. This suggests they predict the heat transfer processes in the engine well. Therefore, their deviation in indicated work, as seen in Section 4.2.4, may not be from inaccuracies in heat transfer but in other processes like flow friction or seal leakage.

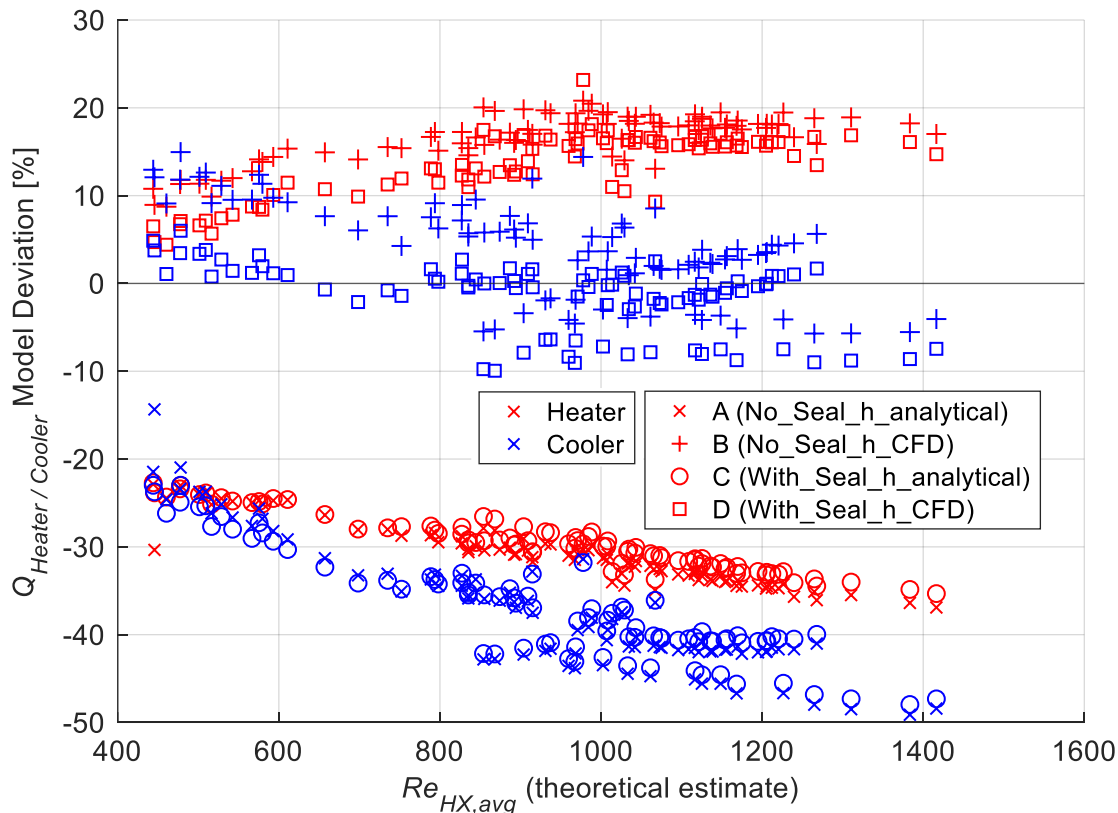


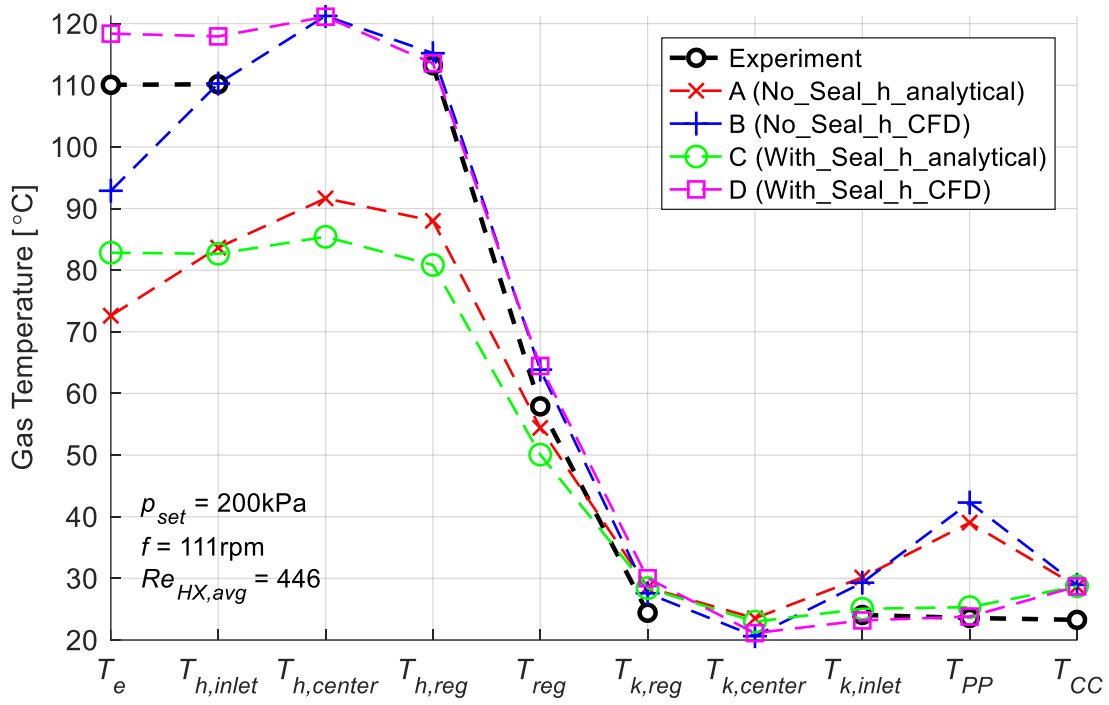
Figure 4.11: Relative deviation of Heater and Cooler heat flow rates over average heat exchanger Reynolds number, all model variants A to D, all datasets.

4.4 Analysis of Gas Temperatures

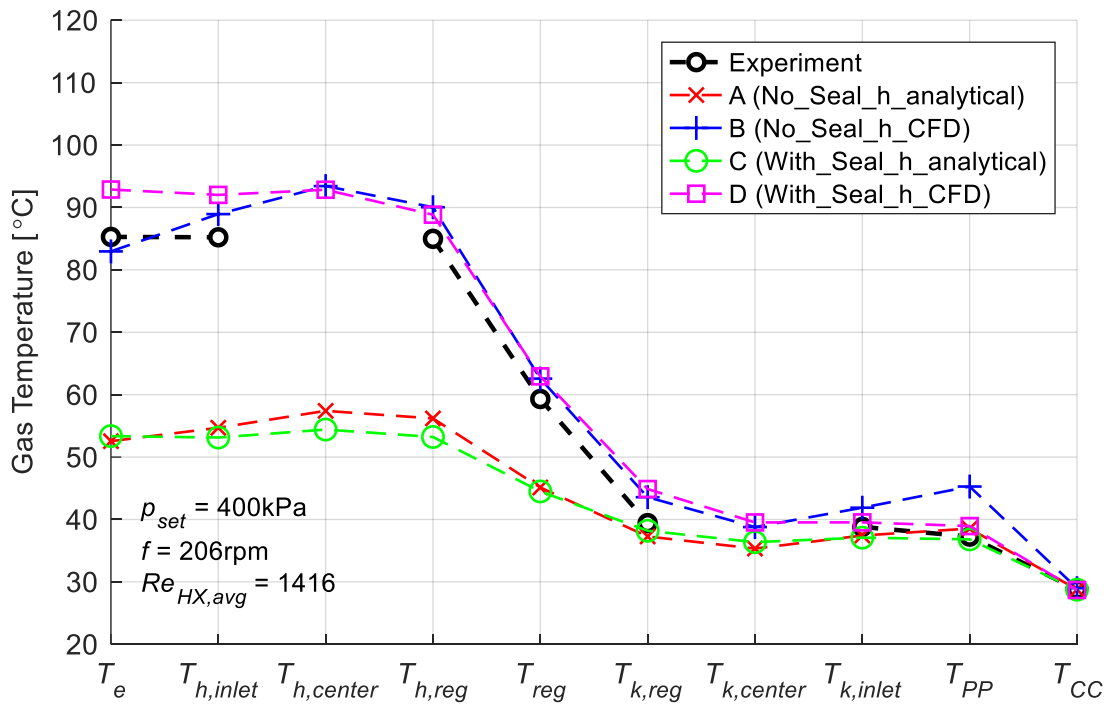
The gas temperatures in different sections of the working space are a direct measure of the heat exchanger performance and are the root cause of the pressure swing and indicated work output of the engine. They are used only as a supporting metric for model validation for several reasons:

- Gas temperatures undergo a strong oscillation during the engine cycle, but due to the limitation of thermocouple response time only the average temperatures are available in the experimental data. The average temperatures convey much less information than the indicator diagram which represents every point in the cycle.
- Gas temperatures are measured at point locations in the experiment, but are calculated and averaged for volume elements by the model. These measurement methods and locations may not be perfectly comparable.
- For each datapoint, temperature data from several locations must be analyzed. This complicates the interpretation of results compared to W_{ind} which is only a single value per datapoint that summarizes the engine performance.

Due to the amount of data, the full set of temperatures from all measurement locations is only shown for the two setpoints with the lowest and highest heat exchanger Reynolds number in Figure 4.12 (a) and (b), respectively. The plots show a temperature profile that follows, from left to right, the measurement locations (see Figure 2.7) along the gas flow path from top to bottom of the engine, starting at the expansion space, through the heat exchangers, to the power piston space and crankcase. See Section 2.7.2 for the equations of the experimental temperatures and Section 3.5.1 for the sensor locations in the model. $T_{h,center}$ and $T_{k,center}$ are not available from the experiment setup and therefore only shown for the model data.



(a)



(b)

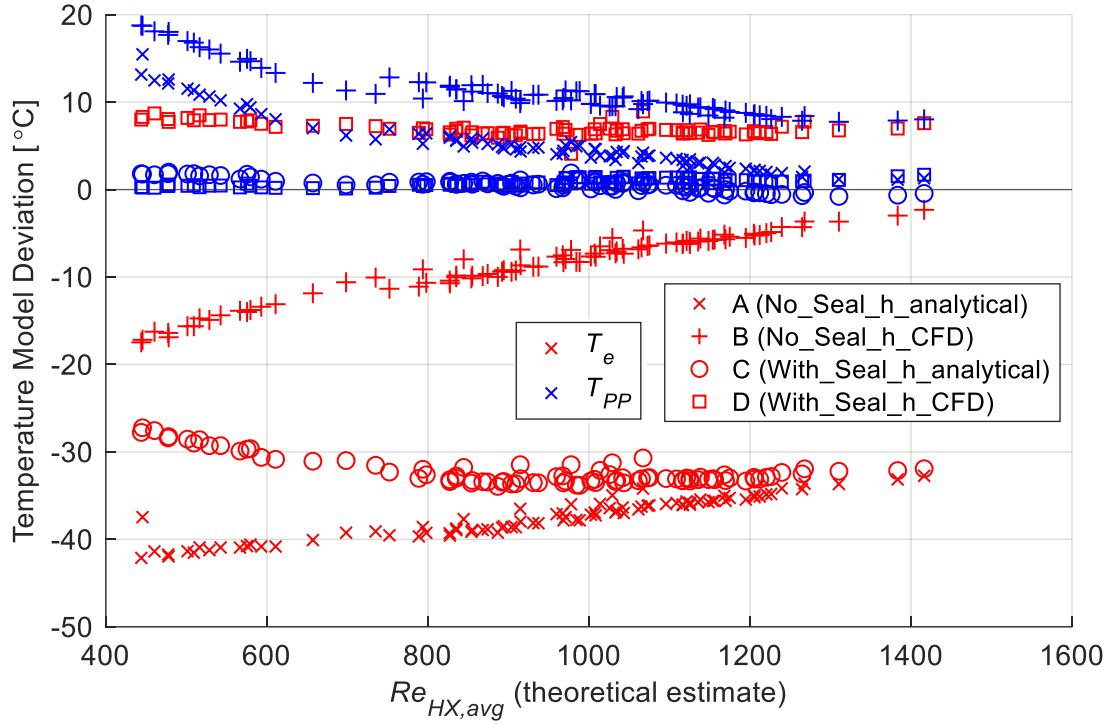
Figure 4.12: Gas temperature profile along locations in working space from Expansion Space (left) to Crankcase (right). Data from experiment and all model variants for datapoints with (a) lowest $Re_{HX,avg}$, (b) highest $Re_{HX,avg}$. $Re_{HX,avg}$ is the estimate from equation (68). Data exists only at the marker positions, dashed lines are for readability.

From the experiment data it is observed that at the lower $Re_{HX,avg}$ (Figure 4.12 a) the temperature difference between the hot side (left) and cold side (right) is about 85 °C whereas at the higher $Re_{HX,avg}$ (Figure 4.12 b) it is much smaller at about 45 °C. This is expected as an increased Reynolds number means an increased mass flow rate of gas to be heated and cooled, which causes the temperature change done by the heat exchangers to decrease as they have a heat transfer limit. At the center of the regenerator the temperature (T_{reg}) is almost equal in both cases. Looking at the model results, variants B and D predict fairly accurate temperatures at most locations, compared to variants A and C which drastically underestimate the hot side temperatures but are similar on the cold side. This is another observation in favour of the heat transfer coefficients obtained from CFD, in addition to the findings from the previous sections.

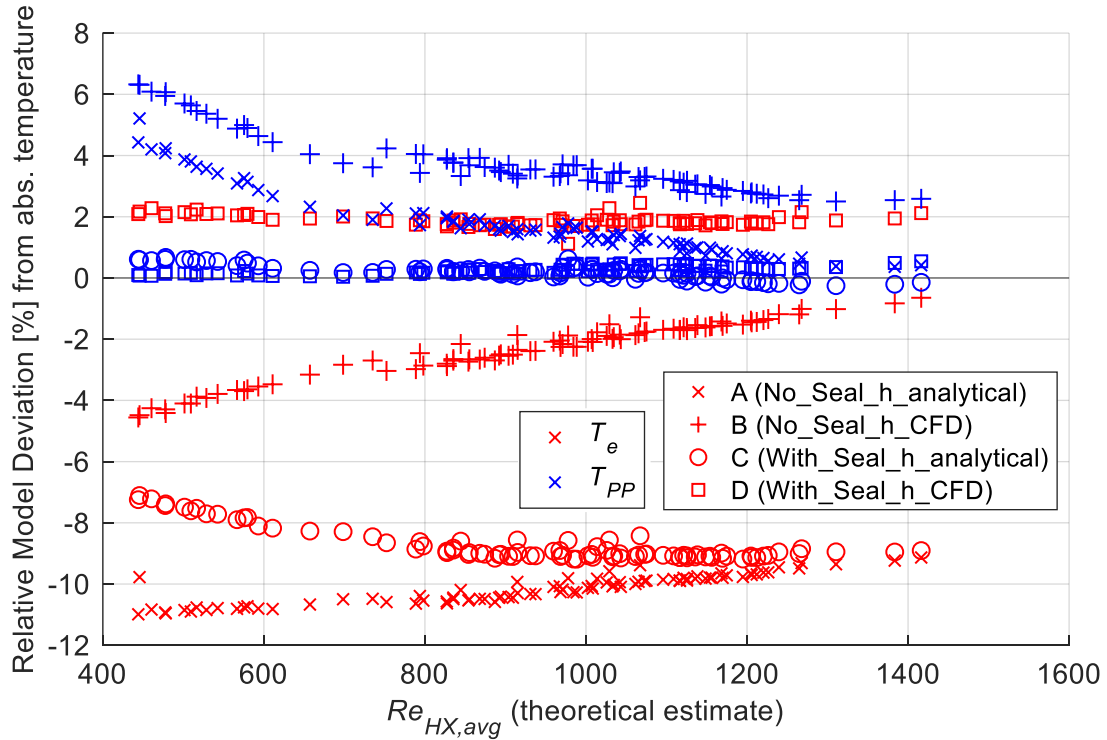
The temperatures that represent the largest volume spaces are the most important in this analysis as they have the greatest influence on the engine pressure and the indicator diagram. These are T_e and $T_{h,inlet}$ on the hot side and T_{PP} and $T_{k,inlet}$ on the cold side. Temperature data from the compression space would be useful but the experimental setup does not allow for a measurement there. The experimental data shows that the differences between T_e and $T_{h,inlet}$, and between T_{PP} and $T_{k,inlet}$, respectively, are small. This trend is predicted correctly by model variants C and D which both have the ‘perfect’ displacer piston seal. In contrast, variants A and B show strong temperature gradients between these locations and predict a much lower T_e (expansion space) and a much higher T_{PP} (power piston space) compared to the experiment. This is especially observed for the low - $Re_{HX,avg}$ datapoint in Figure 4.12 (a) where seal leakage is more significant as found in Section 4.2.5. These deviations in the data from the models without the seal are likely caused by gas leaking through the displacer piston gap. During the heating phase, while the displacer piston moves into the compression space, cold gas from the compression space leaks directly into the expansion space, reducing the temperature there. The opposite takes place during the cooling phase, when hot gas from expansion space leaks into the compression space and from there into the adjacent power piston space, raising the temperature there.

The verdict from Figure 4.12 is that only model D achieved relatively accurate estimates for the values and trends of the average gas temperatures in the two datapoints shown. The remaining datapoints were analyzed and observations consistent with those described were made for all datapoints. To quantify the model deviations, Figure 4.13 (a) shows the deviation in T_e and T_{PP}

between all model variants and the experimental data for all datapoints over $Re_{HX,avg}$. Red points denote the expansion space temperature and blue the power piston space. To enable the comparison with model deviations shown in previous sections, the same data is given in Figure 4.13 (b) as relative deviation from the experimental values, which was calculated after converting the temperatures into absolute units (K).



(a)



(b)

Figure 4.13: Deviation of expansion space (T_e) and power piston space (T_{PP}) gas temperatures predicted by model variants A to D from experiment, over average heat exchanger Reynolds number. (a) Absolute deviation in $^{\circ}\text{C}$, (b) relative deviation in %.

For T_{PP} all models are within 7 % (equivalent to 20 °C) of the experimental measurements, but the variants C and D show remarkably accurate predictions within 1 % (2 °C). For T_e only variant D shows good agreement within 3 % (10 °C) while the other variants underestimate the temperature significantly. Variant D is also the only one to produce consistent results across the entire range of the Reynolds number, with a nearly constant deviation over all datapoints for both temperature locations. Variant B, which does not model the displacer piston seal, underestimates the temperature difference between T_e and T_{PP} , but becomes more accurate as the Reynolds number increases. This supports the earlier finding from Figure 4.12 that the gas temperatures are linked to seal leakage. Overall, the observations from Figure 4.12 hold true for all engine setpoints and model variant D can make reliable predictions of the most relevant gas temperatures for the *Raphael* engine.

4.5 Analysis of Heat Exchanger Pressure Drop

Apart from the indicated work, the pressure drop (Δp_{HX}), caused by viscous flow friction in the heat exchangers and regenerator, is the second major performance parameter the thermodynamic models needs to predict. The pressure drop does not significantly affect the indicator diagram, but it causes a pressure difference between the expansion and compression space which opposes the movement of the displacer piston, thereby creating a loss. With the present experimental setup, Δp_{HX} was to be calculated as the difference between the dynamic pressure data of the expansion and compression spaces as shown in Chapter 0. Upon inspecting the pressure drop data, it was discovered to differ significantly from the expected range and trends. Consequently, a test was run to determine the effect of different measurement locations on the readings of the dynamic pressure sensors and pinpoint the cause of the deviation. It was concluded that the setup was unable to provide reliable data for the pressure drop and alternative experiments were proposed to obtain these measurements. The following sections document these findings.

4.5.1 Experimental Pressure Drop Measurements vs. Model and Theory

The sensor that measures p_{d0} in the expansion space, from which Δp_{HX} is calculated, is located in the displacer cylinder head which is mounted to the heater. Thus, this sensor is exposed to a temperature close to the heater's (T_{Source}). The experimental datasets used in the previous sections were recorded with $T_{Source} = 150$ °C, which is above the dynamic pressure sensor's maximum operating temperature of 135 °C [93]. For this, the sensor had to be removed and the pressure drop could not be obtained from these datasets. Four new datasets were therefore acquired at a reduced source temperature of 130 °C and p_{set} of 100, 200, 350 and 450 kPa. The regenerator was changed to a porosity of 97 % (from 96 %) to decrease the pressure drop and achieve engine speeds comparable to before despite the reduced T_{Source} . The instantaneous pressure drop was computed for each crank angle increment and is displayed in Figure 4.14 along with the predictions from model variant A. From each dataset the datapoints with minimum and maximum speed are shown.

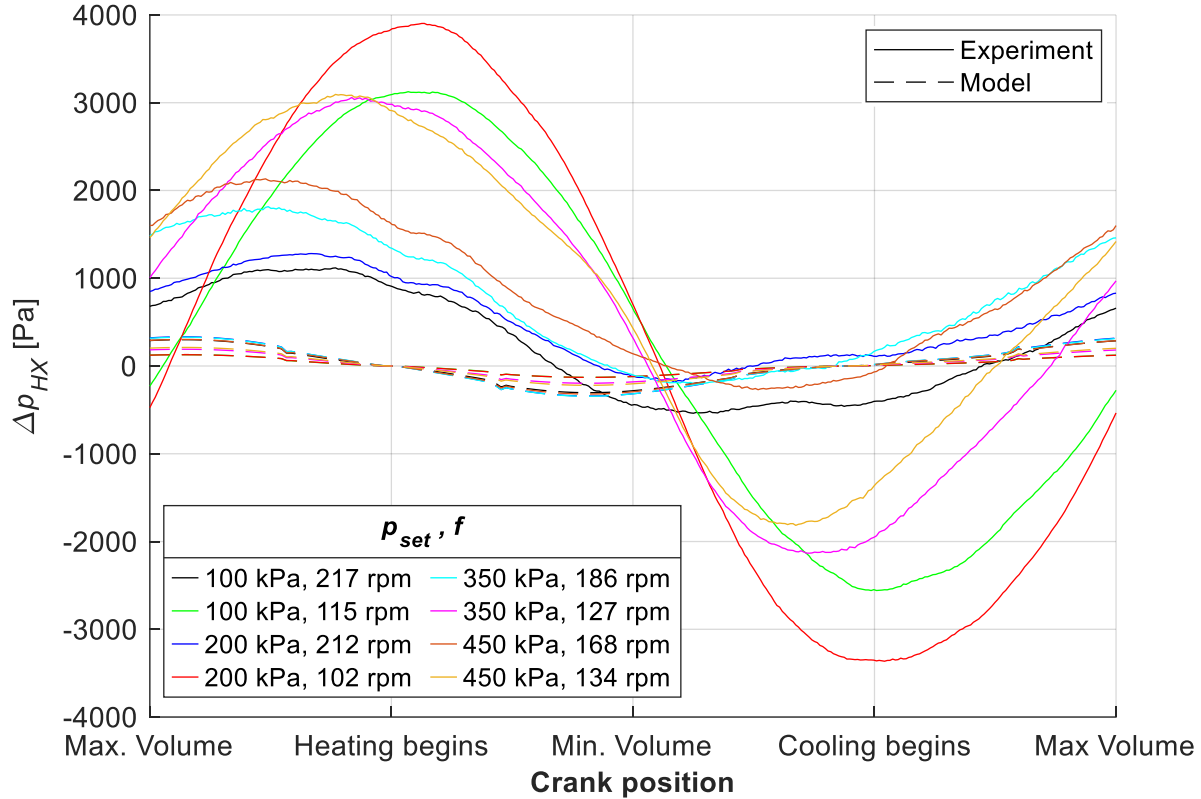


Figure 4.14: Pressure drop over crank position, for 8 different datatypes, from experiment (solid lines) and model variant A (dashed lines).

The pressure drop from experimental data is substantially higher than the model prediction, by about one order of magnitude. Model values are below 400 Pa while the experiment shows close to 4000 Pa. The model Δp_{HX} crosses zero close to the crank positions where the heating or cooling phases begin, which is expected since at these positions the displacer piston is at the top or bottom dead center position and the flow in the heat exchangers is changing direction. In contrast, the experiment curves cross zero close to the minimum and maximum volume positions where the maximum pressure drop should occur. It appears that the experimental data goes against reasonable expectations in both amplitude and phase of Δp_{HX} .

To examine these trends in all datatypes and measure the deviation from expected values, the cycle-averaged pressure drop data is compared to an analytical estimate for a steady-state flow. The total pressure drop is the sum of the pressure drop from two heat exchanger modules ($\Delta p_{HX,module}$) and the regenerator (Δp_{Reg}) expressed as:

$$\Delta p_{HX,analytical} = 2 \Delta p_{HX,module} + \Delta p_{Reg} \quad (70)$$

The two components are obtained through the Darcy-Weisbach equation (see Section 1.3.1):

$$\Delta p_{HX,module} = N_{f,HX} \frac{L_{HX}}{D_{h,HX}} \frac{\rho_{HX,avg} (U_{HX,avg})^2}{2} \quad (71)$$

$$\Delta p_{Reg} = N_{f,Reg} \frac{L_{Reg}}{D_{h,Reg}} \frac{\rho_{HX,avg} (U_{Reg,avg})^2}{2} \quad (72)$$

where: $N_{f,HX}$ = heat exchanger friction factor (-)

L_{HX} = heat exchanger gas channel length (m)

$N_{f,Reg}$ = regenerator friction factor (-)

L_{Reg} = regenerator length (m)

$U_{Reg,avg}$ = average flow velocity in regenerator (m/s)

$D_{h,Reg}$ = hydraulic diameter of regenerator matrix (m)

The friction factor and pressure drop for the heat exchangers and the regenerator matrix are estimated using the same correlations that are implemented into the *MSPM* model. They are listed by Middleton [33] and were checked for their applicability to the *Raphael's* geometry before conducting this study. As seen previously, the heat exchanger Reynolds numbers are in the laminar regime across all datapoints with this engine. The friction factor for the heat exchangers was obtained from a laminar equation for circular pipes [66] with a modification for rectangular channels [114]. $Re_{HX,avg}$ is from equation (68).

$$N_{f,HX} = \frac{-43.94 AR^3 + 123.2 AR^2 - 118.31 AR + 96}{Re_{HX,avg}} \quad (73)$$

$$AR = \min \left(\frac{H_{channel,HX}}{W_{channel,HX}}, \frac{W_{channel,HX}}{H_{channel,HX}} \right) \quad (74)$$

where: AR = heat exchanger gas channel aspect ratio (-)

The regenerator friction factor for a random fiber matrix and laminar flow is [66]:

$$N_{f,Reg} = \frac{25.7 c + 79.8}{Re_{Reg,avg}} + \frac{0.146 c + 3.76}{(Re_{Reg,avg})^{0.00283 c + 0.0748}} \quad (75)$$

$$c = \frac{\beta}{1 - \beta} \quad (76)$$

where: $Re_{Reg,avg}$ = average Reynolds number in regenerator (-)

β = regenerator porosity (-)

$Re_{Reg,avg}$ is defined similarly to $Re_{HX,avg}$ in equation (62), but with the regenerator's flow velocity and hydraulic diameter according to [66].

$$Re_{Reg,avg} = \frac{\rho_{HX,avg} U_{Reg,avg} D_{h,Reg}}{\mu(T_{HX,avg})} \quad (77)$$

$$U_{Reg,avg} = \frac{A_{DP}}{A_{Reg}} U_{DP,avg} \quad (78)$$

$$D_{h,Reg} = \frac{D_{W,Reg}}{1 - \beta} \quad (79)$$

where: A_{Reg} = regenerator flow cross section area, considering porosity (m²)

$D_{W,Reg}$ = regenerator wire diameter (m)

Figure 4.15 shows the averaged Δp_{HX} from experiment, model and the analytical estimate for all datapoints over the heat exchanger Reynolds number. The colours denote the datasets with different p_{set} . The model and analytical estimates are similar, below 250 Pa with an upwards trend related to engine speed as would be expected. The analytical values are slightly higher than the model's, especially in the datasets with lower p_{set} , likely because model variant A has a lower flow velocity in the heat exchangers due to the missing displacer piston seal (see Figure 4.9). The experimental values deviate strongly from the expected range for all datapoints and follow a downward trend with speed. This indicates a flaw in the experimental measurement method.

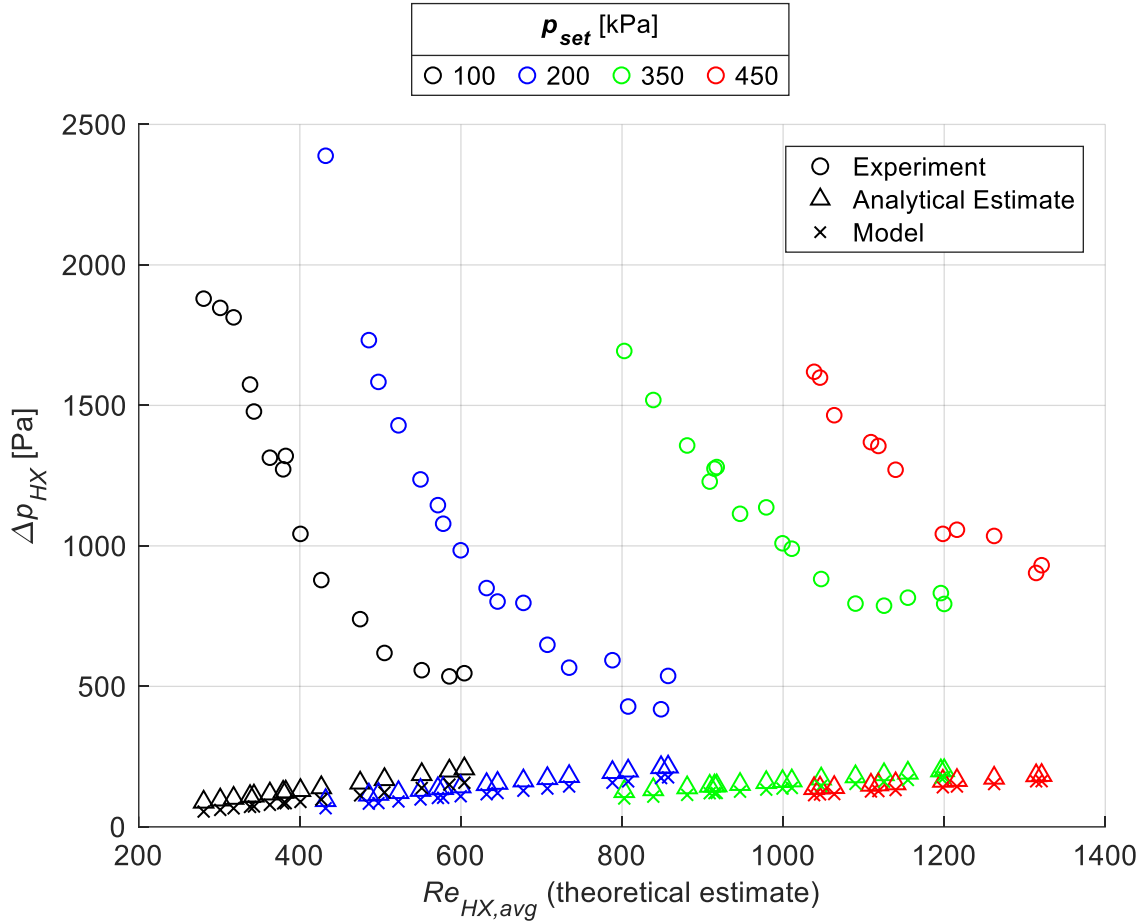


Figure 4.15: Average pressure drop over heat exchanger Reynolds number from equation (68), for all 59 datapoints. Experiment, model variant A, and analytical estimate from equation (70).

To illustrate the unexpected phase of the experimental pressure drop data, the two crank positions at which Δp_{HX} crosses zero are plotted for all datapoints in Figure 4.16. The horizontal axis separates the datapoints by $Re_{HX,avg}$, and each datapoint has two markers on the vertical axis denoting the zero crossings. The points are expected to line up close to the black horizontal lines, where the heating and cooling phases begin, and this is true for the model data. The experimental points are at completely different and inconsistent locations. Thus, not only the magnitude but also the timing of the experimental measurements is unreliable for all datapoints.

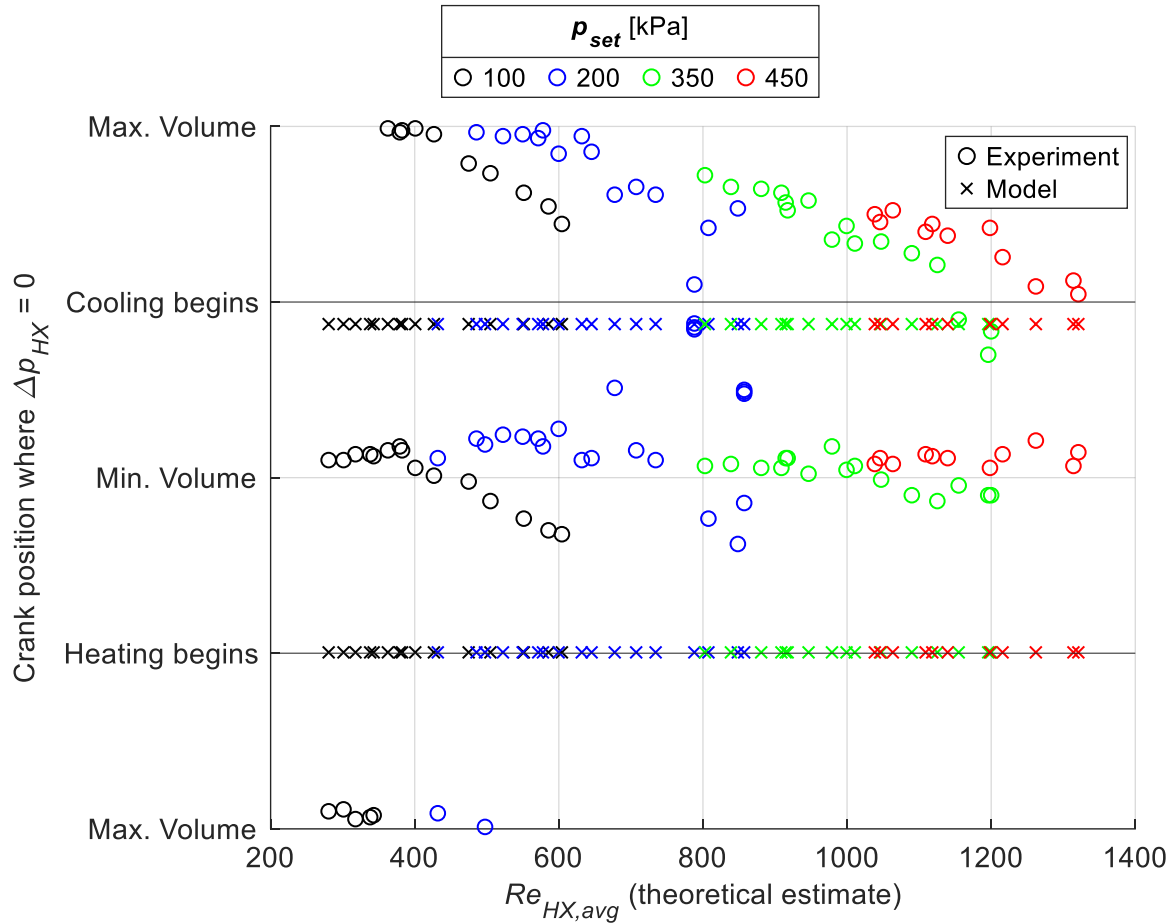


Figure 4.16: Crank positions where pressure drop is zero over heat exchanger Reynolds number from equation (68), for all 59 datapoints. Data from experiment and model variant A.

From these observations a sensor error was suspected. The sensors for p_{d0} and p_{d1} , from which Δp_{HX} is calculated, were swapped to see if there were differences between the individual sensors. This led to even higher pressure drop measurements of up to 10 kPa with similar trends as in Figure 4.15. The sensor arrangement was therefore confirmed as the source of error, and a comprehensive test was conducted to determine the variations between all four dynamic pressure sensors and which external factors influence their readings.

4.5.2 Experiment: Varying Positions of Dynamic Pressure Sensors

It was suspected that there may be deviations due to inherent differences between individual sensors and due to external influences at different sensor positions, for example temperature. Not only the pressure drop, but also the pressure data for the indicator diagram from sensor p_{d2} in the power piston space could be affected. An experiment was carried out in which the four sensors were swapped between the positions so that each sensor was tested at least once in position 0 (displacer cylinder head) and position 2 (power piston cylinder). In position 0 the sensor is at an elevated temperature due to proximity to the heater. See Figure 2.7 for the sensor locations. With each sensor configuration three setpoints with different load torques were acquired at $T_{Source} = 130\text{ }^{\circ}\text{C}$ and $p_{set} = 100\text{ kPa}$. Then, the cyclic pressure data from all sensors was compared at sensor positions 0 and 2.

Figure 4.17 shows the pressures measured by all sensors at position 0 for the two setpoints with the highest (a) and lowest (b) speeds. For both setpoints there are substantial deviations in amplitude and phase between the sensors. The trends between the sensors are similar for both setpoints, e.g., sensor B always has the smallest amplitude and its phase lags behind the others, but the magnitude of the deviations between them is greater in (b) at the lower speed. Figure 4.18 shows the same data but from sensor position 2. Here, the differences between the sensors are much smaller, are of similar magnitude for both setpoints, and there appears to be no visible phase difference. Sensor D, however, still deviates from the others by up to 15 %, which would notably affect the indicated work obtained from this data.

This data proves that the amplitude and phase of the dynamic pressure data are considerably influenced by individual sensor characteristics, sensor positions and engine speed. Firstly, strong deviations occur at position 0, which is the only position where the sensor is at an elevated temperature, whereas little deviations are observed at position 2. The two positions not shown here (compression space and crankcase) were also inspected and showed minimal deviations. This confirms that the sensors produce unreliable readings when operating at high temperature. Secondly, the observation that the temperature effects are greater at a lower speed suggests that it may be the sensitivity and/or response time characteristics of the sensors that are altered by the temperature. In any case, it was established that the instrumentation on the experiment setup is not fit for measuring the pressure drop on the running engine.

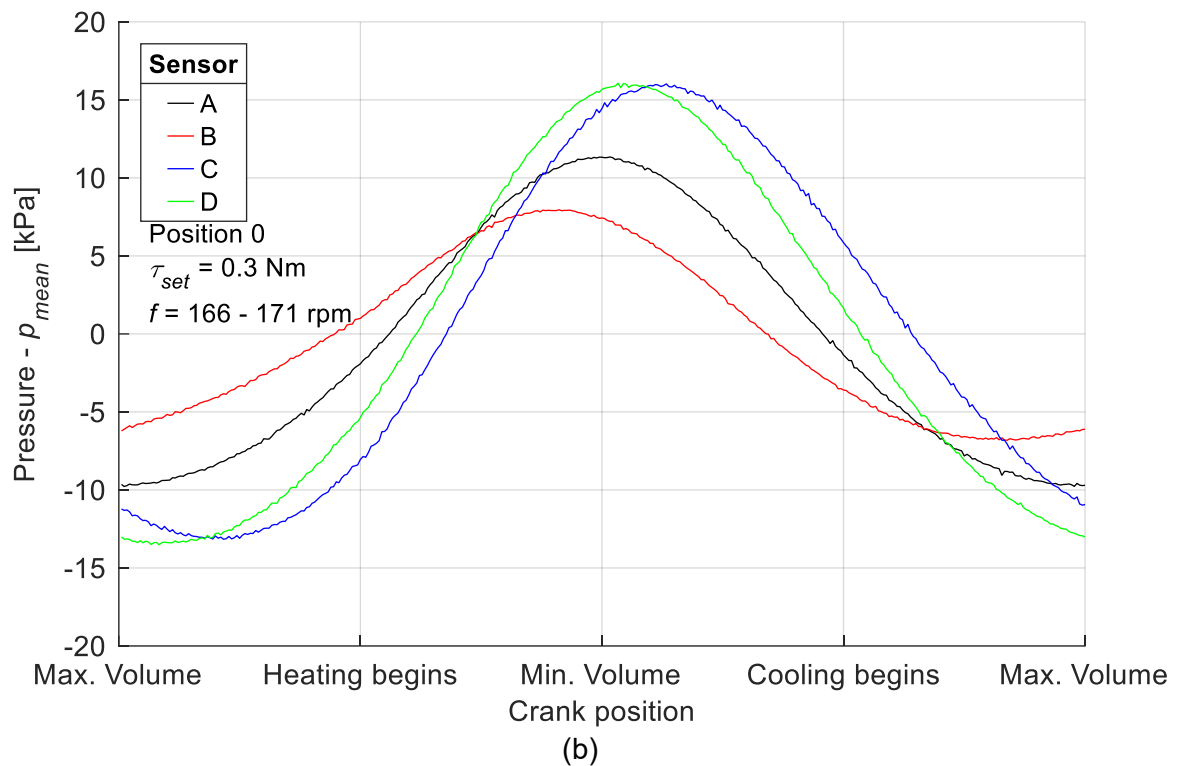
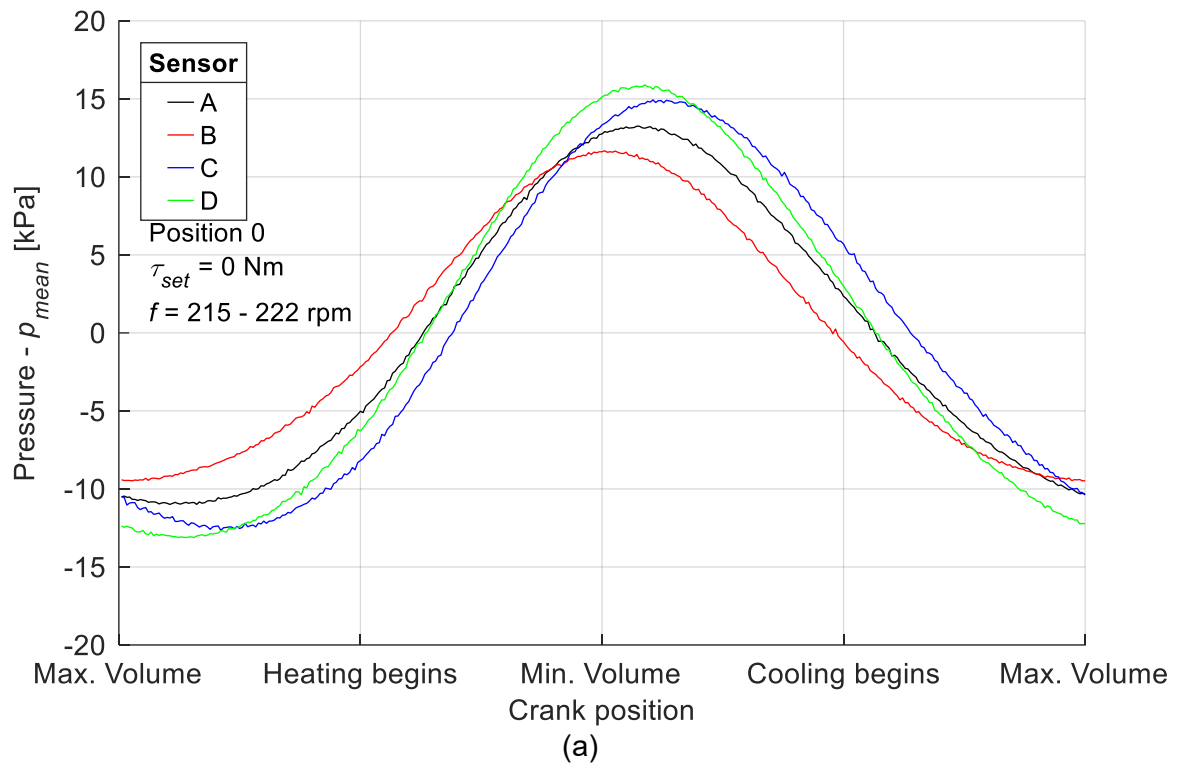


Figure 4.17: Comparison of dynamic pressure measurements from all four sensors at **position 0 (displacer cylinder head)**. Setpoints with higher (a) and lower (b) speed.

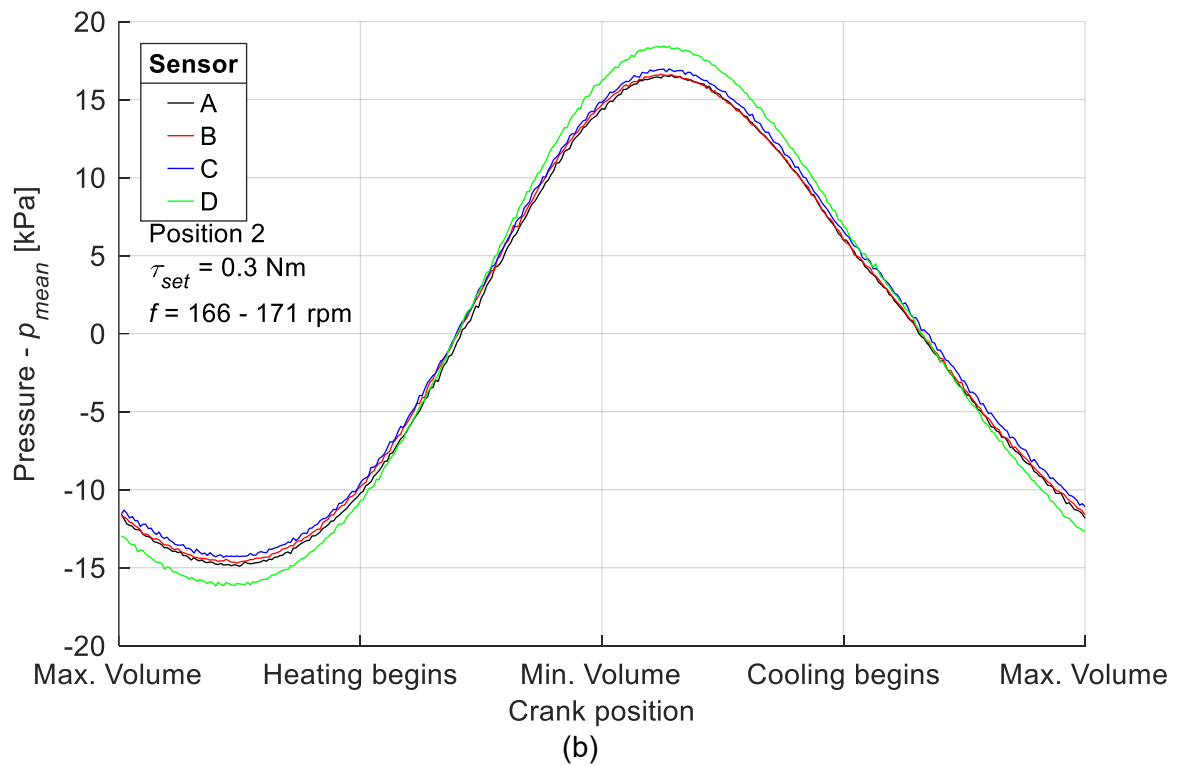
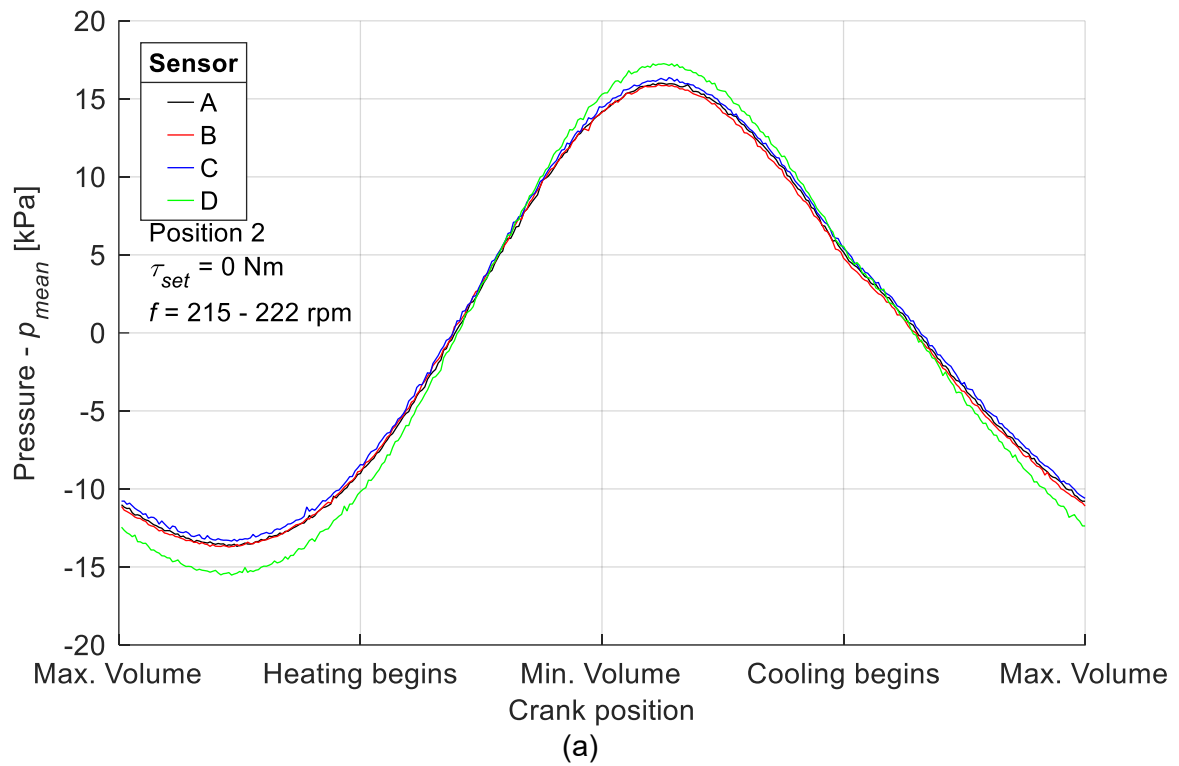


Figure 4.18: Comparison of dynamic pressure measurements from all four sensors at **position 2 (power piston cylinder)**. Setpoints with higher (a) and lower (b) speed.

The effect of the different sensors on the indicator diagram was also analyzed. Figure 4.19 shows the indicator diagrams from all sensors for the second setpoint. Sensor D registered a notably larger pressure swing that affects the area and shape of the curve.

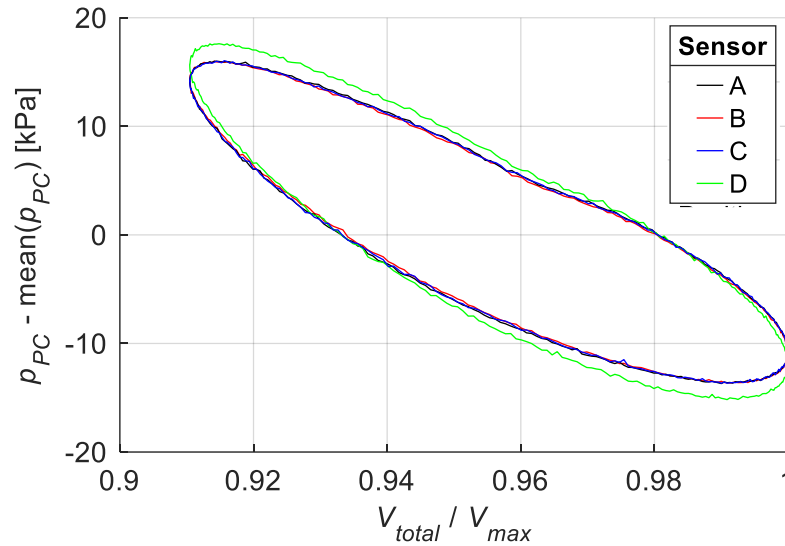


Figure 4.19: Indicator diagrams from all pressure sensors for setpoint with $f = 200 - 210$ rpm.

The resulting values of indicated work for all setpoints are plotted in Figure 4.20. Sensors A, B and C give values that are within 3 % of each other while sensor D is up to 14 % higher than the others. The data for W_{ind} in the validation datasets was recorded by sensor B, which is shown here to be in line with two other sensors, so its data can reasonably be trusted. However, it must be noted that there can apparently be inherent differences between individual sensors large enough to influence the resulting indicated work notably.

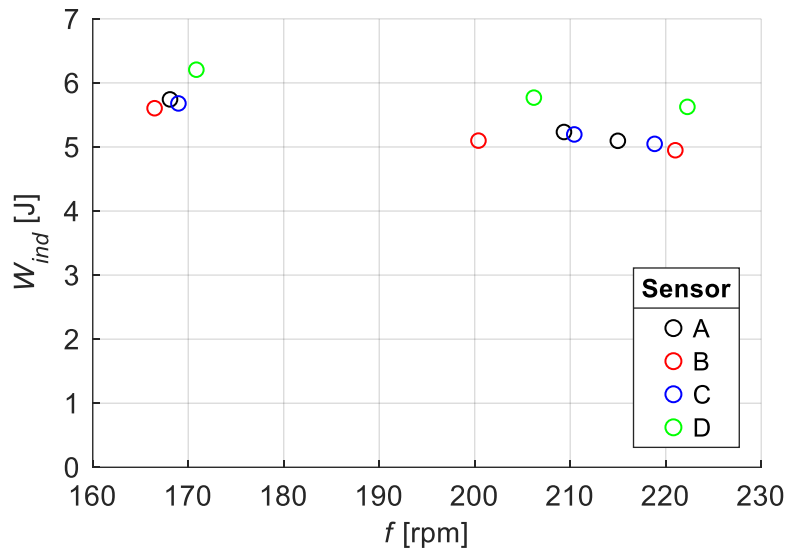


Figure 4.20: Indicated work from all pressure sensors for three setpoints, over speed.

4.5.3 Conclusions and Suggestions for Pressure Drop Measurement

It was found that the heat exchanger pressure drop cannot be measured with the given experimental setup due to deviations between individual pressure sensors. The indicated work data that was used for validation in section 4.2 is likely not affected to a degree that would alter the findings of the analysis. The sensor deviations are likely caused by temperature. According to the manufacturer, the dynamic pressure sensors have a temperature sensitivity of up to 0.054 % of full scale per °C [93], which amounts to 20.5 kPa for a sensor temperature of 130 °C and compensated temperature of 20 °C. This is more than 80 times greater than the expected pressure drop, hence the setup cannot be expected to perform well.

Several issues arise with measuring Δp_{HX} with the current experimental setup. Firstly, the pressure drop is obtained as the difference between two measurements from two separate dynamic pressure sensors at different locations. This means that any deviation between the signal characteristics of the two sensors will be carried over into the calculated pressure drop and will distort the resulting data.

Secondly, the sensors have a measurement range on the order of the highest setpoint pressure, 345 kPa for the sensors used here [93]. However, the expected pressure drop is on the order of 0.25 kPa as seen in Figure 4.15, about a thousand times smaller than the range of the sensors.

Measuring a signal much smaller than the range of the instruments means that the sensor uncertainty, which usually scales with the range, will be significant and may be larger than the signal, which would render the data useless. In this case, the uncertainty is 1 % of the full range [93], which equals 3.45 kPa or about 14 times the order of Δp_{HX} . For this reason alone, the pressure drop from this setup could not be deemed reliable even if the sensors were perfectly identical.

The experiment in the previous section found that the sensor readings deviate strongly from each other in amplitude and phase based on sensor location, most likely because one location is on the hot side of the engine body and the sensor gets close to its maximum operating temperature. For an accurate two-point measurement of the pressure drop both sensors should be in equal conditions, meaning the engine should ideally not be hot.

A number of experiments can be proposed to measure the pressure drop of the *Raphael* engine:

1. Instead of two separate sensors, a single differential pressure measurement can be done with one sensor connected to both the expansion and compression spaces. This eliminates the problems with deviation between sensors and the large sensor uncertainty as the differential sensor's range can be on the same order as the pressure drop. The sensor would not be flush-mounted but connected to the measurement locations with tubing. Speer [31] tested this setup on an engine similar to *Raphael* but encountered another problem that comes with measuring a varying pressure with a sensor that is not flush-mounted. As the pressure waves travel from the working space to the sensing element via the tubing, they can be dampened and phase-shifted from interaction with the tubing walls. This can lead to the pressure seen by the sensor being substantially distorted from the actual pressures in the engine. Thus, a transient pressure should be measured with a sensor that is exposed directly to the measurement location.
2. Instead of measuring the pressure drop directly, it can be observed indirectly through the force it exerts on the displacer piston. If the power consumed by the displacer piston while working against the pressure drop can be measured, the acting pressure difference can be estimated. This was done with the *HTG* engine by Speer [31]. The engine was driven externally with an electric motor, and was operated in different stages of disassembly so that the power going into different frictional loss mechanisms, such as the pressure drop, could be

determined. The electrical power consumed by the motor was measured, from which an estimate for the average Δp_{HX} could be obtained.

3. Rather than measuring the transient pressure drop with oscillating flow, it could be measured at steady state, where distortion from tubing geometry plays no role and a differential sensor could be used. This approach would be in line with standard test procedures for heat exchangers, and would see the heat exchangers mounted into a steady flow setup. Currently this experiment is being developed at *DTECL* with the aim of recording the pressure drop of the *Raphael* heat exchangers for validation of *MSPM*.

The development of additional experiments to measure Δp_{HX} exceeds the scope of this thesis and is left for future work. Nevertheless, it is necessary to complete the validation of the thermodynamic model of *MSPM*. Issues with the existing setup were investigated and suggestions made to aid this process.

4.6 Analysis of In-Cycle Speed Variations

The fluctuations of the engine speed with crankshaft angle due to energy being transferred between the pistons and the flywheel can be modeled by *MSPM* for a pre-defined average speed without requiring a functioning mechanical model with mechanical friction. Though this goes beyond the scope of the thermodynamic model, in this section the speed variation will be modeled and compared to the experimentally measured transient speed for a set of eight datapoints, which are the lowest and highest speed datapoints from each of the four datasets listed in Section 4.1.3. This will validate the model predictions of the forces transmitted through the mechanism and how they interact with the inertia of the system. The only additional model input required is the flywheel moment of inertia, which is listed in Table 2.1. The model will run at the given constant speed until reaching steady state as in a normal constant-speed case, and then run one additional cycle in which varying speed is enabled. Model variant D was used for this study.

Figure 4.21 shows the instantaneous engine speed over the crankshaft position for the two setpoints with the lowest (a) and highest (b) $Re_{HX,avg}$. The original speed data from the model is higher than the experimental values by a constant offset because when enabling varying speed, the model takes the average speed f from the experimental data as its starting speed, not average speed. This deviation has been subtracted in the plots so that the curves start at the same value. The model predicts the two oscillations in the speed curve, which are caused by alternating phases of efficacious and forced work (see Section 1.3.2), accurately in phase and with some deviation in amplitude. At low Reynolds number (a) the speed is overpredicted and at high Reynolds number (b) underpredicted at most crank positions. The mean relative deviation in speed was calculated for all 8 setpoints, and the highest was 25 %. The deviation at higher speed (b) is smaller than at lower speed (a), which aligns with the model author's findings mentioned in Section 3.3.

The indicated work from the model with and without varying speed was compared to determine if the speed variations have a notable effect on it. For all datapoints the values of W_{ind} were within 2 % of each other. However, the true effect, which could be more significant, could only be determined if the model was run with speed variations for more than one cycle. This is not yet possible in *MSPM*, but should be implemented and tested in the future by enabling speed to be input as a vector dependent on crank angle instead of only a scalar. For this validation of the

thermodynamic model it is assumed that the effect of speed variation on indicated work is negligible compared to the model deviation from the experimental data.

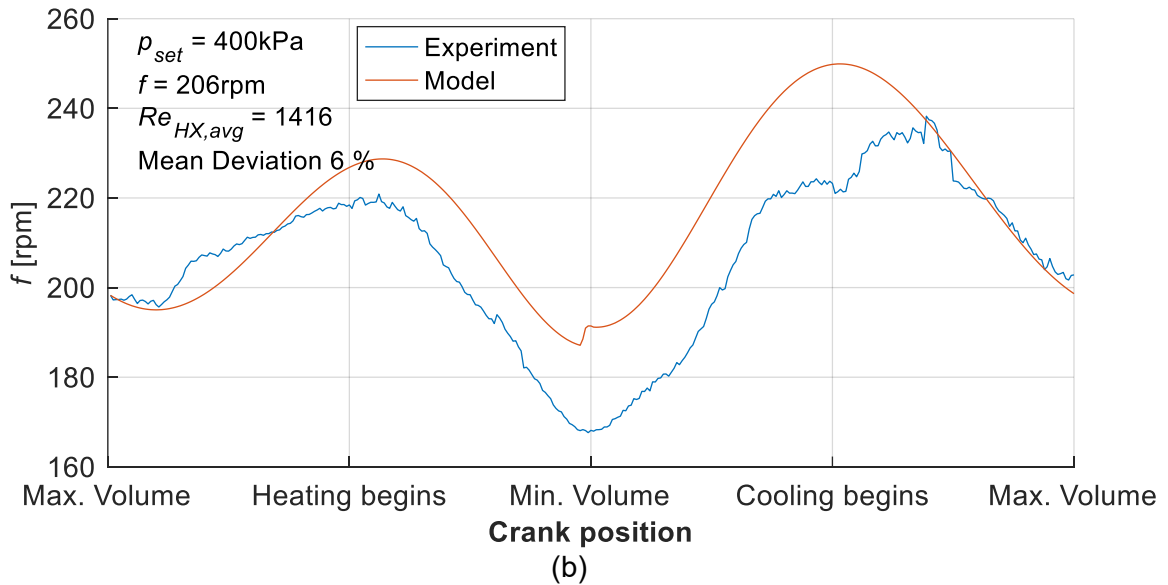
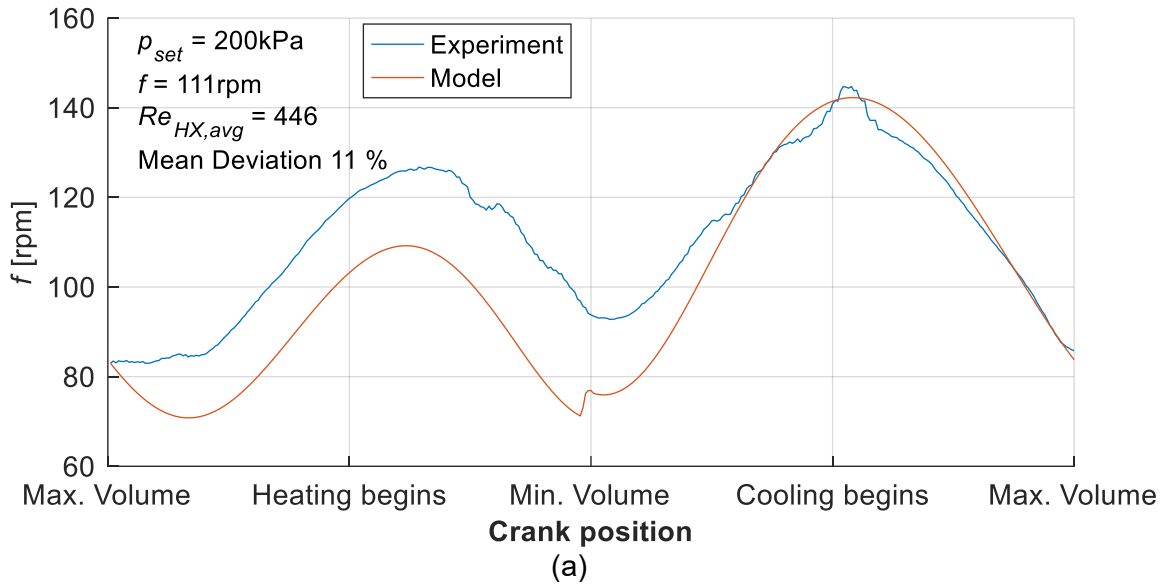


Figure 4.21: Engine speed variation over crank position, comparison between experiment and model variant D. For the two setpoints with lowest (a) and highest (b) $Re_{HX,avg}$.

4.7 Model Sensitivity to Settings and Input Parameters

Most parameters that were used to build the model of *Raphael* in *MSPM* or that are inputs required to run the model are known with a high precision. The geometry of all components is known within manufacturing tolerances from the solid model. However, some parameters with potentially strong influence on the model results could only be estimated with considerable uncertainty or are only applied to the model in a simplified way. These are:

- Heat exchanger liquid side convective heat transfer coefficients h_{Source} and h_{Sink} , which were estimated in section 3.6 and whose strong influence has been observed in sections 4.2 to 4.4.
- Source and sink temperatures T_{Source} and T_{Sink} . They vary between the heat exchanger liquid inlet and outlet, but the model applies them as constant equal to the mean between the measured inlet and outlet temperature.
- Regenerator porosity β and fiber diameter $D_{W,Reg}$. Porosity is roughly known from weighing the regenerator material. Fiber diameter (0.1mm) was measured in a digital image using a ruler with a 0.5 mm scale as reference. The material may also be not uniformly distributed around the regenerator space.

For these parameters, a sensitivity analysis was performed to see if their uncertainties may affect the findings of the validation in previous sections. Additionally, model results were tested for numerical repeatability and dependence on important model settings:

- The effect of different initial conditions of the solver on the model results
- The effect of disabling the modeling of heat conduction in different solid components
- The effect of increasing or decreasing the model mesh density

In section 0 the combined uncertainty in indicated work resulting from the sources that could be quantified is estimated.

4.7.1 Sensitivity to Initial Conditions

The sensitivity of the model results to the initial conditions given to the solver is analyzed by running some datapoints with two different starting conditions and then comparing the resulting

W_{ind} . The default for *MSPM*, also used for all model data presented in this thesis, is running ‘from Snapshot’, which means that the pressure and temperature distribution of the previous run is used as the initial condition for the next run. This greatly reduces the computing time compared to running ‘from Scratch’, which means starting with the default uniform pressure and temperature specified in the model. Running ‘from Scratch’ took an average of 15 minutes per datapoint in this case while running ‘from Snapshot’ required less than 4 minutes per datapoint. Figure 4.22 shows the values of W_{ind} for all datapoints as well as the relative deviation between them. The 78 datapoints are a subset of those shown in the analysis of h_{Source} and h_{Sink} in section 4.7.7. The points to the left of the vertical black line are from the ‘no seal’ model, the ones to the right from the ‘with seal’ model.

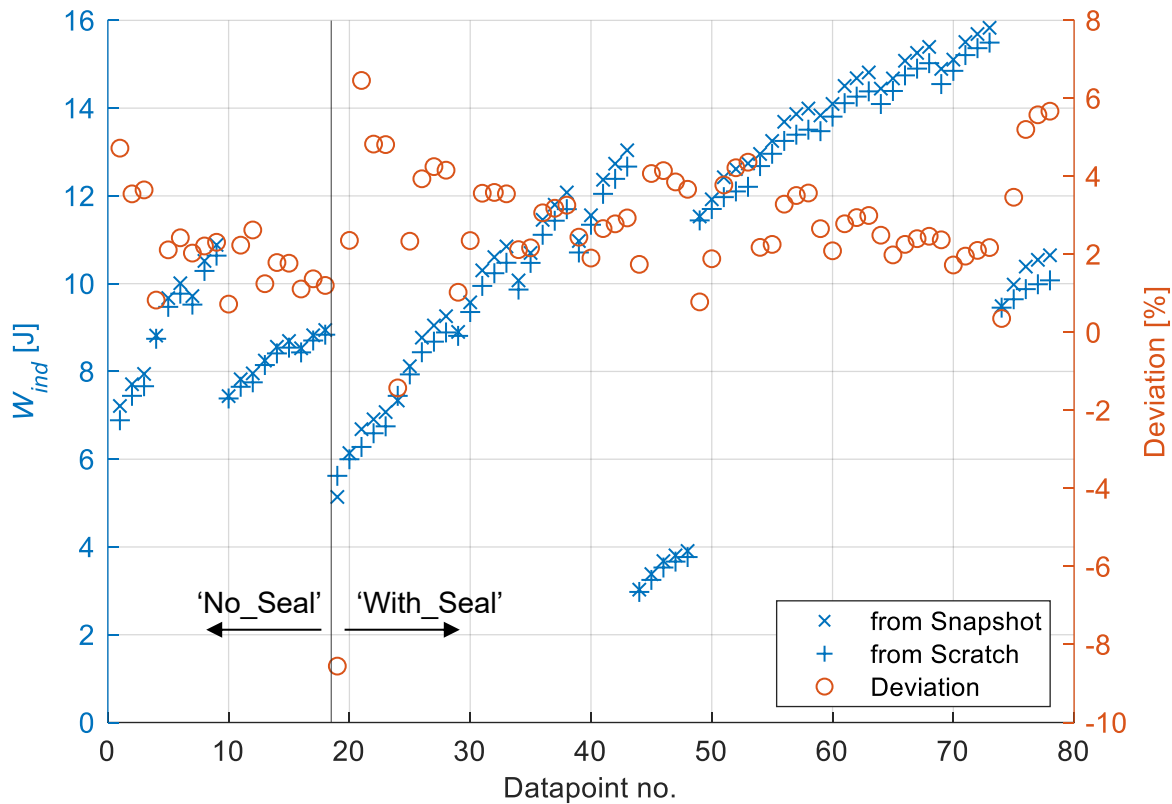


Figure 4.22: Comparison of indicated work model results when starting from different initial conditions ‘from Snapshot’ and ‘from Scratch’ (left axis). Relative deviation between them (right axis). Source heat transfer coefficients vary between the datapoints. Data to the left of the black vertical line is from ‘no seal’ model, to the right from ‘with seal’ model.

For almost all datapoints there is a consistent trend in that the indicated work when running ‘from Snapshot’ is higher than when running ‘from Scratch’ by up to 7 %, and by 2.6 % on average.

Only two outliers out of 78 have a negative deviation, one of these has the highest deviation at 9 %. Hence, the uncertainty in W_{ind} from the ‘scatter’ of the model results caused by varying initial conditions is:

$$u_{initial} = 7 \% \quad (80)$$

Reducing the convergence residual would likely decrease the width of the scatter.

4.7.2 Repeatability of Model Results in Repeated Runs

If a model run has finished by reaching the steady state convergence criterion and is then run again, the result of this second will be slightly different because the model always simulates at least five engine cycles before exiting again due to the convergence criterion. This is another form of random ‘scatter’ of the model results. Its effect was measured by running a setpoint on model variant D 25 times with identical input parameters and observing the scatter in the resulting W_{ind} values. The ‘from Snapshot’ starting conditions were used (see previous section) so that each run would start from the solution of the previous one. Figure 4.23 shows the results and the relative deviation of each value from the mean. All values are within a range of about 2 %. This source of uncertainty is similar to that from the initial conditions (previous section) in that it has a random nature and could be reduced by lowering the convergence criterion. Thus,

$$u_{repeat} = 2 \% \quad (81)$$

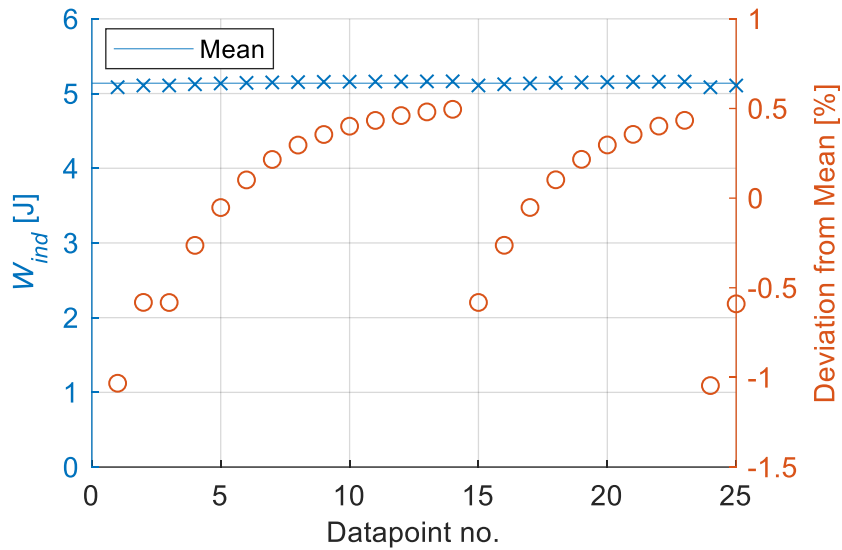


Figure 4.23: Indicated work model results repeatability over 25 repetitions of the same setpoint. For a hypothetical setpoint with $p_{mean} = 300$ kPa and $f = 150$ rpm. Model Variant D.

4.7.3 Effect of Neglecting Heat Conduction in Different Components

The modeling of heat conduction in solid bodies contributes the majority of all nodes to an *MSPM* model (88 % in case of the *Raphael* model, see Section 3.4) because temperature gradients are much steeper in solids compared to gas as there is no heat transfer through advection. At the same time, conduction in most bodies except for the heat exchangers has little effect on the indicated work of the engine, it mostly only affects conduction heat losses which affect thermal efficiency. Thus, neglecting conduction in certain parts of the model may reduce the computation effort without compromising much of the accuracy of the thermodynamic model. In this section, the changes in W_{ind} and the heat flow rates to the heater, cooler and environment when disabling conduction in bodies with large numbers of nodes are investigated. This study was done with model variant A for a hypothetical setpoint with $T_{Source} = 150$ °C, $T_{Sink} = 5$ °C, $p_{mean} = 300$ kPa, and $f = 150$ rpm. Figure 4.24 illustrates which components of the model were investigated. Each of these bodies or groups of bodies were tested separately by setting their material to ‘Perfect Insulator’, which means that they do not exchange any heat with their neighbours and they are reduced to a single node whose constant temperature has no effect. In the case of the power piston and crankcase (PP and CC) bodies, these were modeled as conduction-free already so in this test the conduction was enabled for them.

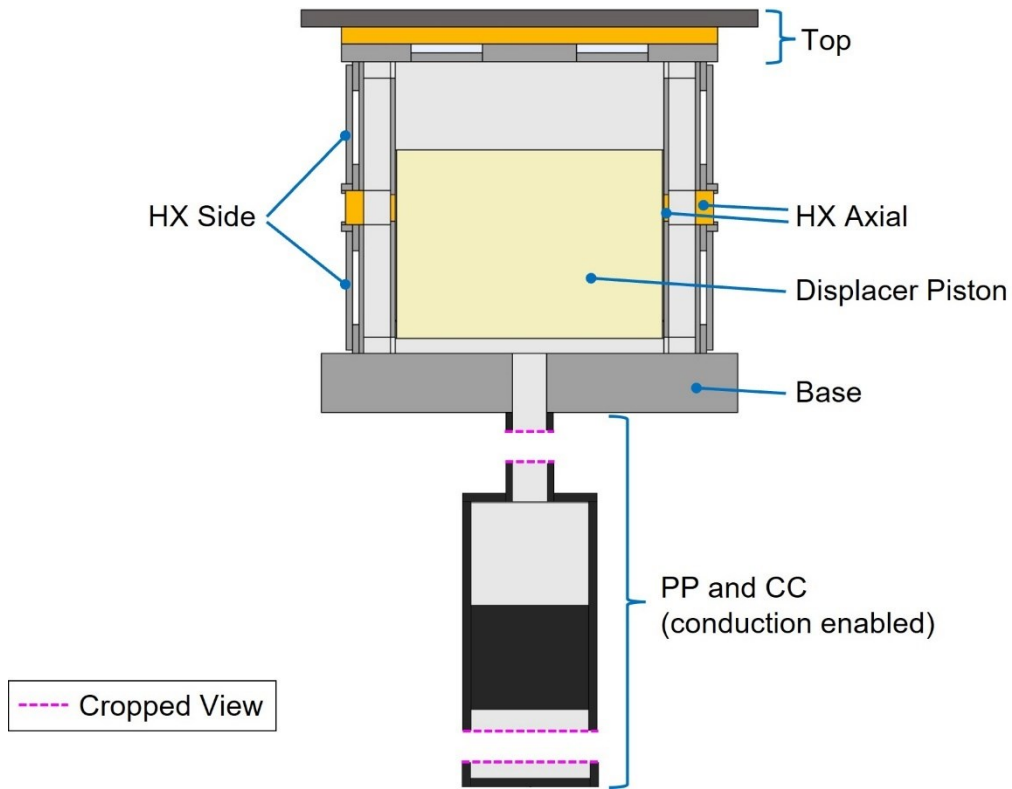


Figure 4.24: *Raphael* engine model in *MSPM* showing the bodies for which the effect of neglecting heat conduction was studied.

Table 4.3 contains the results of the study, highlighting the changes that had notable effect in colors: Greater than 20 % red, greater than 5 % orange, greater than 1 % yellow. By far the greatest change was observed when disabling conduction through the outside walls of the heat exchangers. This was thought to be analogous to installing thermal insulation around the heat exchangers on the real engine, which should reduce the measured heat flow rates and slightly improve the heat exchanger temperatures, leading to a small increase in W_{ind} . The model heat flows decreased as expected, but indicated work also unexpectedly decreased by almost half. Also, materials with different thermal conductivities for the heat exchanger outside walls were tested, and W_{ind} was found to increase with the conductivity in most cases. Thus, according to the model results, the conductivity of the heat exchanger outside walls is actually beneficial to the engine power, likely because it enables more heat to be exchanged with the source and sink overall.

To confirm if the effect of thermal insulation around the heat exchangers is modeled as expected, the model was run with added insulator bodies enclosing the heat exchangers. This led to the expected small increase in W_{ind} and strong decrease in \dot{Q}_{Env} . Therefore, the model results

can be trusted, and the effect of the heat exchanger side wall conduction revealed that the solid geometry of the entire heat exchanger, not only the part directly between the source channel and the gas channel, plays a greater role than expected for heat transfer and overall engine performance.

Table 4.3: Resulting changes in indicated work and heat flows from disabling (for PP and CC: enabling) heat conduction in the listed bodies in the *MSPM* model of *Raphael*.

| Bodies | W_{ind} [J] | Change | \dot{Q}_{Source} [W] | Change | \dot{Q}_{Sink} [W] | Change | \dot{Q}_{Env} [W] | Change |
|------------------------|------------------|--------|---------------------------|--------|-------------------------|--------|------------------------|--------|
| (Default) | 5.05 | - | 619.5 | - | 540.5 | | 53.9 | - |
| HX Axial | 5.17 | +2.5% | 610.4 | -1.5% | 528.6 | -2.2% | 53.0 | -1.6% |
| HX Side | 2.92 | -42.1% | 416.6 | -32.8% | 412.7 | -23.6% | 29.4 | -45.5% |
| Displacer Piston | 5.02 | -0.6% | 620.6 | +0.2% | 541.1 | +0.1% | 53.8 | -0.2% |
| Top | 5.24 | +3.8% | 604.6 | -2.4% | 546.8 | +1.2% | 22.1 | -59.0% |
| Base | 4.48 | -11.2% | 607.6 | -1.9% | 515.6 | -4.6% | 59.3 | +9.9% |
| PP and CC (enabled) | 5.03 | -0.4% | 619.9 | +0.1% | 539.2 | -0.2% | 57.1 | +5.9% |

The ‘Top’ section of the engine (displacer cylinder head) appears to contribute most of the heat lost to the environment as it decreased by 59 % when conduction was disabled. Getting this data for a range of datapoints would be useful to determine where insulation should be installed on a real engine to improve its thermal efficiency. The ‘Base’ of the displacer cylinder has the opposite effect. Disabling conduction here actually increased \dot{Q}_{Env} and reduced W_{ind} considerably by about 10 % each. It also reduced the sink heat flow. This suggests that the ‘Base’ acts as a cooling surface and takes heat from the environment, which is plausible as it is directly connected to the cooler. Enabling conduction in the power piston and crankcase geometry increased \dot{Q}_{Env} slightly due to heat from the working gas being conducted to the environment, but had no effect on the other variables.

A surprising result is that the axial conduction between the heat exchangers and the conduction through the displacer piston had little effect on any of the variables. It was expected that a more significant amount of energy is lost through axial conduction, especially due to the small distance between the heat exchangers. The effect of displacer piston conduction was negligible compared to the scatter in model results (see previous section). For this reason, the node count of the displacer piston, which contained most of the solid nodes, was reduced from 710 to 10 for the validation runs (see section 3.4) to reduce computing time.

4.7.4 Numerical Mesh Sensitivity Study

As with any discretized model, the density of the numerical grid or mesh is critical to the accuracy of the solution. This section analyzes the influence of the spatial mesh in *MSPM* on the results. The temporal grid (time step) was kept unchanged throughout this work, it could be investigated in the future. With a model that allows uniform scaling of the mesh in all dimensions and domains, like with most CFD applications, the aim is to reach a mesh density that makes the solution mesh independent. This is achieved when refining the mesh further only causes the solution variables to converge with the mesh scale towards their final, ‘exact’ values which can then be predicted. In *MSPM*, uniform grid scaling is not yet implemented, but instead, a ‘Node Factor’ can be used to scale various parameters that influence the mesh creation. It is applied to the following parameters of the ‘Mesher’ in *MSPM*:

- ‘oscillation_depth_N’ – Number of solid nodes inside the ‘oscillation depth’ of a solid body, which is the depth from the surface at which temperature oscillations imparted from the gas at the surface become negligible, and depends on the oscillation frequency and the thermal diffusivity of the material [33].
- ‘maximum_thickness’ – Maximum permitted size of solid nodes in either dimension.
- ‘Gas_Entrance_Exit_N’ – Number of gas nodes in the entrance and exit lengths of a matrix (heat exchanger / regenerator), which is defined as 15 % of its length in *MSPM*.
- ‘Gas_Maximum_Size’ and ‘Gas_Minimum_Size’ – Maximum and minimum permitted size of gas nodes in a matrix in flow direction.

The Node Factor is multiplied or divided into these parameters so that a higher Node Factor leads to more and smaller nodes. These parameters are used only by the ‘Smart Discretize’

function. This means the Node Factor applies only to gas bodies with a matrix and to solid bodies for which the discretization function is enabled. It does not affect regular gas and solid bodies for which the number of nodes is fixed. A test was conducted where the Node Factor was varied from 0.2 to 6 in 27 increments, with model variant A for a hypothetical setpoint with $T_{Source} = 150\text{ }^{\circ}\text{C}$, $T_{Sink} = 5\text{ }^{\circ}\text{C}$, $p_{mean} = 300\text{ kPa}$, and $f = 150\text{ rpm}$. Figure 4.25 shows the change of the resulting W_{ind} and heat flow rates from this test.

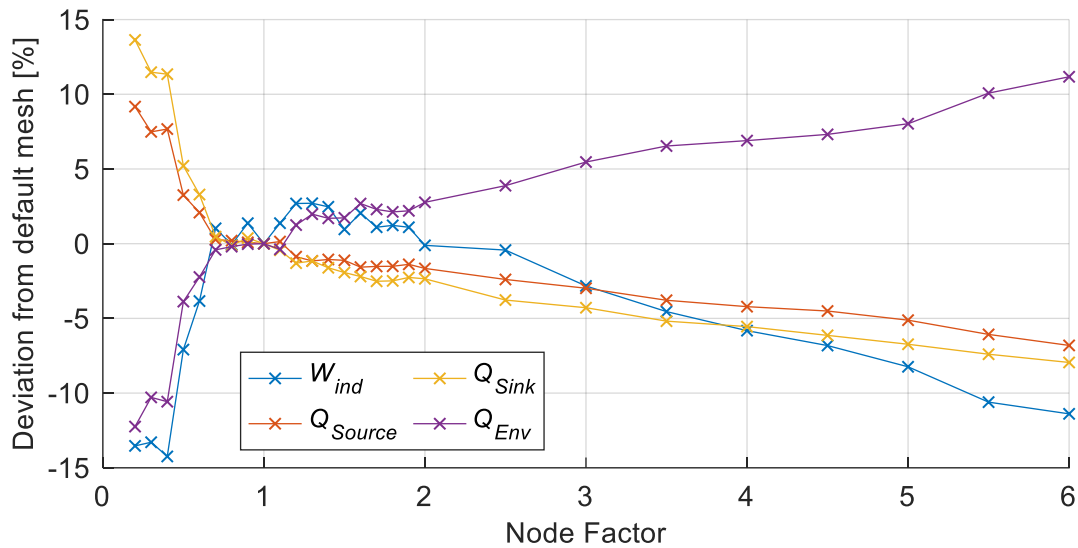


Figure 4.25: Indicated work and heat flow rates over ‘Node Factor’ which scales the mesh density. Shown relative to the respective values of the default model with ‘Node Factor’ of 1.

For all values of the Node Factor the variables did not change by more than 15 %, which is smaller than expected considering the wide range it was varied over. While the Node Factor was between 0.7 and 2 the results were within 3 % of the default mesh. This means that the solution is not very sensitive to the mesh density in this range where the mesh setting is close to the default. However, further increase of the Node Factor did not lead to convergence, but to increasing changes in all variables following relatively linear trends. Since this is not a uniform mesh refinement, a higher node count does not necessarily equate to a better result. It is unclear whether the higher Node Factor increases the accuracy of the model or possibly introduces numerical distortion, for example by creating nodes with high aspect ratios that can cause unphysical effects in the solution. The latter is more plausible, because the default meshing parameters were chosen by the model author with the aim of producing reliable results for a given geometry based on

discretization practices found in the literature [33]. Thus, it is likely that the most accurate results would be achieved with a Node Factor relatively close to 1.

Figure 4.26 shows how the numbers of nodes and faces as well as the computation time scale with the Node Factor. The counts of all mesh elements appear to increase linearly, with some small irregularities because the meshing parameters controlled by the Node Factor can sometimes not all be fulfilled simultaneously depending on the meshed geometry. The counts of gas nodes and gas faces appears as one curve because there is always one more gas face than there are gas nodes for the *Raphael* geometry. The computation time increases more than linearly and may be following a power function as found before by Middleton [33]. The difference is substantial; changing the Node Factor from the default 1 to 6 means the model takes more than 5 hours to solve instead of 45 minutes.

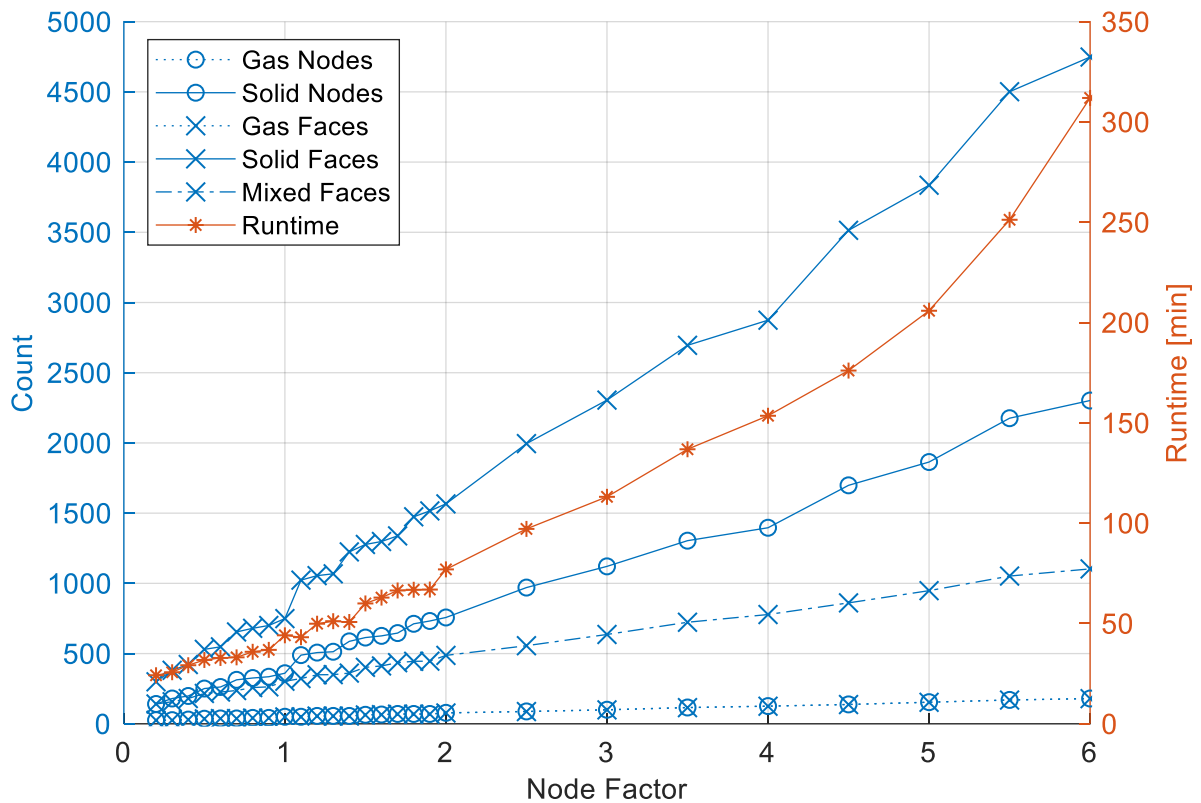


Figure 4.26: Number of nodes, faces and runtime of the computation over the 'Node Factor'.

4.7.5 Sensitivity to Source and Sink Temperatures

In the real engine, the temperatures of the heat transfer liquids in the source channels of the heat exchangers changes from the values measured at the liquid inlets to those at the outlets. The liquid flow rates must be limited so that the temperature change caused by heat transferred with the fluid is sufficiently large to be measured. In the model, the mean of the inlet and outlet temperatures is applied as the uniform temperature for the entire heat exchanger, which is a simplification that may introduce error. There will be some ‘equivalent temperature’ between the inlet and outlet temperature that will produce the same heat transfer rate as in the experiment, but this is not necessarily the mean. The potential scale of this error is estimated in this section by running the same hypothetical setpoint as in previous sections and varying T_{Source} and T_{Sink} independently. Figure 4.27 shows the resulting changes in W_{ind} and the heat flow rates when varying T_{Source} (a) or T_{Sink} (b). The changes are shown relative to the values obtained when running the model with the setpoint temperatures of 5 °C and 150 °C.

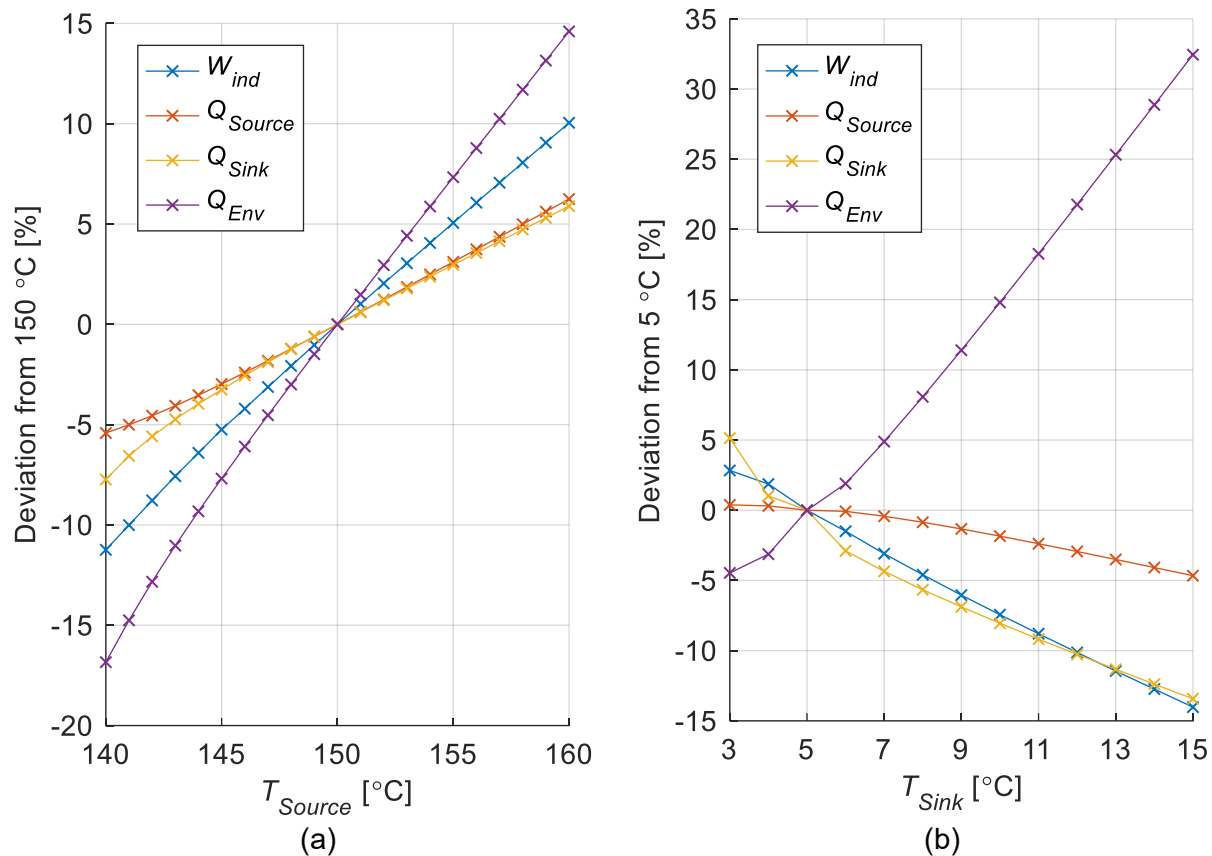


Figure 4.27: Indicated work and heat flow rates over varying source temperature (a) and sink temperature (b). Model variant A. Shown relative to the values at the setpoint temperatures.

All variables appear to follow almost linear trends over T_{Source} and T_{Sink} , and the heat flow to the environment changes more quickly than the others. To estimate the aforementioned error for the datasets used for validation, it must be estimated how far the mean temperature used as the model input might be from the ‘equivalent temperature’. In the experiment, the difference in T_{Source} between inlet and outlet was up to 9.5 °C. Assuming that the ‘equivalent temperature’ is no more than 25 % of this difference away from the mean temperature, and using the slope of W_{ind} in Figure 4.27 (a) which is about 1 % deviation per °C, this gives an estimated maximum error of:

$$u_{T_{source}} = 2.4 \% \quad (82)$$

in W_{ind} caused by the simplified representation of the source temperature in the model. The error for \dot{Q}_{Source} and \dot{Q}_{Sink} is smaller as their slopes are smaller. Following the same logic for the sink temperature, the highest inlet-outlet temperature difference was 13.3 °C, leading to an estimated maximum error in W_{ind} of:

$$u_{T_{sink}} = 4.8 \% \quad (83)$$

The error for \dot{Q}_{Source} is smaller and for \dot{Q}_{Sink} about equal judging by the slopes in Figure 4.27 (b). This analysis brought two findings. Firstly, the indicated work and heat flow rates predicted by the model are proportional to the source and sink temperatures over their ranges measured in the experiment. Secondly, it was roughly estimated that the simplification of uniform source and sink temperatures in the model heat exchangers may incur error in W_{ind} , \dot{Q}_{Source} and \dot{Q}_{Sink} which must be considered when evaluating the validation results. This error could be minimized when using the model in practice by doing a CFD or similar analysis to find an ‘equivalent temperature’ to input to the model.

4.7.6 Sensitivity to Source and Sink Liquid Heat Transfer Coefficients

The process of estimating the convective heat transfer coefficients (h_{source} and h_{sink}) for the liquids in the source channel of the heat exchangers was described in Section 3.6. Two estimates were made, one analytical and one from CFD, and both were tested on the two versions ‘No_Seal’ and ‘With_Seal’ of the *Raphael* model in *MSPM* that were introduced in Section 3.4.2. It was observed in the model validation in Sections 4.2 to 4.4 that the model results in terms of indicated work and source/sink heat flow rates depend strongly on h_{source} and h_{sink} . None of the model variants produced consistently small errors in all variables but it was proposed that varying the heat transfer coefficients between the two estimates may yield a reliable model. Since both estimates are not based on measured data, it is plausible that the ‘true’ values would be somewhere between the estimates. Model variant D (‘With_Seal_h_CFD’) showed strong accuracy in its predictions of heat flow and gas temperatures, but overpredicted W_{ind} . Following the findings from section 4.2.4 this might be improved by decreasing the heat transfer coefficients.

An extensive sensitivity study was conducted that varied h_{source} and h_{sink} independently over ranges where the lowest model deviations were expected. This was done for both model versions ‘No_Seal’ and ‘With_Seal’, and for the two experimental datapoints with the highest and lowest heat exchanger Reynolds number. These datapoints were assumed to represent the trend between all datapoints since the trends observed in Sections 4.2 to 4.4 were mostly linear over $Re_{HX,avg}$. The following ranges of h_{source} and h_{sink} were investigated:

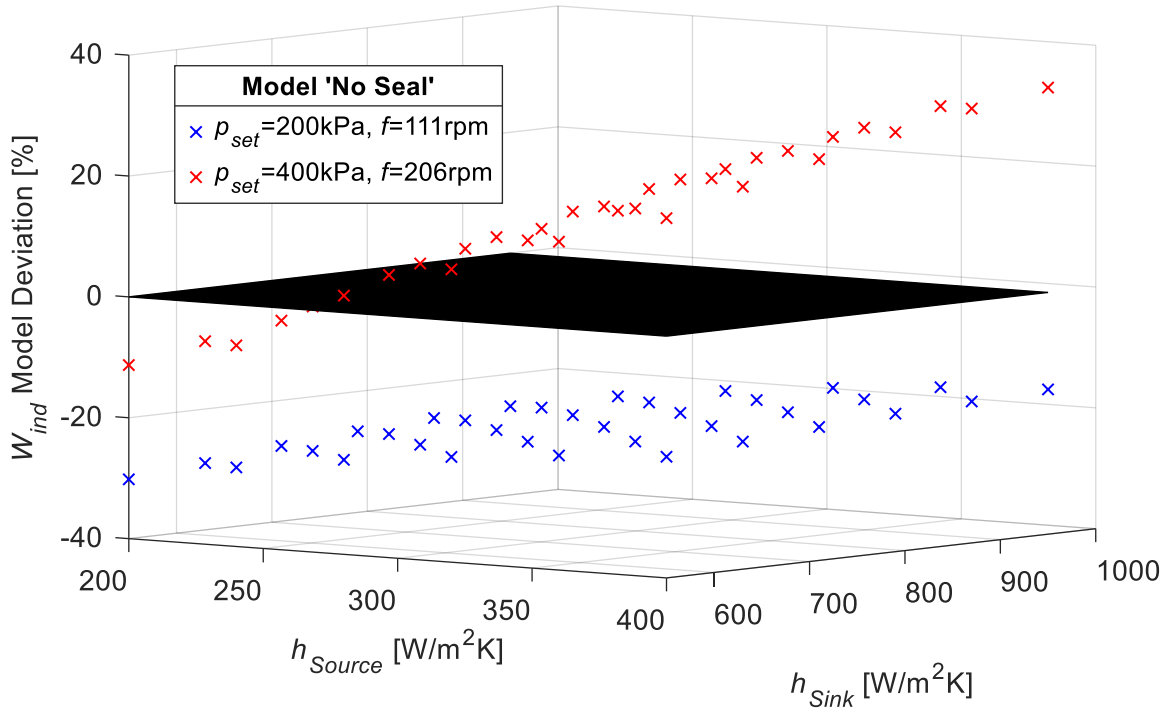
- ‘No_Seal’ model: Optimum expected in a range centred on the CFD estimate.
 - h_{source} : 200 to 400 W/m² K in steps of 40
 - h_{sink} : 550 to 950 W/m² K in steps of 80
- ‘With_Seal’ model: Optimum expected between the analytical and CFD estimates.
 - h_{source} : 80 to 280 W/m² K in steps of 20
 - h_{sink} : 380 to 740 W/m² K in steps of 40

This resulted in 72 combinations that were run with the ‘No_Seal’ model and 220 runs with the ‘With_Seal’ model. The resulting W_{ind} , \dot{Q}_{source} and \dot{Q}_{sink} were analyzed for all runs with the aim to find a combination of heat transfer coefficients that yields low deviation in all variables. Figure 4.28 shows three-dimensional plots of the model deviation in W_{ind} from both ‘No_Seal’ (a)

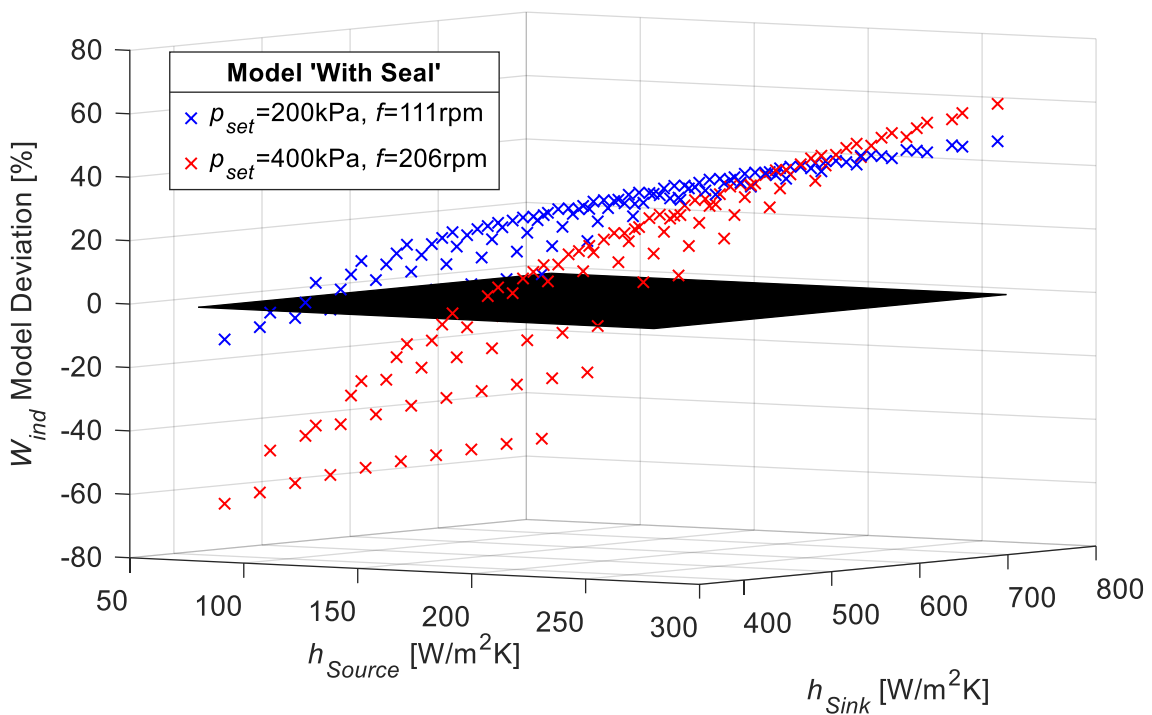
and ‘With_Seal’ (b) over h_{source} and h_{sink} . The two datapoints are displayed in blue (low $Re_{HX,avg}$) and red (high $Re_{HX,avg}$). The black surface indicates zero deviation. With the ‘No_Seal’ model only the high-Reynolds number setpoint crosses zero deviation while for the other setpoint W_{ind} is always underestimated. With the ‘With_Seal’ model a deviation close to zero is achieved for both setpoints, but it does not appear to be at the same combination of heat transfer coefficients.

Since the main goal of this section is to minimize the error in W_{ind} with the ‘With_Seal’ model, plots shown from here will only be for indicated work and for this model. All plots including the ‘No_Seal’ model and the variables \dot{Q}_{source} and \dot{Q}_{sink} can be found in Appendix E.

For a model to be considered reliable, it should firstly make predictions with a low overall error, and secondly the error should be consistent between datapoints. To measure these two factors, two new variables were calculated from the data from Figure 4.28. To measure the overall error, the root sum square (RSS) of the deviations from both datapoints is taken. The consistency is measured from the difference between the deviations (DD) of both datapoints. Both these variables should be minimized; a reliable model would have low values for both at one combination of h_{source} and h_{sink} . The resulting plot is shown in Figure 4.29. It shows that W_{ind} appears to be significantly more sensitive to h_{source} than to h_{sink} , and that the RSS deviation appears to reach a minimum at a lower h_{source} than where the DD has a minimum.



(a)



(b)

Figure 4.28: 3D plot of the model deviation in W_{ind} over the source and sink liquid heat transfer coefficients. For setpoints with highest (red) and lowest (blue) $Re_{HX,avg}$. For model versions 'No_Seal' (a) and 'With_Seal' (b).

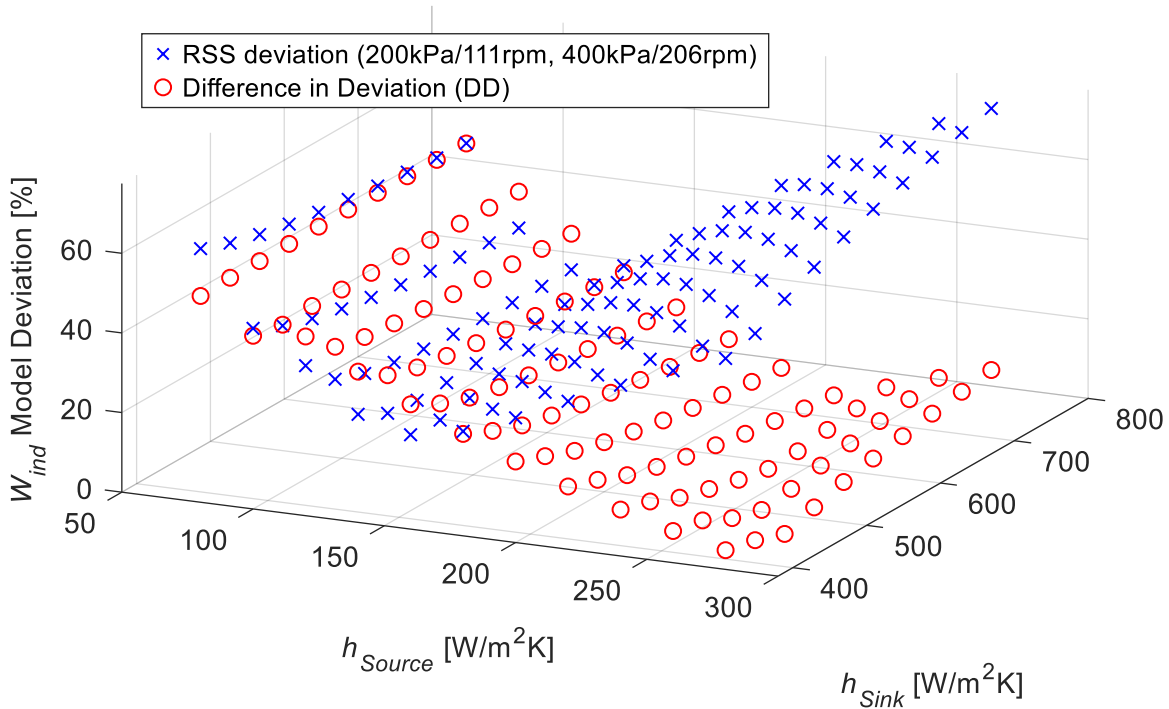


Figure 4.29: **For model version ‘With_Seal’**. RSS deviation in W_{ind} from two setpoints, and difference in deviation (DD) between setpoints, over the source and sink liquid heat transfer coefficients. 3D view.

To quantify and analyze the trends, the data needs to be viewed two-dimensionally so the effects of h_{source} and h_{sink} can be seen individually. This is shown in Figure 4.30, where the RSS deviation and DD are plotted over h_{source} with lines of equal h_{sink} (a), and over h_{sink} with lines of equal h_{source} (b). The two estimates of the heat transfer coefficients used for model validation are highlighted for reference.

The plot in Figure 4.30 (b) shows that the lowest RSS deviation of about 25 % is achieved with h_{source} in the range of 120 to 160 $W/m^2 K$, while the lowest DD of close to zero requires h_{source} to be greater than 220 $W/m^2 K$. Plot (c) shows that W_{ind} has no clear dependence on h_{sink} , and therefore h_{source} is the main parameter of influence. Thus, taking model variant D and decreasing h_{source} from 281 $W/m^2 K$ (CFD estimate) to about 140 $W/m^2 K$ can significantly reduce the average deviation in W_{ind} , but a 25 % error remains. At the same time, the consistency in the deviation as indicated by DD becomes worse. This means that the ‘With_Seal’ model cannot be made reliable through tuning of the liquid heat transfer coefficients, and there remain other sources of model error that should be investigated.

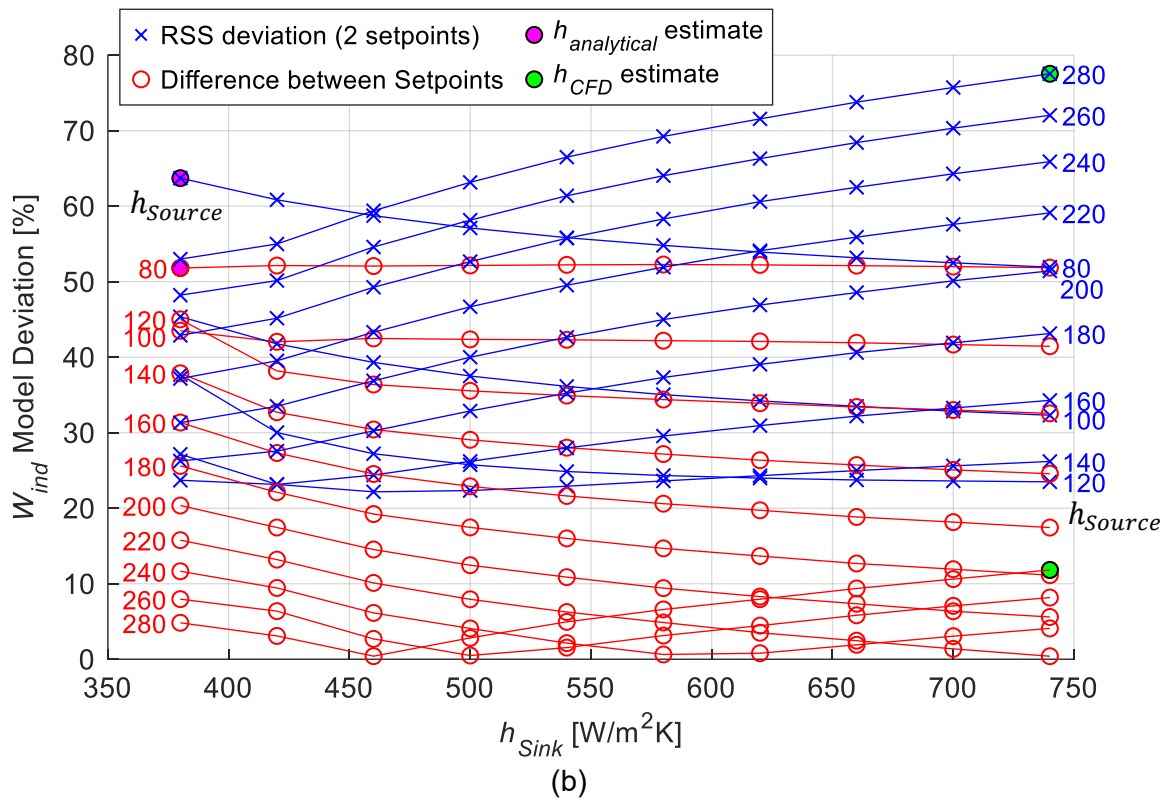
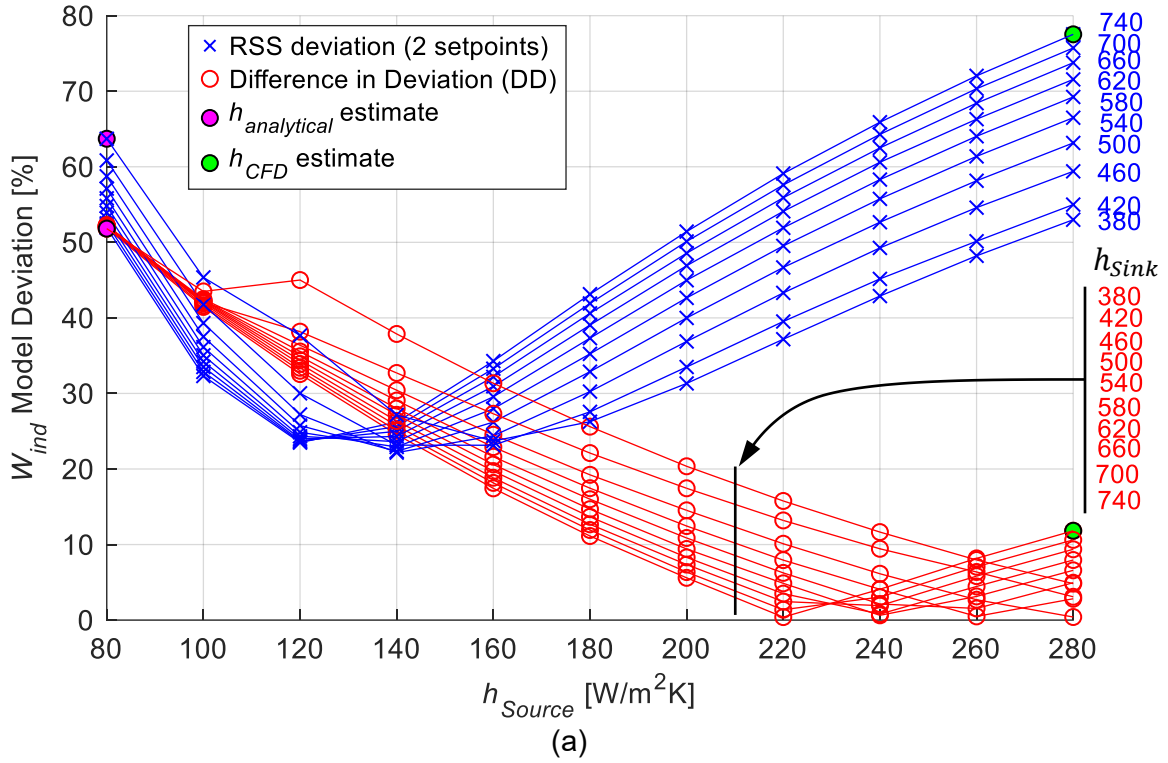


Figure 4.30: For model version 'With_Seal'. RSS deviation in W_{ind} from two setpoints, and difference in deviation (DD) between setpoints, over the source and sink liquid heat transfer coefficients. (a) trend over h_{Source} with lines of equal h_{Sink} annotated, (b) trend over h_{Sink} with lines of equal h_{Source} annotated.

Similar analyses were done for the other variables \dot{Q}_{Source} and \dot{Q}_{Sink} and for the ‘No_Seal’ model using the plots in Appendix E. The findings are summarized in the following.

- For the ‘With_Seal’ model, the deviation in \dot{Q}_{Source} is minimized when h_{Source} is between 160 and 200 W/m² K, while the deviation in \dot{Q}_{Sink} may have a minimum at a h_{Source} of greater than 280 W/m² K, the highest tested. Thus, the optimal values of h_{Source} for predicting W_{ind} , \dot{Q}_{Source} and \dot{Q}_{Sink} differ vastly from each other, which reinforces the conclusion that this model will not become reliable just by tuning h_{Source} and h_{Sink} . Note that the analysis of \dot{Q}_{Source} and \dot{Q}_{Sink} is not as meaningful as W_{ind} due to the uncertainty in the experimental measurements as mentioned in Section 4.3.
- For the ‘With_Seal’ model, all variables show a strong dependence on h_{Source} while the influence of h_{Sink} is insignificant. This is also true for the ‘No_Seal’ model, but less pronounced. It indicates that the engine performance depends more strongly on the liquid convection heat transfer in the heater than in the cooler. This means that h_{Source} , which is smaller than h_{Sink} due to the different fluids, is the main bottleneck limiting the engine performance, and efforts to improve heat transfer should focus on the heater.
- For the ‘No_Seal’ model, as expected, variation of the heat transfer coefficients does not notably improve the RSS deviation in W_{ind} . It reaches its minimum of 25 % when using the CFD estimate, which corresponds to model variant B.

The insight from this sensitivity study is that varying h_{Source} and h_{Sink} , the model input parameters whose values could not be accurately determined, did not lead to either model version producing accurate and consistent predictions of the indicated work and heat flow rates. For the ‘With_Seal’ model h_{Source} can be tuned in the interval between the analytical and CFD estimates to minimize either the RSS deviation or the difference in deviation (DD), but both cannot be minimized simultaneously. Therefore, apart from the liquid heat transfer coefficients, other assumptions and simplifications of the *MSPM*’s thermodynamic model must be the cause of the deviation in W_{ind} between the ‘With_Seal’ model and experimental data.

4.7.7 Sensitivity to Regenerator Properties

As the regenerator filling was made from widely available polyester fiber stuffing for pillows, its porosity β and fiber diameter $D_{W,Reg}$ had to be determined by weighing and visual measurement. The porosity used for validation data (96 %) is assumed to be accurate within ± 1 % since different regenerators were made in increments of 1 %. The fiber diameter of 0.1 mm is estimated to be accurate within ± 0.03 mm judging by the variation between measurement samples.

To test the effect of these uncertainties on the model results, a study was conducted where β was varied from 94 % to 98 % in increments of 0.5 %, and $D_{W,Reg}$ was varied from 0.05 mm to 0.15 mm in increments of 0.01 mm. This was done using model variant D and a hypothetical setpoint with $T_{Source} = 150$ °C, $T_{Sink} = 5$ °C, $p_{mean} = 300$ kPa, and $f = 150$ rpm. Figure 4.31 shows the effect of both properties on the predicted indicated work. For porosity (a) the gradient of the curve increases when moving towards 100 % (empty regenerator), while for the wire diameter (b) the relationship appears linear over the tested interval. Within the estimated boundaries of uncertainty, marked by the black lines, W_{ind} varied by up to 4 % for β and by up to 4.1 % for $D_{W,Reg}$. Thus, the following uncertainties in W_{ind} caused by the regenerator properties must be considered:

$$u_{\beta} = 4 \% \quad (84)$$

$$u_{D_{W,Reg}} = 4.1 \% \quad (85)$$

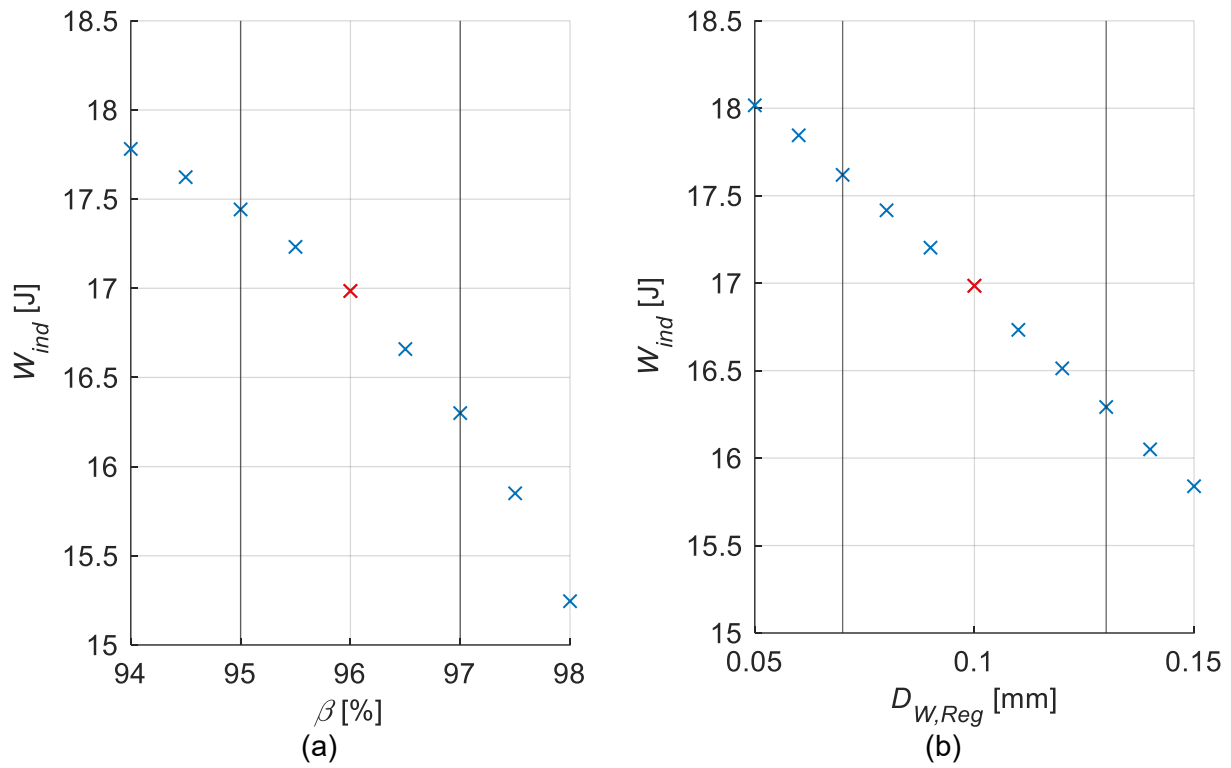


Figure 4.31: Sensitivity of indicated work to varying regenerator porosity (a) and wire diameter (b). Red are the nominal properties used for model validation; black lines are estimated boundaries of uncertainty in regenerator properties.

4.7.8 Summary: Total Estimated Uncertainty in Model Indicated Work

In Sections 4.7.1, 4.7.2, 4.7.5 and 4.7.7 the effects on the predicted indicated work caused by initial conditions, repeated simulation runs, and varying source and sink temperatures and regenerator properties within estimated ranges of uncertainty have been quantified. The total uncertainty in W_{ind} from these sources can be estimated by the root sum square:

$$u_{total} = \sqrt{u_{repeat}^2 + u_{initial}^2 + u_{T_{source}}^2 + u_{T_{sink}}^2 + u_{\beta}^2 + u_{D_{W,Reg}}^2} = 10.7 \% \quad (86)$$

This value is only an order-of-magnitude estimate since the varied parameters were only tested on one model variant and one hypothetical engine setpoint. However, to determine if the deviations between model predictions and experiment data might be within the uncertainty range of the model results, u_{total} can be compared to the predictions of W_{ind} by model variant D (Section 4.2.4), which was found earlier to produce the most accurate overall results out of all variants. u_{total} is much smaller than the deviation of variant D of 50 % to 70 %, meaning that the model results are known with sufficient accuracy to say that shortcomings of the *MSPM* model are most likely the cause of the observed deviations.

4.8 Shaft Power and Thermal Efficiency

In this section, the experimentally measured shaft power (P_{shaft}) and thermal efficiency (η_{shaft}) are shown as these are important metrics in the Stirling literature, and compared against the four model variants' estimates. It must be considered that the data from this model cannot be directly compared to the experiment because the model does not include the mechanism and neglects mechanical losses. It does, however, include flow friction losses from the heat exchangers and regenerator. Therefore, the model is expected to overestimate shaft power, especially at elevated speeds, and overestimate the speed at which maximum shaft power occurs.

Figure 4.32 shows shaft power over engine speed. The experimental engine outputs a relatively stable power between 12 and 15 W at speeds up to 140 rpm, independent of the mean pressure. This is similar to the trend in indicated work that was observed in Figure 4.7. At higher speeds P_{shaft} decreases until reaching zero at the maximum (free-running) speed. The maximum power of 15.1 W is achieved with p_{set} of 400 kPa at a speed of 129 rpm. Model variant A mostly underestimates shaft power except at higher speeds where the power of the real engine decreases more quickly than any of the model variants predict. Variant C overestimates at low p_{set} but underestimates at high pressure, likely because the analytically estimated heat transfer coefficients limit the power too strongly. Variants B and D overestimate P_{shaft} , and show a trend of increasing power with speed and a strong dependence on p_{set} which are not present in the experimental data. Since variant B showed relatively little deviation in its predictions of indicated work (Figure 4.7), the deviation seen here should be mostly due to the neglect of mechanical losses by the model. At the lowest speed and $p_{set} = 400$ kPa, where the maximum shaft power occurred in the experiment, the deviation of model variant B is about 41 %, which could be taken as a rough estimate of the overprediction of shaft power by *MSPM*. The stark differences between the model variants highlight again that a reliable estimate of the source heat transfer and the performance of piston seals is crucial if one hopes to get a meaningful prediction of Stirling engine performance.

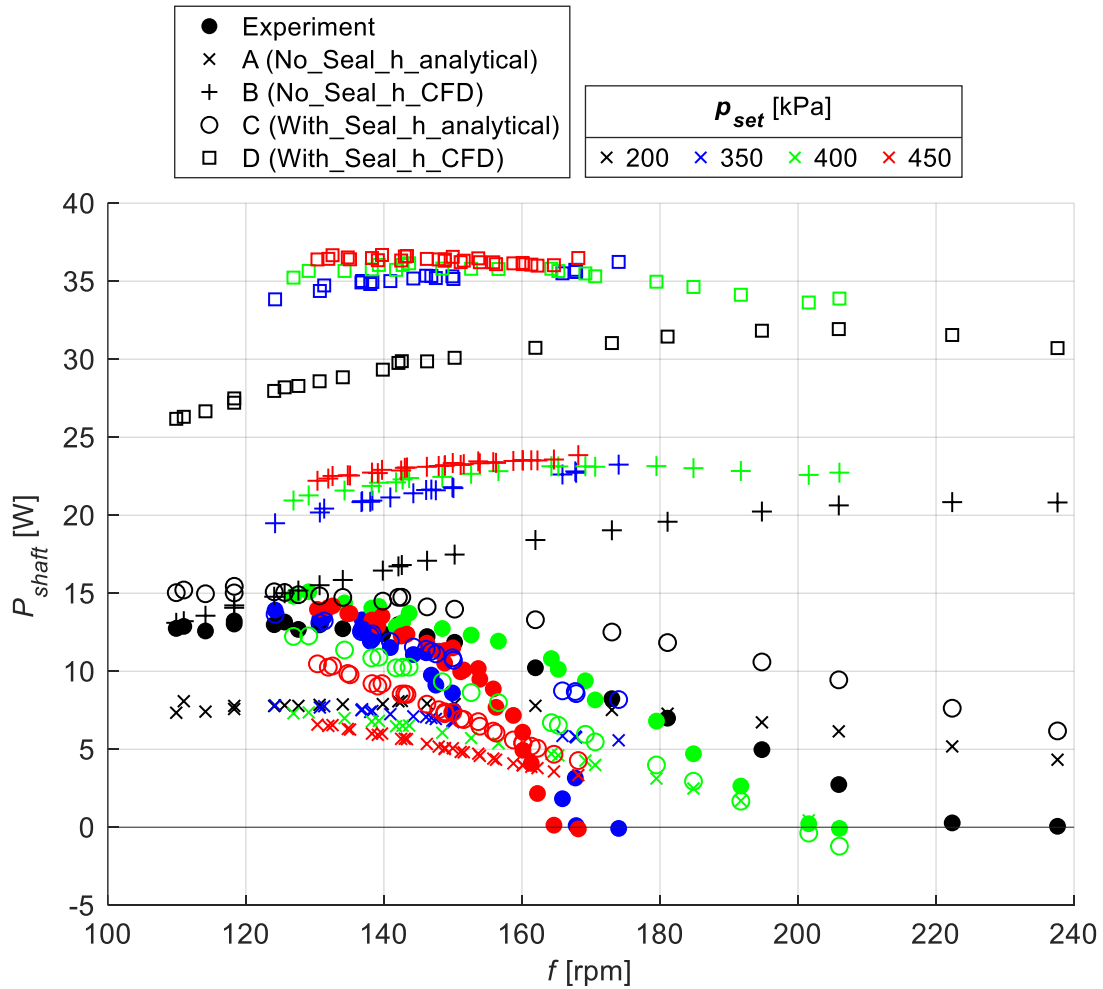


Figure 4.32: Shaft Power of *Raphael* engine over speed. Data from experiment and all model variants, for all setpoints. Colour indicates charge pressure.

Figure 4.33 shows the thermal efficiency, calculated from shaft power, for the same datapoints. The trends are mostly similar to those observed in Figure 4.32 for shaft power. In the experiment, the maximum efficiency of 2.2 % is reached at the lowest speed and setpoint pressure, and an increase in speed always leads to reduced efficiency. This is correctly predicted by all model variants except variant B, which displays a steady efficiency. The models all predict the efficiency to decrease as pressure is increased, but the experimental data shows higher values at $p_{set} = 400$ kPa compared to 350 kPa, which is likely due to variations in the experimental conditions such as the replacement of the power piston seal.

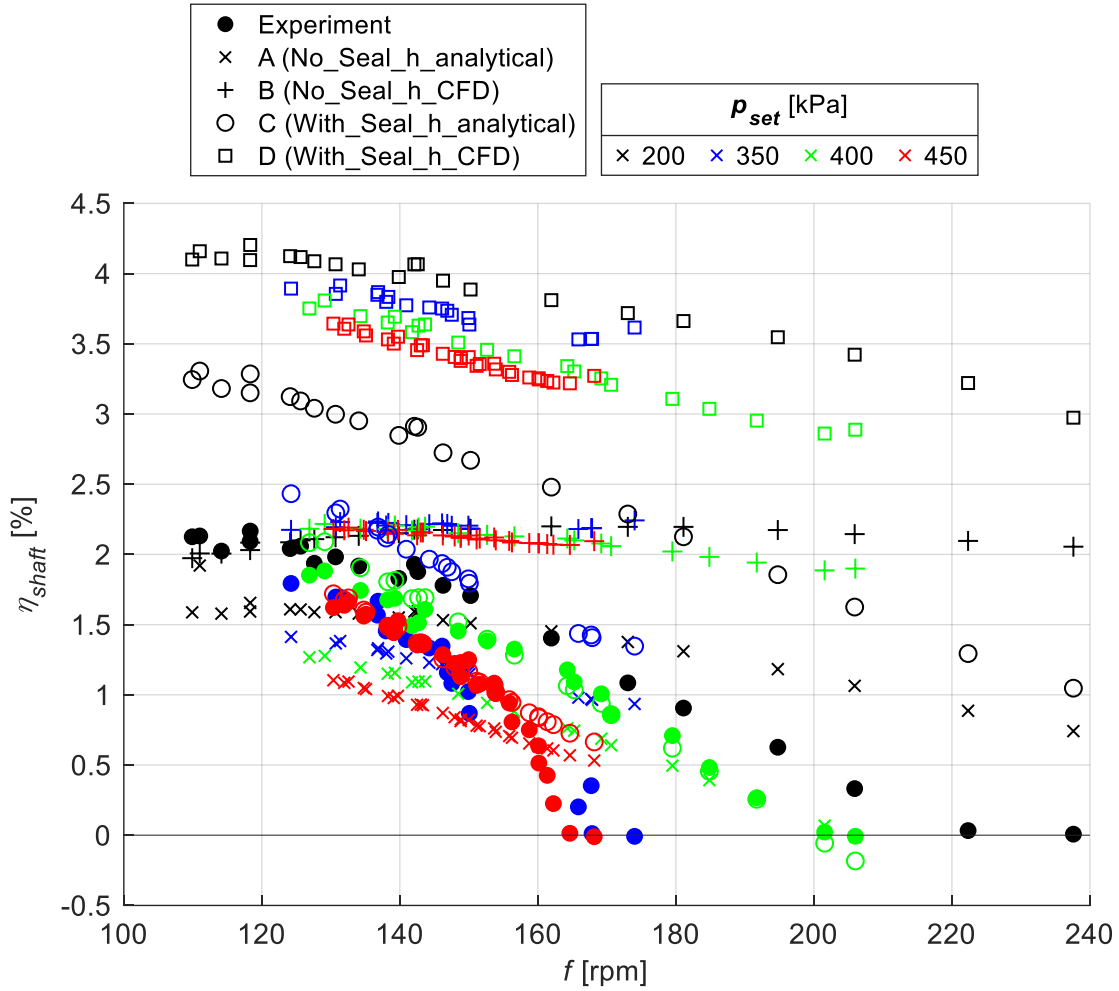


Figure 4.33: Shaft (Thermal) Efficiency of *Raphael* engine over speed. Data from experiment and all model variants, for all setpoints. Colour indicates charge pressure.

The observed peak efficiency of 2.2 % can be compared to the theoretical efficiencies η_{Carnot} and η_{CNCA} (see Section 1.2):

$$\eta_{Carnot} = 1 - \frac{T_{Sink}}{T_{Source}} = 1 - \frac{278.15 \text{ K}}{423.15 \text{ K}} = 34.3 \% \quad (87)$$

$$\eta_{CNCA} = 1 - \sqrt{\frac{T_{Sink}}{T_{Source}}} = 18.9 \% \quad (88)$$

The *Raphael* reached 6.4 % of η_{Carnot} and 11.6 % of η_{CNCA} . This is less than half of what the commercial LTDSE ThermoHeart™ achieved (28 % of η_{CNCA} at $T_{Source} = 150$ °C and $T_{Sink} = 20$ °C [20]). Thus, *Raphael* was significantly less efficient than what has been demonstrated at similar source and sink temperatures, likely due to large heat transfer resistances in its heat exchangers and an underwhelming regenerator performance.

4.9 Experimental Uncertainty

The uncertainty in the experimental data must be assessed to verify that the observations made in this Chapter are valid, and that the deviations between model and experiment could not have been caused by insufficient accuracy in the experimental data acquisition setup and procedures. This Section summarizes the results of an uncertainty analysis that was carried out following methods described by Coleman and Steele [115] and is documented in Appendix A to Appendix C.

A comprehensive uncertainty analysis would account for systematic uncertainty, which is caused by predictable errors from instruments and calibration, and random uncertainty, which refers to statistical errors due to the limited precision of measurements that are taken as a mean of several sample values. Further, uncertainties that depend on the measured value would be calculated separately for each measurement. Such an analysis for a Stirling engine setup comparable to the one used in this work was done by Nicol-Seto [42].

The uncertainty analysis presented here is simplified. Firstly, only systematic uncertainties are considered. It is assumed that random uncertainty is small compared to systematic uncertainty because all variables were calculated as averages of several samples. Scalar variables such as engine speed and temperatures were averaged over the entire datapoint, and cyclic variables such as dynamic pressures were averaged across at least $n_{cyc} = 15$ cycles (Section 0). Secondly, uncertainties for most variables were not determined for each datapoint individually. Instead, to greatly reduce complexity, the ‘worst case’ uncertainty, meaning that the greatest possible uncertainty for the entire range of data, was calculated and taken as a representative uncertainty that can be applied to all data. For example, the uncertainty for all thermocouple temperature measurements was calculated as the ‘worst case’ out of all measured temperatures and applied to all thermocouple data. With this method, uncertainties can be overestimated but never underestimated. Appendix A discusses the uncertainty equations and propagation methods used.

4.9.1 Measured Variables

Table 4.4 lists the resulting uncertainties for measured variables that are relevant for the data shown in this Chapter. The corresponding calculations are in Appendix B. The absolute uncertainties are put into a relative context in the right column. The uncertainty in liquid temperatures amounts to a considerable share of the temperature difference between inlet and outlet. However, this uncertainty is likely significantly lower in reality because of the temperature sensor calibration that was not considered in the uncertainty calculation. There is also an uncertainty in the torque data that is greater than the smallest torque increments between setpoints. This is because a torque sensor with a range almost 10 times higher than the highest measurement was used. However, the torque measurements were observed to be clearly distinguishable between increments, so the real uncertainty is likely lower than estimated here.

Table 4.4: Uncertainties of relevant measured variables

| Variables | Symbols | Uncertainty | Relative Comparison |
|----------------------|---|-------------|--|
| Liquid Temperatures | $T_{source,in}, T_{source,out},$ $T_{sink,in}, T_{sink,out}$ | 0.5 °C | 9 % of smallest $\Delta T = T_{in} - T_{out}$ |
| Gas Temperatures | $T_e, T_{h,inlet}, T_{h,reg}, T_{k,inlet},$ $T_{k,reg}, T_{reg}, T_{PP}, T_{CC}$ | 1.5 °C | 3.2 % of smallest $\Delta T = T_e - T_{PP}$ |
| Atmospheric Pressure | p_{atm} | 0.014 kPa | 0.02 % of 1 atm |
| Torque | τ | 0.0325 Nm | 163% of smallest torque increment |

4.9.2 Calculated Variables

Table 4.5 lists the uncertainties from error propagation into the calculated variables that are used in this Chapter. Appendix C contains the corresponding calculations. Considerable uncertainty was found in the heat flow rates, caused by the liquid temperature and specific heat uncertainties. As discussed in Section 2.4.3, the uncertainty in the heater fluid specific heat was expected to be large, and the deviations between experimental and modeled heater heat flow rate observed in Section 4.3 were suggested to be a result of the experimental uncertainty. However,

the calculated uncertainty of 88 W cannot account for the maximum deviation observed in Figure 4.10, which is about 150 W. The uncertainty of the specific heat might be greater than estimated, and some share of the deviation is likely a result of inaccuracy by the model.

The uncertainty in the pressure drop measurement Δp_{HX} is much greater than the expected pressure drop being measured. This confirms the argument made in Section 4.5.3 that the experimental setup and the method of determining the pressure drop with two separate sensors is too inaccurate to resolve the pressure drop.

The uncertainties in shaft power and efficiency are also considerable, but the trends observed in Section 4.8 are still valid. Considering the uncertainties, model variants A and C may have predicted shaft power and efficiency fairly accurately. However, no model was able to reliably predict the decline of power and efficiency with increasing speed.

Lastly, the uncertainty in indicated work is significant, at 15.7 % to 23.1 % of W_{ind} . It is shown in Figure 4.34 as a function of engine speed for all experimental datapoints. The uncertainty has a stronger effect at higher engine pressures, likely because the volume uncertainties have greater effect, and at higher speeds where the indicated work is smaller. Comparing this to the model deviations in Figure 4.7 shows that the deviation of model variant B was mostly within the experimental uncertainty, while the other variants had greater deviations. It had been found in Section 2.8 that the experimentally measured W_{ind} was repeatable within 3 %, which is much smaller than the estimated uncertainty and indicates that the true accuracy of the measurements may be better than suggested by the uncertainty. The observed trends between experiment and model are still expected to be valid, but for future experiments it should be considered to reduce the engine volume uncertainty by verifying the power piston dimensions and stroke, to reduce the crank angle uncertainty by aligning the encoder more accurately, and to reduce the pressure uncertainty by recording a greater number of cycles per datapoint.

Table 4.5: Uncertainties of relevant calculated variables

| Variables | Symbols | Uncertainty | Relative Comparison |
|-----------------------------------|--|-------------|--|
| Cooler heat flow rate | \dot{Q}_{cooler} | 71 W | 14.2 % of smallest |
| Heater heat flow rate | \dot{Q}_{heater} | 88 W | 14.7 % of smallest |
| Mean working space pressure | p_{mean} | 6.19 kPa | 2.1 % of smallest |
| Mean crankcase pressure | $p_{mean,CC}$ | 10.73 kPa | 3.5 % of smallest |
| Working space pressures | $p_{Exp,avg}, p_{Com,avg}, p_{PC,avg}, p_{CC,avg}$ | 2.8 kPa | 6.2 % of smallest pressure swing (45.2 kPa) |
| Indicator diagram pressure | $p_{d2,avg}$ | 0.9 kPa | 2 % of smallest pressure swing (45.2 kPa) |
| Heat Exchanger Pressure drop | Δp_{HX} | 15.17 kPa | 60 times pressure drop (250 Pa, section 4.5.1) |
| Engine Speed (transient and mean) | f, f_{θ} | 3.3 rpm | 3 % of smallest f |
| Shaft Power | P_{shaft} | 0.81 W | 8.3 % of average |
| Thermal Efficiency | η_{shaft} | 0.34 % | 28 % of average |
| Indicated Work | W_{ind} | Max. 2.1 J | Max. 23.1 % |

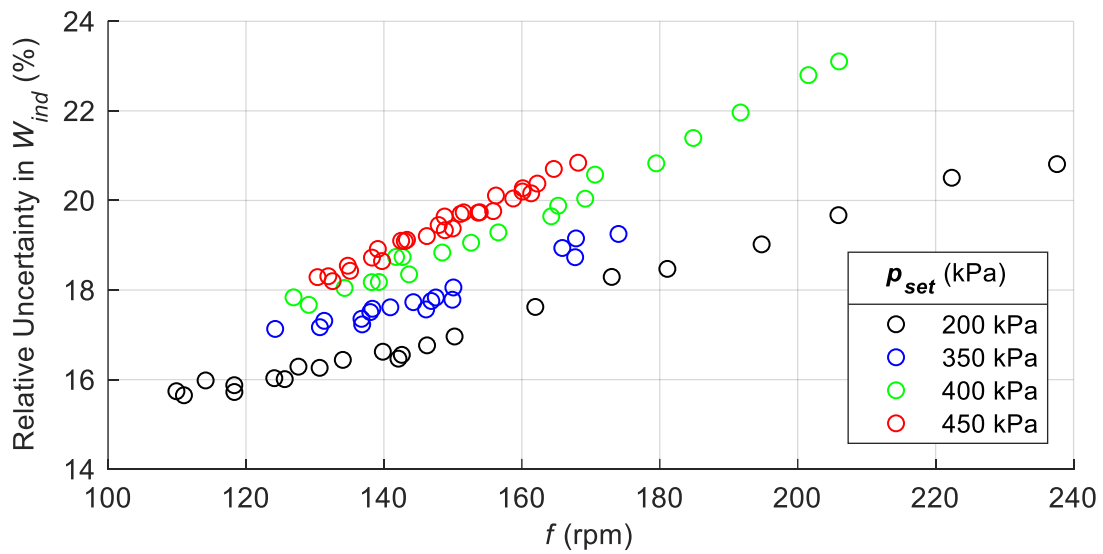


Figure 4.34: Uncertainty in indicated work over engine speed, for all datapoints

4.10 Chapter Conclusion

The numerical model *MSPM* was validated against experimental data from the *Raphael* low temperature difference Stirling engine. This first validation focused only on the thermodynamic model and only at steady state, using as metrics the indicator diagram shape and indicated work, source and sink heat flow rates, gas temperatures, and pressure drop across the heat exchangers and regenerator. 89 experimental datapoints were acquired at source and sink temperatures of 150 °C and 5 °C, respectively, mean pressure between 200 and 450 kPa, speed between 111 and 238 rpm, and the estimated Reynolds number in the heat exchanger channels was between 400 and 1500. Four model variants (A to D) were tested which differed in the modeling of the displacer piston seal (Section 3.4.2) and choice of liquid convection heat transfer coefficients (Section 3.6).

4.10.1 Summary of Results

Model results were analyzed in terms of the relative deviation between model and experiment. It was found that the deviation in indicated work followed approximately linear trends with respect to the heat exchanger Reynolds number for most model variants. Model variant B predicted the indicated work to within 20 % but the deviation was not consistent between the datapoints. Variant D achieved a more consistent deviation, but it was much higher as this model overestimated the indicated work by 50 % to 70 %. The variants B and D also made good predictions of the heater and cooler heat flow rates (within 20 %) and variant D predicted gas temperatures consistently to within 3 % or 10 °C.

Measurement of the pressure drop proved to be infeasible with the experimental setup due to the unsteady measurement with two separate pressure sensors being limited by sensor accuracy and temperature-induced deviation. The model prediction of the pressure drop could not be validated. It was proposed to instead measure a single differential pressure in a steady state experiment or determine the pressure drop indirectly through the losses incurred when driving the engine externally.

Touching on the mechanical model of *MSPM*, in-cycle speed variations were investigated. The model was found to be qualitatively in good agreement with experimental data.

A sensitivity study was conducted to examine the effects of certain model input parameters that were not known precisely from the experiment, and certain model settings such as initial conditions, heat conduction and mesh. Analyzing the input parameters, it was estimated that reasonable variations in the source and sink temperatures, regenerator properties, and initial conditions (related to the tolerance of the convergence criterion) would cause a combined uncertainty in the indicated work of no more than 11 %. The deviation of 50 % to 70 % observed in variant D is greater than this uncertainty and therefore must come from other sources. The convective heat transfer coefficients for the liquid side of the heat exchangers were systematically varied between the two estimates made in Section 3.6 to determine if any reasonable combination of values would yield better predictions of indicated work. It was found that either the overall deviation or the consistency in deviation between setpoints could be optimized, but not both together. Thus, the model deviation was not caused by inaccurate estimates of the heat transfer coefficients alone.

The effect of modeling or not modeling heat conduction in different sections of the solid engine body was analyzed. Axial conduction between the heat exchangers and through the displacer piston was found to have little effect, which allowed the node count of the displacer piston to be reduced significantly to decrease computing time. Disabling conduction in the outside walls of the heat exchangers affected the overall engine performance significantly and revealed a strong influence of the solid geometry of the entire heat exchanger. Overall, the effects of conduction predicted by the model followed expectations.

The numerical mesh density was varied using the ‘Node Factor’ parameter of *MSPM*. The indicated work and heat flow rates did not show convergence with increasing mesh size, which was attributed to the ‘Node Factor’ not being comparable to a uniform mesh refinement as done in CFD studies. The default mesh settings are likely reliable as they take the modeled geometry into account.

Investigating shaft power and thermal efficiency showed that *Raphael* achieved a peak power of 15.1 W at 400 kPa charge pressure and the lowest possible speed. Model predictions varied substantially between the variants, but it was suggested that at peak shaft power the overestimation of shaft power due to neglecting mechanical losses may be around 40 %.

Experimental uncertainty was examined, considering systematic uncertainties only and determining ‘worst-case’ uncertainties for all measured and calculated variables. The heat exchanger heat flow rates showed notable uncertainties due to the combined uncertainties from liquid temperatures, liquid mass flow rates and specific heats. It was confirmed quantitatively that the pressure drop cannot be measured accurately with the setup as its uncertainty was much greater than the expected pressure drop. The relative uncertainty in indicated work was up to 23 %, which may contribute some of the deviations between experiment and model, but does not invalidate the observed trends.

4.10.2 Discussion

The validation of indicated work, heat transfer rates and gas temperatures showed that overall, model variants B and D achieved the best agreement with experimental data but deviated in different ways. These variants used the same source heat transfer coefficients and differed only in the presence of the displacer piston seal. A sensitivity study showed that varying the heat transfer coefficients did not yield consistent results from either of the models, with and without seal. Hence the model error must be rooted elsewhere.

Both variants estimated the heat flow rates well (Section 4.3), but did not predict the effects of this thermal energy entering and leaving the working space correctly. Variant B, without the displacer piston seal, underestimated the gas temperature difference between hot and cold space, likely because of leakage past the displacer piston (Section 4.4). As found in Section 4.2.5, this leakage is more significant at conditions with lower heat exchanger Reynolds numbers. At the same time, the indicated work predicted by variant B was too low at low Reynolds numbers and too high at high Reynolds numbers (Figure 4.7). This suggests that the deviation in indicated work may also, like the temperature deviation, be caused by inaccurate modeling of the displacer piston seal.

Variant D, with the leak-free displacer piston seal, predicted gas temperatures more accurately, but still overestimated the hot side temperatures (Section 4.4), and also substantially overestimated indicated work (Figure 4.7). This may have been caused by the lack of displacer piston leakage in this model. The high indicated work also suggests that a significant leak between working space and crankcase may be present in the real engine, which was not considered in the model, and that

MSPM might be underestimating flow friction, which has the effect of reducing the pressure swing and indicated power. Inaccurate flow friction may be caused by the model using steady state friction factor correlations out of their scope (Section 3.2.6).

To sum up, the model validation showed that the representation of leaks, caused by piston seals and potentially other components like the displacer rod bushing, may be a significant source of error in the models used for this study. Therefore, to obtain accurate predictions of indicated work from the *MSPM* model, the leak rates of seals should be investigated and tested in future modeling efforts.

The goal of this validation was to assess whether *MSPM* can be used to predict thermodynamic metrics, such as indicated work, of new or modified LTDSE designs, which would greatly aid the development of such machines. For the *Raphael* engine, the model made reliable predictions of the gas temperatures and heat flow rates, which are the more direct metrics of thermodynamic performance. However, the less direct but more relevant metric of indicated work could not be predicted consistently. Conclusions regarding the modeling of different machines cannot be drawn with certainty due to this study being limited to a single engine, meaning only one heat exchanger geometry and a limited range of flow conditions within the laminar regime only.

It is proposed that *MSPM* can be expected to predict the thermodynamic performance of an engine reliably only if certain sensitive model inputs are well defined. It was found that two critical inputs are the characteristics of the heat source and sink, such as the source heat transfer coefficients, and the characteristics of leaks, such as piston seals. These are also two of the important loss mechanisms for LTDSEs. Experimental measurements, CFD or other analyses may be necessary to determine these inputs that can be applied in the model. Less well-defined models will likely not yield accurate results in terms of absolute numbers, but may be able to qualitatively predict the performance differences between design variations, and thus help to find optima.

Conclusions about potential sources of model error and suggestions for future work will be made in Chapter 6. This validation gave a first estimate of the accuracy of the *MSPM* model, so that it can now be used to model new designs or modifications of Stirling engines or similar machines. This is demonstrated in the following Chapter by scaling up an LTDSE.

Chapter 5. Scaling Up an LTDSE Using the *MSPM* Model

The core objective of the research at *DTECL*, as outlined in Chapter 1, is to investigate the potential of LTDSEs at a scale where their power output would be large enough for a real application. Small systems for residential combined heat and power (CHP) output roughly between 1 and 10 kW, with large units generating up to 75 kW [25]. The largest commercially available LTDSE, the ThermoHeart™ by Cool Energy Inc. [20], achieves 25 kW of electrical power. Larger scales would possibly be of interest for large industrial waste heat streams or geothermal plants. However, due to the low power density when working with low temperature heat, LTDSEs require larger volumes and piston diameters than high temperature engines with equal power. Therefore, it can be more viable, above a certain power scale, to combine several smaller engines into one unit instead of further increasing the size of a single engine. This is done, for example, by the ThermoHeart™ which uses four engines that share one mechanism [57], and the Swedish Stirling 400 kW high temperature unit with its 14 independent engines [22].

A reliable model can predict and optimize the size and geometry of an engine for a certain power scale, and thus eliminate expensive and tedious development and testing of experimental engines that would otherwise be necessary. In this chapter the *MSPM* model is used to scale up an LTDSE design, which is similar to the *Raphael* engine (Section 2.1), to scales of 1 kW and 10 kW. Additionally, a model is built of the ThermoHeart™ engine [20] and compared to performance data from this engine to see how *MSPM* compares to real data from a large-scale engine.

5.1 Scaling Parameters

Scaling up the power of a Stirling engine can be achieved by scaling a number of variables, as indicated by the West number [34] which was discussed in Section 1.5.1. From it follows the basic relation of proportionality:

$$P_{shaft} \propto p_{mean} V_{sw} f \frac{T_{Source} - T_{Sink}}{T_{Source} + T_{Sink}} \quad (89)$$

where: P_{shaft} = shaft power (W)

p_{mean} = mean cycle pressure (Pa)

V_{sw} = swept volume of displacer piston (m³)

f = mean engine speed (Hz)

T_{Source} = expansion space or heater temperature (K)

T_{Sink} = compression space or cooler temperature (K)

This neglects the influence of mechanical losses, flow losses, dead volume, the heat transfer limit, and other losses that inhibit an engine's performance and depend on the individual geometry and heat exchanger type. However, it shows that for an unchanged geometry the power can be expected to scale proportionally with pressure, speed, and volume, as long as losses and the heat transfer limit are not dominant. When scaling the swept volume V_{sw} all other volumes should be scaled equally so that their relative proportions and the compression ratio remain unchanged. Since in this case only LT applications are of interest, temperatures will remain as $T_{Source} = 150$ °C and $T_{Sink} = 5$ °C. Thus, in this chapter an engine will be scaled by:

- Volume (scaled by diameter)
- p_{mean} , and
- f

with the aim of reaching 1 kW and 10 kW of shaft power. Finally, a combination of these three parameters will be used to obtain a physically feasible geometry that could be developed into a

real machine. The shaft power predicted by *MSPM* is not comparable to experimentally measured shaft power because the mechanical model in this study is not set up to predict mechanical losses. However, it does include losses from flow friction and is therefore a better estimate of the output of a real engine than the indicated power P_{ind} .

5.2 Making a Scalable Model

5.2.1 Scaling of Volumes and Heat Exchanger Properties with Diameter

The model used for this scaling study needs to have a geometry that allows the volumes of all components to be scaled independently. This is difficult with the *Raphael* heat exchangers as they are located around the outside of the displacer piston cylinder, as seen in Figure 2.2, and therefore their diameter is tied to that of the cylinder. It is also desirable that the geometric parameters of the heat exchangers that affect heat transfer can be scaled proportionally with volume, so that the flow conditions and heat transfer coefficients will not be changed by scaling and thus, the heat exchanger geometry can be used irrespective of scale. This means that the flow cross section area and the surface area on both the gas and liquid/source sides should scale uniformly with volume, and the shape of the geometry should not be changed through scaling. The finned geometry of the *Raphael* heat exchangers does not allow this because when its diameter is increased and fin thickness and separation kept constant, more fins can be added to the gas side but not to the finless liquid side, and the gas surface area would scale disproportionately to liquid surface area. Also, the radial length of the fins would increase, and with it the average conduction distance from liquid to gas surface. This means that at larger scales this heat exchanger would suffer from increasing heat transfer resistance from conduction.

To enable proportional scaling, the scaling model uses the ‘Tube Bank Internal’ heat exchanger type instead. Figure 5.1 shows a view of this geometry normal to the direction of the gas flow. It represents a shell-and-tube heat exchanger which is also used in the ThermoHeart™ commercial LTDSE [57]. The working gas flows through parallel tubes while the source/sink liquid flows perpendicularly through the shell surrounding the tubes. Each tube occupies a certain amount of frontal area that depends on the arrangement and spacing of the tubes (see Figure 5.1), and the number of tubes can be scaled proportional to the frontal area of the heat exchanger. Cross section areas and surface areas on the gas and liquid side all scale with the number of tubes, which makes this heat exchanger type highly adaptable.

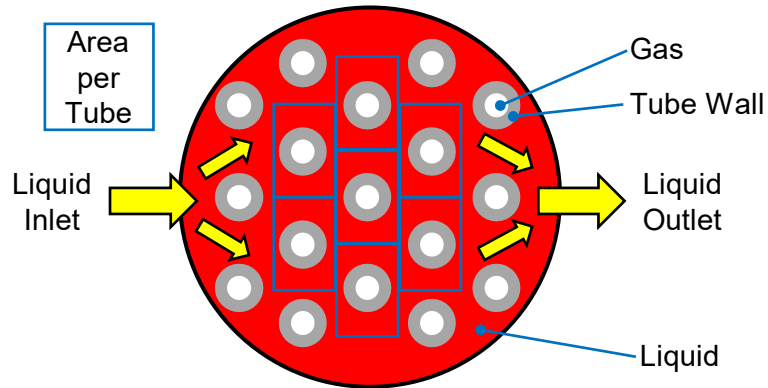


Figure 5.1: Illustration of tube bank heat exchanger, cross section perpendicular to gas flow direction. Tubes arranged in a rectangular grid with each tube taking a rectangular share of the cross section area.

The following equations show that when scaling the engine volume by scaling only the diameter of all components by a factor X and keeping the axial lengths unchanged, the volumes and heat exchanger parameters scale equally with X^2 . The spacing and diameter of the heat exchanger tubes stay constant. It is also shown that the heat exchanger Reynolds number and Nusselt number do not change with X and are dependent on mean pressure and speed. Thus, the heat transfer limit of this heat exchanger is expected to scale with the engine volume and should not inhibit the engine performance at larger scales.

For all diameters (except heat exchanger matrix):

$$D \propto X \quad (90)$$

Axial lengths:

$$L = \text{const.} \quad (91)$$

All volumes (except heat exchanger):

$$V = \frac{\pi}{4} D^2 L \propto X^2 \quad (92)$$

Heat exchangers:

$$D_i, D_o, A_{\text{perTube}} = \text{const.} \quad (93)$$

$$N_{\text{tubes}} = \frac{A_{\text{front}}}{A_{\text{perTube}}} \propto \frac{D^2}{A_{\text{perTube}}} \propto X^2 \quad (94)$$

$$A_{\text{cross,gas}} = N_{\text{tubes}} \frac{\pi}{4} D_i^2 \propto N_{\text{tubes}} \propto X^2 \quad (95)$$

$$A_{s,\text{gas}} = N_{\text{tubes}} \pi D_i L \propto N_{\text{tubes}} \propto X^2 \quad (96)$$

$$A_{s,\text{liquid}} = N_{\text{tubes}} \pi D_o L \propto N_{\text{tubes}} \propto X^2 \quad (97)$$

$$Re_{HX} = \frac{\rho_{\text{mean}} U_{HX,\text{mean}} D_i}{\mu_{\text{air}}} \propto \rho_{\text{mean}} U_{HX,\text{mean}} \propto p_{\text{mean}} f \quad (98)$$

Heat transfer (correlations used by *MSPM* [33]):

$$Nu_l = 6 = \text{const.} \quad (99)$$

$$Nu_t = 0.036 \left(\frac{L_{HX}}{D_i} \right)^{-0.055} Re_{HX}^{0.8} Pr_{\text{air}}^{0.33} \propto Re_{HX}^{0.8} \propto (p_{\text{mean}} f)^{0.8} \quad (100)$$

With:

$$\mu_{\text{air}}, Pr_{\text{air}} \approx \text{const. (for small changes in pressure and temperature)} \quad (101)$$

$$\rho_{mean} = \frac{p_{mean}}{R_{air}T_{mean}} \propto p_{mean} \text{ (Ideal gas)} \quad (102)$$

$$U_{HX,mean} = \frac{2 f V_{sw,d}}{A_{cross,gas}} \propto \frac{f X^2}{X^2} \propto f \quad (103)$$

where: X = diameter Scaling factor

D_i = tube inner diameter (m)

D_o = tube outer diameter (m)

$A_{perTube}$ = heat exchanger frontal area per tube (m²)

N_{tubes} = number of tubes in heat exchanger

A_{front} = heat exchanger total frontal area (m²)

$A_{cross,gas}$ = gas cross section area of heat exchanger (m²)

$A_{s,gas}$ = heat exchanger surface area, gas side (m²)

$A_{s,liquid}$ = heat exchanger surface area, liquid side (m²)

Re_{HX} = average heat exchanger Reynolds number, gas side

ρ_{mean} = average gas density (kg/m³)

$U_{HX,mean}$ = average heat exchanger flow velocity (m/s)

μ_{air} = air dynamic viscosity (Pa s)

p_{mean} = mean pressure (Pa)

f = mean engine speed (Hz)

Nu_l = laminar Nusselt number, tube bank heat exchanger

Nu_t = turbulent Nusselt number, tube bank heat exchanger

L_{HX} = heat exchanger axial length (m)

Pr_{air} = air Prandtl number

R_{air} = specific gas constant of air (J/kg K)

T_{mean} = mean gas temperature (K)

$V_{sw,d}$ = displacer swept volume (m³)

5.2.2 Model Geometry in MSPM

The scalable model with the tube bank heat exchangers is shown in Figure 5.2 as rendered by MSPM. The model was kept as similar as possible to the *Raphael* engine model (see Section 3.4) so this study can be roughly interpreted as a scaling-up of the *Raphael*.

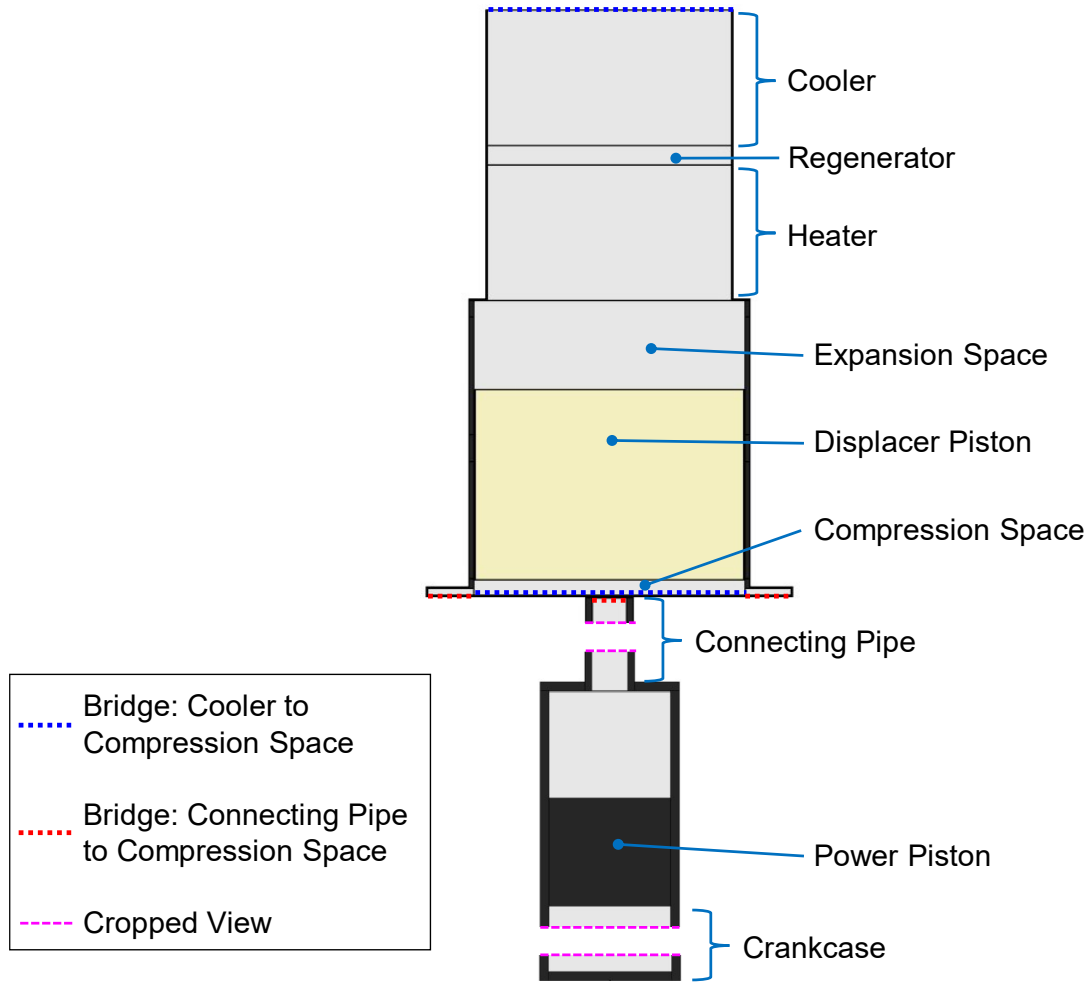


Figure 5.2: Model used for scaling study, as rendered in MSPM.

Both pistons, their stroke lengths and swept volumes are identical to the *Raphael*. The displacer piston seal is assumed to be ‘perfect’ without leak and friction, as had been done for model variants C and D in Chapter 4. The bottom section with the power piston and connecting pipe is unchanged. All solid bodies apart from the displacer piston are modeled as ‘Perfect Insulators’ as conduction will not be investigated. The heat exchangers, which are of the ‘Tube Bank Internal’ type, and regenerator were moved on top of the displacer cylinder so they can be scaled independently. The

top of the cooler cannot be physically connected to the compression space, this is solved by using a ‘Bridge’ component to form a face between the cooler top and the bottom of the compression space, connecting them virtually. The same is done with the connecting pipe, which is linked to the compression space via a ‘Bridge’ to a small annular volume that connects radially with the compression space. The two ‘Bridges’ are highlighted in Figure 5.2 in blue and red, respectively. For a real engine these connections would need to be solved differently, for example by placing the heat exchanger stack next to the displacer cylinder and adding ducts between them, or switching to an alpha layout with the heat exchangers between two pistons as done with the ThermoHeart™ engine [57].

5.2.3 Tube Bank Heat Exchangers: Sizing and Advantages

The axial length of the heat exchangers (L_{HX}) is close to that from the *Raphael*. The number of tubes (N_{tubes}) and tube diameters (D_i and D_o) were chosen so that the resulting heat exchanger has a gas cross section area ($A_{cross,gas}$) equal to that of the *Raphael*, gas surface area ($A_{surf,gas}$) close to the *Raphael*'s, and the tubes are standard sizes that could be obtained off the shelf. The heat exchanger outer diameter (D_{HX}) is not relevant for the modeling of the gas flow inside the tubes, but was chosen slightly larger than the minimum required to fit the tubes if they were arranged in the densest possible pattern, which is the hexagonal arrangement with a packing density of $\eta_{pack} = 90.7\%$ [116]. For a real engine, the heat exchanger would need to have a larger diameter or length to accommodate space for the liquid between the tubes while maintaining the same N_{tubes} . Finally, the regenerator axial length was defined to maintain the same regenerator volume as in the *Raphael*. The regenerator matrix is the same 96 % porosity, 0.1 mm polyester random fiber. The heat exchanger parameters are shown and compared to those of the *Raphael* engine heat exchangers in Table 5.1.

Table 5.1: Properties of heat exchangers and regenerator of the scaling model from this chapter and the *Raphael* engine.

| Parameter | Scaling Model (Tube Bank) | <i>Raphael</i> (Finned) |
|--|--|---|
| Material | 6061 Aluminum | |
| Number of tubes N_{tubes} | 1830 | - |
| Tube diameters D_i, D_o | 2 mm, 4 mm | - |
| Hydraulic diameter | 2 mm | 1.905 mm |
| Heat exchanger axial length L_{HX} | 100 mm | 96 mm |
| $A_{cross,gas}$ | 57.5 cm ² | |
| $A_{s,gas}$ | 11,498 cm ² | 11,180 cm ² |
| $A_{s,liquid}$ | 22,996 cm ² | 439 cm ² |
| Liquid heat transfer coefficients, analytical estimate (Section 5.2.4) | 304.1 W/m ² K (Heater) 776.7 W/m ² K (Cooler) | 79.3 W/m ² K (Heater) 383.2 W/m ² K (Cooler) |
| Avg. conduction distance (liquid to gas surface) | $\frac{D_o - D_i}{2} = 1$ mm | Wall thickness + half fin length \approx 13.5 mm |
| Heat exchanger gas volume | 0.575 L | 0.552 L |
| Heat exchanger and regenerator outer diameter D_{HX} | 180 mm | - |
| Regenerator axial length | 14.2 mm | 25.4 mm |
| Regenerator volume | 362.3 cm ³ | |
| Regenerator Material | Random polyester fibers, \varnothing 0.1 mm, Porosity 96 % | |
| Total working space volume (max) | 4.55 L | 4.62 L |

Comparing the heat transfer properties of these two equally sized heat exchangers reveals that in addition to its superior scalability, the tube bank geometry would likely outperform the finned geometry in terms of heat transfer rate. While nearly identical on the gas side, its liquid side surface

area is more than 50 times greater, liquid heat transfer coefficients are estimated 2 to 3 times higher, and the solid conduction distance through the tube wall is a fraction of the distance between source and gas in the finned heat exchanger. These advantages result from the tubular geometry which inherently has more outside than inside surface area and can be thin-walled because of its pressure-resistant shape. For these reasons Cool Energy Inc. equipped their ThermoHeart™ LTDSE with tube bank heat exchangers instead of plate-fin [57]. Additionally, the hydraulic diameter of the chosen tubes is nearly equal to that of the *Raphael*'s finned geometry, and the same Nusselt number correlations for internal flow apply to both. This means that the Reynolds number, friction factor, heat transfer coefficient and pressure drop on the gas side would be similar for both. Thus, the tube bank geometry would certainly be equal or better in heat transfer and pressure drop at any operating point or physical scale, and its parameters can be optimized independently from other components. For these reasons, a tube bank or similar heat exchanger type should be considered first for any Stirling engine using a liquid heat source and sink.

5.2.4 Liquid Heat Transfer Coefficients for Tube Bank Heat Exchanger

Similar to the source channel in the *Raphael* engine heat exchanger, the liquid domain surrounding the tubes is modeled by *MSPM* as an isothermal node with no convection heat transfer resistance between this node and the tube surface. To model the heat flow path more closely, the liquid convection heat transfer coefficients were estimated analytically as was done for the *Raphael* in Section 3.6.1. It was assumed that the same heat transfer fluids at the same temperatures and mass flow rates are used as with the *Raphael*. The fluid flows from an inlet on the outer wall of the heat exchanger to an outlet on the opposite side as seen in Figure 5.1. To simplify, it is assumed to flow along semicircular streamlines parallel to the outer wall, like in the *Raphael*'s annular heat exchanger. Therefore, the flow cross section area and flow velocity without regarding the tubes are:

$$\begin{aligned}
 A_{cross,liquid} &= D_{HX} L_{HX} \\
 U_{liquid} &= \frac{\dot{m}}{\rho A_{cross,liquid}}
 \end{aligned}
 \tag{104}$$

The following equations are derived from the description of flow across tube banks by Cengel [45]. Assuming that the tubes are arranged uniformly in all directions with a spacing S_T of 1.5 times their diameter, the highest velocity will occur between the tubes:

$$S_T = 1.5 D_o$$

$$U_{liquid,max} = \frac{S_T}{S_T - D_o} U_{liquid} = \frac{1.5}{0.5} U_{liquid} = 3 U_{liquid} \quad (105)$$

The Reynolds number for this flow is defined based on this velocity [45]:

$$Re = \frac{\rho U_{liquid,max} D_o}{\mu} = \frac{U_{liquid,max} D_o}{\nu} \quad (106)$$

Then, assuming the tube arrangement is comparable to a staggered tube bank, the Nusselt number for the relevant range of $0 \leq Re \leq 500$ is [45]:

$$Nu = 1.04 Re^{0.6} Pr^{0.36} \quad (107)$$

This assumes that the change in fluid properties due to temperature between the free stream and the tube surface is negligible, which is expected unless a heat transfer limit causes a substantial thermal gradient between the liquid and the solid. The Prandtl number of the fluid is [45]:

$$Pr = \frac{\mu c_p}{k} = \frac{\nu \rho c_p}{k} \quad (108)$$

Finally, the heat transfer coefficients are obtained from [45]:

$$h_{analytical} = \frac{Nu k}{D_o} \quad (109)$$

The fluid properties and results of these calculations for both the cooler and the heater are listed in Table 5.2. The resulting heat transfer coefficients were applied to the face between the source node and the tube wall node in the heat exchanger component of the model.

Table 5.2: Calculation of liquid heat transfer coefficients for tube bank heat exchangers.

| Parameter | Cooler (30 % Ethylene glycol – water) | Heater (Silicone oil <i>Sil 180</i>) |
|--|--|---|
| ρ (kg/m ³) | 1054 (0 °C) [107] | 932 (measured, 21.5 °C) |
| Viscosity | $\mu = 1.7 \text{ cP} = 0.0017 \text{ Pa s}$ (26.7 °C) [107] | $\nu = 2 \text{ cSt} = 2 \cdot 10^{-6} \text{ m}^2/\text{s}$ (200 °C) [111] |
| Pr | 13.24 | 34.11 |
| Specific Heat c_p (J/kg K) | 3770 (Section 2.4.3) | 1830 (Section 2.4.3, 150 °C) |
| k (W/m K) | 0.484 [112] | 0.1 [111] |
| \dot{m} (kg/s) (Section 2.4.2) | 0.0236 | 0.0546 (150 °C) |
| $A_{cross,liquid}$ (m ²) | 0.018 | |
| U_{liquid} (m/s) | 0.00124 | 0.00325 |
| $U_{liquid,max}$ (m/s) | 0.00373 | 0.00976 |
| Re | 9.3 | 19.5 |
| Nu | 6.4 | 12.2 |
| $h_{analytical}$ (W/m ² K) | 776.7 | 304.1 |

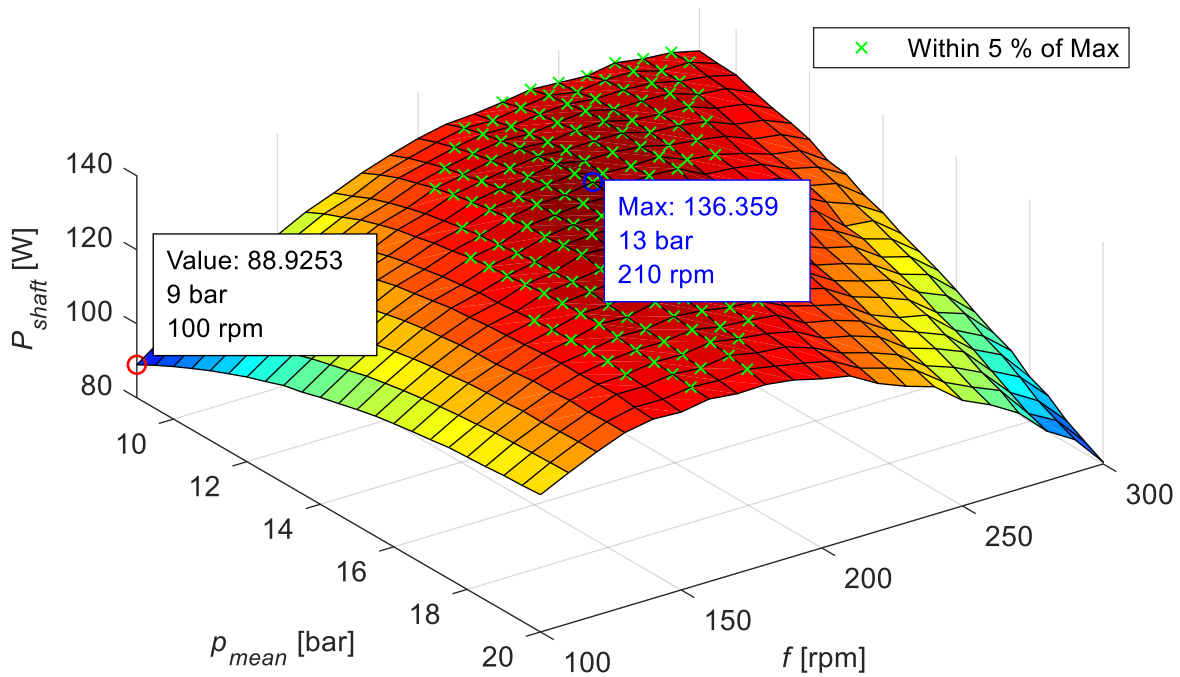
5.3 Scaling Study

To find a ‘baseline’ operating point, the pressure and speed that would produce maximum shaft power were determined for the model described in the previous section. Then, the model was scaled up in volume while maintaining this operating point. Since the flow properties and geometry scale with the volume as described in Section 5.2.1, the optimal operating pressure and speed are expected to remain constant independent of the scale. Note that p_{mean} refers to absolute pressure in this section. The source and sink temperature were equal to those of the *Raphael* engine, at $T_{source} = 150\text{ °C}$ and $T_{sink} = 5\text{ °C}$.

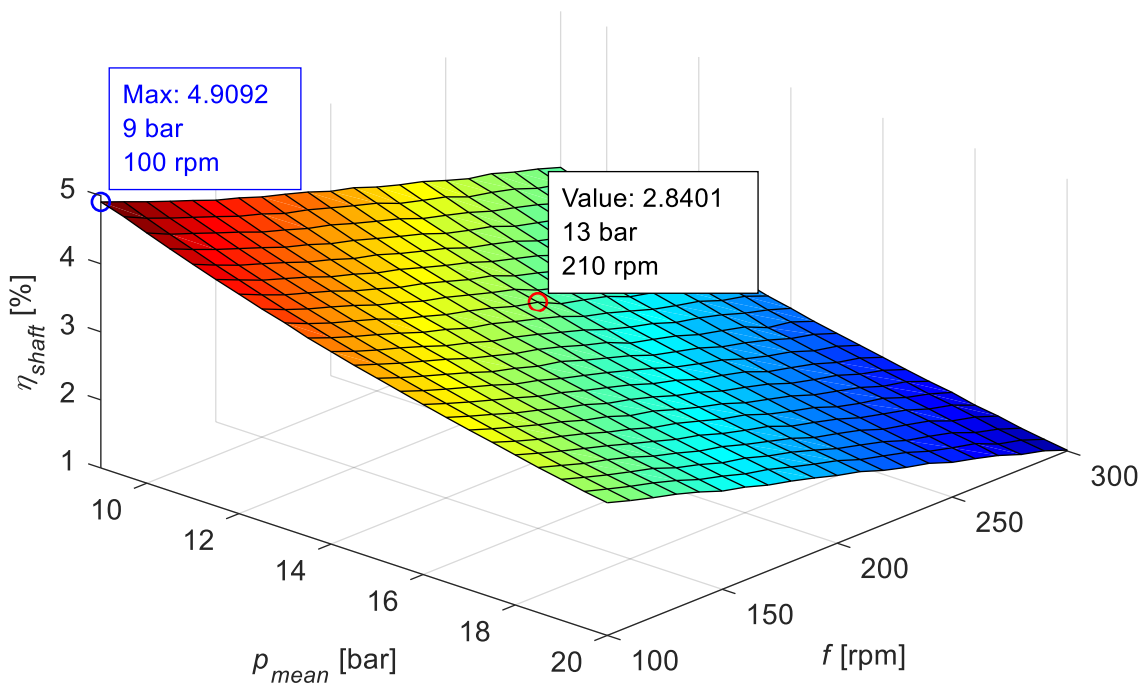
5.3.1 Optimizing Pressure and Speed

The model was run over a wide, coarse grid of p_{mean} and f to locate the shaft power maximum and then the intervals between 9 bar and 20 bar, and 100 rpm to 300 rpm, respectively, which are centred on the maximum, were mapped in steps of 0.5 bar and 10 rpm, respectively. Figure 5.3 shows the resulting maps of power (a) and efficiency (b). The maximum P_{shaft} of 126 W was predicted at 13 bar and 210 rpm, which is a much higher pressure than the operating range of the real *Raphael* engine (~ 6 bar). This indicates the increased heat transfer performance of the tube bank heat exchangers. The optimal speed is not increased compared to the *Raphael* and is in line with the optimum predicted by model variants B and D in Figure 4.32. Thus, according to *MSPM*, pressure is preferred over speed as a means to scale up power. The power maximum is not a sharp peak, there is a broad operating range (marked by green cross) that includes speeds of 150 and 290 rpm and almost the entire range of pressures tested in which P_{shaft} is within 5 % of the maximum.

Thermal efficiency was predicted to be nearly inversely proportional to both pressure and speed. This is expected since the flow friction loss and most other losses in the system increase with the speed of the process and/or the Reynolds number, which in turn scales with pressure and speed (see equation (98)). At the point of maximum shaft power, the efficiency is 2.84 %.



(a)



(b)

Figure 5.3: Shaft power (a) and shaft (thermal) efficiency (b) of the scaling model with tube bank heat exchangers at varying pressure (absolute) and speed. Values at maximum power and efficiency annotated. Area of power within 5 % of maximum is highlighted by green crosses.

5.3.2 Results of Scaling Up

The model was then scaled up in volume as described in Section 5.2.1, up to 100 times the volume of the *Raphael* engine, meaning that all diameters were scaled by up to $X = 10$. At each scale the model was tested at the maximum shaft power conditions of 13 bar and 210 rpm. The resulting shaft power is plotted over the scaling factor in Figure 5.4, where (a) shows the scale up to 10 and (b) shows the full scale up to 100. Power is predicted to scale nearly perfectly linearly with volume, which is sensible as the diameters of the flow geometry and the size of the heat exchangers were scaled proportionally. A volume scaled by about 7.2 is needed to reach a theoretical shaft power of 1 kW, and by about 70 to reach 10 kW.

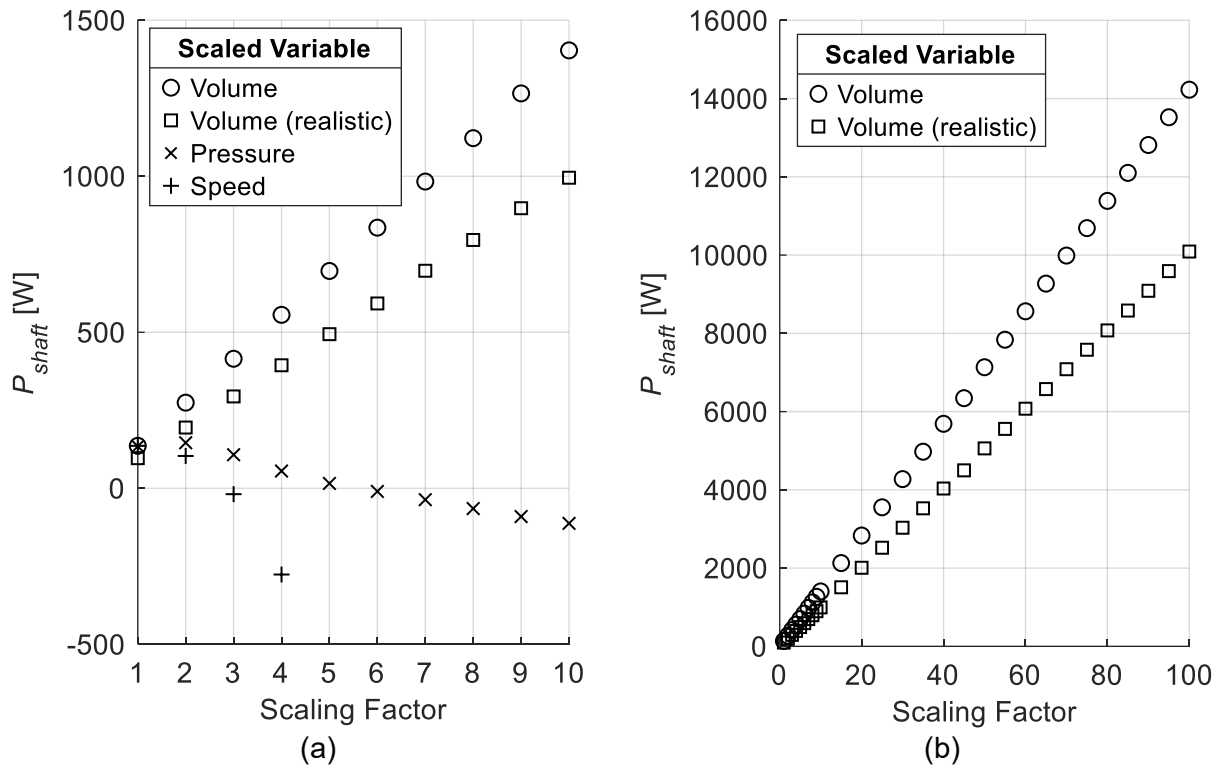


Figure 5.4: Shaft power predicted by scaling up engine volume, mean pressure or speed while scaling number of heat exchanger tubes equally. (a) Factor up to 10, (b) Factor up to 100 (volume only). 'Realistic' values assume that model predictions are 41 % higher than the actual shaft power would be. Starting from $V = 4.55$ L, $p_{mean} = 13$ bar, $f = 210$ rpm (max shaft power).

In a similar way, pressure and speed were also independently scaled by up to 100 while leaving volumes constant, but scaling the number of heat exchanger tubes by the same factor. It can be seen from equations (98), (102) and (103) that Re_{HX} remains constant in this case, so that P_{shaft}

may be expected to scale with pressure and speed like it did with volume. However, Figure 5.4 (a) shows that this was not the case as power decreased through scaling. With a pressure increased by factor 6 or greater, or speed by 3 or greater, the engine became ineffective as power turned negative. The cause for this was most likely that flow cross sections were not scaled, so flow friction increased, and that the scaling of the heat exchanger tubes added substantial amounts of dead volume which reduced the pressure swing and made the engine ineffective. This issue shows that the flow geometry of an engine always must be adapted when one parameter is changed or scaled. An engine can be scaled to higher power by utilizing higher pressure and/or speed instead of only more volume, but this requires optimizing all heat exchanger properties, like in this case tube dimensions, number, and length, and all other flow geometry, such as the size of ducting, at the same time. This would go beyond the scope of this chapter, which is a simplified scale-up study in which a physical layout and proportions close to the *Raphael* engine are maintained.

5.3.3 Estimating Realistic Power and Required Scale

The values from the previous section for shaft power of a scaled engine are model predictions that are most likely higher than what a real engine could achieve due to losses not modeled. The comparison between experimental and model shaft power for the *Raphael* in Section 4.8 can be used as a basis to estimate realistic values. In that section, it was estimated that *MSPM* overpredicted shaft power at its maximum by about 41 %. Assuming that this deviation between predicted and actual shaft power can also be applied to the model scaled in this chapter, one gets an estimate of the realistic power that can be expected at different volume scales, which is also shown in Figure 5.4. Following this estimate, the engine volume would need to be scaled by a factor of 10 to achieve 1 kW of power and by 100 to reach 10 kW. This corresponds to volumes of 45.5 L and 455 L, respectively.

5.3.4 Performance with Different Working Gases

The working gas used in the *Raphael* engine and this study is air, but different gases could be used to improve the power output and efficiency. Pure nitrogen, helium, and hydrogen have been used in the Stirling literature. Advantages can be expected from helium and hydrogen because of their high thermal conductivity compared to air (helium: 5.7 times, hydrogen: 7 times, at 1 atm

and 25 °C [117]) which improves heat transfer at equal flow conditions, and their higher individual gas constants (helium: 7 times, hydrogen: 14 times [118]) which means that an equal temperature change causes a greater pressure change following the ideal gas law. Organ’s [109] theoretical analysis of heat transfer and pressure drop suggests that if operating conditions are fixed, the fluid with the highest gas constant is preferable.

To investigate *MSPM*’s predictions of the effects of a working gas change, the same model that produced Figure 5.4 was run at the optimized conditions for air ($p_{mean} = 13$ bar, $f = 210$ rpm), and the volume was scaled by 1 to 100 with nitrogen, helium, and hydrogen. Figure 5.5 shows the resulting curves of shaft power, with (a) displaying the scale up to 10 in detail. Pure nitrogen brought a slight improvement of 4 % over air, and hydrogen led to an increase by 33 %, but helium was predicted to more than double the engine’s shaft power (230 %). The thermal efficiency achieved with helium was also predicted as multiple times that of the other gases at 7.3 % (hydrogen 3.16 %, nitrogen 3.04 %, air 2.9 %). Helium being superior to the other gases goes against Organ’s analysis [109] and the general expectation.

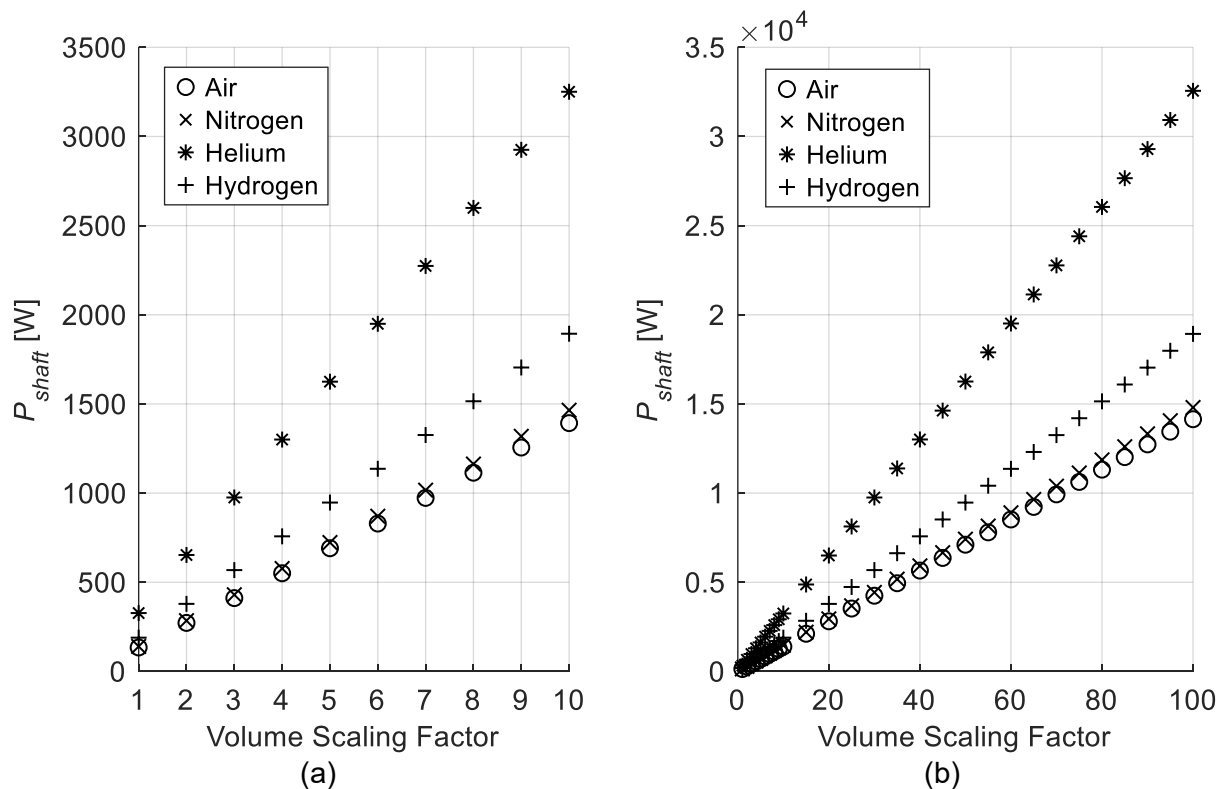


Figure 5.5: Shaft power predicted by scaling up engine volume and number of heat exchanger tubes, with different working fluids. (a) Factor up to 10, (b) Factor up to 100.

Organ [109] estimated in a simplified analysis that if an engine is operated with hydrogen and with air, an identical gas process cycle with equal Reynolds numbers is achieved with both fluids if the air-charged engine runs at 14 % of the speed or at 14 % of the pressure of the hydrogen-charged engine. Therefore, the optimal operating point with hydrogen should be expected at a much higher pressure and/or speed than the optimum with air. Thus, to investigate if *MSPM*'s fluid model may be erroneous and was producing the unexpected results, the same model was run again with air, hydrogen, and helium, this time keeping the engine volume constant and increasing either speed or pressure by up to 10 times from the optimum for air ($p_{mean} = 13$ bar, $f = 210$ rpm). With helium the shaft power was much higher than with air or hydrogen and reached a maximum when speed or pressure was increased by about 5 times. With hydrogen the shaft power was poor, and in the case of increasing speed the power was lower than with air. This went clearly against expected trends. Additionally, as the pressure was increased above 120 bar the power of the air-charged engine suddenly began to increase strongly after having continuously decreased before. At that pressure the error incurred by the ideal gas assumption may be around 6 % [108] and become noticeable, but this could not cause such a trend which seems unphysical. These observations should be verified with different engine models. They indicate that *MSPM* in its current form may not produce reliable results with any other fluid than air.

The volumes required to reach 1 kW and 10 kW with all fluids are summarised in Table 5.3. The 'realistic' estimate accounts for overprediction of shaft power in the way described in Section 5.3.3. As discussed above, the model predictions for helium and hydrogen are most likely incorrect, which is indicated by the (*) markers.

Table 5.3: Engine volumes predicted by *MSPM* to reach shaft power goals with different working fluids. 'Realistic' estimate assumes model overpredicts shaft power by 41 %. Unrealistic predictions with helium and hydrogen indicated by (*).

| | Air | Helium (*) | Hydrogen (*) |
|---------------------------------|------------|------------|--------------|
| $P_{shaft} = 1$ kW (model) | 32.8 L | 14.1 L | 24.6 L |
| $P_{shaft} = 1$ kW (realistic) | 45.5 L | 20.5 L | 34.1 L |
| $P_{shaft} = 10$ kW (model) | 318.5 L | 141.1 L | 245.7 L |
| $P_{shaft} = 10$ kW (realistic) | 455 L | 200.2 L | 341.3 L |

5.3.5 Conclusion of Scaling Study

It must be kept in mind that the results from the preceding Sections are only for an engine with the proportions of the *Raphael*, with tube bank heat exchangers, operating at $T_{source} = 150$ °C, $T_{sink} = 5$ °C, $p_{set} = 13$ bar (absolute) and $f = 210$ rpm. The displacer piston seal was modeled as leak-free and the source/sink liquid heat transfer coefficients were estimated analytically, which makes this model comparable to variant C from the validation in Chapter 4. Many variables such as the engine layout, heat exchanger and regenerator properties and length, piston strokes versus diameter, could be modified to yield different engine designs with comparable power output, possibly with smaller volume. This could be achieved by using the gradient descent optimizer in *MSPM*. After some testing, it was found that the optimizer requires more work on its algorithms before it can produce reliable results. As concluded from Chapter 4, the absolute numbers of indicated work and power predicted by *MSPM* cannot be deemed reliable at this stage, but it should be valuable for comparative analysis of design options and optimization.

5.4 Comparison to ThermoHeart™ Commercial LTDSE

The ThermoHeart™ [20], as discussed in Section 1.4.4, is, to the author's knowledge, the only commercially available Stirling engine for recovery of low temperature heat (150 to 400 °C) at large scale (25 kW). Since *MSPM* is meant to predict the performance of machines for a similar range of temperatures and power, validating the model against real data from this engine will give valuable insight into the model's reliability for its intended purpose.

5.4.1 *MSPM* Model of ThermoHeart™ Engine

As the engine is a proprietary design, few details about the dimensions, volume sizes and heat exchanger properties have been made available. Published experimental data that can be compared to models is also scarce, consisting of electrical power output, heater and cooler heat flow rates, and thermal efficiency at T_{source} between 150 and 400 °C, and fixed $T_{sink} = 20$ °C, $p_{mean} = 580$ psi and $f = 550$ rpm [20]. Therefore, published images and dimensions (overall height and diameter) [20], [57] were used to measure the dimensions of the working spaces and heat exchangers to obtain a model that should roughly represent the thermodynamic unit of the ThermoHeart™ engine. The resulting estimates are listed in Table 5.4, they are for one of the engine's four identical alpha-type thermal units. A significant uncertainty is associated with all dimensions, for instance, different estimates of the piston diameter varied by up to 96 %. The intention of this study is to verify if *MSPM*'s predictions will be on a comparable order of magnitude.

Table 5.4: Properties of ThermoHeart™ engine as published in or estimated from [20], [57].

| | | | |
|------------------------|-----------------------------|---------------------------------|---|
| Heat Exchangers | Type | Tube bank (Gas in tubes) | known |
| | Material | 6061 Aluminum | guess |
| | Outer diameter | 305 mm | |
| | Length (each) | 96.5 mm | |
| | Tube outer diameter (OD) | 1.5875 mm (1/16 inch) | |
| | Tube internal diameter (ID) | 1.3208 mm (0.052 inch) | |
| | Number of tubes (each) | 8100 | known |
| | Tube Spacing | 2 × tube OD | |
| Regenerator | Type | Stainless steel woven screen | known |
| | Length | 57.5 mm | |
| | Outer diameter | 305 mm | |
| | Porosity β | 60 % | Section 5.4.2 |
| | Wire diameter $D_{W,Reg}$ | 0.2 mm | Section 5.4.2 |
| Pistons | Diameter | 127 mm | |
| | Stroke | 190.5 mm | |
| | Phase angle | 20° | Calculated from Volume change. Compression piston leads. |
| Gas Volumes | Gas | Nitrogen | known |
| | Heat Exchangers (each) | 1.071 L | |
| | Regenerator | 2.519 L | |
| | Piston swept volume | 2.413 L | |

| | | | |
|--------------------|--------------------|---------|--|
| Gas Volumes | Volume change | 0.833 L | Estimated in proportion to <i>Raphael</i> engine |
| | Dead volume | 1.714 L | |
| | Total volume (max) | 9.621 L | |

The heat exchangers are tube banks with the gas flowing through the tubes, just like in the model used for scaling in Section 5.3. From a published photo the tube OD was estimated to be 1/16 inch, a commonly available size, and it was found that 0.052 inches is an available ID for thin-walled tubes of this OD. The tubes appear to be arranged in a hexagonal pattern with a spacing of two diameters. The cross-sectional area taken by the tubes in this arrangement fills the available cross-sectional area of the heat exchanger diameter almost exactly (within 4 %), which indicates that the estimated parameters are compatible geometrically. The tube material was presumed to be Aluminum, but it has little effect on heat transfer since the conduction distance is very short in thin-walled tubes. No liquid heat transfer coefficient was used in this model, so the outside surface of the tubes is assumed to be at the source or sink temperature, and the flow rates of the heat transfer liquids is irrelevant.

As an alpha-type, this engine does not have a dedicated power piston, but the compression and expansion are achieved through a phase difference between the two identical pistons. Since there is no information about the phase angle of ThermoHeart™, the volume change was estimated as 10 % of the heat exchanger, regenerator, and swept volume, which is the same ratio as the *Raphael*'s, so that the ThermoHeart™ model has a similar compression ratio as the *Raphael*. The phase angle was calculated to produce this volume change. Figure 5.6 shows the model in *MSPM*. There are clearances between the pistons and the heat exchangers which contribute dead volume, as shown in Figure 5.6. The buffer spaces behind both pistons are connected by a Bridge component to simulate the real engine's buffer space, which is a large pressure vessel that ensures the buffer pressure is nearly constant. All materials except for the heat exchangers and regenerator are modeled as 'perfect insulator', therefore heat conduction is not modeled.

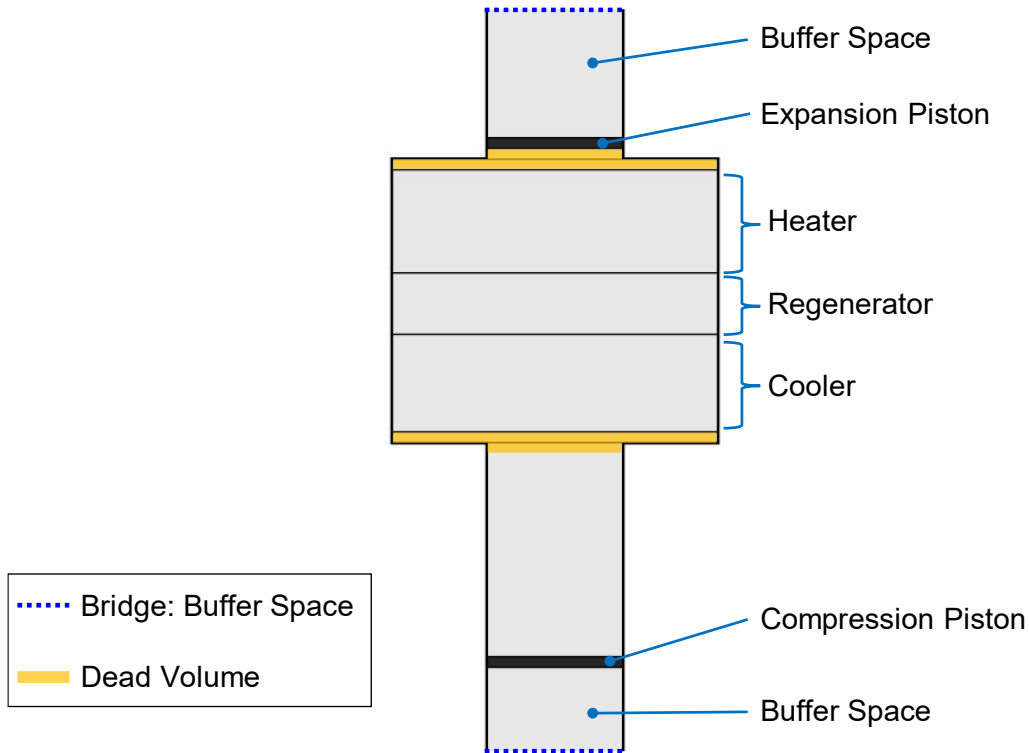


Figure 5.6: Model of ThermoHeart™ engine as rendered in *MSPM*. Expansion piston at minimum volume and compression piston at maximum volume.

5.4.2 Estimating Regenerator Properties

The regenerator porosity β and wire diameter $D_{W,Reg}$ could not be found or estimated from the published information. However, these parameters affect engine performance substantially, so the model was tested with varying β and $D_{W,Reg}$ to find a combination that yields the closest shaft power and efficiency compared to the published data. Porosity was tested between 50 and 95 %, and wire diameter between 0.03 and 0.5 mm, based on values of the *Raphael* regenerator and the woven screen regenerators that were experimentally tested for the correlations used by *MSPM* which are found in [66]. Figure 5.7 shows the resulting predictions of shaft power and efficiency for source temperatures of 150 °C (a,b) and 400 °C (c,d). Only the region of $60 \% \leq \beta \leq 85 \%$ and $0.1 \text{ mm} \leq D_{W,Reg} \leq 0.3 \text{ mm}$ which produced viable results is shown.

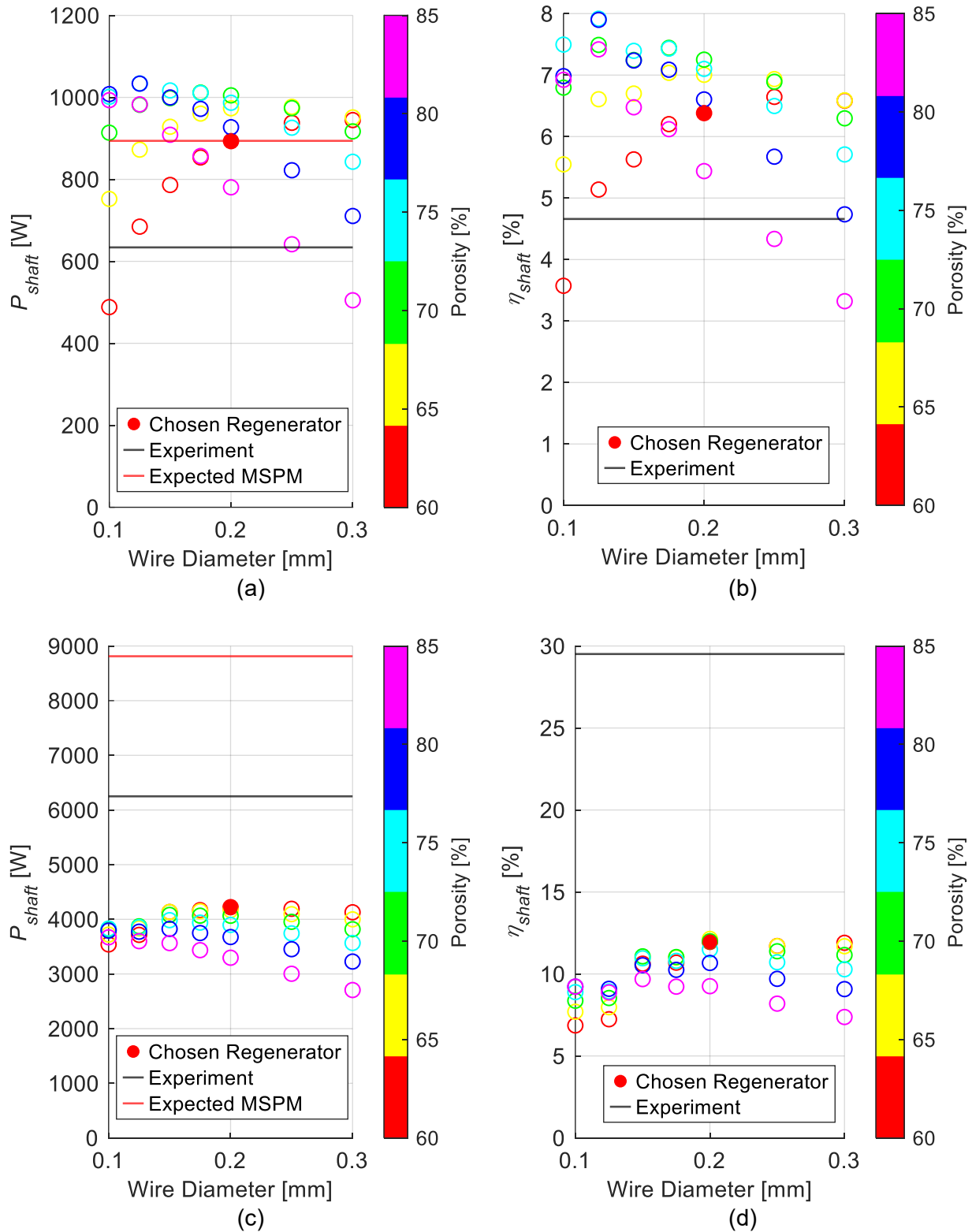


Figure 5.7: Shaft power (a,c) and thermal efficiency (b,d) predicted by *MSPM* model with $T_{source} = 150^\circ\text{C}$ (a,b) and $T_{source} = 400^\circ\text{C}$ (c,d), with varying regenerator wire diameter (x-axis) and porosity (colour). Black horizontal lines are experimental data [20], red lines in (a,c) are shaft power predictions expected from *MSPM* assuming 41 % overprediction.

This data was compared to experimental values [20] (black lines) and the shaft power *MSPM* would be expected to predict following the assumption from Section 5.3.3 that it overpredicts by 41 % (red lines). At low source temperature (a,b) the model returned values close to those expected, but at high temperature (c,d) the same model predicted shaft power and efficiency about 50 % too low compared to the experimental data. No configuration was found that performed better at 400 °C. Thus, the regenerator with the least deviation from the experiment with $\beta = 60\%$ and $D_{W,Reg} = 0.2\text{ mm}$ was chosen for the following section.

5.4.3 Validation at Varying Source Temperature

The model of one thermal unit of the ThermoHeart™ engine, as described in the previous sections, was run at T_{source} of 150 °C to 400 °C and compared against the published datapoints [20] in terms of shaft power, efficiency, and heat input rate. Since liquid side heat transfer was not modeled, the datapoint with the maximum oil flow rate was used for each temperature. The resulting comparison is plotted in Figure 5.8. Figure 5.8 (a) shows that the shaft power predicted by *MSPM* matches the experimental data closely at 150 °C but underestimates increasingly at higher temperatures. As the sink temperature is constant at 20 °C, the temperature ratio is proportional to T_{source} . Thus, both experiment and model show the shaft power to increase nearly linearly with the temperature ratio, but the model predicts about a 50 % lower rate of increase. The predicted efficiency in Figure 5.8 (b) is also accurate at low temperature, but increases at a much slower rate than with the real engine and appears to reach a maximum around 350 to 400 °C, whereas the experimental data show no maximum in the given temperature range. This is due to the heat input rate, Figure 5.8 (c), which is overestimated by *MSPM* increasing with temperature, from about 38 % at 150 °C to about 148 % at 400 °C.

The model takes in significantly more heat but delivers less power, which indicates that the modeled regenerator is most likely recovering less heat than the real one. The model heat exchangers may also cause more flow friction losses than in the real machine and thereby reduce power, but they are not inferior in heat transfer capacity as Figure 5.8 (d) shows. These deviations are probably caused by the high degree of uncertainty in almost all of the model's dimensions and properties, and a sensitivity study on each of these parameters would go beyond the scope of this work. It should be noted that engine speed was assumed to be constant at all temperatures, but

there is a possibility that the actual speed varied because the published data [20] is not clear. However, *MSPM* predicted the performance of ThermoHeart™ within the correct order of magnitude and displayed excellent accuracy at 150 °C source temperature. It also proved capable of optimizing regenerator properties and, correctly predicted that engine performance is much more sensitive to regenerator properties at low temperature (Figure 5.7 a,b) than at high temperature (Figure 5.7 c,d), which is an important trend for LTDSEs. These findings indicate that the model can relatively confidently predict trends in bulk parameters like power and efficiency for LTDSEs with simple geometries.

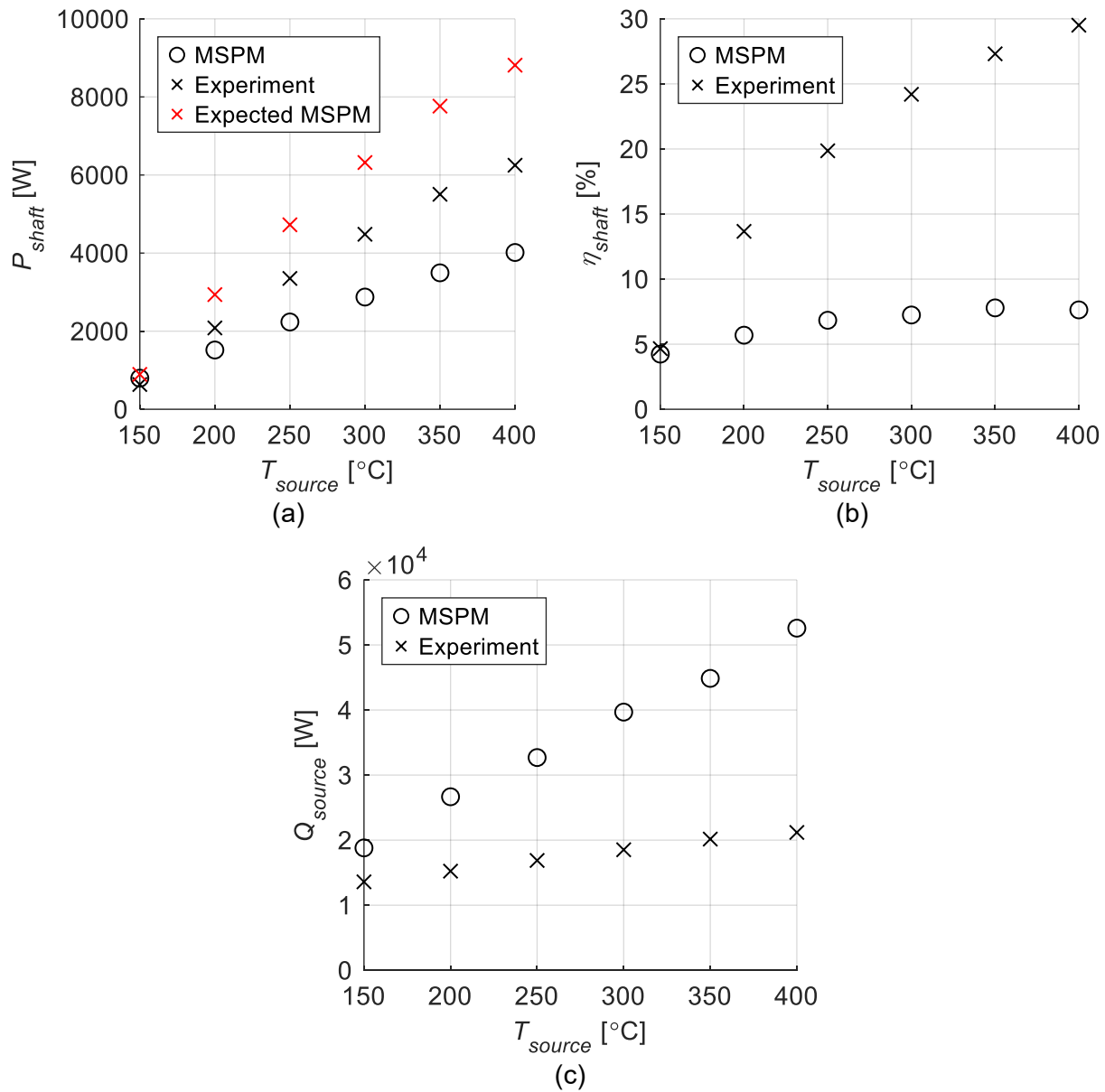


Figure 5.8: Shaft power (a), thermal efficiency (b), and heat input rate (c) predicted by *MSPM* model compared to experimental data [20] over source temperature.

The power output per total volume of the modeled ThermoHeart™ engine at $T_{source} = 150$ °C is about 93 W/L while that of the scaled-up *Raphael* model is three times lower at 31 W/L (see Figure 5.4). This confirms the conclusion of Section 5.3.5 that the volume predicted to reach a certain shaft power can be reduced drastically by optimizing the engine geometry and components, especially the regenerator and heat exchanger properties.

5.5 Chapter Conclusion

The *MSPM* model was used to make predictions of the volume size that would be required for an LTDSE to produce 1 kW or 10 kW of shaft power from temperatures $T_{source} = 150$ °C and $T_{sink} = 5$ °C. The engine model used was based on the *Raphael* model from Chapter 4 and shared its proportions, but a tube bank heat exchanger replaced the finned annular heat exchanger. This enabled the proportional scaling of all gas volumes, flow cross sections, and heat exchanger and regenerator surface area. Liquid heat transfer coefficients were analytically estimated for the tube outer surfaces analogously to what was done for the *Raphael* in Section 3.6.1.

The maximum shaft power of this model was found at a charge pressure of 13 bar and a speed of 210 rpm. At this operating point the model was scaled up in volume by a factor of up to 100. Shaft power increased linearly with volume as expected, and the resulting estimates of volume to reach a power of 1 kW and 10 kW were 45.5 liters and 455 liters, respectively. This includes the assumption from Section 4.8 that *MSPM* overpredicts shaft power by 41 %. Keeping in mind the conclusions from the validation of *MSPM* in the preceding chapter, the results should be taken only as order-of-magnitude estimates. Scaling pressure or speed, instead of volume, along with the heat exchangers was found to be ineffective because if the size of other flow geometry like the regenerator and ducts is not scaled accordingly, power is limited and reduced drastically by flow friction losses.

Changing the model working fluid to helium or hydrogen led to unexpected results, with the model predicting helium to outperform the other gases substantially and hydrogen to produce little more shaft power than air. *MSPM* does not appear to make reliable predictions with other gases than air, or at pressures above 120 bar. The cause for this needs to be investigated. For this it would be favorable to have experimental data with different working fluids to compare the model results against.

Next, *MSPM* was validated against the ThermoHeart™ [20], a commercial 25 kW LTDSE, which was modeled from rough estimates of its dimensions from published images. For lack of information, the regenerator parameters were optimized in *MSPM* to minimize the deviation from published experimental data. The model predicted shaft power on the order of the experimental data, which is a positive result considering the significant potential deviations between the

estimated and true parameters of the ThermoHeart™ engine. At 150 °C source temperature the model predicted the shaft power and efficiency accurately, and the heat input rate relatively well. However, at higher source temperatures up to 400 °C the model underestimated thermal efficiency substantially, indicating a much lower regenerator performance in the model. To verify *MSPM*'s predictions of regenerator performance, it should be experimentally validated against an engine with well-known geometry, such as *Raphael* (Chapter 2), using different regenerators. A well optimized regenerator will be crucial for any LTDSE design to achieve a usable power scale without requiring a substantially inflated engine volume.

To sum up, this chapter showed that *MSPM* is able to scale and optimize various parameters and delivered promising results modeling a real large-scale LTDSE. It can be used with relative confidence to explore varying Stirling engine geometries and scales. However, all properties relevant to heat transfer and flow friction, including the complete heat flow path between source and gas, must be defined with little uncertainty to yield meaningful results. Also, it should only be used with air and at moderate pressures, as its predictions outside of this range need to be investigated. More input of experimental data, particularly with varying heat exchanger and regenerator geometries, is necessary to address the overall reliability of *MSPM*.

Chapter 6. Conclusions and Future Work

Research gaps exist in the development of large-scale low temperature difference Stirling engines (LTDSEs) for power generation from low temperature heat, which is an untapped sustainable energy source. Few LTDSEs have been used in real applications, and no model is accessible to research that has been validated to predict the performance of LTDSEs. The work documented in this thesis aimed to advance the knowledge and tools in this research area by experimentally validating an existing numerical model. In the following sections, the contributions towards the thesis objectives will be summarized and discussed.

6.1 Review of Thesis Goals

6.1.1 Acquire detailed experimental data with a lab scale LTDSE

In Chapter 2, an experimental setup was described that uses a lab-scale gamma LTDSE, called *Raphael*, with source and sink temperatures of 150 °C and 5 °C, liquid-to-gas heat exchangers, a working space volume of 4.6 liters, and a maximum shaft power of about 15 W. The control system allowed automated control of source and sink temperatures, engine pressure, and shaft torque. In experiments the engine was operated at pressures between 200 kPa and 450 kPa (gauge), and speeds between 111 rpm and 238 rpm. The data acquisitions system recorded temperatures of the working gas and the heat source/sink liquids, average and instantaneous pressures, the crankshaft angular position and the shaft torque for samples of 10 seconds. To gather data at operating conditions close to steady state, the engine's behaviour after start-up was observed for up to 7 hours, and wait times of 1 hour after start-up and 10 minutes after torque setpoint changes were found sufficient.

In Chapter 4, an uncertainty analysis found that the accuracy of most data from this setup was sufficient for validating a model, but some variables had significant uncertainties. The pressure sensors were not accurate enough to measure the heat exchanger pressure drop, which prevented the validation of flow friction effects predicted by the model. The heat exchanger heat flow rates were affected by uncertainties mainly from liquid temperature measurements and insufficient information about the hot heat transfer liquid. The uncertainty in indicated work was also higher

than desired, but did not significantly affect the model validation. These limitations should be addressed for future experiments.

The measured shaft power of *Raphael* occurred at its minimum speed, and its peak efficiency at 2.2 % was much lower than that of a known commercial LTDSE at equal temperatures. This indicated that the engine was severely limited by heat transfer and flow friction, since any increase in speed appeared to cause flow losses that negated any gain in indicated power.

6.1.2 Validating the *MSPM* model

In Chapter 3, a model of the *Raphael* engine was created using the numerical code *MSPM*, a 3rd order model for Stirling and similar machines that aims to predict the losses of low temperature engines. The model was limited to the thermodynamic cycle, as the losses of the mechanism were not considered at this stage of the validation. The model also simplified the engine structure to be axisymmetric, though the actual engine layout is not symmetrical. The power piston seal was modeled as perfect (leak-free and frictionless), and the displacer piston seal was modeled in two variants, perfect and non-existent. A custom heat transfer coefficient was implemented to the model to simulate the heat transfer resistance from convection between the heat source/sink liquids and the heat exchanger walls. Two estimates for the heat transfer coefficient values were made by analytical correlations and CFD analysis, leading to two model variants. Combining the different displacer piston seals and heat transfer coefficients, four model variants were tested in the validation.

Chapter 4 showed the validation of the thermodynamic model of *MSPM* at steady state, using as metrics primarily the indicator diagram shape and indicated work, the source and sink heat flow rates, and average gas temperatures. The four model variants of the *Raphael* engine were tested on 89 experimental datapoints in which the estimated average heat exchanger Reynolds number ranged between 400 and 1500. For each metric the relative deviation between model results and experimental data was analyzed. The model deviation in indicated work was found to be close to linear when plotted over the average heat exchanger Reynolds number. The model predictions varied significantly between the four variants. The variants assuming higher heat transfer coefficients (from CFD) predicted indicated work relatively well. Out of these two, the variant with a non-existent displacer seal had deviations below 20 % but they were not consistent across

the datapoints. On the other hand, the variant with the perfect displacer seal made more consistent predictions, but with an error of 50 to 70 %. This variant also made accurate and consistent predictions of the heat flow rates (within 20 %) and gas temperatures (within 3 % or 10 °C). The variants with lower (analytical) heat transfer coefficients strongly underestimated the indicated work and similarly the heat flow rates and temperature differences achieved. Thus, the CFD analysis was able to estimate the heat transfer coefficients of the liquid source and sink much more accurately than analytical correlations.

Overall, it was concluded that *MSPM* can potentially predict the performance of the given LTDSE to an accuracy that would allow to optimize the engine, but the model is highly sensitive to and dependent on certain inputs. Trends in model deviation were analyzed and a comprehensive sensitivity analysis on input parameters, the numerical mesh, and the extent of heat conduction modeling was conducted. It was found that the source and sink heat transfer coefficients and the leak characteristics of both piston seals were the crucial parameters for the model's accuracy. The model had been tested in different variants because these same parameters were difficult to determine experimentally and had to be estimated. The observed model deviations suggested that the 'true' heat transfer coefficients are close to those estimated with CFD, and the 'true' leak rates of the power piston and displacer piston seals are somewhere between the 'perfect' and 'non-existent' seal assumptions and would need to be measured or estimated to make the model reliable.

6.1.3 Investigate upscaling LTDSEs and model a large LTDSE using *MSPM*

The goal of Chapter 5 was to test the capabilities of the *MSPM* model for larger LTDSE development. An LTDSE model was scaled up from lab scale to a potential commercial scale, with 1 to 10 kW of shaft power from temperatures of 150 °C and 5 °C. All volumes and cross section areas of the model were equal to the *Raphael* engine used in the previous chapters. Shell-and-tube heat exchangers were used in this model, which made it possible to scale all gas volumes, flow cross sections, and the heat exchanger and regenerator surface areas proportionally by scaling the diameter of the engine. The shaft power maximum of the model was found at a pressure of 13 bar and a speed of 210 rpm. This was much higher than the optimum pressure and speed of *Raphael*, which indicated a superior performance of the shell-and-tube heat exchangers compared to the finned channels of *Raphael*.

When the engine volume was scaled at the optimum pressure and speed, power output increased linearly with volume. Volumes of 45.5 L and 455 L were predicted to produce the desired 1 kW and 10 kW of power, respectively. This estimate includes the assumption that the model overpredicts shaft power by 41 %, from the observations in Chapter 4. While this scaling study demonstrated the use of the *MSPM* model at larger scales, it produced an engine that would be suboptimal in practice due to its large physical size. By optimizing all components, especially the regenerator which played little role in this study, more compact designs with equal power output could be achieved.

To assess *MSPM*'s capability of modeling a real large-scale LTDSE, it was validated against the ThermoHeart™ [20] engine, where it showed reasonable shaft power predictions at 150 °C source temperature and a strong sensitivity to the regenerator properties. At higher source temperatures the model underestimated thermal efficiency significantly, likely related to the regenerator performance. This demonstrated that the regenerator plays a crucial role even at low temperatures, and that *MSPM*'s modeling of different regenerators should be validated experimentally.

For the design of large LTDSEs these studies found some recommendations. Firstly, the design of the heat exchangers to minimize convection and conduction resistances is critical. By maximizing heat transfer and minimizing flow friction through the choice of heat exchanger type and optimization, higher pressures and speeds can be achieved which in turn reduce the physical size needed for a certain power output. Secondly, while the regenerator may be expendable in lab-scale LTDSEs, it will be an essential component for any real application that must be optimized to achieve a sufficient efficiency to make an engine economical.

6.1.4 Assess capabilities of *MSPM* Model

The validation in Chapter 4 found that overall, *MSPM* has promising potential to model LTDSE performance reliably because while the observed deviations from experimental data were significant, they can likely be attributed to sensitive model inputs that are challenging to define, namely the source heat transfer coefficients and seal leakage. With additional effort to estimate these inputs and tune them in the model to align its predictions with experiments, it is believed that the model agreement could be improved to a reliable level. Since the model cannot predict all

physical processes, for example the leakage and friction caused by a certain seal, experiments and simulations outside of *MSPM*, such as CFD, may be necessary to define the input parameters. The modeling of seal leakage in *MSPM*, either by the *Leak* component or physical gaps between pistons and bore, has not been studied in detail in this work. It was found that the displacer piston seal strongly affected the modeled engine performance, and that it could not be represented by a ‘perfect’ seal or a ‘non-existent’ seal. It must be noted that this assessment is based on a single engine geometry with a limited variety of flow conditions tested, and should be backed up by more experimental validation with different heat exchangers, regenerators etc.

Chapter 3 discussed potential weaknesses of the model, and suggested that the use of steady heat transfer and flow friction correlations in a system with oscillating flow and the neglect of imperfect heat transfer at the heat source/sink may cause notable model deviations. A custom heat transfer coefficient was implemented to allow modeling of all heat transfer resistances, and used successfully in Chapter 4 and Chapter 5, which is an important extension of *MSPM*'s capabilities. Functionality for visual mesh analysis was added which aids primarily the implementation of new heat exchanger types, along with other improvements and corrections, which are described in Appendix D. An area not covered by this work is the mechanical model of *MSPM*. The model has not yet been tested to model mechanical friction. The mechanism implementations in the code require additional work before the mechanical model and transient cases can be validated.

Chapter 5 demonstrated the abilities of *MSPM* to scale up an engine by volumetric size, to show performance differences between types of heat exchangers, and to show the strong influence of the regenerator in an LTDSE and optimize its properties, and to reasonably predict the performance of a large LTDSE based on a rudimentary model. However, this analysis had limitations. Scaling by volume did not investigate variations in any other parameters and the engine geometry, so it was based on a limited scope of geometries and flow conditions and the findings may not hold for modeling different machines. The lack of detailed specifications of the large LTDSE meant that the model accuracy could not be assessed conclusively in this study. Altogether, experimental data with more variation in terms of heat exchangers and regenerator is needed, along with founded knowledge of source heat transfer coefficients and seal leakage as found in Chapter 4, to conduct a validation with more detailed outcomes and to build a reliable model.

It was also found that *MSPM* produced questionable results with other gases than air and at high pressures above 120 bar. This severely limits the scope of the model in its current state.

6.2 Future Work

Based on the findings and limitations of this thesis work, opportunities for experimental research and further validation and development of the *MSPM* model are proposed.

6.2.1 Experimental Work and Validating *MSPM*

A general suggestion for future experiments is to reduce the experimental uncertainty. The accuracy of indicated work measurements can be easily improved by recording datapoints over a longer time so that more engine cycles are recorded and can be averaged. The uncertainty in heat flow rates would be improved by reducing the liquid flow rates to allow a greater temperature drop between inlet and outlet, and by determining the specific heat of the heating oil or ideally replacing the oil altogether with a fluid for which properties are documented.

Work to further validate *MSPM* is listed in order of descending importance or significance.

- Measurement and validation of the pressure drop. As discussed in Section 4.5.3, a single-sensor differential pressure measurement should be done. It could be measured in unsteady flow on the engine, but will be more reliable in a steady-flow experiment. This work is currently in progress. Alternatively, flow friction losses could be measured by powering the engine externally, as done by Speer [31] and Michaud [41].
- Modeling and validation of seal leakage. Seal leak rates could be estimated, but measuring them as a function of pressure would be the only reliable method to validate. West [34] stated that a static measurement of leak rates might underestimate dynamic leak rate found in oscillating pressure conditions. In *MSPM*, a ‘Leak’ component or varying seal gaps could be used.
- Validate with varying regenerator properties. This could be done without modifying the given experimental setup.
- Expand validation to data collected with different length scales, engine layouts, working gases, heat exchanger geometries and flow conditions. The experiments in this work were limited to laminar flow in the heat exchangers.

- Mechanical model should be validated once code implementation is complete. Mechanical losses could be measured in isolation by (powering the engine externally, as done by Speer [31] and Michaud [41]).
- With working mechanical model, simulate transient behaviour from engine start-up to steady state (Section 2.6).
- Experimentally measure solid temperatures on heat exchanger surfaces, which can serve as a metric to directly validate the heat transfer modeling.
- Model other applications that are not engines, such as Stirling coolers and heat pumps.

6.2.2 Expanding the *MSPM* Model

Numerical work with high significance to develop *MSPM* could be:

- Review implementation of working gases and validate predictions especially with helium and hydrogen and at high pressures.
- Review and validate steady state assumption and empirical correlations used by *MSPM*. This could entail implementing more complex treatment of oscillating flow, primarily in the laminar regime, using appropriate correlations, Valensi number (see Sage [66]), surface-based Nusselt number (which could also address developing flow).
- Review implementation of mechanisms with friction to validate mechanical model. See Appendix D.2 for information about code.
- Implement output of forces acting on moving bodies and mechanism components. Not required for evaluating thermodynamic model, but will be useful when testing mechanism model and necessary when designing mechanism.
- Eventually, implement support for free-piston machines to aid development of future LTDSE for real-world application. This would entail modeling dynamics, and multiple mechanisms with differing angles and speeds as stated by Middleton [33].
- Implement other types of heat exchangers (e.g. intercooler), and heat sources (e.g. solar radioisotope, hot gas).
- Accelerate the model code. Currently it uses only a single CPU thread, but has been run in parallel by running multiple MATLAB instances. Parallelizing the code itself

could enable solving several cases simultaneously. To start, code should be timed to analyse potential for time savings by modifying operations.

Additional improvements and studies could be:

- Develop a convergence criterium based on indicated work, not shaft power, which would be more suitable when evaluating the thermodynamic model.
- Vary the numerical time step and observe effects.
- Add uniform mesh refinement option for mesh convergence study.
- Add input of speed as function of crank angle (vector or function). This would enable running the model at a predefined cyclic-steady speed, and testing the effect of speed variations.

References

- [1] L. Clarke *et al.*, “Energy Systems,” in *Climate Change 2022: Mitigation of Climate Change. Contribution of Working Group III to the Sixth Assessment Report of the Intergovernmental Panel on Climate Change*, P.R. Shukla, J. Skea, R. Slade, A. Al Khourdajie, R. van Diemen, D. McCollum, M. Pathak, S. Some, P. Vyas, R. Fradera, M. Belkacemi, A. Hasija, G. Lisboa, and S. LuzJ. Malley, Eds. Cambridge: Cambridge University Press, 2022. doi: 10.1017/9781009157926.008.
- [2] World Meteorological Organization (WMO), “2022 State of Climate Services: Energy (WMO-No. 1301),” 2022. Accessed: Nov. 12, 2022. [Online]. Available: https://library.wmo.int/doc_num.php?explnum_id=11340
- [3] Canada Energy Regulator, “Canada’s Energy Future 2021: Energy Supply and Demand Projections to 2050,” 20[129]22. Accessed: Nov. 12, 2022. [Online]. Available: <https://www.cer-rec.gc.ca/en/data-analysis/canada-energy-future/2021/canada-energy-futures-2021.pdf>
- [4] Canada Energy Regulator, “Canada’s Energy Future Data Appendices,” *Government of Canada*, 2021. <https://doi.org/10.35002/zjr8-8x75> (accessed Nov. 12, 2022).
- [5] J. D. Hughes, “Canada’s Energy Outlook: Current realities and implications for a carbon constrained future,” 2018. Accessed: Nov. 12, 2022. [Online]. Available: https://energyoutlook.ca/wp-content/uploads/2018/05/cmp_canadas-energy-outlook-2018_full.pdf
- [6] J. Banks and N. B. Harris, “Geothermal potential of Foreland Basins: A case study from the Western Canadian Sedimentary Basin,” *Geothermics*, vol. 76, 2018, doi: 10.1016/j.geothermics.2018.06.004.
- [7] CMC Research Institutes, “Community Integrated Energy Mapping Feasibility Study In Alberta’s Industrial Heartland And Strathcona Industrial Area,” Nov. 2014. Accessed: Aug. 12, 2021. [Online]. Available: <https://www.nrcan.gc.ca/science-and-data/funding-partnerships/funding-opportunities/current-investments/community-integrated-energy-mapping-feasibility-study-gateway-albertas-energy-demand/16067>

- [8] I. Oma, "Potential of Stirling Engine and Organic Rankine Cycle for Energy Recovery in Ship Machinery Systems," Norwegian University of Science and Technology, 2015. Accessed: Jan. 30, 2022. [Online]. Available: <http://hdl.handle.net/11250/2494126>
- [9] N. Tauveron, S. Colasson, and J. A. Gruss, "Available systems for the conversion of waste heat to electricity," in *ASME International Mechanical Engineering Congress and Exposition, Proceedings (IMECE)*, 2014, vol. 6A. doi: 10.1115/IMECE2014-37984.
- [10] R. Stirling, "Improvements for diminishing the consumption of fuel and in particular an engine capable of being applied to the moving (of) machinery on a principle entirely new.," 4081, 1816
- [11] R. Bauer, "The Stirling Engine: The 'Cyclical Life' of an Old Technology," *Icon*, vol. 15, pp. 108–118, 2009, [Online]. Available: <http://www.jstor.org/stable/23787099>
- [12] U. R. Singh and A. Kumar, "Review on solar Stirling engine: Development and performance," *Thermal Science and Engineering Progress*, vol. 8, pp. 244–256, Dec. 2018, doi: 10.1016/J.TSEP.2018.08.016.
- [13] N. Boutammachte and J. Knorr, "Field-test of a solar low delta-T Stirling engine," *Solar Energy*, vol. 86, no. 6, pp. 1849–1856, Jun. 2012, doi: 10.1016/J.SOLENER.2012.03.001.
- [14] B. Kongtragool and S. Wongwises, "A review of solar-powered Stirling engines and low temperature differential Stirling engines," *Renewable and Sustainable Energy Reviews*, vol. 7, no. 2, pp. 131–154, Apr. 2003, doi: 10.1016/S1364-0321(02)00053-9.
- [15] T. Schneider, D. Müller, and J. Karl, "A review of thermochemical biomass conversion combined with Stirling engines for the small-scale cogeneration of heat and power," *Renewable and Sustainable Energy Reviews*, vol. 134, p. 110288, Dec. 2020, doi: 10.1016/J.RSER.2020.110288.
- [16] M. Takeuchi, S. Suzuki, and Y. Abe, "Development of a low-temperature-difference indirect-heating kinematic Stirling engine," *Energy*, vol. 229, p. 120577, Aug. 2021, doi: 10.1016/J.ENERGY.2021.120577.

- [17] Z. Jiang *et al.*, “A Stirling generator with multiple bypass expansion for variable-temperature waste heat recovery,” *Appl Energy*, vol. 329, p. 120242, Jan. 2023, doi: 10.1016/J.APENERGY.2022.120242.
- [18] F. Catapano, C. Perozziello, and B. M. Vaglieco, “Heat transfer of a Stirling engine for waste heat recovery application from internal combustion engines,” *Appl Therm Eng*, vol. 198, p. 117492, Nov. 2021, doi: 10.1016/j.applthermaleng.2021.117492.
- [19] K. Laazaar and N. Boutammachte, “Development of a new technique of waste heat recovery in cement plants based on Stirling engine technology,” *Appl Therm Eng*, vol. 210, p. 118316, Jun. 2022, doi: 10.1016/J.APPLTHERMALENG.2022.118316.
- [20] Cool Energy Inc., “ThermoHeart™ 25 kW High Performance Stirling Engine,” 2019. <https://coolenergy.com/wp-content/uploads/2019/09/Cool-Energy-ThermoHeart-25kW-Engine-Overview-20190930.pdf> (accessed Oct. 16, 2022).
- [21] I. Kolin, S. Koscak-kolin, and M. Golub, “Geothermal Electricity Production By Means Of the Low Temperature Difference Stirling Engine,” *World Geothermal Congress 2000*, 2000, Accessed: Nov. 12, 2022. [Online]. Available: <http://www.geothermal-energy.org/pdf/IGAstandard/WGC/2000/R0856.PDF>
- [22] Swedish Stirling AB, “Technical specifications and facts about the PWR BLOK 400-F (generation 3) unit,” 2022. <https://swedishstirling.com/en/technology/technical-specifications/> (accessed Oct. 19, 2022).
- [23] T. Li, D. Tang, Z. Li, J. Du, T. Zhou, and Y. Jia, “Development and test of a Stirling engine driven by waste gases for the micro-CHP system,” *Appl Therm Eng*, vol. 33–34, no. 1, pp. 119–123, Feb. 2012, doi: 10.1016/J.APPLTHERMALENG.2011.09.020.
- [24] I. Szczygieł, W. Stanek, and J. Szargut, “Application of the Stirling engine driven with cryogenic exergy of LNG (liquefied natural gas) for the production of electricity,” *Energy*, vol. 105, 2016, doi: 10.1016/j.energy.2015.08.112.
- [25] S. Zhu, G. Yu, K. Liang, W. Dai, and E. Luo, “A review of Stirling-engine-based combined heat and power technology,” *Appl Energy*, vol. 294, Jul. 2021, doi: 10.1016/j.apenergy.2021.116965.

- [26] S. M. Oriti and S. Wilson, “Dynamic power convertor development for radioisotope power systems at NASA glenn research center,” in *Propulsion and Energy Forum*, 2018. Accessed: Nov. 12, 2022. [Online]. Available: <https://ntrs.nasa.gov/citations/20180007790>
- [27] J. G. Schreiber and L. G. Thieme, “Final results for the GRC supporting technology development project for the 110-watt Stirling Radioisotope Generator (SRG110),” in *Space Technology and Applications International Forum (STAIF-2007)*, 2007, vol. 880. Accessed: Nov. 12, 2022. [Online]. Available: <https://ntrs.nasa.gov/citations/20070023440>
- [28] I. Kolin, *Stirling Motor: History, Theory, Practice*. Dubrovnik: Zagreb University Publications, 1991.
- [29] J. R. Senft, *Ringbom Stirling Engines*. Oxford University Press, 1993.
- [30] C. J. A. Stumpf, “Parameter Optimization of a Low Temperature Difference Gamma-Type Stirling Engine to Maximize Shaft Power,” University of Alberta, 2019. doi: <https://doi.org/10.7939/r3-jb09-7t31>.
- [31] C. P. Speer, “Modifications to Reduce the Minimum Thermal Source Temperature of the ST05G-CNC Stirling Engine,” University of Alberta, 2018. doi: <https://doi.org/10.7939/R3930P94X>.
- [32] K. Wang, S. R. Sanders, S. Dubey, F. H. Choo, and F. Duan, “Stirling cycle engines for recovering low and moderate temperature heat: A review,” *Renewable and Sustainable Energy Reviews*, vol. 62, pp. 89–108, Sep. 2016, doi: 10.1016/J.RSER.2016.04.031.
- [33] S. M. W. Middleton, “A Modular Numerical Model for Stirling Engines and Single-Phase Thermodynamic Machines,” University of Alberta, 2021. doi: <https://doi.org/10.7939/r3-x8qd-p159>.
- [34] C. D. West, *Principles and applications of Stirling engines*. New York: Van Nostrand Reinhold, 1986.
- [35] C. M. Hargreaves, *The Philips Stirling Engine*. Amsterdam: Elsevier Science Publishers B.V., 1991.
- [36] G. Walker, *Stirling-cycle Machines*. Clarendon Press, 1973.

- [37] A. de Vos, "Efficiency of some heat engines at maximum-power conditions," *Am J Phys*, vol. 53, no. 6, 1985, doi: 10.1119/1.14240.
- [38] J. R. Senft, *Mechanical efficiency of heat engines*. Cambridge: Cambridge University Press, 2007. doi: 10.1017/CBO9780511546105.
- [39] W. R. Martini, "Stirling Engine Design Manual (Second Edition)," 1983. Accessed: Nov. 01, 2022. [Online]. Available: <https://ntrs.nasa.gov/citations/19830022057>
- [40] I. Urieli and D. Berchowitz, *Stirling Cycle Engine Analysis*. Bristol: Adam Hilger, 1984.
- [41] J. P. Michaud, "Low Temperature Difference Alpha-Type Stirling Engine for the Experimental Determination of Optimal Parameters to Maximize Shaft Power," University of Alberta, 2020. doi: <https://doi.org/10.7939/r3-m3jj-1646>.
- [42] M. E. Nicol-Seto, "Investigation of a Drive Mechanism Modification to Increase Thermodynamic Power of a Low Temperature Differential Gamma Type Stirling Engine," University of Alberta, 2021. doi: <https://doi.org/10.7939/r3-ex8v-ze72>.
- [43] D. A. Miller, "Experimental Investigation of Stirling Engine Modelling Techniques at Reduced Source Temperatures," University of Alberta, 2019. doi: <https://doi.org/10.7939/r3-jvb2-y408>.
- [44] J. L. Weisbach, *Lehrbuch der Ingenieur- und Maschinen-Mechanik*. Braunschweig: Vieweg und Sohn, 1845. Accessed: Jan. 30, 2022. [Online]. Available: <https://catalog.hathitrust.org/Record/008888915>
- [45] Y. A. Cengel and A. J. Ghajar, *Heat and Mass Transfer, Fundamentals & Application, Fifth Edition in SI Units*, vol. 5th, no. 3. 2015.
- [46] B. Hoegel, "Thermodynamics-based design of stirling engines for low-temperature heat sources," University of Canterbury, 2014. Accessed: Nov. 14, 2022. [Online]. Available: <http://dx.doi.org/10.26021/2499>
- [47] L. Hasanovich, "Effect of Heat Exchanger Volume and Geometry on Power Output of a Low Temperature Difference Stirling Engine," University of Alberta, 2022. Accessed: Nov. 13, 2022. [Online]. Available: <https://doi.org/10.7939/r3-d6nn-sj02>

- [48] L. C. Spencer, “A comprehensive review of small solar-powered heat engines: Part III. Research since 1950—‘unconventional’ engines up to 100 kW,” *Solar Energy*, vol. 43, no. 4, pp. 211–225, Jan. 1989, doi: 10.1016/0038-092X(89)90021-2.
- [49] A. der Minassians, “Stirling engines for low-temperature solar-thermal-electric power generation,” University of California, Berkeley, 2007. Accessed: Nov. 18, 2022. [Online]. Available: <https://www2.eecs.berkeley.edu/Pubs/TechRpts/2007/EECS-2007-172.html>
- [50] M. M. He, “Stirling Engine for Solar Thermal Electric Generation,” University of California, Berkeley, 2016. Accessed: Nov. 18, 2022. [Online]. Available: <https://www2.eecs.berkeley.edu/Pubs/TechRpts/2018/EECS-2018-15.html>
- [51] C. C. Lloyd, “A Low Temperature Differential Stirling Engine for Power Generation,” University of Canterbury, 2009. Accessed: Nov. 17, 2022. [Online]. Available: <http://dx.doi.org/10.26021/2929>
- [52] K. Hirata, “Stirling Engines of Saitama University.” <http://www.bekkoame.ne.jp/~khirata/academic/kiriki/home.html> (accessed Nov. 18, 2022).
- [53] S. IWAMOTO, K. HIRATA, and F. TODA, “Performance of Stirling Engines,” *JSME International Journal Series B Fluids and Thermal Engineering*, vol. 44, no. 1, pp. 140–147, 2001, doi: 10.1299/jsmeb.44.140.
- [54] S. Iwamoto, F. Toda, K. Hirata, M. Takeuchi, and T. Yamamoto, “Comparison of low-and high-temperature differential Stirling engines,” in *8th international Stirling engine conference*, 1997.
- [55] F. Toda and M. Matsubara, “Development of 1kW Low-Temperature Difference Stirling Engine,” in *ISEC International Stirling Engine Conference*, 2018.
- [56] K. Hirata, “The one way piston ring.” <http://www.bekkoame.ne.jp/~khirata/academic/kiriki/ring/index.html> (accessed Nov. 18, 2022).
- [57] L. Smith, B. Nuel, S. P. Weaver, S. Berkower, S. C. Weaver, and B. Gross, “25 kW Low-Temperature Stirling Engine for Heat Recovery, Solar, and Biomass Applications,” in

- 17th International Stirling Engine Conference (ISEC)*, 2016. Accessed: Oct. 16, 2022. [Online]. Available: https://www.ohio.edu/mechanical/stirling/ISEC_papers/ISEC2016-CoolEnergy.pdf
- [58] Cool Energy Inc., “Cool Energy 40 kW ThermoHeart® C Engine Specifications,” 2019. <https://coolenergy.com/wp-content/uploads/2019/09/ThermoHeart-C-40-kW-Engine-Spec-Sheet-20190930.pdf> (accessed Nov. 17, 2022).
- [59] G. R. Dochat, “Stirling space power demonstrator engine test/analytical comparison,” *Acta Astronaut*, vol. 15, no. 6–7, pp. 341–346, Jun. 1987, doi: 10.1016/0094-5765(87)90169-X.
- [60] G. Schmidt, “Theorie der geschlossenen Lehmann’schen Maschine,” *Zeitschrift des Vereines Deutscher Ingenieure*, vol. 15, no. 1, 1871.
- [61] N. C. J. Chen and F. P. Griffin, “A Review of Stirling-engine mathematical models,” 1983. doi: <https://doi.org/10.2172/5948203>.
- [62] B. Kongtragool and S. Wongwises, “Investigation on power output of the gamma-configuration low temperature differential Stirling engines,” *Renew Energy*, vol. 30, no. 3, pp. 465–476, Mar. 2005, doi: 10.1016/j.renene.2004.06.003.
- [63] F. Ahmed, H. Huang, S. Ahmed, and X. Wang, “A comprehensive review on modeling and performance optimization of Stirling engine,” *Int J Energy Res*, vol. 44, no. 8, 2020, doi: 10.1002/er.5214.
- [64] I. Urieli, “Stirling Cycle Machine Analysis.” <https://www.ohio.edu/mechanical/stirling/index.html> (accessed Feb. 10, 2022).
- [65] T. Finkelstein, “Computer Analysis of Stirling Engines,” in *Proceedings of the 10th IECEC*, 1975.
- [66] D. Gedeon, “*Sage User’s Guide. Sage v12 Edition*,” 2021. <http://www.Sageofathens.com/Documents/SageStlxHyperlinked.pdf> (accessed Feb. 10, 2022).

- [67] D. R. Gedeon, "The optimization of Stirling cycle machines," in *Intersociety Energy Conversion Engineering Conference*, 1978.
- [68] E. Rogdakis, G. Antonakos, and I. P. Koronaki, "Influence of a Regenerator on Stirling Engine Performance," *Journal of Energy Engineering*, vol. 142, no. 2, 2016, doi: 10.1061/(asce)ey.1943-7897.0000338.
- [69] H. D. Kuehl, *Generalized thermodynamic description of regenerative gas cycles. Verallgemeinerte thermodynamische Beschreibung regenerativer Gaskreisprozesse*. Duesseldorf (Germany): VDI-Verlag, 1990.
- [70] J. Sauer and H.-D. Kuehl, "Numerical model for Stirling cycle machines including a differential simulation of the appendix gap," *Appl Therm Eng*, vol. 111, pp. 819–833, Jan. 2017, doi: 10.1016/j.applthermaleng.2016.09.176.
- [71] G. Xiao *et al.*, "An approach to combine the second-order and third-order analysis methods for optimization of a Stirling engine," *Energy Convers Manag*, vol. 165, pp. 447–458, Jun. 2018, doi: 10.1016/J.ENCONMAN.2018.03.082.
- [72] R. Shoureshi, "Analysis and design of Stirling engines for waste-heat recovery," Massachusetts Institute of Technology, 1981. Accessed: Nov. 12, 2022. [Online]. Available: <http://hdl.handle.net/1721.1/64834>
- [73] H. Yousefzadeh and A. R. Tavakolpour-Saleh, "A novel unified dynamic-thermodynamic method for estimating damping and predicting performance of kinematic Stirling engines," *Energy*, vol. 224, Jun. 2021, doi: 10.1016/J.ENERGY.2021.120222.
- [74] K. Kraitong, "Numerical modelling and design optimisation of Stirling engines for power production," University of Northumbria at Newcastle (United Kingdom), 2012. Accessed: Nov. 16, 2022. [Online]. Available: <https://www.proquest.com/docview/1221968115>
- [75] H.-S. Yang, C.-H. Cheng, and S.-T. Huang, "A complete model for dynamic simulation of a 1-kW class beta-type Stirling engine with rhombic-drive mechanism," *Energy*, vol. 161, pp. 892–906, Oct. 2018, doi: 10.1016/j.energy.2018.07.159.

- [76] M. Hooshang, R. Askari Moghadam, and S. AlizadehNia, “Dynamic response simulation and experiment for gamma-type Stirling engine,” *Renew Energy*, vol. 86, pp. 192–205, Feb. 2016, doi: 10.1016/J.RENENE.2015.08.018.
- [77] W.-L. Chen, “A study on the effects of geometric parameters in a low-temperature-differential γ -type Stirling engine using CFD,” *Int J Heat Mass Transf*, vol. 107, pp. 1002–1013, Apr. 2017, doi: 10.1016/j.ijheatmasstransfer.2016.11.007.
- [78] W.-L. Chen, Y.-C. Yang, and J. L. Salazar, “A CFD parametric study on the performance of a low-temperature-differential γ -type Stirling engine,” *Energy Convers Manag*, vol. 106, pp. 635–643, Dec. 2015, doi: 10.1016/j.enconman.2015.10.007.
- [79] K. Mahkamov, “An Axisymmetric Computational Fluid Dynamics Approach to the Analysis of the Working Process of a Solar Stirling Engine,” *J Sol Energy Eng*, vol. 128, no. 1, pp. 45–53, Feb. 2005, doi: 10.1115/1.2148979.
- [80] E. Rogdakis, P. Bitsikas, G. Dogkas, and G. Antonakos, “Three-dimensional CFD study of a β -type Stirling Engine,” *Thermal Science and Engineering Progress*, vol. 11, pp. 302–316, Jun. 2019, doi: 10.1016/J.TSEP.2019.04.012.
- [81] L. Kuban, J. Stempka, and A. Tyliczszak, “A 3D-CFD study of a γ -type Stirling engine,” *Energy*, vol. 169, pp. 142–159, Feb. 2019, doi: 10.1016/J.ENERGY.2018.12.009.
- [82] D. García, M. J. Suárez, E. Blanco, and J. I. Prieto, “Experimental correlations and CFD model of a non-tubular heater for a Stirling solar engine micro-cogeneration unit,” *Appl Therm Eng*, vol. 153, pp. 715–725, May 2019, doi: 10.1016/J.APPLTHERMALENG.2019.03.013.
- [83] P. Bitsikas, E. Rogdakis, and G. Dogkas, “CFD study of heat transfer in Stirling engine regenerator,” *Thermal Science and Engineering Progress*, vol. 17, p. 100492, Jun. 2020, doi: 10.1016/j.tsep.2020.100492.
- [84] ve//ingenieure GmbH and Internet Archive, “The ST05G Stirling Engine Project (archived 2017).” https://web.archive.org/web/20171030195800/http://www.ve-ingenieure.de/projekt_st05g_cnc_engl.html (accessed Apr. 06, 2022).

- [85] J. Bert, D. Chrenko, T. Sophy, L. le Moynes, and F. Sirot, "Simulation, experimental validation and kinematic optimization of a Stirling engine using air and helium," *Energy*, vol. 78, pp. 701–712, Dec. 2014, doi: 10.1016/J.ENERGY.2014.10.061.
- [86] M. Hooshang, R. Askari Moghadam, S. Alizadeh Nia, and M. T. Masouleh, "Optimization of Stirling engine design parameters using neural networks," *Renew Energy*, vol. 74, pp. 855–866, Feb. 2015, doi: 10.1016/J.RENENE.2014.09.012.
- [87] S. Alfarawi, R. Al-Dadah, and S. Mahmoud, "Enhanced thermodynamic modelling of a gamma-type Stirling engine," *Appl Therm Eng*, vol. 106, pp. 1380–1390, Aug. 2016, doi: 10.1016/J.APPLTHERMALENG.2016.06.145.
- [88] S. Alfarawi, R. AL-Dadah, and S. Mahmoud, "Influence of phase angle and dead volume on gamma-type Stirling engine power using CFD simulation," *Energy Convers Manag*, vol. 124, pp. 130–140, Sep. 2016, doi: 10.1016/J.ENCONMAN.2016.07.016.
- [89] C. Speer, "Personal Conversation," 2021.
- [90] General Plastics Manufacturing Company, "LAST-A-FOAM® FR-4700 TOOLING FOAM BOARD." <https://www.generalplastics.com/products/fr-4700> (accessed Apr. 07, 2022).
- [91] Thermo Fisher Scientific, "Bath Circulator Fluids *Sil 180*." <https://www.thermofisher.com/order/catalog/product/9990203> (accessed Apr. 10, 2022).
- [92] FUTEK Advanced Sensor Technology Inc., "Pressure Sensor (OEM) PMP300 FSH03103." <https://www.futek.com/store/pressure-sensors/oem-pressure-sensors/pressure-sensor-oem-PMP300/FSH03103> (accessed Apr. 12, 2022).
- [93] PCB Piezotronics Inc., "PCB Model 113B28." <https://www.pcb.com/products?m=113B28> (accessed Apr. 12, 2022).
- [94] Omega Engineering Inc, "Reduced Fine Tip Diameter Thermocouple Probes with Lead Wire." <https://www.omega.ca/en/temperature-measurement/temperature-probes/probes-with-lead-wires/tjft72/p/TJFT72-T-SS-116G-6-SMPW-M> (accessed Apr. 12, 2022).

- [95] Omega Engineering Inc, “Thermocouple Response Time,” 2019.
<https://www.omega.ca/en/resources/thermocouples-response-time> (accessed Apr. 12, 2022).
- [96] Omega Engineering Inc, “RTD Probes with Mounting Threads and Lead Wire.”
<https://www.omega.ca/en/temperature-measurement/temperature-probes/probes-with-lead-wires/p/RTD-810-Series> (accessed Apr. 12, 2022).
- [97] Proportion-Air Inc., “QB3.” <https://proportionair.com/electronic-pressure-regulators/qb3/>
(accessed Apr. 12, 2022).
- [98] Thermo Fisher Scientific, “SAHARA S45 Stainless-Steel Heated Bath Circulators.”
<https://www.thermofisher.com/order/catalog/product/158-1455> (accessed Apr. 12, 2022).
- [99] Thermo Fisher Scientific, “Merlin™ Recirculating Chillers.”
<https://www.thermofisher.com/order/catalog/product/266216992001> (accessed Apr. 12, 2022).
- [100] VWR International LLC, “Masterflex L/S® Digital Computer-Compatible Drive with Easy-Load® II Pump Head; 115/230 VAC.”
<https://us.vwr.com/store/item/NA5139011/masterflex-l-s-digital-drives-with-computer-network-compatibility-pump-systems-avantor> (accessed Apr. 12, 2022).
- [101] Magnetic Brake Systems, “Magnetic Brakes MBZ-5.7.”
<https://www.magbrakesystems.com/mbz-5-7> (accessed Apr. 12, 2022).
- [102] FUTEK Advanced Sensor Technology Inc., “Non-Contact Shaft-to-Shaft Rotary Torque Sensor TRS600 FSH01997.” <https://www.futek.com/store/torque-sensors/shaft-to-shaft-rotary-torque-sensors/non-contact-shaft-to-shaft-rotary-TRS600/FSH01997> (accessed Apr. 12, 2022).
- [103] Encoder Products Company, “Model 15S Accu-Coder™.”
<https://www.encoder.com/model-15s> (accessed Apr. 12, 2022).
- [104] National Instruments, “cDAQ-9189 Specifications.”
<https://www.ni.com/pdf/manuals/376607a.pdf> (accessed Apr. 12, 2022).

- [105] A. R. Ganji and A. J. Wheeler, *Introduction to Engineering Experimentation*, 3rd ed., no. 9. Pearson Higher Education, 2010.
- [106] The Dow Chemical Company, “SYLTHERM™ 800 Stabilized Heat Transfer Fluid.” <https://www.dow.com/en-us/pdp.syltherm-800-stabilized-heat-transfer-fluid.39260z.html#overview> (accessed Apr. 18, 2022).
- [107] Engineering ToolBox, “Ethylene Glycol Heat-Transfer Fluid Properties,” 2003. https://www.engineeringtoolbox.com/ethylene-glycol-d_146.html (accessed Apr. 27, 2022).
- [108] Engineering ToolBox, “The Ideal Gas Law,” 2003. https://www.engineeringtoolbox.com/ideal-gas-law-d_157.html (accessed Nov. 03, 2022).
- [109] A. J. Organ, *Stirling Cycle Engines: Inner Workings and Design*. John Wiley & Sons Ltd, 2014. doi: 10.1002/9781118818428.
- [110] R. Wang, J. Hu, Z. Jia, E. Luo, J. Xu, and Y. Sun, “Performance study of a free-piston Stirling heat pump with a circumferential temperature gradient in the heating heat exchanger,” *International Journal of Refrigeration*, Nov. 2022, doi: 10.1016/J.IJREFRIG.2022.11.007.
- [111] Thermo Fisher Scientific, “MS Excel sheet ‘TOOL_Fluid Selector 1.0’, obtained in private communication.”
- [112] Engineering ToolBox, “Liquids - Thermal Conductivities,” 2008. https://www.engineeringtoolbox.com/thermal-conductivity-liquids-d_1260.html (accessed Jul. 09, 2022).
- [113] Engineering ToolBox, “Air - Dynamic and Kinematic Viscosity,” 2003. https://www.engineeringtoolbox.com/air-absolute-kinematic-viscosity-d_601.html (accessed Jul. 16, 2022).
- [114] E. Fried and I. E. Idelchik, *Flow Resistance: A Design Guide for Engineers*. Philadelphia: Taylor & Francis, 1989. doi: <https://doi.org/10.1201/9780203755754>.

- [115] H. W. Coleman and W. G. Steele, *Experimentation, Validation, and Uncertainty Analysis for Engineers*, 4th ed. John Wiley & Sons, 2018. doi: 10.1002/9781119417989.
- [116] H. C. Chang and L. C. Wang, “A Simple Proof of Thue’s Theorem on Circle Packing,” *arXiv preprint*, vol. arXiv:1009.4322, 2010, Accessed: Oct. 19, 2022. [Online]. Available: <https://arxiv.org/abs/1009.4322>
- [117] Engineering ToolBox, “Solids, Liquids and Gases - Thermal Conductivities,” 2003. https://www.engineeringtoolbox.com/thermal-conductivity-d_429.html (accessed Oct. 25, 2022).
- [118] Engineering ToolBox, “Gases - Specific Heats and Individual Gas Constants,” 2003. https://www.engineeringtoolbox.com/specific-heat-capacity-gases-d_159.html (accessed Oct. 25, 2022).
- [119] PCB Piezotronics Inc., “PCB Model 482C05.” <https://www.pcb.com/products?model=482C05> (accessed Apr. 12, 2022).
- [120] National Instruments, “PS-14 Industrial Power Supply.” <https://www.ni.com/en-ca/support/model.ps-14.html> (accessed Jan. 12, 2022).
- [121] National Instruments, “NI 9411 Datasheet.” https://www.ni.com/pdf/manuals/373506a_02.pdf (accessed Apr. 12, 2022).
- [122] National Instruments, “NI 9212 and TB-9212 Datasheet.” https://www.ni.com/pdf/manuals/374358c_02.pdf (accessed Apr. 12, 2022).
- [123] National Instruments, “NI 9216 Datasheet.” https://www.ni.com/pdf/manuals/378022a_02.pdf (accessed Apr. 12, 2022).
- [124] National Instruments, “NI 9205 Datasheet.” https://www.ni.com/pdf/manuals/378020a_02.pdf (accessed Apr. 12, 2022).
- [125] National Instruments, “NI 9264 Datasheet.” https://www.ni.com/pdf/manuals/378025a_02.pdf (accessed Apr. 12, 2022).
- [126] Omega Engineering Inc, “RTD Sensors.” <https://www.omega.ca/en/resources/rtd-hub> (accessed Nov. 19, 2022).

- [127] Omega Engineering Inc, “ANSI and IEC Color Codes for Thermocouples, Wire and Connectors.” <https://www.omega.ca/en/colorcodes> (accessed Nov. 19, 2022).
- [128] OHAUS CORPORATION, “Scout® Pro Portable Electronic Balances.” <https://dmx.ohaus.com/WorkArea/showcontent.aspx?id=6046> (accessed Nov. 20, 2022).
- [129] R. Gordon, M. Pickering, and D. Bisson, “Uncertainty analysis by the ‘worst case’ method,” *J Chem Educ*, vol. 61, no. 9, p. 780, Sep. 1984, doi: 10.1021/ed061p780.

Appendix A. Uncertainty Analysis Methods

A.1 Systematic Uncertainties of Measured Variables

For each measured variable x the individual systematic uncertainties u_j from various error sources were obtained from equipment specifications or estimated. Following Coleman and Steele [115] they are combined into the combined standard uncertainty u_x by the root-sum-square:

$$u_x = \left(\sum_{j=1}^m (u_j)^2 \right)^{\frac{1}{2}} \quad (110)$$

where: x = measured variable

u_x = combined uncertainty of x

u_j = individual systematic uncertainties of x

m = number of individual systematic uncertainties

A.2 Propagation of Uncertainty

Uncertainties in measured variables were propagated through equations for calculate variables following the methods in Coleman and Steele [115]. Generally, for a calculated variable y that is a function of n measured variables x_i such that $y = y(x_1, x_2, \dots, x_n)$, the combined uncertainty of y is [115]:

$$u_y = \left(\sum_{i=1}^n \left(u_{x_i} \cdot \frac{\partial y}{\partial x_i} \right)^2 \right)^{\frac{1}{2}} \quad (111)$$

where: y = calculated variable

u_y = combined uncertainty of y

x_i = measured variables

u_{x_i} = combined uncertainty of x_i

n = number of variables x_i

$\frac{\partial y}{\partial x_i}$ = sensitivity coefficients

In some cases, the calculations of u_y can be simplified. If y is a summation of variables x_i where k is a constant, then the combined uncertainty of y can be calculated as the root-sum-square of the individual uncertainties as shown in equation (113) [115].

$$y = k \sum_{i=1}^n x_i \quad (112)$$

$$u_y = k \left(\sum_{i=1}^n u_{x_i}^2 \right)^{\frac{1}{2}} \quad (113)$$

If y takes a polynomial form as in equation (114) where k is a constant and a_i are integers, then the combined uncertainty of y can be calculated as in equation (115) [115]:

$$y = k \prod_{i=1}^n x_i^{a_i} \quad (114)$$

$$u_y = y \left(\sum_{i=1}^n \left(a_i \frac{u_{x_i}}{x_i} \right)^2 \right)^{\frac{1}{2}} \quad (115)$$

In the case of a calculated variable y that is a mean of n values x_i which have the same uncertainty u_x associated with them, as shown in equation (116), it can be derived from equation (111) that the combined uncertainty of y is as shown in equation (117):

$$y = \frac{1}{n} * \sum_{i=1}^n x_i \quad (116)$$

$$u_{x_i} = u_x = \text{const. for all } i$$

$$u_y = \frac{u_x}{\sqrt{n}} \quad (117)$$

A.2.1 Cyclic and Averaged Data

Some variables are calculated as the average of a sample of cyclic data, meaning varying, like

$$f = \text{mean}(f_{\theta})$$

$$T_e = \text{mean}(T_{TC0})$$

In these cases, the uncertainty in the cyclic data is also applied to the averaged value.

Other variables are calculated as the average of a number of steady or averaged values, such as the averaging of cyclic speed and pressure data (Section 2.7.6) or the mean pressure

$$p_{mean} = p_{atm} + \text{mean}(p_{Exp}, p_{Com}, p_{PC})$$

Where p_{Exp}, p_{Com}, p_{PC} are averaged first and then their mean is calculated. In these cases, the uncertainty from the individual values being averaged is propagated through the equation of the mean, so that the resulting uncertainty in the mean variable is obtained using equation (117).

A.2.2 Specifications of DAQ and Control System

The table below summarizes all DAQ equipment from the setup described in Chapter 2. The uncertainties from these devices will be calculated in the following appendix sections.

Table 6.1: Specifications of data acquisition and setpoint control equipment.

| Function | Manufacturer & Model | Properties |
|--|---|---|
| Mean Pressure Sensors Measure mean pressure vs. atmosphere | FUTEK PMP300 FSH03103 [92] | 0 – 200 psi (relative) 0 – 10 V analog output |
| Dynamic Pressure Sensors Measure dynamic pressure vs. mean | PCB Piezotronics 113B28 [93] | +/- 50 psi (from mean) |
| | PCB Piezotronics 482C05 [119] | Signal Conditioner +/- 5 V analog output |
| Atmospheric Pressure Sensor Measures atmospheric pressure | Android device LG Electronics LM-G820UM Sensor: Goertek 4864 | Resolution: 1 Pa Android application: 'Sensors Multitool' v1.3.2 weRed Software |
| Thermocouples Measure gas temperatures | Omega TJFT72-T-SS-116G-6-SMPW-M [94] | T-type, grounded junction \varnothing 1/16 inch stainless steel sheath \varnothing 0.02 inch fine tip |
| RTDs Measure liquid temperatures | Omega RTD-810 [96] | 3 wires \varnothing 1/8 inch stainless steel sheath |
| Torque Sensor Measures torque load | FUTEK TRS600 FSH01997 [102] | 10 Nm +/- 5 V analog output |
| Shaft Encoder Measures crankshaft angle | Encoder Products Company 15S-19M1-0500NV1ROC-F03-S1 [103] | 500 pulses/rotation |

| | | |
|---|---|---|
| <p>Magnetic Brake</p> <p>Applies torque load</p> <p>Measures speed for monitoring</p> | <p>Magnetic Brake Systems</p> <p>MBZ-5.7 [101]</p> | <p>Max. torque (zero rpm): 3.94 Nm</p> <p>0 – 10 V analog control</p> <p>0 – 4 V analog speed output</p> |
| <p>Pressure Regulator</p> <p>Controls mean pressure</p> | <p>Proportion Air</p> <p>QB3TANEEZP150PSGBR [97]</p> | <p>0 - 150 psi gauge pressure output</p> <p>0 – 10 V analog control</p> |
| | <p>Gas buffer tank</p> | <p>20 gal (76 L)</p> |
| | <p>Orifice flow restrictor</p> | <p>0.025-inch diameter</p> |
| <p>Heated Bath</p> <p>Heats heat source medium to setpoint temperature</p> <p>Cycles medium through heater</p> <p>Digital control from PC</p> | <p>ThermoFisher</p> <p>Sahara PC201 S-45 [98]</p> | <p>Heating power 3140 W</p> <p>Max. temperature 200 °C</p> <p>Max. Flow Rate 24 L/min</p> <p>Medium: Silicone oil, Fisher Scientific <i>Sil 180</i> [91]</p> <p>Tank: 41 litres</p> |
| <p>Recirculating Chiller</p> <p>Cools heat sink medium to setpoint temperature</p> <p>Cycles medium to tank</p> <p>Digital control from PC</p> | <p>ThermoFisher</p> <p>Merlin M150LR T1 [99]</p> | <p>Cooling power 4832 W</p> <p>Min. temperature -15 °C</p> <p>Medium: Water – Ethylene Glycol 70:30 mixture</p> <p>Tank: 35 litres</p> |
| <p>Peristaltic Pump</p> <p>Cycles heat sink medium through cooler</p> | <p>Masterflex L/S (77924-65) [100]</p> | <p>Easy Load II head (77200-62)</p> <p>Viton tubing size 17 (96412-17)</p> |
| <p>DAQ Chassis</p> <p>Connects DAQ modules to PC</p> | <p>National Instruments Inc.</p> <p>cDAQ-9189 [104]</p> | <p>Part Number: 785065-01</p> <p>Ethernet interface to PC</p> |
| <p>DAQ Power Supply</p> <p>Supplies power for</p> <ul style="list-style-type: none"> • DAQ chassis • Mean pressure sensors • Pressure regulator • Torque sensor • Shaft encoder | <p>National Instruments Inc.</p> <p>PS-14 [120]</p> | <p>24 VDC supply</p> |

| | | |
|---|--|--|
| DAQ Counter Module Reads shaft encoder | National Instruments Inc. 9411 [121] | Part Number: 779005-01 |
| DAQ Thermocouple Input Module Reads thermocouple temperatures | National Instruments Inc. 9212 miniTC [122] | Part Number: 785259-01 2 modules, 8 channels each 1.8 samples/second/channel (High Resolution) |
| DAQ RTD Input Module Reads RTD temperatures | National Instruments Inc. 9216 [123] | Part Number: 785186-01 8 channels 400 samples/second (total) |
| DAQ Analog Input Module Reads inputs from <ul style="list-style-type: none"> • Mean pressure sensors • Dynamic pressure signal conditioner • Torque sensor • Magnetic brake speed | National Instruments Inc. 9205 [124] | Part Number: 785184-01 16 channels (differential voltage) Up to +/- 10 V analog input 250k samples/second (total) |
| DAQ Analog Output Module Sends control voltage to <ul style="list-style-type: none"> • Pressure regulator • Magnetic brake | National Instruments Inc. 9264 [125] | Part Number: 780927-01 16 channels +/- 10 V analog output 25k samples/second/channel |

Appendix B. Uncertainty in Measured Variables

The measured variables are listed in Table 2.3. The equations given in Section A.2 were used to propagate uncertainties.

Except for the RTDs and TCs, all sensors and the DAQ were used at about 25 °C room temperature which is in their compensated temperature range, therefore no temperature error was considered.

B.1 RTD and Liquid Temperatures

As seen in Table 2.7 the gas temperatures are calculated as averages of the cyclic temperature data samples from the RTDs. As discussed in Section 0, the uncertainty $u_{T_{RTD}}$ below is directly applied to all gas temperatures.

The table below lists the individual uncertainties applied to all RTD measurements. Potential improvements in uncertainty from the calibration (see Section 2.4.1) are not considered. The individual uncertainties are used to calculate the combined uncertainty following equation (110) and rounding up:

$$u_{T_{RTD}} = 0.5 \text{ } ^\circ\text{C} \quad (118)$$

Also for

$$T_{source,in}, T_{source,out}, T_{sink,in}, T_{sink,out}$$

Table 6.2: RTD measurement uncertainties

| Uncertainty Source | Instrument | Uncertainty Description | Value | Notes |
|--------------------|---------------|-------------------------|------------------------------------|--|
| Instrument | RTD-810 [96] | Specified Accuracy | $\pm 0.45 \text{ } ^\circ\text{C}$ | Class A deviation at T = 150 °C: $\pm(0.15 + 0.002*T)^\circ\text{C}$ [126] |
| DAQ | NI 9216 [123] | Temperature Accuracy | $\pm 0.20 \text{ } ^\circ\text{C}$ | Typical accuracy for 3-wire, measurement of -200°C to 150°C |

B.2 TC and Gas Temperatures

As seen in Table 2.7 the gas temperatures are calculated as averages of the cyclic temperature data samples from the thermocouples. As discussed in Section 0, the uncertainty $u_{T_{TC}}$ below is directly applied to all gas temperatures.

The table below lists the individual uncertainties applied to all thermocouple measurements. Potential improvements in uncertainty from the calibration (see Section 2.4.1) are not considered. The individual uncertainties are used to calculate the combined uncertainty following equation (110) and rounding up:

$$u_{T_{TC}} = 1.5 \text{ } ^\circ\text{C} \quad (119)$$

Also for

$$T_e, T_{h,inlet}, T_{h,reg}, T_{k,inlet}, T_{k,reg}, T_{reg}, T_{PP}, T_{CC}$$

Table 6.3: TC measurement uncertainties

| Source | Model | Description | Value | Notes |
|------------|---|---|-------------------------------------|---|
| Instrument | Omega TJFT72-T-SS- 116G-6- SMPW-M [94] | Specified Accuracy | $\pm 1.125 \text{ } ^\circ\text{C}$ | Manufacturer specified as $\pm 1 \text{ } ^\circ\text{C}$ or ($\pm 0.75\% \cdot T$), whichever is higher [127]. For $T = 150 \text{ } ^\circ\text{C}$. |
| DAQ | NI 9212 miniTC [122] | Gain Error | $\pm 0.03 \text{ } ^\circ\text{C}$ | Typical, 0.02 % of $150 \text{ } ^\circ\text{C}$ |
| DAQ | NI 9212 miniTC [122] | Measurement Accuracy | $\pm 0.77 \text{ } ^\circ\text{C}$ | Typical for 'High Resolution' mode at $0 \text{ } ^\circ\text{C}$ |
| DAQ | NI 9212 miniTC [122] | Cold-junction compensation accuracy | $\pm 0.6 \text{ } ^\circ\text{C}$ | Typical |

B.3 Mean Pressures

The table below lists the individual uncertainties applied to all mean pressure measurements from the diaphragm pressure sensors. The maximum uncertainty values given by the manufacturer are assumed since the calibration is outdated. These are used to calculate the combined uncertainty following equation (110) and rounding up:

$$u_{p_m} = 10.13 \text{ kPa} \quad (120)$$

Table 6.4: Mean pressure measurement uncertainties

| Source | Model | Description | Value | Notes |
|------------|----------------------------------|------------------------|-----------------------|---|
| Instrument | FUTEK PMP300 FSH03103 [92] | Nonlinearity | $\pm 0.05 \text{ V}$ | $\pm 0.5 \%$ of rated output (RO) RO = 10 V at 1379 kPa (200 psi) |
| | | | $\pm 6895 \text{ Pa}$ | |
| Instrument | FUTEK PMP300 FSH03103 [92] | Zero Balance | $\pm 0.05 \text{ V}$ | $\pm 0.5 \%$ of rated output (RO) RO = 10 V at 1379 kPa (200 psi) |
| | | | $\pm 6895 \text{ Pa}$ | |
| Instrument | FUTEK PMP300 FSH03103 [92] | Hysteresis | $\pm 0.016 \text{ V}$ | $\pm 0.16 \%$ of rated output (RO) RO = 10 V at 1379 kPa (200 psi) |
| | | | $\pm 2206 \text{ Pa}$ | |
| Instrument | FUTEK PMP300 FSH03103 [92] | Non-repeatability | $\pm 0.01 \text{ V}$ | $\pm 0.1 \%$ of rated output (RO) RO = 10 V at 1379 kPa (200 psi) |
| | | | $\pm 1379 \text{ Pa}$ | |
| DAQ | NI 9205 [124] | Accuracy at Full Scale | $\pm 6.23 \text{ mV}$ | Max error for range 10 V At 1379 kPa / 10 V |
| | | | $\pm 860 \text{ Pa}$ | |

B.4 Dynamic pressures

The table below lists the individual uncertainties applied to all dynamic pressure measurements from the piezoelectric sensors. The maximum uncertainty values given by the manufacturer are assumed since the calibration is outdated. These are used to calculate the combined uncertainty following equation (110) and rounding up:

$$u_{p_d} = 3.48 \text{ kPa} \quad (121)$$

Table 6.5: Dynamic pressure measurement uncertainties

| Source | Model | Description | Value | Notes |
|--------------------|-------------------------------|------------------------|-----------------------|---|
| Instrument | PCB Piezotronics 113B28 [93] | Nonlinearity | $\pm 3450 \text{ Pa}$ | 1 % of Full scale (344.7 kPa) |
| Instrument | PCB Piezotronics 113B28 [93] | Resolution | $\pm 3.5 \text{ Pa}$ | Half of resolution (7 Pa) |
| Instrument | PCB Piezotronics 113B28 [93] | Time response | - | Rise time $\leq 1.0 \mu\text{s}$ Lower than voltage sampling period $1/1000 \text{ Hz} = 1 \text{ ms}$ |
| Signal Conditioner | PCB Piezotronics 482C05 [119] | Accuracy | - | Not specified by manufacturer, negligible |
| DAQ | NI 9205 [124] | Accuracy at Full Scale | $\pm 6.23 \text{ mV}$ | Max error for range 10 V At 344.7 kPa / 5 V |
| | | | $\pm 430 \text{ Pa}$ | |

B.5 Shaft Torque

Since random uncertainty is not considered, the uncertainty in the average torque τ is the same as that of the measured unsteady torque τ_{raw} . The table below lists the individual uncertainties applied to the torque sensor measurements. The maximum uncertainty values given by the manufacturer are assumed since the calibration is outdated. These are used to calculate the combined uncertainty following equation (110) and rounding up:

$$u_{\tau} = u_{\tau_{raw}} = 0.0325 \text{ Nm} \quad (122)$$

Table 6.6: Torque measurement uncertainties

| Source | Model | Description | Value | Notes |
|------------|--------------------------------|------------------------|-------------------------|---|
| Instrument | FUTEK TRS600 FSH01997 [102] | Nonlinearity | $\pm 0.01 \text{ V}$ | 0.2 % of rated output (RO) RO = 5 V at 10 Nm |
| | | | $\pm 0.02 \text{ Nm}$ | |
| Instrument | FUTEK TRS600 FSH01997 [102] | Hysteresis | $\pm 0.005 \text{ V}$ | 0.1 % of rated output (RO) RO = 5 V at 10 Nm |
| | | | $\pm 0.01 \text{ Nm}$ | |
| Instrument | FUTEK TRS600 FSH01997 [102] | Non-repeatability | $\pm 0.01 \text{ V}$ | 0.2 % of rated output (RO) RO = 5 V at 10 Nm |
| | | | $\pm 0.02 \text{ Nm}$ | |
| DAQ | NI 9205 [124] | Accuracy at Full Scale | $\pm 6.23 \text{ mV}$ | Max error for range 10 V At 10 Nm / 5 V |
| | | | $\pm 0.0125 \text{ Nm}$ | |

B.6 Crankshaft Angle

The table below lists the individual uncertainties applied to the crank angle measurements. These are used to calculate the combined uncertainty following equation (110) and rounding up:

$$u_{\theta} = 2.3^{\circ} \quad (123)$$

Table 6.7: Angle measurement uncertainties

| Source | Model | Description | Value | Notes |
|------------|---|----------------------|--------------------|------------------------|
| Instrument | Encoder Products Comp. 15S-19M1-0500NV1ROC-F03-S1 [103] | Mechanical Accuracy | $\pm 1^{\circ}$ | Manufacturer specified |
| Instrument | Encoder Products Comp. 15S-19M1-0500NV1ROC-F03-S1 [103] | Specified Accuracy | $\pm 0.17^{\circ}$ | Manufacturer specified |
| Alignment | | Alignment with shaft | $\pm 2^{\circ}$ | estimated |
| Play | | Play in mechanism | - | negligible |
| DAQ | NI 9411 [121] | Delay Time | 500 ns | negligible |

B.7 Time for Voltage / Counter Data

The only data that is used in instantaneous form is the dynamic pressures and the crankshaft angle, which are used to generate the indicator diagram. Both these measurements are acquired simultaneously using the same time stamps from the DAQ. Therefore, any inaccuracy in the time stamp data (e.g. latency) affects the pressure and angle data equally and does not change the link between corresponding pressure and angle values. The resulting indicator data is not affected, hence uncertainty in the time stamp data does not need to be considered.

Timestamp data is used to calculate the engine speed. The latency affecting this data is estimated in the table below. Thus:

$$u_{t_{VC}} = 1 \text{ ms} \quad (124)$$

Table 6.8: Timestamp uncertainties

| Source | Model | Description | Value | Notes |
|------------------|--------------------|----------------------------------|--------------------|------------|
| DAQ and Computer | | Latency | $\pm 1 \text{ ms}$ | estimated |
| DAQ | NI cDAQ-9189 [104] | Network synchronization accuracy | $<1 \mu\text{s}$ | negligible |
| DAQ | NI 9411 [121] | Delay Time | 500 ns | negligible |

B.8 Atmospheric Pressure

The smartphone’s atmospheric pressure sensor was calibrated using a mercury barometer, which introduced a calibration uncertainty as shown in Table 6.9. A resolution of 1 Pa, meaning an uncertainty of 0.5 Pa, was given for the smartphone’s pressure sensor by the application used to access the sensor data. This value is much smaller than the calibration uncertainty and was therefore neglected.

$$p_{atm} = p_{sens} + \Delta p_{corr} \quad (125)$$

$$u_{p_{atm}} = 0.014 \text{ kPa} \quad (126)$$

where: p_{sens} = Smartphone sensor readout (uncertainty neglected)

Δp_{corr} = calibration correction

Table 6.9 – Atmospheric pressure sensor measurement uncertainties

| Source | Model | Description | Value | Notes |
|-------------|-------------------|---------------------------|------------|----------------|
| Calibration | Mercury barometer | Calibration via barometer | ±0.014 kPa | Equation (129) |
| Instrument | Smartphone | Accuracy | ±0.5 Pa | neglected |

B.8.1 Calibration: 2022-06-13

The pressure readings from the atmospheric pressure sensor were calibrated against a mercury barometer at a single point. The mercury barometer column height was measured with a Vernier scale that is part of the barometer and has a resolution of 0.1 mm, leading to an uncertainty of ±0.05 mm. The measured height was then corrected for the effects of gravity (latitude) and temperature following the correction tables shown in Figure 6.1 and Figure 6.2. The measurements and associated uncertainties are listed in Table 6.10 and the corrected barometer reading is calculated in equation (127). Experiments were conducted at a latitude of 53.53° and the uncertainty of the gravity correction factor is assumed to be negligible. The temperature of the

barometer is measured with an analogue thermometer that is attached to the barometer body. It has a resolution of 1 °C and an uncertainty of ± 0.5 °C. The temperature was observed as 20.0 °C.

Table 6.10 – Barometer calibration variables and uncertainties

| Variable | Value | Uncertainty Variable | Uncertainty Value | Unit | Notes |
|----------|--------|----------------------|-------------------|--------|--|
| h | 697.0 | u_h | ± 0.05 | [mmHg] | Convert to kPa with standard ratio |
| h_g | 0.492 | - | - | [mmHg] | Gravity correction changes minimally for small changes in latitude |
| h_T | -2.270 | u_{h_T} | ± 0.09 | [mmHg] | ± 0.5 °C uncertainty converted to mmHg with tables |

$$p_{bar} = h + h_g + h_T = 695.22 \text{ mmHg} = 92.69 \text{ kPa} \quad (127)$$

where: p_{bar} = barometer pressure

h = mercury column height

h_g = gravity correction factor

h_T = temperature correction factor

At the same time the atmospheric pressure sensor read $p_{sens,cal} = 92.66$ kPa. The correction factor Δp_{corr} follows from:

$$\Delta p_{corr} = p_{bar} - p_{sens,cal} = 0.03 \text{ kPa} \quad (128)$$

Uncertainties are propagated through equations (127) and (128) yielding the total calibration uncertainty from the following equation.

$$u_{\Delta p_{corr}} = \left[(u_h)^2 + (u_{h_T})^2 \right]^{\frac{1}{2}} = 0.103 \text{ mmHg} \leq 0.014 \text{ kPa} \quad (129)$$

Table 3. GRAVITY CORRECTION

To reduce the reading of the barometer to standard gravity

| Latitude N or S | Height of the mercury column | | | | | | | | | | | | | | |
|---|------------------------------|-------|-------|-------|-------|-------------|-------|-------|-------|-------|-----------|-------|-------|-------|-------|
| | Inches | | | | | Millimetres | | | | | Millibars | | | | |
| | 26 | 27 | 28 | 29 | 30 | 680 | 700 | 720 | 740 | 760 | 780 | 900 | 950 | 1000 | 1050 |
| LATITUDE 0° TO 45° THE CORRECTION IS TO BE SUBTRACTED | | | | | | | | | | | | | | | |
| LATITUDE 46° TO 90° THE CORRECTION IS TO BE ADDED | | | | | | | | | | | | | | | |
| 90° | +0.67 | +0.70 | +0.73 | +0.75 | +0.78 | +1.76 | +1.82 | +1.87 | +1.92 | +1.97 | +2.02 | +2.33 | +2.46 | +2.59 | +2.72 |
| 88 | .067 | .070 | .072 | .075 | .078 | 1.76 | 1.81 | 1.86 | 1.91 | 1.97 | 2.02 | 2.33 | 2.46 | 2.59 | 2.72 |
| 86 | .067 | .069 | .072 | .074 | .077 | 1.75 | 1.80 | 1.85 | 1.90 | 1.95 | 2.00 | 2.31 | 2.44 | 2.57 | 2.70 |
| 84 | .066 | .068 | .071 | .074 | .076 | 1.72 | 1.77 | 1.83 | 1.88 | 1.93 | 1.98 | 2.28 | 2.41 | 2.54 | 2.66 |
| 82 | .065 | .067 | .070 | .072 | .075 | 1.69 | 1.74 | 1.79 | 1.84 | 1.89 | 1.94 | 2.24 | 2.37 | 2.49 | 2.62 |
| 80 | +0.63 | +0.66 | +0.68 | +0.71 | +0.73 | +1.65 | +1.70 | +1.75 | +1.80 | +1.85 | +1.90 | +2.19 | +2.31 | +2.43 | +2.56 |
| 78 | .061 | .064 | .066 | .069 | .071 | 1.61 | 1.65 | 1.70 | 1.75 | 1.80 | 1.84 | 2.13 | 2.25 | 2.36 | 2.48 |
| 76 | .059 | .062 | .064 | .066 | .068 | 1.55 | 1.60 | 1.64 | 1.69 | 1.74 | 1.78 | 2.05 | 2.17 | 2.28 | 2.40 |
| 74 | .057 | .059 | .061 | .064 | .066 | 1.49 | 1.53 | 1.58 | 1.62 | 1.66 | 1.71 | 1.97 | 2.08 | 2.19 | 2.30 |
| 72 | .054 | .056 | .058 | .061 | .063 | 1.42 | 1.46 | 1.50 | 1.54 | 1.59 | 1.63 | 1.88 | 1.98 | 2.09 | 2.19 |
| 70 | +0.51 | +0.53 | +0.55 | +0.57 | +0.59 | +1.34 | +1.38 | +1.42 | +1.46 | +1.50 | +1.54 | +1.78 | +1.87 | +1.97 | +2.07 |
| 68 | .048 | .050 | .052 | .054 | .056 | 1.26 | 1.30 | 1.33 | 1.37 | 1.41 | 1.44 | 1.67 | 1.76 | 1.85 | 1.94 |
| 66 | .045 | .046 | .048 | .050 | .052 | 1.17 | 1.20 | 1.24 | 1.27 | 1.31 | 1.34 | 1.55 | 1.63 | 1.72 | 1.80 |
| 64 | .041 | .043 | .044 | .046 | .047 | 1.07 | 1.10 | 1.13 | 1.17 | 1.20 | 1.23 | 1.42 | 1.50 | 1.58 | 1.65 |
| 62 | .037 | .039 | .040 | .041 | .043 | 0.97 | 1.00 | 1.03 | 1.06 | 1.08 | 1.11 | 1.28 | 1.36 | 1.43 | 1.50 |
| 60 | +0.33 | +0.34 | +0.36 | +0.37 | +0.38 | +0.86 | +0.89 | +0.91 | +0.94 | +0.97 | +0.99 | +1.14 | +1.21 | +1.27 | +1.33 |
| 58 | .029 | .030 | .031 | .032 | .033 | 0.75 | 0.78 | 0.80 | 0.82 | 0.84 | 0.86 | 1.00 | 1.05 | 1.11 | 1.16 |
| 56 | .024 | .025 | .026 | .027 | .028 | 0.64 | 0.66 | 0.68 | 0.69 | 0.71 | 0.73 | 0.84 | 0.89 | 0.94 | 0.99 |
| 54 | .020 | .021 | .021 | .022 | .023 | 0.52 | 0.54 | 0.55 | 0.57 | 0.58 | 0.60 | 0.69 | 0.73 | 0.77 | 0.80 |
| 52 | .015 | .016 | .016 | .017 | .018 | 0.40 | 0.41 | 0.42 | 0.44 | 0.45 | 0.46 | 0.53 | 0.56 | 0.59 | 0.62 |
| 50 | +0.11 | +0.11 | +0.11 | +0.12 | +0.12 | +0.28 | +0.29 | +0.29 | +0.30 | +0.31 | +0.32 | +0.37 | +0.39 | +0.41 | +0.43 |
| 48 | .006 | .006 | .006 | .007 | .007 | 0.15 | 0.16 | 0.16 | 0.17 | 0.17 | 0.18 | 0.20 | 0.21 | 0.23 | 0.24 |
| 46 | +0.01 | +0.01 | +0.01 | +0.01 | +0.01 | +0.03 | +0.03 | +0.03 | +0.03 | +0.03 | +0.03 | +0.04 | +0.04 | +0.04 | +0.04 |
| 45 | -.001 | -.001 | -.001 | -.001 | -.001 | -.03 | -.03 | -.04 | -.04 | -.04 | -.04 | -.04 | -.05 | -.05 | -.05 |
| 44 | .004 | .004 | .004 | .004 | .004 | 0.10 | 0.10 | 0.10 | 0.11 | 0.11 | 0.11 | 0.13 | 0.13 | 0.14 | 0.15 |
| 42 | .008 | .009 | .009 | .009 | .010 | 0.22 | 0.23 | 0.23 | 0.24 | 0.25 | 0.25 | 0.29 | 0.31 | 0.33 | 0.34 |
| 40 | -.013 | -.014 | -.014 | -.015 | -.015 | -.035 | -.036 | -.037 | -.038 | -.039 | -.040 | -.046 | -.048 | -.051 | -.053 |
| 38 | .018 | .019 | .019 | .020 | .021 | 0.47 | 0.48 | 0.50 | 0.51 | 0.52 | 0.54 | 0.62 | 0.65 | 0.69 | 0.72 |
| 36 | .022 | .023 | .024 | .025 | .026 | 0.59 | 0.61 | 0.62 | 0.64 | 0.66 | 0.67 | 0.78 | 0.82 | 0.86 | 0.91 |
| 34 | .027 | .028 | .029 | .030 | .031 | 0.71 | 0.73 | 0.75 | 0.77 | 0.79 | 0.81 | 0.93 | 0.99 | 1.04 | 1.09 |
| 32 | .031 | .033 | .034 | .035 | .036 | 0.82 | 0.84 | 0.87 | 0.89 | 0.92 | 0.94 | 1.08 | 1.14 | 1.20 | 1.27 |
| 30 | -.036 | -.037 | -.038 | -.040 | -.041 | -.093 | -.096 | -.098 | -.101 | -.104 | -.107 | -.123 | -.130 | -.137 | -.144 |
| 28 | .040 | .041 | .043 | .044 | .046 | 1.04 | 1.07 | 1.10 | 1.13 | 1.16 | 1.19 | 1.37 | 1.45 | 1.52 | 1.60 |
| 26 | .043 | .045 | .047 | .048 | .050 | 1.14 | 1.17 | 1.20 | 1.24 | 1.27 | 1.30 | 1.50 | 1.59 | 1.67 | 1.75 |
| 24 | .047 | .049 | .051 | .053 | .054 | 1.23 | 1.27 | 1.30 | 1.34 | 1.38 | 1.41 | 1.63 | 1.72 | 1.81 | 1.90 |
| 22 | .051 | .052 | .054 | .056 | .058 | 1.32 | 1.36 | 1.40 | 1.44 | 1.48 | 1.52 | 1.75 | 1.85 | 1.94 | 2.04 |
| 20 | -.054 | -.056 | -.058 | -.060 | -.062 | -.141 | -.145 | -.149 | -.153 | -.157 | -.161 | -.186 | -.196 | -.207 | -.217 |
| 18 | .057 | .059 | .061 | .063 | .065 | 1.48 | 1.53 | 1.57 | 1.61 | 1.66 | 1.70 | 1.96 | 2.07 | 2.18 | 2.29 |
| 16 | .059 | .062 | .064 | .066 | .068 | 1.55 | 1.60 | 1.64 | 1.69 | 1.73 | 1.78 | 2.05 | 2.17 | 2.28 | 2.40 |
| 14 | .062 | .064 | .066 | .069 | .071 | 1.61 | 1.66 | 1.71 | 1.76 | 1.80 | 1.85 | 2.14 | 2.26 | 2.37 | 2.49 |
| 12 | .064 | .066 | .069 | .071 | .074 | 1.67 | 1.72 | 1.77 | 1.82 | 1.87 | 1.91 | 2.21 | 2.33 | 2.45 | 2.58 |
| 10 | -.066 | -.068 | -.071 | -.073 | -.076 | -.172 | -.177 | -.182 | -.187 | -.192 | -.197 | -.227 | -.240 | -.252 | -.265 |
| 8 | .067 | .070 | .072 | .075 | .077 | 1.75 | 1.81 | 1.86 | 1.91 | 1.96 | 2.01 | 2.32 | 2.45 | 2.58 | 2.71 |
| 6 | .068 | .071 | .073 | .076 | .079 | 1.78 | 1.84 | 1.89 | 1.94 | 1.99 | 2.05 | 2.36 | 2.49 | 2.62 | 2.76 |
| 4 | .069 | .072 | .074 | .077 | .080 | 1.81 | 1.86 | 1.91 | 1.97 | 2.02 | 2.07 | 2.39 | 2.52 | 2.66 | 2.79 |
| 2 | .070 | .072 | .075 | .078 | .080 | 1.82 | 1.87 | 1.93 | 1.98 | 2.03 | 2.09 | 2.41 | 2.54 | 2.67 | 2.81 |
| 0 | -.070 | -.072 | -.075 | -.078 | -.080 | -.182 | -.188 | -.193 | -.198 | -.204 | -.209 | -.241 | -.255 | -.268 | -.282 |

Tables 1 thru 3 are condensed from the "Smithsonian Meteorological Tables", Sixth Revised Edition 1949, Fifth Reprint 1971; and are corrected for consistency with the recommendations contained in the "International Meteorological Tables", World Meteorological Organization, 1966, with amendments thru July 1973.

Figure 6.1: Gravity correction table for mercury barometer

Table 2. TEMPERATURE CORRECTION, Metric Units

To reduce the reading of the barometer to standard temperature

| Temperature C | Observed Reading of the Barometer in Millimetres or Millibars | | | | | | | | | | | | |
|------------------|---|------|------|------|------|------|------|------|------|------|------|------|------|
| | 540 | 560 | 580 | 600 | 620 | 640 | 660 | 680 | 700 | 720 | 740 | 760 | 780 |
| | ALL CORRECTIONS SUBTRACTIVE | | | | | | | | | | | | |
| 0 | 0.00 | 0.00 | 0.00 | 0.00 | 0.00 | 0.00 | 0.00 | 0.00 | 0.00 | 0.00 | 0.00 | 0.00 | 0.00 |
| 1 | .09 | .09 | .09 | .10 | .10 | .10 | .11 | .11 | .11 | .12 | .12 | .12 | .13 |
| 2 | .18 | .18 | .19 | .20 | .20 | .21 | .22 | .22 | .23 | .24 | .24 | .25 | .25 |
| 3 | .26 | .27 | .28 | .29 | .30 | .31 | .32 | .33 | .34 | .35 | .36 | .37 | .38 |
| 4 | .35 | .37 | .38 | .39 | .40 | .42 | .43 | .44 | .46 | .47 | .48 | .50 | .51 |
| 5 | 0.44 | 0.46 | 0.47 | 0.49 | 0.51 | 0.52 | 0.54 | 0.56 | 0.57 | 0.59 | 0.60 | 0.62 | 0.64 |
| 6 | .53 | .55 | .57 | .59 | .61 | .63 | .65 | .67 | .69 | .71 | .72 | .74 | .76 |
| 7 | .62 | .64 | .66 | .69 | .71 | .73 | .75 | .78 | .80 | .82 | .85 | .87 | .89 |
| 8 | .70 | .73 | .76 | .78 | .81 | .84 | .86 | .89 | .91 | .94 | .97 | .99 | 1.02 |
| 9 | .79 | .82 | .85 | .88 | .91 | .94 | .97 | 1.00 | 1.03 | 1.06 | 1.09 | 1.12 | 1.15 |
| 10 | 0.88 | 0.91 | 0.95 | 0.98 | 1.01 | 1.04 | 1.08 | 1.11 | 1.14 | 1.17 | 1.21 | 1.24 | 1.27 |
| 11 | .97 | 1.00 | 1.04 | 1.08 | 1.11 | 1.15 | 1.18 | 1.22 | 1.26 | 1.29 | 1.33 | 1.36 | 1.40 |
| 12 | 1.06 | 1.10 | 1.13 | 1.17 | 1.21 | 1.25 | 1.29 | 1.33 | 1.37 | 1.41 | 1.45 | 1.49 | 1.53 |
| 13 | 1.14 | 1.19 | 1.23 | 1.27 | 1.31 | 1.36 | 1.40 | 1.44 | 1.48 | 1.53 | 1.57 | 1.61 | 1.65 |
| 14 | 1.23 | 1.28 | 1.32 | 1.37 | 1.41 | 1.46 | 1.51 | 1.55 | 1.60 | 1.64 | 1.69 | 1.73 | 1.78 |
| 15 | 1.32 | 1.37 | 1.42 | 1.47 | 1.52 | 1.56 | 1.61 | 1.66 | 1.71 | 1.76 | 1.81 | 1.86 | 1.91 |
| 16 | 1.41 | 1.46 | 1.51 | 1.56 | 1.62 | 1.67 | 1.72 | 1.77 | 1.82 | 1.88 | 1.93 | 1.98 | 2.03 |
| 17 | 1.50 | 1.55 | 1.61 | 1.66 | 1.72 | 1.77 | 1.83 | 1.88 | 1.94 | 1.99 | 2.05 | 2.10 | 2.16 |
| 18 | 1.58 | 1.64 | 1.70 | 1.76 | 1.82 | 1.88 | 1.93 | 1.99 | 2.05 | 2.11 | 2.17 | 2.23 | 2.29 |
| 19 | 1.67 | 1.73 | 1.79 | 1.86 | 1.92 | 1.98 | 2.04 | 2.10 | 2.17 | 2.23 | 2.29 | 2.35 | 2.41 |
| 20 | 1.76 | 1.82 | 1.89 | 1.95 | 2.02 | 2.08 | 2.15 | 2.21 | 2.28 | 2.34 | 2.41 | 2.47 | 2.54 |
| 21 | 1.85 | 1.91 | 1.98 | 2.05 | 2.12 | 2.19 | 2.26 | 2.32 | 2.39 | 2.46 | 2.53 | 2.60 | 2.67 |
| 22 | 1.93 | 2.01 | 2.08 | 2.15 | 2.22 | 2.29 | 2.36 | 2.43 | 2.51 | 2.58 | 2.65 | 2.72 | 2.79 |
| 23 | 2.02 | 2.10 | 2.17 | 2.25 | 2.32 | 2.40 | 2.47 | 2.54 | 2.62 | 2.69 | 2.77 | 2.84 | 2.92 |
| 24 | 2.11 | 2.19 | 2.26 | 2.34 | 2.42 | 2.50 | 2.58 | 2.66 | 2.73 | 2.81 | 2.89 | 2.97 | 3.05 |
| 25 | 2.20 | 2.28 | 2.36 | 2.44 | 2.52 | 2.60 | 2.68 | 2.77 | 2.85 | 2.93 | 3.01 | 3.09 | 3.17 |
| 26 | 2.28 | 2.37 | 2.45 | 2.54 | 2.62 | 2.71 | 2.79 | 2.88 | 2.96 | 3.04 | 3.13 | 3.21 | 3.30 |
| 27 | 2.37 | 2.46 | 2.55 | 2.63 | 2.72 | 2.81 | 2.90 | 2.99 | 3.07 | 3.16 | 3.25 | 3.34 | 3.42 |
| 28 | 2.46 | 2.55 | 2.64 | 2.73 | 2.82 | 2.91 | 3.00 | 3.10 | 3.19 | 3.28 | 3.37 | 3.46 | 3.55 |
| 29 | 2.55 | 2.64 | 2.73 | 2.83 | 2.92 | 3.02 | 3.11 | 3.21 | 3.30 | 3.39 | 3.49 | 3.58 | 3.68 |
| 30 | 2.63 | 2.73 | 2.83 | 2.93 | 3.02 | 3.12 | 3.22 | 3.32 | 3.41 | 3.51 | 3.61 | 3.71 | 3.80 |
| 31 | 2.72 | 2.82 | 2.92 | 3.02 | 3.12 | 3.22 | 3.32 | 3.43 | 3.53 | 3.63 | 3.73 | 3.83 | 3.93 |
| 32 | 2.81 | 2.91 | 3.02 | 3.12 | 3.22 | 3.33 | 3.43 | 3.54 | 3.64 | 3.74 | 3.85 | 3.95 | 4.05 |
| 33 | 2.89 | 3.00 | 3.11 | 3.22 | 3.32 | 3.43 | 3.54 | 3.64 | 3.75 | 3.86 | 3.97 | 4.07 | 4.18 |
| 34 | 2.98 | 3.09 | 3.20 | 3.31 | 3.42 | 3.53 | 3.64 | 3.75 | 3.87 | 3.98 | 4.09 | 4.20 | 4.31 |

Figure 6.2: Temperature correction table for mercury barometer

Appendix C. Uncertainty in Calculated Variables

C.1 Heater and Cooler Liquid Flow Rates

The pump flow rates were measured in a calibration procedure. Uncertainties from this are discussed in the following section. The table below lists the individual uncertainties. These are used to calculate the combined uncertainty following equation (110) and rounding up:

$$u_{\dot{m}_{Cooler}} = 1.8 \cdot 10^{-4} \text{ kg/s} \quad (130)$$

$$u_{\dot{m}_{Heater}} = 3.1 \cdot 10^{-3} \text{ kg/s}$$

Table 6.11: Cooler flow rate uncertainties

| Source | Model | Description | Value | Notes |
|----------------------|-------------------------------------|---------------------|---------------------------------------|--|
| Pump (Cooler) | Masterflex L/S (77924-65) [100] | Specified Accuracy | $\pm 2.4 \cdot 10^{-5} \text{ kg/s}$ | Specified as 0.1 % $\dot{m}_{Cooler} = 0.0236 \text{ kg/s}$ |
| Pump (Heater) | ThermoFisher Sahara PC201 S-45 [98] | Repeatability | $\pm 2.73 \cdot 10^{-3} \text{ kg/s}$ | Estimated as 5 % of max flow rate (150 °C) |
| Calibration (Cooler) | | Weighing and timing | $\pm 1.78 \cdot 10^{-4} \text{ kg/s}$ | Equation (136) |
| Calibration (Heater) | | Weighing and timing | $\pm 1.43 \cdot 10^{-3} \text{ kg/s}$ | Equation (137) |

C.1.1 Calibration Oct 2021

For each measurement, liquid from the pump loop was captured in a container for a measured time around 10 seconds and weighed. The mass flow rate was calculated for each sample as:

$$\dot{m} = \frac{m_{scale}}{\Delta t} \quad (131)$$

where: p_{bar} = barometer pressure

\dot{m} = mass flow rate (kg/s)

m_{scale} = weighed mass of fluid (kg)

Δt = time recorded (s)

Propagation of uncertainty in this equation following equation (115):

$$u_{\dot{m}} = \dot{m} \left(\left(\frac{u_{m_{scale}}}{m_{scale}} \right)^2 + \left(\frac{u_{\Delta t}}{\Delta t} \right)^2 \right)^{\frac{1}{2}} \quad (132)$$

The mass measurements are affected by uncertainties from the scale, and the time recordings by human error from stopping the time. These uncertainties are listed in the tables below. Following equation (110) and rounding up gives:

$$u_{m_{scale}} = 0.25 \text{ g} \quad (133)$$

$$u_{\Delta t} = 0.5 \text{ s} \quad (134)$$

Table 6.12: Fluid mass uncertainties

| Source | Model | Description | Value | Notes |
|--------|------------------------|---------------|--------|------------------------|
| Scale | Scout Pro SP6001 [128] | Linearity | ±0.1 g | Manufacturer specified |
| Scale | Scout Pro SP6001 [128] | Repeatability | ±0.2 g | Manufacturer specified |

Table 6.13: Recorded time uncertainties

| Source | Model | Description | Value | Notes |
|---------------|-------|-------------|-------------|-----------|
| Time stoppage | | Human error | ± 0.5 s | estimated |

\dot{m}_{Cooler} was measured at 5 °C since the sink temperature was constant during experiments, and \dot{m}_{Heater} was measured at different temperatures (see Section 2.4.2). At each temperature, four or five (n) samples of m_{scale} and Δt were taken, \dot{m} calculated and averaged over the five samples. The uncertainty for each sample was calculated using equation (132) and the combined uncertainty following equation (113):

$$u_{\dot{m},total} = \frac{1}{n} \left(\sum_{i=1}^n u_{m_i}^2 \right)^{\frac{1}{2}} \quad (135)$$

$$u_{\dot{m},total,cooler} = 1.78 \cdot 10^{-4} \text{ kg/s} \quad (136)$$

$$u_{\dot{m},total,heater} = 1.43 \cdot 10^{-3} \text{ kg/s (max of all temperatures)} \quad (137)$$

C.2 Heat Flow Rates

For the purpose of uncertainty, it will be assumed the heat capacities at the inlet and outlet of the heater are equal, and the error in the heat capacity (Section C.2.3) applies equally at the inlet and outlet. If this was not assumed, the heat capacity error could be significantly different between inlet and outlet, which is unreasonable and would vastly overestimate the uncertainty in the heat flow rate. Thus, the equation for the heat flow rate is:

$$\dot{Q} = \dot{m} c (T_{in} - T_{out}) = \dot{m} c \Delta T \quad (138)$$

The uncertainty propagation for \dot{Q} following equation (111) is:

$$u_{\dot{Q}} = \left(\left(u_{\dot{m}} \frac{\partial \dot{Q}}{\partial \dot{m}} \right)^2 + \left(u_c \frac{\partial \dot{Q}}{\partial c} \right)^2 + \left(u_{\Delta T} \frac{\partial \dot{Q}}{\partial \Delta T} \right)^2 \right)^{\frac{1}{2}} \quad (139)$$

$$u_{\dot{Q}} = ((u_{\dot{m}} c \Delta T)^2 + (u_c \dot{m} \Delta T)^2 + (u_{\Delta T} \dot{m} c)^2)^{\frac{1}{2}} \quad (140)$$

This expression was evaluated for each experimental datapoint, using the values from the table below for the uncertainties. The resulting maximum uncertainties for any datapoint are:

$$u_{\dot{Q}_{cooler}} = 71 \text{ W} \quad (141)$$

$$u_{\dot{Q}_{heater}} = 88 \text{ W} \quad (142)$$

Table 6.14: Heat flow rate uncertainty values

| Cooler | | |
|--|---------------------------|------------------------|
| $u_{\dot{m}} = u_{\dot{m},total,cooler}$ | $1.78 \cdot 10^{-4}$ kg/s | Equation (136) |
| u_c | 95 J/kg K | Equation (145)(146) |
| $u_{\Delta T}$ | 0.71 °C | Equation (144) |
| c | 3770 J/kg K | Following Section |
| $\Delta T, \dot{m}$ | Various | From experimental data |
| Heater | | |
| $u_{\dot{m}} = u_{\dot{m},total,heater}$ | $1.43 \cdot 10^{-3}$ kg/s | Equation (137) |
| u_c | 98 J/kg K | Equation (146) |
| $u_{\Delta T}$ | 0.71 °C | Equation (144) |
| c | Various | From experimental data |
| $\Delta T, \dot{m}$ | Various | From experimental data |

C.2.1 Liquid Temperature Difference

Since

$$\Delta T = T_{in} - T_{out} \quad (143)$$

And both temperatures have the uncertainty of RTD measurements $u_{T_{RTD}}$ (Section B.1), the propagated uncertainty following equation (113) and rounding up is:

$$u_{\Delta T} = (2 u_{T_{RTD}}^2)^{\frac{1}{2}} = 0.71 \text{ °C} \quad (144)$$

C.2.2 Cooler Heat Capacity

To determine c_{cold} , first, the density of the water-ethylene glycol mixture was measured by recording the mass (on a scale) and volume (in a graduated cylinder) of five samples (each around 100 g) and calculating the average density from these. Then, this density was matched with interpolated values of densities of water-ethylene glycol mixtures from [107] to find the mass fraction of ethylene glycol to be 30.2 %. This was used to determine the specific heat of the mixture from the corresponding table in [107], resulting in $c_{cold} = 3770$ J/kg K. All values were measured and taken at 5 °C.

It is difficult to trace the uncertainties in this procedure. There may be uncertainties caused by the volume and mass measurements, the true temperature of the measurements, from averaging and from tabular interpolation. As a conservative estimate, an uncertainty of ± 5 % in the measured mass fraction will be assumed, which corresponds to an uncertainty of ± 2.5 % in c_{cold} by interpolation from [107]. This leads to:

$$u_{c_{cold}} = 95 \text{ J/kg K} \quad (145)$$

C.2.3 Heater Heat Capacity

As discussed in Section 2.4.3 the heat capacity of *Sil 180* as a function of temperature had to be estimated based on a single value and the temperature trend in a comparable fluid. A conservative estimate for the resulting uncertainty is made by taking the difference between the specific heats of the actual fluid, *Sil 180*, and the one which was used for the trend, *SYLTHERM 800*, at the temperature where the properties of both are known (20 °C). This leads to:

$$u_{c_{hot}} = 98 \text{ J/kg K} \quad (146)$$

C.3 Calculated Pressures

C.3.1 Raw Pressures for entire Data Sample

The equations for calculated pressures are given in Table 2.9. The calculated pressures are summations of the measured pressures and other calculated pressures. The uncertainties of all mean pressures are equal, and so are the uncertainties of all dynamic pressures. Equation (113) is used for uncertainty propagation of the instantaneous working space pressures:

$$u_{p_{Exp}} = u_{p_{Com}} = u_{p_{PC}} = u_{p_{CC}} = (u_{p_m}^2 + u_{p_d}^2)^{\frac{1}{2}} = 10.72 \text{ kPa} \quad (147)$$

With $u_{p_m} = 10.13 \text{ kPa}$ and $u_{p_d} = 3.48 \text{ kPa}$ from Appendix B.

For p_{mean} , equation (113) for the sum and equation (117) for the mean of three variables with equal uncertainties can be combined to obtain the uncertainty:

$$u_{p_{mean}} = (u_{p_{atm}}^2 + u_X^2)^{\frac{1}{2}} = 6.19 \text{ kPa} \quad (148)$$

$$u_X = \frac{u_{p_{Exp}}}{\sqrt{3}}$$

With $u_{p_{atm}} = 0.014 \text{ kPa}$ from Appendix B.

The remaining $p_{mean,CC}$ and Δp_{HX} are summations and follow equation (113):

$$u_{p_{mean,CC}} = (u_{p_{atm}}^2 + u_{p_{CC}}^2)^{\frac{1}{2}} = 10.73 \text{ kPa} \quad (149)$$

$$u_{\Delta p_{HX}} = (u_{p_{Exp}}^2 + u_{p_{Com}}^2)^{\frac{1}{2}} = 15.17 \text{ kPa}$$

C.3.2 Cycle Averaged Pressures

With the same logic as for the cycle averaged speed f_θ in Section 0, the uncertainty of the cycle averaged pressures is propagated through the averaging operation following equation (117):

$$u_{p_{Exp,avg}} = u_{p_{Com,avg}} = u_{p_{PC,avg}} = u_{p_{CC,avg}} = \frac{u_{p_{Exp}}}{\sqrt{n_{cyc}}} = 2.8 \text{ kPa} \quad (150)$$

$$u_{p_{d2,avg}} = \frac{u_{p_{d2}}}{\sqrt{n_{cyc}}} = 0.9 \text{ kPa} \quad (151)$$

With $n_{cyc} = 15$, $u_{p_{Exp}}$ from Section 0, and $u_{p_{d2}}$ from Section B.4.

C.4 Crankshaft Angle Increment

For calculating engine speed, increments of θ are calculated. θ is subject to the uncertainties listed in Section B.6. For the angle increment ($\Delta\theta = \theta_{mono,i+20} - \theta_{mono,i-20}$), it is assumed that the uncertainty from sensor alignment can be neglected as the misalignment will cancel out when calculating the difference between two angles. The remaining uncertainties, following equation (110) and rounding up, give:

$$u_{\theta_{mono}} = 1.1^\circ \quad (152)$$

Thus, the combined uncertainty following equation (113) and rounding up is:

$$u_{\Delta\theta} = (2 u_{\theta_{mono}}^2)^{\frac{1}{2}} = 1.6^\circ \quad (153)$$

C.5 Speed

C.5.1 Raw speed for entire data sample (f_{raw})

The equation for raw instantaneous engine speed is (Section 2.7.5):

$$f_{raw,i} = \frac{\theta_{mono,i+20} - \theta_{mono,i-20}}{t_{VC,i+20} - t_{VC,i-20}} * \frac{60 \text{ rpm}}{360 \text{ }^\circ/\text{s}} = \frac{\Delta\theta}{\Delta t_{VC}} * \frac{1 \text{ rpm}}{6 \text{ }^\circ/\text{s}} \quad (154)$$

Equation (115) is used for uncertainty propagation, using the uncertainties in the table below. The following uncertainty was calculated for all experimental datapoints, and the maximum is given here:

$$u_{f_{raw}} = f_{raw} \left(\left(\frac{u_{\Delta t_{VC}}}{\Delta t_{VC}} \right)^2 + \left(\frac{u_{\Delta\theta}}{\Delta\theta} \right)^2 \right)^{\frac{1}{2}} = 12.7 \text{ rpm} \quad (155)$$

Table 6.15: Speed uncertainty values

| | | |
|---------------------|--------|---|
| $u_{\Delta t_{VC}}$ | 1.5 ms | Equation (156) |
| $u_{\Delta\theta}$ | 1.6° | Equation (153)(146) |
| Δt_{VC} | 40 ms | 40 increments at 1000 Hz sampling frequency |
| $\Delta\theta$ | varies | $= f_{raw} * \frac{1 \text{ rpm}}{6 \text{ }^\circ/\text{s}} * \Delta t_{VC}$ |
| f_{raw} | varies | From experimental data |

The uncertainty in Δt_{VC} follows from Section B.7 and equation (113), rounding up:

$$u_{\Delta t_{VC}} = (2 u_{t_{VC}}^2)^{\frac{1}{2}} = 1.5 \text{ ms} \quad (156)$$

C.5.2 Speed for each cycle angle (f_θ)

As discussed in Section 2.7.6, the speed data f_{raw} that contains several engine cycles is averaged for each crank angle degree. The minimum number of cycles recorded in each sample is $n_{cyc} = 15$ (from Section 0). Then, following equation (117) the uncertainty propagation for f_θ , obtained as the mean of n_{cyc} cycles, is:

$$u_{f_\theta} = \frac{u_{f_{raw}}}{\sqrt{n_{cyc}}} = 3.3 \text{ rpm} \quad (157)$$

C.5.3 Average Speed (f)

Following Section 0, the uncertainty calculated above also applied to the cycle averaged speed:

$$u_f = u_{f_\theta} = 3.3 \text{ rpm} \quad (158)$$

C.6 Shaft Power

The equation for shaft power from Section 2.7.7:

$$P_{shaft} = \tau f * \frac{2\pi \text{ rad/s}}{60 \text{ rpm}} \quad (159)$$

Equation (115) is used for uncertainty propagation, using the uncertainties in the table below. The following uncertainty was calculated for all experimental datapoints, and the maximum is given here:

$$u_{P_{shaft}} = P_{shaft} \left(\left(\frac{u_{\tau}}{\tau} \right)^2 + \left(\frac{u_f}{f} \right)^2 \right)^{\frac{1}{2}} = 0.81 \text{ W} \quad (160)$$

Table 6.16: Shaft power uncertainty values

| | | |
|-------------|-----------|------------------------|
| u_{τ} | 0.0325 Nm | Equation (122) |
| u_f | 3.3 rpm | Equation (158) |
| τ | varies | From experimental data |
| f | varies | From experimental data |
| P_{shaft} | varies | From experimental data |

C.7 Thermal Efficiency

The equation for thermal efficiency from Section 2.7.7:

$$\eta_{shaft} = P_{shaft} / \dot{Q}_{Heater} \quad (161)$$

Equation (115) is used for uncertainty propagation, using the uncertainties in the table below. The following uncertainty was calculated for all experimental datapoints, and the maximum is given here:

$$u_{\eta_{shaft}} = \eta_{shaft} \left(\left(\frac{u_{P_{shaft}}}{P_{shaft}} \right)^2 + \left(\frac{u_{\dot{Q}_{heater}}}{\dot{Q}_{heater}} \right)^2 \right)^{\frac{1}{2}} = 0.34 \% \quad (162)$$

Table 6.17: Thermal efficiency uncertainty values

| | | |
|------------------------|--------|------------------------|
| $u_{P_{shaft}}$ | 0.81 W | Equation (160) |
| $u_{\dot{Q}_{heater}}$ | 88 W | Equation (142) |
| η_{shaft} | varies | From experimental data |
| P_{shaft} | varies | From experimental data |
| \dot{Q}_{heater} | varies | From experimental data |

C.8 Indicated Work

Indicated work is calculated by numerical integration of pressure and volume increment data as seen in Section 2.7.9. Propagation of uncertainties through this operation is complex and would overestimate the total uncertainty if constant uncertainties are assumed for each pressure value and volume increment. To avoid this, the uncertainty in W_{ind} is determined following a ‘worst-case’ approach along the lines of Gordon et al. [129]. For indicated work, this means that the uncertainties in pressure and volume are applied to the code that determines the volume variations and calculates W_{ind} in a way that realistically maximizes the resulting change in W_{ind} . Stumpf [30] did a similar analysis for indicated work. The method is outlined in the following sections. The resulting uncertainty in W_{ind} was between 15.7 % and 23.1 % of W_{ind} , depending on the datapoint. The highest absolute uncertainty was 2.1 J. A plot showing the uncertainty for all datapoints is given in Section 4.9.2. The Figure below shows the effect of the combined uncertainties on a sample indicator curve. The curves with the largest and smallest possible W_{ind} were calculated for each datapoint. Both curves had an almost equal relative deviation in W_{ind} from the nominal curve.

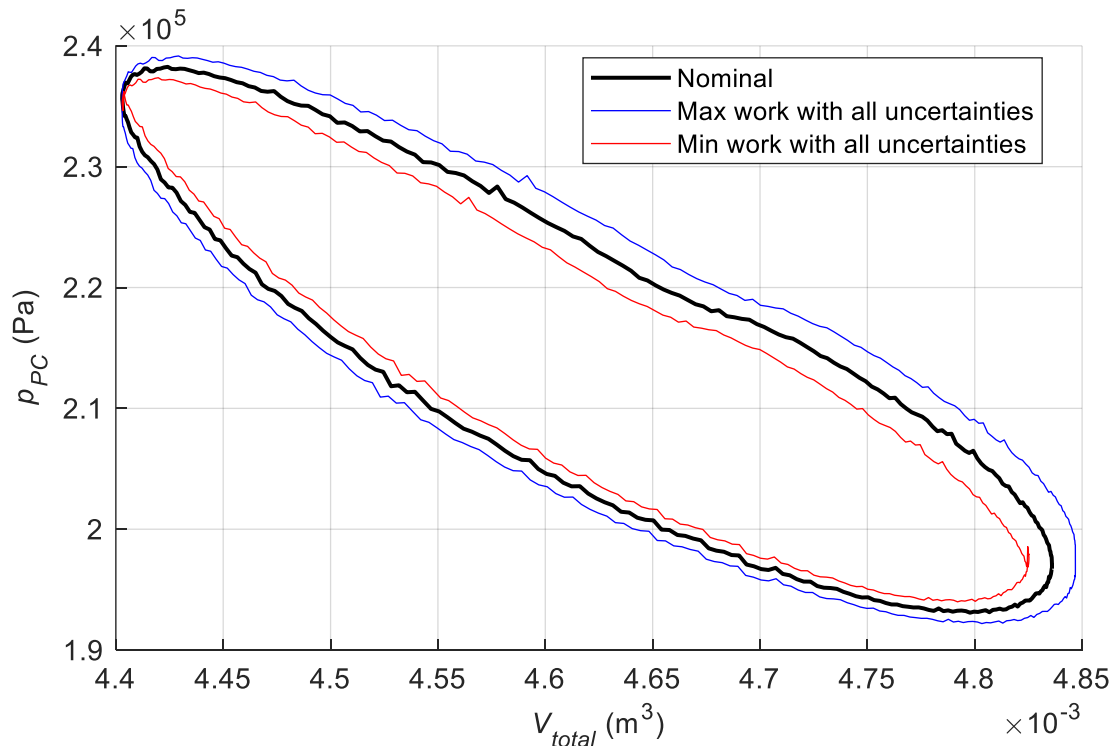


Figure 6.3: Effect of all pressure and volume uncertainties combined on indicator diagram

C.8.1 Pressure Uncertainty

The pressure variable used is $p_{d2,avg}$ and its uncertainty was determined in Section 0 as:

$$u_{p_{d2,avg}} = 0.9 \text{ kPa} \quad (163)$$

This uncertainty is applied to the pressure data for each experimental datapoint so that it maximizes and minimizes W_{ind} , to test the greatest positive and negative change in W_{ind} caused by this uncertainty. This is shown in the sample indicator diagram below.

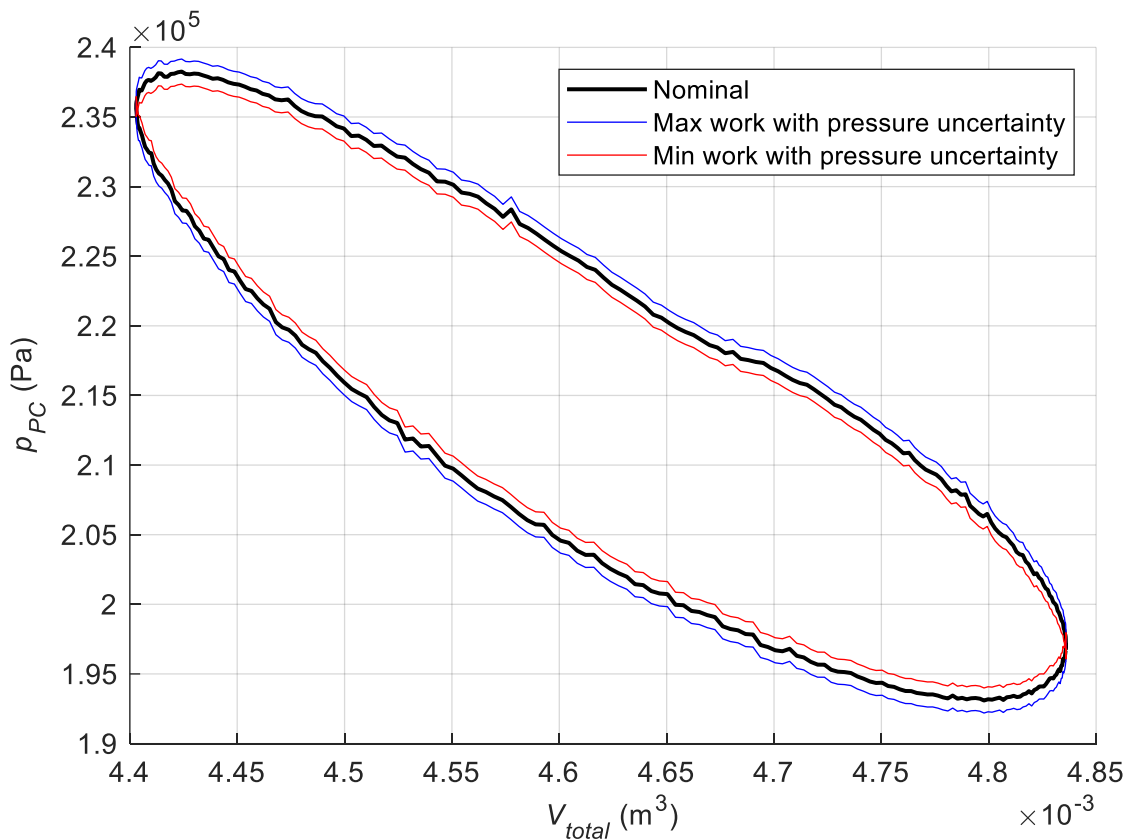


Figure 6.4: Effect of pressure uncertainty on indicator diagram

For maximum W_{ind} the uncertainty is added to the expansion (top) part of the curve and subtracted from the compression (bottom) part. For minimum W_{ind} the opposite is done. The result is a vertical stretching of the indicator curve.

C.8.2 Volume Uncertainty

The only component causing the volume change that extracts work is the power piston, hence only the uncertainties in the power piston's geometry and motion need to be considered for the uncertainty in volume. Uncertainties in the volume increments could come from inaccuracies of the piston diameter, of the mechanism, which is represented here as a stroke uncertainty, and from the uncertainty in crankshaft angle measurement. The table below lists the values considered.

Table 6.18 –Sources of volume uncertainties

| Source | Value | Notes |
|---|--------------------------------|-------------|
| Power Piston Diameter / Bore (manufacturing and wear) | ± 0.5 mm | Estimated |
| Power Piston Stroke (manufacturing and wear) | ± 1 mm | Estimated |
| Crank angle Uncertainty | $u_{\theta} = \pm 2.3^{\circ}$ | Section B.6 |

These values were applied to the volume calculation code similarly to the pressure uncertainty in the previous section. Figure 6.5 shows the effect of the uncertainties in piston bore and stroke. It can be seen that an increased bore and stroke will increase the maximum volume and stretch the curve horizontally, while a reduced bore and stroke do the opposite. Figure 6.6 shows the effect of the crank angle uncertainty. Adding it to the angle data increases the indicated work while subtracting it does the opposite.

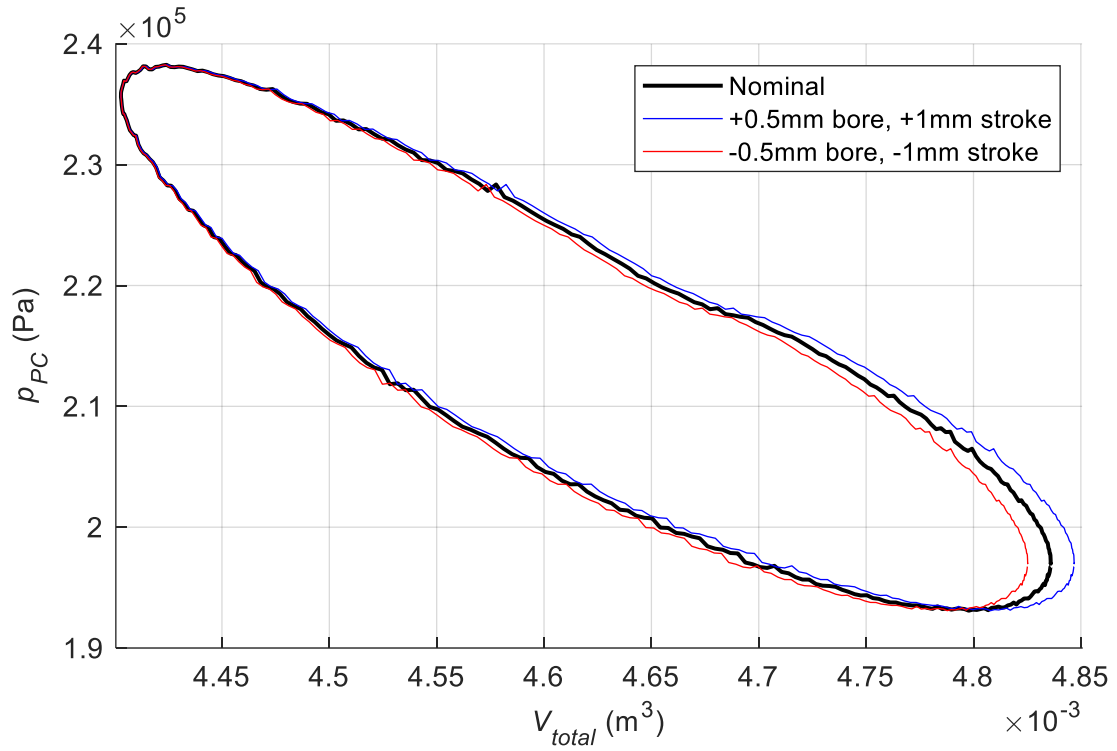


Figure 6.5: Effect of power piston bore and stroke uncertainty on indicator diagram

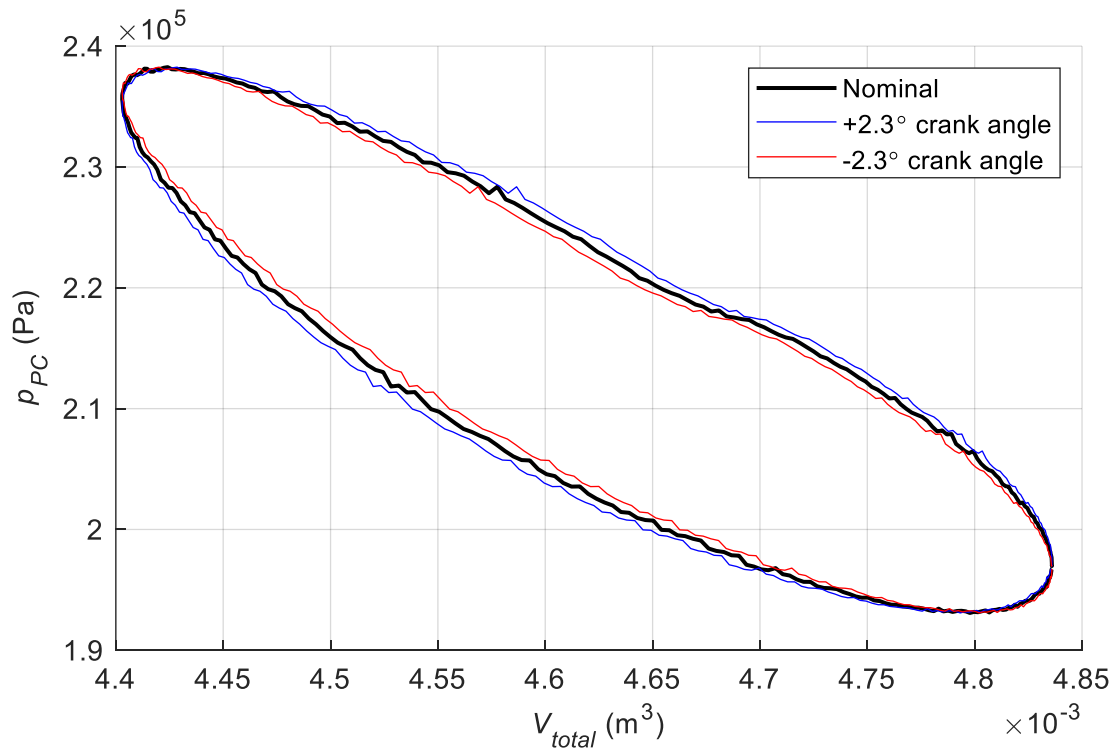


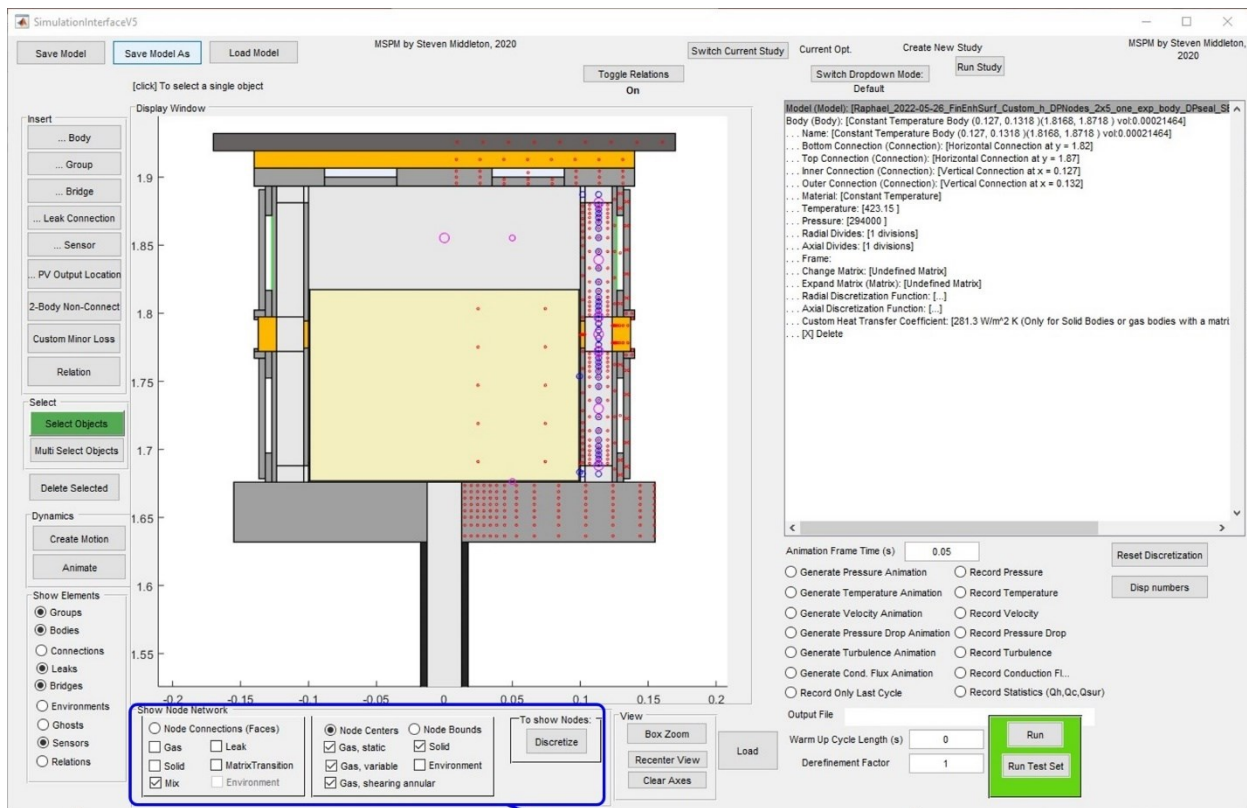
Figure 6.6: Effect of crank angle uncertainty on indicator diagram

Appendix D.Improvements Made to *MSPM* Model

In addition to the custom heat transfer coefficients described in Section 3.6, other changes were made to the *MSPM* code and GUI to add functionality or correct model discretization and results. Constructing a working model of the *Raphael* engine was only possible after implementing the discretization for its heat exchangers. The headings of Sections D.4 to D.11 each refer to a different MATLAB code file. All changes are commented in the code.

D.1 GUI Functionality

The original user interface was able to display all node centerpoints at once as red circles and all faces at once as green lines. This allowed a coarse look at the discretized model, but it was not possible to analyze the mesh in detail because different types of nodes and faces could not be differentiated. To improve this, the GUI was equipped with the ability to render all types of nodes and faces individually and in different styles so they can be told apart. Faces appear as green lines (which could be configured into different colours) and for nodes, their centerpoints and/or outlines (bounds) can be shown in colours depending on node type. The figure below shows the updated GUI window and highlights the added options that allow the user to choose which elements are rendered. This functionality is showcased in Section 3.4.1. It is particularly useful for the implementation and troubleshooting of discretization code and to analyze the validity of a mesh.



Detailed Mesh View

Figure 6.7: Updated GUI highlighting new mesh viewing options.

D.2 Issues with Mechanism Code

The code defining the motion and friction of different mechanisms is in 'LinRotMechanism.m'. No mechanism with friction has so far been implemented and debugged completely. The code for the Slider Crank mechanism is there but requires fixing of errors. For this, the kinematics from which the code was derived should be reviewed.

D.3 Additional Test Set Parameters

Added the following parameters that can be defined in a test set to modify the model automatically for each test:

- 'h_custom_Source' and 'h_custom_Sink' for heat transfer coefficients applied to source and sink bodies, and nodes in heat exchangers (see Section 3.6)
- 'X_Scale': scales diameter (x coordinate) of all bodies, and can scale heat exchanger proportionally. Used in Chapter 5.
- 'Gas': Modifies working gas of entire model to compare different gases easily. Used in Chapter 5.
- 'Reg_dw' and 'Reg_Porosity': Modifies properties of 'Woven Screen' or 'Random Fiber' matrixes. Used in Section 5.4.2 to optimize regenerator.
- 'minCycles': Defines minimum number of engine cycles to simulate before it can be declared steady state. Can be used to prevent simulation from declaring steady state prematurely.

D.4 Model.m

Function 'discretize':

- Corrected the signs assigned to environment heat flow to correct the sign of the 'statistics.ToEnvironment' output. Validated that sign is correct for positive and negative heat flow cases.

Function ‘show’:

- Added code to obtain mesh information and render nodes and faces as described in Section D.1.

Function ‘Run’:

- Added ‘TestSetStatistics’ file that records node and face counts, final speed and shaft power, number of simulated cycles, and computation time for each run in a test set
- Added an animation of the Reynolds number that is output with every run started from a test set. GUI option still needs to be added to generate this animation when running single test.

D.5 Simulation.m

Function ‘Run’:

- Fixed that source and sink temperatures defined in a test set were not actually applied to the model, by updating temperatures after discretization.
- Fixed application of torque load to keep speed steady when running with variable speed and steady state convergence enabled to test in-cycle speed variations. Used in Section 4.6.
- Added convergence plot displayed during simulation showing shaft power, speed and ‘power factor’ (convergence parameter)
- Added workaround to error occurring in gas loop solving code with some particular numbers or configurations of loops. User is notified if the workaround is used, and should change the model to prevent this. Source of error should be investigated.

Function ‘Nusselt’:

- Corrected the weighing function between laminar and turbulent Nusselt numbers to match documentation by model author [33].

D.6 Matrix.m

- ‘Woven Screen’ matrix: Corrected laminar Nusselt number correlation to match source from *Sage* model [66]
- ‘Fin Enhanced Surface’ heat exchanger:
 - Reworked its unfinished code implementation, correcting errors in discretization scheme.
 - Used successfully for model of *Raphael* engine (Section 3.4).
 - Empirical correlations chosen by model author should be verified against literature.
- ‘Tube Bank Internal’ heat exchanger:
 - Replaced the simplified conduction math, which was treating tube walls as flat walls, with more accurate annular conduction.
 - Added support for ‘h_custom’ to be applied to tube outer surface.
- Added code to update all matrix properties and correlations before discretization so that changes made to matrix properties by test set (e.g. ‘Reg_Porosity’) are registered.

D.7 Node.m

The following corrections removed significant errors in parameters that affect the flow in heat exchanger and regenerator matrixes.

- Function ‘calcData’: Corrected calculation of gas volume for gas nodes within a matrix. Volume was calculated too small by factor of the matrix porosity.
- Function ‘recalc_Dh’: Corrected calculation of hydraulic diameter for gas nodes within a matrix. It was being underestimated because gas surface area was overestimated.

D.8 NodeContact.m

Function 'getConductance':

- Added code to apply custom heat transfer coefficient 'h_custom' to heat conduction equations. For a body that has 'h_custom' that is not 'NaN', the coefficient is applied to all solid faces that connect to a node of that body.
- Corrected error in conductance calculation for linear conduction to environment. Verified that heat loss to environment is now correct compared to analytical solution.

D.9 Face.m

- Function 'calcData': Fixed calculation of solid face conductance to use correct thermal conductivity value.

D.10 Material.m

- Added Polyester (PET), Polyetherimide (PEI/ Ultem), *SIL 180* oil (as solid), and 'Rigid Polyurethane Foam, General Plastics FR-4718' materials to model *Raphael* engine
- Corrected property correlations for Hydrogen gas

D.11 Sensor.m

- Added Reynolds number (Re) to options for sensor variables, validated correctness of Re data
- Fixed error with turbulence sensor

Appendix E. Results of Model Sensitivity Study for Liquid Heat Transfer Coefficients

The following plots show the results of varying the liquid heat transfer coefficients h_{source} and h_{sink} for both the 'No_Seal' and 'With_Seal' models. The observed output variables are indicated work W_{ind} , source heat flow rate \dot{Q}_{source} and sink heat flow rate \dot{Q}_{sink} . Results from two engine setpoints are displayed as RSS deviation (indicating scale of deviation) and difference in deviation (DD, indicating consistency between setpoints).

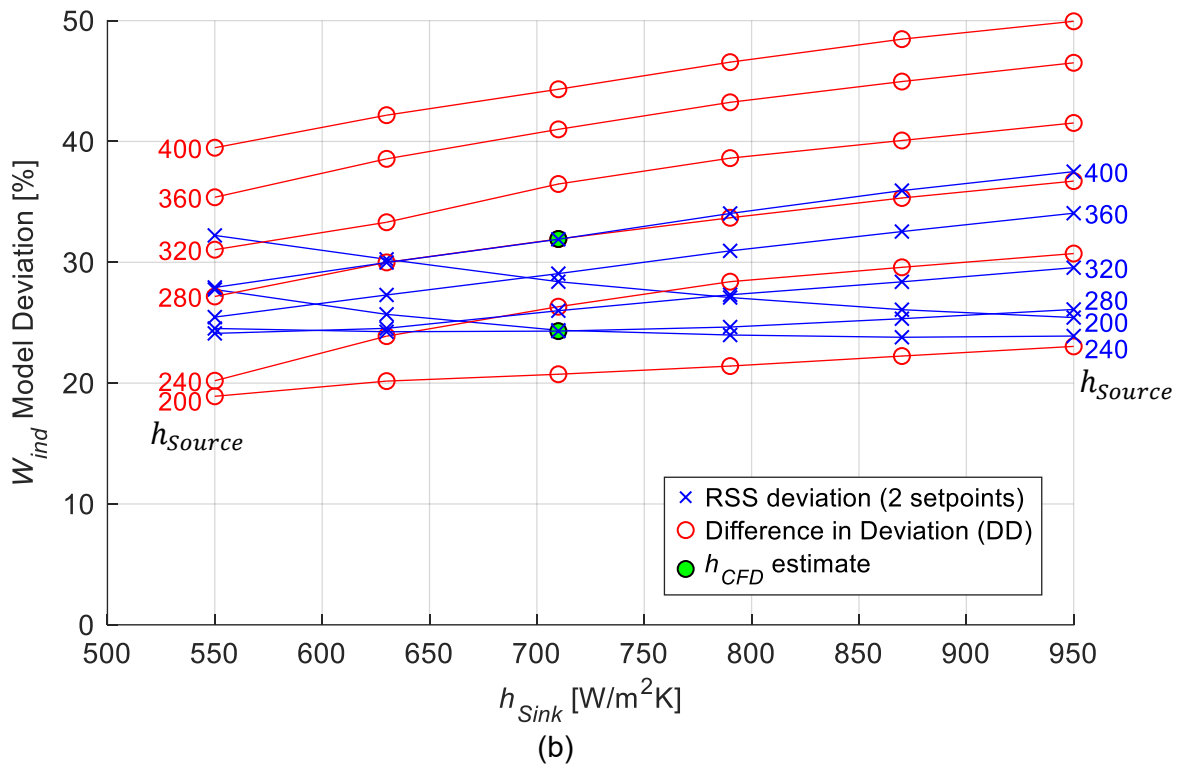
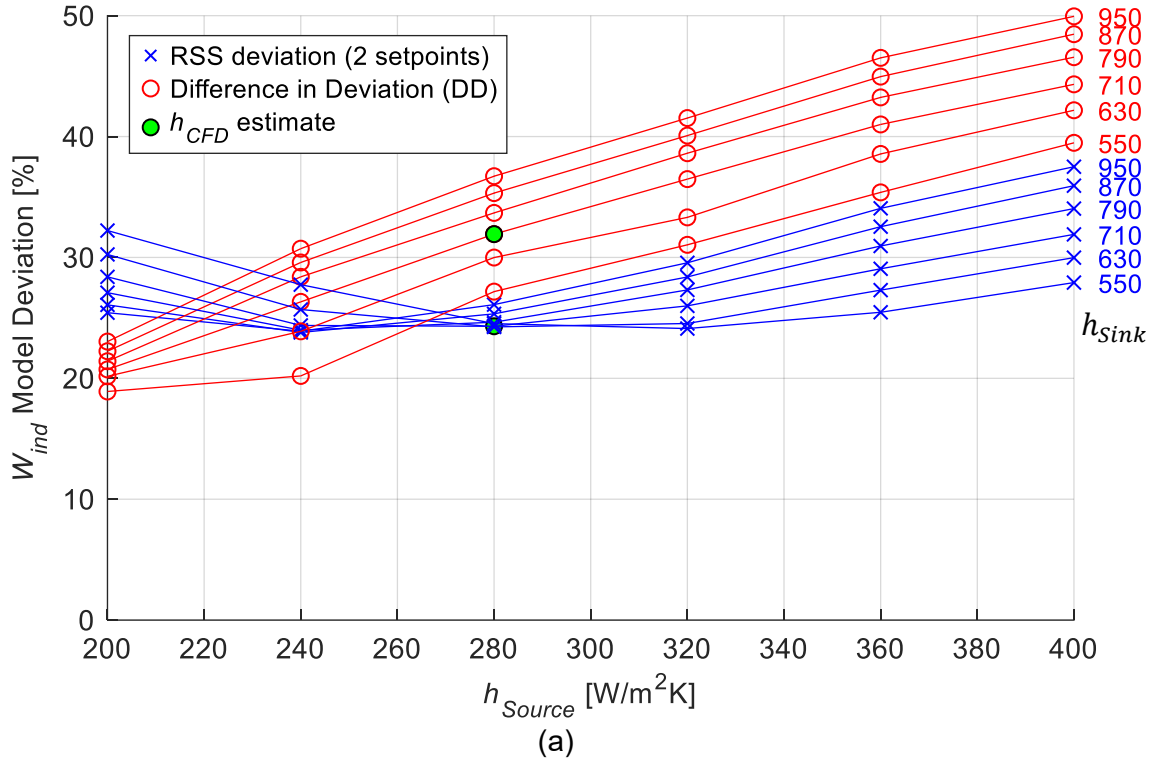


Figure 6.8: For model version 'No_Seal'. RSS deviation in W_{ind} from two setpoints, and difference in deviation (DD) between setpoints, over the source and sink liquid heat transfer coefficients. (a) trend over h_{source} with lines of equal h_{sink} annotated, (b) trend over h_{sink} with lines of equal h_{source} annotated.

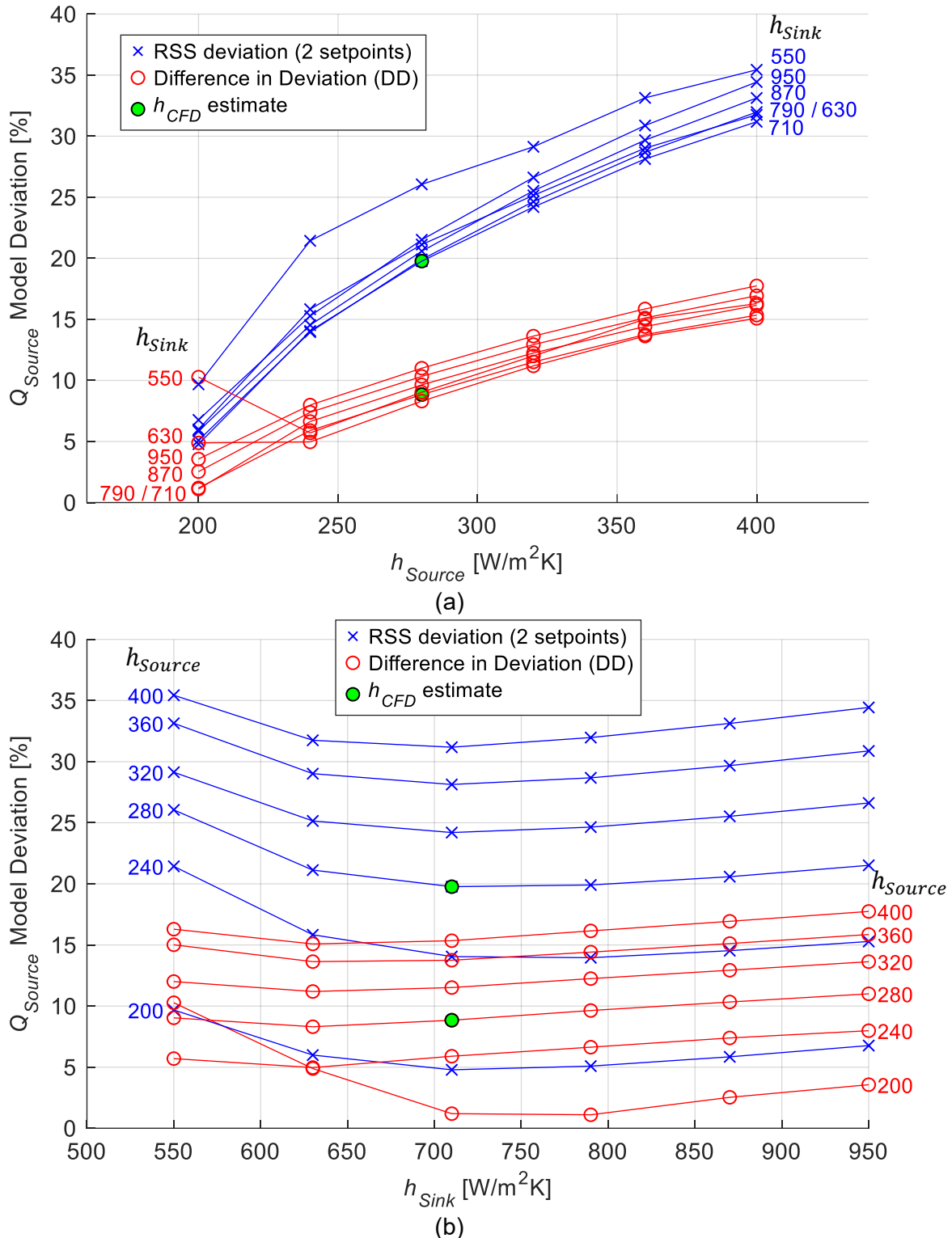


Figure 6.9: For model version 'No_Seal'. RSS deviation in \dot{Q}_{Source} from two setpoints, and difference in deviation (DD) between setpoints, over the source and sink liquid heat transfer coefficients. (a) trend over h_{Source} with lines of equal h_{Sink} annotated, (b) trend over h_{Sink} with lines of equal h_{Source} annotated.

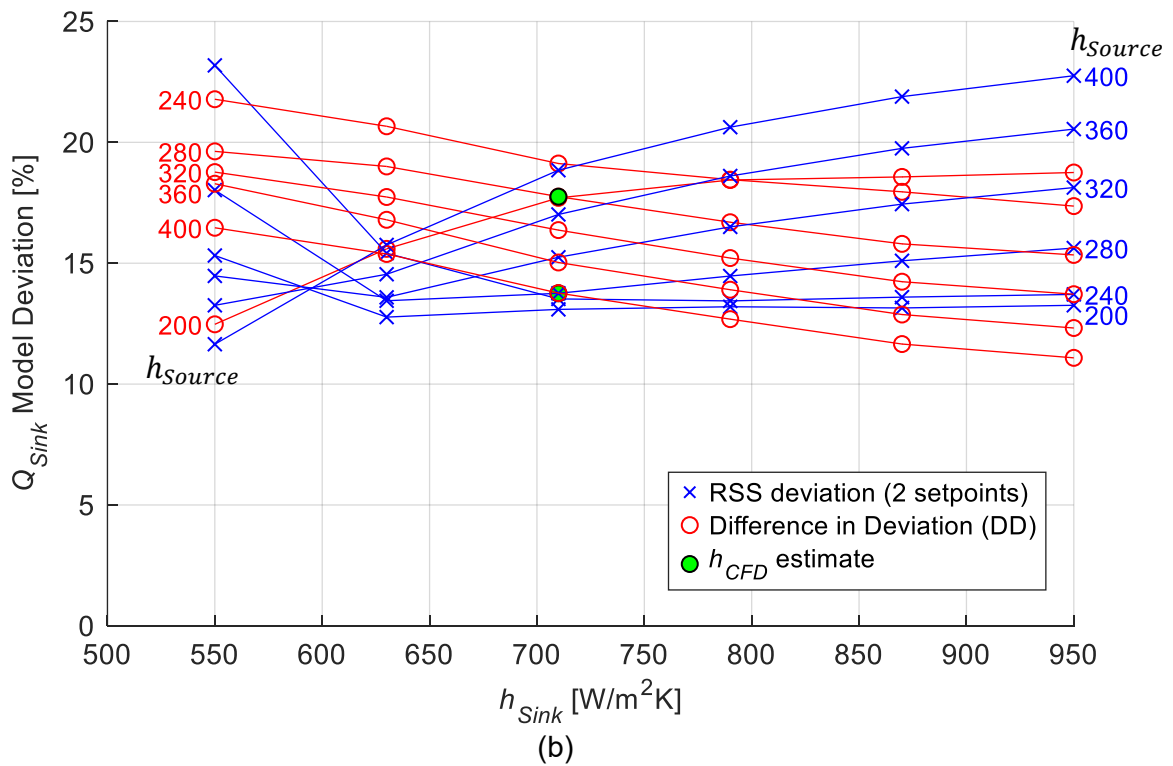
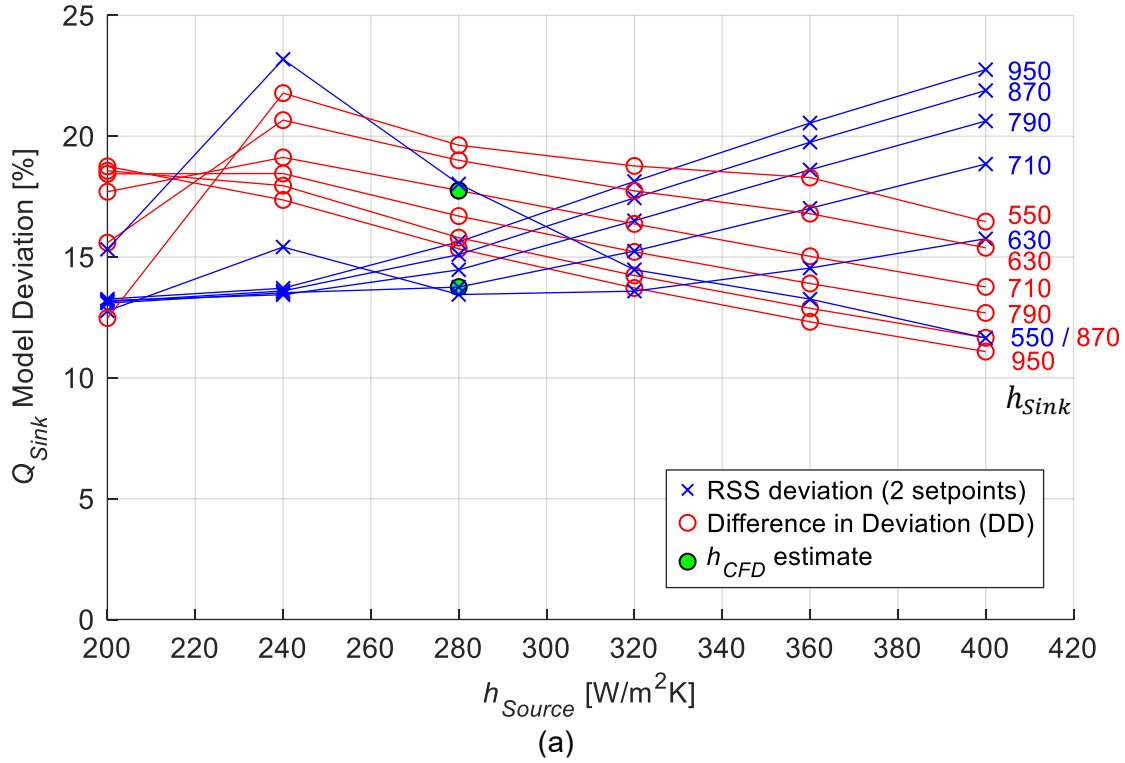


Figure 6.10: For model version 'No_Seal'. RSS deviation in \dot{Q}_{Sink} from two setpoints, and difference in deviation (DD) between setpoints, over the source and sink liquid heat transfer coefficients. (a) trend over h_{Source} with lines of equal h_{Sink} annotated, (b) trend over h_{Sink} with lines of equal h_{Source} annotated.

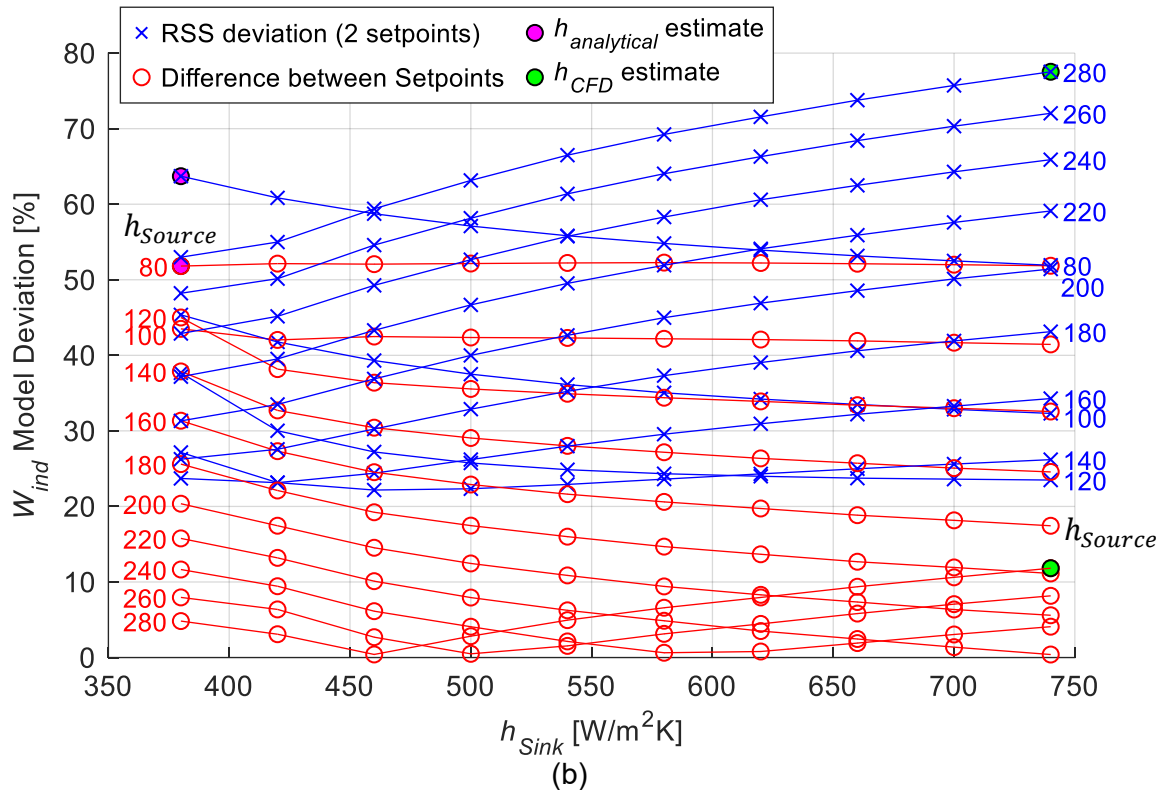
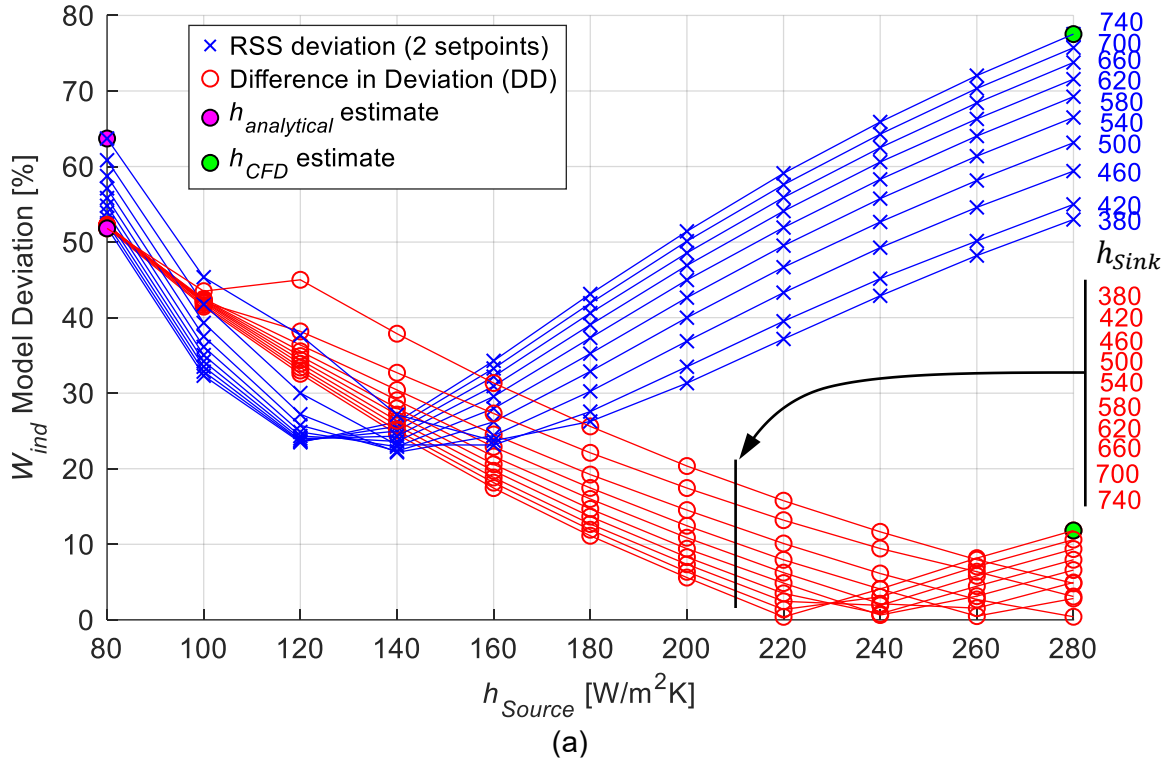


Figure 6.11: For model version 'With_Seal'. RSS deviation in W_{ind} from two setpoints, and difference in deviation (DD) between setpoints, over the source and sink liquid heat transfer coefficients. (a) trend over h_{Source} with lines of equal h_{Sink} annotated, (b) trend over h_{Sink} with lines of equal h_{Source} annotated.

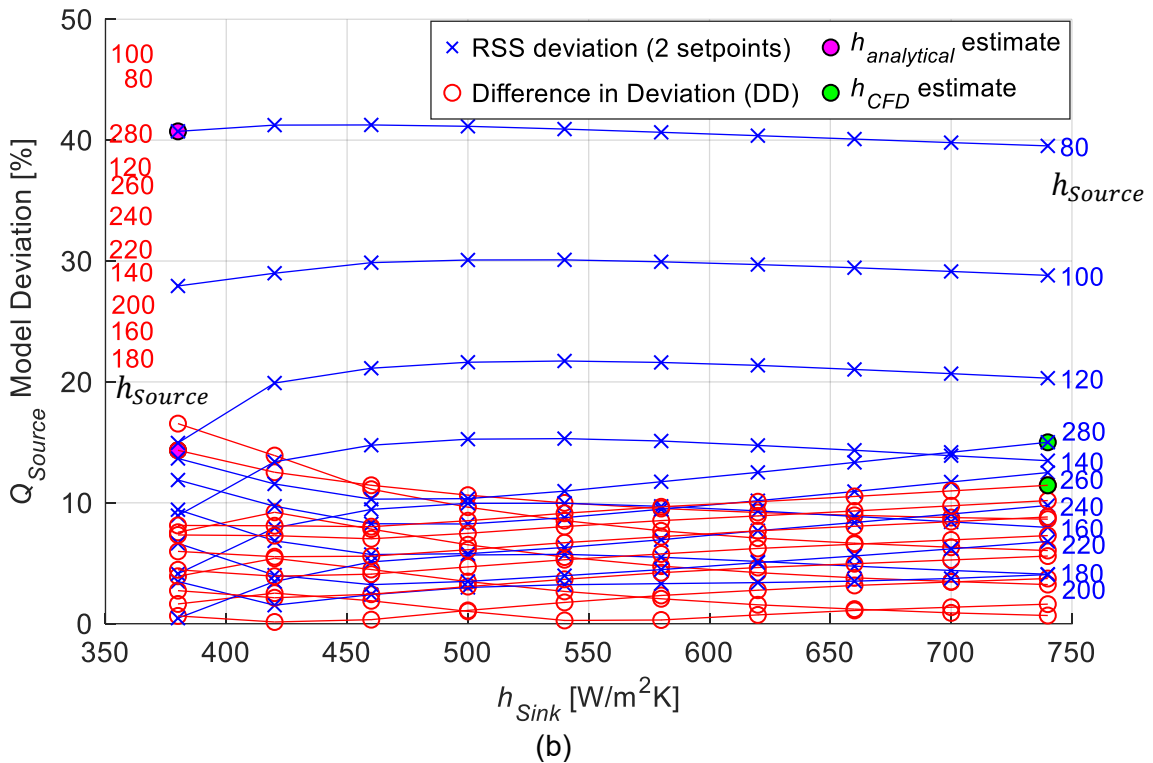
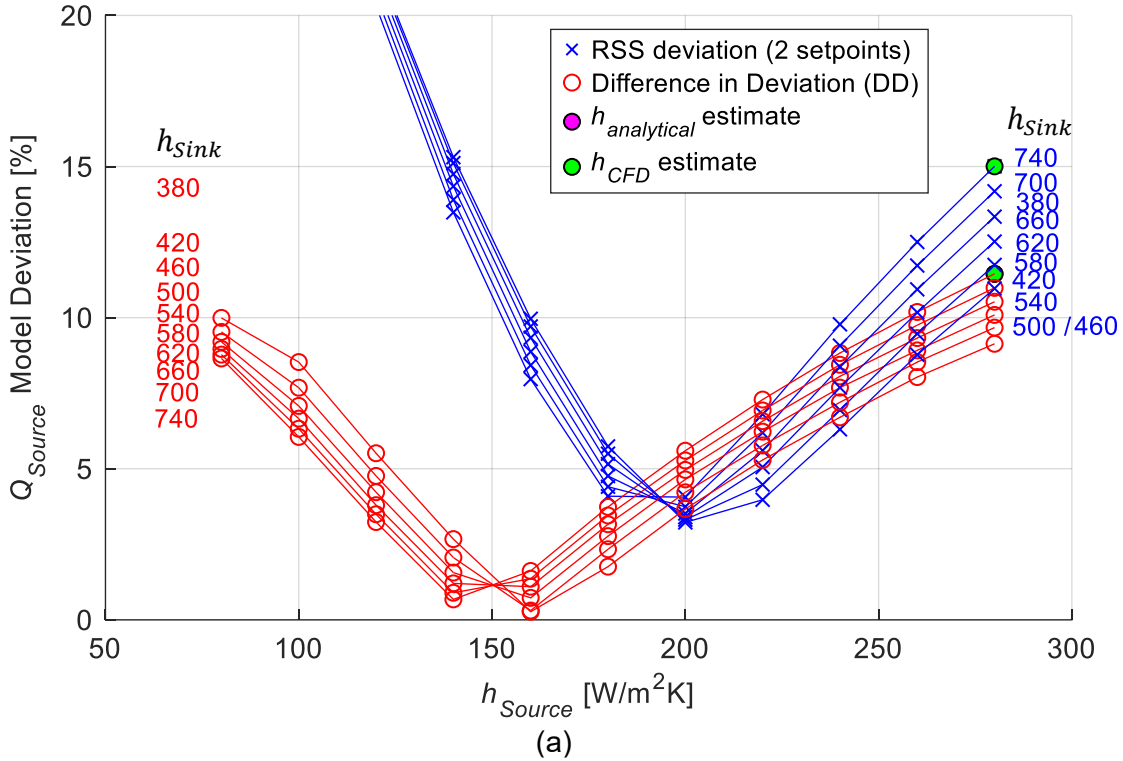


Figure 6.12: For model version 'With_Seal'. RSS deviation in \dot{Q}_{Source} from two setpoints, and difference in deviation (DD) between setpoints, over the source and sink liquid heat transfer coefficients. (a) trend over h_{Source} with lines of equal h_{Sink} annotated (cropped to show minimum), (b) trend over h_{Sink} with lines of equal h_{Source} annotated.

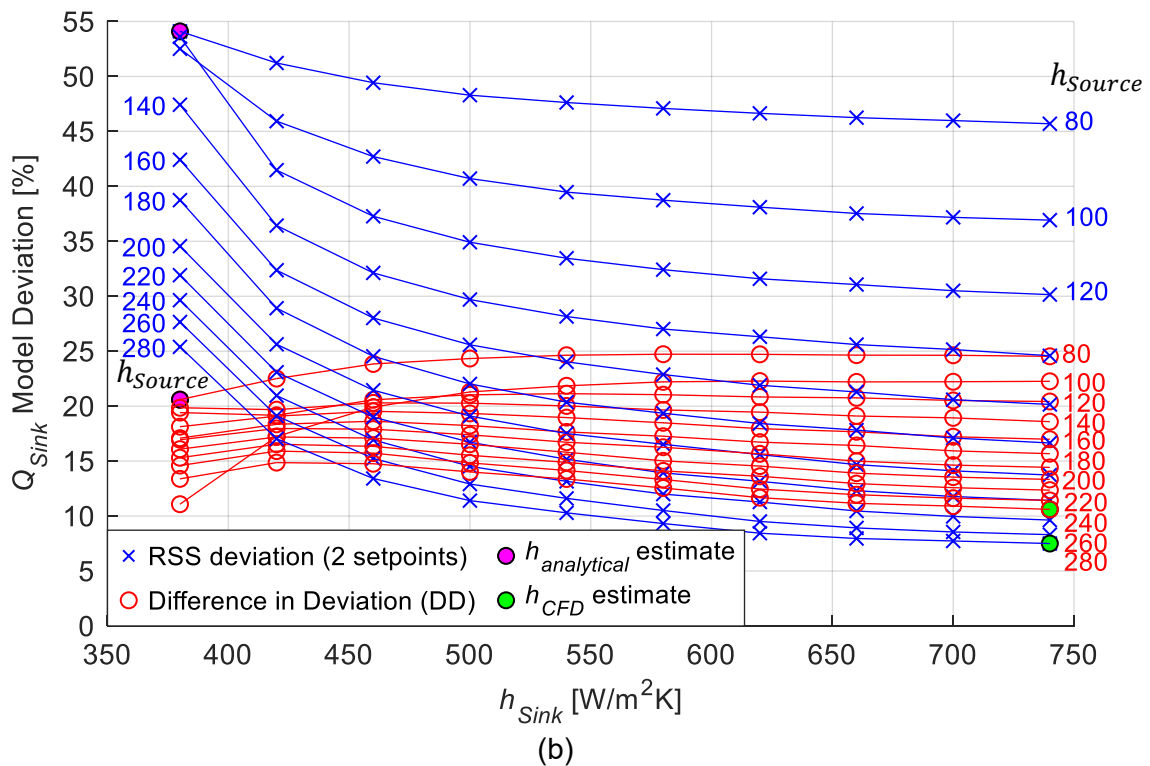
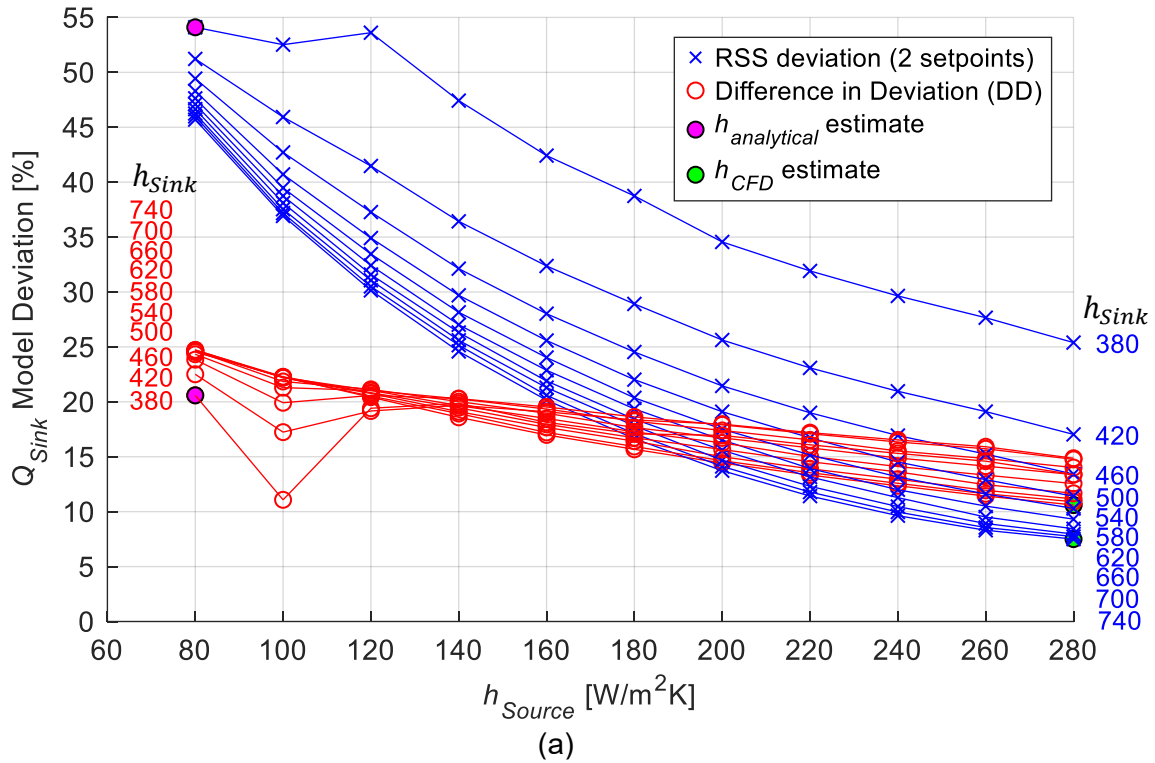
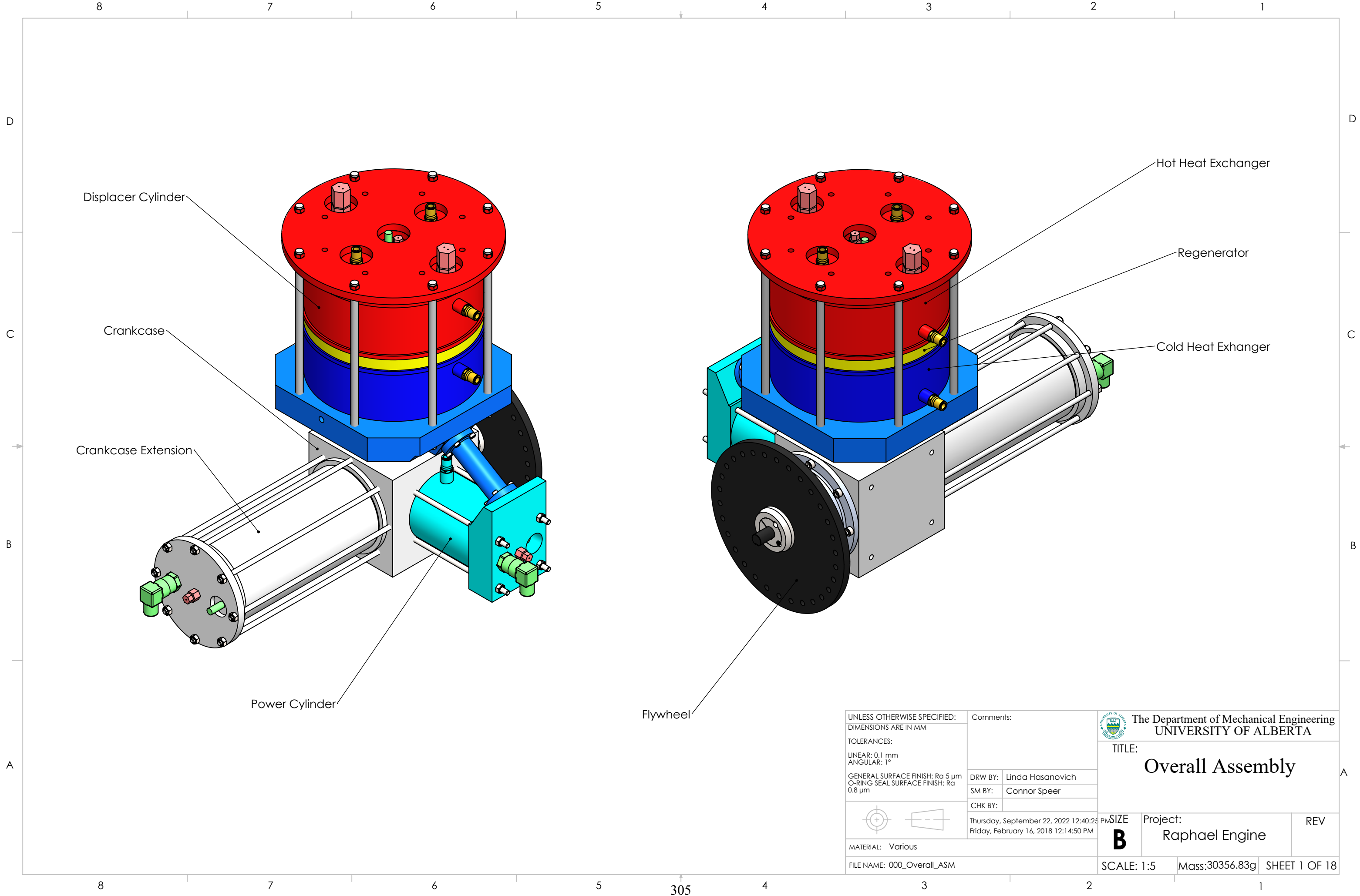


Figure 6.13: **For model version 'With_Seal'**. RSS deviation in \dot{Q}_{Sink} from two setpoints, and difference in deviation (DD) between setpoints, over the source and sink liquid heat transfer coefficients. (a) trend over h_{Source} with lines of equal h_{Sink} annotated, (b) trend over h_{Sink} with lines of equal h_{Source} annotated.

Appendix F. Drawing Package of *Raphael* Engine

The provided drawings of the experimental LTDSE *Raphael* include assembly drawings of the entire engine and more detailed drawings up to the part level of the heat exchangers. The layout and all components of the engine are displayed, and the dimensions of the heat exchanger geometry can be read and reproduced from these drawings. The drawings were prepared by Linda Hasanovich. The final drawing shows the power piston seal. Some seal dimensions were redacted because the seal design is proprietary.



Displacer Cylinder

Crankcase

Crankcase Extension

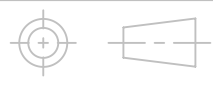
Power Cylinder

Flywheel

Hot Heat Exchanger

Regenerator

Cold Heat Exchanger

| | | | |
|---|--|--|---|
| UNLESS OTHERWISE SPECIFIED: DIMENSIONS ARE IN MM | | Comments: | |
| TOLERANCES: LINEAR: 0.1 mm ANGULAR: 1° | | DRW BY: Linda Hasanovich |  The Department of Mechanical Engineering UNIVERSITY OF ALBERTA |
| GENERAL SURFACE FINISH: Ra 5 µm O-RING SEAL SURFACE FINISH: Ra 0.8 µm | | SM BY: Connor Speer | |
|  | | CHK BY: | |
| MATERIAL: Various | | Thursday, September 22, 2022 12:40:25 PM | SIZE B |
| FILE NAME: 000_Overall_ASM | | Friday, February 16, 2018 12:14:50 PM | Project: Raphael Engine |
| | | SCALE: 1:5 | REV Mass:30356.83g SHEET 1 OF 18 |

| | |
|---|--|
|  The Department of Mechanical Engineering UNIVERSITY OF ALBERTA | |
| TITLE: <h1>Overall Assembly</h1> | |
| SIZE B | Project: Raphael Engine |
| SCALE: 1:5 | REV Mass:30356.83g SHEET 1 OF 18 |

8

7

6

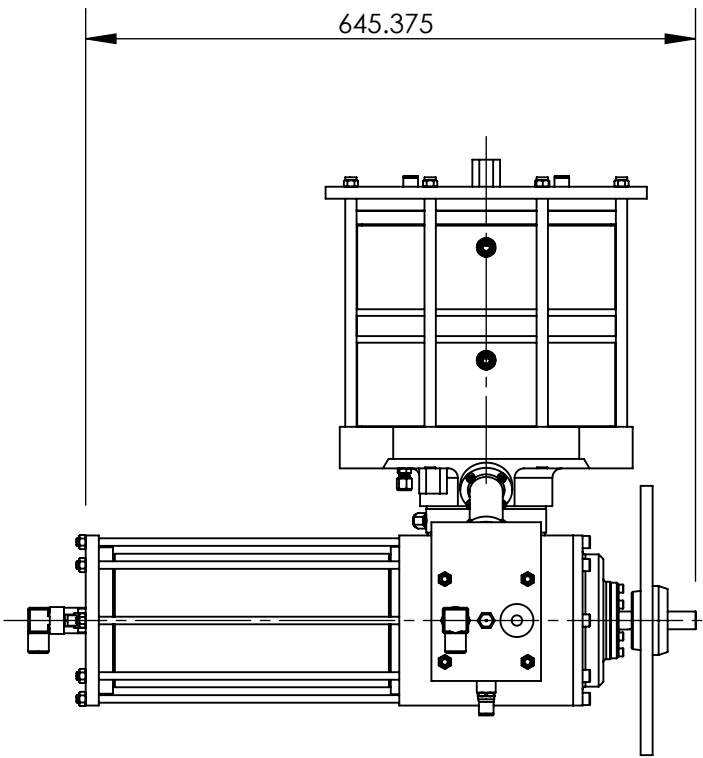
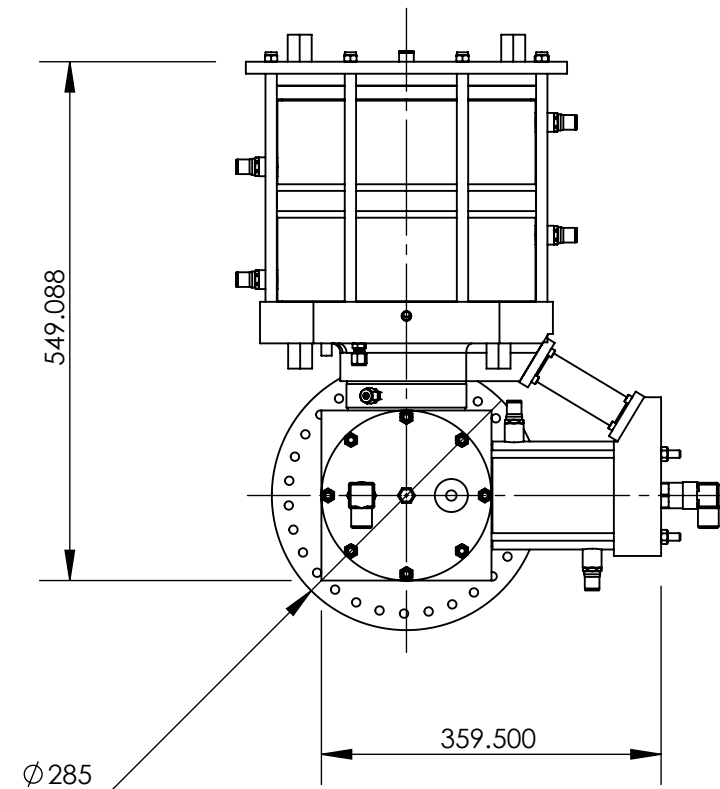
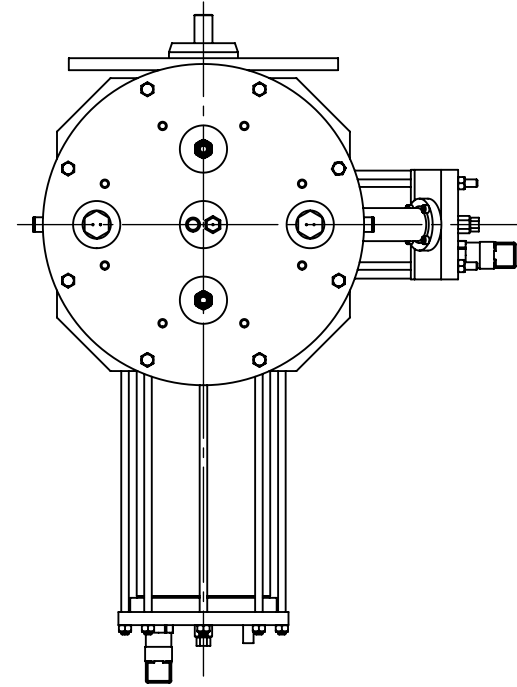
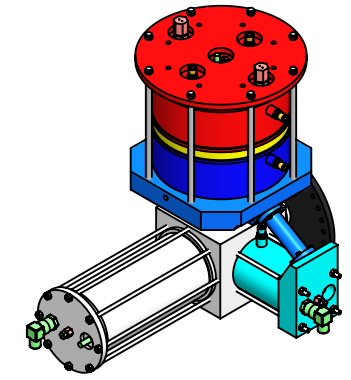
5

4

3

2

1



| | | | |
|---|---|------------------|---|
| UNLESS OTHERWISE SPECIFIED: DIMENSIONS ARE IN MM TOLERANCES: LINEAR: 0.1 mm ANGULAR: 1° GENERAL SURFACE FINISH: Ra 5 µm O-RING SEAL SURFACE FINISH: Ra 0.8 µm | Comments: | |  The Department of Mechanical Engineering UNIVERSITY OF ALBERTA |
| | DRW BY: Linda Hasanovich SM BY: Connor Speer CHK BY: | | |
| MATERIAL: Various FILE NAME: 000_Overall_ASM | Thursday, September 22, 2022 12:40:25 PM Friday, February 16, 2018 12:14:50 PM | SIZE B | Project: Raphael Engine |
| | | SCALE: 1:8 | Mass: 30356.83g SHEET 2 OF 18 |

8

7

6

5

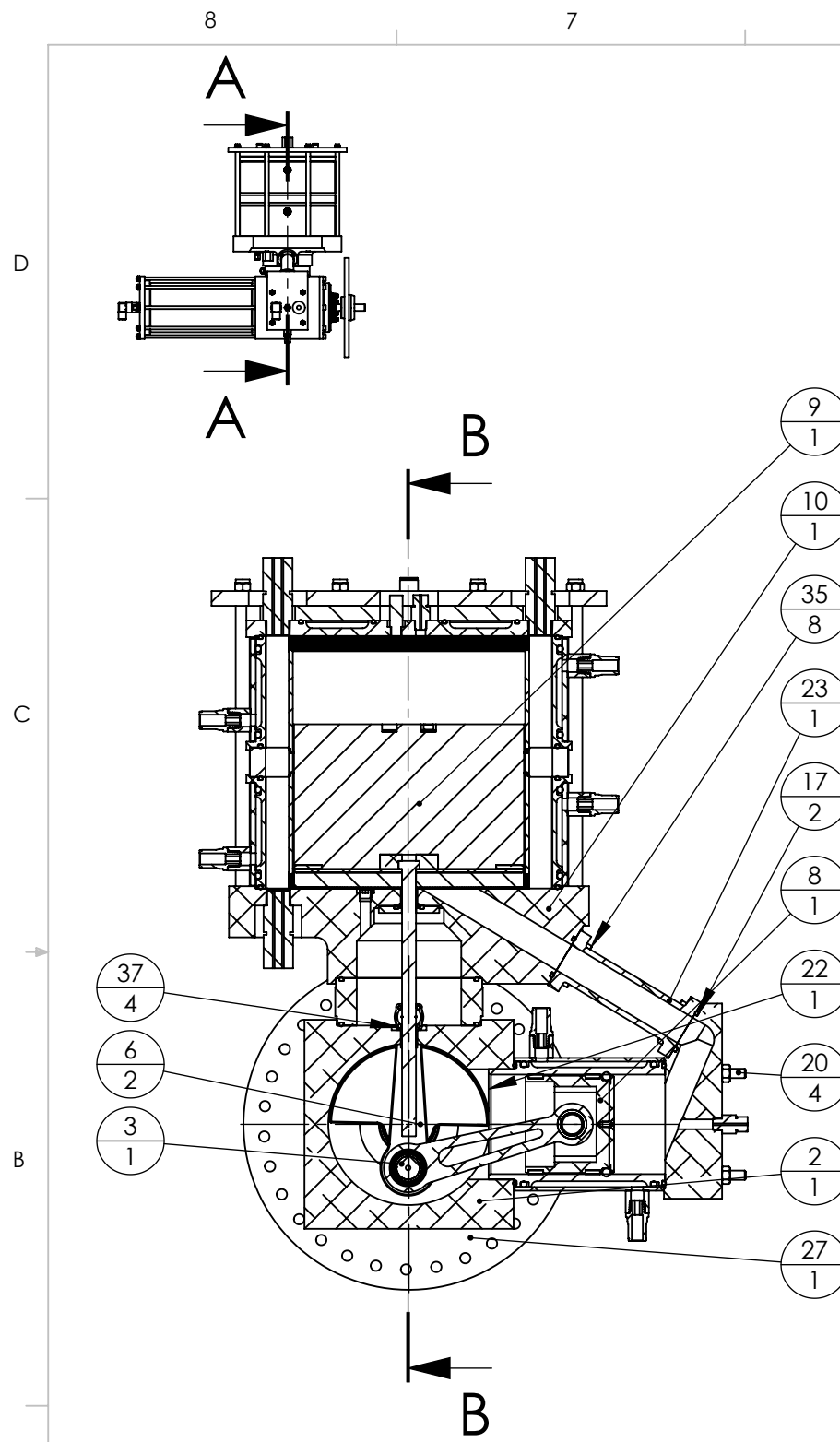
306

4

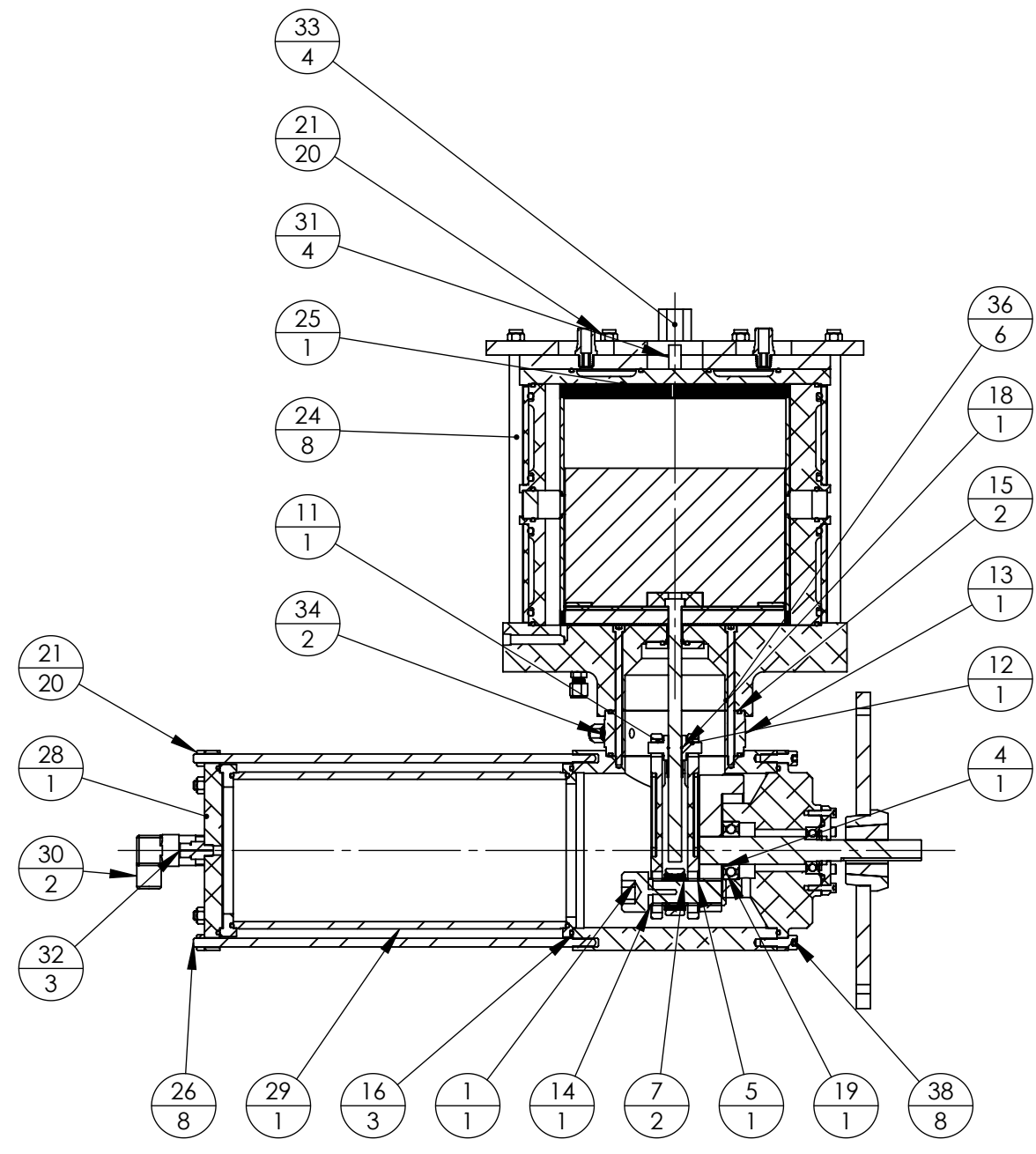
3

2

1



SECTION A-A



SECTION B-B

| ITEM NO. | PART NUMBER | QTY. |
|----------|--|------|
| 1 | socket head cap screw_am | 1 |
| 2 | C-CC-Z-00-CRANKCASE_ASM | 1 |
| 3 | C-CS-Z-00-CRANKSHAFT_ASM.SLDPRT | 1 |
| 4 | C-ZZ-Z-02-SPACER_115 | 1 |
| 5 | C-ZZ-Z-03-SPACER_116 | 1 |
| 6 | A-ZZ-R-00-DISP_CON_ROD_ASM | 2 |
| 7 | C-ZZ-Z-04-SPACER_117 | 2 |
| 8 | B-PP-Z-00-POWER_PISTON_ASM | 1 |
| 9 | A-DP-F-00-DISP_FULL_ASM | 1 |
| 10 | A-DM-Z-00-DISP_MOUNT_ASM | 1 |
| 11 | A-ZZ-Z-02-RIGHT_CROSSHEAD | 1 |
| 12 | A-ZZ-Z-03-LEFT_CROSSHEAD | 1 |
| 13 | A-ZZ-Z-01-FOOT | 1 |
| 14 | C-ZZ-Z-05-SPACER_118 | 1 |
| 15 | 3.5 x 113 mm Nitrile O-Ring | 2 |
| 16 | 3.5 x 145 mm Nitrile O-Ring | 3 |
| 17 | 3.5 x 33 mm Nitrile O-Ring | 2 |
| 18 | 91665A380 | 1 |
| 19 | C-BC-Z-00-BEARING_CARTRIDGE_ASM | 1 |
| 20 | C-ZZ-Z-06-PC_THREADED_ROD | 4 |
| 21 | prevailing torque hex nut_am | 20 |
| 22 | B-PC-Z-00-POWER_CYL_ASM | 1 |
| 23 | B-CP-Z-01-CON_PIPE | 1 |
| 24 | A-DC-Z-04-DISPLACER_CYL_THREADED_ROD | 8 |
| 25 | A-DC-Z-00-DISP_CYL_ASM | 1 |
| 26 | C-ZZ-Z-07-CC_EXT_THREADED_ROD | 8 |
| 27 | C-ZZ-F-00-FLYWHEEL_ASM.SLDPRT | 1 |
| 28 | C-ZZ-Z-01-COVER | 1 |
| 29 | C-ZZ-CE-00-CRANKCASE_EXTENSION_ASM | 1 |
| 30 | I-ZZ-Z-01-STATIC_PRESSURE_TRANSDUCER | 2 |
| 31 | I-ZZ-Z-02-DYNAMIC_PRESSURE_TRANSDUCER | 4 |
| 32 | I-ZZ-Z-03-GAS_TC_FITTING | 3 |
| 33 | I-ZZ-Z-03-TWO_ELEMENT_GAS_TC_FITTING | 4 |
| 34 | 5182K807 | 2 |
| 35 | B18.3.1M - 5 x 0.8 x 20 Hex SHCS -- 20NHX | 8 |
| 36 | B18.3.1M - 6 x 1.0 x 120 Hex SHCS -- 24NHX | 6 |
| 37 | B18.3.1M - 3 x 0.5 x 12 Hex SHCS -- 12NHX | 4 |
| 38 | B18.3.1M - 8 x 1.25 x 25 Hex SHCS -- 25NHX | 8 |

UNLESS OTHERWISE SPECIFIED:
 DIMENSIONS ARE IN MM
 TOLERANCES:
 LINEAR: 0.1 mm
 ANGULAR: 1°
 GENERAL SURFACE FINISH: Ra 5 µm
 O-RING SEAL SURFACE FINISH: Ra 0.8 µm

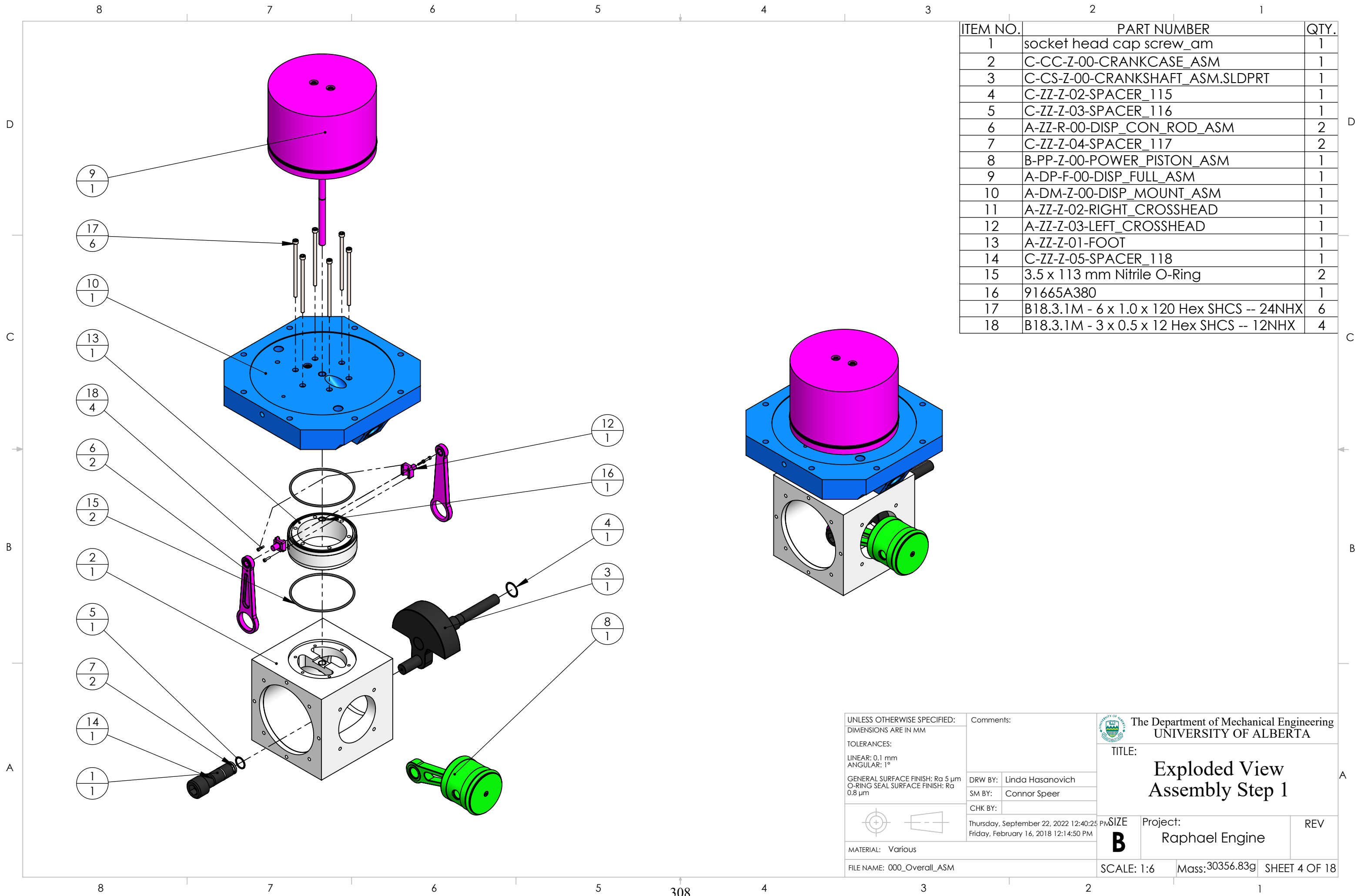
Comments:
 DRW BY: Linda Hasanovich
 SM BY: Connor Speer
 CHK BY:
 Thursday, September 22, 2022 12:40:25 PM
 Friday, February 16, 2018 12:14:50 PM

The Department of Mechanical Engineering
 UNIVERSITY OF ALBERTA

TITLE:
**Overall Assembly
 Section Views**

Project:
Raphael Engine

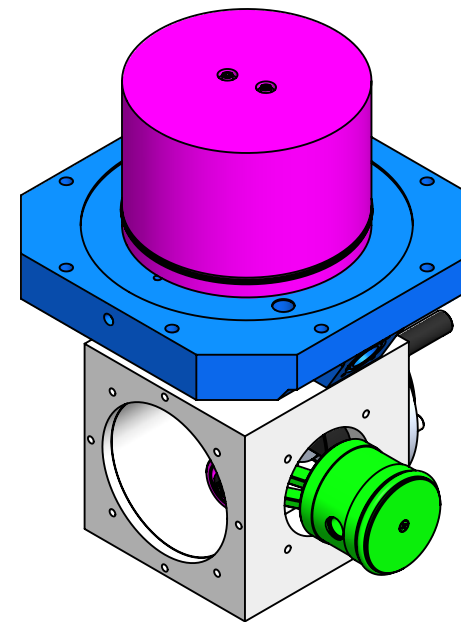
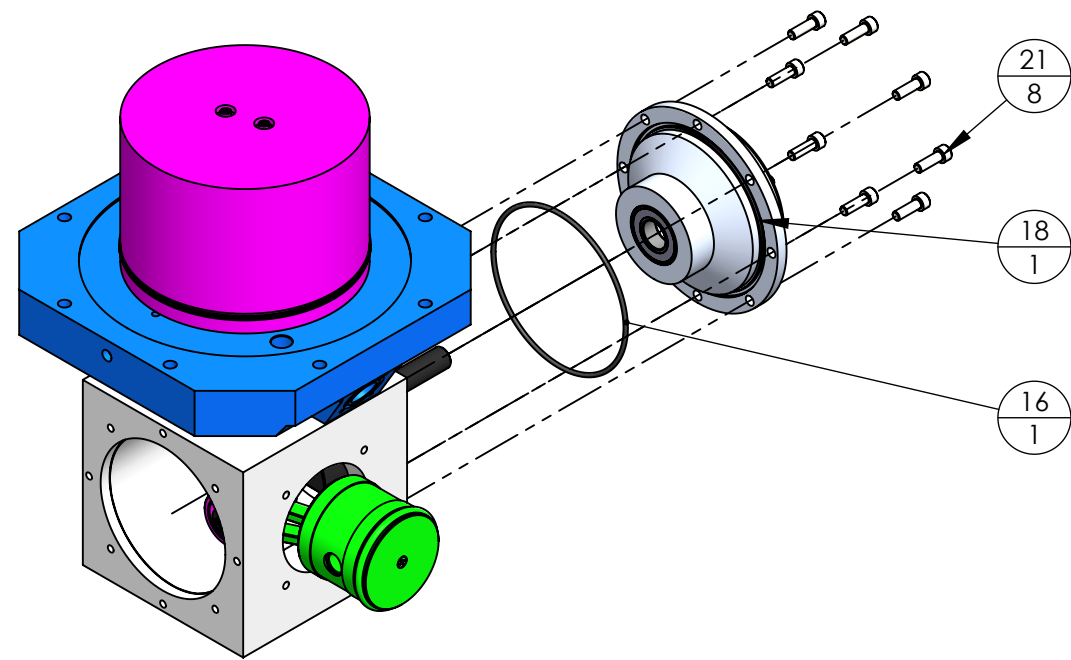
SCALE: 1:6 Mass: 30356.83g SHEET 3 OF 18

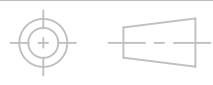


| ITEM NO. | PART NUMBER | QTY. |
|----------|--|------|
| 1 | socket head cap screw_am | 1 |
| 2 | C-CC-Z-00-CRANKCASE_ASM | 1 |
| 3 | C-CS-Z-00-CRANKSHAFT_ASM.SLDPRT | 1 |
| 4 | C-ZZ-Z-02-SPACER_115 | 1 |
| 5 | C-ZZ-Z-03-SPACER_116 | 1 |
| 6 | A-ZZ-R-00-DISP_CON_ROD_ASM | 2 |
| 7 | C-ZZ-Z-04-SPACER_117 | 2 |
| 8 | B-PP-Z-00-POWER_PISTON_ASM | 1 |
| 9 | A-DP-F-00-DISP_FULL_ASM | 1 |
| 10 | A-DM-Z-00-DISP_MOUNT_ASM | 1 |
| 11 | A-ZZ-Z-02-RIGHT_CROSSHEAD | 1 |
| 12 | A-ZZ-Z-03-LEFT_CROSSHEAD | 1 |
| 13 | A-ZZ-Z-01-FOOT | 1 |
| 14 | C-ZZ-Z-05-SPACER_118 | 1 |
| 15 | 3.5 x 113 mm Nitrile O-Ring | 2 |
| 16 | 91665A380 | 1 |
| 17 | B18.3.1M - 6 x 1.0 x 120 Hex SHCS -- 24NHX | 6 |
| 18 | B18.3.1M - 3 x 0.5 x 12 Hex SHCS -- 12NHX | 4 |

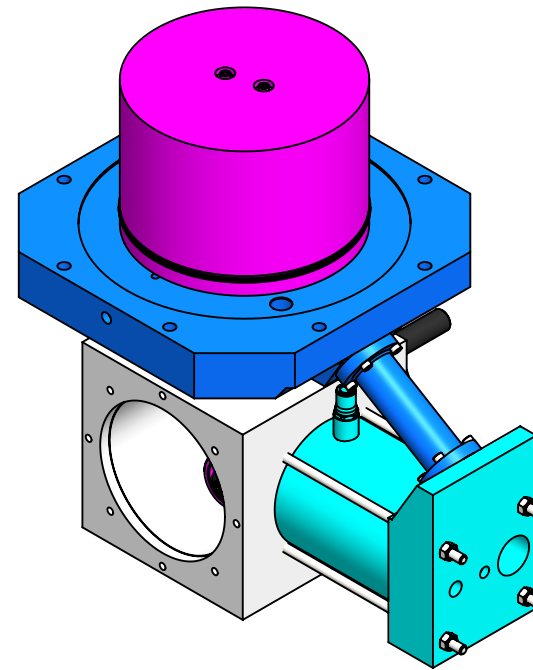
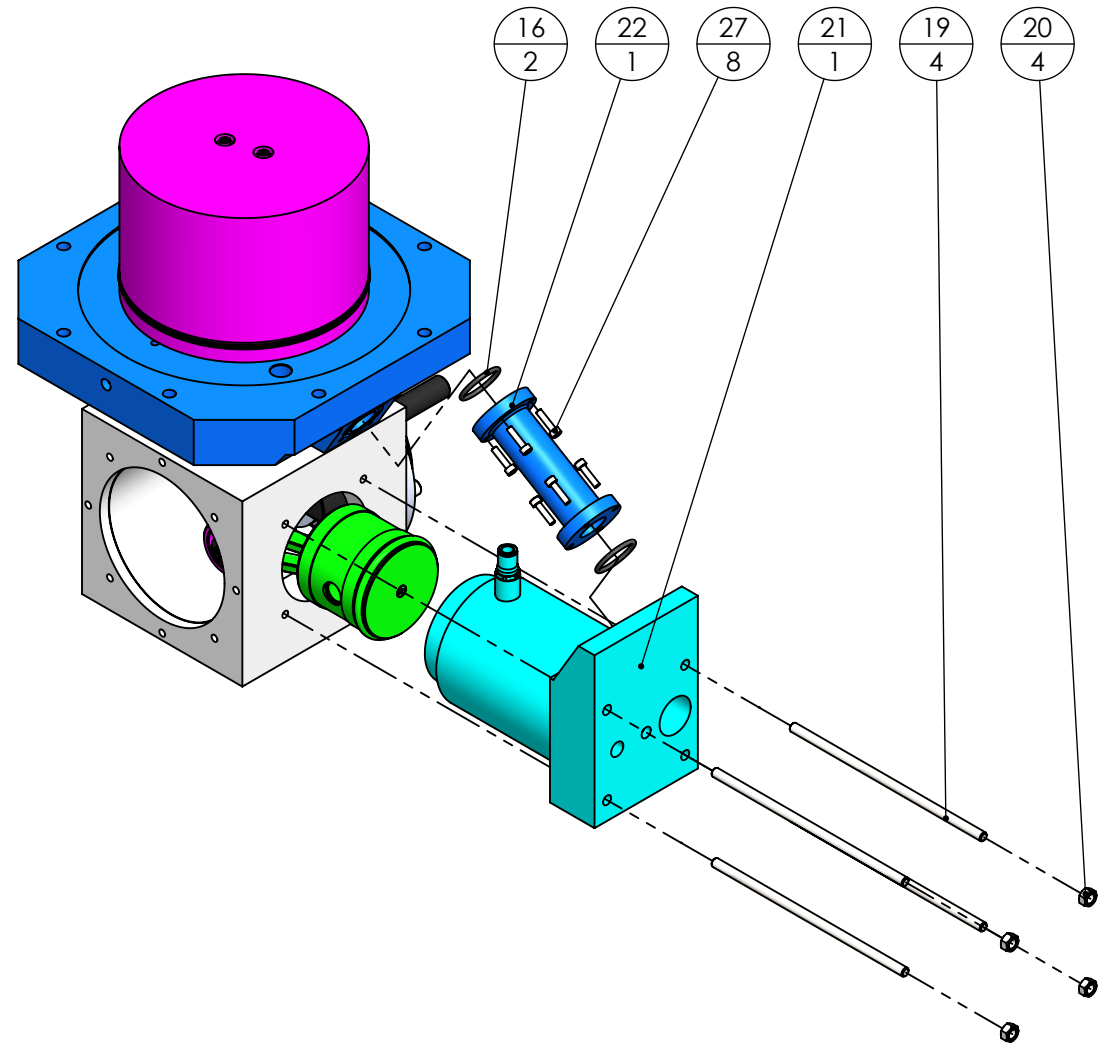
| | | |
|---|---|--|
| UNLESS OTHERWISE SPECIFIED: DIMENSIONS ARE IN MM TOLERANCES: LINEAR: 0.1 mm ANGULAR: 1° GENERAL SURFACE FINISH: Ra 5 µm O-RING SEAL SURFACE FINISH: Ra 0.8 µm | Comments: | The Department of Mechanical Engineering UNIVERSITY OF ALBERTA |
| | DRW BY: Linda Hasanovich SM BY: Connor Speer CHK BY: | |
| MATERIAL: Various FILE NAME: 000_Overall_ASM | Thursday, September 22, 2022 12:40:25 PM Friday, February 16, 2018 12:14:50 PM | SIZE B |
| SCALE: 1:6 | Project: Raphael Engine | REV |
| Mass: 30356.83g | SHEET 4 OF 18 | |

| ITEM NO. | PART NUMBER | QTY. |
|----------|--|------|
| 16 | 145 x 3.5 Nitrile O-Ring | 1 |
| 18 | C-BC-Z-00-BEARING_CARTRIDGE_ASM | 1 |
| 19 | B18.3.1M - 3 x 0.5 x 12 Hex SHCS -- 12NHX | 4 |
| 20 | B18.3.1M - 6 x 1.0 x 20 Hex SHCS -- 20NHX | 1 |
| 21 | B18.3.1M - 8 x 1.25 x 25 Hex SHCS -- 25NHX | 8 |

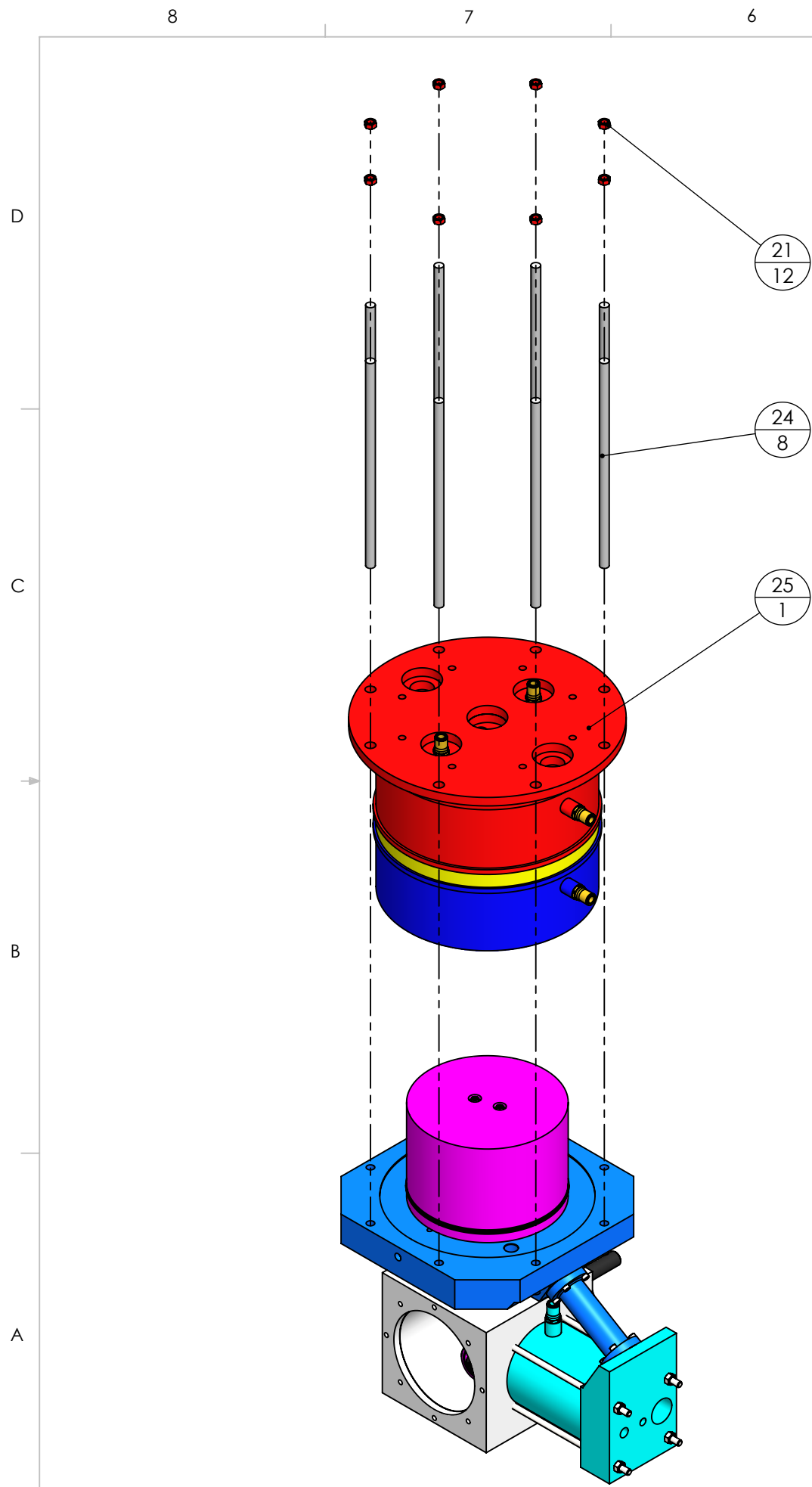


| | | |
|---|---|---|
| UNLESS OTHERWISE SPECIFIED: DIMENSIONS ARE IN MM TOLERANCES: LINEAR: 0.1 mm ANGULAR: 1° GENERAL SURFACE FINISH: Ra 5 µm O-RING SEAL SURFACE FINISH: Ra 0.8 µm | Comments: |  The Department of Mechanical Engineering UNIVERSITY OF ALBERTA |
| | DRW BY: Linda Hasanovich SM BY: Connor Speer CHK BY: | |
|  | Thursday, September 22, 2022 12:40:25 PM Friday, February 16, 2018 12:14:50 PM | SIZE B |
| MATERIAL: Various | Project: Raphael Engine | REV |
| FILE NAME: 000_Overall_ASM | SCALE: 1:6 | Mass: 30356.83g SHEET 5 OF 18 |

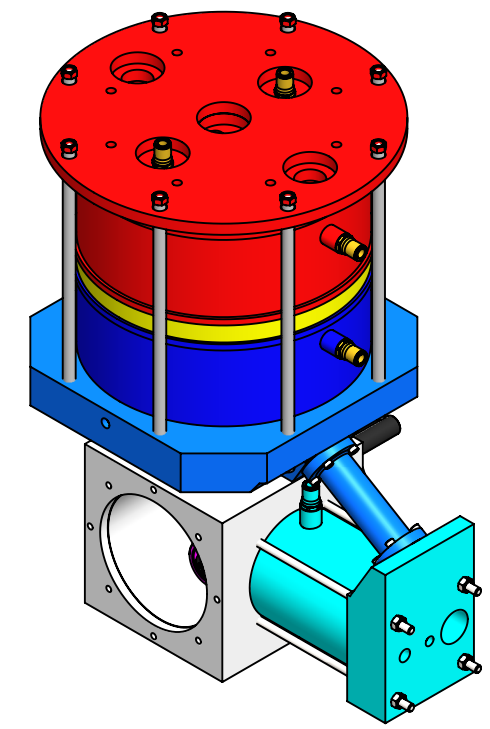
| ITEM NO. | PART NUMBER | QTY. |
|----------|--|------|
| 16 | 33 x 3.5 mm Nitrile O-Ring | 2 |
| 19 | C-ZZ-Z-06-PC_THREADED_ROD | 4 |
| 20 | prevailing torque hex nut_am | 4 |
| 21 | B-PC-Z-00-POWER_CYL_ASM | 1 |
| 22 | B-CP-Z-01-CON_PIPE | 1 |
| 23 | B18.3.1M - 6 x 1.0 x 120 Hex SHCS -- 24NHX | 6 |
| 24 | B18.3.1M - 3 x 0.5 x 12 Hex SHCS -- 12NHX | 4 |
| 25 | B18.3.1M - 6 x 1.0 x 20 Hex SHCS -- 20NHX | 1 |
| 26 | B18.3.1M - 8 x 1.25 x 25 Hex SHCS -- 25NHX | 8 |
| 27 | B18.3.1M - 5 x 0.8 x 20 Hex SHCS -- 20NHX | 8 |



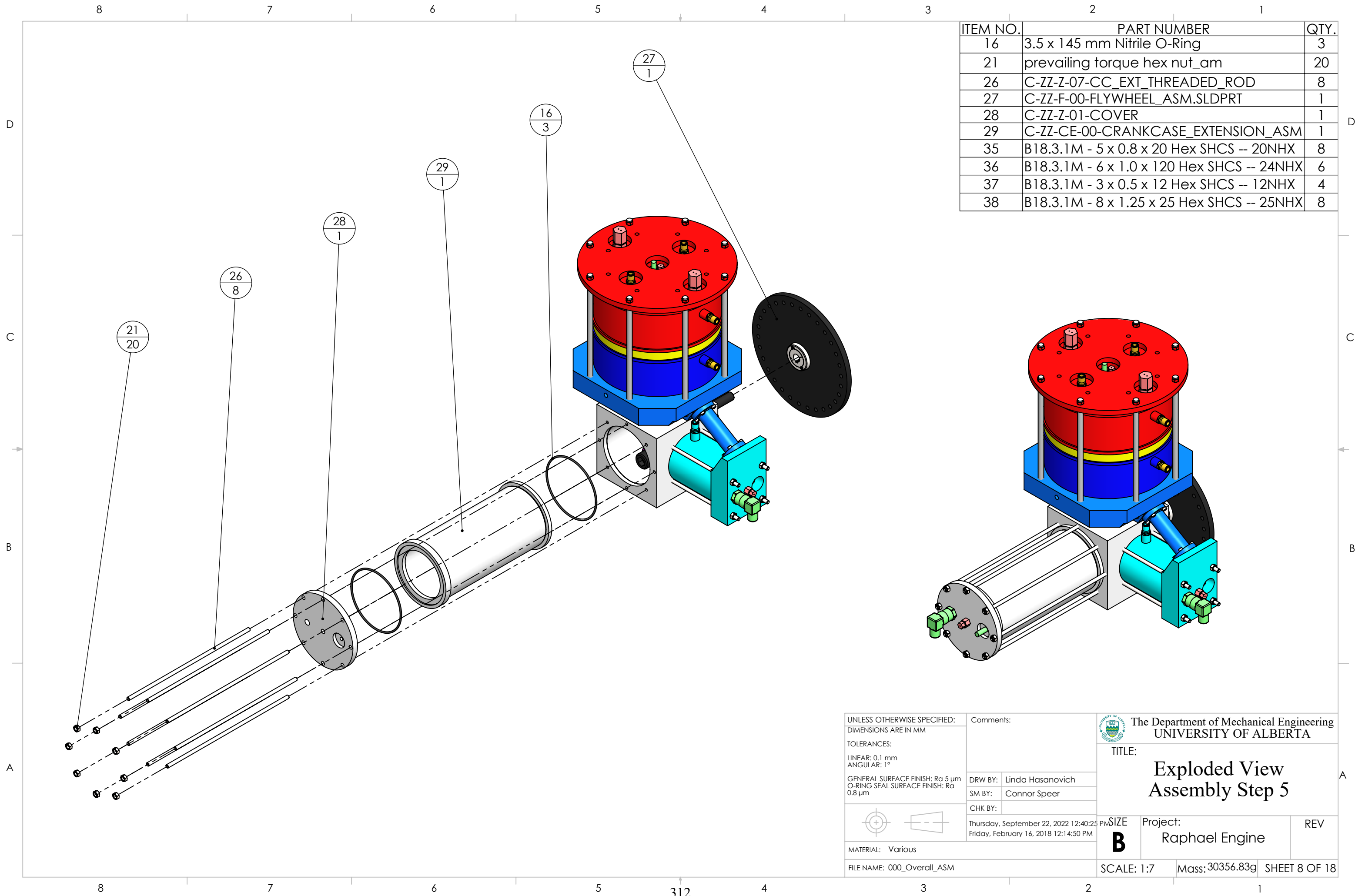
| | | |
|---|--|---|
| UNLESS OTHERWISE SPECIFIED: DIMENSIONS ARE IN MM TOLERANCES: LINEAR: 0.1 mm ANGULAR: 1° GENERAL SURFACE FINISH: Ra 5 µm O-RING SEAL SURFACE FINISH: Ra 0.8 µm | Comments: |  The Department of Mechanical Engineering UNIVERSITY OF ALBERTA TITLE: <h3>Exploded View Assembly Step 3</h3> |
| | DRW BY: Linda Hasanovich SM BY: Connor Speer CHK BY: | |
|  MATERIAL: Various FILE NAME: 000_Overall_ASM | Thursday, September 22, 2022 12:40:25 PM Friday, February 16, 2018 12:14:50 PM Project: Raphael Engine | REV SCALE: 1:6 Mass: 30356.83g SHEET 6 OF 18 |



| ITEM NO. | PART NUMBER | QTY. |
|----------|--|------|
| 24 | A-DC-Z-04-DISPLACER_CYL_THREADED_ROD | 8 |
| 25 | A-DC-Z-00-DISP_CYL_ASM | 1 |
| 26 | B18.3.1M - 3 x 0.5 x 12 Hex SHCS -- 12NHX | 4 |
| 27 | B18.3.1M - 6 x 1.0 x 20 Hex SHCS -- 20NHX | 1 |
| 28 | B18.3.1M - 8 x 1.25 x 25 Hex SHCS -- 25NHX | 8 |
| 29 | B18.3.1M - 5 x 0.8 x 20 Hex SHCS -- 20NHX | 8 |

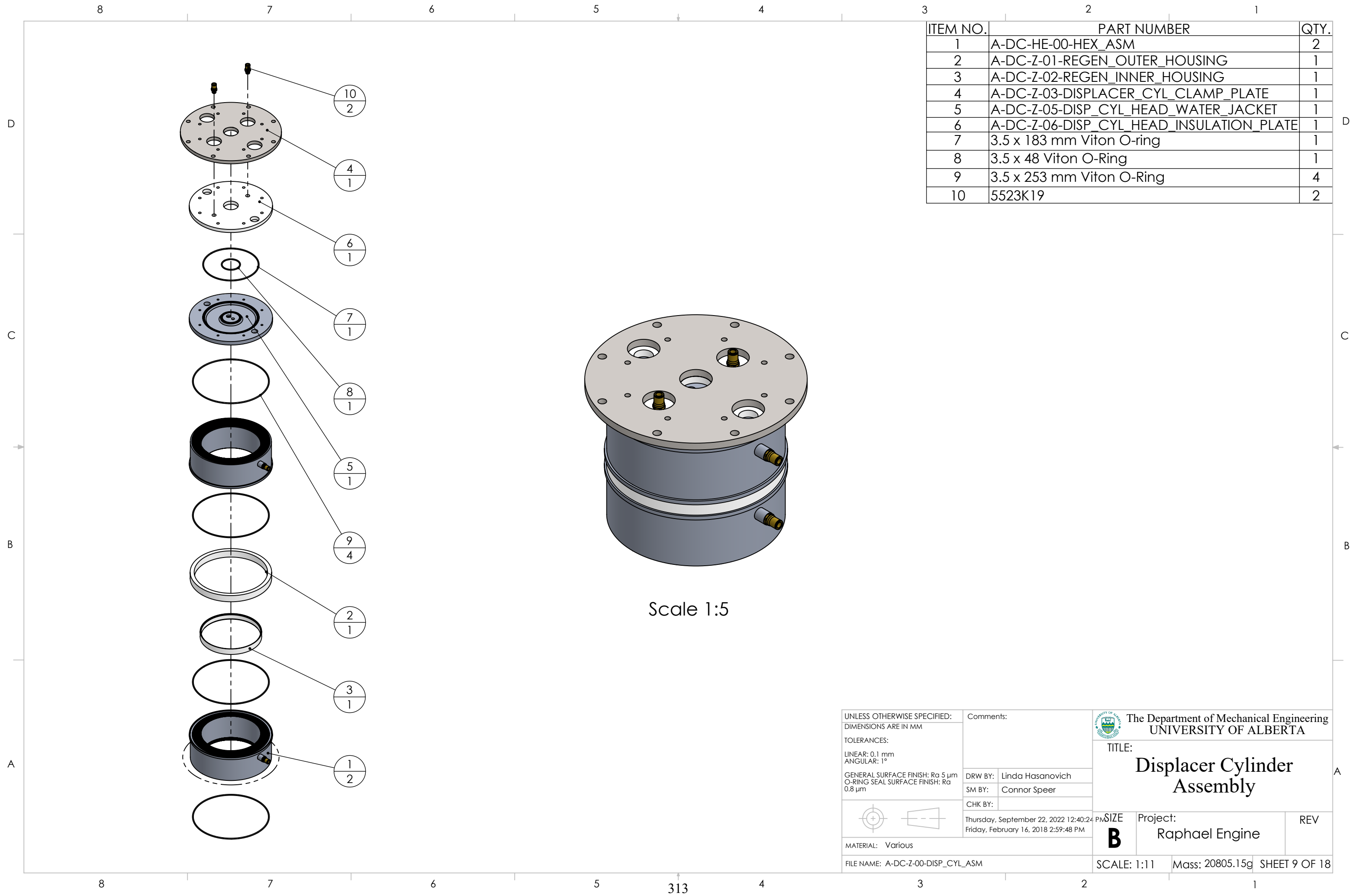


| | | | |
|---|--|---|--|
| UNLESS OTHERWISE SPECIFIED: DIMENSIONS ARE IN MM TOLERANCES: LINEAR: 0.1 mm ANGULAR: 1° GENERAL SURFACE FINISH: Ra 5 µm O-RING SEAL SURFACE FINISH: Ra 0.8 µm | Comments: | The Department of Mechanical Engineering UNIVERSITY OF ALBERTA | TITLE: <h3>Exploded View Assembly Step 4</h3> |
| | DRW BY: Linda Hasanovich | | |
| | SM BY: Connor Speer | SIZE B | REV |
| | CHK BY: Thursday, September 22, 2022 12:40:25 PM Friday, February 16, 2018 12:14:50 PM | SCALE: 1:7 | Mass: 30356.83g |

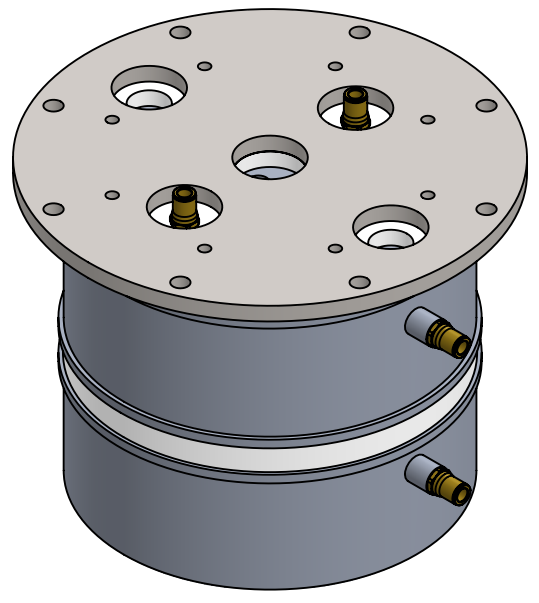


| ITEM NO. | PART NUMBER | QTY. |
|----------|--|------|
| 16 | 3.5 x 145 mm Nitrile O-Ring | 3 |
| 21 | prevailing torque hex nut_am | 20 |
| 26 | C-ZZ-Z-07-CC_EXT_THREADED_ROD | 8 |
| 27 | C-ZZ-F-00-FLYWHEEL_ASM.SLDPRT | 1 |
| 28 | C-ZZ-Z-01-COVER | 1 |
| 29 | C-ZZ-CE-00-CRANKCASE_EXTENSION_ASM | 1 |
| 35 | B18.3.1M - 5 x 0.8 x 20 Hex SHCS -- 20NHX | 8 |
| 36 | B18.3.1M - 6 x 1.0 x 120 Hex SHCS -- 24NHX | 6 |
| 37 | B18.3.1M - 3 x 0.5 x 12 Hex SHCS -- 12NHX | 4 |
| 38 | B18.3.1M - 8 x 1.25 x 25 Hex SHCS -- 25NHX | 8 |

| | | |
|---|---|---|
| UNLESS OTHERWISE SPECIFIED: DIMENSIONS ARE IN MM TOLERANCES: LINEAR: 0.1 mm ANGULAR: 1° GENERAL SURFACE FINISH: Ra 5 µm O-RING SEAL SURFACE FINISH: Ra 0.8 µm | Comments: | The Department of Mechanical Engineering UNIVERSITY OF ALBERTA |
| | DRW BY: Linda Hasanovich SM BY: Connor Speer CHK BY: | |
| MATERIAL: Various FILE NAME: 000_Overall_ASM | Thursday, September 22, 2022 12:40:25 PM Friday, February 16, 2018 12:14:50 PM | Project: B Raphael Engine |
| SCALE: 1:7 Mass: 30356.83g | SHEET 8 OF 18 | REV |

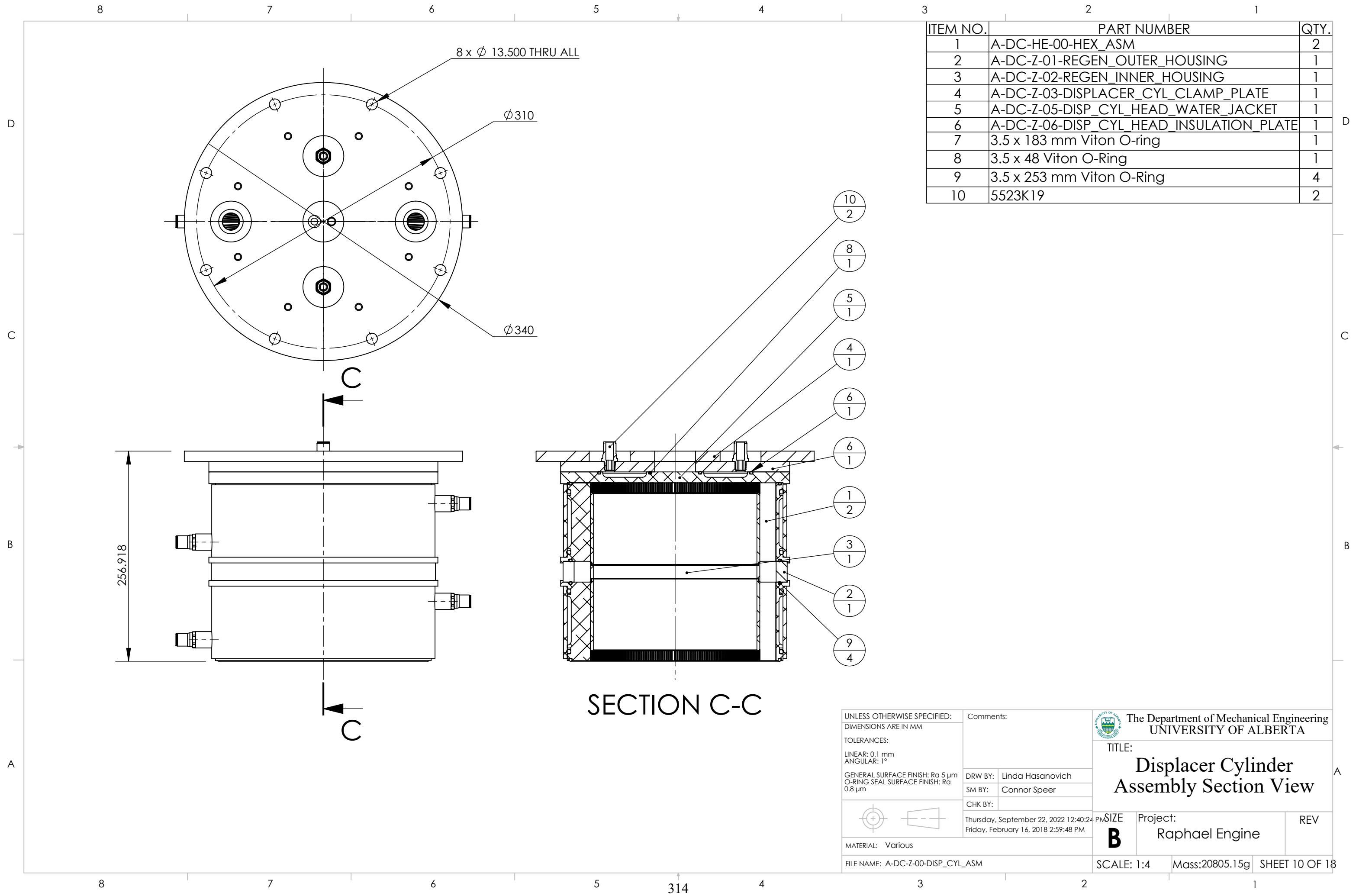


| ITEM NO. | PART NUMBER | QTY. |
|----------|--|------|
| 1 | A-DC-HE-00-HEX_ASM | 2 |
| 2 | A-DC-Z-01-REGEN_OUTER_HOUSING | 1 |
| 3 | A-DC-Z-02-REGEN_INNER_HOUSING | 1 |
| 4 | A-DC-Z-03-DISPLACER_CYL_CLAMP_PLATE | 1 |
| 5 | A-DC-Z-05-DISP_CYL_HEAD_WATER_JACKET | 1 |
| 6 | A-DC-Z-06-DISP_CYL_HEAD_INSULATION_PLATE | 1 |
| 7 | 3.5 x 183 mm Viton O-ring | 1 |
| 8 | 3.5 x 48 Viton O-Ring | 1 |
| 9 | 3.5 x 253 mm Viton O-Ring | 4 |
| 10 | 5523K19 | 2 |



Scale 1:5

| | | | |
|---|---|-----------------------------------|---|
| UNLESS OTHERWISE SPECIFIED: DIMENSIONS ARE IN MM TOLERANCES: LINEAR: 0.1 mm ANGULAR: 1° GENERAL SURFACE FINISH: Ra 5 µm O-RING SEAL SURFACE FINISH: Ra 0.8 µm | Comments: | |  The Department of Mechanical Engineering UNIVERSITY OF ALBERTA |
| | DRW BY: Linda Hasanovich | SM BY: Connor Speer | |
|  | CHK BY: Thursday, September 22, 2022 12:40:24 PM Friday, February 16, 2018 2:59:48 PM | Project: Raphael Engine | REV |
| MATERIAL: Various | FILE NAME: A-DC-Z-00-DISP_CYL_ASM | SCALE: 1:11 | Mass: 20805.15g SHEET 9 OF 18 |

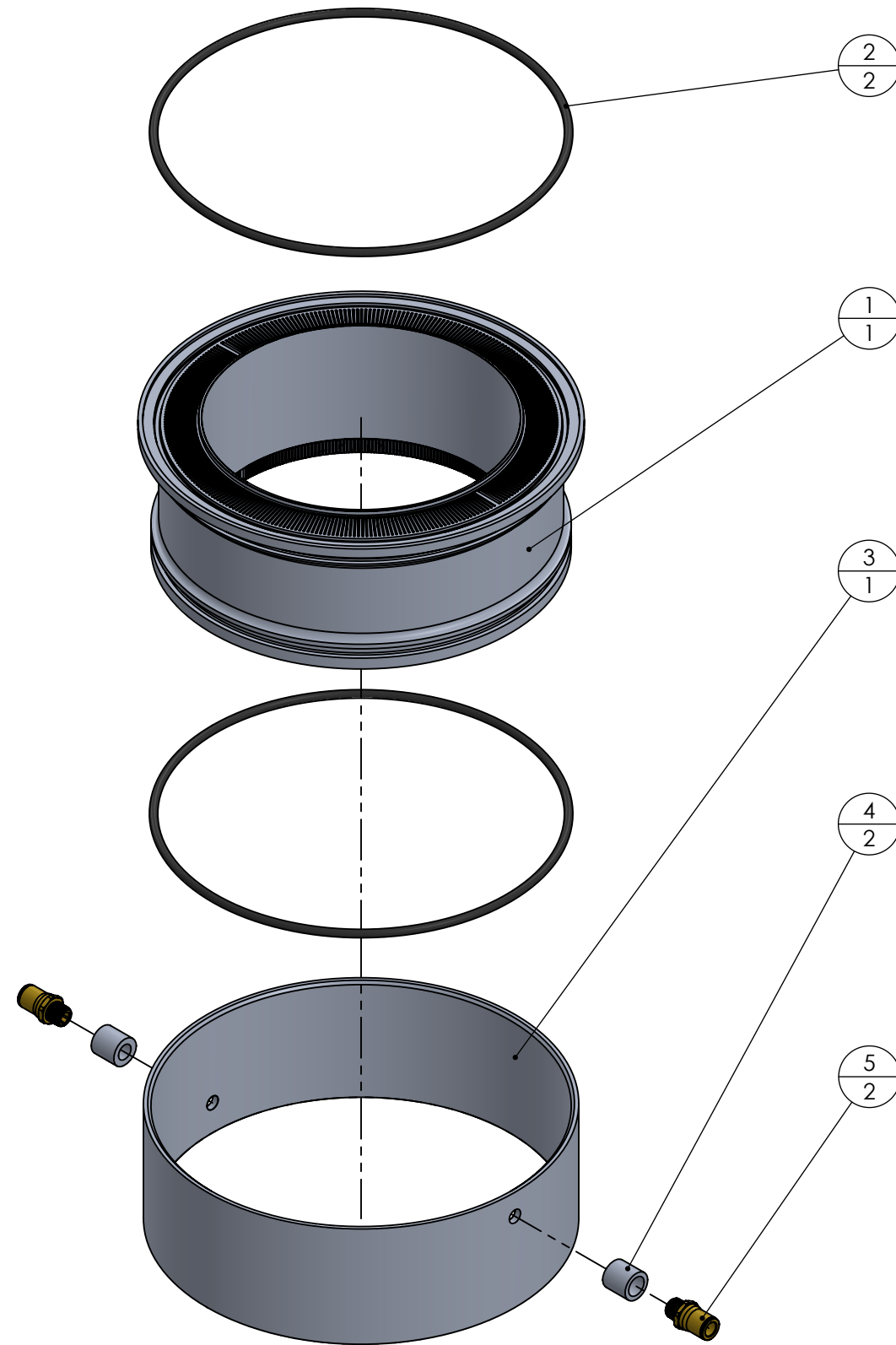


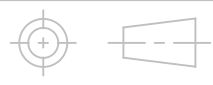
| ITEM NO. | PART NUMBER | QTY. |
|----------|--|------|
| 1 | A-DC-HE-00-HEX_ASM | 2 |
| 2 | A-DC-Z-01-REGEN_OUTER_HOUSING | 1 |
| 3 | A-DC-Z-02-REGEN_INNER_HOUSING | 1 |
| 4 | A-DC-Z-03-DISPLACER_CYL_CLAMP_PLATE | 1 |
| 5 | A-DC-Z-05-DISP_CYL_HEAD_WATER_JACKET | 1 |
| 6 | A-DC-Z-06-DISP_CYL_HEAD_INSULATION_PLATE | 1 |
| 7 | 3.5 x 183 mm Viton O-ring | 1 |
| 8 | 3.5 x 48 Viton O-Ring | 1 |
| 9 | 3.5 x 253 mm Viton O-Ring | 4 |
| 10 | 5523K19 | 2 |

SECTION C-C

| | | | | |
|---|---|--|---|---|
| UNLESS OTHERWISE SPECIFIED: DIMENSIONS ARE IN MM TOLERANCES: LINEAR: 0.1 mm ANGULAR: 1° GENERAL SURFACE FINISH: Ra 5 µm O-RING SEAL SURFACE FINISH: Ra 0.8 µm | Comments: | | The Department of Mechanical Engineering UNIVERSITY OF ALBERTA | |
| | TITLE: <h2 style="text-align: center;">Displacer Cylinder Assembly Section View</h2> | | | |
| | DRW BY: Linda Hasanovich | SM BY: Connor Speer | CHK BY: | Project: <h3 style="text-align: center;">Raphael Engine</h3> |
| | Thursday, September 22, 2022 12:40:24 PM Friday, February 16, 2018 2:59:48 PM | | SCALE: 1:4 Mass:20805.15g | |
| MATERIAL: Various FILE NAME: A-DC-Z-00-DISP_CYL_ASM | | SIZE <h1 style="font-size: 2em;">B</h1> | REV | |

| ITEM NO. | PART NUMBER | QTY. |
|----------|-------------------------------|------|
| 1 | A-DC-HC-00-HEX_CARTRIDGE_ASM | 1 |
| 2 | 5.33 x 266.07 mm Viton O-Ring | 2 |
| 3 | A-DC-HE-01-HEX_JACKET | 1 |
| 4 | A-DC-HE-02-HEX_JACKET_INLET | 2 |
| 5 | 5523K19 | 2 |



| | | | | |
|---|--|---------------------|--|--|
| UNLESS OTHERWISE SPECIFIED: DIMENSIONS ARE IN MM TOLERANCES: LINEAR: 0.1 mm ANGULAR: 1° GENERAL SURFACE FINISH: Ra 5 µm O-RING SEAL SURFACE FINISH: Ra 0.8 µm | Comments: | |  The Department of Mechanical Engineering UNIVERSITY OF ALBERTA | |
| | DRW BY: Linda Hasanovich | SM BY: Connor Speer | | TITLE: Heat Exchanger Assembly Exploded View |
|  | CHK BY: Tuesday, September 6, 2022 12:54:57 PM Friday, February 16, 2018 11:55:32 AM | SIZE B | Project: Raphael Engine | REV |
| FILE NAME: A-DC-HE-00-HEX_ASM | SCALE: 1:4 | Mass: 4845.42g | SHEET 11 OF 18 | |

8 7 6 5 4 3 2 1

D

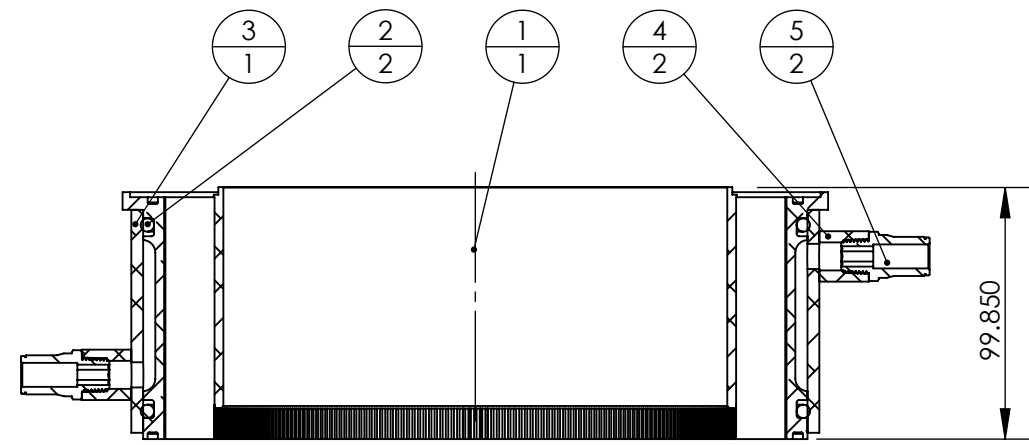
C

B

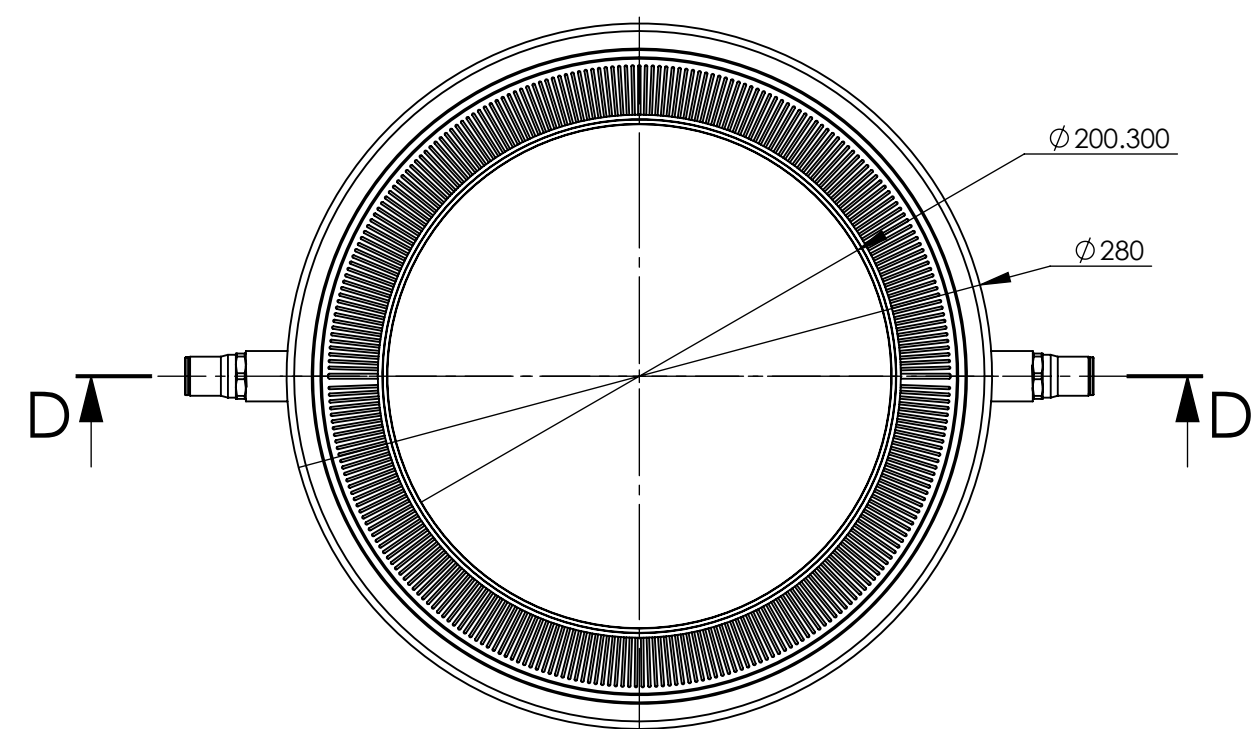
A

8 7 6 5 4 3 2 1

315

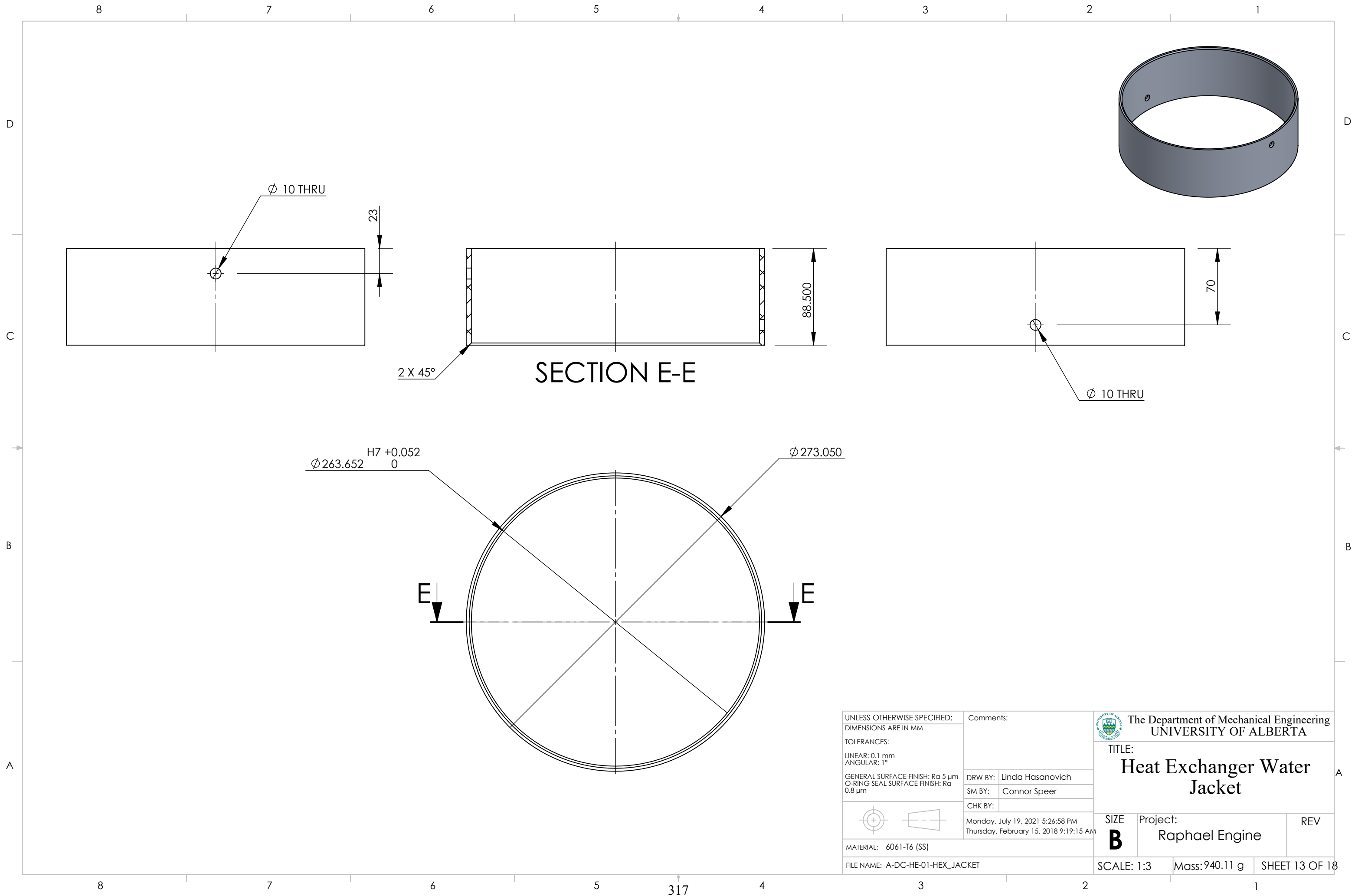


SECTION D-D

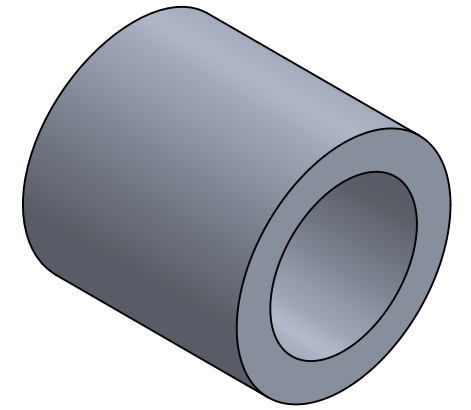


| ITEM NO. | PART NUMBER | QTY. |
|----------|-------------------------------|------|
| 1 | A-DC-HC-00-HEX_CARTRIDGE_ASM | 1 |
| 2 | 5.33 x 266.07 mm Viton O-Ring | 2 |
| 3 | A-DC-HE-01-HEX_JACKET | 1 |
| 4 | A-DC-HE-02-HEX_JACKET_INLET | 2 |
| 5 | 5523K19 | 2 |

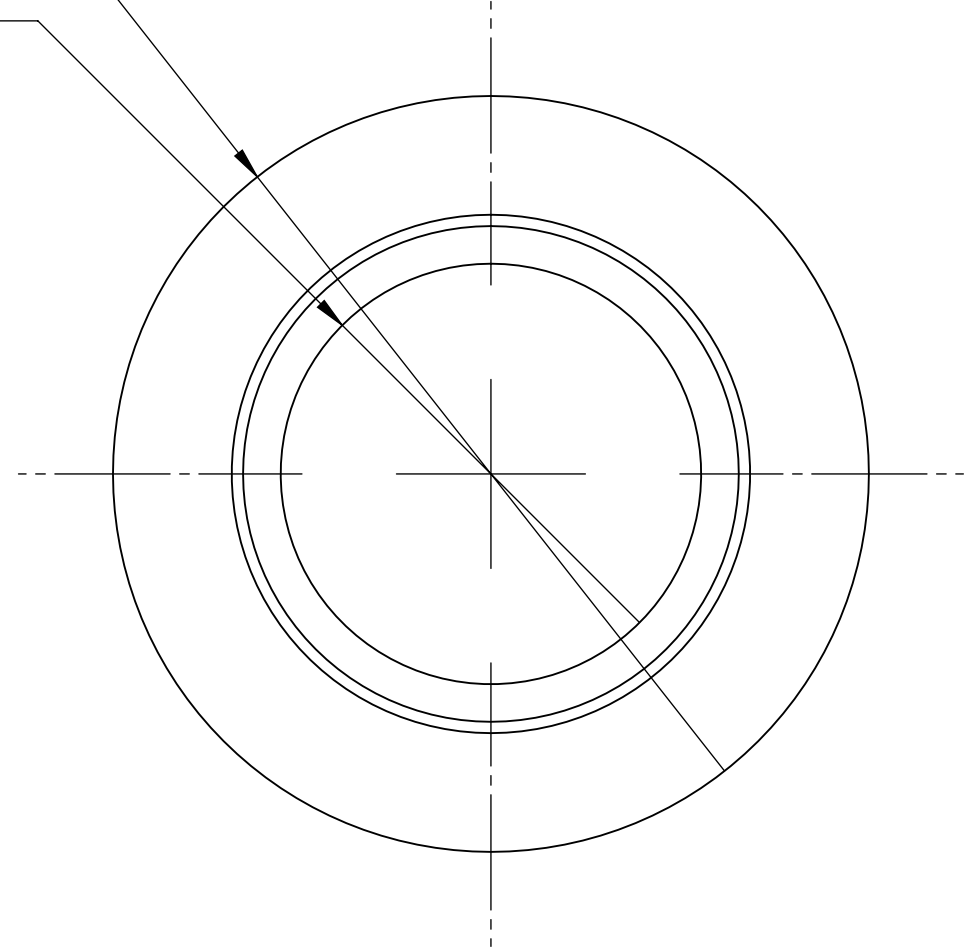
| | | | |
|---|--|---------------------|---|
| UNLESS OTHERWISE SPECIFIED: DIMENSIONS ARE IN MM TOLERANCES: LINEAR: 0.1 mm ANGULAR: 1° GENERAL SURFACE FINISH: Ra 5 µm O-RING SEAL SURFACE FINISH: Ra 0.8 µm | Comments: | |  The Department of Mechanical Engineering UNIVERSITY OF ALBERTA |
| | DRW BY: Linda Hasanovich | SM BY: Connor Speer | |
|   | CHK BY: Tuesday, September 6, 2022 12:54:57 PM Friday, February 16, 2018 11:55:32 AM | SIZE B | Project: Raphael Engine |
| MATERIAL: Various FILE NAME: A-DC-HE-00-HEX_ASM | SCALE: 1:3 | Mass: 4845.42g | REV SHEET 12 OF 18 |



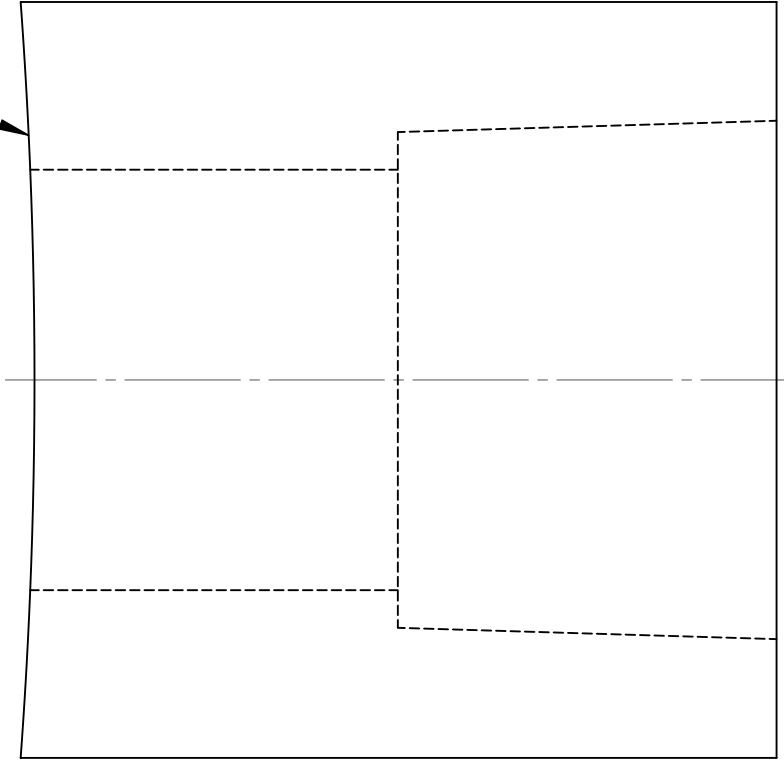
| | | | |
|---|--|------------------|---|
| UNLESS OTHERWISE SPECIFIED: DIMENSIONS ARE IN MM TOLERANCES: LINEAR: 0.1 mm ANGULAR: 1° GENERAL SURFACE FINISH: Ra 5 µm O-RING SEAL SURFACE FINISH: Ra 0.8 µm | Comments: | |  The Department of Mechanical Engineering UNIVERSITY OF ALBERTA |
| | DRW BY: | Linda Hasanovich | |
|   | SM BY: | Connor Speer | Heat Exchanger Water Jacket |
| | CHK BY: | | |
| MATERIAL: 6061-T6 (SS) | Monday, July 19, 2021 5:26:58 PM Thursday, February 15, 2018 9:19:15 AM | | SCALE: 1:3 Mass: 940.11 g SHEET 13 OF 18 |
| FILE NAME: A-DC-HE-01-HEX_JACKET | | | |



Ø 20
 Ø 11.125 THRU ALL
 1/4 NPT



R57.15 FOR POWER CYLINDER INLETS (QTY 2)
 R136.53 FOR DISPLACER CYLINDER INLETS (QTY 4)



UNLESS OTHERWISE SPECIFIED:
 DIMENSIONS ARE IN MM
 TOLERANCES:
 LINEAR: 0.1 mm
 ANGULAR: 1°
 GENERAL SURFACE FINISH: Ra 5 µm
 O-RING SEAL SURFACE FINISH: Ra 0.8 µm

Comments:
 DRW BY: Linda Hasanovich
 SM BY: Connor Speer
 CHK BY:
 Monday, July 19, 2021 5:26:58 PM
 Wednesday, April 11, 2018 8:41:13 AM

The Department of Mechanical Engineering
 UNIVERSITY OF ALBERTA

TITLE:
Weld-On Water Inlet

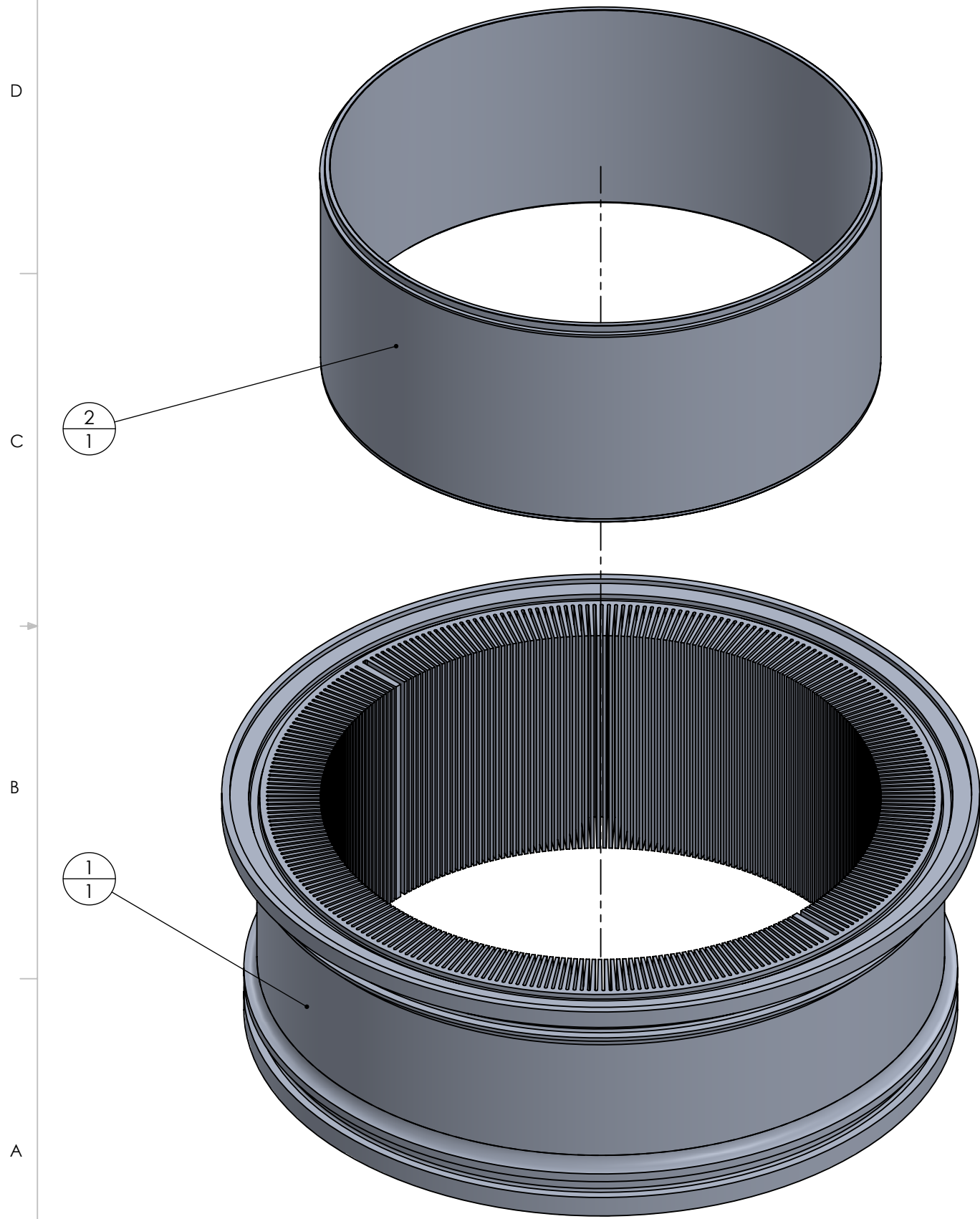


MATERIAL: 6061-T6 (SS)
 FILE NAME: A-DC-HE-02-HEX_JACKET_INLET

SIZE **B** Project: Raphael Engine REV

SCALE: 5:1 Mass: 10.38 g SHEET 14 OF 18

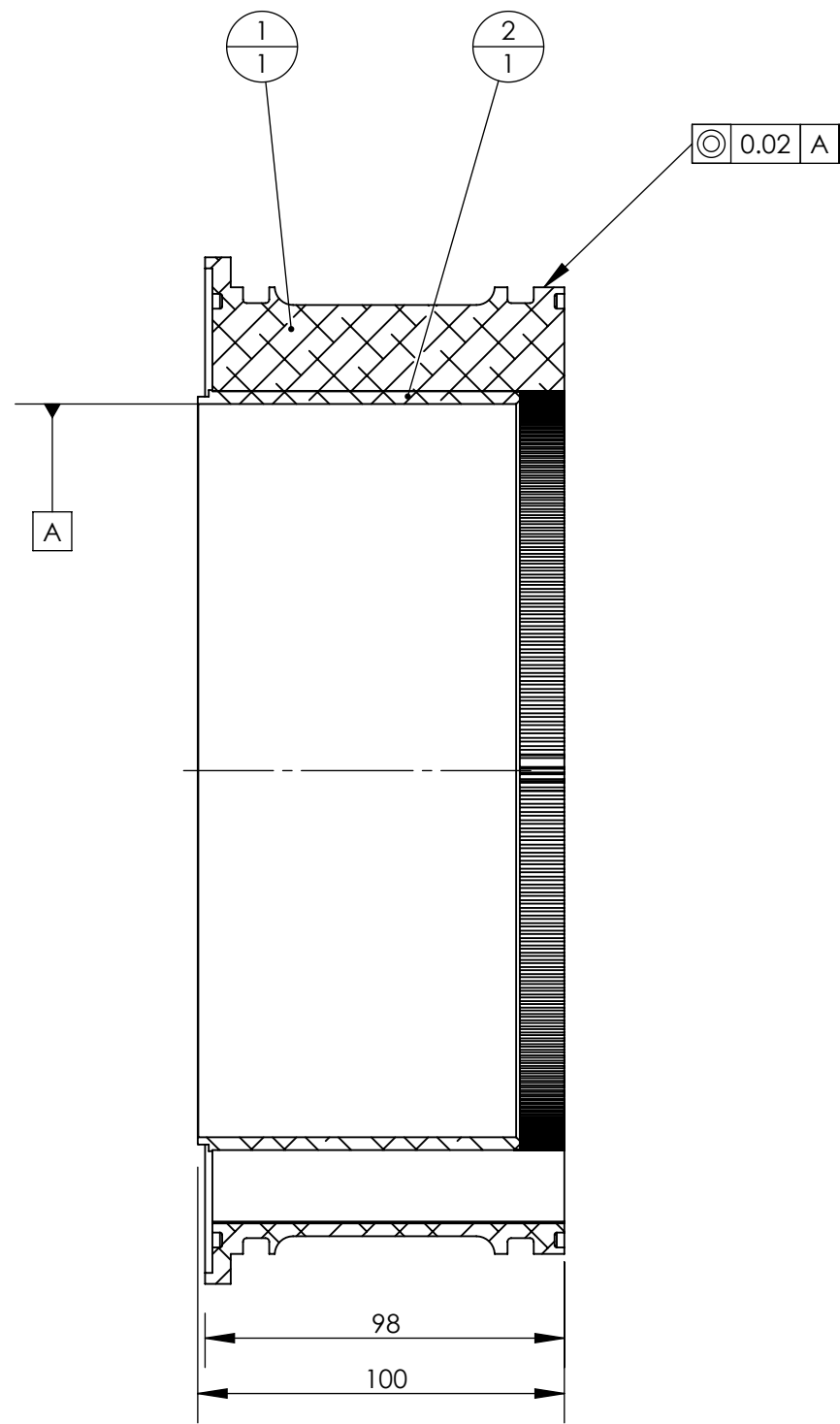
| ITEM NO. | PART NUMBER | QTY. |
|----------|-------------------------------|------|
| 1 | A-DC-HC-01-HEX_CARTRIDGE | 1 |
| 2 | A-DC-HC-02-HEX_CARTRIDGE_PIPE | 1 |



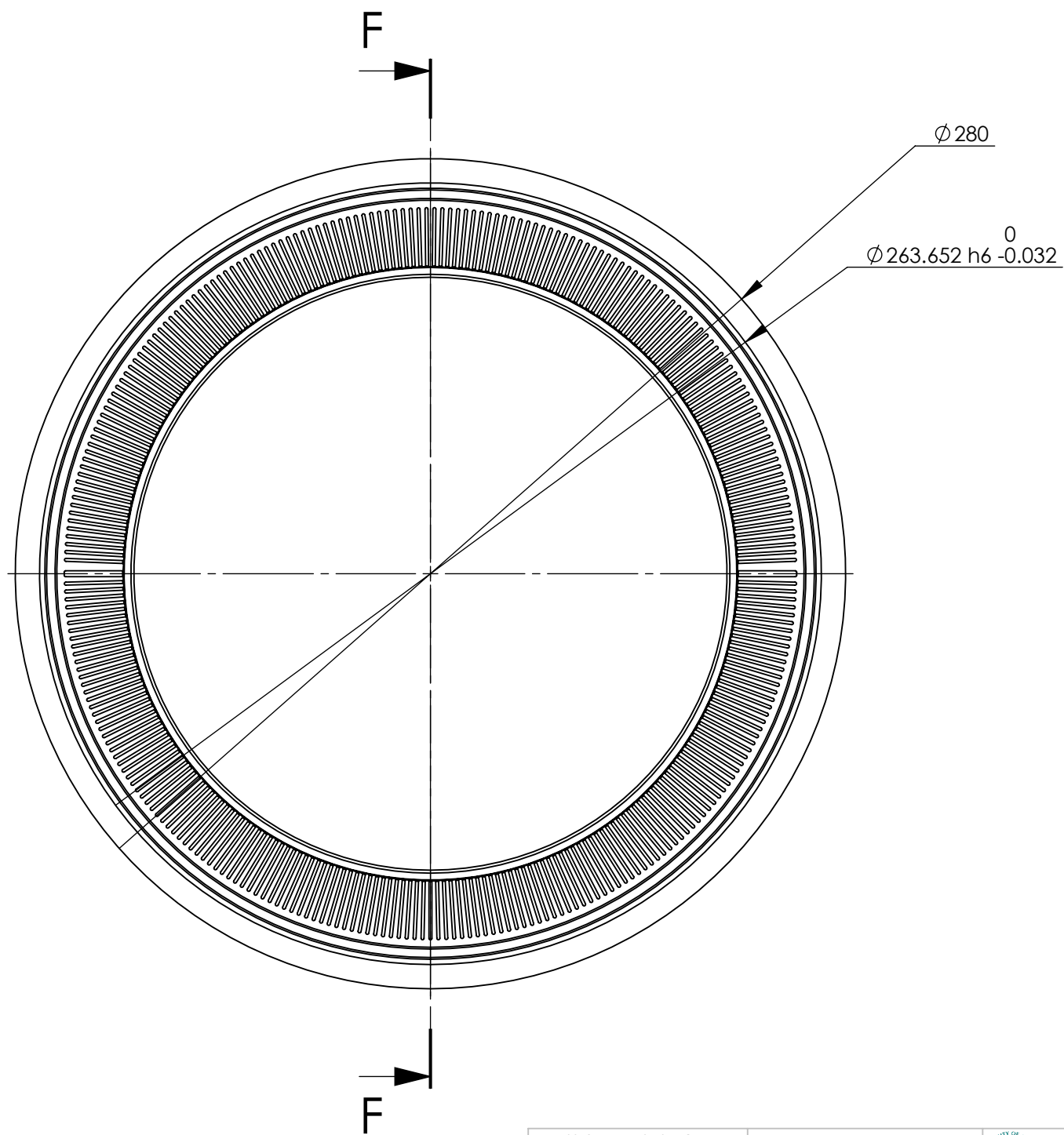
| | | |
|---|---|---|
| UNLESS OTHERWISE SPECIFIED: DIMENSIONS ARE IN MM TOLERANCES: LINEAR: 0.1 mm ANGULAR: 1° GENERAL SURFACE FINISH: Ra 5 µm O-RING SEAL SURFACE FINISH: Ra 0.8 µm | Comments: Shrink fit using liquid nitrogen. |  The Department of Mechanical Engineering UNIVERSITY OF ALBERTA |
| | DRW BY: Linda Hasanovich SM BY: Connor Speer CHK BY: | |
| MATERIAL: Various | Tuesday, September 6, 2022 12:54:55 PM Friday, February 16, 2018 11:53:24 AM | Project: Raphael Engine |
| FILE NAME: A-DC-HC-00-HEX_CARTRIDGE_ASM | SCALE: 1:2 | Mass: 3776.11g |

| | |
|------------------|-----|
| SIZE B | REV |
| SHEET 15 OF 18 | |

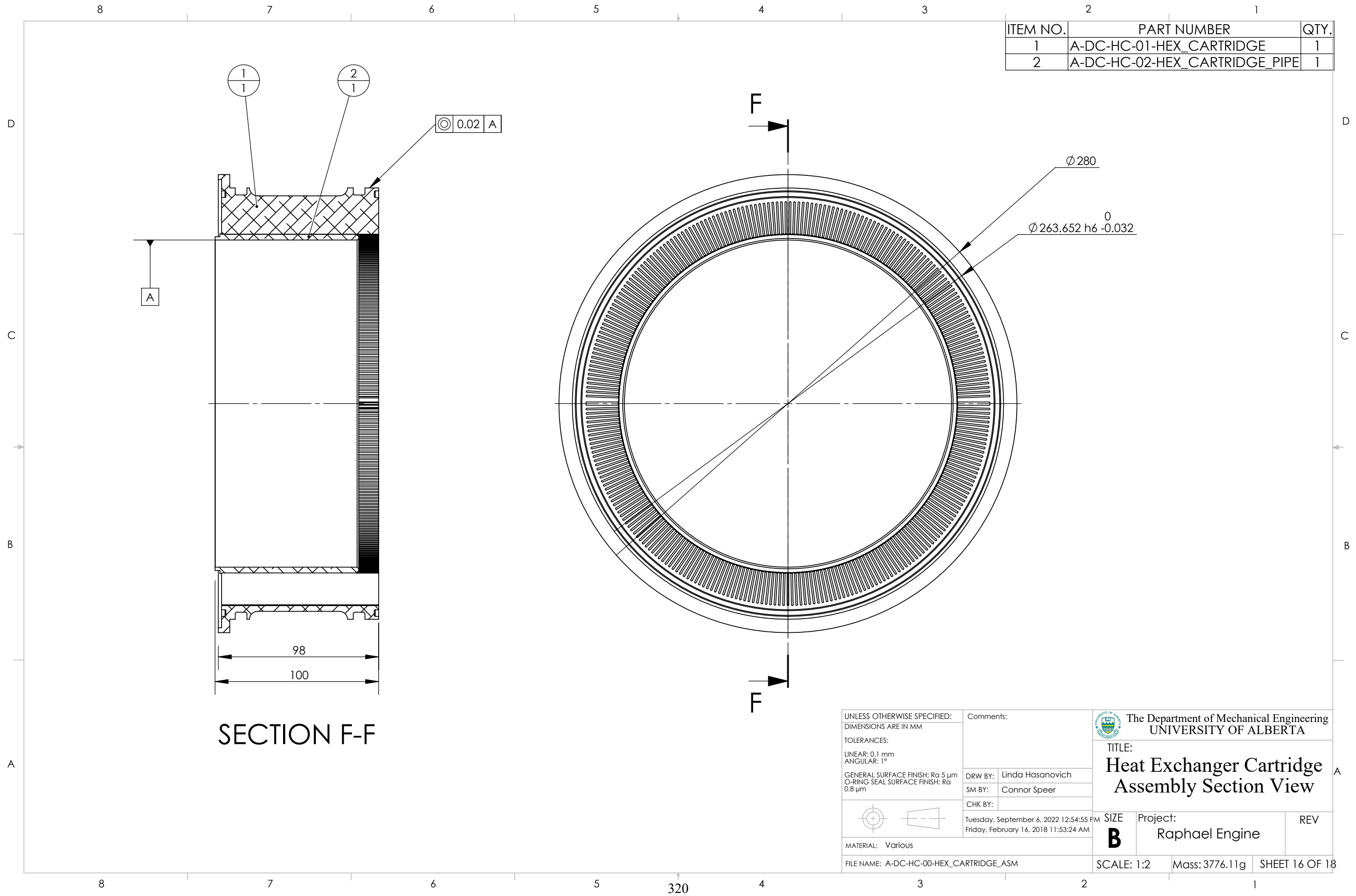
| ITEM NO. | PART NUMBER | QTY. |
|----------|-------------------------------|------|
| 1 | A-DC-HC-01-HEX_CARTRIDGE | 1 |
| 2 | A-DC-HC-02-HEX_CARTRIDGE_PIPE | 1 |

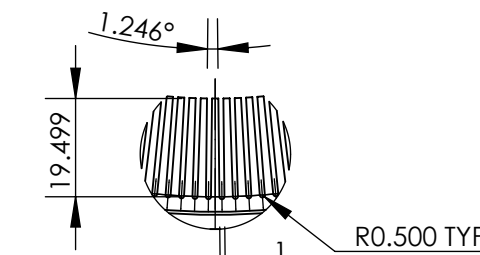
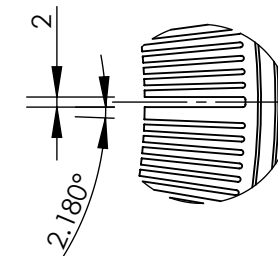
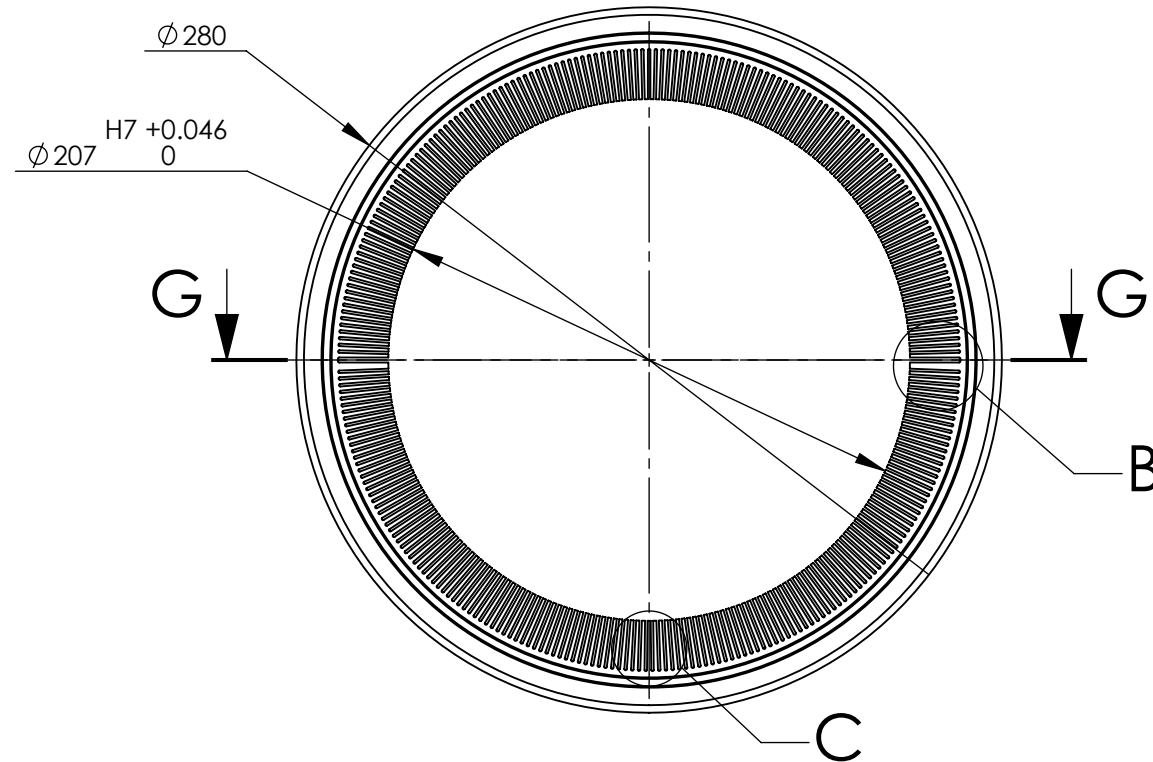
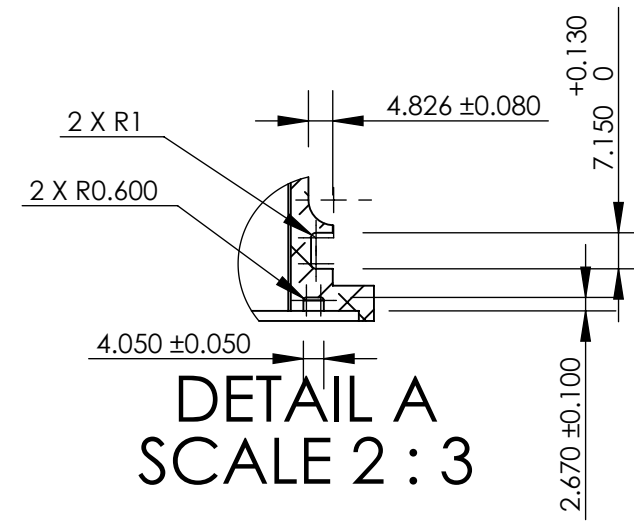
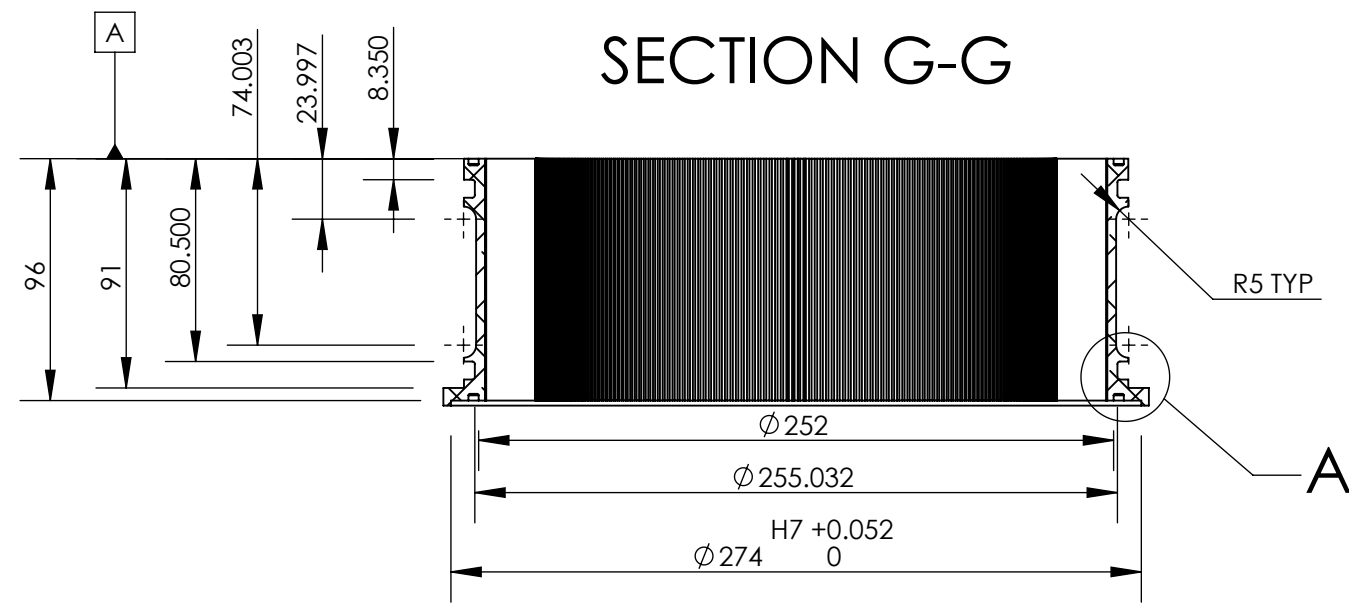


SECTION F-F

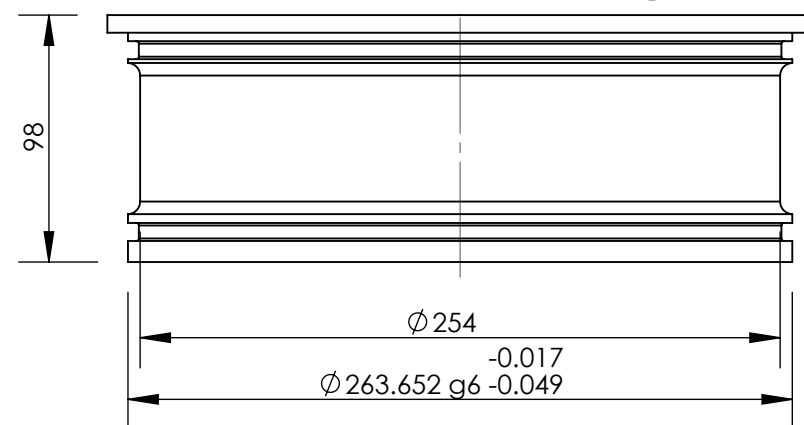


| | | | |
|--|--|---|---|
| <p>UNLESS OTHERWISE SPECIFIED: DIMENSIONS ARE IN MM</p> <p>TOLERANCES: LINEAR: 0.1 mm ANGULAR: 1°</p> <p>GENERAL SURFACE FINISH: Ra 5 μm O-RING SEAL SURFACE FINISH: Ra 0.8 μm</p> <p>MATERIAL: Various</p> <p>FILE NAME: A-DC-HC-00-HEX_CARTRIDGE_ASM</p> | <p>Comments:</p> | <p>The Department of Mechanical Engineering UNIVERSITY OF ALBERTA</p> | <p>TITLE: Heat Exchanger Cartridge Assembly Section View</p> |
| | <p>DRW BY: Linda Hasanovich</p> <p>SM BY: Connor Speer</p> <p>CHK BY:</p> | | |
| | <p>Tuesday, September 6, 2022 12:54:55 PM</p> <p>Friday, February 16, 2018 11:53:24 AM</p> | <p>SIZE B</p> | <p>REV</p> |
| | <p>SCALE: 1:2</p> <p>Mass: 3776.11g</p> <p>SHEET 16 OF 18</p> | | |

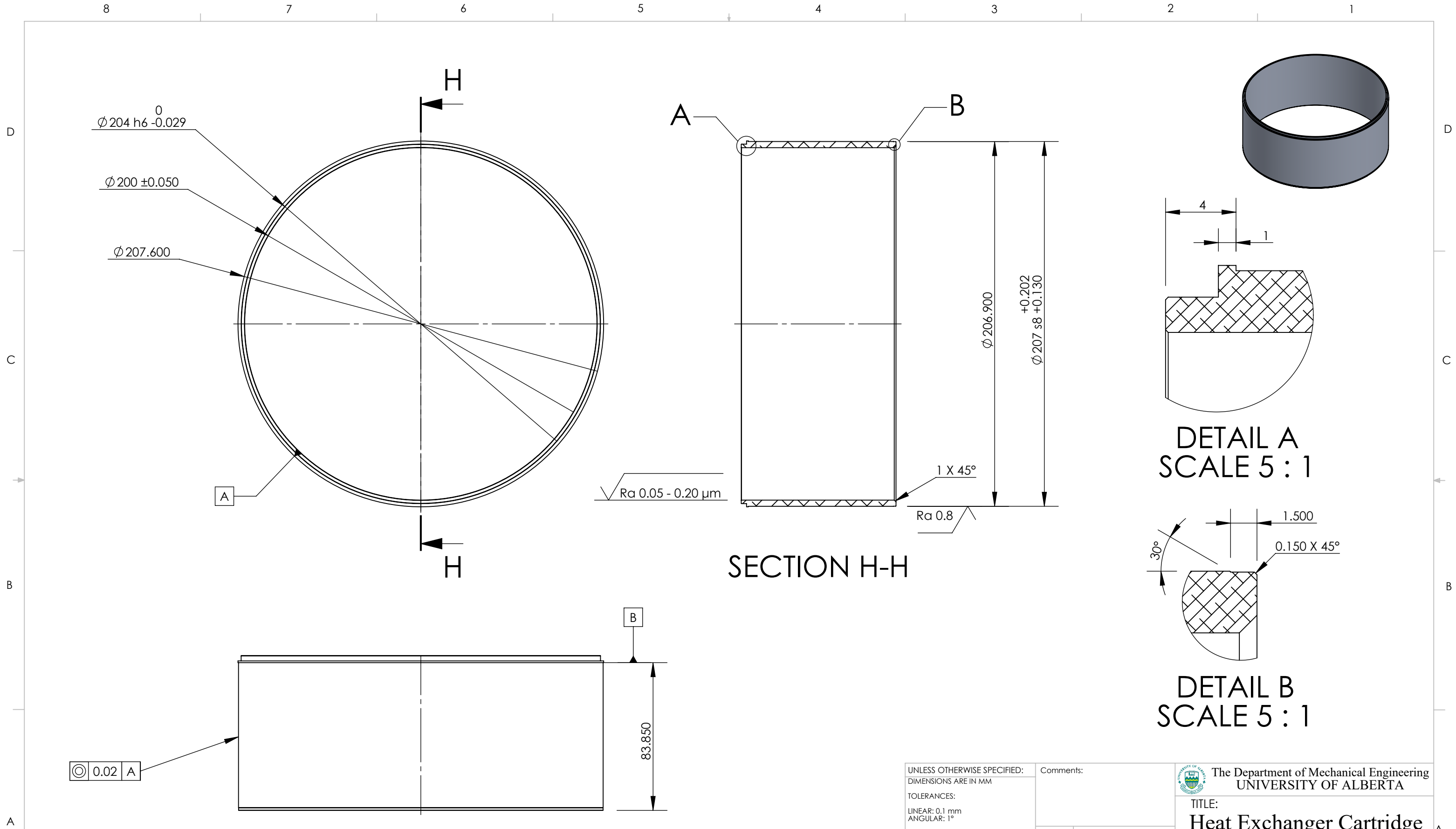




Note: There are 289 slots in total.
Slots are evenly spaced.



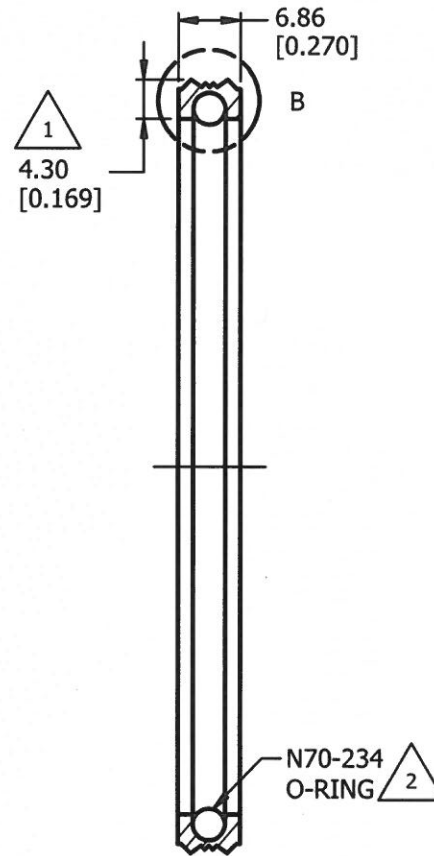
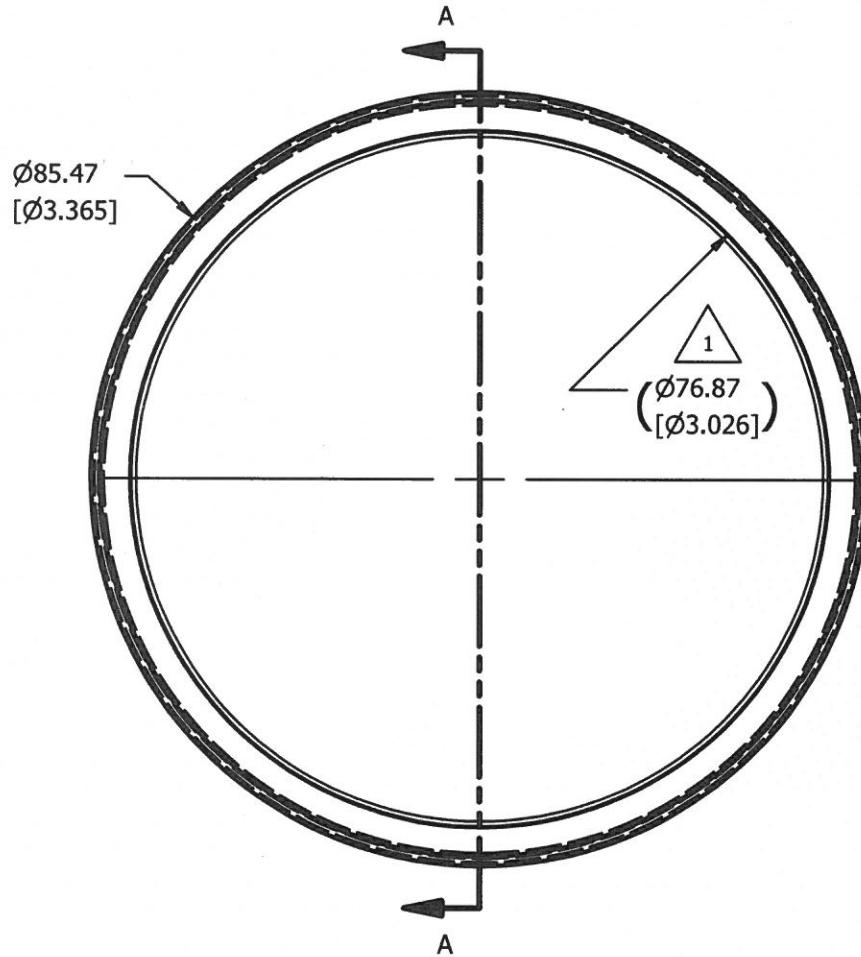
| | | | | |
|---|---|------------------|---|---|
| UNLESS OTHERWISE SPECIFIED: DIMENSIONS ARE IN MM TOLERANCES: LINEAR: 0.1 mm ANGULAR: 1° GENERAL SURFACE FINISH: Ra 5 µm O-RING SEAL SURFACE FINISH: Ra 0.8 µm | Comments: | |  The Department of Mechanical Engineering UNIVERSITY OF ALBERTA | |
| | DRW BY: | Linda Hasanovich | | TITLE: Heat Exchanger Cartridge |
|  MATERIAL: 6061-T6 (SS) | SM BY: | Connor Speer | SIZE Project: B Raphael Engine | |
| | CHK BY: | | | REV |
| FILE NAME: A-DC-HC-01-HEX_CARTRIDGE | Monday, July 19, 2021 5:26:59 PM Thursday, February 15, 2018 12:46:18 PM | SCALE: 1:3 | Mass: 3253.72 g | SHEET 17 OF 18 |



| | | | | | |
|---|----------------------------------|---|---|----------------|-------------------------------|
| UNLESS OTHERWISE SPECIFIED: DIMENSIONS ARE IN MM TOLERANCES: LINEAR: 0.1 mm ANGULAR: 1° GENERAL SURFACE FINISH: Ra 5 μm O-RING SEAL SURFACE FINISH: Ra 0.8 μm | Comments: | |  The Department of Mechanical Engineering UNIVERSITY OF ALBERTA | | |
| | DRW BY: | Linda Hasanovich | | TITLE: | Heat Exchanger Cartridge Pipe |
|  | SM BY: | Connor Speer | SIZE | Project: | REV |
| | CHK BY: | | B | Raphael Engine | |
| MATERIAL: 6061-T6 (SS) | Monday, July 19, 2021 5:26:59 PM | Thursday, February 15, 2018 12:58:28 PM | SCALE: 1:2 | Mass: 522.39 g | SHEET 18 OF 18 |
| FILE NAME: A-DC-HC-02-HEX_CARTRIDGE_PIPE | | | | | |

DRAWING APPROVED FOR PRODUCTION/REFERENCE BY HTS ENGINEERING DEPARTMENT

| REV | INFO | BY: | APPR. | DATE |
|-----|----------------------------------|-----|-------|----------|
| 0 | INITIAL DRAWING | JS | SA | 01/15/18 |
| 1 | REVISED DIMENSIONS | JS | SA | 02/06/19 |
| 2 | REVISED O-RING SIZE FROM N70-233 | JS | SA | 02/27/19 |



SECTION A-A

NOTE: THE VALUES ARE BASED ON 2.5% C/S SQUEEZE.

ALL DIMENSIONS ARE IN mm [INCHES]
REMOVE ALL BURRS AND SHARP EDGES

| TOLERANCES UNLESS STATED OTHERWISE | |
|---------------------------------------|-------------|
| X.X ±0.1 | Frac. ±1/64 |
| X.XX ±0.13 | Ang. ±0.5° |
| X.XXX ±0.005 | |

DO NOT FILE OR COPY, FOR
CONSTRUCTION OR
REFERENCE ONLY. PLEASE
DESTROY AFTER USE.



HiTech Seals - Edmonton
9211-41 AVE NW
780 438 6055
Toll Free: 800 661 6055
Fax: 780 434 5866

www.hitechseals.com

| | | | |
|--------------|--------------------------|-------|--------|
| PART: | CS 337PTFESQMOD | | |
| DESCRIPTION: | PISTON CROWN SEAL | | |
| MATERIAL: | 25% CARBON GRAPHITE PTFE | DURO: | N/A |
| DRAWING: | CS007 | PAGE: | 1 OF 1 |
| | | REV: | 2 |

THIS DRAWING IS PROPERTY OF HI-TECH SEALS INC. AND MUST BE RETURNED ON DEMAND. THE DRAWING IS LOANED IN CONFIDENCE AND IS NOT TO BE REPRODUCED IN WHOLE OR PART WITHOUT WRITTEN CONSENT OF HI-TECH SEALS INC.

| | |
|--------------------|---------------------|
| INTERNAL INFO: N/A | |
| DRF: 5234 | INCLUDED: SEE ABOVE |
| MACHINE: N/A | PROGRAM: N/A |

Appendix G. Experimental Data Processing Code

All code is in MATLAB. The first file is the code that initiates processing of experimental or model (*MSPM*) data. The following files contain engine specifications used for processing, and carry out the processing of experimental data from the setup described in Chapter 2. The basis for this code was written by Connor Speer.

G.1 Starting Point of Experimental and Model Data Processing (‘post_process.m’)

```
% post_process.m - Written by Connor Speer - January 2019
% MSPM post processing added by Matthias Lottmann, January 2022
% Starting point for both experimental and MSPM data post processing.

%% IMPORTANT: For either section, need to specify environment pressure before
processing.
% [Pa]
% p_environment = 93.82 *1000; % 200kpa Dec16
% p_environment = 91.03 *1000; %350kpa 23 Dec
% p_environment = 93.78 *1000; %450kpa 14-Jan
% p_environment = 93.19 *1000; %400kpa 28-Jan

% p_environment = repelem([93.82 91.03 93.78 93.19]*1000, 2); %Combination,
in order of pressure - setpoint number
% p_environment = [93.82 91.03 93.78 93.19]*1000; %Combination, in order as
processed
% p_environment = p_environment([1,2,4,3, 2,4,1,3]);

% p_environment = p_environment([4,4,4,4,1,1,1,1]);
% p_environment = p_environment([4,4,1,1]);
% p_environment = p_environment([4,1]);
% p_environment = p_environment([1,1,4,4,4,4,1,1]);

% p_environment = 94.12 *1000; %TH130 Reg94 16-Feb
% p_environment = 94.25 *1000; %TH130 Reg97 02-Mar
% p_environment = 93.91 *1000; %TH130 Reg97 03-Mar
% p_environment = 93.17 *1000; %TH130 Reg97 16-Mar
% p_environment = 93.20 *1000; %TH130 Reg97 29-Mar
% p_environment = 94 *1000; % Standard pressure

p_environment = 0;

%% Run this section for MSPM data processing %%%%%%%%%%%
% Environment pressure will be subtracted from MSPM
% pressure outputs to obtain relative pressure, which is comparable to
```

```

% experiment pressure data.
% Also specify engine layout so that PVs are processed correctly. In
% 'DataExtract' must adjust 'PV_order' according to order of PV data in
% PVoutput file.
% IMPORTANT: Folder name should contain 'TH', 'TC', 'p' followed by
% setpoint parameters. These are extracted from folder name and included in
% the output.
layout = 'alpha';
% layout = 'gamma';
DataExtract(p_environment,layout);

%% Run this section for experiment data processing %%%%%%%%%%%
% Calls calibration, data reduction, and modeling sub-functions to
% post-process data in a given list of folders. Plotting will be done
% elsewhere.

%   clear, clc, close all;

% User selects an ENGINE_DATA structure to use for model inputs
ENGINE_DATA = T2_ENGINE_DATA;

% User selects a folder to post process.
path = 'G:\Shared drives\NOBES_GROUP\MSPM\[MATLAB_WORKING_FOLDER]\Data
Processing Code\06_Post Processing_Experimental\[Experimental Data]';
Raw_Data_Folder = uigetdir(path, 'Choose folder to post process.');
```

```

% Call to calibrate sub-function
% NOTE: Calibration data path is specified in 'calibrate.m'
calibrate(Raw_Data_Folder)

% Call to 'reduce' sub-function. If 'short_output' is true, raw data is not
included in output file.
% Environment pressure is stored in RD_DATA as 'p_atm'
short_output = true;
have_DCH_source = false;
reduce(Raw_Data_Folder, ENGINE_DATA, short_output, have_DCH_source,
p_environment);

```

G.2 Engine Specifications to Calculate Volumes

('T2_ENGINE_DATA')

```
function ENGINE_DATA = T2_ENGINE_DATA

% This function will define a structure that describes the geometric data,
% operating conditions, and working fluid properties for the engine.

% The values in this particular script correspond to the original displacer
% diameter, and the identical heater and cooler.

%% Drive Mechanism:
% Engine Type
ENGINE_DATA.engine_type = 'x'; % x --> Gamma slider crank

% Link 1 (Base)
ENGINE_DATA.Pr1 = 0; % Desaxe offset of piston in (m).
ENGINE_DATA.Dr1 = 0; % Desaxe offset of displacer in (m).

% Link 2 (Crank)
ENGINE_DATA.Pr2 = 0.0375 ; %[m] Piston crank throw radius (half stroke)
ENGINE_DATA.Dr2 = 0.0375; %[m] Displacer crank throw radius
ENGINE_DATA.Cb = -0.01599; % Distance from output shaft to crank center of
mass (m)
ENGINE_DATA.Cphi = 0; % Angle between Cb line and center line of crank
(radians)
ENGINE_DATA.Cm = 2.57134; % Mass of crank (kg). Entire crankshaft assembly.
Sans flywheel assembly since the flywheel center of mass doesn't move.
ENGINE_DATA.CIG = 0.00966444; % Moment of inertia of crank about the axis of
rotation (kg*m^2)

% Link 3 (Connecting Rod for Piston)
ENGINE_DATA.Pr3 = 0.146; % Center to center distance of con rod (m).
ENGINE_DATA.PRb = 0.06932; % Distance from wrist pin to con rod center of
mass (m).
ENGINE_DATA.PRphi = 0; % Angle b/w Rb line and center line of con rod
(radians)
ENGINE_DATA.PRm = 0.238; % Mass of connecting rod (kg)
ENGINE_DATA.PRIG = 0.00049283; % Moment of inertia about center of mass
(kg*m^2)

% Link 4 (Piston)
ENGINE_DATA.Pm = 0.788; % Mass of piston in (kg) (Piston + Wrist Pin + Bushing
+ Snap Rings) ADD MASS OF SEALS AND WEAR RINGS!!
ENGINE_DATA.Pbore = 0.08573 ; %[m]

% Link 5 (Connecting Rods for Displacer)
ENGINE_DATA.Dr3 = 0.130; % Center to center distance of con rod (m).
ENGINE_DATA.DRb = 0.07294; % Distance from wrist pin to con rod center of
mass (m).
```

```

ENGINE_DATA.DRphi = 0; % Angle b/w Rb line and center line of con rod
(radians)
ENGINE_DATA.DRm = 2*0.130; % Mass of connecting rod (kg)
ENGINE_DATA.DRIG = 2*0.00017865; % Moment of inertia about center of mass
(kg*m^2)

% Link 6 (Displacer)
ENGINE_DATA.Dm = 1.858; % Mass of displacer in (kg) (Displacer Body, Displacer
Base ASM, and Crossheads)
ENGINE_DATA.Dbore = 0.200; %[m]

% Crankshaft Axial Geometry
ENGINE_DATA.LCB2 = 0.07335; % Distance b/w large and small crankshaft
bearings (m)
ENGINE_DATA.LPR = 0.05131; % Distance b/w large crankshaft bearing and center
of power con rod bearing (m)

% Flywheel
ENGINE_DATA.FIG = 0.06237836; %(kg*m^2) Moment of inertia of the flywheel
assembly about the axis of rotation.

%% Volumes: DISPLACER ROD SHOULD BE ADDED TO VOLUME VARIATIONS
% Total Dead Volume
ENGINE_DATA.Vdead = 1831.788987/1e6; %[m^3]

% Power Piston Clearance Volume for Gamma Engines
% --> Includes the Cyl Head, Con Pipe, Disp Mount, and clearance disk in this
case.
ENGINE_DATA.Vclp = 170.6/1e6; %[m^3]

% Power Piston Swept Volume for Sinusoidal Gammas (and Schmidt analysis)
ENGINE_DATA.Vswp = ENGINE_DATA.Pr2*(pi/4)*ENGINE_DATA.Pbore^2; %[m^3]

% Total Displacer Clearance Volume (above, below, annular, and appendix gap)
for Gammas
ENGINE_DATA.Vcld_bottom = (pi/4)*(ENGINE_DATA.Dbore^2)*0.001+... % 1mm
clearance of displacer
0.01215*(pi/4)*(0.207^2-ENGINE_DATA.Dbore^2); % Heat exchanger annular
space
ENGINE_DATA.Vcld_top = pi/4*(ENGINE_DATA.Dbore^2)*0.001+... % 1mm clearance
0.01215*(pi/4)*((0.207^2)-(ENGINE_DATA.Dbore^2))+... % Heat exchanger
annular space
(pi/4)*((ENGINE_DATA.Dbore^2)-(0.198^2))*0.1404; % Appendix gap

% Displacer Swept Volume for Sinusoidal Gammas (and Schmidt analysis)
ENGINE_DATA.Vswd = ENGINE_DATA.Dr2*(pi/4)*ENGINE_DATA.Dbore^2; %[m^3]

% Displacer Phase Angle Advance for Gamma
ENGINE_DATA.beta_deg = 90.0; %[deg]

% Displacer Drive Rod Volume
ENGINE_DATA.d_disprod = 0.012; %(m) Diameter of the displacer rod.
ENGINE_DATA.V_disprod_min = ((ENGINE_DATA.d_disprod)^2)*(pi/4)*0.001; %(m^3)
Minimum volume of the displacer rod in the working space. 1 mm clearance.

```

```

%% Cooler:
% Cooler Type
% p --> smooth pipes
% a --> smooth annulus
% s --> slots
ENGINE_DATA.cooler_type = 's';

% Cooler Slot Width for Slot Cooler (circumferential direction)
ENGINE_DATA.cooler_slot_width = 1.00e-03; %[m]

% Cooler Slot Height for Slot Cooler (radial direction)
ENGINE_DATA.cooler_slot_height = 2.00e-02; %[m]

% Cooler Heat Exchanger Length (flow direction)
ENGINE_DATA.cooler_length = 9.600e-02; %[m]

% Cooler Number of Slots
ENGINE_DATA.cooler_num_slots = 289; %[m]

% Hydraulic Diameter [m]
ENGINE_DATA.cooler_D_h = 2*ENGINE_DATA.cooler_slot_width / (1 +
ENGINE_DATA.cooler_slot_width/ENGINE_DATA.cooler_slot_height);

ENGINE_DATA.cooler_A_cross = 5749e-6;
%% Regenerator:
% Regenerator Configuration
% t --> tubular regenerator
% a --> annular regenerator
ENGINE_DATA.regen_config = 'a';

% Regen Housing I.D. for Annular Regenerator
ENGINE_DATA.regen_housing_ID = 0.247; %[m]

% Matrix I.D. for Annular Regenerator
ENGINE_DATA.regen_matrix_ID = 0.207; %[m]

% Regenerator Length
ENGINE_DATA.regen_length = 0.0254; %[m]

% Regenerator Number of Tubes
ENGINE_DATA.regen_num_tubes = 1;

% Regenerator Matrix Type
% m --> mesh
% f --> foil
% n --> no matrix
ENGINE_DATA.regen_matrix_type = 'm';

% Matrix Porosity for Mesh Matrix
ENGINE_DATA.regen_matrix_porosity = 0.96;

% Matrix Wire Diameter for Mesh Matrix
ENGINE_DATA.regen_wire_diameter = 0.0001; %[m]
% ENGINE_DATA.regen_wire_diameter = 5.08e-05; %[m] (Connor)

```

```

%% Heater:
% Heater Type
% p --> smooth pipes
% a --> smooth annulus
% s --> slots
ENGINE_DATA.heater_type = 's';

% Heater Slot Width for Slot Heater (circumferential direction)
ENGINE_DATA.heater_slot_width = ENGINE_DATA.cooler_slot_width; %[m]

% Heater Slot Height for Slot Heater (radial direction)
ENGINE_DATA.heater_slot_height = ENGINE_DATA.cooler_slot_height; %[m]

% Heater Heat Exchanger Length (flow direction)
ENGINE_DATA.heater_length = ENGINE_DATA.cooler_length; %[m]

% Heater Number of Slots for Slot Heater
ENGINE_DATA.heater_num_slots = ENGINE_DATA.cooler_num_slots;

ENGINE_DATA.heater_D_h = ENGINE_DATA.cooler_D_h;

%% Operating Conditions:
% Working Fluid
% hy --> hydrogen
% he --> helium
% ai --> air
ENGINE_DATA.gas_type = 'ai';

% Mean Pressure
ENGINE_DATA.pmean = 1000000.0; %[Pa]  (= 10 bar)

% Cold Sink Temperature
ENGINE_DATA.Tsink = 5 + 273.15; %[K]

% Cooler Gas Temperature
ENGINE_DATA.Tgk = 21 + 273.15; %[K]

% Cooler Wall Temperature
ENGINE_DATA.Twk = 21 + 273.15; %[K]

% Compression Space Temperature
ENGINE_DATA.Tgc = 21 + 273.15; %[K]

% Hot Source Temperature
ENGINE_DATA.Tsource = 273 + 150; %[K]

% Heater Gas Temperature
ENGINE_DATA.Tgh = 273 + 130; %[K]

% Heater Wall Temperature
ENGINE_DATA.Twh = 273 + 130; %[K]

% Expansion Space Temperature

```

```

ENGINE_DATA.Tge = 273 + 130; %[K]

% Operating Frequency
ENGINE_DATA.freq = 2; %[Hz]

%% Cooling System
% ENGINE_DATA.c_coolant = 4184; % Specific heat capacity of water in [J/kgK]
% ENGINE_DATA.dens_coolant = 1000; % Water density [kg/m^3]
ENGINE_DATA.c_coolant = 3118.57; %(J/kgK) - for 50% ethylene glycol water mix
at 10 deg C
ENGINE_DATA.dens_coolant = 1101.12; %(kg/m^3) - for 50% ethylene glycol water
mix at 10 deg C

%% Heating System
% ENGINE_DATA.c_hot_liquid = 4184; % Specific heat capacity of water in
[J/kgK]
% ENGINE_DATA.dens_hot_liquid = 1000; % Water density [kg/m^3]
ENGINE_DATA.c_hot_liquid = 1510; %(J/kgK) - for SIL 180 at 20 deg C
ENGINE_DATA.dens_hot_liquid = 930; %(kg/m^3) - for SIL 180 at 20 deg C

%% Data for Engine Specific Loss Calculations:
% Maximum volume of the buffer space
% Volume of crankcase extension has been added
% Matthias from Solidworks (300mm extension)
ENGINE_DATA.V_buffer_max = 0.007312332;
% Connor (460mm extension)
% ENGINE_DATA.V_buffer_max = 0.0032 + (0.460*(pi/4)*(0.1282^2)); %[m^3]

% Constant mechanism effectiveness
ENGINE_DATA.effect = 0.8; % [unitless]

% Configuration code for GSH calculation
ENGINE_DATA.GSH_config = 1; % Big CC extension

```

G.3 Reading and Calibration of Raw Experimental Data (‘calibrate.m’)

```
function calibrate(Raw_Data_Folder)

% Written by Connor Speer, September 2018
% Torque Sensor added, variables added, code for fits simplified by Matthias
Lottmann, 2021

% This script uses the calibration data to adjust the raw log files and
% saves them as MATLAB files for future post processing. The MATLAB file
% will contain information for the entire folder and share the folder's
% name.

%% Input Parameters
PSI_to_Pa = 6894.757;

% RTD Calibration Data Folder
% RTD_Cal_Folder = 'G:\Shared
drives\NOBES_GROUP\MSPM\[MATLAB_WORKING_FOLDER]\Data Processing Code\06_Post
Processing_Experimental\[Experimental Data]\00_Calibration\October 6th
Calibration Data\RTD';
RTD_Cal_Folder = 'G:\Shared
drives\NOBES_GROUP\MSPM\[MATLAB_WORKING_FOLDER]\Data Processing Code\06_Post
Processing_Experimental\[Experimental
Data]\00_Calibration\Cal_2022_06_10\RTD';

% TC Calibration Data Folder
TC_Cal_Folder = 'G:\Shared
drives\NOBES_GROUP\MSPM\[MATLAB_WORKING_FOLDER]\Data Processing Code\06_Post
Processing_Experimental\[Experimental
Data]\00_Calibration\Cal_2022_06_10\TC';

%% Preallocate Space For the DATA Structure
% Collect all the log file names from the RTD calibration data folder
log_files_info = dir(fullfile(Raw_Data_Folder, '*.txt'));
n_setpoints = length(log_files_info)/3;

C_DATA(n_setpoints).filename = [];
C_DATA(n_setpoints).time_RTD = [];
C_DATA(n_setpoints).RTD_0 = [];
C_DATA(n_setpoints).RTD_1 = [];
C_DATA(n_setpoints).RTD_2 = [];
C_DATA(n_setpoints).RTD_3 = [];
C_DATA(n_setpoints).RTD_4 = [];
C_DATA(n_setpoints).RTD_5 = [];
C_DATA(n_setpoints).RTD_6 = [];
C_DATA(n_setpoints).RTD_7 = [];
C_DATA(n_setpoints).time_TC = [];
C_DATA(n_setpoints).TC_0 = [];
```

```

C_DATA(n_setpoints).TC_1 = [];
C_DATA(n_setpoints).TC_2 = [];
C_DATA(n_setpoints).TC_3 = [];
C_DATA(n_setpoints).TC_4 = [];
C_DATA(n_setpoints).TC_5 = [];
C_DATA(n_setpoints).TC_6 = [];
C_DATA(n_setpoints).TC_7 = [];
C_DATA(n_setpoints).TC_8 = [];
C_DATA(n_setpoints).TC_9 = [];
C_DATA(n_setpoints).TC_10 = [];
C_DATA(n_setpoints).time_VC = [];
C_DATA(n_setpoints).theta = [];
C_DATA(n_setpoints).p_DCH = [];
C_DATA(n_setpoints).p_DM = [];
C_DATA(n_setpoints).p_PC = [];
C_DATA(n_setpoints).p_CC = [];
C_DATA(n_setpoints).p_PC_static = [];
C_DATA(n_setpoints).p_CC_static = [];
C_DATA(n_setpoints).MB_speed = [];
C_DATA(n_setpoints).MB_speed_transient = [];

C_DATA(n_setpoints).p_regulator = [];
C_DATA(n_setpoints).torque_sensor_transient = [];

% C_DATA(n_setpoints).dens_hot = [];
% C_DATA(n_setpoints).dens_cold = [];
% C_DATA(n_setpoints).c_hot = [];
% C_DATA(n_setpoints).c_cold = [];
C_DATA(n_setpoints).hot_bath_setpoint = [];
C_DATA(n_setpoints).cold_bath_setpoint = [];
C_DATA(n_setpoints).hot_liquid_flowrate = [];
C_DATA(n_setpoints).cold_liquid_flowrate = [];
C_DATA(n_setpoints).pmean_setpoint = [];
C_DATA(n_setpoints).torque_setpoint = [];
C_DATA(n_setpoints).teknik_setpoint = [];

%% Fit Curves to the Calibration Data (Only do this once)
% RTDs %%%%%%%%%%%%%%%%%%%%%%%%%%%%%%%%%%%%%%%%%%%%%%%%%%%%%%%%%%%%%%%%%%%%%%%%%%
% --> Same procedure as TCs. See below.

% Collect all the log file names from the RTD calibration data folder
RTD_log_files_info = dir(fullfile(RTD_Cal_Folder, '*.txt'));

% Preallocate space for the structure array
RTD_DATA(length(RTD_log_files_info)).RTD_0_corr = [];
RTD_DATA(length(RTD_log_files_info)).RTD_1_corr = [];
RTD_DATA(length(RTD_log_files_info)).RTD_2_corr = [];
RTD_DATA(length(RTD_log_files_info)).RTD_3_corr = [];
RTD_DATA(length(RTD_log_files_info)).RTD_4_corr = [];
RTD_DATA(length(RTD_log_files_info)).RTD_5_corr = [];
RTD_DATA(length(RTD_log_files_info)).RTD_6_corr = [];
RTD_DATA(length(RTD_log_files_info)).RTD_7_corr = [];

% Initialize counter variable
counter = 1;
counter_max = 0.5*length(RTD_log_files_info);

```

```

WaitBar = waitbar(0, 'Analyzing RTD calibration data...');

% Open Calibration Log Files
for i = 1:1:length(RTD_log_files_info)
    filename_RTD = strcat(RTD_Cal_Folder, '\', RTD_log_files_info(i).name);
    [~,~,~,~,...
    ~,~,~,...
    ~,~,~,RTD_0,RTD_1,RTD_2,RTD_3,...
    RTD_4,RTD_5,RTD_6,RTD_7] = importfile_RTD(filename_RTD);
%     RTD_0 --> Displacer Cylinder Head Inlet
%     RTD_1 --> Displacer Cylinder Head Outlet
%     RTD_2 --> Heater Inlet
%     RTD_3 --> Heater Outlet
%     RTD_4 --> Cooler Inlet
%     RTD_5 --> Cooler Outlet
%     RTD_6 --> Power Cylinder Inlet
%     RTD_7 --> Power Cylinder Outlet

% Calculate the average reading for each RTD
RTD_DATA(counter).RTD_0_avg = mean(RTD_0); % (°C)
RTD_DATA(counter).RTD_1_avg = mean(RTD_1); % (°C)
RTD_DATA(counter).RTD_2_avg = mean(RTD_2); % (°C)
RTD_DATA(counter).RTD_3_avg = mean(RTD_3); % (°C)
RTD_DATA(counter).RTD_4_avg = mean(RTD_4); % (°C)
RTD_DATA(counter).RTD_5_avg = mean(RTD_5); % (°C)
RTD_DATA(counter).RTD_6_avg = mean(RTD_6); % (°C)
RTD_DATA(counter).RTD_7_avg = mean(RTD_7); % (°C)

% Calculate the "true" temperature as the average of all RTDs
RTD_true = mean([mean(RTD_0) mean(RTD_1) mean(RTD_2) mean(RTD_3)
mean(RTD_5) mean(RTD_6) mean(RTD_7)]); % (°C)
%mean(RTD_4)
% Calculate the correction term for each RTD
RTD_DATA(counter).RTD_0_corr = RTD_true - mean(RTD_0); % (°C)
RTD_DATA(counter).RTD_1_corr = RTD_true - mean(RTD_1); % (°C)
RTD_DATA(counter).RTD_2_corr = RTD_true - mean(RTD_2); % (°C)
RTD_DATA(counter).RTD_3_corr = RTD_true - mean(RTD_3); % (°C)
RTD_DATA(counter).RTD_4_corr = RTD_true - mean(RTD_4); % (°C)
RTD_DATA(counter).RTD_5_corr = RTD_true - mean(RTD_5); % (°C)
RTD_DATA(counter).RTD_6_corr = RTD_true - mean(RTD_6); % (°C)
RTD_DATA(counter).RTD_7_corr = RTD_true - mean(RTD_7); % (°C)

% Increment the counter variable
counter = counter + 1;

% Update Wait Bar
waitbar(counter / counter_max)
%%%%%%%%%%%%%%%%%%%%%%%%%%%%%%%%%%%%%%%%%%%%%%%%%%%%%%%%%%%%%%%%%%%%%%%%
RTD_true_log(i)=RTD_true;
end
close(WaitBar);

% Fit curves to correction terms

```

```

[fits.RTD_0, gofs.RTD_0] =
fit([RTD_DATA.RTD_0_avg]', [RTD_DATA.RTD_0_corr]', 'poly3');
[fits.RTD_1, gofs.RTD_1] =
fit([RTD_DATA.RTD_1_avg]', [RTD_DATA.RTD_1_corr]', 'poly3');
[fits.RTD_2, gofs.RTD_2] =
fit([RTD_DATA.RTD_2_avg]', [RTD_DATA.RTD_2_corr]', 'poly3');
[fits.RTD_3, gofs.RTD_3] =
fit([RTD_DATA.RTD_3_avg]', [RTD_DATA.RTD_3_corr]', 'poly3');
[fits.RTD_4, gofs.RTD_4] =
fit([RTD_DATA.RTD_4_avg]', [RTD_DATA.RTD_4_corr]', 'poly3');
[fits.RTD_5, gofs.RTD_5] =
fit([RTD_DATA.RTD_5_avg]', [RTD_DATA.RTD_5_corr]', 'poly3');
[fits.RTD_6, gofs.RTD_6] =
fit([RTD_DATA.RTD_6_avg]', [RTD_DATA.RTD_6_corr]', 'poly3');
[fits.RTD_7, gofs.RTD_7] =
fit([RTD_DATA.RTD_7_avg]', [RTD_DATA.RTD_7_corr]', 'poly3');

%%
% THESIS plots
% x = RTD_true_log;
% colors = {'k', 'b', 'r', 'g'};
% colors = repmat(colors,1,2);
% markers = repelem({'o', '>'},4);
%
% figure
% hold on
% xlabel('"True" reference temperature [\circC]')
% ylabel('Error before calibration [\circC]')
% for i=[0:3,5:7]
%     scatter(x, eval("-[RTD_DATA.RTD_"+i+"_corr]"), 30,colors{i+1},
markers{i+1})
% end
% nicefigure('thesis_half')
%
% figure
% hold on
% xlabel('"True" reference temperature [\circC]')
% ylabel('Error after calibration [\circC]')
% for i=[0:3,5:7]
%     scatter(x, (eval("[RTD_DATA.RTD_"+i+"_avg] +
fits.RTD_"+i+"([RTD_DATA.RTD_"+i+"_avg])'") - x), 30,colors{i+1},
markers{i+1})
% end
% nicefigure('thesis_half')

% Other plots
% figure
% plot(fits.RTD_0, [RTD_DATA.RTD_0_avg]', [RTD_DATA.RTD_0_corr]', '*')
% xlabel('RTD 0 avg (°C)')
% ylabel('Correction Term (°C)')
%
% figure
% plot(fits.RTD_1, [RTD_DATA.RTD_1_avg]', [RTD_DATA.RTD_1_corr]', '*')
% xlabel('RTD 1 avg (°C)')
% ylabel('Correction Term (°C)')
%

```

```

% figure
% plot(fits.RTD_2,[RTD_DATA.RTD_2_avg]',[RTD_DATA.RTD_2_corr]','*')
% xlabel('RTD 2 avg (°C)')
% ylabel('Correction Term (°C)')
%
% figure
% plot(fits.RTD_3,[RTD_DATA.RTD_3_avg]',[RTD_DATA.RTD_3_corr]','*')
% xlabel('RTD 3 avg (°C)')
% ylabel('Correction Term (°C)')
%
% figure
% plot(fits.RTD_4,[RTD_DATA.RTD_4_avg]',[RTD_DATA.RTD_4_corr]','*')
% xlabel('RTD 4 avg (°C)')
% ylabel('Correction Term (°C)')
%
% figure
% plot(fits.RTD_5,[RTD_DATA.RTD_5_avg]',[RTD_DATA.RTD_5_corr]','*')
% xlabel('RTD 5 avg (°C)')
% ylabel('Correction Term (°C)')
%
% figure
% plot(fits.RTD_6,[RTD_DATA.RTD_6_avg]',[RTD_DATA.RTD_6_corr]','*')
% xlabel('RTD 6 avg (°C)')
% ylabel('Correction Term (°C)')
%
% figure
% plot(fits.RTD_7,[RTD_DATA.RTD_7_avg]',[RTD_DATA.RTD_7_corr]','*')
% xlabel('RTD 7 avg (°C)')
% ylabel('Correction Term (°C)')

%% Thermocouples %%%%%%%%%%%%%%%%%%%%%%%%%%%%%%%%%%%%%%%%%%%%%%%%%%%%%%%%%%%%%%%
% --> Calculate the average temperature measurement at each calibration
% point.
% --> Take these average temperatures to be the "true" temperatures.
% --> Calculate the correction terms for each TC at each calibration point
% as the difference between the measured value and the "true" value.
% --> Fit curves to the correction terms of each TC.
% --> Use the equations of the curves to calculate the corresponding
% correction term for each TC measurement
% --> Add the correction terms to the measured data points to apply the
% calibration

% Collect all the log file names from the thermocouple test data folder
TC_log_files_info = dir(fullfile(TC_Cal_Folder, '*.txt'));

% Preallocate space for the structure array
TC_DATA(length(TC_log_files_info)).TC_0_corr = [];
TC_DATA(length(TC_log_files_info)).TC_1_corr = [];
TC_DATA(length(TC_log_files_info)).TC_2_corr = [];
TC_DATA(length(TC_log_files_info)).TC_3_corr = [];
TC_DATA(length(TC_log_files_info)).TC_4_corr = [];
TC_DATA(length(TC_log_files_info)).TC_5_corr = [];
TC_DATA(length(TC_log_files_info)).TC_6_corr = [];
TC_DATA(length(TC_log_files_info)).TC_7_corr = [];
TC_DATA(length(TC_log_files_info)).TC_8_corr = [];

```

```

TC_DATA(length(TC_log_files_info)).TC_9_corr = [];
TC_DATA(length(TC_log_files_info)).TC_10_corr = [];

% Initialize counter variable
counter = 1;
counter_max = 0.5*length(TC_log_files_info);

WaitBar = waitbar(0, 'Analyzing TC calibration data...');

% Open Calibration Log Files
for i = 1:length(TC_log_files_info)
    filename_TC = strcat(TC_Cal_Folder, '\', TC_log_files_info(i).name);
    [~, TC_0, TC_1, TC_2, TC_3, TC_4, TC_5, TC_6, TC_7, TC_8, TC_9, ...
    TC_10, ~, ~, ~, ~, ~] = importfile_TC(filename_TC);
    % TC_0 --> Displacer Cylinder Head (Expansion Space)
    % TC_1 --> Heater/Expansion Space Interface, Bypass Side (Far Side)
    % TC_2 --> Heater/Expansion Space Interface, Connecting Pipe Side
    % TC_3 --> Regen/Heater Interface, Bypass Side
    % TC_4 --> Regen/Heater Interface, Connecting Pipe Side
    % TC_5 --> Cooler/Regenerator Interface, Bypass Side
    % TC_6 --> Cooler/Regenerator Interface, Connecting Pipe Side
    % TC_7 --> Compression Space/Cooler Interface, Bypass Side
    % TC_8 --> Compression Space/Cooler Interface, Connecting Pipe Side
    % TC_9 --> Power Cylinder
    % TC_10 --> Crankcase
    % TC_11 -->
    % TC_12 -->
    % TC_13 -->
    % TC_14 -->
    % TC_15 -->

    % Calculate the average reading for each thermocouple
    TC_DATA(counter).TC_0_avg = mean(TC_0); % (°C)
    TC_DATA(counter).TC_1_avg = mean(TC_1); % (°C)
    TC_DATA(counter).TC_2_avg = mean(TC_2); % (°C)
    TC_DATA(counter).TC_3_avg = mean(TC_3); % (°C)
    TC_DATA(counter).TC_4_avg = mean(TC_4); % (°C)
    TC_DATA(counter).TC_5_avg = mean(TC_5); % (°C)
    TC_DATA(counter).TC_6_avg = mean(TC_6); % (°C)
    TC_DATA(counter).TC_7_avg = mean(TC_7); % (°C)
    TC_DATA(counter).TC_8_avg = mean(TC_8); % (°C)
    TC_DATA(counter).TC_9_avg = mean(TC_9); % (°C)
    TC_DATA(counter).TC_10_avg = mean(TC_10); % (°C)

    % Calculate the "true" temperature as the average of all TCs
    TC_true = mean([mean(TC_0) mean(TC_1) mean(TC_2) mean(TC_4) ...
    mean(TC_5) mean(TC_6) mean(TC_7) mean(TC_8) mean(TC_9) mean(TC_10)]);
    % (°C)

    % Calculate the correction term for each TC
    TC_DATA(counter).TC_0_corr = TC_true - mean(TC_0); % (°C)
    TC_DATA(counter).TC_1_corr = TC_true - mean(TC_1); % (°C)
    TC_DATA(counter).TC_2_corr = TC_true - mean(TC_2); % (°C)
    TC_DATA(counter).TC_3_corr = TC_true - mean(TC_3); % (°C)
    TC_DATA(counter).TC_4_corr = TC_true - mean(TC_4); % (°C)
    TC_DATA(counter).TC_5_corr = TC_true - mean(TC_5); % (°C)

```

```

TC_DATA(counter).TC_6_corr = TC_true - mean(TC_6); % (°C)
TC_DATA(counter).TC_7_corr = TC_true - mean(TC_7); % (°C)
TC_DATA(counter).TC_8_corr = TC_true - mean(TC_8); % (°C)
TC_DATA(counter).TC_9_corr = TC_true - mean(TC_9); % (°C)
TC_DATA(counter).TC_10_corr = TC_true - mean(TC_10); % (°C)

% Increment the counter variable
counter = counter + 1;

% Update Wait Bar
waitbar(counter / counter_max)
%%%%%%%%%%%%%%
TC_true_log(i) = TC_true;
end
close(WaitBar);

% Fit curves to correction terms
[fits.TC_0, gofs.TC_0] =
fit([TC_DATA.TC_0_avg]', [TC_DATA.TC_0_corr]', 'poly3');
[fits.TC_1, gofs.TC_1] =
fit([TC_DATA.TC_1_avg]', [TC_DATA.TC_1_corr]', 'poly3');
[fits.TC_2, gofs.TC_2] =
fit([TC_DATA.TC_2_avg]', [TC_DATA.TC_2_corr]', 'poly3');
[fits.TC_3, gofs.TC_3] =
fit([TC_DATA.TC_3_avg]', [TC_DATA.TC_3_corr]', 'poly3');
[fits.TC_4, gofs.TC_4] =
fit([TC_DATA.TC_4_avg]', [TC_DATA.TC_4_corr]', 'poly3');
[fits.TC_5, gofs.TC_5] =
fit([TC_DATA.TC_5_avg]', [TC_DATA.TC_5_corr]', 'poly3');
[fits.TC_6, gofs.TC_6] =
fit([TC_DATA.TC_6_avg]', [TC_DATA.TC_6_corr]', 'poly3');
[fits.TC_7, gofs.TC_7] =
fit([TC_DATA.TC_7_avg]', [TC_DATA.TC_7_corr]', 'poly3');
[fits.TC_8, gofs.TC_8] =
fit([TC_DATA.TC_8_avg]', [TC_DATA.TC_8_corr]', 'poly3');
[fits.TC_9, gofs.TC_9] =
fit([TC_DATA.TC_9_avg]', [TC_DATA.TC_9_corr]', 'poly3');
[fits.TC_10, gofs.TC_10] =
fit([TC_DATA.TC_10_avg]', [TC_DATA.TC_10_corr]', 'poly3');

%%
% % THESIS plots
% colors = {'k','b','r','g','m','c'};
% colors = repmat(colors,1,3);
% markers = repelem({'o','>','s'},6);
%
% np = 1;
% ys = [];
% figure
% hold on
% xlabel('"True" reference temperature [\circC]')
% ylabel('Error before calibration [\circC]')
% for i=0:10
%     y = eval("-[TC_DATA.TC_" + i + "_corr]");
%     ys = [ys y];
%     scatter(TC_true_log, y, 30, colors{np}, markers{np})

```

```

%     np = np+1;
% end
% for i=[0:3,5:7]
%     y = eval("-[RTD_DATA.RTD_" + i + "_corr]");
%     ys = [ys y];
%     scatter(RTD_true_log, y, 30, colors{np}, markers{np})
%     np = np+1;
% end
% nicefigure('thesis_half')
% rsserror = rssq(ys);
% disp("RSS error before cali: " + rsserror)
%
% np = 1;
% ys = [];
% figure
% hold on
% xlabel('"True" reference temperature [\circC]')
% ylabel('Error after calibration [\circC]')
% for i=0:10
%     y = eval("[TC_DATA.TC_" + i + "_avg] +
fits.TC_" + i + "([TC_DATA.TC_" + i + "_avg])'" ) - TC_true_log;
%     ys = [ys y];
%     scatter(TC_true_log, y, 30, colors{np}, markers{np})
%     np = np+1;
% end
% for i=[0:3,5:7]
%     y = eval("[RTD_DATA.RTD_" + i + "_avg] +
fits.RTD_" + i + "([RTD_DATA.RTD_" + i + "_avg])'" ) - RTD_true_log;
%     ys = [ys y];
%     scatter(RTD_true_log, y, 30, colors{np}, markers{np})
%     np = np+1;
% end
% nicefigure('thesis_small')
% rsserror = rssq(ys);
% disp(newline + "RSS error after cali: " + rsserror)
%
%
% % % Other plots
% figure
% plot(fits.TC_0, [TC_DATA.TC_0_avg]', [TC_DATA.TC_0_corr]', '*')
% xlabel('TC 0 avg ( $^{\circ}$ C)')
% ylabel('Correction Term ( $^{\circ}$ C)')
%
% figure
% plot(fits.TC_1, [TC_DATA.TC_1_avg]', [TC_DATA.TC_1_corr]', '*')
% xlabel('TC 1 avg ( $^{\circ}$ C)')
% ylabel('Correction Term ( $^{\circ}$ C)')
%
% figure
% plot(fits.TC_2, [TC_DATA.TC_2_avg]', [TC_DATA.TC_2_corr]', '*')
% xlabel('TC 2 avg ( $^{\circ}$ C)')
% ylabel('Correction Term ( $^{\circ}$ C)')
%
% figure
% plot(fits.TC_3, [TC_DATA.TC_3_avg]', [TC_DATA.TC_3_corr]', '*')
% xlabel('TC 3 avg ( $^{\circ}$ C)')
% ylabel('Correction Term ( $^{\circ}$ C)')

```

```

%
% figure
% plot(fits.TC_4,[TC_DATA.TC_4_avg]',[TC_DATA.TC_4_corr]','*')
% xlabel('TC 4 avg (°C)')
% ylabel('Correction Term (°C)')
%
% figure
% plot(fits.TC_5,[TC_DATA.TC_5_avg]',[TC_DATA.TC_5_corr]','*')
% xlabel('TC 5 avg (°C)')
% ylabel('Correction Term (°C)')
%
% figure
% plot(fits.TC_6,[TC_DATA.TC_6_avg]',[TC_DATA.TC_6_corr]','*')
% xlabel('TC 6 avg (°C)')
% ylabel('Correction Term (°C)')
%
% figure
% plot(fits.TC_7,[TC_DATA.TC_7_avg]',[TC_DATA.TC_7_corr]','*')
% xlabel('TC 7 avg (°C)')
% ylabel('Correction Term (°C)')
%
% figure
% plot(fits.TC_8,[TC_DATA.TC_8_avg]',[TC_DATA.TC_8_corr]','*')
% xlabel('TC 8 avg (°C)')
% ylabel('Correction Term (°C)')
%
% figure
% plot(fits.TC_9,[TC_DATA.TC_9_avg]',[TC_DATA.TC_9_corr]','*')
% xlabel('TC 9 avg (°C)')
% ylabel('Correction Term (°C)')
%
% figure
% plot(fits.TC_10,[TC_DATA.TC_10_avg]',[TC_DATA.TC_10_corr]','*')
% xlabel('TC 10 avg (°C)')
% ylabel('Correction Term (°C)')

%% Dynamic Pressure Transducers %%%%%%%%%%%
% --> Same procedure as static pressure

% Calibration Data for LW37338 Transducer
PSI_LW37338 = [1 2 3 4 5 10 20 30 40 50]; %(psig)
Vdc_LW37338 = [0.0996 0.1988 0.2971 0.3960 0.4940 0.989 1.986 2.985 3.975
4.980]; % Calibration outputs in (Volts)

[fits.DP_LW37338, gofs.DP_LW37338] = fit(Vdc_LW37338',PSI_LW37338','poly1');

% Calibration Data for LW37354 Transducer
PSI_LW37354 = [1 2 3 4 5 10 20 30 40 50]; %(psig)
Vdc_LW37354 = [0.101 0.202 0.302 0.403 0.502 1.016 2.028 3.041 4.052 5.073];
% Calibration outputs in (Volts)

[fits.DP_LW37354, gofs.DP_LW37354] = fit(Vdc_LW37354',PSI_LW37354','poly1');

% Calibration Data for LW37355 Transducer
PSI_LW37355 = [1 2 3 4 5 10 20 30 40 50]; %(psig)

```

```

Vdc_LW37355 = [0.102 0.205 0.306 0.409 0.510 1.029 2.056 3.088 4.118 5.151];
% Calibration outputs in (Volts)

[fits.DP_LW37355, gofs.DP_LW37355] = fit(Vdc_LW37355',PSI_LW37355','poly1');

% Calibration Data for LW37337 Transducer
PSI_LW37337 = [1 2 3 4 5 10 20 30 40 50]; %(psig)
Vdc_LW37337 = [0.0951 0.1905 0.2870 0.3805 0.4761 0.953 1.903 2.863 3.816
4.751]; % Calibration outputs in (Volts)

[fits.DP_LW37337, gofs.DP_LW37337] = fit(Vdc_LW37337',PSI_LW37337','poly1');

% figure
% plot(fits.DP_LW37337)
% hold on
% plot(Vdc_LW37337, fits.DP_LW37337(Vdc_LW37337),'o');
% plot(-Vdc_LW37337, fits.DP_LW37337(-Vdc_LW37337),'o');
% legend('1','2','3')

%% Static Pressure Transducers %%%%%%%%%%%
% --> Fit curve to calibration data to get an equation that converts
% voltage to Pa for each transducer
% --> Use equations to convert measured voltages into pressures

% Calibration Data for 772967 Transducer
PSI_772967 = [0 40 80 120 160 200 0]; %(psig)
Vdc_772967 = [0.000 2.006 4.002 5.998 7.986 9.968 0.000]; % Calibration
outputs in (Volts)

fits.SP_772967 = fit(Vdc_772967',PSI_772967','poly1');

% Calibration Data for 772966 Transducer
PSI_772966 = [0 40 80 120 160 200 0]; %(psig)
Vdc_772966 = [0.000 2.008 4.010 6.002 7.987 9.971 0.000]; % Calibration
outputs in (Volts)

fits.SP_772966 = fit(Vdc_772966',PSI_772966','poly1');

%% Torque Sensor (Futek TRS600 - FSH01997 10Nm) %%%%%%%%%%%
NM_TRS600 = [0 1.695 3.389 5.084 6.779 8.474 9.999 0];
Vdc_TRS600 = [0 0.846 1.698 2.543 3.391 4.238 5.001 0.013];
% using only points for 0, 1.695, 0 Nm since others are out of experiment
range
fits.TRS600 = fit(Vdc_TRS600([1,2,end])', NM_TRS600([1,2,end])', 'poly1');

%% Convert Raw Measured Data into Calibrated Data
% --> Do this in a loop that repeats for every log file in the specified
% folder.

% Collect all the log file names from the raw data folder
Raw_Data_Files_Info = dir(fullfile(Raw_Data_Folder, '*.txt'));

% Initialize counter variable
counter = 1;

```

```

% Open Raw Data Files, Calibrate, and Save
for i = 1:3:length(Raw_Data_Files_Info)
    filename_RTD = strcat(Raw_Data_Folder, '\', Raw_Data_Files_Info(i).name);

    [~,~,hot_bath_setpoint,cold_bath_setpoint,...
    hot_liquid_flowrate,cold_liquid_flowrate,pmean_setpoint,...

torque_setpoint,teknic_setpoint,RTD_time,RTD_0_raw,RTD_1_raw,RTD_2_raw,RTD_3_
raw,...
    RTD_4_raw,RTD_5_raw,RTD_6_raw,RTD_7_raw] = importfile_RTD(filename_RTD);
%     RTD_0 --> Displacer Cylinder Head Inlet
%     RTD_1 --> Displacer Cylinder Head Outlet
%     RTD_2 --> Heater Inlet
%     RTD_3 --> Heater Outlet
%     RTD_4 --> Cooler Inlet
%     RTD_5 --> Cooler Outlet
%     RTD_6 --> Power Cylinder Inlet
%     RTD_7 --> Power Cylinder Outlet

% Time for RTDs
time_inc_RTD = (RTD_time(end)-RTD_time(1))/length(RTD_time); %(s)
N_RTD = length(RTD_time);
time_RTD = (0:N_RTD-1)*time_inc_RTD;
time_RTD = time_RTD(:);
%Use this if data has jump in time (e.g. several txt files stitched
together)
% time_RTD = RTD_time-RTD_time(1);

filename_TC = strcat(Raw_Data_Folder, '\', Raw_Data_Files_Info(i+1).name);
[TC_time,TC_0_raw,TC_1_raw,TC_2_raw,TC_3_raw,TC_4_raw,TC_5_raw,...
TC_6_raw,TC_7_raw,TC_8_raw,TC_9_raw,TC_10_raw,~,~,...
~,~,~] = importfile_TC(filename_TC);
%     TC_0 --> Displacer Cylinder Head (Expansion Space)
%     TC_1 --> Heater/Expansion Space Interface, Bypass Side
%     TC_2 --> Heater/Expansion Space Interface, Connecting Pipe Side
%     TC_3 --> Regen/Heater Interface, Bypass Side
%     TC_4 --> Regen/Heater Interface, Connecting Pipe Side
%     TC_5 --> Cooler/Regenerator Interface, Bypass Side
%     TC_6 --> Cooler/Regenerator Interface, Connecting Pipe Side
%     TC_7 --> Compression Space/Cooler Interface, Bypass Side
%     TC_8 --> Compression Space/Cooler Interface, Connecting Pipe Side
%     TC_9 --> Power Cylinder
%     TC_10 --> Crankcase
%     TC_11 -->
%     TC_12 -->
%     TC_13 -->
%     TC_14 -->
%     TC_15 -->

% Time for Thermocouples
time_inc_TC = (TC_time(end)-TC_time(1))/length(TC_time); %(s)
N_TC = length(TC_time);
time_TC = (0:N_TC-1)*time_inc_TC;
time_TC = time_TC(:);
%Use this if data has jump in time (e.g. several txt files stitched together)

```

```

%         time_TC = TC_time-TC_time(1);
        filename_Volt_Count =
strcat(Raw_Data_Folder, '\\',Raw_Data_Files_Info(i+2).name);

[VC_time,ctr0,AI_0_raw,AI_1_raw,AI_2_raw,AI_3_raw,AI_4_raw,AI_5_raw,AI_6_raw,
...
AI_7_raw,AI16_raw,~,~,~,~,~,...
~,~] = importfile_Volt_Count(filename_Volt_Count);
%   ctr0 --> 500 PPR Rotary Encoder Output
%   AI_0 --> Displacer Cylinder Head Dynamic Pressure
%   AI_1 --> Displacer Mount Dynamic Pressure
%   AI_2 --> Power Cylinder Dynamic Pressure
%   AI_3 --> Crankcase Dynamic Pressure
%   AI_4 --> Power Cylinder Static Pressure
%   AI_5 --> Crankcase Static Pressure
%   AI_6 --> Speed Output Signal from Magnetic Brake
%   AI_7 --> Pressure Measurement Output from Regulator
%   AI_16 --> Torque Sensor (Futek TRS600 - FSH01997 10Nm) torque signal
%   AI_17 -->
%   AI_18 -->
%   AI_19 -->
%   AI_20 -->
%   AI_21 -->
%   AI_22 -->
%   AI_23 -->

% Time for Voltages and Counter
time_inc_VC = (VC_time(end)-VC_time(1))/length(VC_time); %(s)
N_VC = length(VC_time);
time_VC = (0:N_VC-1)*time_inc_VC;
time_VC = time_VC(:); %(s)
%Use this if data has jump in time (e.g. several txt files stitched together)
%         time_VC = VC_time-VC_time(1);

% Apply calibration to RTDs
corr_terms_RTD_0 = fits.RTD_0(RTD_0_raw); %(°C)
RTD_0 = RTD_0_raw + corr_terms_RTD_0; %(°C)

        corr_terms_RTD_1 = fits.RTD_1(RTD_1_raw); %(°C)
RTD_1 = RTD_1_raw + corr_terms_RTD_1; %(°C)

        corr_terms_RTD_2 = fits.RTD_2(RTD_2_raw); %(°C)
RTD_2 = RTD_2_raw + corr_terms_RTD_2; %(°C)

        corr_terms_RTD_3 = fits.RTD_3(RTD_3_raw); %(°C)
RTD_3 = RTD_3_raw + corr_terms_RTD_3; %(°C)

        corr_terms_RTD_4 = fits.RTD_4(RTD_4_raw); %(°C)
%   RTD_4 = RTD_4_raw + corr_terms_RTD_4; %(°C)
%% Disable calibration for RTD 4 as there is no cal data at its temp
range.
RTD_4 = RTD_4_raw; %(°C)
%%%%%%%%%%%%%%%%%%%%%%%%%%%%%%%%%%%%%%%%%%%%%%%%%%%%%%%%%%%%%%%%%%%%%%%%

```

```

    corr_terms_RTD_5 = fits.RTD_5(RTD_5_raw); %(°C)
    RTD_5 = RTD_5_raw + corr_terms_RTD_5; %(°C)

    corr_terms_RTD_6 = fits.RTD_6(RTD_6_raw); %(°C)
    RTD_6 = RTD_6_raw + corr_terms_RTD_6; %(°C)

    corr_terms_RTD_7 = fits.RTD_7(RTD_7_raw); %(°C)
    RTD_7 = RTD_7_raw + corr_terms_RTD_7; %(°C)

% Apply calibration to TCs
    corr_terms_TC_0 = fits.TC_0(TC_0_raw); %(°C)
    TC_0 = TC_0_raw + corr_terms_TC_0; %(°C)

    corr_terms_TC_1 = fits.TC_1(TC_1_raw); %(°C)
    TC_1 = TC_1_raw + corr_terms_TC_1; %(°C)

    corr_terms_TC_2 = fits.TC_2(TC_2_raw); %(°C)
    TC_2 = TC_2_raw + corr_terms_TC_2; %(°C)

    corr_terms_TC_3 = fits.TC_3(TC_3_raw); %(°C)
    TC_3 = TC_3_raw + corr_terms_TC_3; %(°C)

    corr_terms_TC_4 = fits.TC_4(TC_4_raw); %(°C)
    TC_4 = TC_4_raw + corr_terms_TC_4; %(°C)

    corr_terms_TC_5 = fits.TC_5(TC_5_raw); %(°C)
    TC_5 = TC_5_raw + corr_terms_TC_5; %(°C)

    corr_terms_TC_6 = fits.TC_6(TC_6_raw); %(°C)
    TC_6 = TC_6_raw + corr_terms_TC_6; %(°C)

    corr_terms_TC_7 = fits.TC_7(TC_7_raw); %(°C)
    TC_7 = TC_7_raw + corr_terms_TC_7; %(°C)

    corr_terms_TC_8 = fits.TC_8(TC_8_raw); %(°C)
    TC_8 = TC_8_raw + corr_terms_TC_8; %(°C)

    corr_terms_TC_9 = fits.TC_9(TC_9_raw); %(°C)
    TC_9 = TC_9_raw + corr_terms_TC_9; %(°C)

    corr_terms_TC_10 = fits.TC_10(TC_10_raw); %(°C)
    TC_10 = TC_10_raw + corr_terms_TC_10; %(°C)

% Apply calibration to static pressure transducers
    SP_772967 = fits.SP_772967(AI_4_raw) *PSI_to_Pa; %(Pa)

    SP_772966 = fits.SP_772966(AI_5_raw) *PSI_to_Pa; %(Pa)

% Apply calibration to dynamic pressure transducers
    DP_LW37338 = fits.DP_LW37338(AI_0_raw) *PSI_to_Pa; %(Pa)

    DP_LW37354 = fits.DP_LW37354(AI_1_raw) *PSI_to_Pa; %(Pa)

```

```

DP_LW37355 = fits.DP_LW37355(AI_2_raw) *PSI_to_Pa; %(Pa)

DP_LW37337 = fits.DP_LW37337(AI_3_raw) *PSI_to_Pa; %(Pa)

% Apply calibration for Torque Sensor Measurement (10 Nm / 5 Volt)
torque_sensor_transient = fits.TRS600(AI16_raw); % (Nm)

% Add Static and Dynamic Pressure Measurements
%%%%%%%% Standard setup %%%%%%%%%%
%   p_DCH --> Displacer Cylinder Head Pressure, transducers LW37338 and
772967 (Pa)
p_DCH = mean(SP_772967) + DP_LW37338; %(Pa)

%   p_DM --> Displacer Mount Pressure, transducers LW37354 and 772967 (Pa)
p_DM = mean(SP_772967) + DP_LW37354; %(Pa)

%   p_PC --> Power Cylinder Pressure, transducers LW37355 and 772967 (Pa)
p_PC = mean(SP_772967) + DP_LW37355; %(Pa)

%   p_CC --> Crankcase Pressure, transducers LW37337 and 772966 (Pa)
p_CC = mean(SP_772966) + DP_LW37337; %(Pa)
%%%%%%%%

% % %%%%%%%%% Setup 1 %%%%%%%%%%
%%%%%%%%
%   p_DCH = mean(SP_772967) + DP_LW37354; %(Pa)
%   p_DM = mean(SP_772967) + DP_LW37338; %(Pa)
%   p_PC = mean(SP_772967) + DP_LW37355; %(Pa)
%   p_CC = mean(SP_772966) + DP_LW37337; %(Pa)
% %%%%%%%%%

% %%%%%%%%% Setup 2 %%%%%%%%%%
%%%%%%%%
%   p_DCH = mean(SP_772967) + DP_LW37355; %(Pa)
%   p_DM = mean(SP_772967) + DP_LW37338; %(Pa)
%   p_PC = mean(SP_772967) + DP_LW37354; %(Pa)
%   p_CC = mean(SP_772966) + DP_LW37337; %(Pa)
% %%%%%%%%%

% %%%%%%%%% Setup 3 %%%%%%%%%%
%%%%%%%%
%   p_DCH = mean(SP_772967) + DP_LW37338; %(Pa)
%   p_DM = mean(SP_772967) + DP_LW37355; %(Pa)
%   p_PC = mean(SP_772967) + DP_LW37337; %(Pa)
%   p_CC = mean(SP_772966) + DP_LW37354; %(Pa)
% %%%%%%%%%

% %%%%%%%%% Setup 4 %%%%%%%%%%
%%%%%%%%
%   p_DCH = mean(SP_772967) + DP_LW37337; %(Pa)
%   p_DM = mean(SP_772967) + DP_LW37355; %(Pa)
%   p_PC = mean(SP_772967) + DP_LW37338; %(Pa)
%   p_CC = mean(SP_772966) + DP_LW37354; %(Pa)
% %%%%%%%%%

% Convert crank angles from degrees to radians.
theta = ctr0*(pi/180); % (rad)

```

```

% Magnetic Brake Speed Output (250 RPM/volt)
MB_speed_transient = AI_6_raw*250;
MB_speed = mean(MB_speed_transient); % Speed Output Signal from Magnetic
Brake (RPM)

% Regulator Measured Pressure (15 PSI/Volt)
p_regulator = AI_7_raw *15 *PSI_to_Pa; % (Pa)

%% Store Results in Output Structure
C_DATA(counter).filename = Raw_Data_Files_Info(i).name;
C_DATA(counter).time_RTD = time_RTD;
C_DATA(counter).RTD_0 = RTD_0;
C_DATA(counter).RTD_1 = RTD_1;
C_DATA(counter).RTD_2 = RTD_2;
C_DATA(counter).RTD_3 = RTD_3;
C_DATA(counter).RTD_4 = RTD_4;
C_DATA(counter).RTD_5 = RTD_5;
C_DATA(counter).RTD_6 = RTD_6;
C_DATA(counter).RTD_7 = RTD_7;
C_DATA(counter).time_TC = time_TC;
C_DATA(counter).TC_0 = TC_0;
C_DATA(counter).TC_1 = TC_1;
C_DATA(counter).TC_2 = TC_2;
C_DATA(counter).TC_3 = TC_3; % <-- CHANGE BACK WHEN THERMOCOUPLE 3 IS
FIXED (DONE)
C_DATA(counter).TC_4 = TC_4;
C_DATA(counter).TC_5 = TC_5;
C_DATA(counter).TC_6 = TC_6;
C_DATA(counter).TC_7 = TC_7;
C_DATA(counter).TC_8 = TC_8;
C_DATA(counter).TC_9 = TC_9;
C_DATA(counter).TC_10 = TC_10;
C_DATA(counter).time_VC = time_VC;
C_DATA(counter).theta = theta;
C_DATA(counter).p_DCH = fillmissing(p_DCH, 'linear'); % Fill in NaNs with
linearly interpolated values.
C_DATA(counter).p_DM = fillmissing(p_DM, 'linear');
C_DATA(counter).p_PC = fillmissing(p_PC, 'linear');
C_DATA(counter).p_CC = fillmissing(p_CC, 'linear');
C_DATA(counter).p_PC_static = fillmissing(SP_772967, 'linear');
C_DATA(counter).p_CC_static = fillmissing(SP_772966, 'linear');
C_DATA(counter).MB_speed = MB_speed;
C_DATA(counter).MB_speed_transient = MB_speed_transient;
C_DATA(counter).p_regulator = p_regulator;
C_DATA(counter).torque_sensor_transient = torque_sensor_transient;

% C_DATA(counter).dens_hot = dens_hot;
% C_DATA(counter).dens_cold = dens_cold;
% C_DATA(counter).c_hot = c_hot;
% C_DATA(counter).c_cold = c_cold;
C_DATA(counter).hot_bath_setpoint = hot_bath_setpoint;
C_DATA(counter).cold_bath_setpoint = cold_bath_setpoint;
C_DATA(counter).hot_liquid_flowrate = hot_liquid_flowrate;
C_DATA(counter).cold_liquid_flowrate = cold_liquid_flowrate;

```

```

C_DATA(counter).pmean_setpoint = pmean_setpoint;
C_DATA(counter).torque_setpoint = torque_setpoint;
C_DATA(counter).teknik_setpoint = teknik_setpoint;

counter = counter + 1;
end

reversed_file_path = reverse(Raw_Data_Folder);
reversed_folder_name = strtok(reversed_file_path, '\\');
folder_name = reverse(reversed_folder_name);
Calibrated_Data_Filename =
strcat(Raw_Data_Folder, '\\', folder_name, '_CAL.mat');

save(Calibrated_Data_Filename, 'C_DATA', '-v7.3')

% %%
% for i=1:length(C_DATA)
%     equal1(i) = all([C_DATA(i).RTD_2]==[C_DATA2(i).RTD_2]);
%     equal2(i) = all([C_DATA(i).RTD_4]==[C_DATA2(i).RTD_4]);
%
% end

```

G.4 Processing of Experimental Data and Calculation of Variables (‘reduce.m’)

```
function reduce(Raw_Data_Folder, ENGINE_DATA, short_output, have_DCH_source,
p_environment)
```

```
% Written by Connor Speer - October 2017
% Modified by Connor Speer - July 2018
% Modified by Matthias Lottmann - 2021-2022:
% New variables, function options added, code simplifications

% Process experimental data and return it in a structure for plotting
% elsewhere.
%% Use this if running this script on its own.
% Raw_Data_Folder = uigetdir;

%% Inputs
% Properties of Heat Transfer Liquids

% IRRELEVANT (not used later)
% dens_hot = 930; %(kg/m^3) - for SIL 180 at 20 deg C
% RELEVANT
% hot liquid specific heat now calculated temperature dependent in loop.
% c_hot = 1510; %(J/kgK) - for SIL 180 at 20 deg C

% Matthias 2021 Dec 08: Water/Ethylene glycol 70/30 mix, 5 deg C
% https://www.engineeringtoolbox.com/ethylene-glycol-d\_146.html
% IRRELEVANT (not used later)
% dens_cold = 1057.5; %(kg/m^3)
% RELEVANT
c_cold = 3770; %(J/kgK)

m_dot_Cooler = 0.0235576; %(kg/s) THIS WAS MEASURED VIA BUCKET TEST!!!!
    % Connor's value
%     m_dot_Cooler = 0.027624; %(kg/s) THIS WAS MEASURED VIA BUCKET TEST!!!!

% Connor's values
% dens_cold = 1101.12; %(kg/m^3) - for 50% ethylene glycol water mix at 10
deg C
% c_cold = 3118.57; %(J/kgK) - for 50% ethylene glycol water mix at 10 deg C
% dens_cold = 1000; %(kg/m^3) - for water
% c_cold = 4184; %(J/kgK) - for water

%%
reversed_file_path = reverse(Raw_Data_Folder);
reversed_folder_name = strtok(reversed_file_path, '\\');
folder_name = reverse(reversed_folder_name);
Calibrated_Data_Filename =
strcat(Raw_Data_Folder, '\\', folder_name, '_CAL.mat');
```

```

% Collect all the log file names from the test data folder
load(Calibrated_Data_Filename, 'C_DATA');
[~,number_of_files] = size(C_DATA);

%% Preallocate Space For DATA_STRUCTURE
% RD_DATA(number_of_files).filename = [];
%
% if ~short_output
%     RD_DATA(number_of_files).time_RTD = [];
%     RD_DATA(number_of_files).RTD_0 = [];
%     RD_DATA(number_of_files).RTD_1 = [];
%     RD_DATA(number_of_files).RTD_2 = [];
%     RD_DATA(number_of_files).RTD_3 = [];
%     RD_DATA(number_of_files).RTD_4 = [];
%     RD_DATA(number_of_files).RTD_5 = [];
%     RD_DATA(number_of_files).RTD_6 = [];
%     RD_DATA(number_of_files).RTD_7 = [];
%     RD_DATA(number_of_files).time_TC = [];
%     RD_DATA(number_of_files).TC_0 = [];
%     RD_DATA(number_of_files).TC_1 = [];
%     RD_DATA(number_of_files).TC_2 = [];
%     RD_DATA(number_of_files).TC_3 = [];
%     RD_DATA(number_of_files).TC_4 = [];
%     RD_DATA(number_of_files).TC_5 = [];
%     RD_DATA(number_of_files).TC_6 = [];
%     RD_DATA(number_of_files).TC_7 = [];
%     RD_DATA(number_of_files).TC_8 = [];
%     RD_DATA(number_of_files).TC_9 = [];
%     RD_DATA(number_of_files).TC_10 = [];
%     RD_DATA(number_of_files).time_VC = [];
%     RD_DATA(number_of_files).theta = [];
%     RD_DATA(number_of_files).p_DCH = [];
%     RD_DATA(number_of_files).p_DM = [];
%     RD_DATA(number_of_files).p_PC = [];
%     RD_DATA(number_of_files).p_CC = [];
%     RD_DATA(number_of_files).p_regulator = [];
%     RD_DATA(number_of_files).torque_sensor_transient = [];
%     RD_DATA(number_of_files).MB_speed_transient = [];
% end
%
% RD_DATA(number_of_files).MB_speed = [];
% RD_DATA(number_of_files).encoder_speed = [];
% % RD_DATA(number_of_files).dens_hot = [];
% % RD_DATA(number_of_files).dens_cold = [];
% RD_DATA(number_of_files).c_hot_in = [];
% RD_DATA(number_of_files).c_hot_out = [];
% RD_DATA(number_of_files).c_cold = [];
% RD_DATA(number_of_files).hot_bath_setpoint = [];
% RD_DATA(number_of_files).cold_bath_setpoint = [];
% RD_DATA(number_of_files).hot_liquid_flowrate = [];
% RD_DATA(number_of_files).cold_liquid_flowrate = [];
% RD_DATA(number_of_files).pmean_setpoint = [];
% RD_DATA(number_of_files).torque_setpoint = [];
% RD_DATA(number_of_files).torque_sensor = [];
% RD_DATA(number_of_files).teknik_setpoint = [];

```

```

%
% % From the post_process sub-function
% RD_DATA(number_of_files).p_DCH_avg = [];
% RD_DATA(number_of_files).p_DM_avg = [];
% RD_DATA(number_of_files).p_PC_avg = [];
% RD_DATA(number_of_files).p_CC_avg = [];
% RD_DATA(number_of_files).pmean = [];
% RD_DATA(number_of_files).pmean_CC = [];
% RD_DATA(number_of_files).p_atm = [];
%
% RD_DATA(number_of_files).Tge = [];
% RD_DATA(number_of_files).Tgh_far = [];
% RD_DATA(number_of_files).Tgh_pipe = [];
% RD_DATA(number_of_files).Tgh = [];
% RD_DATA(number_of_files).Tgr = [];
% RD_DATA(number_of_files).Tgk = [];
% RD_DATA(number_of_files).Tgc = [];
% RD_DATA(number_of_files).TgCC = [];
%
% RD_DATA(number_of_files).Tgh_inlet_far = [];
% RD_DATA(number_of_files).Tgh_inlet_pipe = [];
% RD_DATA(number_of_files).Tgh_inlet = [];
% RD_DATA(number_of_files).Tgh_reg_far = [];
% RD_DATA(number_of_files).Tgh_reg_pipe = [];
% RD_DATA(number_of_files).Tgh_reg = [];
%
% RD_DATA(number_of_files).Tgk_inlet_far = [];
% RD_DATA(number_of_files).Tgk_inlet_pipe_1 = [];
% RD_DATA(number_of_files).Tgk_inlet_pipe_2 = [];
% RD_DATA(number_of_files).Tgk_inlet = [];
% RD_DATA(number_of_files).Tgk_reg = [];
% RD_DATA(number_of_files).TgPP = [];
%
% if have_DCH_source
%     RD_DATA(number_of_files).Tsource_DCH_in = [];
%     RD_DATA(number_of_files).Tsource_DCH_out = [];
% end
% RD_DATA(number_of_files).Tsource_in = [];
% RD_DATA(number_of_files).Tsource_out = [];
% RD_DATA(number_of_files).Tsink_in = [];
% RD_DATA(number_of_files).Tsink_out = [];
%
% RD_DATA(number_of_files).Wind = [];
% RD_DATA(number_of_files).FW = [];
% RD_DATA(number_of_files).W_CC = [];
% RD_DATA(number_of_files).CC_GSH = [];
%
% RD_DATA(number_of_files).Qdot_DCH = [];
%
% RD_DATA(number_of_files).Qdot_heater = [];
% RD_DATA(number_of_files).Qdot_cooler = [];
% %RD_DATA(number_of_files).Qdot_PC = [];
%
% RD_DATA(number_of_files).P_shaft_tsensor = [];
% RD_DATA(number_of_files).P_shaft_tsensor_MB_speed = [];
% RD_DATA(number_of_files).P_shaft_setpoint_MB_speed = [];
% RD_DATA(number_of_files).efficiency_shaft = [];

```

```

% RD_DATA(number_of_files).efficiency_ind = [];
% RD_DATA(number_of_files).Beale = [];
% RD_DATA(number_of_files).West = [];
%
% if ~short_output
%     RD_DATA(number_of_files).Ve = [];
%     RD_DATA(number_of_files).Vc = [];
%     RD_DATA(number_of_files).Vtotal = [];
% end
%
% RD_DATA(number_of_files).Ve_rounded = [];
% RD_DATA(number_of_files).Vc_rounded = [];
% RD_DATA(number_of_files).Vtotal_rounded = [];
% RD_DATA(number_of_files).V_CC_rounded = [];

% Initialize counter variable
counter = 1;

WaitBar = waitbar(0, 'Processing experimental data ...');

% Open pre-calibrated log files
for i =1:number_of_files
    %% Calculate Data from the File %%%%%%%%%%%%%%%%%%%%%%%%%%%%%%%%%%%%%%%%%%%%%%%%%%%%%%%%%%%%%%%%%%%%%%%%%
    % Gas temperatures
    Tge = mean(C_DATA(i).TC_0); % Average Expansion Space Gas Temperature
    (°C)

    Tgh_inlet_far = mean(C_DATA(i).TC_1); % Far Side Average Heater
    Inlet/Outlet Gas Temperature (°C)
    Tgh_inlet_pipe = mean(C_DATA(i).TC_2); % Conn Pipe Side Average Heater
    Inlet/Outlet Gas Temperature (°C)
    Tgh_inlet = mean([mean(C_DATA(i).TC_1), mean(C_DATA(i).TC_2)]); % Average
    Heater Inlet/Outlet Gas Temperature (°C)

    Tgh_reg_far = mean(C_DATA(i).TC_3); % Far Side Average Heater/Regenerator
    interface Gas Temperature (°C)
    Tgh_reg_pipe = mean(C_DATA(i).TC_4); % Conn Pipe Average
    Heater/Regenerator interface Gas Temperature (°C)
    Tgh_reg = mean([mean(C_DATA(i).TC_3), mean(C_DATA(i).TC_4)]); % Average
    Heater/Regenerator interface Gas Temperature (°C)

    Tgh_far = mean([Tgh_inlet_far, Tgh_reg_far]); % Far Side Average Heater
    Gas Temperature (°C)
    Tgh_pipe = mean([Tgh_inlet_pipe, Tgh_reg_pipe]); % Conn Pipe Side Average
    Heater Gas Temperature (°C)
    Tgh = mean([Tgh_inlet, Tgh_reg]); % Average Heater Gas Temperature (°C)

    % TC_6 is at same position as TC_8 because it cannot be pushed up into
    % the cooler due to design error in crankcase!
    Tgk_inlet_far = mean(C_DATA(i).TC_7); % Far Side Average Cooler
    Inlet/Outlet Gas Temperature (°C)
    Tgk_inlet_pipe_1 = mean(C_DATA(i).TC_8); % Conn Pipe Side Average Cooler
    Inlet/Outlet Gas Temperature (°C)

```

```

    Tgk_inlet_pipe_2 = mean(C_DATA(i).TC_6); % Conn Pipe Side Average Cooler
    Inlet/Outlet Gas Temperature (°C)
    Tgk_inlet = mean([mean(C_DATA(i).TC_7), mean(C_DATA(i).TC_8)]); % Average
    Cooler Inlet/Outlet Gas Temperature (°C)

    Tgk_reg = mean(C_DATA(i).TC_5); % Average Cooler/Regenerator interface
    Gas Temperature (°C)
    % this sensor sometimes loses connection and produces measurements wildly
    out of bounds. replace these with NaN.
    if ~(Tgk_reg<160 && Tgk_reg>0)
        Tgk_reg = NaN;
        Tgk = NaN;
        Tgr = NaN;
    else
        Tgk = mean([Tgk_reg, Tgk_inlet]); % Average Cooler Gas Temperature
    (°C)
        % Average Regenerator Gas Temperature (Log Mean Method)
        Tgr = (Tgh_reg - Tgk_reg) / log(Tgh_reg / Tgk_reg); %(°C)
    end

    TgPP = mean(C_DATA(i).TC_9); % Average Power Piston Space Gas Temperature
    (°C)
    Tgc = mean([TgPP, Tgk_inlet]); % Average Compression Space Gas
    Temperature (°C), aprx. from PP and cooler inlet
    TgCC = mean(C_DATA(i).TC_10); % Average Crankcase Gas Temperature (°C)

    % Liquid Temperatures
    if have_DCH_source
        Tsource_DCH_in = mean(C_DATA(i).RTD_0); % Average Displacer cylinder head
    Inlet Liquid Temperature (°C)
        Tsource_DCH_out = mean(C_DATA(i).RTD_1); % Average Displacer cylinder
    head Outlet Liquid Temperature (°C)
    end
        Tsource_in = mean(C_DATA(i).RTD_2); % Average Heater Inlet Liquid
    Temperature (°C)
        Tsource_out = mean(C_DATA(i).RTD_3); % Average Heater Outlet Liquid
    Temperature (°C)
        Tsink_in = mean(C_DATA(i).RTD_4); % Average Cooler Inlet Liquid
    Temperature (°C)
        Tsink_out = mean(C_DATA(i).RTD_5); % Average Cooler Outlet Liquid
    Temperature (°C)

    % Calculate Crankshaft Speed from Encoder Measurement %%%%%%%%%%%
    % Convert theta to monotonically increasing
    %--> Step through theta one row at a time
    %--> For each row, check if it is larger or smaller than the previous row
    %--> If larger, add the difference to the total crank angle count
    %--> If smaller, add the entire value to the total crank angle count

    theta_mono = zeros(length(C_DATA(i).theta),1); % Preallocate space
    theta_mono(1) = C_DATA(i).theta(1);
    for j = 2:length(C_DATA(i).theta)
        if C_DATA(i).theta(j) >= C_DATA(i).theta(j-1)
            theta_mono(j) = theta_mono(j-1) + (C_DATA(i).theta(j)-
    C_DATA(i).theta(j-1));

```

```

        else
            theta_mono(j) = theta_mono(j-1) + C_DATA(i).theta(j);
        end
    end
end
%%
% Calculate encoder speeds
%--> This is a moving average with an interval of 40 samples. At 1000
% Hz sampling rate and 200 RPM this corresponds to 50 degrees of
% rotation.
avg_int = 40;
delta_theta_mono = zeros(length(C_DATA(i).theta),1); % Preallocate space
delta_time = zeros(length(C_DATA(i).theta),1); % Preallocate space
omega = zeros(length(C_DATA(i).theta),1); % Preallocate space

for k = (avg_int/2+1):(length(C_DATA(i).theta)-avg_int/2)
    delta_theta_mono(k) = theta_mono(k+avg_int/2) - theta_mono(k-
avg_int/2); %(rad)
    delta_time(k) = C_DATA(i).time_VC(k+avg_int/2) - C_DATA(i).time_VC(k-
avg_int/2); %(s)
    omega(k) = delta_theta_mono(k)/delta_time(k); %(rad/s)
end
% fill start and end values
omega(1:avg_int/2) = omega(avg_int/2+1); %(rad/s)
omega((end-avg_int/2-1):end) = omega(end-avg_int/2); %(rad/s)

encoder_speed_raw = omega.*(60/(2*pi)); %(RPM)

% Average for each crank angle degree
[encoder_speed_transient] =
PV_data_avg(C_DATA(i).theta,encoder_speed_raw); %(RPM)
% Remove any remaining NaN. not sure why sometimes there is still a NaN
value.
nans = isnan(encoder_speed_transient);
if any(nans)
    warning(nnz(nans)+" NaN values in encoder speed at setpoint index
"+counter)
end
encoder_speed = mean(encoder_speed_transient(~nans));

% % Plot encoder speed
% figure(1)
% hold on
% plot(0:359, encoder_speed, 'k', 'Displayname', num2str(avg_int))
% xlim([0,359])
% xlabel('Crank angle [deg]')
% ylabel('Speed [rpm]')
% legend

%%
% Calculate Liquid Mass Flow Rates
[m_dot_DCH, m_dot_Heater] =
SIL_180_flow_rate_calc(C_DATA(i).hot_bath_setpoint);

```

```

%      m_dot_Cooler = C_DATA(i).cold_liquid_flowrate*C_DATA(i).dens_cold;
% (kg/s)
%      m_dot_PC = m_dot_Cooler; % (kg/s)

% Calculate Temperature dependent Specific heat
c_hot_in = SIL_180_specific_heat_calc(Tsource_in);
c_hot_out = SIL_180_specific_heat_calc(Tsource_out);

% Calculate Heat Transfer Rates
if have_DCH_source
    %Add c_hot_in and c_hot_out if using this Heat exchanger!
    Qdot_DCH = m_dot_DCH*c_hot*(mean(C_DATA(i).RTD_0) -
mean(C_DATA(i).RTD_1)); % (W)
else
    Qdot_DCH = 0;
end
Qdot_heater = m_dot_Heater* (c_hot_in*Tsource_in -
c_hot_out*Tsource_out); % (W)
Qdot_cooler = m_dot_Cooler*c_cold*(Tsink_out-Tsink_in); % (W)
%      Qdot_PC = m_dot_PC*c_cold*(mean(C_DATA(i).RTD_7) -
mean(C_DATA(i).RTD_6)); % (W)
Qdot_PC = 0; % (W) THIS WATER JACKET IS NOT BEING USED RIGHT
NOW!!!!!!!!!!!!!!!!!!!!!!!!!!!!!!!!!!!!!!!!!!!!!!!!!!!!!!!!!!!!!!!!!!!!

% Torque measured by sensor
torque_sensor = mean(C_DATA(i).torque_sensor_transient);
% Calculate the measured power output
% MATT: Power calculated from Magnetic brake speed? Inaccurate? Why not
'encoder_speed'? -----
-----
% MATT May 20 2022: Changed 'P_shaft_tsensor' to use encoder speed
% MATT: Could also calculate power from transient torque & speed
P_shaft_tsensor = torque_sensor*encoder_speed*((2*pi)/60); % (W)
P_shaft_tsensor_MB_speed =
torque_sensor*(C_DATA(i).MB_speed*((2*pi)/60)); % (W)
P_shaft_setpoint_MB_speed =
C_DATA(i).torque_setpoint*(C_DATA(i).MB_speed*((2*pi)/60)); % (W)

% Calculate the mean pressure
pmean = mean([mean(C_DATA(i).p_DCH), mean(C_DATA(i).p_DM),
mean(C_DATA(i).p_PC)]);
pmean_CC = mean(C_DATA(i).p_CC);
% Calculate the Beale number
Beale =
P_shaft_tsensor/((pmean)*(C_DATA(i).MB_speed/60)*ENGINE_DATA.Vswp);

% Calculate the West Number
T_factor = ((Tsource_in+273.15)+(Tsink_in+273.15)) / (Tsource_in-
Tsink_in);
West = Beale*T_factor;

% Average the Pressures for Each Crank Angle Degree
[p_DCH_avg] = PV_data_avg(C_DATA(i).theta,C_DATA(i).p_DCH); % (Pa)
[p_DM_avg] = PV_data_avg(C_DATA(i).theta,C_DATA(i).p_DM); % (Pa)
[p_PC_avg] = PV_data_avg(C_DATA(i).theta,C_DATA(i).p_PC); % (Pa)
[p_CC_avg] = PV_data_avg(C_DATA(i).theta,C_DATA(i).p_CC); % (Pa)

```

```

    p_DCH_avg = fillmissing(p_DCH_avg, 'linear'); % Fill in NaNs with linearly
interpolated values.
    p_DM_avg = fillmissing(p_DM_avg, 'linear');
    p_PC_avg = fillmissing(p_PC_avg, 'linear');
    p_CC_avg = fillmissing(p_CC_avg, 'linear');

    %     % Calculate the work lost to regenerator flow friction
    %     dW_regen_FF = (p_DCH_avg -
p_DM_avg).*(pi/4).*(0.096.^2).*dVe_rounded; %[J]
    %     W_lost_regen_FF = sum(dW_regen_FF); %[J]
    %     P_lost_regen_FF = W_lost_regen_FF*Engine_Hz; %[W]

    % Calculate volumes at measured crank angles
    [Vc,Ve,~,~,~] = volume(C_DATA(i).theta, ENGINE_DATA);
    Vtotal = ENGINE_DATA.Vdead + Vc + Ve;
    Vtotal = Vtotal(:);

    % Calculate volumes at rounded crank angles to go with average pressures
    theta_deg_rounded = (0:1:359)+10;
    theta_rounded = theta_deg_rounded*(pi/180);
    theta_rounded = theta_rounded(:);
    [Vc_rounded,Ve_rounded,~,~,V_CC_rounded] = volume(theta_rounded,
ENGINE_DATA);
    Vtotal_rounded = ENGINE_DATA.Vdead + Vc_rounded + Ve_rounded;
    %     Vtotal_rounded = Vtotal_rounded(:);

% Matthias: code below is identical to that in 'volume' function. Using
output of 'volume' instead (above).
%     % Crankcase Volume Variations
%     Pbore = ENGINE_DATA.Pbore; % piston bore [m]
%     Pr1 = ENGINE_DATA.Pr1; % piston desaxe offset in [m]
%     Pr2 = ENGINE_DATA.Pr2; % piston crank radius in [m]
%     Pr3 = ENGINE_DATA.Pr3; % piston connecting rod length [m]
%
%     Ptheta2 = pi - theta_rounded;
%
%     Ptheta3 = pi - asin((-Pr1+(Pr2*sin(Ptheta2)))/Pr3);
%     Pr4 = Pr2*cos(Ptheta2) - Pr3*cos(Ptheta3);
%     Pr4max = sqrt(((Pr2+Pr3)^2)-(Pr1^2));
%
%     % Crankcase Volume Variations in (m^3)
%     V_CC_rounded = ENGINE_DATA.V_buffer_max - ((Pr4max-
Pr4)*((pi/4)*(Pbore^2))); % (m^3)
%     V_CC_rounded = V_CC_rounded(:);

    % Calculate Experimental Indicated Work and Power
%     Wind_exp = polyarea(Vtotal_rounded,p_PC_avg); %OBSOLETE
    V_closed = [Vtotal_rounded; Vtotal_rounded(1)];
    p_closed = [p_PC_avg; p_PC_avg(1)];
    Wind = trapz(V_closed,p_closed);

    % Calculate the measured thermal efficiency

```

```

    efficiency_shaft = P_shaft_tsensor / (Qdot_DCH+Qdot_heater); %(dim.less)
    efficiency_ind = Wind * encoder_speed /60 / (Qdot_DCH+Qdot_heater);
%(dim.less)

%    polyarea(V_CC_rounded,p_CC_avg)*C_DATA(i).MB_speed*(1/60); %OBSOLETE
V_CC_closed = [V_CC_rounded; V_CC_rounded(1)];
p_CC_closed = [p_CC_avg; p_CC_avg(1)];
% Crankcase indicated work
W_CC = trapz(V_CC_closed,p_CC_closed);
% Crankcase Gas Spring Hysteresis Loss
CC_GSH = W_CC*encoder_speed*(1/60);

% Calculate Experimental Forced Work %%%%%%%%%%%
P_engine_exp = p_PC_avg; %[Pa]
P_buffer_exp = p_CC_avg; %[Pa]

% Call forced work subfunction
FW = FW_Subfunction_v4(P_engine_exp, P_buffer_exp, Vtotal_rounded);
%    [~, FW_old, ~] =
FW_Subfunction_v3(theta_rounded,P_engine_exp,P_buffer_exp,Vtotal_rounded,ENGI
NE_DATA.effect,0);

%% Store Results in Output Structure %%%%%%%%%%%
% From the calibrate sub-function
RD_DATA(counter).filename = C_DATA(i).filename;

if ~short_output
    RD_DATA(counter).time_RTD = C_DATA(i).time_RTD;
    RD_DATA(counter).RTD_0 = C_DATA(i).RTD_0;
    RD_DATA(counter).RTD_1 = C_DATA(i).RTD_1;
    RD_DATA(counter).RTD_2 = C_DATA(i).RTD_2;
    RD_DATA(counter).RTD_3 = C_DATA(i).RTD_3;
    RD_DATA(counter).RTD_4 = C_DATA(i).RTD_4;
    RD_DATA(counter).RTD_5 = C_DATA(i).RTD_5;
    RD_DATA(counter).RTD_6 = C_DATA(i).RTD_6;
    RD_DATA(counter).RTD_7 = C_DATA(i).RTD_7;
    RD_DATA(counter).time_TC = C_DATA(i).time_TC;
    RD_DATA(counter).TC_0 = C_DATA(i).TC_0;
    RD_DATA(counter).TC_1 = C_DATA(i).TC_1;
    RD_DATA(counter).TC_2 = C_DATA(i).TC_2;
    RD_DATA(counter).TC_3 = C_DATA(i).TC_3;
    RD_DATA(counter).TC_4 = C_DATA(i).TC_4;
    RD_DATA(counter).TC_5 = C_DATA(i).TC_5;
    RD_DATA(counter).TC_6 = C_DATA(i).TC_6;
    RD_DATA(counter).TC_7 = C_DATA(i).TC_7;
    RD_DATA(counter).TC_8 = C_DATA(i).TC_8;
    RD_DATA(counter).TC_9 = C_DATA(i).TC_9;
    RD_DATA(counter).TC_10 = C_DATA(i).TC_10;
    RD_DATA(counter).time_VC = C_DATA(i).time_VC;
    RD_DATA(counter).theta = C_DATA(i).theta;
    RD_DATA(counter).p_DCH = C_DATA(i).p_DCH;
    RD_DATA(counter).p_DM = C_DATA(i).p_DM;
    RD_DATA(counter).p_PC = C_DATA(i).p_PC;
    RD_DATA(counter).p_CC = C_DATA(i).p_CC;
    RD_DATA(counter).p_regulator = C_DATA(i).p_regulator;

```

```

        RD_DATA(counter).torque_sensor_transient =
C_DATA(i).torque_sensor_transient;
        RD_DATA(counter).MB_speed_transient = C_DATA(i).MB_speed_transient;
end

RD_DATA(counter).MB_speed = C_DATA(i).MB_speed;
RD_DATA(counter).encoder_speed = encoder_speed;
RD_DATA(counter).encoder_speed_transient = encoder_speed_transient;
%   RD_DATA(counter).encoder_speed_raw = encoder_speed_raw;

%   RD_DATA(counter).dens_hot = C_DATA(i).dens_hot;
%   RD_DATA(counter).dens_cold = C_DATA(i).dens_cold;
RD_DATA(counter).c_hot_in = c_hot_in;
RD_DATA(counter).c_hot_out = c_hot_out;
RD_DATA(counter).c_cold = c_cold;
RD_DATA(counter).hot_bath_setpoint = C_DATA(i).hot_bath_setpoint;
RD_DATA(counter).cold_bath_setpoint = C_DATA(i).cold_bath_setpoint;
RD_DATA(counter).hot_liquid_flowrate = C_DATA(i).hot_liquid_flowrate;
RD_DATA(counter).cold_liquid_flowrate = C_DATA(i).cold_liquid_flowrate;
RD_DATA(counter).pmean_setpoint = C_DATA(i).pmean_setpoint;
RD_DATA(counter).torque_setpoint = C_DATA(i).torque_setpoint;
RD_DATA(counter).torque_sensor = torque_sensor;
RD_DATA(counter).teknik_setpoint = C_DATA(i).teknik_setpoint;

% From the post_process sub-function
RD_DATA(counter).p_DCH_avg = p_DCH_avg;
RD_DATA(counter).p_DM_avg = p_DM_avg;
RD_DATA(counter).p_PC_avg = p_PC_avg;
RD_DATA(counter).p_CC_avg = p_CC_avg;
RD_DATA(counter).pmean = pmean;
RD_DATA(counter).pmean_CC = pmean_CC;
RD_DATA(counter).p_atm = p_environment;

RD_DATA(counter).Tge = Tge;
RD_DATA(counter).Tgh_far = Tgh_far;
RD_DATA(counter).Tgh_pipe = Tgh_pipe;
RD_DATA(counter).Tgh = Tgh;
RD_DATA(counter).Tgr = Tgr;
RD_DATA(counter).Tgk = Tgk;
RD_DATA(counter).Tgc = Tgc;
RD_DATA(counter).TgCC = TgCC;

RD_DATA(counter).Tgh_inlet_far = Tgh_inlet_far;
RD_DATA(counter).Tgh_inlet_pipe = Tgh_inlet_pipe;
RD_DATA(counter).Tgh_inlet = Tgh_inlet;
RD_DATA(counter).Tgh_reg_far = Tgh_reg_far;
RD_DATA(counter).Tgh_reg_pipe = Tgh_reg_pipe;
RD_DATA(counter).Tgh_reg = Tgh_reg;

RD_DATA(counter).Tgk_inlet_far = Tgk_inlet_far;
RD_DATA(counter).Tgk_inlet_pipe_1 = Tgk_inlet_pipe_1;
RD_DATA(counter).Tgk_inlet_pipe_2 = Tgk_inlet_pipe_2;
RD_DATA(counter).Tgk_inlet = Tgk_inlet;
RD_DATA(counter).Tgk_reg = Tgk_reg;

```

```

RD_DATA(counter).TgPP = TgPP;

if have_DCH_source
    RD_DATA(counter).Tsource_DCH_in = Tsource_DCH_in;
    RD_DATA(counter).Tsource_DCH_out = Tsource_DCH_out;
end
RD_DATA(counter).Tsource_in = Tsource_in;
RD_DATA(counter).Tsource_out = Tsource_out;
RD_DATA(counter).Tsink_in = Tsink_in;
RD_DATA(counter).Tsink_out = Tsink_out;

RD_DATA(counter).Wind = Wind;
RD_DATA(counter).FW = FW;
% RD_DATA(counter).FW_old = FW_old; %%%%%%%%%%%%%%%REMOVE later
RD_DATA(counter).W_CC = W_CC;
RD_DATA(counter).CC_GSH = CC_GSH;

RD_DATA(counter).Qdot_DCH = Qdot_DCH;
RD_DATA(counter).Qdot_heater = Qdot_heater;
RD_DATA(counter).Qdot_cooler = Qdot_cooler;
RD_DATA(counter).Qdot_PC = Qdot_PC;

RD_DATA(counter).P_shaft_tsensor = P_shaft_tsensor;
RD_DATA(counter).P_shaft_tsensor_MB_speed = P_shaft_tsensor_MB_speed;
RD_DATA(counter).P_shaft_setpoint_MB_speed = P_shaft_setpoint_MB_speed;
RD_DATA(counter).efficiency_shaft = efficiency_shaft;
RD_DATA(counter).efficiency_ind = efficiency_ind;
RD_DATA(counter).Beale = Beale;
RD_DATA(counter).West = West;

if ~short_output
    RD_DATA(counter).Ve = Ve;
    RD_DATA(counter).Vc = Vc;
    RD_DATA(counter).Vtotal = Vtotal;
end

RD_DATA(counter).Ve_rounded = Ve_rounded;
RD_DATA(counter).Vc_rounded = Vc_rounded;
RD_DATA(counter).Vtotal_rounded = Vtotal_rounded;
RD_DATA(counter).V_CC_rounded = V_CC_rounded;

counter = counter + 1;

% Update Wait Bar
waitbar(counter / number_of_files)

end

% Save Data
% reversed_file_path = reverse(Raw_Data_Folder);
% reversed_folder_name = strtok(reversed_file_path, '\');
% folder_name = reverse(reversed_folder_name);
% Post_Processed_Data_Filename = 'G:\Shared
drives\NOBES_GROUP\MSPM\[MATLAB_WORKING_FOLDER]\Data Processing Code\06_Post

```

```
Processing_Experimental\[Experimental Data]\2021-12-23-newBumpy-p350\2021-12-23-newBumpy-p350-T0-0.97\2021-12-23-newBumpy-p350-T0-0.97_RD_short.mat';
Post_Processed_Data_Filename =
strcat(Raw_Data_Folder, '\', folder_name, '_RD.mat');

save(Post_Processed_Data_Filename, 'RD_DATA', '-v7.3')

close(WaitBar)
```

G.5 Secondary Functions

G.5.1 Calculation of Cycle Averaged Pressures and Speed ('PV_data_avg')

```
function [avg_pressures] = PV_data_avg(angles,pressures)
% Written by Connor Speer, March 2017
% Matthias 2022: Fixed 'NaN' output in case of no matching angle

% Inputs:
% angles --> angles corresponding to pressures in [radians].

% Round angles to the nearest whole number and convert to degrees
rounded_angles = round(angles*180/pi);

% Average all pressures which share the same angle

% Initialize vectors
avg_pressures = zeros(360,1);
% Matthias: p_log to log how pressure samples are assigned to angles for plot
% p_log = cell(360,1);

for current_angle = 0:1:359
indices = rounded_angles == current_angle;
% p_log{current_angle+1} = pressures(indices);
% In case there is no datapoint that matches the current angle, take the
previous value
if isempty(indices)
    avg_press = avg_pressures(current_angle);
else
    avg_press = mean(pressures(indices));
end
avg_pressures(current_angle+1) = avg_press;
end
% disp('done')
```

G.5.2 Calculate Flow Rate of Heater Fluid from Calibration Data at Setpoint Temperature ('SIL_180_flow_rate_calc')

```
function [m_dot_DCH, m_dot_heater] =
SIL_180_flow_rate_calc(hot_bath_setpoint)

% Written by Connor Speer, May 2019
% Calculates the mass flow rate of SIL 180 for the given hot bath setpoint
% using results of a bucket test calibration.

% Inputs
% hot_bath_setpoint --> hot bath setpoint in deg C

% Outputs
% m_dot_DCH --> Displacer Cylinder Head SIL 180 mass flow rate in (kg/s).
% m_dot_heater --> Heater SIL 180 mass flow rate in (kg/s).

%% Input Calibration Results
% Connor's values
% temps = [60 80 100 120 150]; % Hot bath setpoints in deg C for calibration
test.
% mfrate_DCH = [0.03165 0.03580 0.03885 0.04185 0.04460]; % DCH mass flow
rates in (kg/s).
% mfrate_heater = [0.03175 0.03505 0.03830 0.04075 0.04280]; % Heater mass
flow rates in (kg/s).

% Matthias, 2021 Dec 08 (measured Toan and Nico)
temps = 70:20:150; % Hot bath setpoints in deg C for calibration test.
% DCH heat exchanger disabled!!!!!!!!!!!!!!!!!!!!!!
% mfrate_DCH = [0.03165 0.03580 0.03885 0.04185 0.04460]; % DCH mass flow
rates in (kg/s).
mfrate_heater = [0.047050568 0.05155111 0.053543139 0.054037953 0.054598534];
% Heater mass flow rates in (kg/s).

% Fit curves to calibration data
% [fit_DCH,gof_DCH] = fit(temps',mfrate_DCH','poly2');
[fit_heater,gof_heater] = fit(temps',mfrate_heater','poly3');

%% Calculate the Flow Rate of SIL 180
% m_dot_DCH = p1_DCH*hot_bath_setpoint^2 + p2_DCH*hot_bath_setpoint + p3_DCH;
m_dot_DCH = 0;

m_dot_heater = fit_heater(hot_bath_setpoint);

%% Plot Set-Up
%
% % % Plot results to characterize curves
% % figure('Position', [x y width height])
% % plot(fit_DCH,temps,mfrate_DCH)
% % xlabel('Hot Bath Setpoint (\circC)')
% % ylabel('SIL 180 Mass Flow Rate (kg/s)')
```

```

% % title('Displacer Cylinder Head')
% % set(gca,'fontsize',font_size)
% % set(gca,'FontName',font)
%
% figure
% plot(fit_heater,temps,mfrate_heater)
% xlabel('Bath Setpoint (\circC)')
% ylabel('Mass Flow Rate (kg/s)')
% cv = coeffvalues(fit_heater);
% txt = "y = " +cv(1)+"*x^3 + " + cv(2)+"*x^2 + " + cv(3)+"*x + " + cv(4)...
%     +newline+ "R^2 = "+ gof_heater.rsquare;
% text(mean(temps), mean(mfrate_heater), txt)
% nicefigure('thesis_small_wide')

% % Cooler flowrate
% hold on
% plot(5, 0.0235576, 'DisplayName','Cooler')

```

G.5.3 Calculate Specific heat of Heater Fluid from Calibration Data at Setpoint Temperature ('SIL_180_specific_heat_calc')

```
function c_hot = SIL_180_specific_heat_calc(T_hot)

% Written by Matthias Lottmann, Jan 2022
% based on Connor's flow rate calc function
% Calculates the specific heat of SIL 180 for a given temperature.

% Data for SIL 180 only available at 20C:
% c_hot = 1510; %(J/kgK) - for SIL 180 at 20 deg C
% Temperature dependent data available for similar oil Dow SYLTHERM 800:
% https://www.dow.com/documents/en-us/app-tech-guide/176/176-01435-01-syltherm-800-heat-transfer-fluid.pdf
% https://www.dow.com/content/dcc/en-us/category/market/mkt-building-construction/sub-build-heating-cooling-refrigeration/heat-transfer-fluid-synthetic-calculator?ffc_type=synthetic
% https://www.dow.com/en-us/pdp.syltherm-800-stabilized-heat-transfer-fluid.39260z.html

% Inputs
% T_hot --> oil temperature in deg C

% Outputs
% c_hot --> Specific Heat Capacity in (J/kgK).

%% Inputs
c_SIL_180_20C = 1510; %(J/kgK) - for SIL 180 at 20 deg C
c_S800_20C = 1608; %(J/kgK) - for SYLTHERM 800 at 20 deg C
temps = 70:10:160; % (deg C)
c_S800 = [1694 1711 1728 1745 1762 1779 1796 1813 1830 1847]; %(J/kgK) - for SYLTHERM 800 at temps

% Fit curve to data
[fit_c,gof] = fit(temps',c_S800','poly1');

%% Estimate the Heat Capacity of SIL 180
% assume that specific heat curve of SIL 180 has constant offset from curve of SYLTHERM 800.
c_hot = fit_c(T_hot) +c_SIL_180_20C -c_S800_20C;

%% Plot Set-Up
%
% figure
% hold on
% plot(temps, fit_c(temps), 'b','DisplayName','SYL800 data')%,temps,c_S800)
% plot(temps, fit_c(temps)+c_SIL_180_20C -c_S800_20C, 'r','DisplayName','Sil 180 estimate')%,temps,c_S800)
% plot(20, c_S800_20C, 'ob', 'DisplayName','SYL800, 20 \circC')
% plot(20, c_SIL_180_20C, 'or', 'DisplayName','Sil 180, 20 \circC')
```

```
% % plot(temps,c_hot,'g', 'DisplayName','SIL 180 estimate')
%
% legend
% xlabel('Temperature (\circC)')
% ylabel('Specific Heat (J/kg K)')
% nicefigure('thesis_small_wide')
% % text(mean(temps), mean(c_S800), "R^2 = "+ gof.rsquare)
```

G.5.4 Engine Volume Calculations ('volume')

```
function [Vc, Ve, dVc, dVe, V_buffer] = volume(theta, ENGINE_DATA)
% determine working space volume variations and derivatives
% Israel Urieli, 7/6/2002
% Modified 2/14/2010 to include rockerV (rockdrive)
% Modified by Connor Speer October 2017

% Argument: theta - current cycle angle [radians]
% Returned values:
%   vc, ve - compression, expansion space volumes [m^3]
%   dvc, dve - compression, expansion space volume derivatives

% *** Note: For gamma engines, the total workspace volume is maximum at
% crank angle 0. For alpha engines, the compression space volume is maximum
% at crank angle zero.

%% Raphael engine is slider-crank gamma
[Vc, Ve, dVc, dVe, V_buffer] = gammacrankvol(theta, ENGINE_DATA);
%=====

function [Vc, Ve, dVc, dVe, V_buffer] = gammacrankvol(theta, ENGINE_DATA)
% gamma crankshaft drive volume variations and derivatives
% Added by Connor Speer - February 2017
% Argument: theta - current cycle angle [radians]
% Returned values:
%   vc, ve - compression, expansion space volumes [m^3]
%   dvc, dve - compression, expansion space volume derivatives

Vclp = ENGINE_DATA.Vclp;
Vcld_top = ENGINE_DATA.Vcld_top;
Vcld_bottom = ENGINE_DATA.Vcld_bottom;
Dbore = ENGINE_DATA.Dbore;
Pbore = ENGINE_DATA.Pbore;
Dr1 = ENGINE_DATA.Dr1;
Dr2 = ENGINE_DATA.Dr2;
Dr3 = ENGINE_DATA.Dr3;
Pr1 = ENGINE_DATA.Pr1;
Pr2 = ENGINE_DATA.Pr2;
Pr3 = ENGINE_DATA.Pr3;
beta = ENGINE_DATA.beta_deg*(pi/180);

% vclp vcl d % piston, displacer clearance vols [m^3]
% Dbore Pbore % displacer, piston bores [m]
% Dr1 Pr1 % displacer, piston desaxe offset in [m]
% Dr2 Pr2 % displacer, piston crank length (half stroke) in [m]
% Dr3 Pr3 % displacer, piston connecting rod lengths [m]
% beta % phase angle advance of displacer motion over piston [radians]

%*** Total volume is maximum at theta = 0 for gammas.
```

```

Ptheta2 = pi - theta;
Dtheta2 = Ptheta2 - beta;

Dtheta3 = pi - asin((-Dr1+(Dr2*sin(Dtheta2)))/Dr3);
Dr4 = Dr2*cos(Dtheta2) - Dr3*cos(Dtheta3);
Dr4max = sqrt(((Dr2+Dr3)^2)-(Dr1^2));
Dr4min = sqrt(((Dr3-Dr2)^2)-(Dr1^2));
Ve = (Vcld_top) + ((pi/4)*(Dbore^2))*(Dr4max-Dr4);

V_disprod = ENGINE_DATA.V_disprod_min +
Dr4*(pi/4)*((ENGINE_DATA.d_disprod)^2); % Added displacer rod.
DVc = (((pi/4)*(Dbore^2))*(Dr4max-Dr4min)) - Ve - V_disprod; % Added
displacer rod.

Ptheta3 = pi - asin((-Pr1+(Pr2*sin(Ptheta2)))/Pr3);
Pr4 = Pr2*cos(Ptheta2) - Pr3*cos(Ptheta3);
Pr4max = sqrt(((Pr2+Pr3)^2)-(Pr1^2));
PVc = (((pi/4)*(Pbore^2))*(Pr4max-Pr4));
Vc = (Vcld_bottom) + Vclp + DVc + PVc;

dDtheta3 = (Dr2.*cos(Dtheta2))./(Dr3.*sqrt(1-(((
-Dr1+(Dr2.*sin(Dtheta2)))/Dr3).^2)));
dDr4 = Dr2.*sin(Dtheta2) + Dr3.*sin(Dtheta3).*dDtheta3;
dVe = -(pi/4)*(Dbore^2).*dDr4;

dPtheta3 = (Pr2.*cos(Ptheta2))./(Pr3.*sqrt(1-(((
-Pr1+(Pr2.*sin(Ptheta2)))/Pr3).^2)));
dPr4 = Pr2.*sin(Ptheta2) + Pr3.*sin(Ptheta3).*dPtheta3;
dPVc = -(pi/4)*(Pbore^2).*dPr4;

dDVc = -dVe - dDr4*(pi/4)*((ENGINE_DATA.d_disprod)^2);

dVc = dDVc + dPVc;

% Crankcase Volume Variations in (m^3) --> COULD ADD DISPLACER ROD TO THIS,
BUT IT WOULD MAKE A VERY SMALL DIFFERENCE.
V_buffer = ENGINE_DATA.V_buffer_max - PVc;
%=====

```

Appendix H. Model Data Processing Code

This single MATLAB script runs through a folder containing any number of folders with datapoints from MSPM, and extracts, processes, and stores all data as described in Chapter 3.

H.1 MSPM Data Processing ('DataExtract.m')

```
%% MSPM Data extraction, processing and storing in struct format
% Written by Matthias Lottmann, 2021

% JUST RUN, INPUTS WILL POP UP.
% To extract data from a set of MSPM results folders, calculate additional
% data and store everything in a struct 'MSPM_DATA' that is saved to a .mat
% file in the same folder as the input data. Input: Path to MSPM 'Runs'
% folder containing folders of individual MSPM runs. Output: Struct
% 'MSPM_DATA' that is saved to a file '*foldername*_MSPM'.

% 'p_environment' is the atmospheric pressure that must be subtracted from
% MSPM pressure to compare to experiment data. It can be scalar (one value
% for all datapoints) or vector (one value per datapoint)

function DataExtract(p_environment, layout)
% clc, clear

% IMPORTANT: Environment pressure that will be subtracted from MSPM
% pressure outputs to obtain relative pressure, which is comparable to
% experiment pressure data.
% p_environment = 93.79 *1000; % Pa

% Set the names of the MSPM output files to be used. (PV outputs, sensors)
% Can contain wildcards (*)
query_enginePV = 'Engine-PV*.mat';
query_crankcasePV = 'Crankcase-PV*.mat';

% User chooses a folder to process
msg = 'Choose folder containing MSPM results folders to process.';
start_path = 'G:\Shared
drives\NOBES_GROUP\MSPM\[MATLAB_WORKING_FOLDER]\MSPM\Runs';
Folder_path = uigetdir(start_path,msg);

%%%%%%%%%%%%%%%%%%%%%%%%%%%%%%%%%%%%%%%%%%%%%%%%%%%%%%%%%%%%%%%%%%%%%%%%
% PV_order: order of Comp, Exp, PP spaces in PV output data.
% For Gamma engines (three variable volume spaces):
% Put indexes as follows: [Com Exp PP]
% 1 = Compression Space, 2 = Expansion Space, 3 = Power Piston <-----
-----CHECK if using new MSPM model!
if strcmp(layout, 'gamma')
    havePP = true;
```

```

%     PV_order = [1 3 2]; % For Raphael model
PV_order = [3 2 1]; % For Scaling_tube_bundle model
end

if strcmp(layout, 'alpha')
    havePP = false;
% For Alpha engines:
% 1 = Compression Space, 2 = Expansion Space
PV_order = [1 2];
end
%%%%%%%%%%%%%%%%%%%%%%%%%%%%%%%%%%%%%%%%%%%%%%%%%%%%%%%%%%%%%%%%%%%%%%%%

%%
% list directories to work through
dirs = dir(Folder_path);
dirs = dirs(3:end); % remove the '.' and '..' folders
dirs = dirs([dirs.isdir]); % consider only folders, not files
n = length(dirs);

% For each results folder, extract data and write into struct
for d = 1:n
    %% load all relevant data from MSPM result folder
    name = dirs(d).name;
    this_folderpath = fullfile(Folder_path, name);

    % extract setpoint parameters from name
    T_source = FindInName(name, 'TH', '_');
    T_sink = FindInName(name, 'TC', '_');
    p_mean_setpoint = FindInName(name, 'p', '_') *1000; %Pa

    % extract h_custom values from name if present
    h_Source = FindInName(name, 'hSource_', '_'); % heat transfer coeff in
W/m^2 K
    h_Sink = FindInName(name, 'hSink_', '_');

    % load MSPM 'Statistics' output. Loads any file with name matching
    % 'query'. Sometimes this file can have a missing '.mat' extension.
    % Therefore enforce loading as 'mat'.
    % Will load 'statistics' struct.
    query = '*_Statistics*';
    thisfile = dir(fullfile(this_folderpath, query));
    if size(thisfile, 1) ~= 1
        error("Folder:"+newline+ name +newline+"File:"+newline+...
            query +newline+"None or several found.");
    end
    load(fullfile(this_folderpath, thisfile.name), '-mat');

    % load working space PV data. Will load 'data' struct.
    query = query_enginePV;
    thisfile = dir(fullfile(this_folderpath, query));
    if size(thisfile, 1) ~= 1 % Error if not exactly one file found.
        error("Folder:"+newline+ name +newline+"File:"+newline+...

```

```

        query +newline+"None or several found.");
end
load(fullfile(this_folderpath, thisfile.name), '-mat');

% allow p_environment to be a vector (if different between setpoints)
if length(p_environment) > 1
    p_env = p_environment(d);
else
    p_env = p_environment;
end

% Extract Pressure (p) and Volume (V) data.
p = data.DependentVariable - p_env; % see header of code file
V = data.IndependentVariable;
if havePP; np_expect = 3; else; np_expect = 2; end
if size(p, 2) ~= np_expect % Error if number of columns unexpected.
    error("Folder:"+newline+ name +newline+"File:"+newline+...
        query +newline+"Unexpected number of data columns found.");
end

% If crankcase PV output exists
% load Crankcase PV data. Will load 'data' struct.
query = query_crankcasePV;
thisfile = dir(fullfile(this_folderpath, query));
if isempty(thisfile)
    haveCC = false;
elseif size(thisfile, 1) > 1
    error("Folder:"+newline+ name +newline+"File:"+newline+...
        query +newline+"Several found.");
else
    haveCC = true;
    load(fullfile(this_folderpath, thisfile.name), '-mat');
    % Extract Pressure (p) and Volume (V) data.
    p_CC = data.DependentVariable - p_env; % see header of code file
    V_CC = data.IndependentVariable;
    if size(p_CC, 2) ~= 1 % Error if number of columns unexpected.
        error("Folder:"+newline+ name +newline+"File:"+newline+...
            query +newline+"Unexpected number of data columns found.");
    end
end

% Load sensor data for all point sensors (1D data) Does not deal with
line sensors.
% Loads files that match multiple queries, for multiple sensor types.
query = {
    '*Temperature vs angle.mat'
    '*center - Reynolds Number vs angle.mat'...
};
Sfiles = struct([]);
for q = 1:length(query)
    Sfiles = [Sfiles; dir(fullfile(this_folderpath, query{q}))];
end
nS = length(Sfiles);
haveS = ~isempty(Sfiles);
%     haveS = 0;

```

```

if haveS
    Sstruct(nS).data = []; % initialize struct for sensor data
    Sstruct(nS).name = [];
    % Get the sensor variable name from the file name. First part
    % of file name equals folder name ('name'),
    name_start_length = length(name)+2;
    % Extract data for each sensor
    for i = 1:nS
        name_flip = flip(Sfiles(i).name);
        % Sensor name ends at the dash
        name_end_length = length(flip( strtok(name_flip, '-') )) + 2;
        load(fullfile(this_folderpath, Sfiles(i).name), '-mat');
        Sstruct(i).name = Sfiles(i).name( name_start_length:(end-
name_end_length) );
        if Sstruct(i).name(1) == 'T'
            adjust = -273.15; % K to CELSIUS
        else
            adjust = 0;
        end
        Sstruct(i).data = data.DependentVariable' + adjust;
    end
    % Get crank angle from one of the sensors just for reference
    theta_rad = data.IndependentVariable;
end

%% Perform calculations on data
% Include p and V for each volume in output struct.
PV_Com.p = p(:,PV_order(1));
PV_Exp.p = p(:,PV_order(2));
PV_Com.V = V(:,PV_order(1));
PV_Exp.V = V(:,PV_order(2));
if havePP
    PV_PP.p = p(:,PV_order(3));
    PV_PP.V = V(:,PV_order(3));
end
if haveCC
    PV_CC.p = p_CC;
    PV_CC.V = V_CC;
end

% Mean pressure for each volume
PV_Com.p_mean = mean(PV_Com.p);
PV_Exp.p_mean = mean(PV_Exp.p);
if havePP; PV_PP.p_mean = mean(PV_PP.p); end
if haveCC; PV_CC.p_mean = mean(PV_CC.p); p_mean_CC = PV_CC.p_mean; end
% engine mean pressure for reference
if havePP
    p_mean = mean([PV_Com.p_mean, PV_Exp.p_mean, PV_PP.p_mean]);
else
    p_mean = mean([PV_Com.p_mean, PV_Exp.p_mean]);
end

% delta-P for each volume
PV_Com.deltaP = max(PV_Com.p)-min(PV_Com.p);
PV_Exp.deltaP = max(PV_Exp.p)-min(PV_Exp.p);
if havePP; PV_PP.deltaP = max(PV_PP.p)-min(PV_PP.p); end

```

```

if haveCC; PV_CC.deltaP = max(PV_CC.p)-min(PV_CC.p); end

% Indicated work by integrating the PV loops separately. there is a
% ~2-6% difference between separate and averaged PV work, depending on
% the small but present pressure difference between the volume spaces.
% Separate calculation is more accurate and also matches the PV work
% calculated by MSPM as displayed on the PV plots.

% first close the PV loops so that Wind calculations reflect the
% entire cycle.
p_closed = [p; p(1,:)];
V_closed = [V; V(1,:)];
if haveCC
    p_CC_closed = [p_CC; p_CC(1)];
    V_CC_closed = [V_CC; V_CC(1)];
end

% Integrate for PV work.
PV_Com.Wind = trapz(V_closed(:,PV_order(1)), p_closed(:,PV_order(1)));
PV_Exp.Wind = trapz(V_closed(:,PV_order(2)), p_closed(:,PV_order(2)));
if havePP; PV_PP.Wind = trapz(V_closed(:,PV_order(3)),
p_closed(:,PV_order(3))); end
if haveCC; PV_CC.Wind = trapz(V_CC_closed, p_CC_closed); end

%      % Integrating the average PV loop
% Inaccurate, don't use!
%      P_inst_closed = [p_inst; p_inst(1)]; V_tot_closed = [V_tot;
%      V_tot(1)]; Wind = trapz(V_tot_closed, P_inst_closed);

% Forced work (not implemented for alpha engine)
if haveCC && havePP; FW = FW_Subfunction_v4(PV_PP.p, PV_CC.p, PV_PP.V);
end
P_shaft = mean(statistics.Power);

speed_transient = statistics.Omega / (2*pi); % [Hz]
speedHz = mean(speed_transient); % [Hz]
speedRPM = speedHz * 60; % [rpm]

% 'statistics.To_...' Contain values in unit of energy (J) for each
% cycle increment. For energy flow, sum and multiply with speed.
Qdot_fromSource = - sum(statistics.To_Source)*speedHz;
Qdot_toSink = sum(statistics.To_Sink)*speedHz;
% Sign of 'statistics.To_Environment; has been fixed in MSPM code.
Qdot_toEnv = sum(statistics.To_Environment)*speedHz;
Qdot_flowloss = sum(statistics.Flow_Loss)*speedHz; % should be same unit
as 'To_Source' according to code analysis

if havePP
    Wind = PV_PP.Wind;
else
    Wind = PV_Exp.Wind + PV_Com.Wind;
end
efficiency_ind = Wind*speedHz / Qdot_fromSource; % [dim.less]
efficiency_shaft = P_shaft / Qdot_fromSource; % [dim.less]

```

```

% Temperature calculations
% Find indices of required temperatures in Sstruct
if haveS
    for S=Sstruct
        switch S.name
            case 'Tgh_reg'
                Tgh_reg = mean(S.data);
            case 'Tgk_reg'
                Tgk_reg = mean(S.data);
        end
    end
    try
        Tgr_log = (Tgh_reg - Tgk_reg) / log(Tgh_reg / Tgk_reg); % C
    end
end

%% Write to struct
MSPM_DATA(d).filename = name;
MSPM_DATA(d).speed_transient = speed_transient;
MSPM_DATA(d).speedHz = speedHz;
MSPM_DATA(d).speedRPM = speedRPM;
MSPM_DATA(d).T_source = T_source;
MSPM_DATA(d).T_sink = T_sink;
MSPM_DATA(d).h_Source = h_Source;
MSPM_DATA(d).h_Sink = h_Sink;
MSPM_DATA(d).p_mean_setpoint = p_mean_setpoint;
MSPM_DATA(d).p_mean = p_mean;
if haveCC; MSPM_DATA(d).p_mean_CC = p_mean_CC; end

MSPM_DATA(d).PV_Com = PV_Com;
MSPM_DATA(d).PV_Exp = PV_Exp;
if havePP; MSPM_DATA(d).PV_PP = PV_PP; end
if haveCC; MSPM_DATA(d).PV_CC = PV_CC; end

MSPM_DATA(d).Wind = Wind;
if haveCC && havePP; MSPM_DATA(d).FW = FW; end

MSPM_DATA(d).Qdot_fromSource = Qdot_fromSource;
MSPM_DATA(d).Qdot_toSink = Qdot_toSink;
MSPM_DATA(d).Qdot_toEnv = Qdot_toEnv;
MSPM_DATA(d).Qdot_flowloss = Qdot_flowloss;

MSPM_DATA(d).P_shaft = P_shaft;
MSPM_DATA(d).efficiency_ind = efficiency_ind;
MSPM_DATA(d).efficiency_shaft = efficiency_shaft;

if haveS
    % Write data from each sensor into variable name
    % obtained from MSPM results file name
    for S = Sstruct
        try
            eval("MSPM_DATA(d)." + S.name + "= S.data;");
        catch
    end
end

```

```

        warning("Invalid Sensor Name: "+S.name +newline+ "Will not be
included in MSPM.mat output file.")
    end
end

MSPM_DATA(d).theta_rad = theta_rad;
try
    MSPM_DATA(d).Tgr_log = Tgr_log;
end
end

end

%% Save Data
reversed_file_path = reverse(Folder_path);
reversed_folder_name = strtok(reversed_file_path, '\\');
folder_name = reverse(reversed_folder_name);
Processed_Data_Filename = strcat(Folder_path, '\\', folder_name, '_MSPM.mat');

% Processed_Data_Filename = 'G:\Shared
drives\NOBES_GROUP\MSPM\[MATLAB_WORKING_FOLDER]\MSPM\Runs\22-02-xx-
Fin_Enhanced_Surface\B - HX insulated\[]22-02-
18_p450_FinEnh_HXisolated_EqualThickness';
% Processed_Data_Filename = [Processed_Data_Filename '\new.mat'];
% Processed_Data_Filename = ['new.mat'];
save(Processed_Data_Filename, 'MSPM_DATA', '-v7.3')
disp('Success')
end

% Function that returns parameters from string 'name' that it finds after
% 'tok' until next delimiter 'delim'
function output = FindInName(name, tok, delim)
    i_start = strfind(name, tok) + length(tok);
    output = str2double( strtok(name(i_start:end), delim) );
end

```